5. INTERNATIONALES SYMPOSIUM

INTERAKTION KONVENTIONELLER MUNITION

mit

SCHUTZBAUTEN

19941209 094

DTIC
ELECTE
DEC 1 4 1994

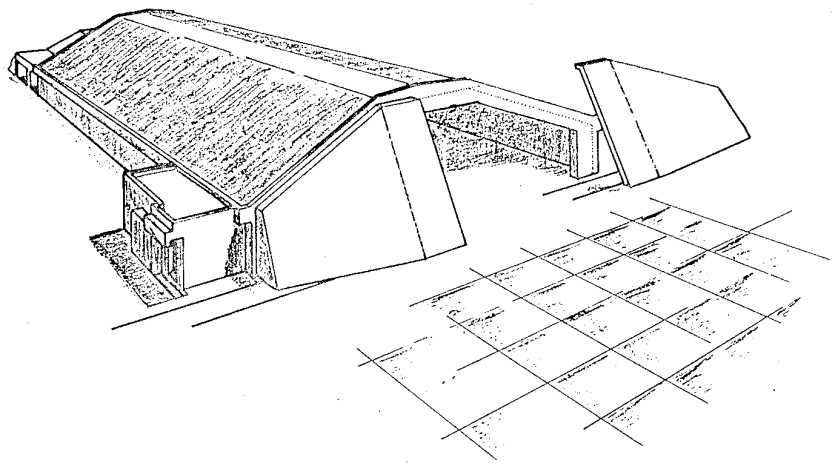

DISTRIBUTION STATEMENT A
Approved for public release;
Distribution Unlimited

BUNDESREPUBLIK DEUTSCHLAND
MANNHEIM, 22.-26. APRIL 1991

DTIC QUALITY INSPECTED 5

REPORT DOCUMENTATION PAGE

Form Approved
OMB No. 0704-0188

Public reporting burden for this collection of information is estimated to average 1 hour per response, including the time for reviewing instructions, searching existing data sources, gathering and maintaining the data needed, and completing and reviewing the collection of information. Send comments regarding this burden estimate or any other aspect of this collection of information, including suggestions for reducing this burden, to Washington Headquarters Services, Directorate for Information Operations and Reports, 1215 Jefferson Davis Highway, Suite 1204, Arlington, VA 22202-4302, and to the Office of Management and Budget, Paperwork Reduction Project (0704-0188), Washington, DC 20503.

1. AGENCY USE ONLY (Leave blank)	2. REPORT DATE	3. REPORT TYPE AND DATES COVERED
	December 1991	ESL-TR-9155, 22-26 Apr 91

4. TITLE AND SUBTITLE
Symposium Proceedings on Interaction of nonnuclear Weapons with Structures

5. FUNDING NUMBERS

6. AUTHOR(S)
Dr. Douglas Merkle, et al

7. PERFORMING ORGANIZATION NAME(S) AND ADDRESS(ES)
Air Force Engineering and Services Center
Air Force Engineering and Services Laboratory
Tyndall AFB, Florida 32403

8. PERFORMING ORGANIZATION REPORT NUMBER
ESL-TR-91-55

9. SPONSORING/MONITORING AGENCY NAME(S) AND ADDRESS(ES)

10. SPONSORING/MONITORING AGENCY REPORT NUMBER

11. SUPPLEMENTARY NOTES
Approved for Public Release, Distribution Unlimited
Project Manager: Dr. Douglas Merkle, (904) 283-3431

12a. DISTRIBUTION/AVAILABILITY STATEMENT
Approved for Public Release. Distribution Unlimited

12b. DISTRIBUTION CODE
A

13. ABSTRACT (Maximum 200 words)

This technical report contains a variety of papers presentd at the Fifth International Symposium on the Interaction of Conventional Munitions with Protective Structures. Papers were presented by international authors, to include both the English and German Language. The report is submitted as presented. All papers included in the technical report have been cleared for public release.

14. SUBJECT TERMS
Finite Element Models, Microcomputer Structural Response Models, Survivable Collective Protection System, Blast Load Analysis, Passive Airblast Attenuation Valves, Hydrocode Analysis

15. NUMBER OF PAGES

16. PRICE CODE

17. SECURITY CLASSIFICATION OF REPORT	18. SECURITY CLASSIFICATION OF THIS PAGE	19. SECURITY CLASSIFICATION OF ABSTRACT	20. LIMITATION OF ABSTRACT
Unc	Unc	Unc	Unlimited

5. INTERNATIONALES SYMPOSIUM

INTERAKTION KONVENTIONELLER MUNITION

mit

SCHUTZBAUTEN

Accesion For
NTIS CRA&I ☒
DTIC TAB ☐
Unannounced ☐
Justification
By
Dist. Ibution /
Availability Codes
Dist | Avail and / or Special
A-1

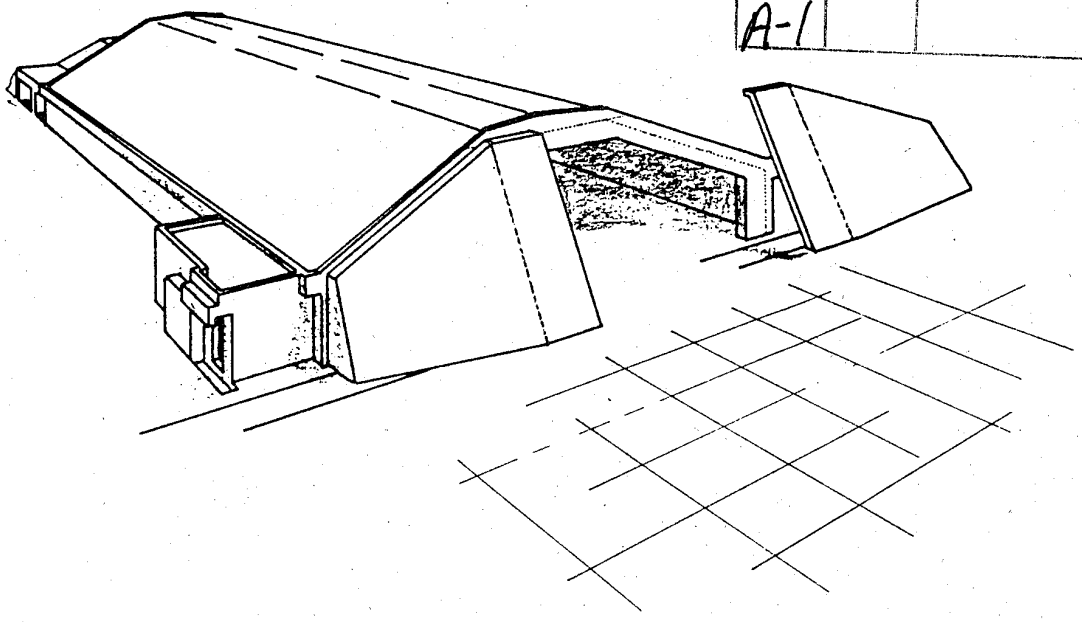

VORTRÄGE
PROCEEDINGS

Dieses Dokument enthält die Sammlung der Vorträge, die auf dem 5. Internationalen Symposium über Interaktion konventioneller Munition mit Schutzbauten (Manhheim, 22. - 26. April 1991) gehalten wurden. Vorträge, die für die Drucklegung nicht zeitgerecht vorlagen, sind in Kurzfassung beigefügt.

Veranstalter des Symposiums ist der

Bundesminister der Verteidigung
5300 Bonn 1

Das Symposium wurde vorbereitet und organisiert von:

Amt für Studien und Übungen der Bundeswehr
Bereich Sonderaufgaben-Infrastruktur
Friedrich-Ebert-Str. 72
5060 Bergisch Gladbach 1

und

Bundesakademie für Wehrverwaltung und Wehrtechnik
Seckenheimer Landstr. 8 - 10
6800 Mannheim 25

Sämtliche Beiträge dieses Dokumentes sind durch den Autor oder durch die zuständigen Bundesdienststellen zur Veröffentlichung freigegeben.

* * * * *

This document represents the proceedings of the 5th International Symposium on the Interaction of Conventional Munitions with Protective Structures, Mannheim, Federal Republic of Germany, April 22 - 26, 1991. Papers not received in time for printing, are attached as abstracts.

The symposium is implemented under supervision of the

Federal Ministry of Defence
D - 5300 Bonn 1

The Symposium was coordinated through

Amt für Studien und Uebungen der Bundeswehr
Bereich Sonderaufgaben-Infrastruktur
Friedrich-Ebert-Str. 72
D - 5060 Bergisch Gladbach 1

and

Bundesakademie für Wehrverwaltung und Wehrtechnik
Seckenheimer Landstr. 8 - 10
D - 6800 Mannheim 25

All the manuscripts in this document have been approved for public release either by the author or the cognizant federal agency.

---- INHALT / CONTENTS ----

*** Allgemeines / Modellversuche *** General Topics / Modelling

Comparison of Finite Element Model with Measured Field Test Data A 3
John R. Hayes, Jr., US Army CERL, USA
W.J. Hall, US Army CERL, USA
Dr. S.L. Paul, US CERL, USA

Postattack Airbase Facility Recovery 4
Dr. Douglas H. Merkle, Applied Research Ass., USA
J. Jeffrey Howard, Applied Research Ass., USA
Capt Richard A. Reid, US AFESC, USA
Lt (USN) James M. Underwood, US AFESC, USA
Thomas L. Warren, Applied Research Ass., USA

Comparison of Microcomputer Structural Response Models with Measured Field Test Data A 11
Dr. S.L. Paul, US Army CERL, USA
J.D. Haltiwanger, US Army CERL, USA
D. Grossman, US Army CERL, USA
J.B. Gambill, US Army CERL, USA
John R. Hayes, Jr., US Army CERL, USA

Full-Scale Blast Test of a Reinforced Soil Bunker 12
Capt Richard A. Reid, US AFESC, USA

*** Bemessung von Bauwerken *** Structural Design

Evaluation of the Survivable Collective Protection System(SCPS) 19
Capt USAF Timothy L. Boone, Phillips Laboratory (AFSC), USA
Dr. Harold C. Sorenson, Washington State University, USA

Full Scale Test of a Blast Resistant Structure 27
Edward H. Bultmann, Jr., Ph.D., MMPI, USA

Optimal Design of Protective Structures Using Computer-Aided Risk Analysis 34
Reuben Eytan, Eytan Building Design Ltd., Israel

Anmerkung / Remark:

N = Vorträge der Sessionen mit eingeschränktem Zutritt
Papers held in a classified session

A = Nur Kurzfassung der Vorträge
Abstracts only

An Experimental Evaluation of the Protection from Conventional Weapons Effects Provided by the Base Damage Control Center 43
Maj USAF Clarence J. Fennell, Phillips Laboratory (AFSC), USA
Capt USAF Timothy L. Boone, Phillips Laboratory (AFSC), USA
Brent Satterwaite, Phillips Laboratory (AFSC), USA

Effects of Enhanced Blast Munitions on Aircraft Shelters 51
Eugene R. Fosness, Phillips Laboratory (AFSC), USA
Rodney Galloway, Phillips Laboratory (AFSC), USA
Capt USAF Timothy L. Boone, Phillips Laboratory (AFSC), USA
Capt John E. Higgins, Phillips Laboratory (AFSC), USA

Modified Analysis of Reinforced Concrete Structures under Impulsive Loads 59
Prof. Theodor Krauthammer, Pennsylvania State University, USA
H.H. Shanaa, Pennsylvania State University, USA

The Effect of Berming on the Response of Structures Subjected to Nearby Explosions 67
Helge Langberg, Defence Research Establishment, Norway

Analysis of Semi-Hardened Structures Subjected to Conventional Weapons Environmments 75
Capt USAF David H. Pyle, US Air Force Europe, Germany
Prof. Thomas T. Barber, University of Virginia, USA

Development of a Working Tool for the Protection, Risk and Cost Benefit Evaluation of Provisional Shelters (PRICE) 83
Tan See Ting, Public Works Department, Singapore

The Failure Mode of Concrete Structures Due to Contact Charges 91
R.J.M. van Amelsfort, Prins Maurits Laboartory TNO, Netherland
Ir. Jaap Weerheijm, Prins Maurits Laboratory TNO, Netherland

Collapse of Shear Wall Buildings Under Blast Loading 101
Prof Chen Zhaoyuan, Tsinghua University, Republic of China
Miao Qisong, Tsinghua University, Republic of China
Wang Zhihao, Tsinghua University, Republic of China

Analysis of Buried R.C. and Metal Structures Subjected to Blast Loading 109
Dr. George M. Zintilis, Advanced Mechanics & Engineering, United Kingdom
S. Syngellakis, Advanced Mechanics & Engineering, United Kingdom
Alastair C. Walker, Advanced Mechanics & Engineering, United Kingdom

*** Boden-Bauwerk-Interaktion ***
Soil-Structure-Interaction

Validation of a Finite Difference Code Using Model Tests of Dynamic Soil Structure Interaction 119
Major Kevin J. Claber, RARDE, United Kingdom
Dr. Michael C.R. Davies, University of Wales, United Kingdom
Mark C. Saunders, RARDE, United Kingdom

Effects of Cushion Layer for Underground Structure Subjected to Impact Loadings 126
Dr.Eng. Kazuo Fujimoto, 4th Research Center, Japan
Ms.Eng Hiroshi Yamaguchi, 4th Research Center, Japan
Mitunori Sayama, 4th Research Center, Japan
Yasuhisa Kuzuha, 4th Research Center, Japan

Untersuchung zum Einfluß der Baugrunddämpfung bei explosionsartiger Belastung auf die Verformungs- und Lastzustände von unterirdischen Bauwerken mit Hilfe einer geotechnischen Großzentrifuge A 132
Prof. Dr.-Ing. Hans Ludwig Jessberger, Ruhr Universität Bochum, Germany
Dr.-Ing. Gerhard Thiel, Ruhr Universität Bochum, Germany

Foundation Systems of Civil Defence Shelters and Protective Structures 137
Pahamim Melamed, Star Engineers Ltd., Israel
S. Schwarz, Technion I.I.T - Haifa, Israel

Tests on the Interaction of Contained Explosives with a Small Burried Shelter in Saturated Sand 145
Harry J. van der Graaf, Delft Geotechnics, Netherland

Numerische/Experimentelle Untersuchung des dynamischen Verhaltens eines Flugzeugshelters der 3. Generation infolge einer Detonation im Boden 153
Otto von Estorff, IABG, Germany
Dr. W. Pfrang, IABG, Germany
Dipl.-Ing. Wilfried Bergerhoff, IABG, Germany
BOR Ferdinand Glaser, WTD 91, Germany

Modeling of Explosively-Formed Craters / Analysis and Comparison of Prototype and Reduced-Scale Test Events A 161
Maj John J. Gill,Ph.D., Phillips Laboratory (AFSC), USA

A Study of Cratering Phenomena from Conventional Weapons Using Small Charges in a Half Space Apparatus A 162
Dr. Robert W. Henny, Phillips Laboratory (AFSC), USA

Dynamic Response of Embedded Circular Reinforced Micro-Concrete Slabs - An Experimental Study 163
A.N. Dancygier, Northwestern University, USA
Prof. Surendra P. Shah, Northwestern University, USA
Prof. Leon M. Keer, Northwestern University, USA

Hydrocode Analysis of Ground Shock Environment from Buried Subscale Munition Tests in Wet Clay Backfill A 171
N - 27
Harold D. Zimmerman, California Research and Technology, USA
Marvin Y. Ito, California Research and Technology, USA
Jon E. Windham, US Army Corps of Engineers WES, USA

*** Computer-Programme ***
Computer Simulation

SABER-PC: A Ground-Shock Software Package for the PC A 175
N - 3
Stephen A. Akers, US Army Corps of Engineers WES, USA
Jill Stelter, California Research & Technology, USA

Numerische Simulation eines Luftstoßes gegen das Ausblasbauwerk eines Shelters 176
Dr. B. Fießler, IABG, Germany
BOR Ferdinand Glaser, WTD 91, Germany

Kurzdarstellung ausgewählter APC-Rechenprogramme zur Ermittlung von Waffenwirkungsparametern und zum Standsicherheitsnachweis von Baustrukturen gegen Wirkungskomponenten 186
OTL Ronald Kaufmann, AStudUbBu, Germany

Survivability Assessment Methodology A 194
Capt Diane Miller, US AFESC, USA
William L. Hacker, Applied Research Ass., USA

DYNA/NIKE Modeling of Shock Wave Interactions and High Explosive Effects on a Personal Computer A 195
Dr. Michael J. Murphy, Hydrosoft International, USA

INBLAST -- A New and Revised Computer Code for the Prediction of Blast Inside Closed or Vented Structures 196
Michael M. Swisdak, Jr., US Naval Surface Warfare Center, USA
Paul E. Montanaro, US Naval Surface Warfare Center, USA

A PC Based Program for Blast Load Analysis and Damage Estimation 197
Dr. Alan J. Watson, University of Sheffield, United Kingdom
Brian Hobbs, University of Sheffield, United Kingdom
Dr. Andrew K. Chan, University of Sheffield, United Kingdom
Jeffrey Peters, University of Sheffield, United Kingdom
R. Westaway, University of Sheffield, United Kingdom

Penetration of a Rigid Projectile into a Semi-Infinite Layered Medium A 205
Prof. Dr. David Yankelevsky, Israel Institute of Technology, Israel

*** Druck in Tunneln/Detonation im Innern ***
Pressure in Tunnels/Internal Detonation

Experimentelle Untersuchung der Ausbreitung konventioneller Luftstösse in Tunnelsystemen 209
Eduard Binggeli, AC-Laboratorium Spiez, Switzerland
Dipl.-Ing. Bernard Anet, AC Laboratorium Spiez, Switzerland

Computer Code SPIDS / Shock Propagation in Ducting Systems Utilizing a PC Computer 218
Prof. Richard H. Fashbaugh,Ph.D. University of Nevada, USA

Experiments to Validate the Structural Behaviour of a New Laboratory for Ballistic Research A 226
Ir. W.P.M. Mercx, Prins Maurits Laboratory TNO, Netherland
Ir. Jaap Weerheijm, Prins Maurits Laboratory TNO, Netherland

Parameterstudien zum Luftstoß in Expansionskammern und Zuführungskanälen 227
Dipl.-Phys. Dr. Günter Scheklinski-Glück, Ernst Mach Institut, Germany

*** Druckstoßventile ***
Blast Valves

Analytical Study of Passive Airblast Attenuation Valves A 237
Quentin A. Baker, Wilfred Baker Engineering Inc., USA
Dr. Wilfred E. Baker, Wilfred Baker Engineering Inc., USA
Dr. Christopher Y. Tuan, Wilfred Baker Engineering Inc., USA

Blast Valves - Unnecessary Expense or Vital Components in Structure Hardening 238
Ann-Sofie Forsberg, Royal Swedish FortF, Sweden

Passive Blast Attenuators - A Possible Alternative to Active Blast Valves? 246
Jürg Hasler, LUWA Ltd, Switzerland

An Experimental Study of Airblast Attenuation Devices A 253
Randy L. Holmes, US Army Corps of Engineers WES, US N –
Paul W. Graham, US Army Corps of Engineers WES, USA
Gayle E. Albritton, US Army Corps of Engineers WES, USA

*** Eigenschaften von Material ***
Material Properties

The Use of Shotcrete for Expedient Repair of Bomb - Damaged Structures 259
Mark Anderson, Ph.D., Applied Research Ass., USA

Fracture Mechanics Model for Concrete under High Loading Rates 267
Prof. Theodor Krauthammer, Pennsylvania State University, USA
D. Chandra, Pennsylvania State University, USA

Strain-Rate Effects on Compressive Testing of Foam 275
Capt USAF Steven T. Kuennen, US AFESC, USA
Prof. C. Allen Ross, US AFESC, USA
Prof. J.W. Tedesco, Auburn University, USA

Experimentelle Untersuchungen zum dynamischen Tragverhalten von Sonderfaserbeton - Sifcon 281
Dipl.-Ing. Christoph Mayrhofer, Ernst Mach Institut, Germany

Fibrous Shotcrete for Expedient Repair of Structures 291
Dr. L.C. Huszynski, Applied Research Ass., USA
M.A. Pochefort, Applied Research Ass., USA

Material Modelling for Hydrocode Analysis of Concrete Response to Explosive Loading 301
Dr. A. James Sheridan, Royal Aerospace Establishment, United Kingdom
A.D. Pullen, Imperial College, United Kingdom
Prof.-Dr. Simon H. Perry, Trinity College, Ireland

Impact Resistance and Toughness of Polymer-Modified Steel Fiber Reinforced Concrete 309
Prof. Parviz Soroushian, Ph.D., Michigan State University, USA
Atef Tlili, Michigan State University, USA

Strain Rate Effects on Dynamic Response of Reinforced Concrete Plate Under Impact Loading 317
Ms.Eng Hiroshi Yamaguchi, 4th Research Center, Japan
Dr.Eng. Kazuo Fujimoto, 4th Research Center, Japan

*** Eigenschaften von Waffen ***
Weapons-Characteristica

Measured Parameters of the Airblast Loading of Generic Models from Shock Tube Tests and Comparison with SHARC-Code Calculations 327
Dr.-Ing. Werner Heilig, Ernst Mach Institut, Germany

Enhanced Blast Munitions Effects Program A 329
Stan Lokaj, Phillips Laboratory (AFSC), USA

The Design and Evaluation of Shaped Charges Using Codes Developed for Micro-Computers 330
Mark E. Majerus, California Research and Technology, USA
Dr. Ronald E. Brown, California Research and Technology, USA

*** Munitionssicherheit ***
Munition Safety

Scale Model Analysis of an Ammunition Plant 339
Prof ir. Roger Bourgois, Royal Military Academy, Belgium
Guido C. Maeyaert, Ministry of Defence, Belgium
Bruno Peymen, Royal Military Academy, Belgium
P. Joos, Royal Military Academy, Belgium

Splittermassenverteilung der Trümmer von gesprengten Flugzeugsheltern 346
Dr. Manfred Held, Messerschmitt-Bölkow-Blohm, Germany

Fragment and Debris Hazard Evaluation Project 355
A.G. Papp, Mason & Hanger-Silas Mason Co., USA
S.L. Young, Mason & Hanger-Silas Mason Co., USA
D.D. Barker, Mason & Hanger-Silas Mason Co., USA

Identification of Wall Concepts to Prevent Sympathetic Detonation in Munitions Storage Magazines 363
Capt USAF Glen J. Pappas, Phillips Laboratory (AFSC), USA

*** Penetration ***

Eindringleistung und Sprengwirkung eines Penetrators gegen Runway - Ziele 373
Dipl.-Phys Hans-Dieter Ackermann, MBB Deutsche Aerospace, Germany
Dipl.-Ing. Stefan Junger, MBB Deutsche Aerospace, Germany

High Velocity Projectile Penetration into Cementitious Materials 381
Dr. William F. Anderson, University of Sheffield, United Kingdom
Dr. Alan J. Watson, University of Sheffield, United Kingdom
Dr. Jeffrey Peters, University of Sheffield, United Kingdom

Effectiveness of Steel Bars for Inducing Yaw in the Flight Path of a Subscale Armor-Piercing Projectile A 388
N - 11
James D. Cargile, US Army Corps of Engineers WES, USA
Toney K. Cummins, US Army Corps of Engineers WES, USA

Scaled Underground Computer Center / Test and Analysis 389
John A. Collins, US AFATL, USA
Martin J. Schmidt, US AFATL, USA
Dr. Frank A. Haestas, Applied Research Ass., USA
John C. Galloway, Applied Research Ass., USA
Mr. Larry L. Brown, Denver Research Institute, USA
James A. Keller, Denver Research Institute, USA

The Effect of Rebar on Projectile Penetration 397
John A. Collins, US AFATL, USA
Dr. Frank A. Haestas, Applied Research Ass., USA
John C. Galloway, Applied Research Ass., USA
Barry L. Bingham, Applied Research Ass., USA

Impact of Bombs on Hard Layers A 101
Dr.Sc.Nat. Daniel Favarger, Gruppe für Rüstungsdienste, Switzerland

Computer Modelling of Small Arms Penetration of Concrete 105
Dr. Michael J. Iremonger, Royal Military College, United Kingdom

Penetration Mitigation for Theater Air Bases 413
Dr. Frank A. Haestas, Applied Research Ass., USA
Dr. John C. Galloway, Applied Research Ass., USA
James C. Partch, Applied Research Ass., USA
Lt.Col. Carlos Pulio, Defense Nuclear Agency, USA
Capt Rayment E. Hoxley, US Army Corps of Engineers WES, USA

Ein semiempirisches Programm zur Strukturauslegung von Penetratoren 420
Dipl.-Phys. Ernst Rottenkolber, Messerschmitt-Boelkow-Blohm, Germany

Projectile Penetration into Conventional and High-Strength Concrete A 426
N - 19
L.F. Tidwell, US Army Corps of Engineers WES, USA
Dr. Robert Rohani, US Army Corps of Engineers WES, USA

Local Response of Concrete Slabs to Low Velocity Impact A 127
Prof. Dr. David Yankelevsky, Israel Institute of Technology, Israel

*** Probabilistische Verfahren/Bedrohung ***
Probabilistics/Threat

Ein probabilistisches Schutzraum-Risiko-Modell 431
Dr.-Ing. Erwin Kessler, Switzerland
Dipl.-Ing. Bernard Anet, AC Laboratorium Spiez, Switzerland

Reliability-Based Design of R/C Structures for Protection Against Projectiles and Fragments 438
R.H. Sues, Applied Research Ass., USA
C.-W. Huang, Applied Research Ass., USA
Dr. Laurence A. Twisdale, Applied Research Ass., USA

Research to Develop Reliability-Based Design Methodology for Protective Structures 441
Dr. Laurence A. Twisdale, Applied Research Ass., USA
R.H. Sues, Applied Research Ass., USA
Capt Diane Miller, US AFESC, USA

*** Schock im Bauwerk ***
Instructure Shock

Conventional Weapon-Induced Shock Environment in a Prototype Structure A 445
James W. Ball, US Army Corps of Engineers WES, USA
Stanley C. Woodson, US Army Corps of Engineers WES, USA
Prof.Dr. Sam A. Kiger, University of West Virginia, USA

Die Schockbelastung von Schutzbauten infolge konventioneller Waffenwirkung 446
Peter Hunziker, AC-Laboratorium Spiez, Switzerland
Dr.-Ing. Erwin Kessler, Switzerland

Untersuchung der schocksicheren Lagerung, Aufstellung und Befestigung von Ausstattungsteilen in Schutzbauten bei hoher, kurzzeitiger Belastung 451
OTL Hans-Georg Hett, AStudUbBw, Germany

Entwicklung von Schockprüfständen zur Simulation konventioneller Waffenwirkungen im Hochschockbereich 463
Dr. Fritz Pischbieter, BATTELLE, Germany
P. Corvin, BATTELLE, Germany

Isolation of Large Displacement Stochastic Shock Loadings 472
Jyrki Ronkainen, TEMET Oy, Finland

A Simplified Two-Dimensional Methodology for Predicting In-Structure Shock for Complex Structures 478
Joseph L. Smith, JAYCOR, USA
Dr. Paul F. Hlakar, JAYCOR, USA

*** Tragverhalten von Bauteilen ***
Bearing Capacity of Construct. Members

Stahlbetonplatten unter Stoß- und Explosionseinwirkung 189
Prof.Dr.-Ing. Josef Eibl, Universität Karlsruhe, Germany

Die Wirkung von Versteifungen bei der Verformung von Stahlplatten unter impulsartiger Blastbelastung 197
Dipl.-Phys. Gerhard H. Gürke, Ernst Mach Institut, Germany

Localized Failure of Concrete and Fibrous Concrete Slabs - Some Wave Propagation and Panel Damage Studies A 501
Kirk A. Marchand, Southwest Research Institute, USA
Luis H. Vargas, Southwest Research Institute, USA
LT (USN) James H. Underwood, US AFESC, USA

Protective Glazing for Blast and Fragment Loadings A 505
Gerald Meyers, US Department of Energy, USA

Analysis of the Response of Reinforced Concrete to Severe, Close-in Explosive Loading 506
Charles J. Oswald, Southwest Research Institute, USA
Kirk A. Marchand, Southwest Research Institute, USA

Response of Reinforced Concrete Slabs to Close-In Explosive Loads A 514
James E. Tancreto, Naval Civil Engineering Laboratory, USA

* * * AUTORENVERZEICHNIS * * *
List of Authors

H.-D.	Ackermann	373
S.A.	Akers	175, N 3
G.E.	Albritton	253, N __
M.	Anderson	259
W.F.	Anderson	381
B.	Anet	209, 431
Q.A.	Baker	237
W.E.	Baker	237
J.W.	Ball	445, N __
T.T.	Barber	75
D.D.	Barker	355
W.	Bergerhoff	153
E.	Binggeli	209
B.L.	Bingham	397
T.L.	Boone	19, 43, 51
R.	Bourgois	339
L.L.	Brown	389
R.E.	Brown	330
E.H.	Bultmann, Jr.	27
J.D.	Cargile	388, N 11
A.K.	Chan	197
D.	Chandra	267
K.J.	Claber	119
J.A.	Collins	389, 397
P.	Corvin	463
T.K.	Cummins	388, N 11
A.N.	Dancygier	163
M.C.	Davies	119
J.	Eibl	489
R.	Eytan	34
R.H.	Fashbaugh	218
D.	Favarger	404
C.J.	Fennell	43
B.	Fießler	176
A.-S.	Forsberg	238
E.R.	Fosness	51
K.	Fujimoto	126, 317
J.C.	Galloway	389, 397, 413
R.	Galloway	51
J.B.	Gambill	11
J.J.	Gill	161
F.	Glaser	153, 176
P.W.	Graham	253, N __
D.	Grossman	11
G.H.	Gürke	497
W.L.	Hacker	194
W.J.	Hall	3
J.D.	Haltiwanger	11
J.	Hasler	246
J.R.	Hayes, Jr.	3, 11
W.	Heilig	327
M.	Held	346
R.W.	Henny	162
J.E.	Higgins	51
B.	Hobbs	197
R.L.	Holmes	253, N __
J.J.	Howard	4
P.	Hunziker	446
C.-W.	Hwang	438
M.J.	Iremonger	405
M.Y.	Ito	171, N 27
H.L.	Jessberger	132
P.	Joos	339
R.R.	Kaufmann	186
L.M.	Keer	163
J.A.	Keller	389
E.	Kessler	431, 446
S.A.	Kiger	445, N __
T.	Krauthammer	59, 267
S.T.	Kuennen	275
Y.	Kuzuba	126

H.	Langberg	67
S.	Langer	373
S.	Lokaj	329
F.A.	Maestas	389, 397, 413
M.E.	Majerus	330
K.A.	Marchand	504, 506
C.	Mayrhofer	284
R.	Melamed	137
W.P.	Mercx	226
D.H.	Merkle	4
H.-G.	Mett	454
G.	Meyers	505
D.	Miller	194, 441
P.F.	Mlakar	478
P.E.	Montanaro	196
R.E.	Moxley	413
M.J.	Murphy	195
L.C.	Muszynski	294
G.C.	Naeyaert	339
C.J.	Oswald	506
A.G.	Papp	355
G.J.	Pappas	363
J.C.	Partch	413
S.L.	Paul	3, 11
S.H.	Perry	301
J.	Peters	197, 381
W.	Pfrang	153
A.D.	Pullen	301
D.M.	Pyle	75
M.	Qisong	101
R.A.	Reid	4, 12
B.	Reymen	339
F.	Rischbieter	463
M.A.	Rochefort	294
R.	Rohani	426, N 19
J.	Ronkainen	472
C.A.	Ross	275
E.	Rottenkolber	420
C.	Rubio	413
B.	Satterwaite	43
M.C.	Saunders	119
M.	Sayama	126
G.	Scheklinski-Glück	227
M.J.	Schmidt	389
S.	Schwarz	137
S.P.	Shah	163
H.M.	Shanaa	59
A.J.	Sheridan	301
J.L.	Smith	478
H.C.	Sorenson	19
P.	Soroushian	309
J.	Stelter	175, N 3
R.H.	Sues	438, 441
M.M.	Swisdak, Jr.	196
S.	Syngellakis	109
J.E.	Tancreto	514
J.W.	Tedesco	275
G.	Thiel	132
L.E.	Tidwell	426, N 19
T.S.	Ting	83
A.	Tlili	309
C.Y.	Tuan	237
L.A.	Twisdale	438, 441
J.M.	Underwood	4, 504
R.J.	van Amelsfort	91
H.J.	van der Graaf	145
L.M.	Vargas	504
O.	von Estorff	153
A.C.	Walker	109
T.L.	Warren	4
A.J.	Watson	197, 381
J.	Weerheijm	91, 226
R.	Westaway	197
J.E.	Windham	171, N 27
S.	Woodson	415, N __
H.	Yamaguchi	126, 317
D.Z.	Yankelevsky	205, 427
S.L.	Young	355
C.	Zhaoyuan	101
W.	Zhihao	101
H.D.	Zimmerman	171, N 27
G.M.	Zintilis	109

Allgemeines / Modellversuche

General Topics / Modelling

ABSTRACT for Presentation at
Fifth International Symposium
on
Interaction of Conventional Munitions with Protective Structures

Comparison of Finite Element Model with Measured Field Test Data

J.R. Hayes, Jr.; W.J. Hall; S.L. Paul
US Army Construction Engineering Lab., Champaign, IL,USA

The Israeli Defense Forces (IDF) conducted a series of full-scale high explosive tests, in which two complete reinforced concrete structures were subjected to airblasts from the above-ground detonations of bare explosive charges that simulated general purpose bomb detonations in the medium to far field. In a cooperative research effort, the Israeli Air Force (IAF) and US Air Force Engineering and Services Center (AFESC) initiated a project to anlayze the test data, with emphasis on exposed wall acceleration-time histories, and use of the actual wall motion histories to validate several available structural response models that have been developed for use in designing protective structures.

This paper reports on the efforts of the University of Illinois Civil Engineering Department and the US Army Construction Engineering Research Laboratory (USACERL), in support of AFESC, to compare wall motions predicted by finite element models with observed wall motions in the actual field tests, and with motions predicted by established single-degree-of-freedom (SDOF) analysis procedures. The objective was to determine the relative merits of performing structural analyses using the more sophisticated finite element modelling technique, versus simplified SDOF models that are available.

Accelerometers were located on the "inner" faces of the field test wall sections at several key points for response measurements. The paper will compare motion histories of the walls that were derived from integrating the accelerometer data with the finite element models and summaries of the SDOF model results.

The commercially available program ADINA is being used for the finite element analyses. The ADINA program is noted for its nonlinear and dynamic analysis capabilities; it is currently being used at several US Department of Defense organizations and thus is a program of choice. Different material and element modelling techniques will be covered in the paper.

The paper will report the results of these finite element analyses and compare them with both the observed data and the SDOF models, to provide analysts and designers with assistance in determining the most appropriate method to use in modelling reinforced concrete box structures subjected to airblast effects in the mid to far field.

POSTATTACK AIRBASE FACILITY RECOVERY

By Dr. Douglas H. Merkle[1]
J. Jeffrey Howard[1]
Capt. Richard A. Reid[2]
LT (USN) James M. Underwood[2], and
Thomas L. Warren[1]
1) Applied Research Associates, Inc., Tyndall AFB, FL 32403
2) HQ AFESC/RDCS, Tyndall AFB, FL 32403

ABSTRACT

Modern warfare grants no safe haven. A few years ago an airbase well behind the front line was considered immune from the threat of death and destruction characterizing an infantry battlefield. Now there is no front line, and the lethality of the battlefield threatens every major overseas airbase. This is because the range, accuracy, and destructive power of modern weapons pose the same threat to an airbase command post as to a tank. That situation mandates that Air Force civil engineers anticipate the nature, extent, and mission capability consequences of facility damage, and develop strategies to recover from it.

To meet this threat, the United States Air Force Engineering and Services Center at Tyndall AFB, FL is developing a computer-based, expert system-assisted, postattack facility damage assessment system for airbases, and expedient repair methods for bomb-damaged, mission-critical structural facilities. Taken together, facility damage assessment and expedient repair are called facility recovery.

BACKGROUND

In 1985 at Spangdahlem AB, FRG the NATO airbase survivability exercise SALTY DEMO dramatically underscored the need for reliable postattack communications and a facility recovery plan. The Air Base Operability (ABO) concept evolved from SALTY DEMO. Its five phases are defense, survival, recovery, aircraft sortie generation, and sortie support. This article deals with the recovery phase of ABO, called Base Recovery After Attack (BRAAT), and specifically with rapid assessment of damage to mission-critical structural facilities, and expedient repair of those facilities, using preplanned methods and prepositioned resources.

Expert Systems

In general, expert systems are computerized databases consisting of specialized knowledge, combined with decision logic based on rules (heuristic, or rule of thumb, and exact), which can be accessed through a user-friendly interface. Figure 1 shows the basic concept of an expert system. The inference engine shown in the figure is a set of logical rules used to apply the knowledge base. An example of an expert system is an automobile trouble-shooting system, which diagnoses breakdowns and suggests repair methods.

Expert System Design For Airbase Postattack Facility Damage Assessment

The computerized expert system POST-DAM will assess damage to structural facilities. Its major features are:

(1) Uses the C Language Integrated Production System (CLIPS), developed by NASA's Mission Planning and Support Division at the Lyndon B. Johnson Space Center.

(2) POST-DAM will operate on a personal computer, without requiring extensive memory or storage.

(3) The POST-DAM system will be located in the Base Civil Engineer Damage Control Center (DCC), with damage assessment teams (DATs) in the field observing damage and feeding information into POST-DAM through a two-way digital burst communication system which is part of the Survivable BRAAT Communication System (SBCS).

(4) POST-DAM will use information from a DAT to assess a structure's condition, and, if the damage is not too severe, will recommend expedient repair procedures consistent with available materials, equipment, personnel, and repair time.

Facility Damage Assessment

The first step in airbase facility recovery is damage assessment, as shown in Figure 2. Initial estimates of mission-critical facility damage are obtained from observations reported to the DCC by personnel assigned to those facilities. Next, a more detailed damage assessment is accomplished by dispatching DATs to those mission-critical facilities known to have been damaged. By using two-way digital burst transmitters, the DATs can communicate with the DCC.

The next step is for DCC personnel to evaluate the information from the DATs. The evaluation begins with a basic decision: whether to accomplish expedient repair. Three factors are considered: mission impact, degree of damage, and resource availability. Table 1 shows the expedient repair decision logic. Expedient repair of structural facilities (ERSF) is attempted only if the damage has caused significant mission impact, is of moderate degree, and repair resources are available.

At this point, the expert system POST-DAM is employed to assist the assessment. POST-DAM is a personal computer database program of anticipated, expediently repairable damage modes, and the results of a continuing real time inventory of available repair resources. Expedient repair estimates include the repair strategy and the required labor, materials, and equipment. The field assessment data is fed into the POST-DAM survivable personnel computer, and POST-DAM returns feasible expedient repair strategies. These are prioritized, and transmitted to the Base Commander in the SRC, who makes the final decision on whether and how to accomplish expedient repair.

Facility Expedient Repair

The key to rapid postattack facility recovery is to have thought through the process beforehand, and thus be prepared for all reasonably likely expediently repairable damage modes for each mission-critical structural facility. This means knowing what expedient repair method will

be used for each damage mode, having sufficient material, equipment, and skilled personnel on hand to execute the repairs, and constantly training repair personnel to maintain proficiency. Expedient repair must be accomplished in 3-4 hours, so the methods must be quick and simple. Table 2 shows criteria used to screen possible expedient repair methods, prior to evaluating the most promising candidate methods in greater detail. Table 3 shows the detailed numerical method used to rank candidate methods for each damage mode. Each criterion, for each category, was scored between 1 (poor) and 5 (excellent). A total score of 38.5 was the highest possible. Table 4 summarizes expedient repair methods evaluated for the most likely, expediently repairable damage modes for mission-critical airbase structures. The repair methods are listed in order of merit for each damage mode, and are described in detail in Reference 1.

Summary

The connection between the facility damage assessment program, POST-DAM, and the expedient repair methods being developed is that the expedient repair methods for all anticipated damage modes, plus the resources, personnel, and time to execute them, will be stored in POST-DAM. This minimizes facility recovery time, by doing everything possible beforehand. The repair process itself is also shortened, because everyone involved knows what to do, and how to do it as efficiently as possible. This is the essence of military readiness.

References

1. Read, D.L., D.H. Merkle, M. Anderson, and M.A. Rochefort, Expedient Repair of Structural Facilities (ERSF) (2 Vols), Applied Research Associates, Inc. final report to the Air Force Engineering and Services Center (HQ AFESC), (February 1991).

2. Jirsa, J.O., A. Teran, and P.T. Nash, Expedient Repair of Structural Facilities, The University of Texas at Austin and Southwest Research Institute final report to the Air Force Engineering and Services Center (HQ AFESC), (November 1988).

3. Warren, T.L., and J.J. Howard, Software User's Manual for the POST-DAM System, 9 volumes, Applied Research Associates, Inc. report to the Air Force Engineering and Services Center, (Feb. 1991).

4. Merkle, D.H., D.L. Read, M.A. Rochefort, J.M. Underwood, and T.L. Warren, "Expert Systems for Airbase Damage Assessment", The Military Engineer, Vol. 32, No. 537, (Aug. 1990), pp. 38-41.

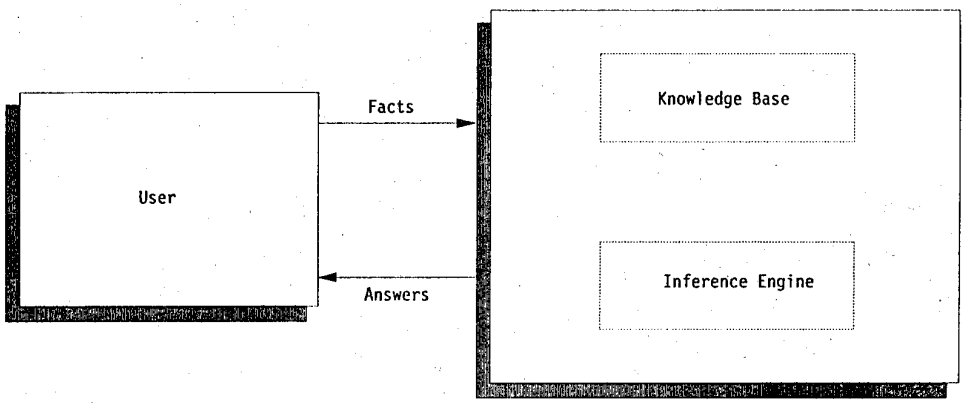

Figure 1. Basic Concept Of An Expert System Function.

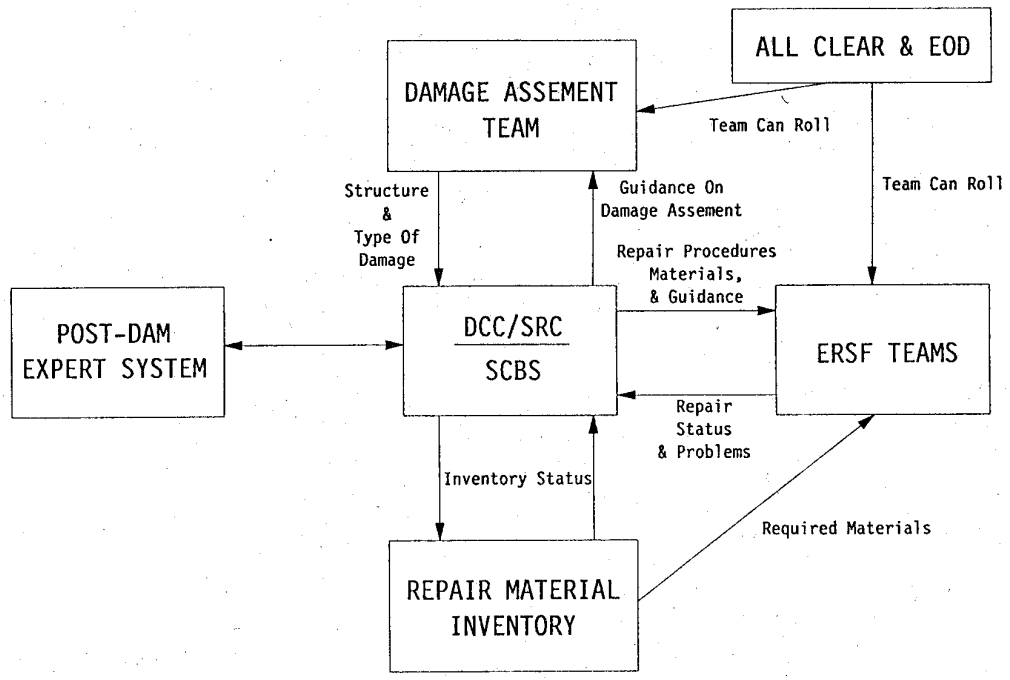

Figure 2. The Facility Recovery Process.

TABLE 1. EXPEDIENT REPAIR OF STRUCTURAL FACILITIES (ERSF) DECISION LOGIC.

	DEGREE OF DAMAGE	
MISSION IMPACT	Moderate	Major
Insignificant	do nothing	do nothing
Significant	repair if resources available; otherwise abandon	abandon

TABLE 2. EXPEDIENT REPAIR SYSTEM SCREENING CRITERIA.

Operational	Structural
simplicity	strength
versatility	stiffness
speed	toughness
pot life	durability
number of components	protection
environmental limitations	airtightness
bulk	
weight	Logistic
special equipment	availability
skill requirements	peacetime use
training	storage life
manpower	cost
safety	reliability
environmental reaction	maintainability
no hazardous waste	

TABLE 3. EVALUATION MATRIX FOR COLUMN REPLACEMENT ERSF SYSTEMS.

		Scores For Candidate ERSF Systems	
Category	Criterion	Glulam Column	Shoring Jack
Operational	Manpower	4	5
	Safety	3	4
	Simplicity	3	4
	Versatility	5	5
Weight Factor	Skill Requirements	4	5
0.40	Heavy Equipment	4	5
	Environmental Range	5	5
	# Of Components	4	5
	Special Equipment	4	4
	Redundancy	5	5
	Transportability	5	5
	Category Score	46	52
	Weighted Score	18.4	20.8
Structural	Strength	4	3
Weight Factor	Durability	4	3
0.30	Blast Resistance	---	---
	Fragment Resistance	---	---
	Airtightness	---	---
	Category Score	8	6
	Weighted Score	2.4	1.8
Logistic	Storage Life	5	4
	Cost	5	4
Weight Factor	Reliability	5	5
0.30	Maintainability	5	4
	Peacetime Use	2	2
	Availability	4	4
	Category Score	26	23
	Weighted Score	7.8	6.9
	Total Score	28.6 (74%)	29.5 (77%)

TABLE 4. SUMMARY OF ERSF SYSTEMS VERSUS DAMAGE MODES.

STRUCTURAL DAMAGE MODE	EVALUATED ERSF SYSTEMS
DAMAGED STEEL FRAMED STRUCTURE	1) CUTTING AND WELDING
DESTROYED CONCRETE COLUMN	1) INSERT SHORING JACK 2) INSERT GLULAM TIMBER COLUMN
CRACKED CONCRETE COLUMN	1) INSTALL COLUMN SPLINT
DAMAGED BEAM/GIRDER	1) USE VERTICAL SHORING - GLULAM COLUMN - SHORING JACK 2) INSTALL KING POST
DESTROYED NON-LOAD-BEARING WALL	1) ATTACH PLYWOOD PATCH 2) PLACE EARTH BERM COVER 3) PLACE PRECAST SLAB COVER 4) SHOTCRETE REPAIR 5) MASONRY BLOCK REPAIR
WALL BREACH	1) ATTACH PLYWOOD PATCH 2) PLACE EARTH BERM COVER 3) PLACE PRECAST SLAB COVER 4) SHOTCRETE REPAIR 5) MASONRY BLOCK REPAIR
FLOOR/ROOF BREACH	1) ATTACH PLYWOOD PATCH 2) RAPID SET CONCRETE REPAIR 3) SHOTCRETE REPAIR
SYSTEMS FOR SEALING STAIRS ACCESSING DAMAGED BUILDING STORY	1) PLYWOOD PATCH 2) SHOTCRETE REPAIR
DAMAGED OVER-PRESSURE DOOR SYSTEM	1) INSTALL CANVAS/SHEETING COVERING 2) REPLACE DAMAGED DOOR 3) INSERT THIRD DOOR 4) SEAL DOOR WITH SHOTCRETE
DAMAGED BLAST DOOR - AIRCRAFT SHELTER BLAST DOOR - OTHER BLAST DOORS	1) PRY OPEN DOOR
DESTROYED WINDOW	1)COVER WITH PLASTIC SHEETING 2) COVER WITH ACRYLIC PANELS
RUPTURED AIRCRAFT SHELTER FLOOR SLAB	1) INSTALL RAMP WITH AM2 MATTING 2) INSTALL RAMP WITH RAPID SET CONCRETE 3) INSTALL RAMP WITH SHOTCRETE

ABSTRACT for Presentation at
Fifth International Symposium
on
Interaction of Conventional Munitions with Protective Structures

Comparison of Microcomputer Structural Response Models with Measured Field Test Data

S.L. Paul, J.D. Haltiwanger, D. Grossman,
J.B. Gambill, J.R. Hayes, Jr.
US Army Construction Engineering Lab., Champaign, IL, USA

The Israeli Defense Forces (IDF) conducted a series of full-scale high explosive tests, in which two complete reinforced concrete structures were subjected to airblasts from the above-ground detonations of bare explosive charges that simulated general purpose bomb detonations in the medium to far field. In a cooperative research effort, the Israeli Air Force (IAF) and US Air Force Engineering and Services Center (AFESC) initiated a project to analyze the test data, with emphasis on exposed wall acceleration-time histories and the use of actual wall motion histories to validate several available structural response models that have been developed for use in designing protective structures.

This paper reports on the efforts of the University of Illinois Civil Engineering Department, the US Army Construction Engineering Research Laboratory (USACERL), and the IAF, in support of AFESC, to reduce the field test data and subsequently, to compare the observed wall motions with motions predicted by established analysis procedures.

Accelerometers were located on the "inner" faces of the test wall sections at several key points for response measurements. The paper will briefly describe the reduction of the accelerometer data and its integration to obtain velocity and displacement histories.

Motion histories were "back-predicted" using several available analytical techniques that use single-degree-of-freedom (SDOF) structural models. First, motions were predicted using the standard procedures found in US Army TM 5-855-1, "Fundamentals of Protective Design for Conventional Weapons," and ESL-TR-87-57, "Protective Construction Design Manual." Next, motions were predicted using the microcomputer program "SASDE," which was developed at the University of Minnesota for AFESC. Finally, the motions were predicted using the computer program "REICON," developed at the University of Florida for the US Air Force Armament Laboratory.

The paper will compare the wall responses to the observed loading environments in these full-scale tests, as determined by each of the several analytical procedures identified above, with the measured test data, and will discuss the relative merits of each analytical method when applied to this type of problem. These comparative studies should enable analysts and designers to use these analytical methods in a more informed and effective manner.

FULL-SCALE BLAST TEST OF A REINFORCED SOIL BUNKER

Captain Richard A. Reid, PE

HQ AFESC/RDCS Tyndall AFB, Florida 32403-6001

Abstract

United States military forces have typically conducted warfighting operations from a network of main and satellite operating bases. However, US participation in regional conflicts outside the sphere of influence of existing US bases requires the rapid buildup of a warfighting airbase, typically called a "bare base". The expedient nature of these bases necessitates the use of temporary construction methods: tents, wood frame structures, or lightweight metal buildings. Although functional, these structures provide little protection from blast overpressure or small arms fire. Structural hardening can be beyond the capabilities of the logistical trail and engineering forces. Reinforced soil systems may provide a means for rapid construction of protective shelters.

The response of a full-scale, conventionally reinforced soil shelter to a variety of conventional blast loadings has been evaluated. The test was instrumented to record the soil/wall interface pressures, interior wall/roof/floor accelerations, strain in the soil reinforcing strips, and free field blast pressures. Displacement of the structure was recorded through integration of the recorded accelerations, and permanent displacements were recorded via a survey. This paper will discuss the various elements of this test program.

Introduction

Conventional reinforced concrete protective structures are currently used by the United States Air Force to shelter aircraft, munitions, command and control facilities and other critical warfighting functions from conventional weapons attack. The advantages of reinforced concrete as a construction material include its ability to be designed to a specific strength, ability to be placed in any size or shape, and well known blast response characteristics. Some disadvantages to reinforced concrete include its high cost, long construction time, reliance on large amounts of quality construction materials, and the need for skilled labor. Therefore, reinforced concrete is not well suited for use where modern construction techniques and support are not available, or when expedient construction is required. Because of these disadvantages, an alternative to reinforced concrete construction was investigated.

As part of a joint effort between Terre Armee LTD, the Israeli Air

Force, and the United States Air Force Engineering and Services Center(AFESC), a reinforced soil structure was built and tested with conventional weapons. This paper discusses the test program, including what reinforced soil is, the construction process, test program, and conclusions. It explains how this innovative construction technique provides an alternative to reinforced concrete construction.

Reinforced Soil

The reinforcement of soil is analogous to the reinforcement of Portland cement concrete. Both soil and concrete are weak in tension, but strong in compression. To exploit on their strengths, and minimize their weaknesses, each is made into a composite material by adding reinforcement. This reinforcement gives the soil or concrete higher tensile strength without adversely affecting compressive strength. Therefore, the reinforcement of soil can be defined as the "inclusion of resistant elements in a soil mass to improve its mechanical properties" (Mitchell and Villet, 1987). The reinforcements used in soil may be synthetic materials, steel, or natural fibers. Since the test structure was built by Terre Armee LTD of Tel Aviv, the patented Reinforced Earth wall system was used. This particular system uses steel strips for reinforcement.

Comparison with Reinforced Concrete

The investigation of reinforced soil systems for protective structures is of interest because it has many advantages when compared to reinforced concrete. First of all, a structure built of reinforced soil is mostly made from soil.

In many cases, the soil indigenous to the construction site is adequate for use in the structure. This eliminates hauling of large quantities of materials to the job site. Secondly, this process requires little skilled labor. Reinforced soil walls are built primarily by unskilled laborers and a foreman, using only a front-end loader and a roller. Although detailed cost comparisons between reinforced soil and reinforced concrete structures have not been performed, conservative estimates show reinforced soil to be 30% less costly then a reinforced concrete structure. The reinforced soil structure can also be built much faster then a reinforced concrete structure. Reinforced soil requires no formwork, rebar placement, or long curing time. Use of a precast roof and floor, as opposed to the cast-in-place roof and floor used in this test, would further reduce both cost and construction time. Finally, reinforced soil is a mobile system. Innovative uses of this construction technique will permit its rapid deployment worldwide.

The design and construction of this Reinforced Earth structure generally followed the standard design procedure for static loading. Initially, lightly reinforced concrete was poured at the test site to provide a floor for the structure and a level bearing surface for the first course of concrete panels. The first course of concrete panels was placed on the foundation, and backfill placed and compacted up to the first level of reinforcement. The first layer of steel strip reinforcement was placed on the backfill and bolted to special anchors embedded in the concrete panels. The reinforcing strips were approximately 4 centimeters wide, 0.5

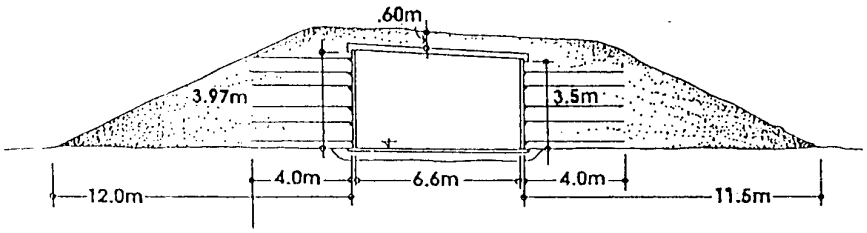

Figure 1. Test Structure - Section. From /2/.

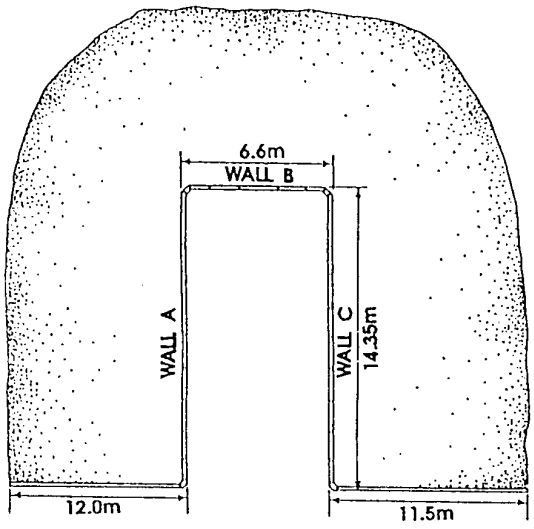

Figure 2. Test Structure - Plan. From /2/.

centimeters thick, and 4 meters long. The second course of concrete panels was placed, and backfill compacted up to the next level of reinforcement. The reinforcing strips were installed, and the entire process repeateduntil the wall had achieved its desired height. Once all panels were in place, forms were built for the cast in place reinforced concrete roof. Once the roof had been placed and cured, a layer of soil was placed over it.

Test Program

The primary objective of the explosive test was to determine whether a Terre Armee shelter would survive the effects of an explosion in an adjacent munitions storage bunker. Assuming the structure would survive, five subsequent tests were planned. In these tests, weapons were to be detonated in the backfill of the test structure at varying distances from its interior walls. A final test was the detonation of a number of weapons inside the test shelter. Because of security requirements, the exact number, sizes and locations of the weapons cannot be discussed in this article.

Instrumentation

In order to maximize the benefit of this test to the scientific community, detailed test instrumentation was used to measure the response of the structure to conventional weapon effects.

A total of five different gage types were used to measure data during this test. Soil interface gages were installed between the concrete wall panels and backfill soil, to determine the blast pressure on the panels at selected locations. Free field soil pressure gages were placed in the soil, to measure the blast pressure in the soil. Air blast pressure gages were used on the surface burst tests to measure blast pressure near the point of detonation and inside the shelter. Accelerometers were placed on the same wall panels that had soil interface pressure gages. Finally, strain gages were installed on selected reinforcing strips. These gages were connected to a 32 channel Pacific Instruments portable data acquisition system having a maximum sampling rate of 1,000,000 samples per second. High speed cameras were also used both inside and outside the shelter, to provide detailed video documentation of the test.

Results

The author is prevented by security requirements from discussing the size and placement of weapons used in this test. Therefore, the measured pressures, accelerations, and deflections are not presented here, because they would mean little without the associated weapon information. In general terms, the response of this structure to some very large and some very close detonations was impressive. Blasts beyond the reinforced soil berm had no noticeable effect on the structure. Detonations in the backfill had various effects. As expected, the closer the weapon was to the interior wall the greater the damage. However, some blasts in the berm caused no wall damage. At worst, failure was localized and never threatened the integrity of the entire structure. Because of the nature of the construction, local failures causing damage to a limited number of panels were thought to be rapidly repairable. This is a significant advantage over reinforced concrete.

Conclusions and Recommendations

Based on this test, reinforced soil is viewed as a very effective protective construction technique. To exploit this initial success, further work is needed to determine how to design reinforced soil structures for a given weapon loading, what type of reinforcement is best for this purpose, and what are the best size, shape, and material for wall panel construction. Explosive ground shock behavior in reinforced soil, failure modes, and the effect of blast loads on the interface between soil and reinforcement have yet to be determined. The Air Force Engineering and Services Center is actively pursuing research to answer these questions, and to develop valid design methodologies for the construction of protective reinforced soil structures.

Acknowledgements

The author wishes to thank Mr. Ermi Negri af Terre Armee LTD, Tel Aviv Israel, Mr Reuben Eytan of Eytan Building Design LTD, Tel Aviv Israel, and Major Emanuel Raudanski of the Israeli Air Force for their roles in the development of the test structure and overall management of the entire test program. Dr Doug Merkle of Applied Research Associates, Panama City Florida provided valuable editorial comments to this report. SMSgt Carl Hollopeter and SSgt Scott Kortum of the Air Force Engineering and Services Center and Mr Mike Purcell of Applied Research Associates in Panama City Florida are recognized for their significant efforts during the execution of this test program.

References

1. Mitchell, J.K. and Villet, W.B., "Reinforcement of Earth Slopes and Embankments", National Cooperative Highway Research Program Report 290, Transportation Research Board, 1987, p.323.

2. Raudanski, E., Eytan, R., and Sweiry, G., "Reinforced Soil Ammunition Magazine, Full-Scale Tests-1990, Testing Program", Headquarters Israeli Air Force Civil Engineering Division, Engineering and Products Branch, 1990.

Bemessung von Bauwerken

Structural Design

EVALUATION OF THE SURVIVABLE COLLECTIVE PROTECTION SYSTEM (SCPS)

Timothy L. Boone, Capt, USAF
PL/NTESR, Kirtland AFB, NM 87117-6008
Dr Harold C. Sorensen
Wash. State Univ., Pullman, WA 99164-2910

The Shock Physics Division of the Phillips Laboratory (PL/NTE), KAFB, NM has conducted theoretical studies to determine the response of a SCPS-2 which is subjected to a shock loading. In this study, the structure was analyzed for a loading generated by a buried 1000-lb bomb and for a loading generated by a surface enhanced blast munition (EBM). The analysis of the SCPS was based on the criterion that a breach in the structure that would allow contamination of the internal chemical environment from external sources constitutes failure. For the analysis associated with the bomb, the critical element (the wall) was modelled as a SDOF system. The natural period was calculated, a resistance function for flexural capacity was determined, and a load function which was associated with the peak pressure produced by the ground shock wave was developed. Soil models were chosen based on the existing data base and engineering judgment. Minimum stand-off-distances (SODs) were then calculated and plotted for four generic soils as functions of the soil saturation level. A vertical shock load that resulted from an EBM burst was generated with the use of a hydrodynamic code (GUSH) and applied to a simplified 2-D model of the SCPS for which a finite element analysis was performed with the use of the DYNA2D code.

INTRODUCTION. The Systems Response Section (NTESR) of PL/NTE was tasked by HQ HSD/YAGD to perform an evaluation of the performance sensitivity of the SCPS-2 shelter to dynamic/explosive environments. The evaluation was to include both the present design threat and future design threats. The analysis of a partially buried, partially bermed structure is difficult to perform with regard to ground shock loads because of the large number of parameters which must be quantified. However, a simplified, rational, first order solution has been obtained which was based on data which were available in the literature and on currently acceptable analysis techniques. In the dynamic analysis of the structure, the effects of the pre-existing static earth pressures and the

increases in structural capacities due to high strain rates were neglected since the increases in capacities nearly balance the static pressures.

ANALYSIS FOR GROUND SHOCK WAVE.

Structural Model. The SCPS shelter is assembled from prefabricated rectangular concrete box units as shown in Figure 1.

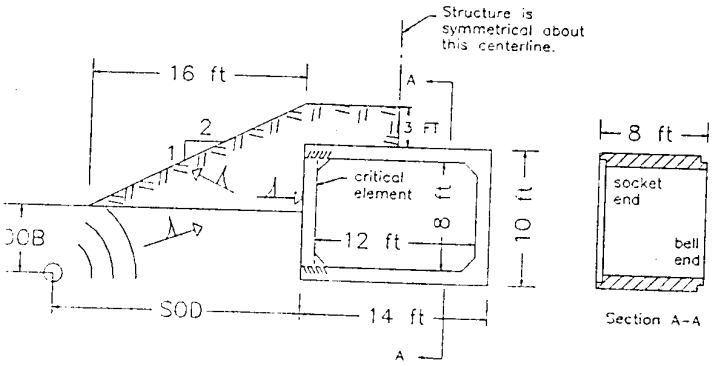

Figure 1. Details of SCPS Shelter.

A 1000-lb bomb is assumed to penetrate the earth surface to a specific depth-of-burial (DOB) on one side of the structure and explode. A ground shock is subsequently transmitted to the soil and induces a compressive wave that imparts an outward velocity to the soil particles at the wave front. For this analysis, it was assumed that the shock wave impacted on and reflected from the various sides of the shelter. Because of the location of the bomb, the vertical wall element was chosen to be the critical element and was modelled as a fixed-fixed beam with a span of 8 ft and a constant rectangular cross-section.

Natural Period. The dynamic analysis requires that the natural period of vibration of the structural element be known. The solution for a fixed-fixed prismatic beam exists in the literature /1/. The natural period of the wall element when the adjacent soil mass is neglected is $T_n = 0.0089$ sec. When the adjacent soil mass which is frequently assumed to influence the dynamic response /2/ is considered, the natural period is $T' = 0.0170$ sec.

Equivalent Single-Degree-of-Freedom (SDOF) Model. The solutions to many equivalent SDOF systems which are subjected to various types of dynamic loads exist in the literature /3/. If an equivalent SDOF system which exhibits the same fundamental frequency and period as the critical element of the shelter could be determined, then the use of existing solutions in this study is

possible. However, the use of existing equivalent SDOF solutions requires that; (1) the natural period, (2) the duration of load or rise time to the maximum value of the forcing function, (3) the maximum value of the forcing function, (4) the shape of the forcing function, (5) the structural resistance function, and, (6) an acceptable ductility factor be known.

The parameters that can be used to represent the equivalent SDOF system are an equivalent applied force, F_e, an equivalent mass, M_e, and an equivalent stiffness, k_e /3/. The equivalent system is dependent upon the load function applied to the original beam (wall). A typical distribution of the pressure on the wall which results from the shock wave is shown in Figure 2.

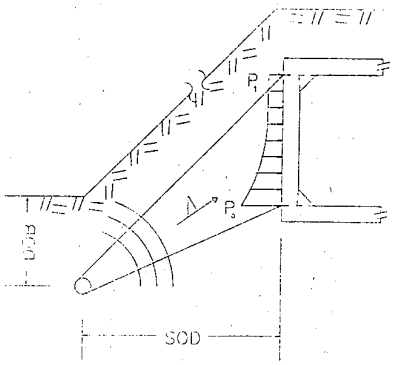

Figure 2. Typical Distribution of Pressure on Wall.

The values of P_0 and P_1 change according to the location of the bomb. Hence a "once through " solution is not possible. However, the pressure distribution has two extremums which can be postulated:

1. $P_1 = P_0$ (a uniform pressure distribution)
2. $P_1 = 0$ (a non-uniformly varying pressure distribution)

The solution for case 1 exists in the literature /3/. The value of the natural frequency for the equivalent system (Case 1) is only 0.4% lower than the value for the original beam. The solution for case 2 does not exist in the literature but was obtained by personnel at NTESR. The value of the natural frequency for the resulting equivalent SDOF system (Case 2) is only 5.4% higher than the value for the original beam. Since the "real" equivalent SDOF system is between the two extremums, it was concluded that the natural frequency and the natural period of the original beam can be used, without appreciable error, in conjunction with an equivalent SDOF model to obtain the desired solution in this study. Hence, an existing solution involving an equivalent SDOF system can

be used, if the real load function considered in this evaluation matches one for which the solution exists.

Load Function. During the conduct of the MUST-IV series of experimental tests on SCPS shelters /4/, pressures were obtained on the external surface of the wall of the concrete box unit. Each experimental pressure trace was different, but a typical shape is as shown in Figure 3. A typical pressure pulse can be characterized /5/ by a linear rise time to peak value and an exponential decay. For this evaluation, the pressure trace was modelled with a linear rise time to peak value with a parabolic decay, and the equivalent SDOF system was solved by

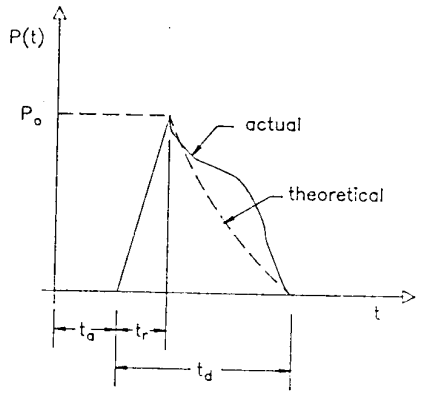

Figure 3. Typical Experimental Pressure Trace.

direct integration of the differential equation of motion (DEOM). The maximum value of the dynamic load factor (DLF) and the time of occurrence of this maximum were 1.95 and 5 ms, respectively.

These answers were then compared to two equivalent solutions as follows.

1. A constant force with a finite rise time /3/ for which the maximum DLF and time to maximum value were 1.9 and 5.2 ms, respectively.

2. A triangular load pulse /3/ for which the maximum DLF and time to maximum value were 1.94 and 4 ms, respectively.

Therefore, the solutions which exist in the literature for SDOF systems involving an applied constant load with a finite rise time or a triangular load pulse with zero rise time can be used in this evaluation to obtain a solution. If the natural period based on the inclusion of the earth zone is used in the calculations, the use of a triangular load pulse with zero rise time is more realistic. For the triangular load pulse which includes the earth zone, the maximum DLF and the time to maximum value become 1.87 and 4.8 ms, respectively. These comparisons confirm that, since the rise time of the force to its peak

value and the time to maximum displacement are both short, the actual shape of the pressure trace for times greater than the rise time is of little consequence to the solutions required in this evaluation as long as the value of the first peak of pressure is the absolute largest value that occurs during the duration of the load. A study was made of the interface pressure traces which were obtained during the MUST-IV series of tests, and the initial peak value was the absolute maximum value in 99% of the records which were considered.

Resistance Function. This evaluation of the SCPS shelter involves the determination of the minimum SOD for which the structure will survive without a breach of the chemical environment. Some yielding in the critical element may be tolerated, i.e., the structure need not remain elastic. The amount of inelastic motion or yielding is defined by a ductility factor. The general practice in the design of protective structures is to allow the ductility factor to be as large as 20 /2/. Since the internal environment in the shelter is to be maintained at a slight positive pressure, a more conservative value of 5 was chosen as the maximum value of the ductility ratio for use in this evaluation. As a result, the cracking of the concrete would be minimal. Since the critical structural element is now allowed to deform into the plastic range, the existing solutions for displacements restricted to the elastic range are no longer applicable. However, elasto-plastic solutions exist in the literature for SDOF systems subjected to various dynamic load pulses /3/. Since the answers associated with this evaluation compared well with the existing elastic solutions, it is tacitly assumed that the existing elasto-plastic solutions can be used to obtain solutions in this evaluation with acceptable accuracies.

The use of existing elasto-plastic solutions for SDOF systems requires that a resistance function be known for the element that is being analyzed. The resistance function is based on the strength capacity of the element. For the critical fixed-fixed wall element chosen for use in this evaluation, the maximum value of the resistance function is based on a collapse mechanism which involves the formation of three structural plastic hinges. These three hinges will form in the element at the locations of the three largest moments. In general in a fixed-fixed beam subjected to a lateral load, a plastic hinge will develop at each end and near the midspan of the beam as shown in Figure 4. The actual location of the internal plastic hinge is dependent upon the load distribution.

The resistance function is a graph relating load and displacement from the initial application of the load to the formation of the collapse mechanism. The

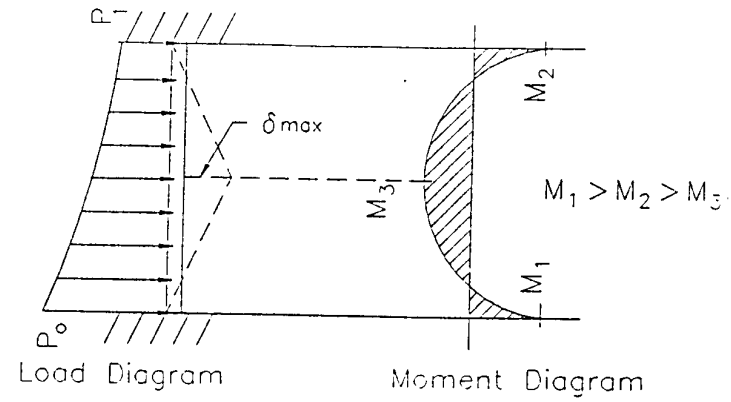

Figure 4. Collapse Mechanism.

development of the resistance function is based on linear elastic structural mechanics techniques (superposition), and the maximum plastic moment is taken as the useful ultimate moment capacity, i.e.,

$$M_p = M_u = 0.90*M_n = R_m$$

The resistance function depends on the distribution of the load. For this evaluation, the load distribution was characterized by a parabolic shape completely defined by P_0 and P_1. As the load was increased to cause the sequential formation of the hinges, the ratio of P_1 to P_0 for each increment was kept constant in order to keep the analysis from "mushrooming". A typical resistance function is shown in Figure 5. The three points (δ_i, R_i) represent the displacement and load conditions at the successive formation of the three plastic hinges. The "real" curve is then idealized to a bi-linear curve on the basis of equal areas (shaded) /2/. The ratio δ_m to δ_{el} is the ductility ratio. Both load and resistance are referenced to the maximum value of P_0.

Eight separate solutions were performed to cover the range of possibilities for the ratio, $r = P_1/P_0$, from 1 to 0 which are the two extremums. The maximum values of the resistance functions from these eight solutions were then plotted

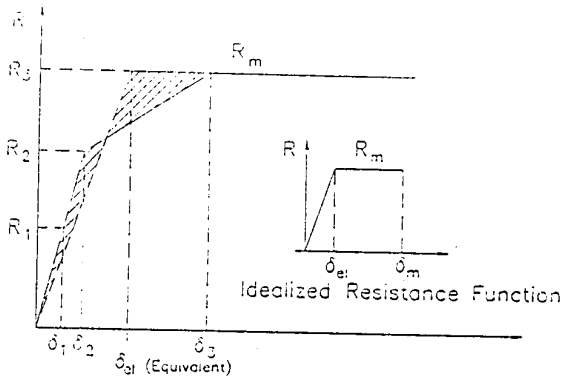

Figure 5. Typical Resistance Function.

to produce a graph relating R_m to r which was used to obtain the answers during the performance of this evaluation of the SCPS shelter. The graph resulting from this series of calculations is shown in Figure 6.

Determination of Minimum SODs . Parameters for four generic soils were determined by experts in soil mechanics at the Phillips Laboratory. The calculations for the minimum SODs for these four soil types under various soil saturation conditions were performed. This calculational process was lengthy and iterative for each SOD which was determined. The results are presented in the form of graphs as shown in Figure 7 for an f_c' of 6000 psi.

It is readily apparent by viewing the graphs that, as the soil saturation level goes above 85%, the safe survivable distance increases dramatically. Hence, good judgment should be used in the siting process for the SCPS shelters.

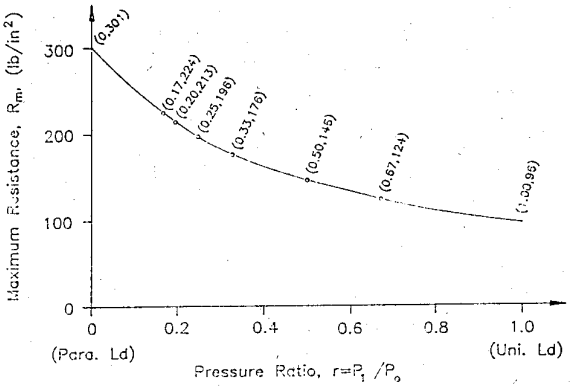

Figure 6. Calculated Resistance Function.

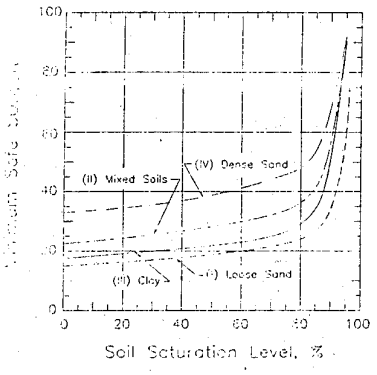

Generic Soil Type I: Loose Sand (γ_d' = 80 pcf)
Generic Soil Type II: Mixed Soils (γ_d' = 95 pcf;
Sandy Clays, Silty Sands, Clayey Sands, Clayey Silts)
Generic Soil Type III: Clay (γ_d' = 100 pcf)
Generic Soil Type IV: Dense/Cemented Sand (γ_d' = 105 pcf)

Soil Sat. Level	Generic Soil Type I	II	III	IV
0	15'	22.5'	17.5'	33'
25	16.5'	24.5'	19.5'	34.5'
50	18.5'	28'	21.5'	38'
75	22'	32.5'	25'	45.5'
85	25.5'	39'	32'	49.5'
95	54'	90'	90.5'	92'
100	>300'	>300'	>300'	>300'

Figure 7. Curves Depicting Safe SODs.

ANALYSIS FOR EBM SHOCK WAVE.

A 2-D finite element analysis was performed on a cross-section of a typical

SCPS-2 shelter. This analysis included many simplifications and served only as an initial study into the effects of an EBM burst on the SCPS shelter. Loads, which resulted from the detonation of an EBM and which were generated with the use of a hydrodynamic code called GUSH, were applied to the structure. Two types of soil (wet sandy clay and dry loose sand) were modelled separately around the shelter. These two soils were considered to be the extremums of those most likely encountered in the field. The load was applied as an equivalent vertical load to the surface of the earth on top of the shelter. The results of these analyses were evaluated, and it was concluded that, although there would be some minor permanent deformations and cracking existing in the structure, the structure would survive intact. Failure of the shelter was defined the same as for the analysis associated with the underground burst. A typical sample of the output from the 2-D analysis (with displacements greatly magnified) involving the dry loose sand is given in Figure 8.

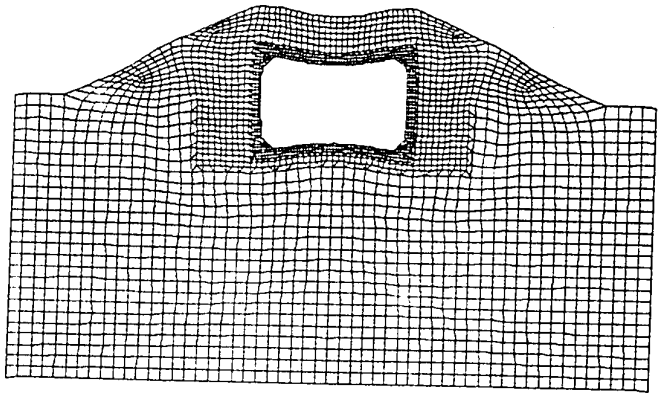

Figure 8. Sample Output From the 2-D Finite Element Analysis.

REFERENCES.

1. James, M.I., et. al., Vibration of Mechanical and Structural Systems, Harper and Row, Publishers, 1989.
2. Crawford, R.E., et. al., "Protection from Nuclear Weapons", AFWL-TR-70-127, February 1971. (Limited Distribution)
3. Biggs, J.W., Introduction to Structural Dynamics, McGraw-Hill Book Company, 1964.
4. Meyer, V.A., "Data Report for MUST-IV (Fourth Multi-Unit Structure Test, Full-Size Rectangular Shelter), Events A through G, Part I, AFWL-TR-84-120, February 1985. (Limited Distribution)
5. Drake, J.L., et. al., "Protective Construction Design Manual", FINAL REPORT, ESL-TR-87-57, November 1989. (Limited Distribution)

FULL SCALE TEST OF A BLAST RESISTANT STRUCTURE

by

Edward H. Bultmann, Jr., Ph.D., P.E.
Manager, Structural Mechanics Division
New Mexico Engineering Research Institute

The detonation of conventional high explosive bombs in the near vicinity of a structure subjects the structure to a very severe loading environment. There are four general components of this environment: airblast, bomb fragments, groundshock and high temperatures. Most blast resistant structures are constructed of concrete and steel and the short duration, high temperatures are of little structural significance. The relative importance of the other three components depends upon the characteristics of the bomb, the height or depth of the center of gravity of the bomb relative to the ground surface, and the distance of the bomb from the structure.

Most aerially delivered general purpose bombs fall in the weight range of 250 to 2000 pounds, with the total weight about equally divided between explosives and bomb casing. At close ranges a high explosive bomb can apply pressures on the order of 5000 to 10,000 psi to the surface of a structure. Fortunately for the structural designer, and the occupants of the structure, these very high pressures are fairly localized and rapidly decrease with distance from the center of the explosion. The smaller the bomb the more rapidly the peak pressures decrease with range from the bomb. At very close ranges, however, the extremely high pressures generated by a bomb detonation may breach walls of the structure.

Detonation of the bomb breaks the casing of the bomb into a large number of fragments with weights ranging from fractions of an ounce to a couple of pounds or more. At short ranges these fragments can impact the surface of the structure at velocities as great as 9000 feet per second. These fragments are capable of perforating thinner concrete or steel wall sections or removing significant amounts of concrete from thicker walls. In the process of perforating or spalling the surfaces of the structure they can also deliver significant impulsive loads to the structure. As in the case of the airblast loading the more severe damage

due to fragment impacts occurs over a relatively small surface of the structure. One factor which can be of importance is whether the fragments or the airblast loading arrives at the structure first. At short ranges both arrive at about the same time. At greater ranges the fragments normally strike the structure before the shock front. In the latter case the structures resistance to the airblast loading may be reduced by fragment damage.

Both high intensity airblast loading and bomb fragment impacts induce compressive stress waves in the walls of the structure. These compressive stress waves are reflected from the inner surface of the wall as tensile waves and can cause spalling of the inner surface concrete. In some instances the spalled concrete fragments may be projected with sufficient velocity to injure personnel or damage equipment. Some structures incorporate steel spall plates securely anchored to the concrete to eliminate or minimize the spall hazard.

If the bomb is detonated on or above the ground surface, airblast loading and fragment impacts are normally of greater significance to aboveground structures, since a much smaller portion of the total energy of the detonation goes into groundshock. If the weapon is detonated below the ground surface, ground shock loading will probably be of greater significance than airblast or fragment impacts, because most of the energy will go into groundshock. The interaction of groundshock waves with the structure is still not fully understood, and the prediction of groundshock loading is subject to much greater uncertainties than airblast loading or fragment penetration.

In the case of buried structures groundshock loading is the only loading mechanism. Both airblast induced and direct induced groundshock may have to be considered, depending on the burst conditions for the bomb.

The design of structures to protect personnel and equipment against all types of weapons effects is of great interest to the US military services and the Air Force Weapons Laboratory has been conducting research in this field for many years. The test program I will briefly review today was part of an Air Force Weapons Laboratory research program. The tests were conducted in 1987 and 1988 to evaluate the response of a full-size, blast resistant structure to near miss detonations of high explosive bombs. This structure was designed to protect against this and other weapon threats. Buried and aboveground detonation of bombs were included in the program. The objectives of the program included the gathering of data on airblast, bomb fragment and groundshock loading of the structure, measurement of the response of the structure to these loadings, and an

evaluation of the level of protection provided by the structure to installed equipment and personnel.

The test structure was a lightly reinforced concrete arch with a clear span of 71 feet (21.6 m), a maximum clear height of 30 feet (9.2 m) and a length of 120 feet (36.6 m). The arch wall thickness varied from 18 to 32 inches (0.46 to 0.81 cm). A 0.125 inch thick steel plate covered the inner surface of the arch. The arch was supported by spread footings 10 feet (3.0 m) wide by 120 feet (36.6 m) long. Reinforced concrete doors and walls closed the two ends of the structure. Grade 60 reinforcing steel and 6000 psi (41.4 MPa) compressive strength concrete were used in constructing the arch. Various items of equipment were installed in the shelter to obtain data on equipment response and evaluate techniques for attaching equipment to shelter walls and floors.

The structure was heavily instrumented to measure the airblast, groundshock and bomb fragment environments generated by detonation of the bombs and the response of the structure and equipment to these environments. Airblast gages, accelerometers and high speed photography were included in the measurements program. Pre and posttest surveys were made to determine permanent displacements of the structure.

One of the surface detonations is shown in Figure 1. Peak pressures measured on the surface of the structure varied from 0.6 to 3200 psi (0.004 to 22 MPa). The measured values agreed reasonably well with predictions, except at the very low pressures which occurred on the opposite side of the structure from the detonation. Bomb fragments removed 6 to 8 inches (15 to 20 cm) of concrete from the surface of the structure nearest the bomb (Figures 2 and 3). This thickness was close to the predicted maximum depth of penetration of bomb fragments. One fragment penetrated to a depth of 12 inches (30 cm). No fragments perforated the wall of the shelter. Peak accelerations measured on the interior surface of the structure varied from 6 to 16,000 g. The maximum structural velocity obtained from integration of accelerometer records was 52 feet per second (15.9 m/s). Shock response spectra and power spectral density plots were developed for many of the accelerometer records. Because the airblast shock front and the bomb fragments arrived at the surface of the structure at about the same time, it was impossible to determine the separate contributions of these two loading mechanisms to structural motions. The significance of these structural motions to items of equipment attached to the walls of the structure depends on the natural frequency of the equipment and the structural elements connecting it to the walls and the frequency content of the wall motions. Very strong, rigid connections can result in very high accelerations being

transmitted to the equipment. More flexible connections usually result in much lower accelerations transmitted to the equipment. The latter approach is normally chosen in shock isolating equipment from high shock environments. Very few items of equipment can withstand accelerations of 16,000 g, so some modification of shock inputs is necessary if the equipment is to survive. The floor of this structure was isolated from the exterior walls and much lower accelerations were observed on the floor than on the exterior walls in the aboveground detonations.

The buried detonations produced very low blast pressures and no bomb fragment impacts on the surface of the structure. The buried burst condition causes more of the energy of the detonation to be coupled into the soil forming larger bomb craters and generating higher groundshock levels. Figure 4 shows the crater formed by one of the buried detonations. It is obvious that this type of detonation can result in loss of foundation support and perhaps settlement of the structure. The buried detonation also resulted in larger accelerations of the structure floor slab due to higher groundshock levels.

One simple approach to reducing damage to structures from aboveground detonations is shown in Figure 5. A partial earth berm was placed against the side of the structure for a near surface detonation. The earth berm has been shown to greatly reduce fragment damage and reduce peak airblast pressures applied to the structure.

This series of tests demonstrated that the structure provided the desired level of protection and added to the experimental data base for design of similar structures.

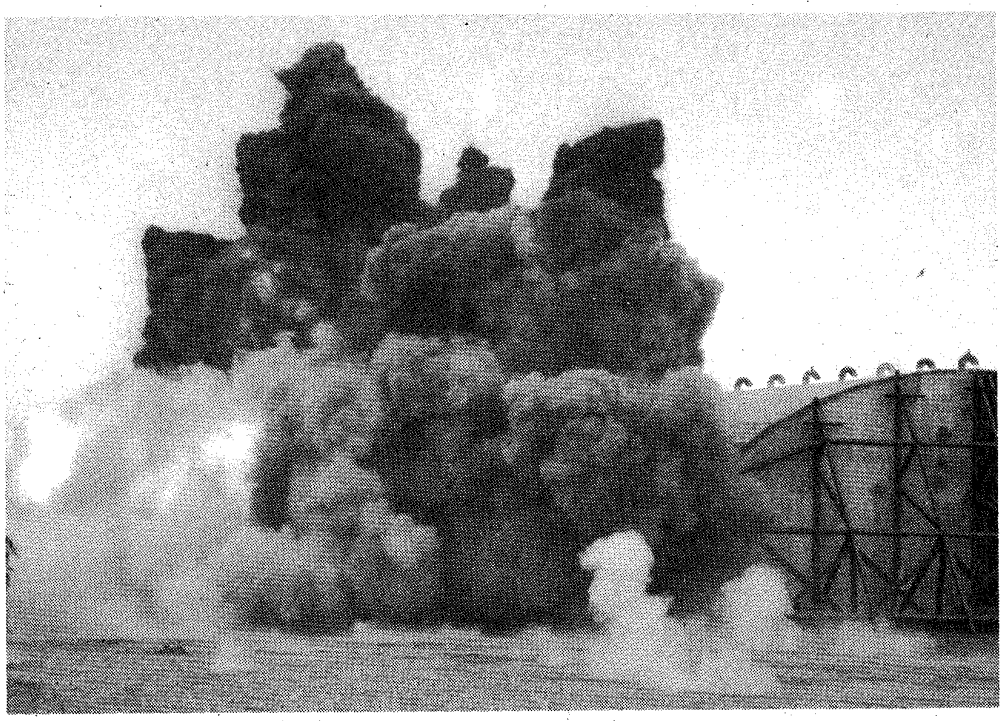

Figure 1. Surface Detonation of General Purpose Bomb.

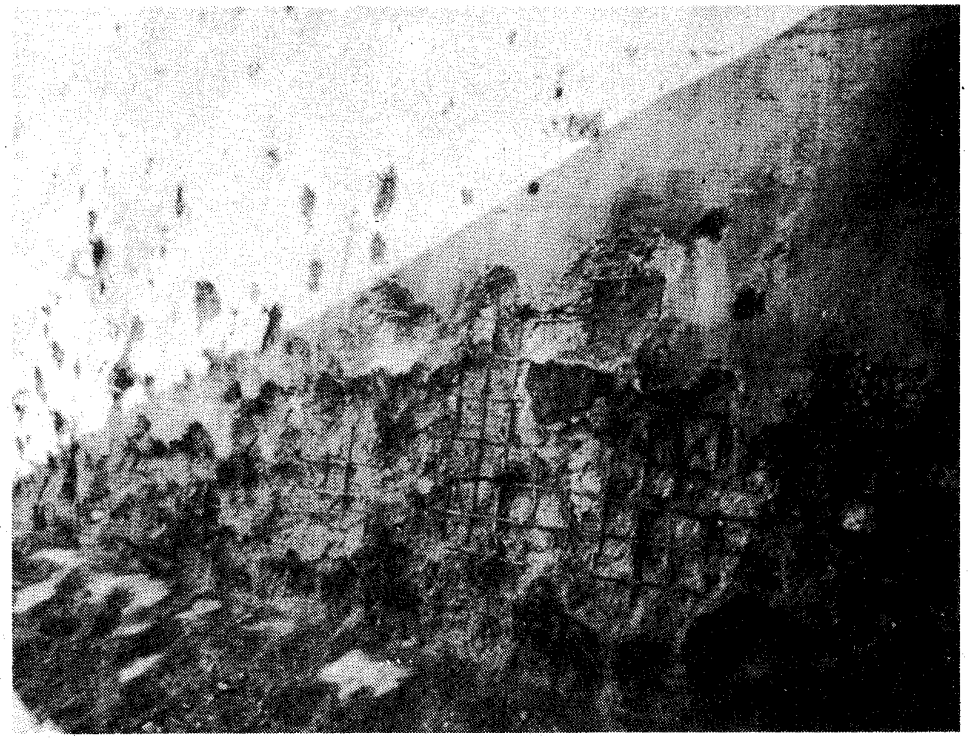

Figure 2. Bomb Fragment Damage to Structure Wall.

Figure 3. Bomb Fragment Damage to Personnel Entrance.

Figure 4. Crater Formed by Underground Detonation.

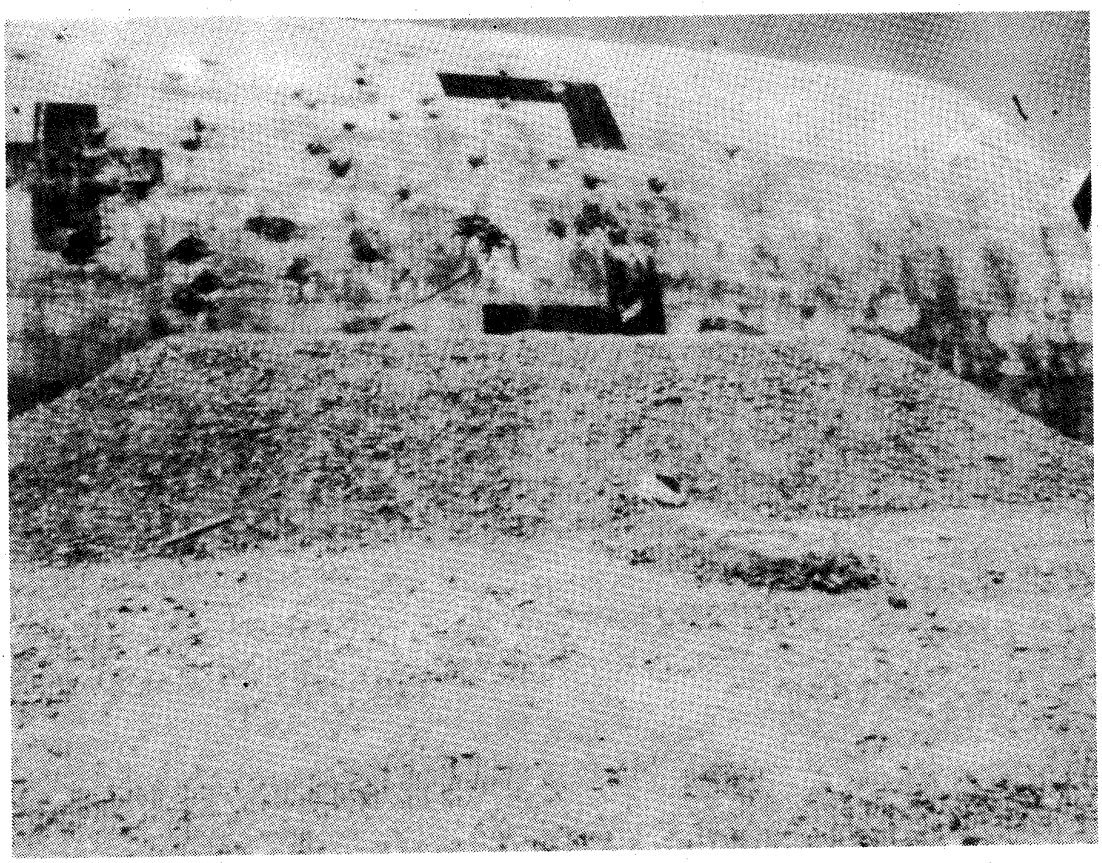

Figure 5. Earth Berm at Side of Structure.

OPTIMAL DESIGN OF PROTECTIVE STRUCTURES USING COMPUTER-AIDED RISK ANALYSIS

Reuben Eytan

Eytan Building Design Ltd.

ABSTRACT

The paper includes the description of the procedures for the optimal design of protective structures using computer-aided risk analysis. The procedures are part of a comprehensive analythical set of computer programs compiled by the author and called SEcurity, Protection and Hardening Risk Analysis (SEPHRA).

The paper emphasizes the damage analysis stage which is based on the author's extensive practical experience and on our database including more than 19,000 real events of conventional weapons effects on different structures and installations.

SEPHRA has been used lately in numerous projects worldwide and is applicable to all types of protective structures and installations.

INTRODUCTION

SEPHRA includes five major stages of analysis:

a. Threat analysis, including the consideration of the probabilities of hit for the defined threats as well as the installation characteristics.

b. Damage analysis, resulting in quantitative estimation of the expected damages to structures, equipment, etc. as well as possible injuries to personnel.

c. Risk assessment, with the final result expressed as a risk level for the structure/facility.

d. Countermeasures cost-effectiveness analysis, consisting of assessing the reduction in the risk level by different hardening/strengthening measures related to the respective cost of the measures, and

e. Countermeasures optimization - leading to the definition of the optimal countermeasures.

The major analysis modes of SEPHRA are:

1. Survivability analysis mode.
2. Optimal countermeasures design mode.
3. Damage control analysis mode.
4. Upgrading analysis mode.

The SEPHRA optimal countermeasures design mode includes the following subroutines:

a. OPTSIT - Optimal Site mode.
b. OPTHAR - Optimal Hardening mode.
c. OPTPRO - Optimal Protection mode.
d. OPTSEC - Optimal Security mode.
e. OPTSTR - Optimal Structure mode.
f. OPTFAC - Optimal Facility mode.

In this paper we are addressing mainly the Optimal Hardening mode (OPTHAR).

GENERAL DESCRIPTION OF SEPHRA

- **SEPHRA** is a computer-aided analysis involving the continuos interface between the analyst and the computer.

- **SEPHRA** is based on the combination of numerous basic subroutines, manually chosen and used by the analyst.

- **SEPHRA** makes use of our extensive database of observed damages to structures under real attacks summarizing 23 years of field practical experience.

- **SEPHRA** is developed for use on PC computers.

- **SEPHRA** has proven to be the most effective because:
  - the experience and judgement of the analyst is fully used.
  - the intermediate results can be easily checked.
  - any required changes can be simply implemented.

- **SEPHRA** <u>is not</u>:

  - a "black-box" computer code (where inputs are compiled and then outputs are received at the end of the computer run).
  - a computer code "for sale", but a man-machine analysis procedure.

The general SEPHRA flowchart is shown in figure no.1.

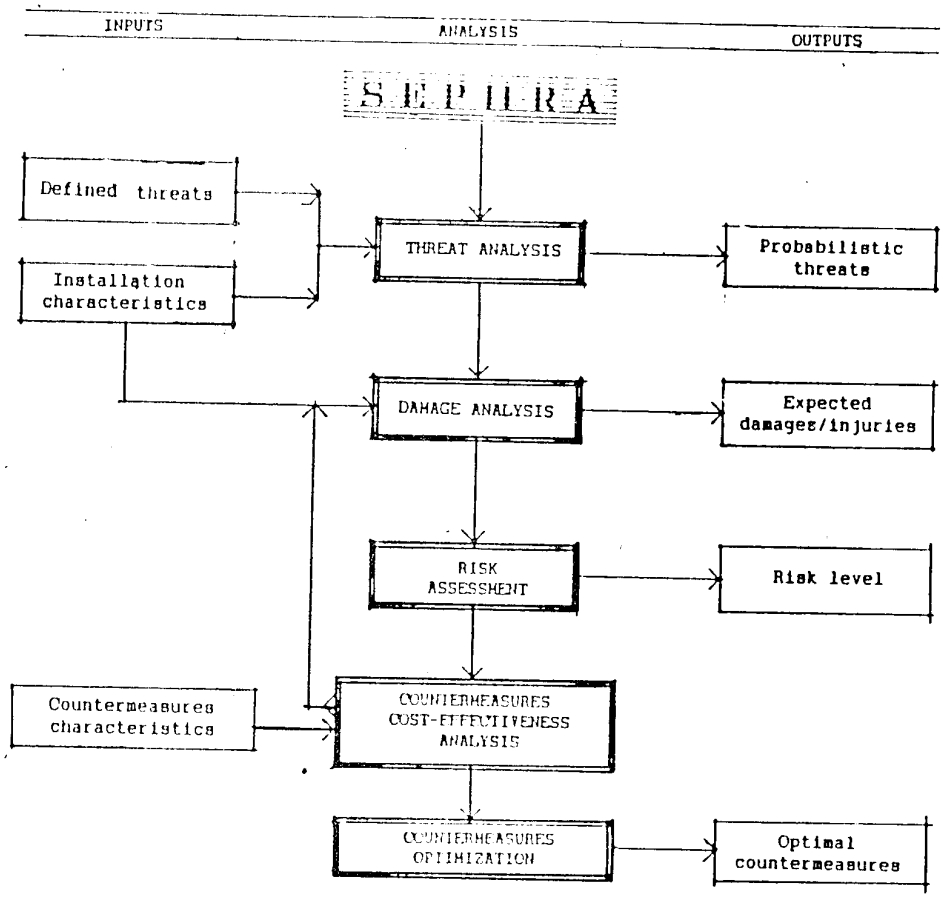

Figure no. 1 SECURITY, PROTECTION and HARDENING RISK ANALYSIS (SEPHRA)
General description

SEPHRA STAGE 1 - THREAT ANALYSIS

Defined threats

The client/user provides the definition of the threats to be considered in the analysis, including the types of attacks, the kind and size of weapons and their hit characteristics, such as direct hit, near miss (distance from installation), single or multiple hits.

Threats probabilities of occurence

The following options are available for the SEPHRA analysis:

- **OPTION 1** - Single threat with probability of occurence equal to 1.

- **OPTION 2** - Several threats, each with probability of occurence equal to 1. The damage analysis is performed for all the threats and the maximal damage from a single threat is further considered for the risk assessment.

- **OPTION 3** - Several threats, each with probability of occurence less than 1. The threat probabilities are either defined by the client or calculated by SEPHRA using the computer-modeled installation characteristics.

Installation characteristics

The following installation characteristics are modeled and compiled as computer inputs by the analysts in full coordination with the client:

- Topography of the installation site and the surroundings.
- Types and characteristics (dimensions, coordinates) of the site surrounding features: buildings, roads, open areas, parkings, etc.
- Site layout and perimeter characteristics (dimensions, coordinates of all structures/facilities, details of the perimeter features).
- Characteristics of all structures/facilities on site - dimensions, building materials, openings, contents (people, equipment, materials, etc.).

At the end of SEPHRA Stage 1 - Threat Analysis - the final defined threats are approved by the user, including the respective threat probabilities.

SEPHRA STAGE 2 - DAMAGE ANALYSIS

The damage assessment is based on:

- Observed weapons/destructive devices effects on real structures.
- Full-scale tests on real structures.
- Recorded damages to structures during real attacks (summarized in our extensive database ODS-Observed Damages to Structures - including more than 19,000 events).
- Calculations of weapons effects and structural response.
- Engineering judgement based on practical experience, including the analysis of damages to normal structures (see figure no.2) as well as hardened structures (see figure no.3).

Figure no.2 - Damaged structures from a SCUD missile attack on Tel Aviv (January 1991).

Figure no.3 - Civil defence shelter damaged by a close-in conventional warhead explosion.

The ODS database includes the description of damages to structures, facilities, equipment, etc. as well as injuries to people from real conventional weapons attacks including:

- Shooting of bullets from small arms and machine guns.
- Shooting of bullets from large machine guns and anti-aircraft guns.
- Direct hits of rocket propelled grenades.
- Direct hits of anti-tank weapons-recoiless guns, etc.
- Direct hits of tank projectiles.
- Direct hits/near misses of mortar shells.
- Direct hits/near misses of rockets and missiles.
- Direct hits/near misses of artillery shells.
- Direct hits/near misses of air bombs.
- Direct hits/near misses of ground-to-ground missiles.
- Small explosive devices - up to 5 kg. TNT.
- Medium explosive devices - up to 20 kg. TNT.
- Large explosive devices - up to 100 kg. TNT.
- Very large explosive devices - up to 2000 kg. TNT.
- Special weapons deviced for specific targets.

In the SEPHRA analysis, the damage can be expressed as:

. Costs for repairs of the direct damage.
. Costs for indirect damage.
. Number of people injured.
. Time required to return to normal functioning.
. Relative capability to perform the required functions.

SEPHRA STAGE 3 - RISK ASSESSMENT

The risk assessment is performed by summarizing the values of the expected damages multiplied by the respective threat probabilities.

The risk for each threat is expressed in the same manner as the damages : costs for the structural repairs/replacing equipment, number of injured people, etc.

However, the total risk for the installation is calculated as a risk level value normally expressed in percentages, relative to 100%, representing the total loss (in property value or injuries to personnel or capability of functioning).

The presentation of a single risk level value for the whole installation, as a result of SEPHRA Stage 3, gives the user a quantified value of the risk and allows the decision making on the present risk acceptability or the need for additional countermeasures.

SEPHRA STAGE 4 - COUNTERMEASURES COST-EFFECTIVENESS ANALYSIS

In this stage, all feasible countermeasures are analyzed: their effectiveness in risk reduction for the defined threats on the specific installation is assessed in quantitative terms, based on our practical experience and engineering judgement, using also the SEPHRA stages 1-3. The countermeasures costs are estimated and diagrams of risk versus cost of protective measures are compiled (see example in figure no.4).

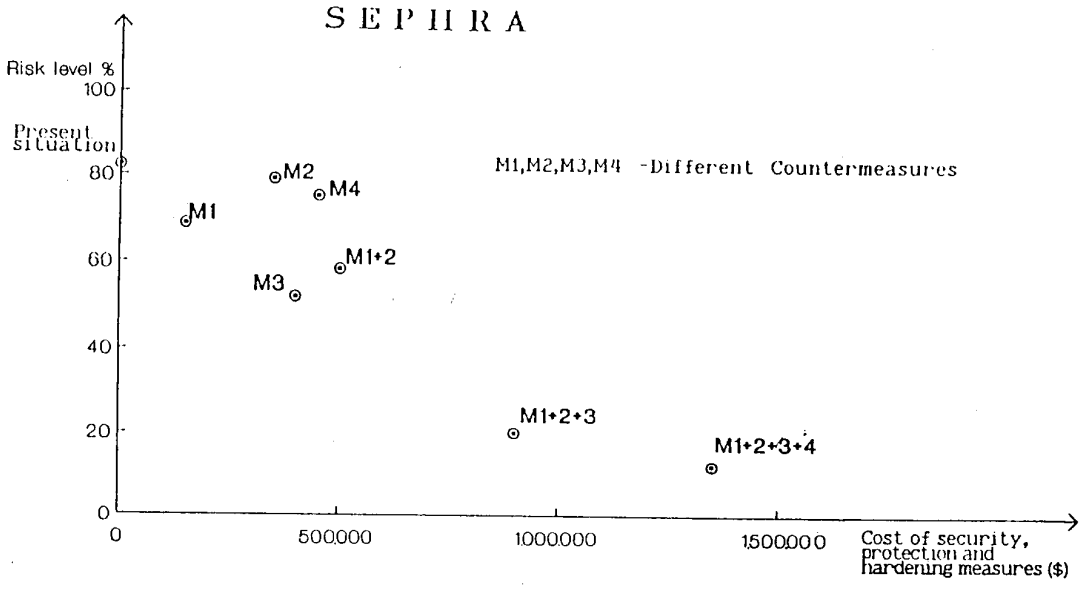

Figure no.4 - Countermeasures cost-effectiveness diagram

SEPHRA STAGE 5 - COUNTERMEASURES OPTIMIZATION

By using the risk-cost diagrams, the optimal range of countermeasures can be defined, as shown in figure no.5.

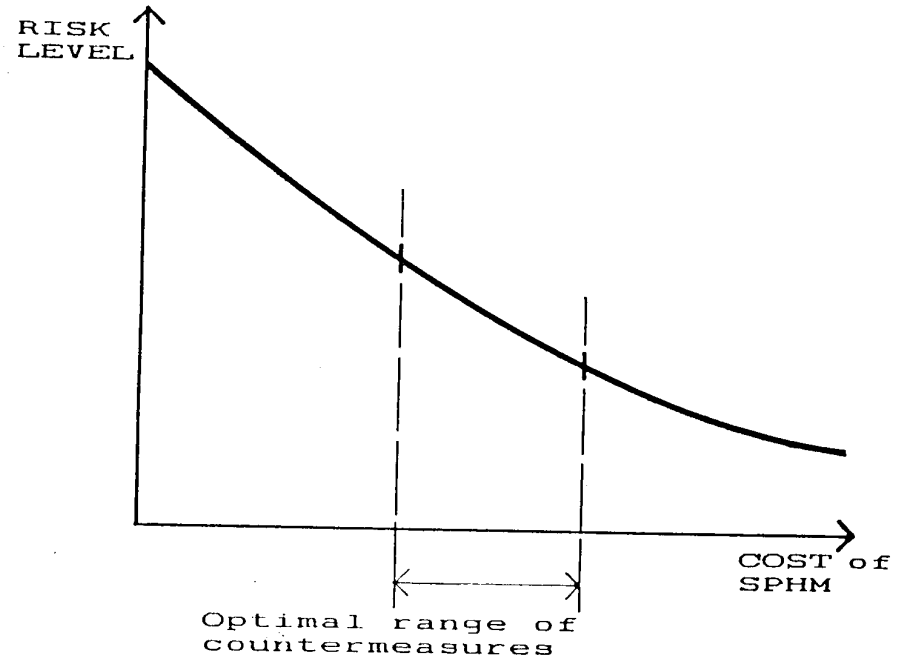

Figure no.5 - Deciding on the optimal security, protection and hardening measures (SPHM).

RISK REDUCTION BY HARDENING AND ADDITIONAL SECURITY MEASURES

The risk reduction by additional security measures, such as security systems and security guards, can be quantified by using additional SEPHRA subroutines. A typical diagram of risk reduction by hardening and additional security measures is presented in figure no.6.

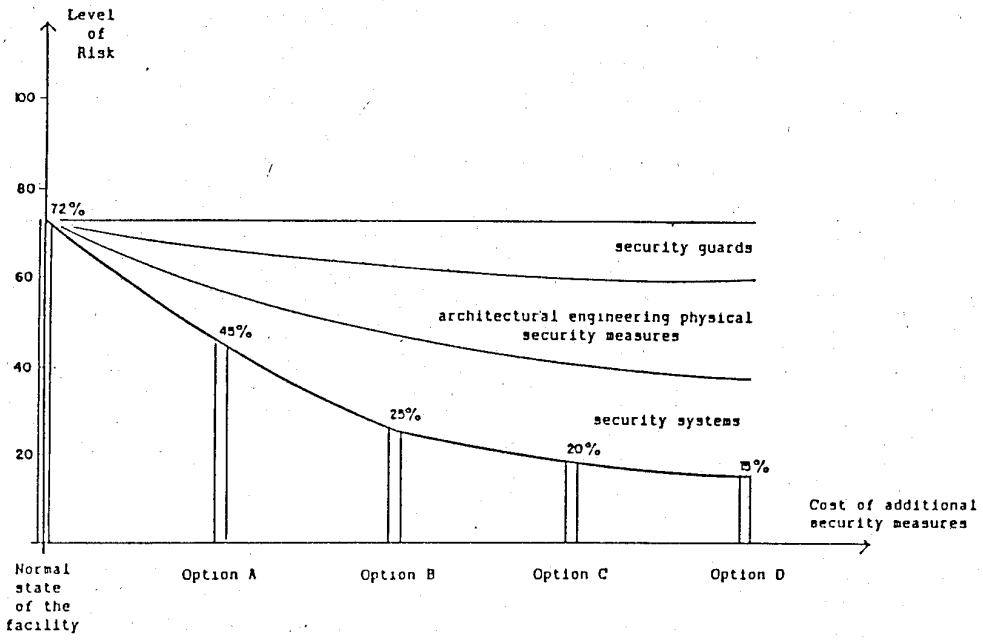

Figure no.6 - Reduction of risk by different security measures

SUMMARY

We have presented our SEPHRA risk analysis procedures used to optimize the hardening measures of protective installations.

The SEPHRA specific characteristics are:

- Can deal with numerous threats simultaneously including considering/calculating the weapons hit probabilities and the relative probabilities of occurence.

- Calculates weapons effects, structural response and expected damages/injuries based on extensive practical experience.

- Correlates all security, hardening and protection measures with the respective reduction in risk, based on extensive practical experience and engineering judgement.

- Presents the analysis results in a "managerial" format providing an optimal tool for decision making.

SEPHRA has been applied in numerous projects, worldwide, with the following goals:

- THREAT DEFINITION - types of attacks, kind and size of weapons, hit characteristics (direct hit, near miss - distance, single or multiple hits) - now and in the future.

- QUANTIFY RISK LEVEL to existing/newly designed structures, facilities, installations, sites, etc.

- FIND OPTIMAL COUNTERMEASURES - security, protection and hardening measures.
  a. For existing installations.
  b. For newly designed installations.

- FIND OPTIMAL UPGRADING - security, protection and hardening measures.

- DEFINE OPTIMAL MASTER PLAN FOR SECURITY, HARDENING AND PROTECTION including optimal site, optimal facility layout, optimal structures layout, optimal security measures.

- DAMAGE CONTROL - assessment of all types of damages and the optimal repair measures and procedures.

- ANALYZE ENVIRONMENTAL HAZARDS - calculate the level of risk to the surroundings.

AN EXPERIMENTAL EVALUATION OF THE PROTECTION FROM CONVENTIONAL WEAPONS EFFECTS PROVIDED BY THE BASE DAMAGE CONTROL CENTER

Maj Clarence J. Fennell, Capt Timothy L. Boone, and Brent Satterthwaite

Shock Physics Division, Phillips Laboratory, Kirtland AFB, NM 87117-6008

A segmented reinforced concrete structure possessing blastproof doors, blast protection valves, auxiliary power supply, and Chemical, Biological and Radiation (CBR) filters is being developed to provide protection from conventional weapons effects for civil engineering personnel who are directing postattack base recovery efforts. This paper emphasizes the predictive methods used in the fullscale experimental test which investigated the structural and equipment survivability provided by this design. The results of this investigation show clearly the importance of ductile and energy absorbing connections. In the event of an unfortunate failure of a structural element, there should be sufficient ductility to prevent catastrophic failure of the entire system. The equipment response was very close to what was expected, and it validated present prediction techniques. The study was significant because it identified items that could be implemented or investigated in order to advance the state of the art in predictive methods.

1.0 INTRODUCTION

The Base Damage Control Center (BDCC) /1/ is being developed by the Air Base Operability Office (AD/YQ) to provide a system for the protection of civil engineering personnel who are directing postattack base recovery efforts. The BDCC must provide protection from conventional weapons blast, shock and fragments, as well as from chemical and biological weapons. To meet these requirements, a segmented reinforced concrete box is provided with blast doors, blast valves, backup power supply, and Chemical, Biological and Radiation (CBR) filters. The BDCC has a larger cross section than the Survivable Collective Protection System (SCPS) family of shelters and does not provide for continuous access and egress as does the SCPS. Rather, the BDCC is intended to operate

in a buttoned-up mode with personnel entering the shelter prior to an attack and remaining there for up to seven days. The baseline system is a half-buried, half-bermed arrangement; the system could also be constructed as fully buried or fully bermed.

The BDCC was designed by the New Mexico Engineering Research Institute (NMERI) under a contract administered by the Air Force Engineering Services Center. Dieterich Beratende Ingenieure (DBI), a German design firm, was contracted to provide the design with German specifications and European construction details. The Air Force Phillips Laboratory's Civil Engineering Research Division (PL/NTE) was funded by AD/YQ to perform weapon effects tests against the BDCC, analyze the difference between a segmented BDCC and one which is cast-in-place, and make recommendations for design improvements.

2.0 OBJECTIVE

The primary objective of this test series was to validate the BDCC design for structural integrity and equipment survivability, but a secondary objective was to collect data on the response and loading mechanisms of the BDCC in order to verify and improve the associated prediction methods. The test objectives were accomplished with a series of four test events which exposed different aspects of the shelter to a Mark (Mk) 83 General-Purpose (GP) Bomb. In Event A, the bomb was placed near the sidewall directly opposite the work area. This location was selected in order to maximize the loading on the sidewall and the Remote Control Panel (RCP). In Event B, the bomb was placed in front of the door. This event was the only surface burst and tested the structure against fragments and airblast. In Event C, the bomb was placed near the dirty mechanical room to maximize loading on the generator and blower assembly. In Event D the bomb was placed near the endwall in order to place loading in a direction normal to the loading in Event C.

3.0 SYSTEM DESCRIPTION

The BDCC shelter is constructed of precast reinforced concrete panels. The structure is 15 m (49.2 ft) long, 8 m (26.2 ft) wide, and 2.5 m (8.2 ft) high on the interior and is divided longitudinally into 5 modules and 2 entryways. Each module consists of two sidewall panels, a floor panel, and a roof panel, welded together to form a rigid box section. The ends of the shelter are capped with concrete endwalls. Ramped entryways formed with retaining wall

elements provide access to the interior on each end of the shelter. Blast doors protect the entrances, and a blast-proof hatch on one end of the shelter provides an emergency egress. All air vents are blasted-protected. The interior of the structure is divided into six areas with reinforced concrete partitions: (1) entryway, (2) work/rest area, (3) latrine area, (4) work/mess area, (5) clean mechanical room (CMR), and (6) dirty mechanical room (DMR). The Toxic Free Area (TFA) is protected from chemical/biological contamination and includes the work/rest area, the latrine area, the work/mess area, and the CMR. The test article has four modules and one entryway. The electrical and mechanical subsystems provide one week of self-sustained operation in a hostile chemically toxic environment. The major components of these systems, as well as the bomb locations, are shown in Fig. 1. The shelter has an emergency power supply (diesel generator) located in the DMR. The ventilation system is designed to mitigate contamination from chemical and biological agents by maintaining a positive interior pressure of 25.4 mm (1 in) of water. Contaminated air is brought into the shelter through the blast valves and blown through the CBR filter to the TFA, pressurizing the TFA. The plumbing system includes a chemical toilet, in addition to a conventional one, and the sinks in the latrine and mess areas can operate from base, as well as the shelter, water supply. The electrical system provides power for operation of the heating, ventilating and air conditioning (HVAC) system, lights, and user-provided items, and operates through various control and breaker panels. The shelter is half-buried and bermed above grade; that is, the spring line of the shelter is approximately even with the ground surface. Below the existing ground surface, the area around the shelter is backfilled with compacted earth. Above the ground surface, the shelter is bermed with loose soil from excavation.

4.0 MODULE PANELS

The modules are made from reinforced concrete flat plate wall, roof, and floor panels. Wall and roof/floor panels are welded together using the embedded base plates at interior locations, and using these plates along with steel cover plates at exterior sidewalls to roof/floor locations. Then, using neoprene material to seal the TFA, modules are fitted together longitudinally with bell and spigot joints.

5.0 ENDWALL

The endwall has planar dimensions of 8.0 m x 4.0 m (315.0 in x 157.5 in) nominal. As an addition, neoprene seals partially embedded in the endwall were used to seal all rooms adjacent to endwalls to maintain the TFA and provide a uniform bearing surface. The endwall panels are bolted into anchors embedded in the adjacent modules.

6.0 GENERATOR

Button-up power is provided to the shelter by a diesel generator set. The unit which consists of the generator and diesel engine is mounted on top of a 1362 liter (360-gal) fuel tank. The entire system with full fuel tank weighs 2721 kg (6000 lbs). The generator and diesel engine are attached to two parallel steel rails using rubber motor mounts. The tank is hard-mounted to the floor of the structure.

7.0 INSTRUMENTATION

The BDCC structure was constructed with instrumentation cast in place to record the four separate events. This system included approximately 220 different gages, most of them being triaxial accelerometers, rebar strain gages and interface pressure (IP) gages. Structural accelerometers were used to substantiate expected motion, and passive displacement (scratch gages) were used to obtain peak and permanent displacements. High-speed photography within the shelter provided coverage of the intermodule motions. Ground-shock instrumentation was used for free field measurements during Events A and D. Each gage location included a canister assembly containing a biaxial pair of accelerometers, sensing both horizontal and vertical directions. Located with the canisters were soil stress paddles which were oriented to measure horizontal stress. IP gages were fielded on each module and were selectively turned on during each test event to document pressure time histories for structural analysis and to obtain correlations to pretest predictions. Strain gages were attached to the steel rebar in the panels at each face, providing strain at both interior and exterior panel faces. Triaxial accelerometers were located at the base of each equipment item with the exception of the air ducts. The electrical instrumentation consisted of voltage and current measurements tracing two circuits. The purpose was to determine if any electrical transients were introduced by the shock environment.

8.0 TEST RESULTS

The main loading mechanism in all three buried shots is the directed-induced ground-shock. This source-generated compressive loading wave imparts soil motions and stresses radially outward from the explosion. Secondary ground-shock loading is caused by tensile reflections from the free surface and compressive reflections from deeper soil or rock layers. Data recovery from accelerometers was good. Irregular waveforms from some stress gages, however, suggest gage-soil coupling problems. Profiles of craters for Events A, C and D are consistent except for minor variations near the structural wall. Pretest cratering calculations obtained using /2/ predicted crater dimensions well. Recorded peak accelerations and stress measurements were also in agreement with predictive calculations.

9.0 GROUND-SHOCK

In Events A and D, the energy source was a U.S. Mk-83 1000-lb GP bomb buried vertically with its center of gravity (CG) positioned 4.28 m (14.0 ft) below the surface. The bomb was near its optimum depth of burial (DOB) which was calculated using /2/. The direct-induced ground shock traveling at a loading velocity slightly lower than the seismic P-wave velocity, produced soil stresses and particle motions radially outward from the explosion. The bomb's cylindrical shape appears to have produced strong tangential or shear waves. Spalling was also evident in readings from near surface accelerometers. Spall occurs when the tensile surface reflected shock imparts stresses greater than the tensile strength of the soil. At the depth the spall occurs, material closer to the surface separates from that at greater depth, leaving a void. The upper material then falls, after passage of the tensile stress, and rejoins the lower material creating a distinctive signal. The acceleration history of a spall typically shows the direct shock, quickly followed by a sharp decay which levels off at -1 g for several milliseconds (called a "-1 g dwell") /3/. Figure 2 shows a well defined spall.

Peak attenuations of particle accelerations, particle velocities, and stresses plotted against their respective predicted attenuations are shown in Figures 3 to 5. Along the bomb CG, data scatter of recorded peak accelerations, peak velocities, and peak stresses fell within a factor of 1.68, 1.41 and 1.61, respectively of the predicted line. Peak particle acceleration attenuation appears to be insensitive to target location, whether above or along the bomb

CG. Peak velocity readings from target locations above the bomb CG were much higher than predicted peaks. The difference is due to the effect of surface-reflected tensile waves on vertical particle motions. Although data recovery was not optimum for peak stresses, data points along the bomb CG were in good agreement with the predictions. Stress peaks measured above the bomb CG were lower than predicted primarily due to the nonradial gage orientation with respect to the bomb CG. Recorded velocity and stress time history waveforms were also compared with predicted waveforms. Both the Waterways Experiment Station (WES) semi-empirical method /4/ and AFTON /4.2/ finite difference computer runs were used in this comparison. It can be seen in Fig. 6 that agreement was good except that, at the closest range, the WES method calculation decayed faster than the observed waveform.

10.0 CRATERING

Predictive methods from /2/ (Air Force Method) and /4/ (WES Method) were used to estimate cratering diameter and depth. Both methods have an empirical basis. For this particular test, the Air Force Method produced predictions very close to the observed size. The WES Method overpredicted crater radius by 15 percent and depth by 65 percent.

11.0 SYSTEM RESPONSE

The primary structural response consisted of low-level intermodule gap opening and closing, module uplift, and slight flexure of floor, wall, and roof panels. The system survived with no apparent distress in the module panels; however, cumulative intermodule gap openings became significant. Strain levels were well within the elastic range of response for the reinforced concrete panels. In addition, some severe cracking, spalling, and joint seal slippage occurred at intermodule joints, but did not threaten system survivability. Brittle behavior was expected for the connections and was verified in subsequent tests (See /5/). Direct result of efforts to provide more ductile connections is given in /6/.

The electrical response was characterized by minor power fluctuations. The system remained on line and no circuit breakers were tripped. A portion of the conduit system failed to flex with the modules because of improper installation.

Detonations produced no appreciable damage to any of the mechanical equipment in the BDCC structure. The experienced environment, for each equipment item, in terms of Shock Response Spectra (SRS) was overlayed with SAFEGUARD shock tolerance curves. The close relative position of the two curves indicated damage was not likely.

REFERENCES

1. Satterthwaite, B., et al., Base Damage Control Center (BDCC) Final Analysis Report, NTE-TN-003-89, Civil Engineering Research Division, Air Force Weapons Laboratory, Kirtland AFB, NM, January 1989.

2. Crawford, R.F., et al., Protection from Nonnuclear Weapons, AFWL-TR-70-127, Air Force Weapons Laboratory, Kirtland AFB, NM, 1971. (Limited Distribution)

3. Stump, B.W. and Reinke, R.E., Spall Observations and Mechanisms in Alluvium, Journal of Geophysical Research, Vol. 89, No. B13, pp. 11,495-11506, 1984. (Limited Distribution)

4. Fundamentals of Protective Design for Conventional Weapons, Structures Laboratory, Waterways Experiment Station, Corps of Engineers, Vicksburg, Mississippi, 1984. (Limited Distribution)

5. Satterthwaite, B., et al., Modular Structural Fragility Test Event, NTE-TN-005-88, Civil Engineering Research Division, Air Force Weapons Laboratory, Kirtland AFB, NM, October 1988.

6. Krauthammer, T., and DeSutter, M.A., Analysis and Design of Connections, Openings and Attachments for Protective Construction, WL-TR-89-44, Civil Engineering Research Division, Air Force Weapons Laboratory, Kirtland AFB, NM, October 1989.

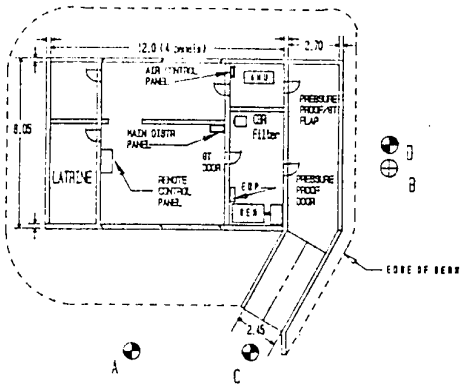

Figure 1. Plan view of test BDCC with bomb locations.

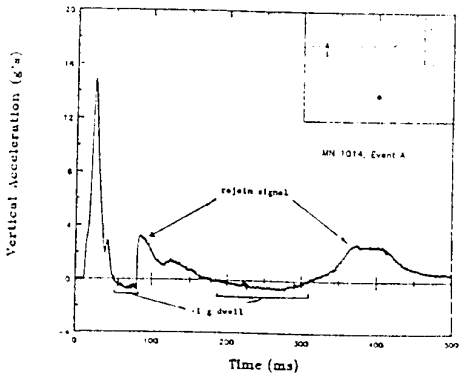

Figure 2. Spall effects on a vertically sensing accelerometer.

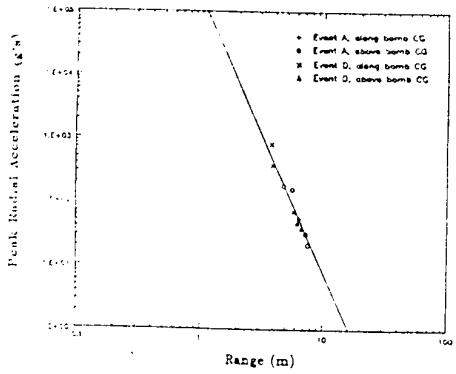

Figure 3. Comparison between recorded and predicted peak radial acceleration.

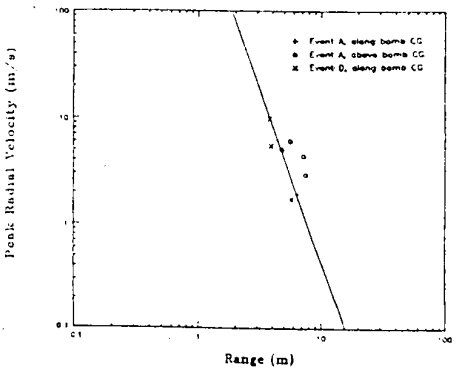

Figure 4. Comparison between recorded and predicted peak radial velocity.

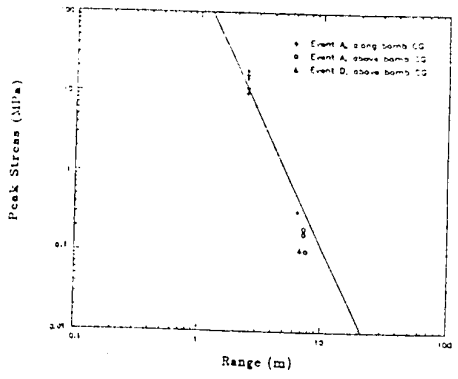

Figure 5. Comparison between recorded and predicted peak stress.

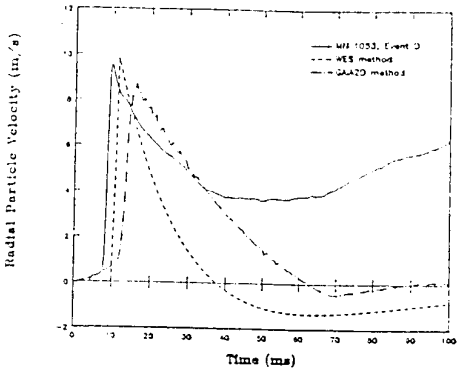

Figure 6. Comparison between recorded and predicted radial particle velocity waveforms.

EFFECTS OF ENHANCED BLAST MUNITIONS ON AIRCRAFT SHELTERS

Eugene R. Fosness, Rodney Galloway, Capt John E. Higgins, and
Capt Timothy L. Boone
Shock Physics Division, Phillips Laboratory, Kirtland AFB, NM 87117-6008

The purpose of this paper is to present the results of the blast and shock effects on a Third Generation Aircraft Shelter to various amounts of dispersed liquid fuel clouds detonated at various standoff distances from the shelter. The specific components of the shelter which were analyzed are the arch and the door. The primary thrust of this analysis may be separated into two areas; load definition and structural analysis. The structural elements were analyzed for three separate volumes of dispersed liquid fuel; 1000 kg, 500 kg, and 250 kg. The appropriate overpressure functions for the dispersed liquid fuel clouds at various ranges are determined by comparing actual experimental results to hydrocode calculations (GUSH and HULL). These overpressure functions are then applied to and reflected from the structure to create structural load functions. These structural load functions are applied to the structural model in such a manner as to simulate an attenuating shock wave passing over the structure. The structural response calculations for these load inputs were performed with finite element codes. The shelter door was modeled in three dimensions. The results for each of these analyses are discussed for each loading.

1.0 BACKGROUND

During the Vietnam War, the U.S. military used fuel-air-explosives (FAE) to remove vegetation from sites to create temporary helicopter landing areas. Because FAE provided a quick, easy method to remove jungle vegetation, this concept led to additional FAE research and development. Finite element analyses were performed to numerically characterize the structural response of the shelter components to FAE effects. The finite element code that was used in this analysis (DYNA3D) was developed at Lawrence Livermore Laboratories.

DYNA3D is an explicit three-dimensional Lagrangian finite element code.

2.0 SHELTER PHYSICAL DIMENSIONS

The shelter has a length of 120.25 feet, width of 76.15 feet, and a height of 30.33 feet. The reinforced concrete arch has a maximum thickness of 32 inches and a minimum thickness of 18 inches. The inside surface of the arch is double corrugated with a 0.125 inch steel liner that acts as a spall plate. The steel liner is attached to the arch with bolts embedded in the concrete at locations where sections of the steel liner overlap.

The front closure (door and space frame) of the shelter is composed of two 85 ton door sections and a space frame. The two door sections are attached by rollers to a guided door track that is parallel to the front of the shelter. The two door sections are composed of 11.875 inch thick reinforced concrete. The inside surface of each section has a 0.125 inch thick steel liner attached to the concrete by studs. The steel liner acts as a spall plate. A steel space frame is attached to each of the door sections to resist out-of-plane motion. The space frame is supported by rollers on tracks, parallel to the front door of the structure.

3.0 AIRBLAST LOADS

In modeling the structural loads, the first step was to establish acceptable free-field environments for selected threats which are based on test data and hydrocode calculations. The Phillips Laboratory (PL) has conducted field tests for the 1000 kg FAE yield. These tests provided free-field overpressure vs time histories at various ranges from the point of detonation. Two-dimensional hydrocode calculations (GUSH) were performed for all three FAE yields to provide pressure vs time histories for various ranges from the source. The GUSH and HULL /1/ calculations compared favorably with the test data within the ranges of interest for the 1000 kg yield, thereby establishing an acceptable level of confidence for all GUSH calculations. The GUSH pressure pulses were simplified into triangular pressure-time functions and were used to generate the structural load inputs.

The method chosen /2/ to convert the established FAE free-field pressures into structural loads parallels the methods typically used for converting airblast from conventional munitions into estimated structural loads. This approach

uses empirical reflection factors based on the magnitude of the incident overpressure (Pso), as well as the angle of incidence between the overpressure and the surface of interest. For side-on detonations, the curved surface of the shelter affects the magnitude and duration of the reflected pressure. The HULL calculations included a generic aircraft shelter modeled as a rigid semi-cylinder placed in the free-field environment. These calculations indicated that the peak pressure at the upwind base of the cylinder is approximately five times higher than the corresponding free-field. This reflection factor, 5, compares favorably with the reflection factor obtained from /2/ for the same conditions. The structural loads predicted by the HULL calculations around the remainder of the cylinder were somewhat less than those obtained from /2/. This may be due, in part, to the fact that /2/ assumes a flat surface of reflection whereas the curved surface of the arch provides additional relief. Reductions in the reflection factors obtained from /2/ were made based on the results of the SRI study. The duration of the amplified pressure curves using HULL was essentially the same as those of the corresponding free-field. A factor of less than one was used on the downwind portion of the arch to account for the outward 'drag' that occurs there.

The structure was placed just outside the cloud boundary for all scenarios. An assumption was made that the airblast formed outside the FAE cloud is similar to that of a conventional airblast. If this is true, the free-field overpressures just outside the cloud would be significantly magnified (due to the formation of a conventional airblast) on a "drag sensitive" target. However, these higher overpressures were not assumed to be as greatly magnified on the structure since the formation of a travelling airblast has not yet occurred. Since the cloud for a 1000 kg FAE has a diameter of approximately 130 feet and the shelter is approximately 120 feet long, the structural loads were assumed to be uniform along the entire length of the structure for a side-on blast. For the 500 kg and 250 kg threats, the cloud diameters are approximately 85 feet and 65 feet, respectively. Because the 500 kg and 250 kg FAE clouds have diameters smaller than the length of the shelter, peak pressure and impulse decrease rapidly along the length of the shelter with increasing distance from the center of the FAE. The load variations were approximated for the lower FAE yields to estimate the extent of damage along the length of the arch.

For maximum structural response the structure/cloud orientation was rotated 90 degrees with the front door of the shelter facing the FAE cloud. The front

door was placed at the boundary of the cloud for each load case. The door was divided into regions for loads based on the relative size of the FAE cloud compared to the overall width of the door. The load function applied to the center region of the door is based on a 90 degree angle of incidence at the cloud radius. Load functions for the outer edges/regions of the door were established as they were for the outer regions of the structure in the three-dimensional arch analyses. A load function was applied based on the appropriate angles of incidence (α) and the average distance of the zone from the center of the cloud.

4.0 ARCH MODEL AND FAILURE CRITERION

The shelter is composed of reinforced concrete that was modelled with an unconfined compressive strength of 5000 psi and a Poisson's ratio, of 0.2. The contributions of the steel liner and reinforcing bars were "smeared" into the concrete model, resulting in an effective elastic modulus, E, of 4.64E6 psi. An elastic-plastic model was chosen to reflect an anticipated compression failure mode in the in-plane circumferential direction. The unconfined compressive strength of concrete was used as the yield stress limit in the elastic-plastic model. Unreinforced concrete is tending toward failure when compressive strains greater than 0.003 occur. A failure mechanism for the arch is predicted to occur when the strain in the concrete reaches 0.006 which is the failure criterion used in this study. Initial calculations indicate strain rates at early times are on the order of 1./sec. Information on rate effects in concrete /3/ suggests that, for the strain rates observed in this analysis, the net plastic strain energy at failure (monotonic loads) can be enhanced over the static value. Also, biaxial (out of plane) confinement contributes to increased plastic strain energy at failure. Hence, a factor of two was applied to the failure strain in this analysis.

5.0 THREE DIMENSIONAL ARCH MODEL

The three-dimensional response of the arch was investigated to determine the effects of load localization and end restraints. The arch was constructed of 4-node Belytschko-Tsay shell elements for solution using DYNA3D. The arch shell was constructed of multiple regions having different uniform pressure distributions and radii of curvature matching the actual structure.

The arch was modeled (Figure 1) with 80 nodes around the circumference and 61 nodes longitudinally. The circumferential nodes were concentrated in sectors within 60 degrees of the foundation to capture the principal inelastic responses in these areas. A uniform spacing of nodes was chosen in the longitudinal direction.

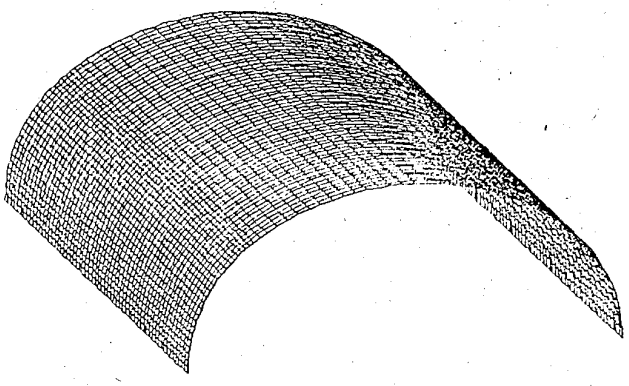

Figure 1. Three-dimensional finite element arch model.

For each of the FAE yields, the FAE cloud boundaries are nearly tangent to the foundation of the arch closest to ground zero. Edge effects were simulated by the following boundary conditions: (1) nodes along the door edge of the arch were unrestrained against translation and rotation (free), (2) nodes along the rear wall of the shelter were restrained against translation and rotation in all directions (fixed), and (3) nodes along the foundation were restrained against all rotation and vertical and lateral (radial) translation. Translation along the length of the foundation was unrestrained to avoid generation of unrealistic stresses resulting from in-plane Poisson's effects.

The arch thickness (25 inches) is consistent with the average thickness of the corrugated arch wall section (25.2 inches). The effective thickness required to equal the uncracked moment of inertia of the corrugated arch section about the longitudinal (z) axis is 28.2 inches. Error in moment of inertia to the point of initial cracking is approximately 30 percent below actual values. Since initial failure of the arch was believed to be compression dominated, a thickness of 25 inches was considered reasonable and appropriate for these calculations.

6.0 CLOSURE MODEL AND FAILURE CRITERION

Failure of the closure is assumed to occur when the out-of-plane displacements of the door panels are greater than 30 percent of the span of the panel or when the plastic strains in the reinforced concrete door panels are greater than 10 percent. A 10 % strain is the maximum ductility that is allowed for a plate (door) in bending. This is a conservative estimate of total strain and deflection of the closure because the attachment points of the steel space frame members to the door are ideal and allow for no break in welds. Catastrophic failure in bending is associated with strains greater than 30 %.

The door was constructed of 4-node Belytschko-Tsay shell elements for solution using DYNA3D. The concrete door was modeled as an elastic-plastic material. The effects of the steel liner and the internal reinforcement were "smeared" to get an elastic modulus of 4.04E6. The door is expected to fail in flexure. An effective yield stress of 1500 psi (compression/tension) was calculated for the elastic-plastic model, in order to provide an equivalent ultimate moment capacity in the door.

The steel members of the space frame were modelled to have an elastic modulus of 29E6 psi, a yield strength of 36 ksi, and a strain hardening slope of 5 degrees. Each door is composed of four reinforced concrete panels that are framed by channel sections. These panels were attached to a space frame that provides lateral support to the door and is intended to resist rebound forces from a dynamic load. A simple-support boundary condition was used to model the bottom and curved edge of the closure. The third (vertical) edge of the door was free. A total of 341 beam elements and 184 shell elements were used to model the door and the attached space frame (Figure 2).

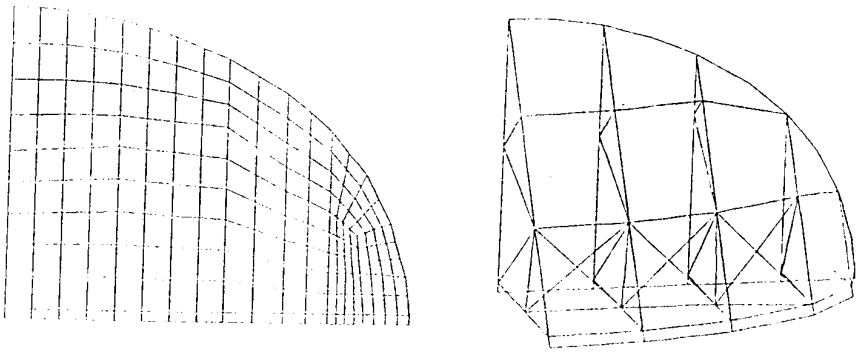

Figure 2. Three-dimensional finite element door and space frame model.

7.0 RESULTS AND CONCLUSIONS

The FAE source region is basically characterized by a distributed cloud of explosive, atomized fuel particles, ignited at a discrete number of points. This distributed source region is very different in nature from typical conventional explosives. The ramifications of this difference are not sufficiently understood yet.

Preliminary test data for FAE airblast/structure reflection factors suggest that actual structural loads may be as much as 50 percent less than the loads which were determined with the use of the equivalent procedure given in the design manual. Similar over-estimates of loads are apparent in the direct modeling of the rigid arch structure in the HULL calculations. The results of HULL calculations and field tests confirm that travelling wave effects with delayed TOA and rapid pressure attenuation are characteristic of arch loads for structures located outside the cloud.

On the upwind side, the arch is expected to respond primarily in circumferential compression, with secondary bending. An early rise in circumferential stress on the upwind side of the arch is predicted. Plastic response of the arch is expected to occur at two regions on the upwind side of the arch. The region of largest plastic strains occurred at the inner face of the arch near the foundation. A second region of plastic strain is centered about 15 degrees above the foundation. Maximum plastic strains in this second region are located at the outer face of the arch and are approximately half the maximums computed at the foundation. Differences in peak strains for the 1000 and 500 kg yields were marginal. Beyond initial development of plastic mechanisms described previously, very little additional structural deformation or growth in plastic strain is noted.

The following edge effects and load localization effects were noted: (1) the response at the free end of the arch was very similar to the response near the midlength of the arch. Response within ten feet of the rear wall of the shelter, simulated by edge fixity, was limited to elastic response only, (even for the largest yield), and (2) for the 1000 kg yield, the pressure was distributed uniformly along the length of the arch. A very uniform distribution of plastic strains developed along this entire length, except in the vicinity of the constrained rear wall. For the 500 and 250 kg yields, plastic strains were limited to regions of maximum loads, centered on the location

tangent to the cloud radius in plan view. This localization effect was observed in both free-end and mid-length arch locations of the load.

The elastic-plastic material model assumed for these arch analyses probably underestimates early strains, but correctly identifies the nature and location of the initial failure mechanism. Late time response, to 100 msec, is probably grossly under estimated as the character of structure response changes with time to weaker response modes.

For the three-dimensional closure analyses, the door response is characterized by inelastic out-of-plane deflections. The deflections and rotations predicted for the space frame members in this analysis may cause welds to fail in several places on the space frame. The failure of welds in the space frame would reduce the overall stiffness of the closure resulting in larger deflections.

It is recommended that additional analytical studies and field testing be performed associated with FAE/structure interaction to better characterize loads to be distributed to the structure. As more is known about the nature of pressure development and flow inside, as well as outside, the cloud for FAE type munitions, modelling refinements may be needed to correctly assess reflected pressures on the shelter. In the interim, it is strongly recommended that direct field testing be performed on FAE loaded shelters to confirm the level of structural response described in the present study.

REFERENCES

1. Simons, J. W., Sanai, P. R. Gefken, and Colton, J. D., (1989), "Effectiveness of FAE Weapons", Defense Nuclear Agency (DNA) Contract: DNA 001-89-C-0003, SRI International, Menlo Park, CA 94025, Progress Report No. 2.

2. Crawford, R. E., et al, (1971), "Protection From Nonnuclear Weapons", Technical Report AFWL-TR-70-127, Air Force Weapons Laboratory, Kirtland Air Force Base, NM, 8-6 pp. Distribution limited to U.S. Government and associated contractors.

3. Gran, J. K., (1987), "Research on Advanced Silo Hardening (ASH) Instrumentation and Material Properties, Vol III: Dynamic Triaxial Compression Tests on High-Strength Concrete", Defense Nuclear Agency (DNA) Contract: DNA 001-85-C-0085, SRI International, Menlo Park, CA 94025.

MODIFIED ANALYSIS OF REINFORCED CONCRETE STRUCTURES UNDER IMPULSIVE LOADS

T. Krauthammer and H.M. Shanaa

Penn State University, University Park, Pennsylvania, U.S.A.

INTRODUCTION

An analytical/numerical approach for the investigation of reinforced concrete structures subjected to localized high intensity short duration dynamic loads is presented. The approach utilizes the Timoshenko Beam Theory for modelling the structure, the solution is obtained using the Finite Difference method, and nonlinear material models are used for obtaining the structural resistance. This study is aimed at expanding a previous approach by Assadi-Lamouki and Krauthammer (1989) by including the effects of concentrated loads, and by introducing new failure criteria.

STRUCTURAL MODELING

The present approach is based on the Timoshenko beam theory (1921), as follows:

$$\frac{\partial M}{\partial x} - Q = -\rho_m I \frac{\partial^2 \beta}{\partial t^2} \tag{1}$$

$$\frac{\partial Q}{\partial x} + q + P \frac{\partial \beta}{\partial x} = \rho_m A \frac{\partial^2 W}{\partial t^2} \tag{2}$$

where, M,Q are the bending moment and shear force, respectively, I is the moment of inertia, A is the cross-sectional area, ρ_m is the material density, β is the rotation of the cross section due to bending, W is the transverse displacement of the midplane of the beam, P is the axial force in the member acting at the plastic centroid of the cross section, and q is the uniformly distributed dynamic load transverse to beam length. In this study the goal is to enable consideration of localized loads.

To simplify the problem, Timoshenko (1921) assumed that the shear stress is constant over the cross sectional area. To correct for the error stemming from this assumption, a factor K was introduced, such that:

$$Q = K A \tau_{xz} \tag{3}$$

where, K is the shear deformation correction coefficient, A is the cross-sectional area, and τ_{xz} is the shear stress. Ross (1983) argued that, under the high frequency loading considered, where shear is critical, K should be:

$$K = \pi^2 / 12 \tag{4}$$

The bending moment, M, and the shear force, Q, are related to the deformation of the structure through curvature, ϕ, and shear strain, γ_{xz}, respectively. For an elastic material with elasticity modulus E and shear modulus G these relationships can be expressed as:

$$Q = K A G \gamma_{xz} \tag{5}$$

$$M = E I \phi \tag{6}$$

In the case of nonlinear material models, these relationships are expressed as numerical functions given by the shear force-strain relationship, relating the shear force to the shear strain, and by the moment-curvature relationship, relating the moment to the curvature. The method used to compute the moment-curvature relationship is that discussed by Krauthammer et al. (1987), while the compression field theory is used to derive the shear force-strain relationship, as discussed by Collins and Mitchell (1991). Nonlinear constitutive laws for concrete and steel are used to derive these relationships. In addition, strain rate effects are used to enhance the properties of each material before it is used in the above models. Following previous studies by Ross (1983) and Assadi-Lamouki and Krauthammer (1989) it is assumed that the stress rate is equivalent to the loading rate. This may not be generally true since one is an external phenomenon, while the other is the internal response. Nevertheless, this assumption allows the determination of the enhancement factor from experimentally observed loading rates.

As in the previous study, this model can address non-ideal support conditions, such as nonlinear rotational and transverse springs. This allows better modeling for elements that are continuous with other neighboring elements. In this case the moment at the support is related to the rotation at the support through the rotational spring representing the restraint that neighboring members impose. On the other hand, the shear force at the support, i.e. the vertical reaction, is related to the slip at the support through the transverse spring. In addition, a similar approach is implemented under the load, where a direct shear slip may occur.

DYNAMIC RESISTANCE MODEL

The resistances models (moment-curvature, shear force-strain, moment-rotation, and shear force-slip) described in the previous section were derived for loading in the static domain, and were further modified to include strain rate effects. In order to use these models in the dynamic domain, however, provisions must be included for unloading, re-loading, and load reversals. Krauthammer et al. (1990) proposed such a model to construct from the static force-deformation relationships, a dynamic force-deformation resistance function for nonlinear analysis. The model shown in Figure 1 provides the means for incorporating cyclic and hysteretic behavior in reinforced concrete. It is stipulated that the dynamic resistances are bounded by the envelope of the strain rate enhanced static resistances, as represented by curve OAC in Figure 1. Point C represents the failure point of the resistance function in question. If during a loading cycle the deformation exceeds the value of deformation at point C, i.e. the ultimate resistance (or failure) point on the load-deformation curve, failure is assumed.

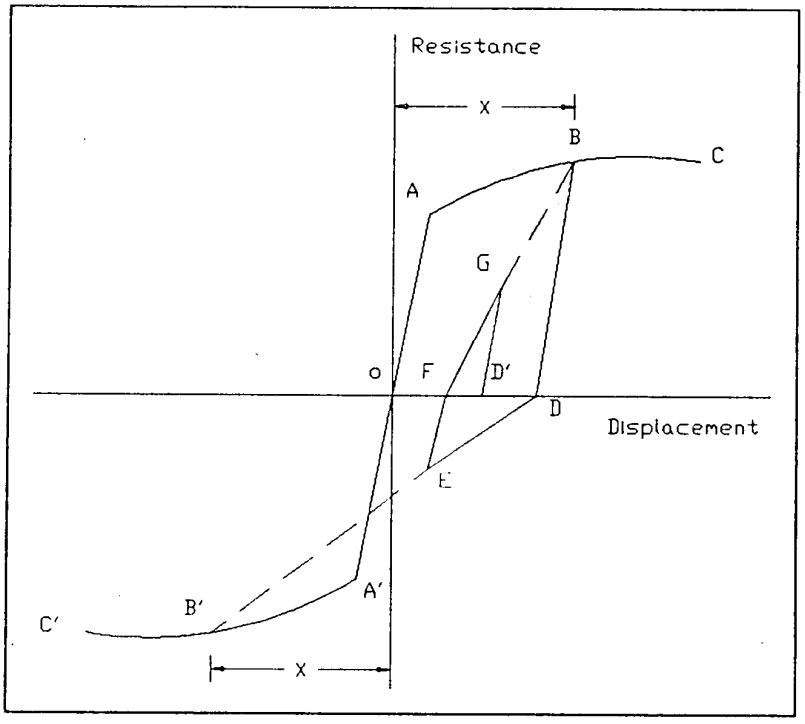

Figure 1. Dynamic Resistance Model.

FAILURE CRITERIA

In the earlier study (Assadi-Lamouki and Krauthammer 1989), the failure point of a given resistance, such as point C in Figure 1, was taken as the peak point on the enhanced static resistance model. The beam was classified as "failed" in a certain mode based on that specific resistance function whose peak capacity had been reached first. For instance, a direct shear failure was declared as soon as the shear slip at the support reached its slip value at the peak strength. Similarly, a flexural failure was concluded if the curvature of the cross section at the support (location of maximum moment) reached its threshold limit (ultimate curvature). Whereas the diagonal shear failure was noted when the shear strain at a particular point reached the corresponding ultimate shear strain. Hence, the failure type was attributed to the failure criterion triggered first. This failure definition, however, is simplistic and may not be precise for predicting failure. A structure "failing" according to the above criteria will still have reserve strength when reaching the above thresholds. This is evident in cases that fail by reaching the ultimate moment at the support, for this threshold only marks the initiation of a plastic hinge. The structure can actually fail in flexure only when a sufficient number of "full hinges" develop, as discussed by Krauthammer et al. (1990). The same argument can also be presented for the other resistance models.

A new approach for studying failure is proposed herein. It is understood that the above thresholds only indicate failure initiation. However, the ductility and the strength of the different resistance functions considered and the dynamic stress redistributions, will determine whether the first mode to reach its threshold may lead to the actual failure of the structure. Such ductility and strength may subdue the effects of the first "failure" mode, while another mechanism is triggered, which in turn may or may not cause the actual failure. Eventually, it is hypothesized that the sequence of these events, and the times when they occur, gives a clearer and truer picture of what happened to the structure. Then, careful evaluation of this sequence could lead to a more realistic, and hopefully more accurate, indication of failure.

NUMERICAL TECHNIQUE & SOLUTION PROCESS

The finite difference method was utilized in this study for obtaining the structural response. This method is based on discretizing the continuum into an assemblage of nodes, and then, expressing the partial derivatives of a function at a node in terms of the difference (i.e. slope) in that function with respect to neighboring nodes (Godunov and Ryabenkii 1987). The equations of motion of the Timoshenko beam (Eqs. 1 and 2), are transformed to algebraic equations by the finite difference formulations leading to the following two equations:

$$\beta(x,t+\Delta t) = 2\,\beta(x,t) - \beta(x,t-\Delta t) - \frac{(\Delta t)^2}{\rho_m I}\left(\frac{M(x+\Delta x,t) - M(x-\Delta x,t)}{2\,\Delta x} - Q(x,t)\right) \tag{7}$$

$$W(x,t+\Delta t) = 2\,W(x,t) - W(x,t-\Delta t) + \frac{(\Delta t)^2}{\rho_m A}\left[\frac{Q(x+\Delta x,t) - Q(x-\Delta x,t)}{2\,\Delta x} + q(x,t) + p\,\frac{\beta(x+\Delta x,t) - \beta(x-\Delta x,t)}{2\,\Delta x}\right] \tag{8}$$

Eqs. (7 and 8) exhibit an explicit form since the only unknown quantities, β and W at a typical node x at time $t+\Delta t$, appear on the left hand side. While, only known quantities, which belong to the preceding time steps t and $t-\Delta t$, appear at the right hand side. Thus, these two unknown quantities are readily computable once the values at the previous two time steps are known. Therefore, given initial conditions at time zero, a marching through time is initiated and the quantities will be easily computed for the next time steps. One should note, however, that Eqs. (7 and 8) will introduce a problem when the node is at a boundary, since there are no nodes at $x-\Delta x$ for the left boundary, or $x+\Delta x$ for the right boundary. Traditionally, this was overcome by implementing imaginary nodes at the boundaries. This is not an easy task, if at all possible, where the boundary is complex. The present solution for this difficulty is that at the boundary a different difference formulation is used than that used for the central nodes. At the boundaries a forward difference scheme is used at the left support, while a backward scheme is utilized at the right support. These formulations do not require any nodes outside the supports.

At this stage the differential equations of the Timoshenko beam have been transformed to explicit functions expressing the deformations, W and β, at a location x at time $t+\Delta t$, as a function of the state of the beam at the previous time steps. First, initial and boundary conditions are applied to the deformations, moments, and shears at each node at the

first two time steps. Next, the transformed equations of motions (Eqs. 16 and 17) are applied to find β and W for all the nodes at time $t+\Delta t$. Then these new values of β and W at this time step are utilized to obtain the shear strain and curvature of the cross section at all nodal points. After the deformations are computed, the internal forces and reactions are obtained from the moment-curvature, shear force-strain and the shear force-slip relationships. Then, a new time step is executed, utilizing the values (β, W, M, and V) from the latest two time steps. In addition, at each time step the failure criteria are checked.

STABILITY AND CONVERGENCE

In order to utilize the explicit time integration method, the time step should be small enough so that information (e.g. disturbances) cannot travel from one node to another within one time step. Hence, the time step must be limited by:

$$\Delta t < \Delta x / v_{max} \tag{9}$$

Δx is the nodal spacing, and v_{max} is the highest speed of disturbance propagation, C_L given by (Fung 1965):

$$C_L = \left[\frac{E(1-\nu)}{(1+\nu)(1-2\nu)\rho_m} \right]^{1/2} = v_{max} \tag{10}$$

where, E is the elastic modulus, ν is poisson's ratio, and ρ_m is the mass density. Any Δt satisfying Eq. (9) will guarantee stability of the solution process. These limits are true for elastic materials, but for nonlinear materials such a formulation is not a straight forward matter. Qualitatively, however, for typical strain softening materials, E decreases along the stress-strain curve, hence, if the initial E is used in Eq. (10), the time step obtained will be the smallest possible value. In addition to this limit, the time step must be sufficiently small to get a reasonably resolution on the loading function.

Another important issue in the finite difference modelling of a beam is the number of nodes, and hence, the increment Δx, used in the discretization of the beam. This has a direct effect on the time step, on the solution accuracy, and on the solution speed. Therefore, it is desirable to obtain an estimate on the minimum number of nodes that must be used for obtaining a certain accuracy. Two factors influence this selection. First, the node spacing should not exceed a dimension equal to the beam depth in order to obtain a realistic shear deformation. Second, The number of nodes affects primarily the number of modes that can be modeled in a vibration problem, which in turn controls how high a frequency may be modeled accurately. The lower the frequency required, the lower the number of modes needed for accurate modeling, and hence, the lower the number of nodes. The highest frequency that should be modeled is governed by the frequency content of the load. The loads considered in this study could contain high frequencies, hence, one must decide on how high a frequency should be included in the analysis, and hence, the number of nodes. Ideally, the consideration of the entire frequency content of the load may require an infinite number of nodal points, an impossible task to achieve.

LOCALIZED LOAD APPLICATION

There were two problems associated with the application of a concentrated force. The first, was that the original Timoshenko beam formulation corresponds to distributed loads only. This was overcome by assuming that the load was uniformly distributed over the node where it is applied. Hence, the concentrated load was divided by the nodal spacing to obtain an equivalent uniform load to be applied at the node. The second difficulty was due to that the application of a single concentrated force resulted in a discontinuity in the shear diagram at the point of application. The sign of the shear force is opposite on each side of the load, hence, at one point there are two different shear forces, one positive and one negative. This problem was eliminated by splitting the load into two concentrated forces at two adjoining nodes where the load was applied.

There are two other reasons for applying the load at two nodes instead of one node. The first follows the requirement that hinges must develop at points of maximum moment, as observed in experiments. If the load is applied over two nodes, there will be a region between the two nodes where the moment will be constant, over which concentrated rotations occur, and hence simulating a hinge. Of course, in this case the solution may become dependent on the nodal spacing. The second reason is that in practice, concentrated loads are usually applied over a finite distance.

EXAMPLE CASE

The numerical procedure was used to analyze several cases of impact loaded reinforced concrete beams tested by Feldman and Siess (1958). One such case, beam C-1, was simply supported over a span of 106" and loaded at midspan with an impact load. The beam was 6" wide, 12" deep, with an effective depth of 10.063". The beam had 2-#7 bars at the bottom, and 2-#6 at the top. The steel yield strength was 46 ksi, and the concrete compressive strength was 5635 psi. For these test case the initial strain rates were recorded during the experiments, which provided for case C-1 an enhancement of 35%. The experimental load was digitized and applied to the beam, as shown in Figure 2. The computed moment-curvature diagram is shown in Figure 3.

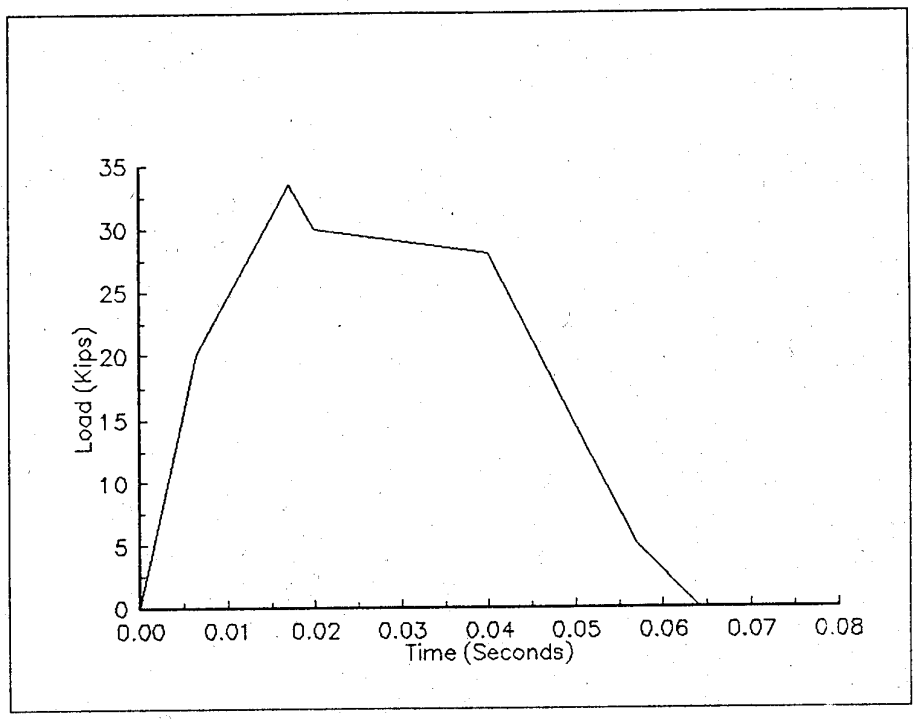

Figure 2. Idealized Load - Time History for Beam C-1.

For this illustration, the beam was discretized into nineteen elements with 20 nodes, and hence, the nodal spacing was 5.579". A critical time step of 0.038 msec was derived from Eq. (9), using a mass density of $2.172*10^{-7}$ kips*sec^2/inch^4, an elastic modulus of 4300 ksi, and a Poisson ratio of 0.17. A time step of 0.01 msec was used, and the solution was obtained up to 60 msec (6000 time steps). The solution required about 1.5 minutes on a 25 Mhz 386/387 micro-computer. The results from the analysis are presented in Figures 4 through 6, and compared to experimental results where available. First, the midspan deflection, with peak value of 3.1" at 43 msec, compares well with the experimental peak value of 3.0" at 50 msec, as shown in Figure 4. Second, the computed reaction follow closely the measured reactions, as shown in Figure 5. The midspan moment is shown in Figure 6.

CONCLUSIONS

The proposed approach can be used very effectively for the analysis of reinforced concrete structures under uniformly distributed and/or localized impulsive loads. This study is continuing, and the issues of failure criteria, development of plastic hinges, support modeling, and the judicious application of the concentrated forces are under consideration. In addition, the computer program will be extended to handle different types of loads, and combinations of loads.

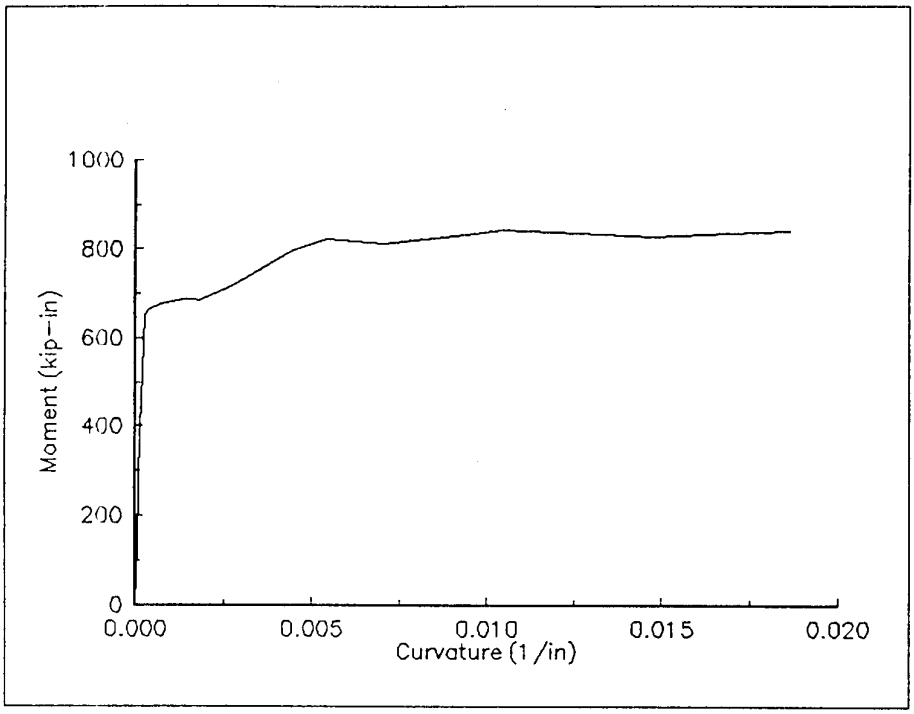

Figure 3. Computed Moment - Curvature Relationship for Beam C-1.

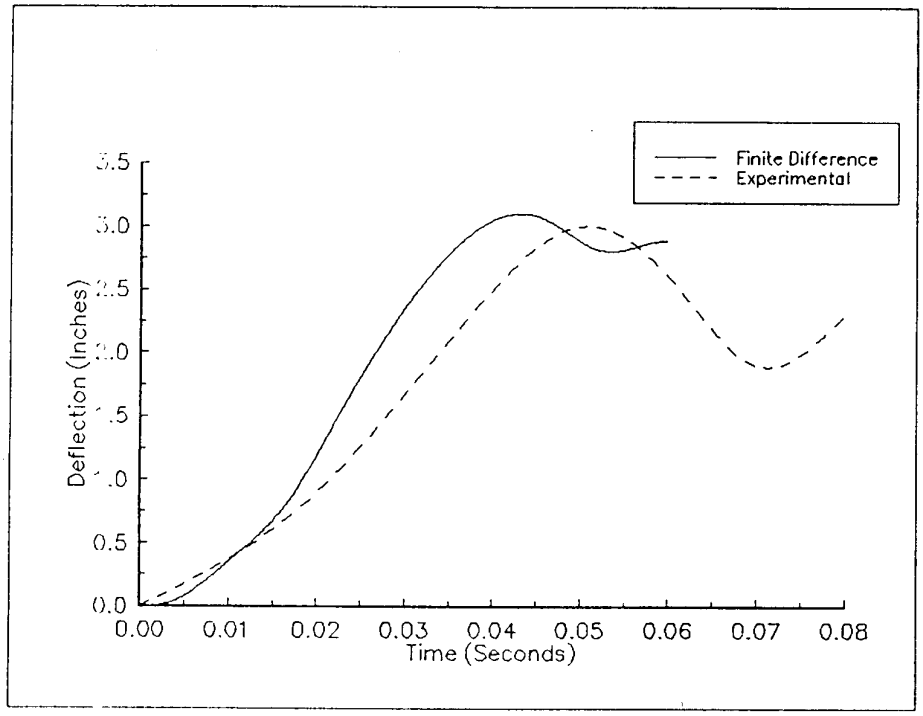

Figure 4. Computed and Experimental Midspan Deflections for Beam C-1.

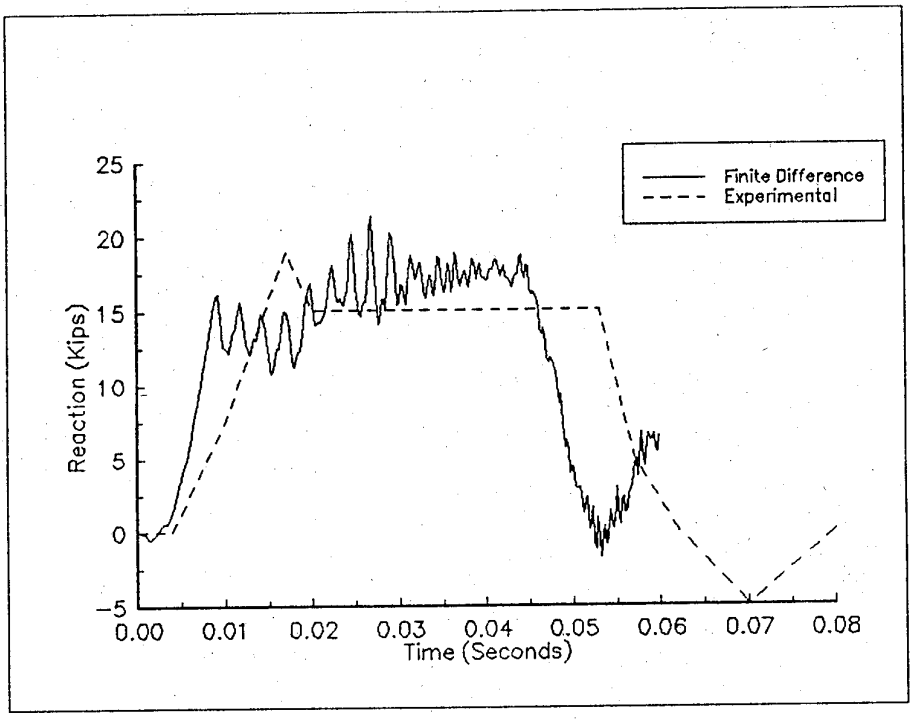

Figure 5. Computed and Experimental Support Reactions for Beam C-1.

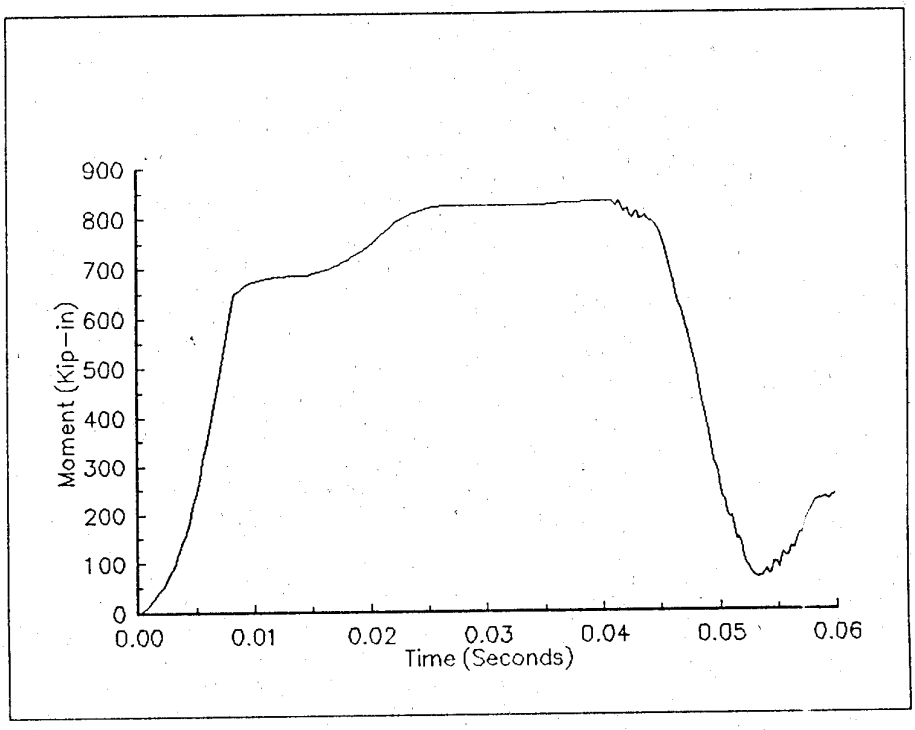

Figure 6. Computed Midspan Bending Moment for Beam C-1.

REFERENCES

Assadi-Lamouki, A. and Krauthammer, T. (1989), "A Modified Timoshenko Beam Approach for the Analysis of Reinforced Concrete Structures Under Impulsive Loads", Proc. 4th International Symposium on the Interaction of Non-nuclear Munitions with Structures, Panama City Beach, Florida, 17-21 April, pp 196-201.

Collins, M. P., and Mitchell, D. (1991), "Prestressed Concrete Structures", Prentice-Hall, Englewood Cliffs, New Jersey.

Feldman, A., and Siess, C. P. (1985), "Investigation of Resistance and Behavior of Reinforced Concrete Members Subjected to Dynamic Loading, Part II", Structural Research Series No. 165; Civil Engineering Department, University of Illinois. Urbana, Illinois.

Fung, Y.C. (1965), "Foundation of Solid Mechanics", Prentice-Hall, Englewood Cliffs, New Jersey.

Godunov, S.K., and Ryabenkii, V.S. (1987), "Difference Schemes", Elsevier, New York.

Krauthammer, T., Shahriar, S., and Shanaa (April 1990), H. M., "Response of RC Elements to Severe Impulsive Loads", Journal of Structural Engineering, ASCE, Vol. 116, No. 4, pp. 1061-1079.

Krauthammer, T., Shahriar, S., and Shanaa, H.M. (November-December 1987), "Analysis of Reinforced Concrete Beams Subjected to Severe Concentrated Loads", Structural Journal, ACI, Vol. 84, No. 6, pp. 473-480.

Ross, T.J. (September 1983), "Direct Shear Failure in Reinforced Concrete Beams Under Impulsive Loading", Report No. AFWL-TR-83-84, Air Force Weapons Laboratory, Kirtland Air Force Base, New Mexico.

Timoshenko, S.P. (1921), "On the Correction for Shear of the Differential Equation for Transverse Vibrations of Prismatic Bars", Philosophical Magazine, Series 6, Vol. 41, London, England, pp. 744-746.

THE EFFECT OF BERMING ON THE RESPONSE OF STRUCTURES SUBJECTED TO NEARBY EXPLOSIONS

Helge Langberg

Norwegian Defence Research Establishment

ABSTRACT

A series of small scale blast experiments was performed in order to study the effect of having a soil berm outside the wall of a structure. The experimental results showed in general good agreement with the results based on the Pressure–Impulse (P–I) diagram theory. This theoretical approach could then be used for the study of a large concrete wall exposed to nearby detonations, showing that in most situations a soil berm tends to reduce the vulnerability of protected structures.

1. INTRODUCTION

In the design of protected structures, considerable concern has been expressed to the problem of having a soil berm outside the wall of a structure. It has been argued that a soil berm will increase the blast effect and hence the damage level of a structure. Several blast experiments, however, have indicated that a soil berm tends to reduce and not increase the blast effect.

In order to investigate this problem, a series of small scale blast experiments was carried out using two steelplates with the same dimensions (300 mm x 300 mm), but different thicknesses as the blast targets. These experiments were designed to give strain and pressure levels for a range of stand–off distances for both buried bursts and air blasts. The experimental results were also compared with the results obtained from a theoretical approach.

2. SMALL SCALE BLAST EXPERIMENTS

The first experimental test–series was performed with a 10 mm thick steelplate exposed to C–4 charges detonated at different stand–off distances in air. This test set–up was repeated keeping both the charge and the steelplate buried in sand, allowing the difference in plate response to be studied. Figure 1 shows the test set–up. An identical test–series was carried out against a 30 mm thick steelplate. Table 1 gives the total number of blast experiments in the test series. It is beyond the scope of this short report to present all test results, however, typical results for the two plate thicknesses are compared in Figure 2.

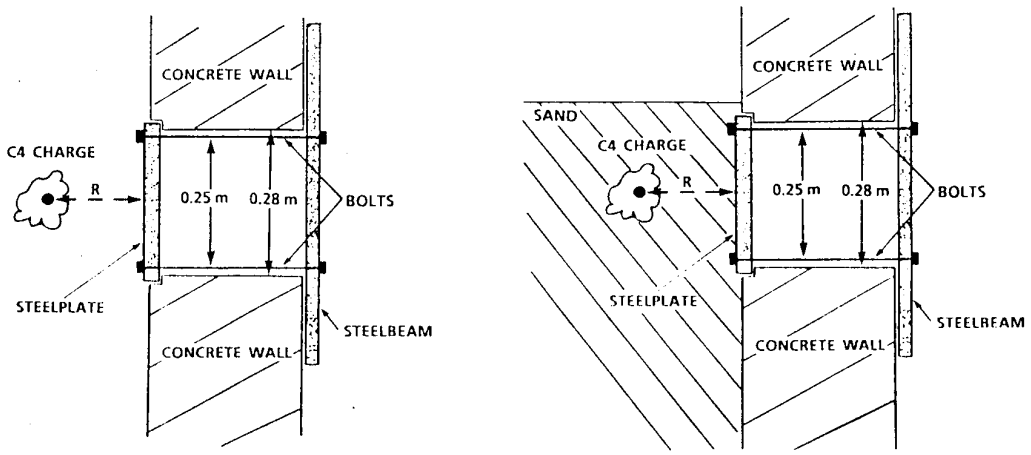

a) Airblast b) Buried detonation

Figure 1 *Test set–up*

AIR/SOIL TYPE	PLATE THICKNESS	CHARGE WEIGHT			TOTAL NO. OF TESTS
		6.5 g	13.2 g	20.0 g	
AIR	10 mm	4	4	–	8
	30 mm	–	6	5	11
DRY SAND	10 mm	5	4	–	9
	30 mm	–	5	5	10
WET SAND	10 mm	4	4	–	8
	30 mm	–	4	5	9

Table 1 *Total number of blast experiments in the test series.*

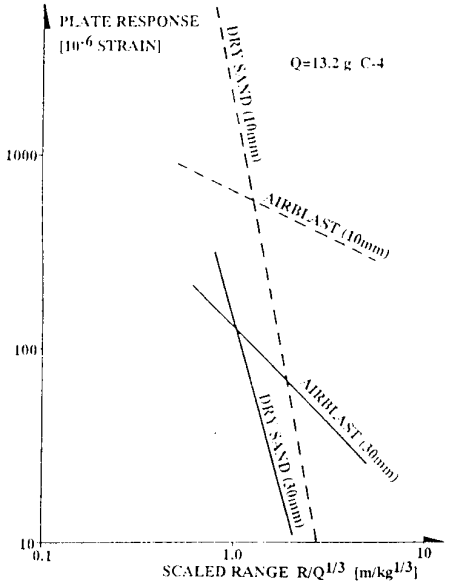

Figure 2 *A comparison of the results obtained with the 10 mm and the 30 mm thick steelplate exposed to 13.2 g C–4 charges.*

For simplicity, only results from the 13.2 g C–4 charges detonated in air and in dry sand are considered in the Figure, which for both plates shows the following main features:

- The air blast response curve has a different slope than the curve for detonations in dry sand.
- The air blast response curve intersects the dry sand detonation curve.

These findings clearly demonstrate that detonations in the air give larger response than buried detonations in dry sand at large scaled distances (ie to the right hand side of the point of intersection in Figure 2). However, moving to the left hand side of this point, the buried detonations yield the largest response values. It should also be noted that the point of intersection for the thickest plate is located closer to the steelplate than the corresponding point for the 10 mm plate.

3. PRESSURE–IMPULSE (P–I) DIAGRAMS

The difference in the results may be explained from theory, by establishing a theoretical pressure–impulse (P–I) diagram for the steelplates used in the blast experiments. Consider the general P–I diagram for a blast loaded plate given in Figure 3. The diagram is valid for plates that are assumed to be homogeneous, isotropic, flat slabs which respond in bending to uniformly applied pressures and impulses.

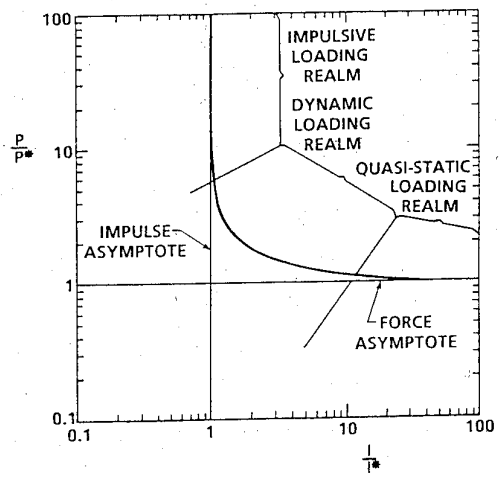

Figure 3 *A general P–I diagram. (1)*

In Figure 3, the continous line defines a threshold load. This threshold could be described in several ways. It may for instance, describe a stress or strain value being constant along the line, or a line describing the failure load on the plate. By plotting the actual load into the diagram, the plate deformation may be determined.

If the point describing the load falls above or to the right of the threshold line, the plate should deform more than the prescribed value. On the other hand, if the point is located below or to the left of the threshold line, the plate deformation is less than the prescribed value.

The threshold line may be divided into three different loading realms; the impulsive, the dynamic and the quasi–static.

When the load period (T) is very much less than the natural period (T_N) of the plate, i.e

$$\frac{T}{T_N} << 1$$

the load is defined as impulsive. For plates that exhibit impulsive loading, the response is determined by the impulse alone, and it should be stressed that it is independent of the maximum pressure. If

$$\frac{T}{T_N} >> 1$$

the load is defined as quasi–static. In this case, the plate response is only determined by the maximum pressure, and being independent of the total impulse and the load duration. When the load neither may be defined as impulsive nor quasi–static, it is referred to as dynamic. For dynamic loads the plate response depends on both the maximum pressure and the total load impulse.

Figure 4 presents a theoretical P–I diagram for the steelplates used in the blast experiments. It consists of a plot of I_r/d versus P_r/d^2 for different strain values, where I_r is the total reflected load impulse, P_r is the maximum reflected pressure and d is the plate thickness. The strain levels have been chosen in order to give the same distance between them in a log–log plot. In order to compare the experimental data with the theoretical ones, all test results are plotted into the P–I diagram. For simplicity all results are divided into the six different strain regions, as seen in Figure 4.

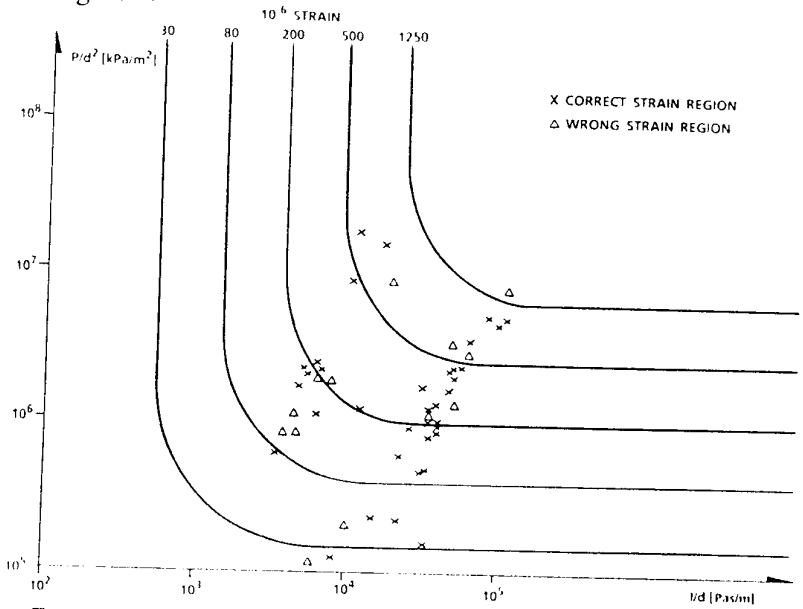

Figure 4 *Experimental results plotted into the P–I diagram for steelplates.*

An "x" indicates a test result where the maximum pressure and impulse value falls into the correct strain region. If the result should have been located in another region, it is denoted by a "Δ". From the Figure, it is apparant that the experimental data fit the quasi–static loading realm fairly well. To a certain degree, this is also the situation for the dynamic loading realm. The impulsive loading realm, however, is more poorly described, since there only are a few data points in this area. Obviously further testing should be carried out in order to obtain more information regarding this part of the P–I diagram. However, by assuming the diagram is reasonably well defined, it is adopted for further analysis of the berming effect.

4. THE WALL THICKNESS' INFLUENCE ON THE RESPONSE OF STRUCTURES.

The experimental results in terms of pressure and impulse values may be plotted into the theoretical P–I diagram for a given charge weight at a range of stand–off distances. This has been done in Figure 5, which shows response levels for detonations in air and in dry sand for both the 10 mm and the 30 mm thick steelplates. The charge weight has been taken as 13.2 g as used in the experiments, and the response plotted for scaled stand–off distances ($R/Q^{1/3}$) ranging from 0.8 m/kg$^{1/3}$ to 3 m/kg$^{1/3}$

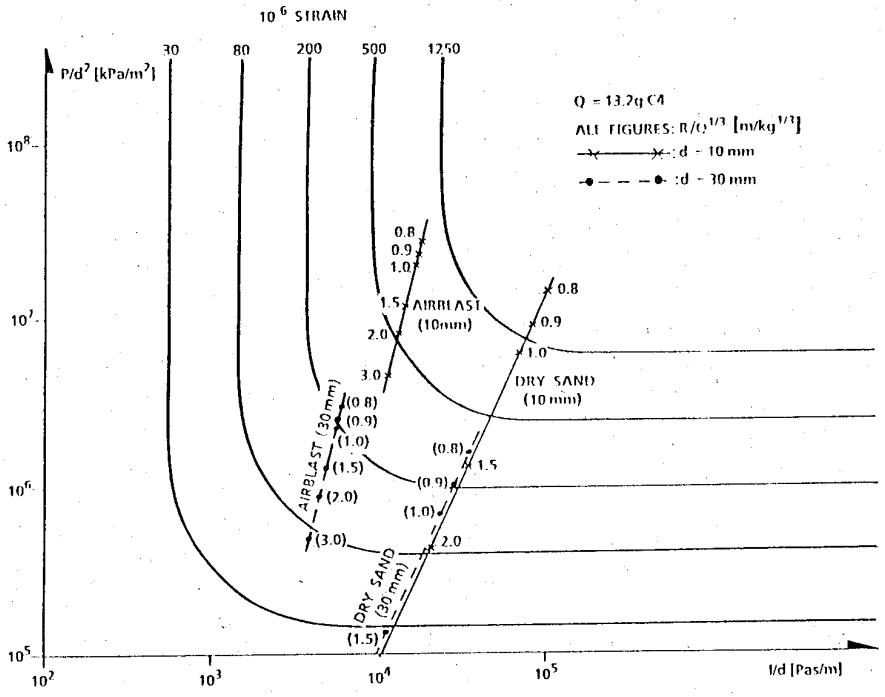

Figure 5 *Theoretical response of the 10 mm and the 30 mm thick steelplate, based on experimental pressure and impulse values.*

It is observed that the curves for the explosions in dry sand for both plate thicknesses are situated in the quasi–static region. The curves showing the airblast response, however, is for the 10 mm thick plate located in the impulsive region for small stand–off distances and in the dynamic region for larger ranges. By studying the air blast curve for the 30 mm thick steelplate it is observed to be in the dynamic region for small stand–off distances and tends towards the quasi–static region for larger ranges.

Thus increasing the plate thickness results in moving the airblast response curve from the impulsive region towards the quasi–static region. This is also obvious from a theoretical point of view, since increasing the plate thickness leads to a shorter natural periode of the plate.

It is also important to note the difference in scaling between pressure and impulse. The correct scaled pressure is P/d^2, while the scaled impulse is I/d. The response of the buried plates is mainly determined by P/d^2, while the response of the plates exposed to airblasts depends on both P/d^2 and I/d. Thus, it is reasonable to assume the response curves for dry sand and airblast in Figure 2 will be different since the response depends on different parameteres which also scales differently.

This study demonstrates the importance of establishing whether the load is impulsive or quasi–static. However, the conclusion may change by altering the thickness of the plate, hence the plate thickness is an essential parameter to consider.

In Figure 5 the response of a 10 mm and a 30 mm thick steelplate is studied. In the same way, other thicknesses may be studied, showing the difference in response to air blasts and buried bursts over a range of plate thicknesses.

This work has been carried out, and Figure 6 gives the result as a plot of response in micro-strain versus plate thicknesses for $R/Q^{1/3} = 1.0$. The Figure clearly shows that for most plate thicknesses, detonations in air give increased response levels compared to detonations in the ground. If the plate is very thin however, the conclusion changes. In this case detonations in the ground give the largest plate response values. Hence, it must be stressed that the location of the point of intersection between the air blast and the buried burst response curves depends on the $R/Q^{1/3}$ value studied. Increasing the scaled stand–off distance moves this point to the left, while decreasing the distance implies that it moves to the right.

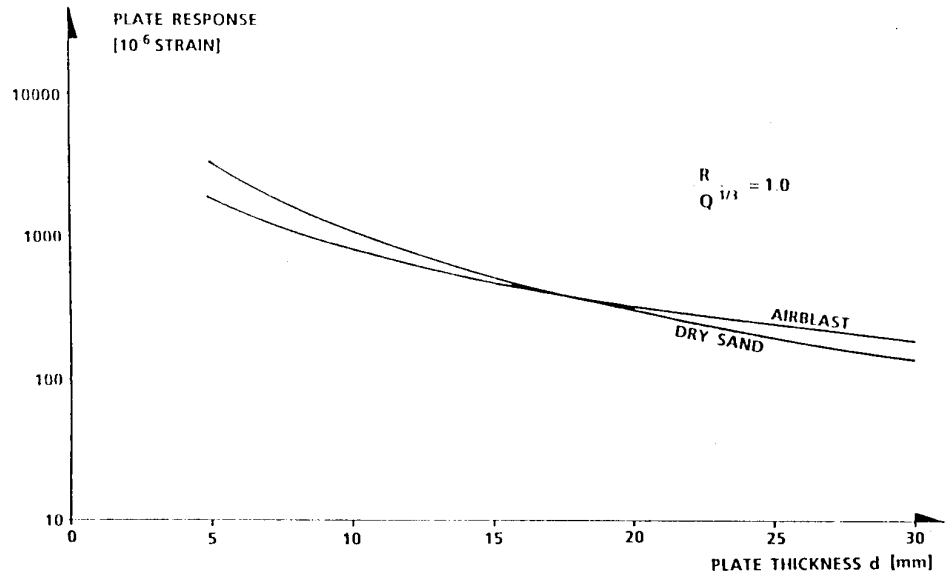

Figure 6 *Response of steelplates to detonations in air and in dry sand for different plate thicknesses at $R/Q^{1/3} = 1.0$*

5. THEORETHICAL APPROACH FOR A LARGE CONCRETE WALL

The P–I theory will now be used to study the response of a typical concrete wall to blast loadings.

For simplicity, a model of fully fixed, elastic, linear concrete wall of dimensions 4m x 4m x 0.5 m is considered. Since a given concrete wall is studied, the thickness of the wall is multiplied into the equation for the P–I asymptotes. Figure 7 presents the P–I diagram for this wall. In the same Figure, the response of the wall to a 500 kg GP bomb detonated at a range of stand–off distances in both air and in sand, is plotted.

All pressure and impulse values are taken from TM 5–855–1 (2). In order to study the worst case, reflective blast parameters have been used throughout this analysis.

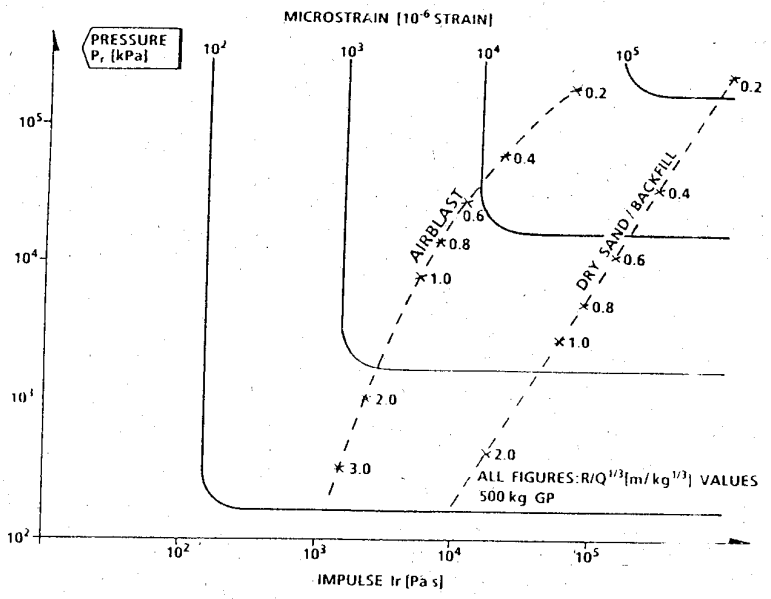

Figure 7 *P–I diagram for a concrete wall of dimensions 4 m x 4 m x 0.5 m, including the response to a 500 kg GP bomb detonated at different stand–off distances in both air and dry sand.*

For the buried detonations which are considered being fully coupled, values for "sandy loess, dry sand and backfill" in (2) were adopted. Following the TM 5–855–1 manual, an average reflection factor of 0.5 is reasonable for buried detonations. Thus the analysis was accomplished with reflected pressures and impulses being 1.5 their free field values.

For the air blast response, the reflected pressure and impulse values are well known for all stand–off distances. Also for this situation the worst case is assumed, that is all detonations occure at the ground surface.

In both cases all loads are assumed to act uniformly over the wall and they are also thought to load the wall at the same time.

The response of the wall to detonations of the 500 kg GP bomb at different stand–off distances is given in Figure 8. This Figure clearly shows that for most stand–off distances, a buried detonation yields much lower response values than the air blast. For close–in detonations the effect will be different, and the buried detonations give the largest response. At these short ranges, however, the structure will not resist the blast effect from neither the buried burst nor the air blast. Hence, the main conclusion is that for this wall, a soil "berm" will reduce the structural response.

It is worthwhile to stress that this conclusion was obtained by only applying the TM 5–855–1 in combination with the P–I theory.

It is also of interest to study the effect of changing some of the wall dimensions. From the analysis of the small–scale steelplates, it is known that by increasing the wall–thickness, the point where the curves for the air blast and the buried detonation intersects, will move to the left. The effect of the soil berm would then increase. On the other hand, if the wall thickness is decreased, the point of intersection moves to the right.

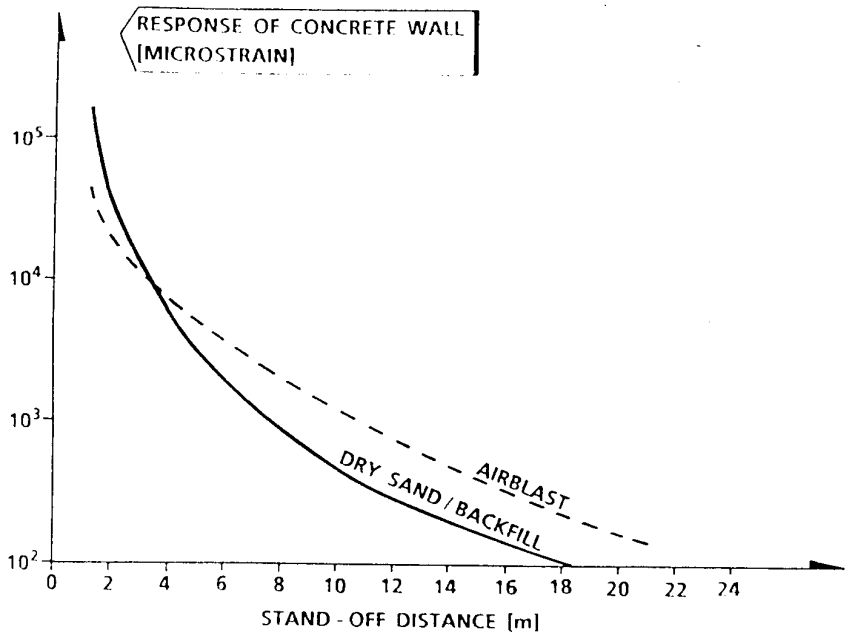

Figure 8 *Response of a 4 m x 4 m x 0.5 m concrete wall to a 500 kg GP bomb detonated at different stand–off distances in air and in dry sand.*

7. CONCLUSION

In this project it has been emphasized to study the parameters that seem to be important in evaluating the difference between buried burst and airblast response of structures. Neglecting the soil–structure interaction effect, the two situations give different load input into the analysis. Generally, it is observed that buried detonations at most stand–off distances give larger impulses and durations, but lower maximum pressures than corresponding bursts in air. Both situations may however, cause damage to the structure.

This project has shown that the plate– or wall thickness is a most important parameter in assessing when the largest response level will occure. For most structural elements, a soil berm decreases the blast response.

So far only the blast effect from above–ground and buried charges has been considered. It is well known that a soil berm will decelerate or stop fragments from an explosion. It will in addition cause a valuable camouflage effect. Altoghether these effects are strengthening the above conclusion.

Based on this study, a soil berm is strongly recommended as a measure in reducing the vulnerability of protected structures.

REFERENCES

(1) Baker, W.E, Cox, P.A, Westine, P.S., Kulesz, J.J and Strehlow, R.A. A short course on explosion hazards evaluation, Southwest Research Institute, USA.

(2) U.S. Army: Fundamentals of protective design for conventional weapons, TM 5–855–1 (1986).

ANALYSIS OF SEMIHARDENED STRUCTURES SUBJECTED TO LOADS FROM CONVENTIONAL WEAPONS

David M. Pyle, Capt., USAF
HQ USAFE/DENT, Ramstein AB, GE

Thomas T. Baber, Associate Professor
University of Virginia, Charlottesville, Va.

ABSTRACT

This paper describes the development of models aimed at representing the loading and subsequent response of typical semihardened structures subjected to loads from the nearby detonation of a conventional weapon. A nondimensionalized wall unit is modeled as a continuous, hysteretic beam. This allows the generation of response statistics for varying wall configurations at any point along the height of the section choosen as the beam element. The loading model will generate then apply the resultant reflected pressure loading at any number of points along the length of the beam element, at any designated time step. The equations of motion of the system are solved by the method of weighted residuals, on an iterative basis. Results of the model compared to documented test series are presented.

INTRODUCTION

This paper describes the development of load and structural models to be used to generate response statistics for typically loaded NATO semihardened facilities. The statistics generated will be used in future work aimed at formulating a stochastic model to predict the response of similar structures to randomly applied loads. The following assumptions/statements are made as a preface to this and the follow-on work:

1. The attack scenario posits blanket bombing of a large target area.
2. The structure in question is not a primary target, therefore the burst locations in its vicinity may be considered random.
3. A wall of a semihard structure in the vicinity of the blast will respond as a one-way slab (Biggs,1962; Coltharp,1985; Hyde,1989), therefore its response characteristics may be generated accurately using a beam model. The portion of the structure to be described by the beam model will be called the region of interest as shown in figure 1.
4. The weapon is assumed to be a general purpose bomb detonating at or near a vertical orientation. The casing effects will not be considered in this paper.

Results of simulations run with the models developed herein will be compared to full scale and reduced scale tests results found

in the literature.

LOADING MODEL

In order to accurately represent the loading of a structure from the near field explosion of a conventional weapon, a model is required that can represent both the spatial and temporal characteristics of this phenomena. Given the attack scenario above, the burst location relative to the region of interest may be defined by the range(r) and angle of incidence(α), which are functions of the lateral and incident standoffs, x and z respectively (see figures 2 and 3). For this work the detonation location as a function of x and z will be assumed as will the throw weight of the weapon. The exclusion of the casing effects is not meant to infer their unimportance but is an initial simplifying assumption deemed necessary to set up the method. Recent studies (Coltharp,1985; Kropatscheck,1983) have shown that the fragment effects are very significant in the loading and response of above ground structures. The underlying premise in describing the distribution of fragments from a cased ordnance is based on a probability law and should lend itself to inclusion in subsequent work.

The parameters which describe the load environment from a surface or midair explosion of a conventional weapon are presented in graphical and equation form in Kingery,1966. A weapons effect program entitled CONWEP, developed by the Army Waterways Experiment Station in Vicksburg Mississippi (Hyde,1989), uses coded versions of these equations to generate loading data given the weapon TNT equivalent throw weight and detonation location. Segments of the program CONWEP were modified and incorporated into this load model. The input needed to generate the required parameters at any point along the region of interest are the variables x and z above, the distance up the region of interest, y, and the weapon throw weight, w. Together they generate what is referred to as the scaled range(SR). SR is defined as:

$$SR = \frac{(x^2+z^2+y^2)^{1/2}}{w^{1/3}} \qquad (1)$$

with the scaled range one goes to the curves of Kingery,1966 and read off the following parameters:

(1) Time of arrival, after detonation, of the blast wave to the structure. (t_a, msec)

(2) Positive pressure phase duration of blast after arrival at structure (t_d,msec)

(3) Peak positive incident pressure seen by the structure. (P_{so},psi)

(4)Positive incident impulse delivered to the structure. (IMP, msec*psi)

Taking the incident impulse, the peak incident pressure, the positive phase duration and the arrival time, an exponential function can be derived to describe the history of the pressure at the point corresponding to that scaled range distance. This function is termed the Modified Friedlander equation(Baker,1973). When the blast wave hits a rigid surface the particle velocities are arrested and the pressure, density and temperature are all increased above the values in the free field incident wave. The magnification resulting from the reflection of the blast wave is a function of the incident wave pressure and the angle of incidence. Curves generated

from experimental data to represent this reflection factor (Crawford,1971) as functions of the above parameters are coded in CONWEP and were incorporated into this load model.

The model generates parameters across the region of interest with the majority generated across the lower half of the wall where the loading changes most rapidly. The result is the further Modified Friedlander Equation below which is applied to the structure model and integrated numerically at each time step.

$$P(y,t) = P_{so}(y) * H[t - t_a(y)] * \left[1 - \left(\frac{t - t_a(y)}{t_d(y)}\right)\right] * \exp\left[-A(y) * \left(\frac{t - t_a(y)}{t_d(y)}\right)\right] \qquad (2)$$

The value $P_{so}(y)$ is the reflected pressure seen at the point y at time t. The Heaviside function $H[t - t_a(y)]$ ensures the loading at a specific point is not applied prior to its time of arrival.

STRUCTURE MODEL

Reinforced concrete wall structures subjected to the conventional weapons effects of interest in this work have been shown to respond essentially as one way slabs, therefore the use of a beam model to represent the response characteristics is justified. It is desired to model the beam so that the response can be evaluated along its entire length in such a way as to include the higher modes of vibration. It is also desired that the model not be too detailed as to cause unwanted complexity requiring long and expensive computer runs, as in a nonlinear finite element analysis. The nonlinear response of the structure is therefore modeled as a continuous hysteretic beam. The beam model is taken to represent the vertically centered section of the wall referred to as the region of interest in figure 1.

The support conditions that best represent the response of similar structures has been characterized as being somewhere between fixed and simply supported(Ross,1985). To gain insight into the method proposed the example developed in this work assumes simply supported conditions. Other support conditions could be incorporated into the model relatively easily. This assumption however is not unique as can be seen in the literature (Coltharp,1985; Biggs,1962).

The equation of motion of the system can be written as

$$m_{,xx} + \rho A v_{,tt} = q_{ext}(x,t) \qquad (3)$$

where the comma and subscript letters represent the derivative of that term with respect to the subscripted letter. The moment curvature relationship can be defined in terms of linear and nonlinear portions. The moment term of equation 1 can be written as:

$$m(x,t) = A_0 EI v_{,xx} + (1 - A_0)\mathbf{M} \qquad |A_0| \le 1 \qquad (4)$$

The term **M** represents the nonlinear, hysteretic portion of the total moment. The term A_0 can be interpreted as the post yield to preyield moment-curvature ratio and controls the degree of nonlinearity that the system will exhibit (see figure 4). For example, if A_0 equals 1 the system is effectively linear while if A_0 equals = 0, the system is fully nonlinear hysteretic.

Substituting equation 4 into equation 3 the governing differential equation may be written as

$$(1-A_0)\mathbf{M}_{,xx} + A_0 EIv_{,xxxx} + \rho A v_{,tt} = q_{ext}(x,t) \qquad (5)$$

The hysteretic moment curvature relationship may be expressed in various ways. One particularly convenient form is the rate type smooth hysteretic system attributed to Bouc(1967),

$$\frac{\mathbf{M}_{,t}}{M_u} = \frac{v_{,xtt}}{\phi_u} - A_1\left|\frac{v_{,xxt}}{\phi_u}\right| \left|\frac{\mathbf{M}}{M_u}\right|^{n-1} \frac{\mathbf{M}}{M_u} - A_2 \frac{v_{,xxt}}{\phi_u} \left|\frac{\mathbf{M}}{M_u}\right|^n \qquad (6)$$

Where the terms A_1, A_2 and n control the shape of the hysteresis as seen in figure 4. This and similar models were developed to represent response of structures to seismic type dynamic loadings which would normally take it through several cycles. The model may also be modified to include system degradation . At this time there is not sufficient data to generate an appropriate degradation model for the types of loadings under consideration herein. Further work in the response of typical structures to multiple shock loadings is required and would be warranted. The motion of the system is now totally defined by equations 5 and 6. Closed form solution of these equations is difficult, so a reasonable approximate solution is desired.

Prior to developing a solution technique the equations are nondimensionalized. The resulting equations become, after rearranging to solve for the derivative of the displacement with respect to time:

$$v_{,\tau\tau} = \bar{q}(\xi,\tau) - (1 - A_0)\mu_{,\xi\xi} - A_0 v_{,\xi\xi\xi\xi} \qquad (7)$$

$$\mu_{,\tau} = v_{,\xi\xi\tau} - A_1\left|v_{,\xi\xi\tau}\right|\left|\mu\right|^{n-1}\mu - A_2 v_{,\xi\xi\tau}\left|\mu\right|^n \qquad (8)$$

The details of the nondimensionalization are in the appendix.

The approach chosen to solve these equations is the method of weighted residuals(Cunningham,1958). Following this methodology, a set of complete functions that satisfy the physical boundary conditions are chosen to approximate the response of the system. The displacement of the system is approximated by a finite sum of terms in the form

$$v(\xi,\tau) = \sum_{k=1}^{n_v} \alpha_k(\tau)\Psi_k(\xi) \qquad (9)$$

where the complete set of functions Ψ_k are chosen to be the set of eigenfunctions that satisfy the assumed end conditions. In a like manner the moment solution may be approximated as a series taking the form:

$$\mu(\xi,\tau) = \sum_{I=1}^{n_\mu} \beta_I(\tau)\Phi_I(\xi) \qquad (10)$$

Substituting the assumed solutions of the associated linear systems into the differential equations results in a residual difference e that is minimized in order to find the optimal values for the coefficients α and β. The residuals of equations 7 and 8 become:

$$\sum_{k=1}^{n_\nu} \Psi_k \alpha_{,\tau\tau} = \overline{q}(\xi,\tau) - (1 - A_0) \sum_{I=1}^{n_\mu} \Phi_{I,\xi\xi}\beta_I - A_0 \sum_{k=1}^{n_\nu} \Psi_{k,\xi\xi\xi\xi}\alpha_k \qquad (11)$$

$$\sum_{I=1}^{n_\mu} \Phi_I \beta_{I,\tau} = \sum_{k=1}^{n_\nu} \Psi_{k,\xi\xi}\alpha_{k,\tau} - A_1 \left|\sum_{k=1}^{n_\nu} \Psi_{k,\xi\xi}\alpha_{k,\tau}\right| \left|\sum_{I=1}^{n_\mu} \Phi_I \beta_I\right|^{n-1} \left(\sum_{I=1}^{n_\mu} \Phi_I \beta_I\right)$$
$$-A_2 \left(\sum_{k=1}^{n_\nu} \Psi_{k,\xi\xi}\alpha_{k,\tau}\right) \left|\sum_{I=1}^{n_\mu} \Phi_I \beta_I\right|^{n} \qquad (12)$$

Introducing

$$\alpha_{k,\tau} = \gamma_k \qquad k=1,2,\ldots,n_\nu \qquad (13)$$

then substituting this variable into equations 11 and 12 results in three first order, partial differential equations.

Following the weighted residual method, the new equations 11 and 12 are minimized inorder to find the optimal values for the solution coefficients. The minimization equations take the form

$$\int_0^1 e_{11}(\xi,\tau)\Psi_k(\xi)\,d\xi = 0 \qquad k=1,2,\ldots,n_\nu \qquad (14)$$

$$\int_0^1 e_{12}(\xi,\tau)\Phi_I(\xi)\,d\xi = 0 \qquad I=1,2,\ldots,n_\mu \qquad (15)$$

Where e_{11} and e_{12} denote the residual equations 11 and 12 above. The model solves equations 13, 14 and 15 simultaneously for the coefficients alpha, beta, and gamma at specific times tau. The total number of equations to be solved is equal to twice the number of terms used in equation 9 plus the number of terms used in equation 10. Inclusion of more terms in these series allows the influence of higher modes of vibration to be seen in the response. These higher modes of vibration influence the response significantly the closer the detonation occurs to the structure, which results in even shorter duration impulse type loadings.

Once the coefficients are determined the displacements, moments, shears and curvatures at any point along the beam and at any time during the response history, can be evaluated. Shear failure criteria after work done by Ross,1982 will be used to predict shear failure along the beam or at the supports in future work. It is recognized that a separate shear model based on a

Timoshenko beam would better approximate the shear response, however the inclusion of such a model is outside of the scope of the current work.

Results of the model under a unit load were validated against single degree of freedom (SDOF) and finite element representations of the system. The SDOF analysis was run using a program entitled Biggs (Baker,1989). The finite element model consisted of 10 two-dimensional beam elements (ANSYS,1986) which represented half the beam recognizing symmetry. Deflection results at various points along the beam were computed. Maximum deflections at three points, including the midspan and quarter points were within 2% of each other. Figure 5 shows a graph of the midspan deflections.

LOAD MODEL APPLIED TO STRUCTURE MODEL RESULTS

Initial validation of the two models developed in this paper was accomplished by comparison of deflection results from the application of actual weapon loadings on structures for which test results are available in the literature. The tests series used tt validate results to date are resported in Wright,1988 and Hyde,1989. From the Wright,1988 tests the following results are presented:

Charge Weight (W) lb TNT	Standoff ft	Reported Midspan Deflection in	Calculated Deflection in
64	20	.1	.35
64	5	.64	.76
194	20	.9	.85

The structure in the Hyde,1989 tests was subjected to the NATO semihardened threat. A bare wall loading in these tests resulted in a maximum measured displacement of .847 in. The models predicted a maximum deflection of .873 in.

STATUS AND CONCLUSIONS

Further validation of the models is on going. Comparisons to test results presented here appear to validate the ability of the model to predict at least the maximum deflection of the structural configurations evaluated. Extension of the this validation to the prediction of shear failures will be more difficult, but is underway. Accumulation of response statistics for all reasonable loading configurations and subsequent development of a stochastic model to predict the random influence of a bombing attack on a typical airbase facility also continues.

APPENDIX

NONDIMENSIONALIZATION

Equations 7 and 8 of the section entitled Structure are nondimensionalized with respect to the ultimate bending moment, M_u, and ultimate curvature, ϕ_u. As shown in figure 4, M_u is only truly the ultimate moment when $A_0 = 0$. For this model $A_0 = .05$. The ultimate curvature and nondimensional moment are defined as:

$$\phi_u = \frac{M_u}{EI} \qquad \mu = \frac{M}{M_u}$$

The nondimensional length and displacement are:

$$\xi = \frac{x}{L} \qquad \nu = \frac{v}{\phi_u L^2}$$

The nondimensional time is defined as:

$$\tau = \overline{\omega} t$$

where

$$\overline{\omega} = \sqrt{\frac{EI}{\rho A L^4}}$$

The nondimensional load and load per unit lenght are:

$$f = \frac{f_{ext} L}{M_u} \qquad \overline{q} = \frac{q_{ext} L^2}{M_u}$$

Incorporating these conversions into equations 5 and 6 results in equations 7 and 8 of the same section.

REFERENCES

Baker,W.E.,"Explosions in Air,"University of Texas Press, Austin and London, 1973.

Baker,W.E.,"User's Manual For Biggs Program," Wilfred Baker Engineering, San Antonio, Texas, Jan 18, 1989.

Bouc,R.,"Forced Vibration of Mechanical Systems with Hysteresis," Abstract, Proceedings of the Fourth Conference on Nonlinear Oscillations, Prague, Czechoslavakia,1967.

Cunningham,W.J., "Introduction to Nonlinear Analysis",McGraw-Hill Book Company,1958.

Hyde,D.W.,"User's Guide For Microcomputer Programs CONWEP and FUNPRO, Applications of TM 5-855-1, 'Fundamentals of Protective Design for Conventional Weapons' ," U. S. Army, Waterways Experiment Station, Vicksburg, Mississippi, April 1988.

Hyde,D.W.,"NATO Semihardened Facility Test,ESL-TR-89-06," HQ USAFE/RDCS, Tyndall AFB, Florida, June 1989.

Kingery,C.N., "Air Blast Parameters Versus Distance for Hemispherical TNT Surface Bursts", BRL Report No. 1344, Aberdeen Proving Ground, Md.,1966.

Kropatscheck,M.O.,"Tests and Evaluations of Close-In Detonations," Proceedings of the International Symposium on the Interaction of Non-nuclear Munitions with Structures, USAFA, Colorado Springs, Co., May, 1983.

Ross,T.J., Krawinkler,H., "Impulsive Direct Shear Failure in RC Slabs", ASCE Journal of Structural Engineering, Vol. 111, No. 8,

August, 1985.

Wright,R.S.,"High Explosive Tests of Swedish-Norwegian Defense Structures, TR-SL-88-23," U.S. Army Waterways Experiment Station, Vicksburg, Mississippi, July 1988.

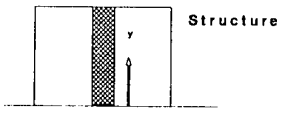

Figure 1: Region of interest

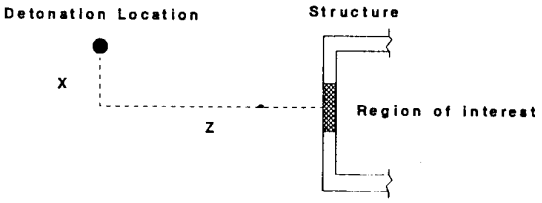

Figure 2: Weapon standoff

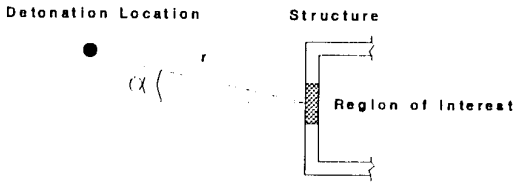

Figure 3: Range and angle of incidence

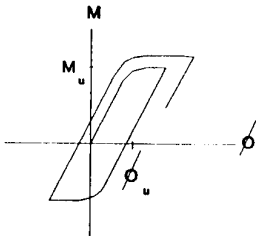

Figure 4: Moment curvature relationship

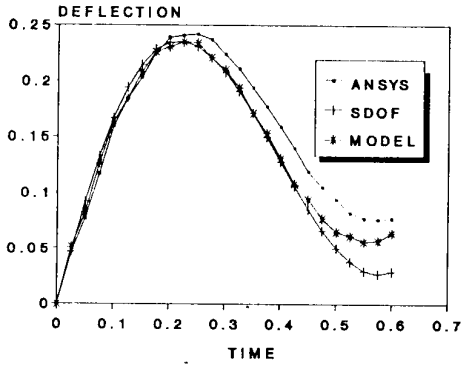

Figure 5: Structure model validation, midspan deflection

DEVELOPMENT OF A WORKING TOOL FOR THE PROTECTION RISK AND COST BENEFIT EVALUATION OF PROVISIONAL SHELTERS (PRICE)

TAN SEE TING
PUBLIC WORKS DEPARTMENT
SINGAPORE

Abstract

The provision of civil defence shelters for a whole population would take a few decades to build. Within the interim period of building dedicated shelters, there is a need to search for provisional shelters in existing buildings such as underground car parks. In doing so, the problem arises in assessing the protection potential of an existing building. In order that comprehensive strengthening measures can be recommended for provisional shelters, we must have answers to the following questions : -

i What is the protection level offered by the provisional shelter concerned? Could this be quantified?

ii How do we maximise the existing protection level by strengthening?

iii What are the protection levels achieved and its corresponding risks relating to various strengthening measures?

iv What are the most cost effective strengthening measures in relation to protection?

v Could an overall protection level indicator be obtained which could be used as a common frame of reference in comparing the protection levels of different provisional shelters?

I have developed a tool which provides the answers to the questions.

Introduction

The total floor area available in underground car parks and storage facilities in an urban city area, poses an attractive potential sheltering area which could be mustered. An example of a partially underground car park is given which should illustrate the concepts and methodology involved. Results of analysis are presented without detailed computations, and figures are given in the Annex.

Concept of Risk

The risk level is given by the multiplication of the probability of occurrence of an event and the estimated no. of injured in the provisional shelter as a result of the event. In probabilistic terms, it is a mathematical expectation of the no. of injured. Hit probabilities of conventional weapons on target areas are calculated for different scenarios.

Description of Car Park Shelter

Fig 1 shows a plan view of the semi-buried car park shelter. There are 2 ramps, one leading into and the other leading out of the car park. The potential shelter area is approximately 1758 sq m, harbouring about 4400 shelterees.

Scenarios

The following 4 scenarios are considered in the assumed conventional bombardment :-

Scenario	Description
I	Debris collapse
II	Direct to near miss hits on the walls of the provisional shelter;
III	Weapons hits at the entrance and exit openings of the car park ramps; and
IV	Direct hit on the roof.

Scenario I : Debris Collapse

4 debris collapse scenarios on the roof of the car park shelter could occur from collapse of nearby buildings due to direct hits on these buildings. The various hit probabilities are given in Fig 2

Scenario II : Direct to Near Miss Hits for Walls of Car Park

The protection and risk analysis are assessed for each of the car park walls. The Western wall is not considered as it is sufficiently protected by an adjacent building. The weapon standoff distances of 2, 4, 6, 10 and 14 metres are used to assess the no. of casualties and hit probability of the event corresponding to each standoff distance.

The natural protection and shielding against bombardment of the above zones by adjacent and nearby multi-storied buildings is also taken into consideration in the hit probabilities (Fig 3).

Scenario III : Weapon hits at Entrance and Exit Openings of Car Park Ramps

Fig 4 shows the shaded areas A and B, into which a bomb falling into either area would cause casualties in the car park. The extent of the hit zone has been calculated based on 5 psi blast pressure as the limit of the "threshold" of eardrum rupture for injuries in the shelter.

Scenario IV : Direct Hit on the Roof

The hit probability of a direct hit on the roof of the car park Building is calculated at 2.25% (See Scenario I).

Casualty Estimation From Aboveground Wall Fragmentation and Blast Effects

The nos. of casualties in the provisional shelter has been calculated for

blast and fragmentation effects on the walls (Fig 5) for the different standoff distances in Scenario II.

Strengthening Measures

Certain strengthening measures are shown in Fig 6. These have been condensed into one figure for convenience of illustration, and appropriate combinations of the various strengthening measures are shown in Fig 7. The strengthening measures are as follows:

Strengthening Measure (SM)	Description
1	Erection of steel props (Fig 6);
2	In-situ hardening of existing 250mm car park walls;
3	Installation of external precast "inverted - T" concrete transportable shielding panels (Fig 6);
4	Installation of anti-spalling plates on the walls;
5	Compartmentalisation I by precast shielding panels (Fig 6);
6	Compartmentalisation II by precast shielding panels (Fig 6);
7	Shielding of entrance and exit openings of ramps (Fig 6);
8	Insitu hardening of roof;
9	Anti spalling plates and Compartmentalisation II
10	Any other feasible strengthening measure.

Risk Levels

Appropriate combinations of strengthening measures are proposed to give an overall protection. Various risk levels corresponding to the relevant combination of strengthening measures are calculated. There are altogether 8 Risk Levels being investigated and their corresponding strengthening measures are given in Fig 7.

Protection, Risk and Cost Benefit Evaluation (PRICE)

Fig 8 show the estimated no. of injured corresponding to the different scenarios of loading, and the type of strengthening measure used.

The risk level in Fig 8 for each strengthening measure is the multiplication of the probability of occurrence with the estimated no. of injured. These values are summed up for the appropriate combination of Strengthening Measures according to the Risk Level concerned(Fig 7) and are given in Fig 9.

PRICE Analysis:
Graphical Plot of Results

The results in Fig 9 are translated into graphical plots. Fig 10 shows the overall relationship between the risk levels and the cost of various strengthening measures plotted on a logarithmic scale. Fig 11 shows the region of our interest in which the strengthening measures are plotted on a normal scale. The sensitivity relationship between protection, risk levels and cost is evident from the graph. It enables a sensitivity analysis to be made between cost and risk for any level of protection.

The provision of props reduces the risk level very significantly, and should be a mandatory requirement. Points A and H represent the extremes of "no strengthening" measures and an upper protection bound respectively. Risk

level B is the most cost effective one. Management however, could prefer other risk level but with full knowledge of its implications from the graph.

Conclusion

I have developed an effective working tool which would enable a very comprehensive protection, risk and cost benefit evaluation to be made for any provisional shelter. It helps to translate technical jargon relating to such an analysis into something which management could understand and use in making decisions on the required protection level of a provisional shelter. It enhances better decisions as it would be made with full awareness of the implications on risk levels and cost.

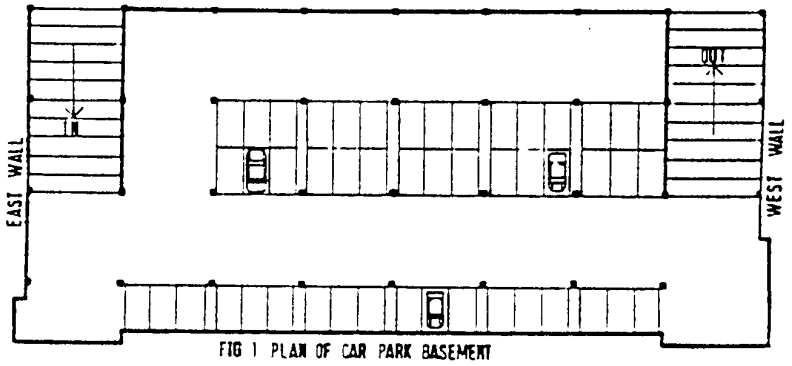

FIG 1 PLAN OF CAR PARK BASEMENT

S/No	Debris Collapse From	Probability %
A	Car park Building and adjacent car park building	1.91
B	Nearby 30 storey building	0.95
C	Nearby 20 storey building	1.68
D	Direct hit on roof of car park building	2.25
	Total	6.69%

FIGURE 2: HIT PROBABILITY FOR DEBRIS COLLAPSE

S/No	Location of Wall	Weapon Standoff Distance	Probability %
A	South or North Wall	(1) 2 metres (2) 6 metres (3) 10 metres (4) 14 metres	(1) 0.32 (2) 0.32 (3) 0.32 (4) 0.32
		Total :	1.28%
B	West Wall	(1) 2 metres (2) 6 metres (3) 10 metres (4) 14 metres	(1) 0.11 (2) 0.11 (3) 0.11 (4) 0.11
		Total :	0.44%

FIGURE 3: HIT PROBABILITY FOR WEAPON STANDOFF DISTANCES FROM WALL

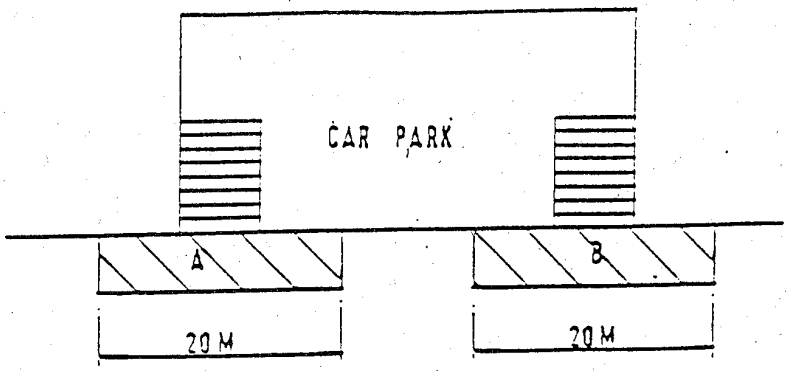

Figure 4 Explosion at Entrance and Exit

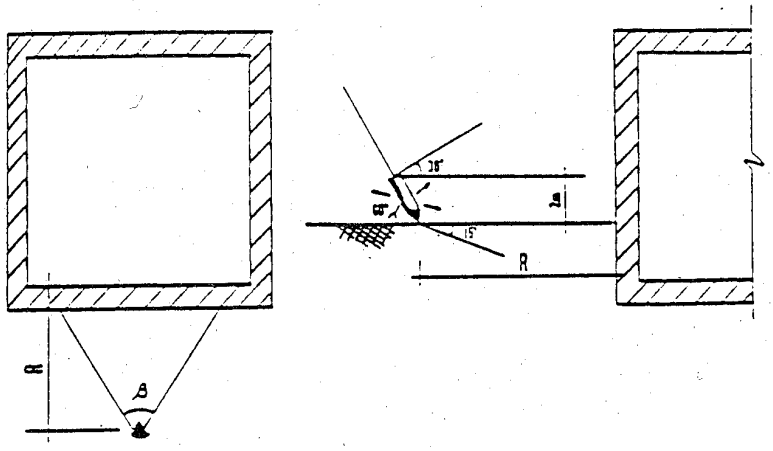

Figure 5 Blast and Fragmentation Effects on Aboveground Wall

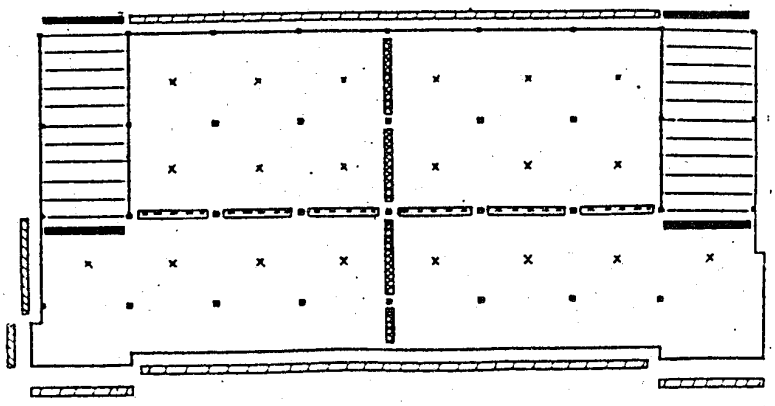

Legend

- External Shield Panels
- Shielding at Openings
- Compartmentalisation I
- Compartmentalisation II
- × Props
- • Building Columns

Figure 6 Strengthening Measures

Risk Level	Combination of Strengthening Measures (SM)
A	No Strengthening Measures
B	SM 1 + 2 + 7
C	SM 1 + 3 + 7
D	SM 1 + 4 + 7
E	SM 1 + 5 + 7
F	SM 1 + 6 + 7
G	SM 1 + 4 + 6 + 7 or 1 + 9 + 7
H	SM 1 + 2 + 8 + 7

FIG 7. Risk Level

Location	Scenario	Probability %	No Strengthening	SM1 and SM2	SM1 and SM3	SM1 and SM4	SM1 and SM5	SM1 and SM6	SM1 and SM7	SM1 and SM8
Roof of Bldg with Shelter	Debris Collapse	6.69	4396	NA	NA	NA	NA	NA	NA	NA
	Cost of Strengthening		NIL	$ 8,850	$ 8,850	$ 8,850	$ 8,850	$ 8,850	$ 8,850	$ 8,850
North Wall	A. Direct hit	0.32	2,450	640	800	2,450	1,900	1,100	-	-
	B. 4m Stand off	0.32	500	70	300	0	500	500	-	-
	C. 6m	0.32	280	0	0	0	280	280	-	-
	D. 10m	0.32	190	0	0	0	190	190	-	-
	Cost of Strengthening		NIL	$15,000	$22,600	$ 6,200	$15,500*	$32,500*	-	-
South Wall	A. Direct Hit	0.30	2,450	640	800	2,450	1,600	1,100	-	-
	B. 4m Stand off	0.30	500	70	300	0	400	350	-	-
	C. 6m	0.30	280	0	0	0	200	150	-	-
	D. 10m	0.30	190	0	0	0	100	70	-	-
	Cost of Strengthening		NIL	$13,000	$17,000	$4,700	$15,000*	$32,000*	-	-
East Wall	A. Direct Hit	0.11	1,190	420	500	1,190	1,190	1,100	-	-
	B. 4m Stand off	0.11	140	20	200	0	140	140	-	-
	C. 6m	0.11	80	0	0	0	80	80	-	-
	D. 10m	0.11	50	0	0	0	50	50	-	-
	Cost of Strengthening		NIL	$ 9,900	$ 5,000	$1,400	$15,500*	$32,500*	-	-
Ramp Openings	Explosion at Openings	0.18	1,200	N.A.	N.A	N.A.	N.A.	N.A.	0	N.A.
	Cost of Strengthening		NIL						$11,300	0
Roof of Shelter	Delay Fused Bomb	0.12	3,480	N.A.	N.A	N.A.	$ 2,200	$ 1,100	N.A.	0
	Cost of Strengthening						$15,000*	$32,500*	-	$640.0

FIGURE 8: PRICE ANALYSIS - STRENGTHENING MEASURES EVALUATION

Location	Scenario	Total Probability %	Quantification of Risk Level							
			Level A	Level B	Level C	Level D	Level E	Level F	Level G	Level H
Roof of Bldg with Shelter	Debris Collapse	6.89	294	0	0	0	0	0	0	0
	Cost of Strengthening		NIL	$ 8,850	$ 8,850	$ 8,850	$ 8,850	$ 8,850	$ 8,850	$ 8,850
North Wall	Direct to near miss	1.28	10.94	2.27	3.52	7.84	9.18	6.62	3.52	2.27
	Cost of Strengthening		NIL	$15,000	$22,600	$ 6,200	$15,500*	$32,500*	$ 6,200+ $32,250*	$15,000
South Wall	Direct to near miss	1.2	10.26	2.13	3.30	7.35	6.9	5.01	3.3	2.13
	Cost of Strengthening		NIL	$13,000	$17,000	$4,700	$15,500*	$32,500*	$ 4,700*+ $32,500*	$13,000
East Wall	Direct to near miss	0.44	1.60	0.48	0.77	1.31	1.61	1.51	1.21	0.48
	Cost of Strengthening		NIL	$ 9,900	$ 5,000	$1,400	$15,500*	$32,500*	$ 1,400+ $32,500*	$ 9,900
Ramp Openings	Explosion at Openings	0.18	2.16	0	0	0	0	0	0	0
	Cost of Strengthening		NIL	$11,300	$11,300	$11,300	$11,300	$11,300	$11,300	$11,300
Roof of Shelter	Delay Fused Bomb	0.12	4.18	4.18	4.18	4.18	2.64	1.32	1.32	0
	Cost of Strengthening		NIL	NIL	NIL	NIL	$15,500*	$32,500*	$32,500*	$640,300
Whole Shelter	TOTAL RISK		323	9.06	11.77	20.68	20.33	14.46	9.25	4.88
	TOTAL COST OF STRENGTHENING		NIL	$58,000	$64,800	$32,400	$35,700	$52,700	$64,700	$698,000

FIGURE 9: PRICE ANALYSIS : RISK LEVEL AND COST PARAMETERS

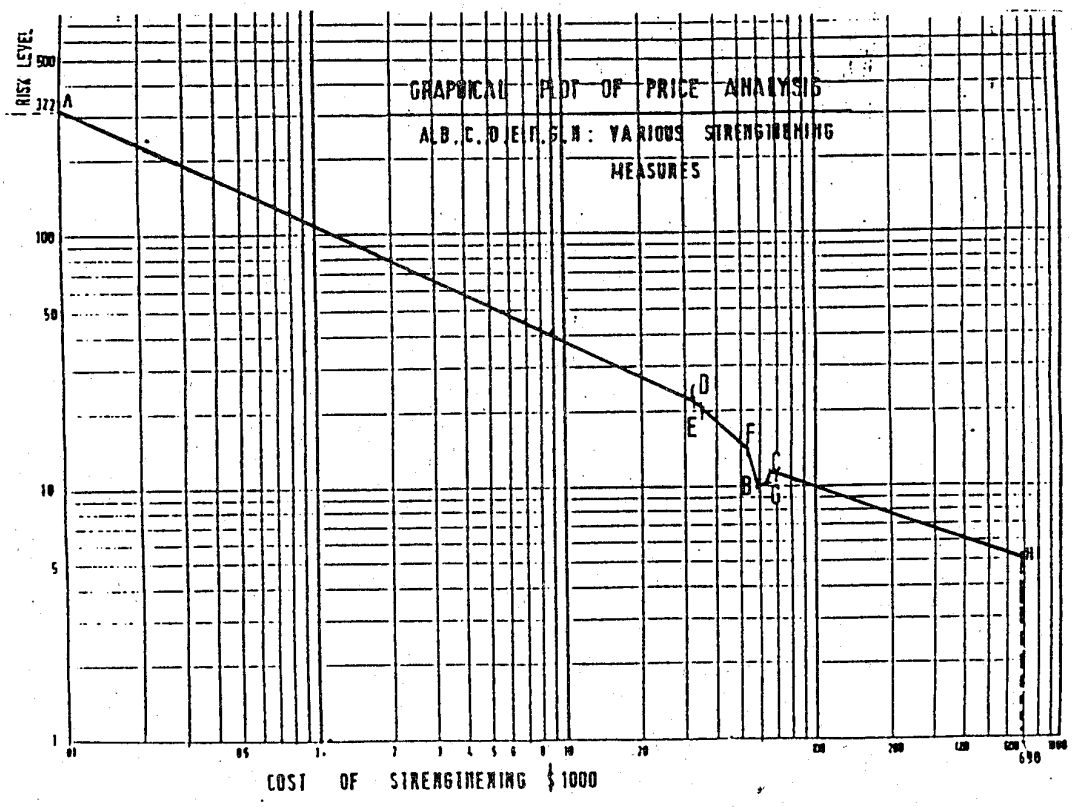

Figure 10 Risk Level versus Cost (log plot)

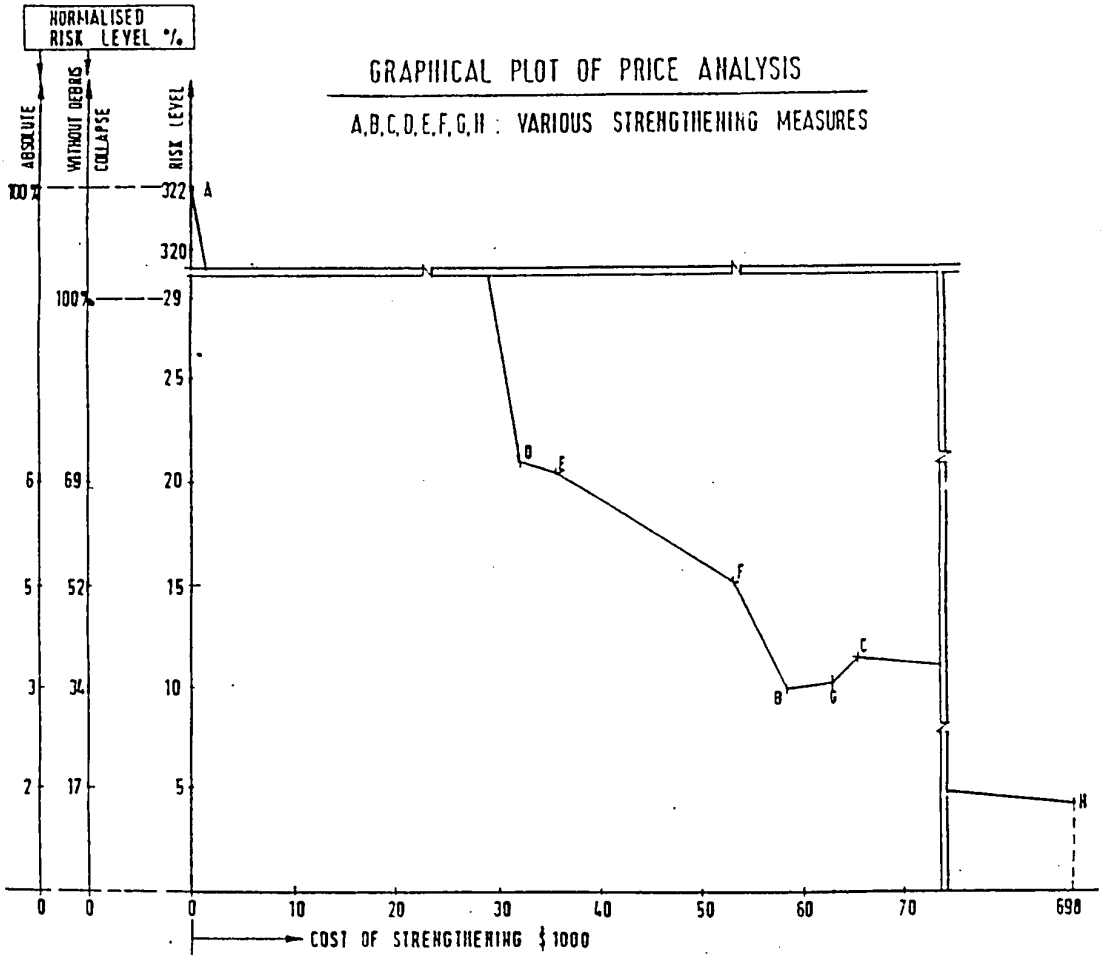

Figure 11 Risk Level versus Cost

THE FAILURE MODE OF CONCRETE STRUCTURES DUE TO CONTACT CHARGES

R.J.M. van Amelsfort and J. Weerheijm

TNO Prins Maurits Laboratory
P.O. Box 45
2280 AA Rijswijk, The Netherlands

ABSTRACT

An experimental and theoretical programme was set up and performed in order to gain more information about the optimal construction of a (layered) protective structure for underground military shelters.

These structures are mostly composed of two reinforced concrete slabs with an intermediate layer of reinforced concrete, lightweight concrete with polystyrene pellets, polystyrene pellets sec, sand or air. These layers can be defined as a penetration layer (in which the bomb must be stopped), an intermediate pressure distributing and shock absorbing layer, and a third layer, mostly the actual construction to be protected.

For a general insight, a literature study was performed on penetration depths of missiles into concrete and explosion effects (failure mode of concrete slabs, cratering, spalling).

Early experiments performed by the TNO Prins Maurits Laboratory (PML) in co-operation with the KMA (Royal Netherlands Military Academy) showed an alternative failure mechanism when loading a concrete slab with a contact charge, namely the punching of successive layers by a high energy concrete particle stream originating from the directly loaded layer.

More recent experiments performed by the PML gave detailed information about this particle stream, such as an estimate of the force that may be exerted by the stream on following slabs, which represents a severe threat to the shelter to be protected.

This paper deals with the state-of-the-art of the investigations performed at the PML concerning the failure mode of (layered) concrete structures due to contact charges.

The consequences are included of the results obtained so far for the construction of protective structures.

1 INTRODUCTION

For an optimal design of layered protective structures for military shelters, knowledge of the phenomena occurring during the impact of a possible threat is necessary. These structures are mostly composed of two reinforced concrete slabs with an intermediate layer. The first slab can be defined as a penetration layer in which the threat must be stopped. The function of the intermediate layer is to distribute and to absorb the induced shock due to the impact and the subsequent explosion. The third layer is mostly the actual construction to be protected.

Several types of intermediate layers were involved in an experimental programme. To design the thickness of the first slab necessary to stop the threat, a literature study on penetration depths of missiles into concrete was performed. When the threat is stopped, an explosive charge can be initiated, which in its turn poses a severe threat to the intermediate layer. This explosion was simulated by a contact charge on a concrete slab.

During the experiments performed by the TNO Prins Maurits Laboratory (PML) in co-operation with the Royal Netherlands Army Academy (KMA), an alternative mechanism of a high energy punching concrete particle stream was observed and appeared to be the major threat to the next layer. A new series of experiments was performed to examine this particle stream and to determine its characteristics.

This paper first gives the results of the penetration study and a short theoretical consideration of concrete slabs loaded by contact charges. The experimental results of contact charges on (layered) structures are then discussed. Finally the results of some scaling principles are given.

2 PENETRATION DEPTH INTO CONCRETE

In this study the considered threat to the protective structure was either a 500 kg General Purpose (GP) or Semi Armour Piercing (SAP) bomb. The main differences between the two are the explosive contents, the diameter, and the nose contour.

Many penetration formulae are given in literature. The calculated penetration depth into reinforced concrete varies with these formulae. For the GP bomb values of 0.6 to 1.0 m, and for the SAP bomb, values of 1.1 to 1.6 m were calculated. A review of the formulae used is given in [1]. On account of the uncertainty and the possible variations of the threat, for instance the angle of incidence, and assuming enough knowledge of penetration into concrete is available, further attention was paid to the load on the layered structure when the bomb explodes, after it is stopped in the first layer.

3 THEORETICAL CONSIDERATIONS

An extensive theoretical description of the failure process of reinforced concrete loaded by a contact charge is given in [2]. A short summary is given here.

Immediately after the explosion, a stress wave corresponding with a very high stress level of 10 to 20 GPa is initiated. This stress level, together with the shape of the stress wave, determine the strength of the concrete, and this strength in its turn determines the propagation velocity of the stress wave. The pressure rapidly decreases with increasing distance from the initiation point and the lower stress level causes a different stress wave shape.

Figure 1 gives the load deformation curve for concrete under volumetric compression. The high value of the bulk modulus for the elastic response up to point C leads to an elastic precursor with a stress level of about 8 to 10 times the static compressive strength f_c behind the precursor front. The stress level increases and the concrete is crushed. The expansion velocity of the region in which the concrete is fully crushed appears to be smaller than the longitudinal elastic wave velocity. This means that the cratering process in a concrete slab, which can only occur in the crushed zone, can be influenced and disturbed by the elastic waves reflected from the back of the slab, being tensile waves.

The particle velocity due to a plane stress wave is given by the quotient of the pressure and the acoustic impedance (product of density and longitudinal wave velocity). For crushed material, the particle velocity will increase due to the increasing stress and the decreasing impedance. The radial movement of the particles will be obstructed by less crushed material. When this resistance is sufficient, the radial trajectories are deflected, the crushed material is ejected and a crater is formed at the back face. The interference of waves at the back face, during the cratering process, results in principal tensile and compressive stresses. Because of the small tensile strength of concrete, spalling can occur over nearly the whole area, covered by the reflected wave. In front of the crushed zone the resistance to the radial movement of the particles in the cratering zone decreases continuously by the expansion of the crushing zone and by spalling and cracking at the rear of the slab. When the reflected wave reaches the crushing zone in the concrete slab, the particles are ejected downwards through a hole and the cratering is stopped. Owing to the high stresses in the area around the charge, the energy of the concentrated particle stream can be very high. This process of forming a concentrated particle stream will occur above some critical charge weight.

The objective of the intermediate layer is to decrease the stress level; it must distribute the concentrated load and it must stop the particle stream when the first layer has the critical failure as described above.

- To decrease the stress level, the intermediate layer must have a lower acoustic impedance than the first layer. But this causes the first layer to spall more. Another possibility is to dissipate the energy of the stress wave by geometrical or internal damping by which the stress level decreases

and the wave duration increases. To distribute the concentrated load, sufficient strength and stiffness of the intermediate layer is required.

- To stop the particle stream, a high density, modulus of elasticity and strength are required.

These points show that there is no ideal material for the intermediate layer. An attempt is made to gain more insight in these problems with an experimental programme, set up to find answers to the questions: Can the particle stream be avoided? When the particle stream appears, can it be stopped?

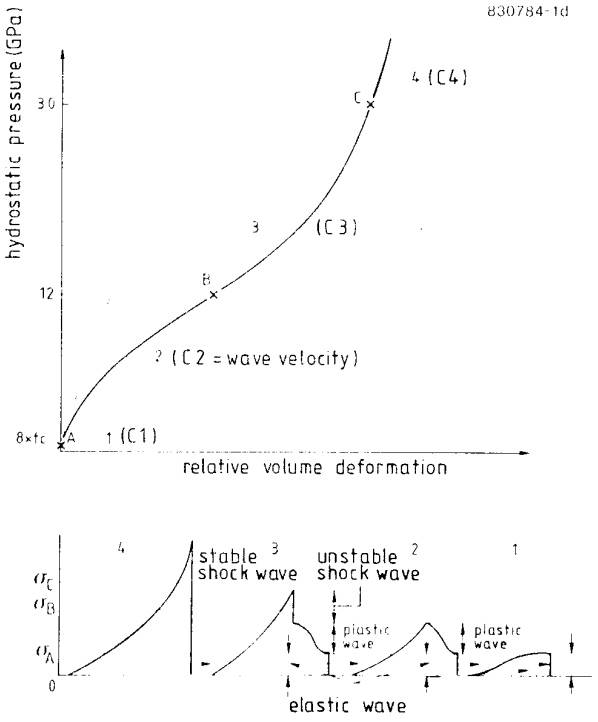

Figure 1 Relationship between compression stresses and relative volume deformations and the variation in the profile of the pressure wave for the different regions

4 CONTACT CHARGES ON LAYERED STRUCTURES

An initial experimental programme was set up to investigate the behaviour of layered structures loaded by contact charges. Layered structures of two reinforced concrete slabs with (reinforced) concrete, polystyrene concrete, rough sand, quartz sand, polystyrene, or air between them, were examined. The thickness of each slab was 0.06 m and its dimension was 1 m^2 [3]. For reference, concrete slabs of 0.12 and 0.18 m thickness were also examined. Hemispherical contact charges of high explosives with 80 % penthrite and 20 % inert material (1.3 TNT equivalent) and charge masses varying from 75 to 400 g were used.

The experiments showed a good damping capacity of intermediate layers containing polystyrene concrete and a good spreading capacity of intermediate layers containing concrete reinforced with steel fibres. The experiments also showed more spalling at a concrete-air interface at relatively small charges and a favourable effect of steel fibres in the concrete with respect to spalling. Monolithic constructions fail by crater formation and spalling due to the expansion of the stress waves from the explosion point. From these experiments it appeared that the failure mechanism of the layered structure is dominated by a particle stream which arises when the charge Q exceeds a critical charge Q_c [4]. This particle stream passes the next layer and hits the bottom layer as a concentrated load (see section 3).

A second series of experiments [5] was then set up to examine the influence of the layered structures on this phenomenon. Two designs were used, one with a thicker upper slab, intended to prevent the particle stream occurring, and one with a thicker intermediate slab, intended to resist the particle stream and to spread the load onto the lower slab. To give the intermediate slab some additional strength and stiffness, a steel plate was also involved in some experiments.

From these experiments it appeared that a thick upper slab is preferable to a thick intermediate layer. In other words: avoid the initiation of a particle stream! Decreasing the thickness of the upper slab cannot be compensated by increasing the thickness of the intermediate slab [6].

The experiments with a steel plate in the intermediate layer showed that the steel plate does not represent an attractive structural alternative for a thick upper plate.

The test results also indicated that the failure mechanism of the particle stream could be scaled. A critical particle stream will be initiated for thicknesses h:

$$h < h_c = 0.0134\, Q^{1/3}\ (m), \qquad (1)$$

with the charge Q in g [6]. This relation was verified for thicknesses up to 0.13 m and charges up to 800 g.

The diameter of the punch cone at the rear of the first slab appeared to be between the hole diameter and the spall diameter. This second series confirmed the mechanism and necessitated quantifying the threat posed by the particle stream. For this purpose a new series of experiments was set up.

5 QUANTIFICATION OF THE PARTICLE STREAM

If the upper slab is not thick enough, the severe threat to the construction to be protected is the particle stream initiated in the intermediate layer. To obtain data on the particle stream, sixty-four experiments with 0.06 m reinforced concrete slabs and contact charges ranging from 20 to 170 g PETN were performed in total [7].

The formula for the critical value (1) has been confirmed to be 85 g for these slabs.

The crater hole diameter can be approximated [9] by:

$$d = 0.0309\ Q^{0.36}\ (m), \tag{2}$$

with the charge Q in g. Similar equations were developed for the diameter of the craters at the front and rear side of the slab.

The velocity of the particle stream was measured with a filming technique. For charges ranging from 50 to 170 g, the average velocities V of the stream range from 160 to 335 m/s, and its widths range from 0.22 to 0.50 m, which is about 2d [7]. As shown in Figure 2, the stream has no divergence. A fit of the obtained velocity data, with the charge Q in g, results in:

$$V = 16.25\ Q^{0.587}\ (m/s) \tag{3}$$

The mass distribution of the particles was also determined for charges ranging from 20 to 170 g. The total retrieved masses of the stream ranges from about 1300 to 4200 g.

To determine the impulse of the particle stream, a ballistic pendulum was used [7, 8]. For the first part of the trajectory (about 1 m), the impulse transmitted to the pendulum is not dependent on the distance between the concrete slab and the target plate in the pendulum. The order of magnitude for the impulse transmitted to the pendulum, I_t, amounts to about 50 Ns for the 50 g load up to about 220 Ns for the 170 g load. A fit of the obtained data, with the charge Q in g, results in:

$$I_t = 0.777\ Q^{1.1}\ (Ns) \tag{4}$$

6 DISCUSSION

The experiments confirm the theory of a critical charge when a concrete slab is loaded with a contact charge. For charge weights above the critical charge, the dominant force on following slabs is formed by the mass stream of small particles ejected through the hole that is punched in the loaded slab [7, 9].

The retrieved concrete mass has a maximum at the critical charge. Since the crater dimensions increase with increasing charge, the mass of the particle stream should increase too. This means that the amount of dust which cannot be caught increases with increasing charge.

From the experiments it appeared that the total mass m of the stream conforms to the mass of a cylinder with diameter d and half the slab thickness h/2 as height:

$$m = 1000\ \pi/4\ d^2\ h/2\ \rho\ (g), \tag{5}$$

with the slab thickness h = 0.06 m, the hole diameter d according to (2) in m, and the concrete density $\rho = 2200\ kg/m^3$.

6.1 Limits of the load produced by the particle stream

A theoretical estimate of the load produced by this stream gives the precursor stress (8-10 f_c) as the lower limit and the crushing stress (30-50 f_c) as the upper limit. So, theoretically, the magnitude of this load will be between 300 and 1500 MPa.

An estimate made with the experimental results leads to the same order of magnitude when the particle velocity is 3000 m/s, being the velocity of the longitudinal wave. The duration time of the load is the ratio of half the slab thickness (0.03 m) and the particle velocity: $t_d = 10^{-5}$ s. Since loss of energy is included in the measured transmitted impulse I_t (4), an underestimate of the force produced by the particle stream, F_u, is given by the ratio of I_t and t_d. The diameter of the stream is 2d, and when a triangular load time distribution is supposed, the ratio of $2F_u$ and πd^2 gives an underestimate of the load produced by the particle stream, P_u. Again, P_u is about 10 times the dynamic compressive strength (f_c = 30 MPa).

The maximal impulse supplied by the stream is $I_s = mV$, where V is the velocity according to (3). The ratio of this impulse and the time t_d gives an overestimated force F_o, and the ratio of $2F_o$ and πd^2 gives the resulting overestimated particle stream load P_o.

The table below shows a review of the limit values calculated in this way for different charges:

Q (g)	d (m)	πd^2 (m^2)	I_t (Ns)	F_u (MN)	P_u (MPa)	I_s (Ns)	F_o (MN)	P_o (MPa)
85	153	0498	103	10.3	280	264	26.4	718
170	196	1207	221	22.1	366	662	66.2	1096

The fact that in the tests, with a concrete slab as second layer, the material was completely crushed by the particle stream, indicates that the lower limit of about 300 MPa is quite accurate.

6.2 Scaling of the experimental results

The literature study on penetration indicates a minimum thickness for the first layer, which must stop the threat, of 1.5 m.
Use of (1) for a contact charge of 250 kg of explosives results in a critical thickness of h_c = 0.85 m.
Use of the Hopkinson scaling law [4]:

$$d_{scale} = c\,(\beta\,Q)^{1/3}, \tag{6}$$

where d_{scale} is the dimension to be scaled, c is equal to 0.0134 according to (1), and β is 1.5 - 2.0 for a confined charge, which is the case here, results in values for the scaled critical thickness of 0.96 - 1.06 m, necessary to prevent the particle stream phenomenon, a somewhat higher value than obtained with (1). These results mean that the residual thickness of the layer, after stopping the bomb, must be at least 1.1 m, so the penetration layer must have a thickness of 1.5 + 1.1 = 2.6 m.
To estimate the required thickness R_{scale} for preventing the perforation of a layered structure by a 250 kg contact charge (Q_{scale}) use is made of:

$$R_{scale}/R = (\beta\,Q_{scale}/Q)^{1/3} \tag{7}$$

Experiments showed a threshold perforation charge of 0.3 kg (Q) for a structure containing 3 layers and with a total thickness of 0.18 m (R). In this case (7) leads to R_{scale} = 1.9 - 2.1 m, the thickness required to prevent perforation by a 250 kg charge. Therefore the thickness of the intermediate layer should be at least 2.1 - 1.1 = 1.0 m. To prevent spalling at the back of this intermediate layer, another layer should be added.
To verify these recommendations and to examine the decreasing quality of concrete with increasing thickness, some full-scale experiments are required.

7 CONCLUSIONS

Assuming enough knowledge is available about the penetration into concrete, the following conclusions can be drawn.

- A critical slab thickness does exist. Below this critical thickness a phenomenon like a concrete particle stream consisting of an increasing percentage of small particles of high energy occurs at a given load. This particle stream has no divergence, and the magnitude of the stress level at the

back of the directly loaded slab is estimated to be between 280 and 720 MPa for charges up to the critical charge of 85 g, and increases to between 360 and 1100 MPa for charges of 170 g. From experiments it appeared that when this particle stream is formed, it will punch through the following layer(s) and poses a severe threat to the construction to be protected. The intermediate layer no longer functions as a pressure distribution and shock absorbing layer.

- To prevent this phenomenon, the thickness of the penetration layer should be at least 2.6 m, and the intermediate layer should be at least 1.0 m thick. An experimental programme for scaling purposes is required to verify these recommendations and to check the validity of the scaling laws used.

8 REFERENCES

1 Harmanny, A., Karthaus, W., Weerheijm, J.
Introductory study on shelters.
PML 1982-20 (in Dutch).

2 Weerheijm, J., Karthaus, W., Opschoor, G.
The failure mode of layered concrete constructions due to contact charges.
21st DoD Explosives Safety Seminar, 1984, USA.

3 Griensven, J.F.A.M. van.
Protective structures. The behaviour of layered structures under an explosive load.
KMA, May 1983 (in Dutch).

4 Weerheijm, J.
Contact explosions on layered structures. Theoretical considerations and structural aspects.
PML 1983-25 (in Dutch).

5 Vriends, E.A.I.M.
Contact explosions on layered structures.
KMA, April 1984 (in Dutch).

6 Weerheijm, J.
Continuing study for an optimal construction of protective structures.
PML 1984-49 (in Dutch).

7 Amelsfort, R.J.M. van, Weerheijm, J.
The failure mode of concrete slabs due to contact charges.
PML 1988-57.

8 Kolkert, W., Amelsfort, R. van.
Study of armour/anti-armour interactions at oblique impact with a ballistic pendulum methodology.
7th International Symposium on Ballistics, 1983, NL.

9 Amelsfort, R.J.M. van, Weerheijm, J., Opschoor, G.
Critical failure of concrete slabs due to contact charges.
24th DoD Explosives Safety Seminar, 1990, USA.

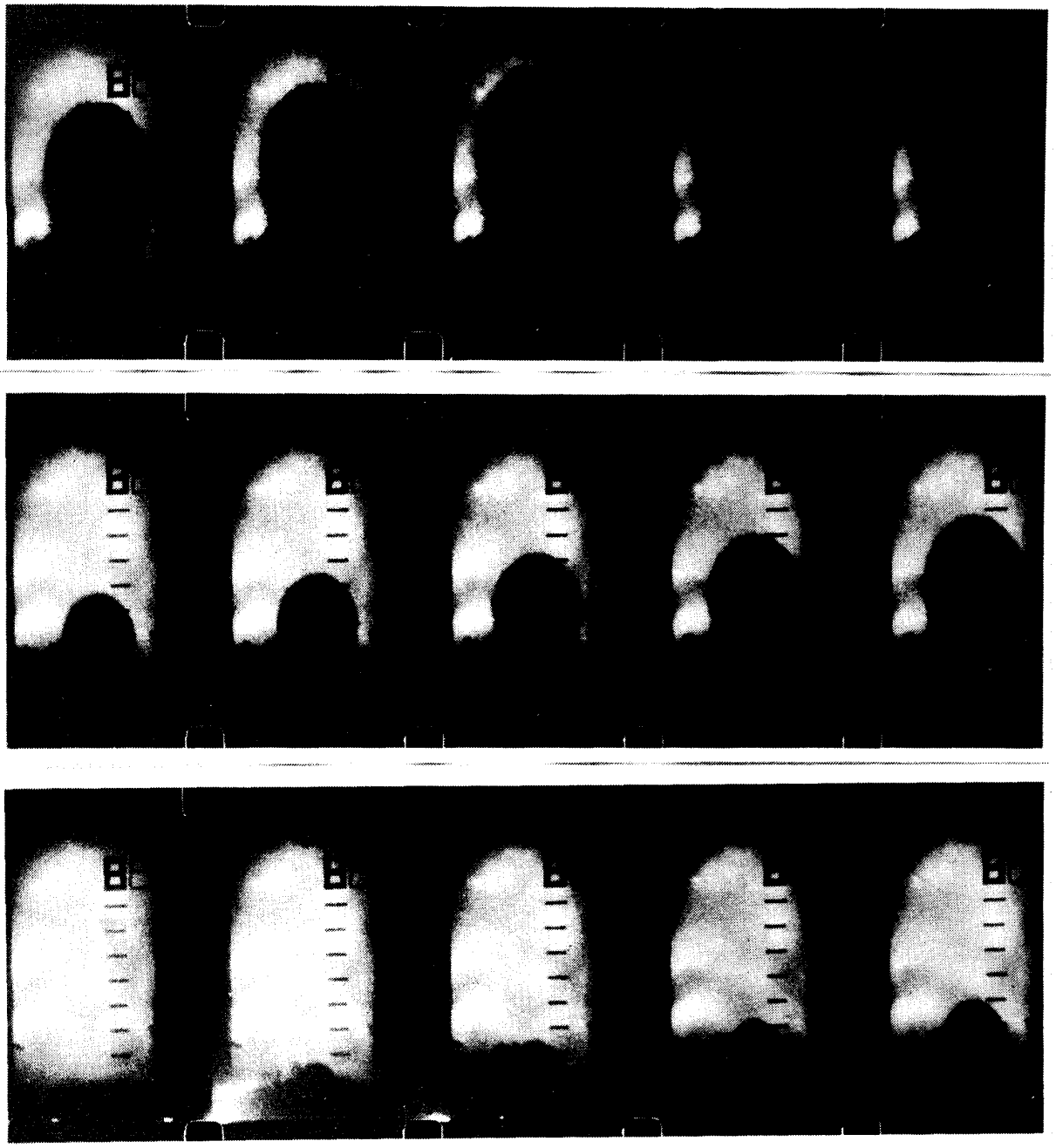

Figure 2 The formation of the concrete particle stream. (Charge 170 g, film speed 4000 frames/s, scale marks 100 mm)

COLLAPSE OF SHEAR WALL BUILDINGS UNDER BLAST LOADING

Zhihao Wang, Qisong Miao, Zhaoyuan Chen

Department of Civil Engineering, Tsinghua University
Beijing, China

Abstract

This paper presents a method for evaluating the collapse process of lightly reinforced shear wall buildings subjected to horizontal external blast loading. Based on the small-scale model test under static loads, a simplified resistance function of the wall structure against collapse is established. The structure can then be analysed dynamically as a rigid body rotating around the base center since the wall deformation is mainly concentrated at the bottom crack section. The results given are essential for estimating the overturning effect on basement shelter under the building.

Model test

Description of the test

The objective of the test is to obtain the resistance curve of lightly reinforced multistory shear wall structures against collapse under horizontal loads. Fig.1 shows the eight-story model structure casted with cement mortar and reinforced with No.16 mild steel wire (diameter 1.65 mm.) on 1:20 scale to the prototype structure. The mechanical properties of the model materials are summarized in Tab.1. All shear walls have a equal thickness of 16 mm with same steel ratio of 0.28% in both horizontal and vertical direction. There are no wall openings in model structure for simplicity.

Tab. 1

Material	Mechanical property	
Cement mortar	Cube strength Modulus of elasticity	23.5 Mpa 1.93 10 Mpa
Steel wire	Yield strength Ultimate strength Elongation of rupture	330-350 Mpa 383 Mpa 12%

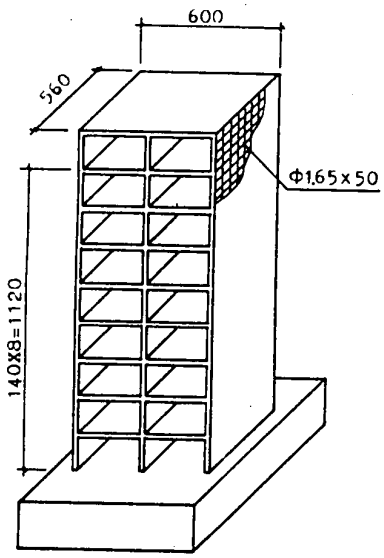

Fig.1 Model structure

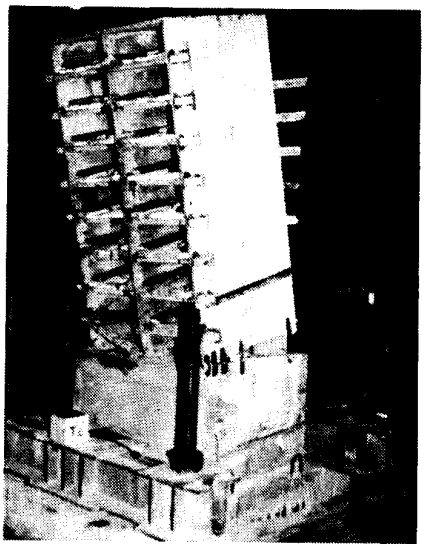

Fig.2 Test device and failure mode

The loading test was undertaken in the Research Laboratory of Earthquake and Blast-Resistant Engineering at Tsinghua University. Shown in Fig.2 is the loading installation with the model fixed to the test bed and loaded in horizontal direction at each floor level by using 4 synchro controlled hydraulic-jacks through load cells and distributed members. Lead blocks were added on each floor which in addition to the self weight of the model increased the total gravity force to 940 kg per floor.

The horizontal deflections at each floor level were measured with LVDT. Elctric resistance strain gages were used to detect the tension cracks and to measure the compressive strain of shear walls at bottom story. The model was forced to deform by jacks at a static speed, and all signals of measurement, including load, deflection and strain, were recorded with a programmed data recorder.

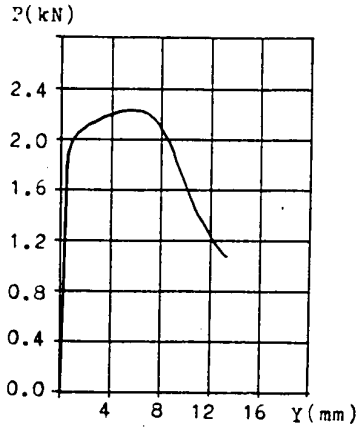

Fig.3 Measured P-y curve

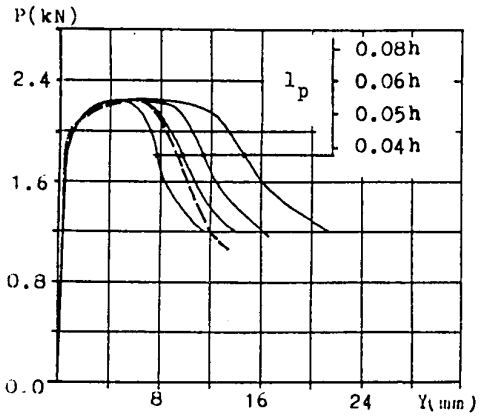

Fig.4 Calculated P-y curves

Test results

Fig.3 is the measured relationship between top floor deflection y and load P. The flexural tension crack appeared at the bottom wall section when the horizontal load P at each floor level increased to 1.75 kN. The wall deflection was really small before cracking (less than 0.4 mm). After the load P reached its maximum value 2.24 kN, the bottom tension steel wires nearest to the wall edge began to break off, causing a sharp descending branch in P-y curve. The whole structure then rotated around the center of the compressive zone at the failed section (Fig.2). According to the measured strength of model materials, the calculated cracking and ultimate loads are 1.67 kN and 2.10 kN respectively and are in good agreement with the tested values.

Discussion

1) Behavior of lightly reinforced shear walls

For lightly reinforced walls with low axial gravity force as examined above, the difference between tension cracking load and yielding load is not significant in magnitude, leading to a single crack occured in first story. The wall deformation is largely concentrated at the single crack region which acts as a plastic hinge with the hinge length much less than that in ordinary reinforced concrete flexural members. Another important feature for shear walls of this kind is the failure mode by fracture of tension steel. All of these results in poor ductility to the structure.

Fig.4 illustrates P-y curves calculated by a computer program for the model structure with different assumed hinge lengths. The following rules are taken in the program: 1) Bernoulli's assumption of plane section; 2) Complete stress-strain relationship including strain softening or hardening for both concrete (mortar) and steel; 3) Computation on deformation increment basis at each step. As seen in the figure, the measured P-y curve (dotted line) coincides well with the calculated ones if the length of plastic hinge l_p is set to be 0.05h, where h is the depth of wall.

2) Post-failure restoring moment

After flexural failure by fracture of tension steel, the upper structure rotates around the corner, and the gravity force N now provides a restoring moment M against wall collapse,

$$M = N \left[\frac{h-x}{2}\cos\theta - \frac{H}{2}\sin\theta \right]$$

where x - length of compressive zone, $x \doteq N/(b \times fc)$
b - wall thickness,
fc - compressive strenth of concrete (mortar).
h, H - the depth and hight of wall.

The above relationship $M - \theta$ can be replaced by a linear one without lossing of much accuracy,

$$M = N \frac{h-x}{2}\left(1 - \frac{\theta}{\theta_1}\right) \qquad (1)$$

in which $\theta_1 = \text{arctg}\,[(h - x/2)/H]$

If the bottom shear force overcomes friction resistance at failed section, the structure would translate horizontally in addition to rotation. No slip displacement however was observed during the model test in which the angle of rotation reached 8° at last.

Dynamic analysis of wall sturcture

Computational model and simplified resistance curve

Based on the test results, it is convenient to consider the wall structure as a rigid body supported by a concentrated rotational spring at the base center (Fig.5). The resistance function of the spring $M - \theta$ against wall collapse can be evaluated from the analysis discussed above and simplified with a multi-linear relationship (Fig.5). Rotation angles at point A,B, can be calculated from load-deflection curve in Fig.4 by using formula $\theta = y/H$, which in correspondence with the beginning of tension crack, and steel fracture. θ_B and θ_c in Fig.5 can also be estimated as

$$\theta_B = \varepsilon_a l_p / (h - x/2)$$

$$\theta_c = 2\theta_B$$

where ε_a - ultimate strain of steel at ultimate strength,
l_p - hinge length, $l_p = 0.05h$,

The resistance beyond point C in Fig.6 comes from gravity action, and is expressed by Eq.1.

It should be noted that a large number of shear walls in engineering practice have substantially different failure modes other than that by tension steel fracture. Different simplified models and resistance functions must be applied to shear walls with moderate and heavy reinforcement, or with large openings and weak couple beams.

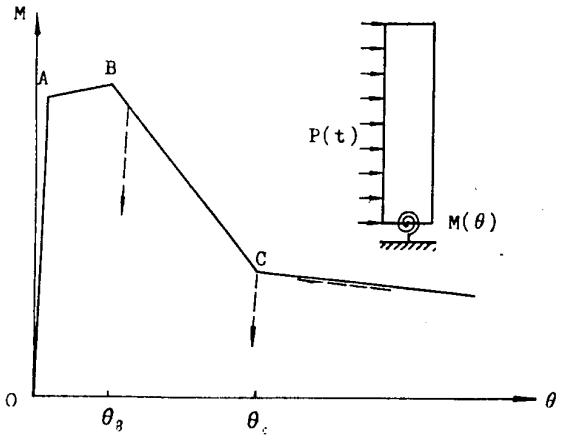

Fig.5 Computational model and resistance curve $M - \theta$

Dynamic equation and its solution

One-degree-freedom system shown in Fig.5 is used for dynamic analysis of wall collapse. The dynamic equation of the system is known to be

$$J_o \ddot{\theta} + M(\theta) = P(t)\, H/2 \qquad (2)$$

where J_o - Rotation inertia of mass
$M(\theta)$ - Resistance function of the spring
$P(t)$ - Distributed dynamic load

Equation (2) is dynamic nonlinear with spring stiffness negative when $\theta > \theta_s$ (Fig.5), hence it will probably become unstable in numerical integration. The stability of different numerical methods has been studied in reference [1] and [2]. An implicit-explicit transient integration algorithm proposed by the authors[2] is used in this paper to ensure numerical integration unconditionally stable in both positive and negative stiffness cases.

The flexibility of soil foundation is not considered here in analysis. It has been discussed in Reference [3].

Example

A shear wall building with underground basement shelter is subjected to explosive loading (Fig.6). The main parameters of the structure are listed in Table 2. Shown in Fig.7 is the time history of net external load P(t).

The danamic responses calculated by Eq.(2) are as follows.

Rotation of structure $\theta(t)$, and internal resistance moment

Tab.2

H = 24 m h = 11.2 m N = 9670 kN θ_t = 0.43 rad	M (θ), see Fig.5	Pt.A	Pt.B	Pt.C
	M 10 kN-m	9.4	10.32	5.24
	θ rad	0.0004	0.006	0.013

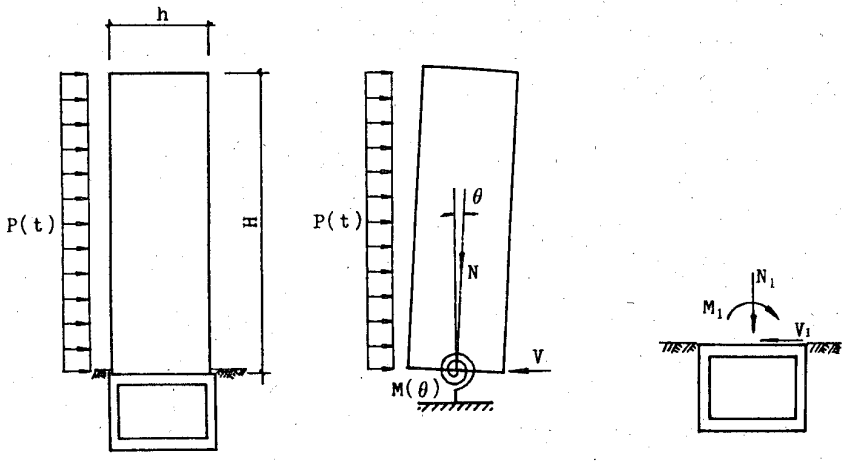

Fig.6 Example for computation

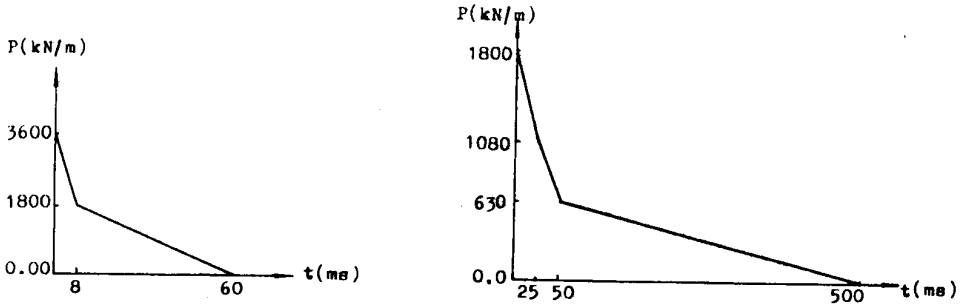

Load case A

Load case B

Fig.7 Load-time history

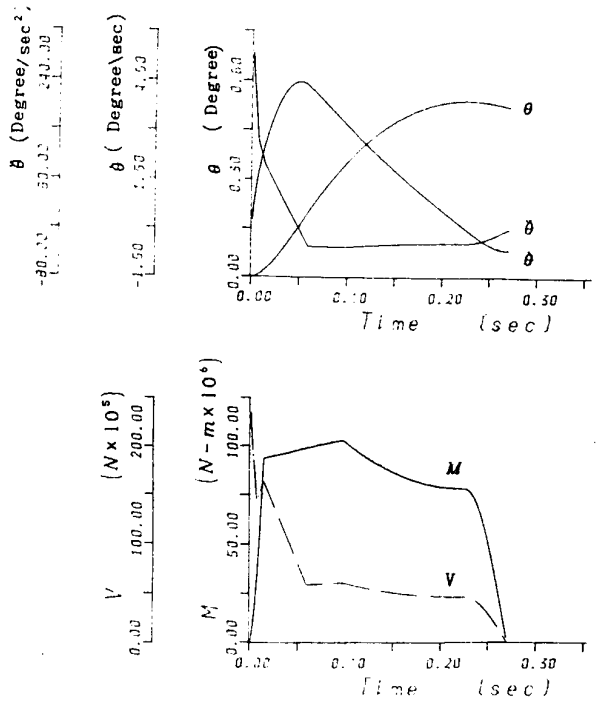

Fig.8 Dynamic response under load case A

M(t) in the assumed spring are plotted in Fig.8 and 9. Maxmum θ amounts 0.54 degrees at t= 220 ms in load case A and 5.74 degrees at t= 1100 ms in load case B. After that the structure rotates in opposite direction and settles down on its original position. The shear force V(t) after fracture of tension steel is no more than friction force at the failed section which implies any translation of structure is unlikely to occur.

Maximum θ will be increased from 5.74 to 16.9 degrees at 2434 ms as load in case B is increased by 1/3. If external load is strong enough to cause $\theta > \theta_1$ ($\theta_1 = 24°$), the structure will no longer rotate back to its original position and fall down.

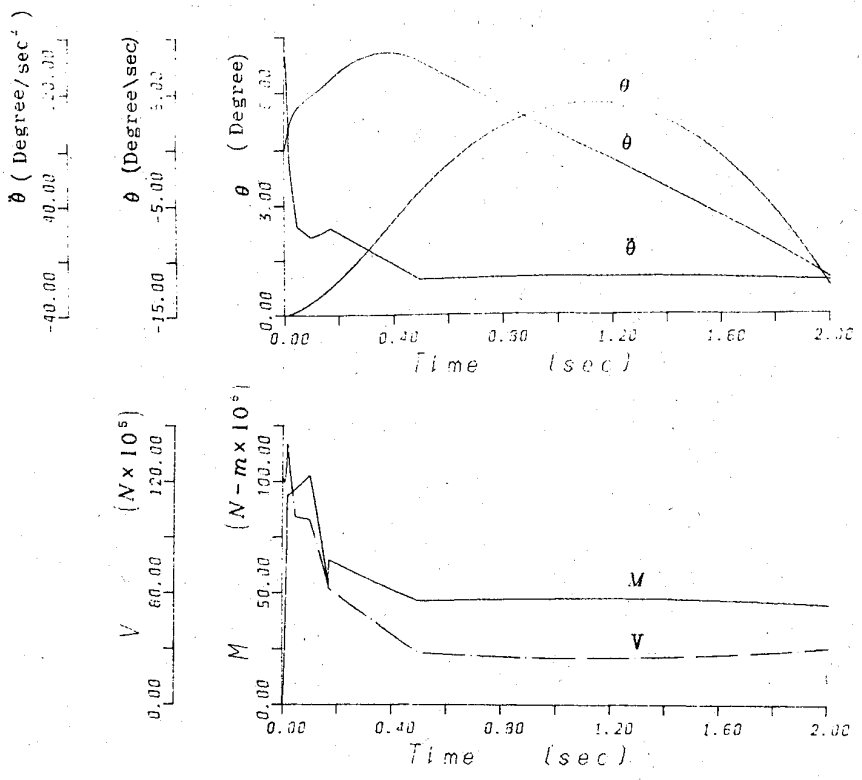

Fig.9 Dynamic response under load case B

Effects on basement shelter

The overturing effects on basement shelter will be (Fig.6)

$V_1(t) = V(t)$

$N_1(t) = N = \text{const}$

$M_1(t) = M(t)$ for $\theta \le \theta_c$

and $= N(h-x)/2$ for $\theta > \theta_c$

After fracture of tension steel, though the section of first floor has failed completely, the upper structure still gives a very strong overturing moment M which must be considered in the vulnerability analysis for basement shelter.

Conclusion

1. For lightly reinforced shear walls with failure mode of tension steel fracture, it is reasonable to use a computational model as shown in Fig.5 and Fig.6 for collapse analysis.
2. The restoring moment by gravity force is of great importance and can not be neglected in collapse analysis.
3. The result given from the collapse analysis is essential for evaluating the vulnerability of basement shelter.

References

[1] Cheng Minxian, Convergence and Stability of Step-by-step Intergration for Model with Negative-Stiffness , Earthquake Engineering and Structure Dynamics, Vol.16, 1988.

[2] Miao Qisong, Yuan Si, Chen Zhaoyuan, Stability in Dynamic Analysis with Negative-Stiffness --- A Mixed Numerical Method for Sturctures with Negative and Positive Stiffness, Proc. of 2nd National Colloquium on Numerical Methods and Its Application to Geotechnical Engineering, Nov. 1990, (in Chinese).

[3] Zhu Hongliang, Chen Zhaoyuan, Overturning Effect of Tall Shear-Wall Buildings on Basement Shelters under Blast Loading, Proc. of 10th National Colloquium on High-Rise Buildings, Jan. 1988, (in Chinese).

ANALYSIS OF BURIED R.C. AND METAL STRUCTURES SUBJECTED TO BLAST LOADING

G M Zintilis[1], S Syngellakis[1,2], and A C Walker[1]

(1) Advanced Mechanics & Engineering Ltd, Guildford, UK
(2) University of Southampton, UK

INTRODUCTION

Two types of buried blast resistant structures are considered: fixed, heavy reinforced concrete bunkers and mobile, light metal emplacements. The former are usually multi-storey buildings intended to protect and support personnel and equipment. Lightweight metal structures, such as battle trenches, are also widely used though it would appear, that these are still of the type developed during and after the Second World War and as such provide limited protection, primarily from air blast and fragments, rather than from underground explosions of artillery and other weapons. The need, therefore, for emplacements of increased resistance against underground explosions is also discussed.

The essential difference between reinforced concrete buildings and metal emplacements is their mass and the way it affects their dynamic response to blast loading. The rather simplistic concept of equivalent soil mass taken to act with a structure has often been relied upon to produce reasonable approximations of the actual soil-structure interaction phenomena. The attractiveness of the simplicity of such added mass methods is tempered by the lack of adequate and validated means of estimating the added mass. There are, however, methods recently developed to calculate the effects of soil-structure interaction (SSI) directly during the response of the structure. One such SSI method of analysis is presented which has been found to lead to more economical designs than those based on approximations of added soil mass. This is because the relative motion of the soil and structure results in load reductions.

BLAST ANALYSIS

The loading on a buried structural wall is determined by integration of the spatial distribution of the blast pressure over the area. A common expression for the empirical maximum pressure is:

$$p_o = f\,K\,(R/w^{1/3})^{-n} \qquad (1)$$

where f is a 'depth-of-burial' factor, K is related to the acoustic impedance (or dynamic modulus) of the soil, R is the distance from a point (x,y) on the wall to the centre of the charge whose weight is w. The index n is an attenuation parameter dependent on soil properties. Formulae such as the above can be introduced into the generic form of blast pressure time history.

An underground blast generates a radially propagating pressure impulse that is usually assumed to be given by an expression of the form:

$$p_R\,(R,t) = AR^{-n}\,f(t) \qquad (2)$$

where f is a time-dependent function representing the impulse decay. Any magnification factor due to the reflection of the incident wave may also be incorporated in A. There are various, mostly empirical, formulae for A to be found in the technical literature as well as design manuals. The more accurate modelling for f(t) is an exponential function which is usually replaced by a triangular impulse in actual calculations.

In addition to making an allowance for the spatial distribution of the loading, it is necessary to obtain the dynamically equivalent load for the idealised system [1]

$$\int_x \int_y p_o(x,y)\ \phi(x,y)\, dxdy = K_L P_o \qquad (3)$$

where ϕ is the normalised deflection shape of the wall element, P_o is the peak load and K_L the load transformation factor. Close-form solutions can be derived if n is an integer number and ϕ is a relatively simple algebraic function. However, in general, numerical integration would be necessary to derive the equivalent loading.

Reinforced Concrete Structures

Individual structural elements are analysed dynamically as single-degree-of-freedom systems, that is, their response to a total blast load P(t) is governed by the equation

$$K_M m\ddot{w} + K_L F = K_L \bar{P}(t) \qquad (4)$$

where w is the central deflection of the element, m its the total mass and F its resistance to deformation. A bilinear elastoplastic model with zero post-yield stiffness is normally adopted for F. The initial elastic stiffness k, the maximum resistance F_m marking the end of the elastic response as well as the transformation factors K_M and K_L generating the equivalent SDOF properties, are determined according to Biggs [1]. The solution incorporates the soil-structure interaction model of Weidlinger and Hinman [2] in the form of an equivalent damping force so that, in Eqn (2), the blast load is modified to

$$\bar{P}(t) = P(t) - K_{LM} C\dot{w} \qquad (5)$$

where $K_{LM} = K_M/K_L$. The damping coefficient C depends on the exposed area of the element and the soil impedance. Furthermore, the condition that $\bar{P}$ cannot become negative applies. As mentioned above the evaluation of the present design loading accounts for the non-uniform distribution of pressure over the buried structure. This is particularly important in cases where the blast is very close to the structure. Then the response is highly localised [3] since the blast pressure would resemble more closely to the action of a concentrated force.

The analysis is therefore based on the pressure formula (2) which is used with n=3. This choice, describes adequately the behaviour of certain types of soil but also is mathematically convenient for yielding closed-form answers to certain analytical integrations over circular domains. Clearly, extending the applicability of the developed software involves only converting analytical to numerical integration so that any value of n can be introduced to the program. The peak normal pressure on the plate is thus given by [2]:

$$p_o = \frac{A}{R^{2+n}} (kr^2 + z_B^2) \qquad (6)$$

with

$$r = \sqrt{(x-x_B)^2 + (y-y_B)^2}, \qquad k = \frac{\nu}{1-\nu} \qquad (7)$$

where x_B, y_B, z_B are the coordinates of the explosive relative to a coordinate system with the face of the plate as its x-y plane, and ν is the Poisson ratio of the soil material.

Plates

The discussion here is restricted to rectangular plates which are assumed to be equally reinforced in their two orthogonal directions and, therefore, isotropic for analysis purposes. This is justified by the axisymmetric nature of the blast load that generates internal stresses in all directions. All the parameters defining the equivalent SDOF which are required for the dynamic analysis are computed using pressure formula (6) in conjunction with the elastoplastic plate characteristics. The elastic deflection of clamped plates due to a centrally applied static load distribution described by (6) is determined by a Galerkin procedure [4]. This solution, considered to be associated with the most unfavourable blast position gives the elastic stiffness and the transformation factors in the elastic range.

Plastic moments corresponding to two types of collapse mechanism [5] are obtained for the same non-uniform pressure distribution. The first mechanism is likely to be generated by an explosion with a large stand-off resulting in a near-uniform pressure distribution. The second is a fan collapse mechanism which is more appropriate for a close-range blast. The latter type of analysis has the additional advantage of being applicable to plates of any shape and support conditions since only the portion of the plate opposite to the explosion is

assumed to respond plastically. The importance of this collapse mechanism was made apparent through the large number of cases already treated using this analysis.

It is accepted that the plate responds plastically according to the collapse mechanism corresponding to the greatest of the two calculated plastic moments. The maximum plate resistance F_m is then found from

$$\frac{F_m}{P_o} = \frac{M_u}{M_p} \tag{8}$$

where M_u is the ultimate moment of the R.C. section and M_p the plastic collapse moment associated with P_o. The mass and load transformation factors in the plastic range are calculated on the basis of the deflection shape associated with the expected collapse mechanism.

Another feature of the present analysis is the rigorous determination of the maximum shear in the plate. This is usually given in tables as the dynamic reaction [1]. Here it is generated as the reaction of a centrally circular portion of the plate subjected to an axisymmetric blast pressure time history. Considering the dynamic equilibrium of this circular element, the following equation is obtained

$$m_s \ddot{w} + C_s \dot{w} = P_s f(t) - 2\pi r_s q \tag{9}$$

where m_s is its effective mass, C_s its effective damping due to SSI, P_s its total peak load and q the uniform shear distribution over its periphery. The time history of q is thus computed as part of the step-by-step integration of Eqn (4). The radius r_s is normally taken equal to the shortest distance between the centre and the edge of the plate. In the case of very close-range blasts however, it is advisable to search for a value of r_s such that the shear q becomes greatest.

Beams Under Slabs

The usual approach in the analysis and design of beams is to identify the beam load as the reaction to plate loading. The present analysis considers the blast at the most unfavourable position, i.e. above the mid-span of the beam. The pressure load is then converted to line load through integration over plate widths that are expected to transmit loads to the beam. This approach is certainly more conservative but also more rational since the location of the blast is in most cases quite arbitrary. The analysis for modelling the beam as a s.d.o.f. follows the same steps as for a plate but it is simpler since it is essentially one-dimensional.

Wall Reactions

Again an approach similar to that adopted for beams is used to yield the axial force transmitted to walls supporting plates or beams subjected to blast. An additional simplification is possible here that does not require dynamic analysis. This is because of the high axial stiffness of the walls such that it is reasonable to assume that the shock is transmitted to them at its peak intensity.

Examples

A FORTRAN program implements the analysis described above. The program also contains useful design features such as the rigorous determination of sectional R.C. properties based on code recommendations for material behaviour. Subroutines dealing with the elastic and plastic analyses of plates with various support conditions can easily be added to the program. The dynamic response is calculated according to a standard numerical integration scheme [1].

The program was tested using data from two papers from American literature. This necessitated the conversion from American to British concrete strength values. Moreover, the characteristic strengths of steel and concrete were assumed dynamically enhanced in both cases. All the numerical input to the program is detailed in Table 1.

The first paper [3] reported analytical and experimental results for two plates with sufficient information for numerical data to be deduced for analysis. The factor K appearing in the pressure formula (1) was obtained from the given maximum pressure at the centre of the plate. The size and spacing of flexural reinforcement were chosen to produce the given reinforcement ratio. Triangular pressure time history was used in the paper with an impulse duration t_d=0.5 ms. This value was notably smaller than durations predicted by established formulae.

The present analysis applied to one of the plates tested, predicts a maximum deflection of 86mm compared to the reported experimental value of 71 mm. The analysis also predicts the fan collapse mechanism observed in the experiments. There is however considerable uncertainty in the choice of proper values for most of the parameters describing the simple SDOF model. The soil properties were not clearly described in [3]. On the other hand the response is found to be particularly sensitive to the value of t_d which varies over the plate while its prediction from various formulae also varies widely. Accounting for all these factors the comparison of the results is deemed satisfactory.

A second example [2] considers a one-way slab with its stiffness and mass characteristics obtained from tabulated results associated with uniform loading. The present analysis admits a long span in the transverse direction and yields an equivalent model of lower stiffness and higher resistance than the one used in the paper. This results in a higher yield displacement so that a maximum deflection of 106 mm is predicted compared to 73.3 mm found by Weidlinger and Hinman. The respective results for the ductility ratio were 8.23 and 9.8. It appears therefore that safe predictions are obtained consistently by the present approach. The same plate was reanalysed without SSI but with the usually employed reflection factor of 1.5 instead of 2.0. This results in an increased ductility ratio of 26.5 thus confirming the benefit of better and direct estimates for SSI. It is also worth mentioning that a fan collapse mechanism is predicted also in this case which highlights the importance of considering the non-uniformity of pressure distribution.

DATA	PLATE 1 [Ref.3]	PLATE 2 [Ref.2]
plate width (m)	0.91	12.8
plate length (m)	0.91	40.0
plate thickness (m)	0.1	1.35
blast stand-off (m)	0.61	6.4
explosive mass (kg)	3.02	464.5
reinf. ratio in tension	0.1	0.0045
concrete strength (MPa)	40	40
steel yield stress (MPa)	400	400
soil constant K (psi)	3200	3520
depth of burial factor	1.	0.4

Table 1 Numerical data for the example reinforced concrete plates

Metal Structures

Typical metal structures such as the panel-post combination shown in Figure 1, can be modelled as a two-degree-of-freedom (d.o.f.) system. The equations of motion are:

$$K_{M1}\, m_1 \ddot{w}_1 + K_{L1}\, F_1 = K_{L1}\, [\bar{P}(t) - m_1\, \ddot{w}_2] \tag{10}$$

$$K_{M2}\, m_2\, \ddot{w}_2 + K_{L2}\, F_2 = 0.5\, K_{L2}\, [\bar{P}(t) - m_1 \ddot{w}_2 - K_D m_1\, \ddot{w}_1 + (K_{LM1} - K_D)\, C \dot{w}_1] \tag{11}$$

where

$$\bar{P}(t) = P(t) - C\,(K_{LM1} \dot{w}_1 + \dot{w}_2) \tag{12}$$

with the indices 1 and 2 denoting panel and post respectively. The transformation factor K_D accounts for the non-uniform distribution of the inertia force $m_1 \ddot{w}_1$ as it is transmitted to the post. It is noted that damping due to soil-panel interaction depends on the total panel velocity $\dot{w}_1 + \dot{w}_2$.

The elastic bending stiffness of the panel is neglected so that its initial stiffness is provided by its resistance to plastic membrane deformation. Thus, although the dynamic analysis admits unloading, the FORTRAN program implementing it stops when the first maximum plate deflection is reached. The maximum resistance F_{1m} corresponds to rupture so that the design objective is a ductility of 1 for the panel. Conventional elastoplastic analysis provides the stiffness and maximum resistance F_{2m} of the post.

Because of the lightness of the metal structure, in the absence of soil damping its own inertia is not sufficient to mitigate the effects of the dynamic loading on its integrity. For a rational design, consideration of an alternative model for the soil-mass interaction is therefore essential. A simple such alternative to the damping

model included in Eqns (10) and (11) is to consider the soil moving together with the panel thus providing the additional inertia required to resist the blast. This approach, although resulting in a simpler and stabler numerical integration scheme, is certainly very empirical and for that reason less reliable than representing the soil effects as a damping force.

The main purpose of the numerical studies was therefore to compare the predictions from the two soil modelling approaches described above. Calculations were initially performed with C=0 in (10) and (11) but with a very substantial contribution from the soil to m_1. This contribution depends on the assumed shape of the interacting soil mass and the blast stand-off. An additional consideration in the context of this crude modelling is reducing the reflection factor for the blast load from 2 to 1.5. This is a code of practice recommendation. It is also obvious that the mass factor for the panel is irrelevant in this case and therefore K_{M1} is set equal to 1.

The design case study was based on the data of Table 2. A triangular load time history was assumed. Solving the problem initially with the soil contributing to the inertia of the system, the acceptable ductilities of 0.86 and 8.11 for panel and post, respectively, were obtained. The time histories of the deflections are shown in Figures 2(a) and 2(b). With the soil effect modelled as damping, the ductilities predicted by the program were 0.0045 for the panel and 0.8941 for the post. The respective time histories of the deflections are shown in Figures 3(a) and 3(b).

It is obvious from these results that the effective soil mass assumption is a very conservative one. It is worth mentioning that, with the soil damping model, the cross-section of the post had to be reduced almost by half for the design limit of the ductility ratio to be reached. Another interesting comparison can be made regarding the nature of the response. Thus, due to the very large amount of damping relative to the masses and stiffnessess of the system, maximum response is reached very quickly and without any post oscillation. Furthermore, the damping model predicts a safe panel response with little sensitivity to substantial variations of the initially considered geometric data.

PROPERTIES	PANEL		POST
	soil mass	soil damping	
mass (kg)	7374	1.72	6.83
mass factor	1	0.5	0.33
stiffness MN/m	0.28		788.5
maximum resistance (MN)	0.114		0.785
damping coefficient (MN.s/m)		2.186	
peak load (MN)	4.731	6.308	
impulse duration (s)	0.01		
load factor	0.61		0.5

Table 2 Properties and applied load for the two d.o.f. system

DETAILED DESIGN CONSIDERATIONS

One of the main characteristics of blast-resistant structures is their ability to absorb large amounts of impulsive energy through mechanisms involving extensive plastic deformations. In order to achieve this it is necessary to design joints and other locations of large plastic strains such that the full ductility is generated and utilised.

For concrete structures this ductility is achieved by proper choice of aggregate, size and distribution of bending reinforcement, lap lengths and shear reinforcement. The allowable rotation before failure is maximised when equal tension and compression reinforcement is provided. If this is a requirement it may then be necessary to provide lacing (zig-zag) bars. Such reinforcement is also necessary where the ultimate shear capacity of the concrete is not sufficient to sustain the bending action.

For metal structures ductility is an inherent material property. It is necessary though to choose the best material for the application in question. Aluminium can be attractive over steel because of its lightness and durability. It is, however, expensive, its ductility is about $^1/_3$ that of mild steel and welding can reduce its strength significantly.

Another important consideration for blast resistant structures relates to the properties of the 'in-situ' soil and of the backfill subsequent to excavation. For temporary light metal structures it is advisable, and often practicable, to minimise the compaction of the backfill and ideally leave an air gap between the structure and the surrounding soil. Thus, by careful backfill specification it is possible to reduce the loading significantly.

The situation for large, permanent r.c. buildings is more involved. This is because on the one hand it is desirable to minimise bomb penetration into the surrounding soil and to keep long term settlement low. On the other hand the higher the soil stiffness the greater the blast effects on the building and its contents. It is possible to achieve economic compromises by specifying as low as possible a level of backfill compaction, in conjunction with a so-called 'burster' slab. Thus, the attenuation of shock pressures on the building is achieved in two ways: first, the bomb is forced to detonate at a greater distance and second by the low soil stiffness. In addition it may be possible to keep the water table low which will also help reduce the blast pressures. The benefits and the corresponding costs of such measures can be optimised by performing 'trade-off' analyses.

SUMMARY AND CONCLUSIONS

Buried protective structures in reinforced concrete or metal are fast becoming commonplace in many countries, both for military and for civilian applications. An analysis method which deals directly with the effects of soil-structure interaction and non-uniform loading, is presented for both r.c. and metal structures. A comparison of the results with the conventional 'added mass' method is made. Finally, some important detailed design considerations are presented with a view to produce economic designs for buried r.c. and metal structures.

REFERENCES

1. Biggs, JM (1964) "Introduction to Structural Dynamics", McGraw-Hill, New York.
2. Weidlinger, P and Hinman, E (1988) "Analysis of Underground Protective Structures", J. Struct. Engng, Proc. ASCE, 144(7), 1658-1673.
3. Ross, CA, Schauble and Nash, PT, (1980) "Response and Failure of Underground Reinforced Concrete Plates subjected to Blast", The Shock and Vibration Bulletin, No. 50, Part 3, pp. 71-83.
4. Timoshenko, SP and Woinowsky-Kreiger (1959) "Theory of Plates and Shells", McGraw-Hill, New York.
5. Johansen, KW (1972) "Yield-line Formulae for Slabs", C&CA London.

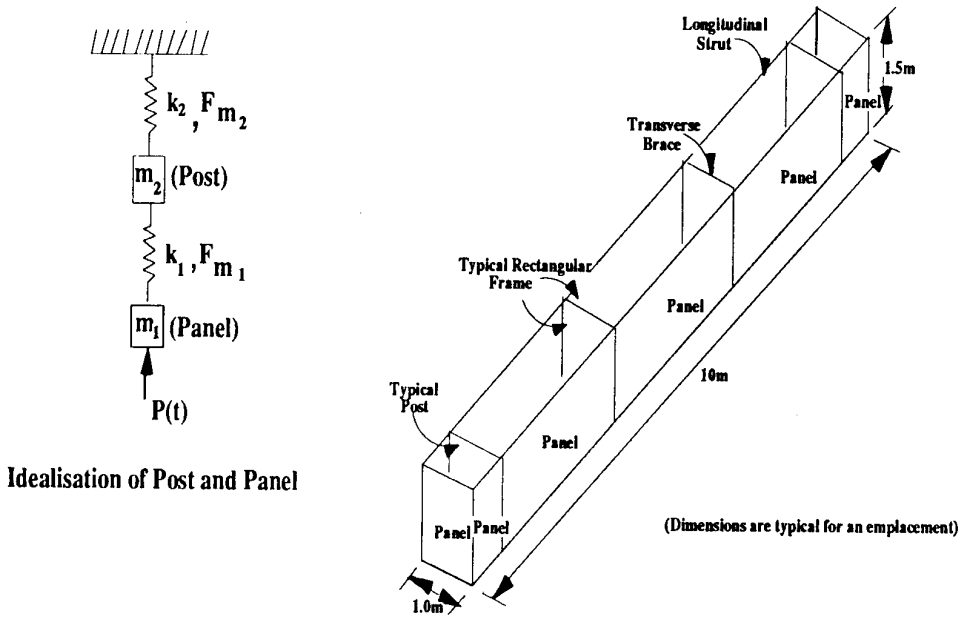

Figure 1. Typical Buried Metal Emplacement and its Idealisation

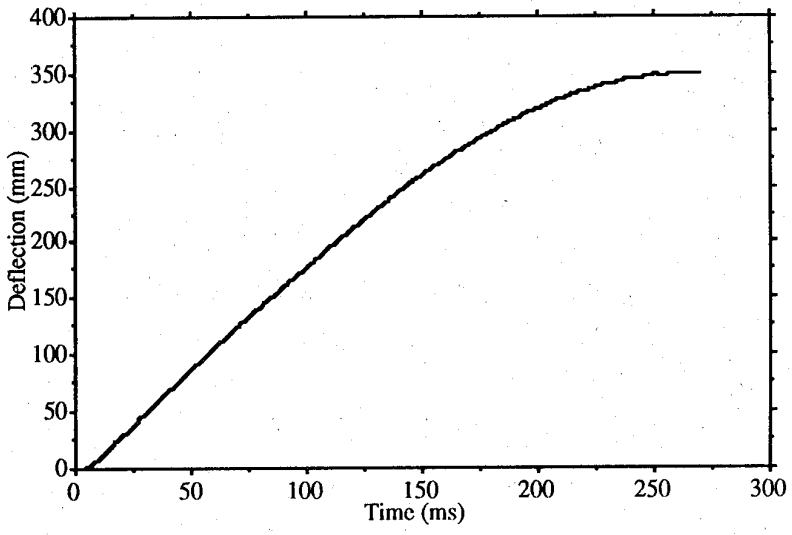

Figure 2(a) Panel Deflection Time History Predicted using the Soil Inertia Model

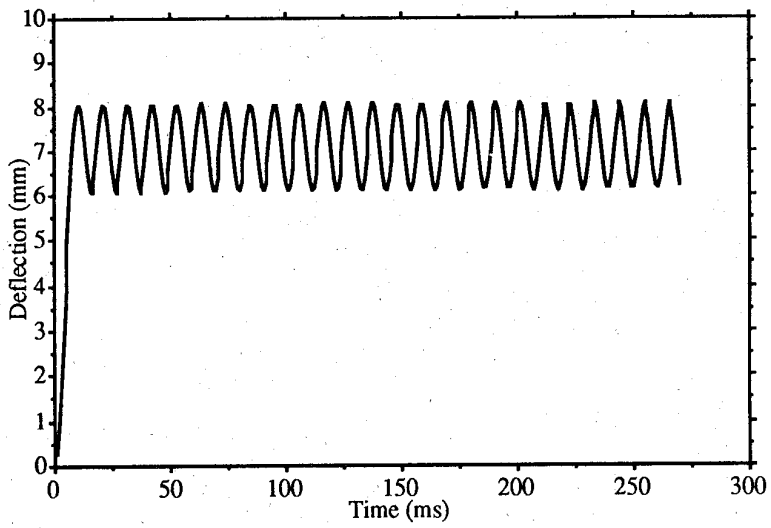

Figure 2(b) Post Deflection Time History Predicted using the Soil Inertia Model

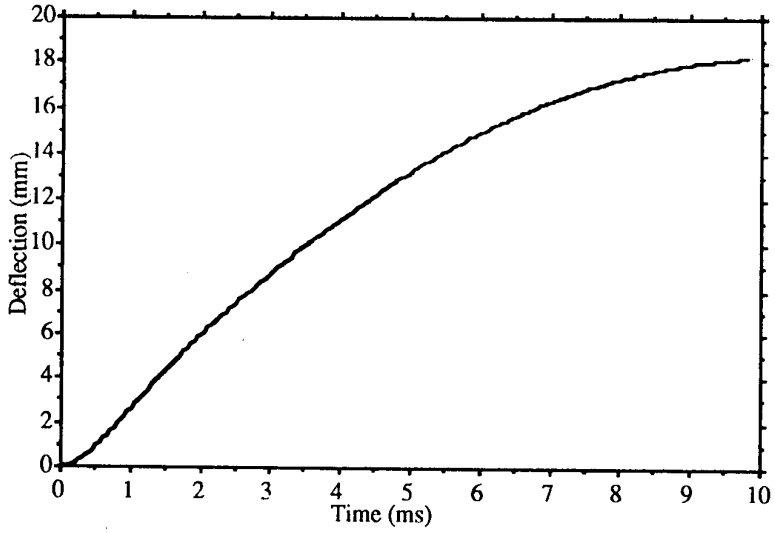

Figure 3(a) Panel Deflection Time History Predicted by the Soil Damping Model

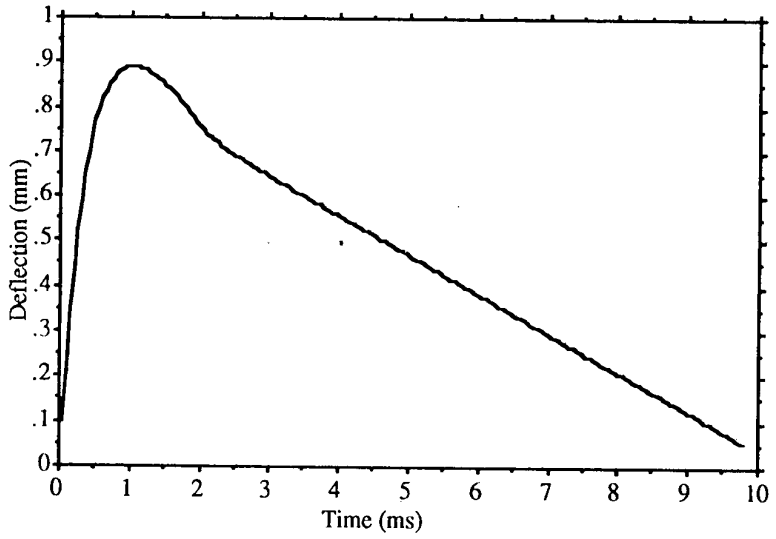

Figure 3(b) Post Deflection Time History Predicted by the Soil Damping Model

Boden-Bauwerk-Interaktion

Soil-Structure-Interaction

VALIDATION OF A FINITE DIFFERENCE CODE USING MODEL TESTS OF DYNAMIC SOIL STRUCTURE INTERACTION

Major Kevin J. Claber R.E.[1]
Michael C.R. Davies[2]
and
Mark C. Saunders[1]

[1] RARDE (Christchurch), U.K.
[2] University of Wales College of Cardiff, U.K.

ABSTRACT

The results of laboratory floor model tests of impulsive surface loading on soil and soil/structure systems were used in a validation exercise of a dynamic loading finite difference code. The structure in the experiments was a buried flexible cylinder. Predictions of free-field stresses, soil/structure interface stresses and cylinder hoop strains were obtained using two material models to represent the soil. The accuracy of these models was assessed as part of the validation exercise.

1 INTRODUCTION

In common with all forms of analysis, the results of predictions using non-linear codes for dynamic loading require validation before complete confidence can be placed in the technique. To conduct such an exercise, geometric and material parameters of the system under analysis must be closely specified together with the loading history. There should also be sufficient measurements of the response of the system to loading - which provides the data for comparison with the predictions in the validation exercise.

Two aspects have to be considered when analysing the effect of dynamic loading on a buried soil/structure system. First, the magnitude of the stress wave reaching the structure from the source of disturbance, i.e. the free-field stress, has to be quantified. The dynamic soil structure interaction resulting from the intersection of the stress wave by the structure may then be calculated. In order to validate all aspects of a dynamic loading finite difference code it is necessary, therefore, to examine the response of the two major components of the system, i.e. the structure and the surrounding soil medium.

Validation exercises may be conducted by comparing the measured response of full or large scale prototype systems (or elements of such systems) with predicted values. Such an exercise has been conducted Stevens et al, [1] and [2], in which the results obtained from field trials of 1/4 scale buried reinforced concrete arches subjected to surface generated blast loading were compared with values predicted from a hybrid finite difference/finite element code. Although the analyses were based on limited available material parameters, good agreement was obtained in comparisons of measured and predicted structural strains, accelerations and displacements, and soil structure interface pressures.

Physical model tests provide an alternative, and often less expensive, technique for conducting comparisons of analysis with physical data. Boundary conditions are exactly specified in a model; removing the necessity for making approximations of boundary locations in the analysis. Materials which have well defined properties may be chosen for the model and repeatability of model tests permits the applied loading and system response to be closely monitored.

Herein is described a validation exercise conducted to assess the accuracy of a general dynamic loading finite difference code when applied to the prediction of soil/structure interaction.

2 PHYSICAL MODEL

The model tests used in the validation exercise were conducted as part of an investigation into impulse loading on buried flexible structures. Detailed results from this series of experiments have been previously presented [3]. In this study brass cylinders were buried in a dry sand medium at varying depths of cover and loaded dynamically with a surface impact. In addition to these experiments a free-field test was performed in which the stress propagation through the soil alone was monitored. The experiment in which the cylinder was buried at a depth of cover of 50mm and the free-field test were selected for analysis in the validation exercise.

2.1 Apparatus, instrumentation and experimental procedure

A 1.5m cubic tank, into which sand could be poured from a hopper to form a medium having a repeatable uniform density of 16.8 $\pm$ 0.1kN/m^3, was used for the experiments. The cylinder, 100mm in diameter and with a wall thickness of 0.127mm, was fabricated from five lengths - joined together with adhesive tape - to span the tank. Segmental construction isolated the instrumented central section from end effects, resulting from confinement in the tank, thus ensuring plane strain conditions for the instrumented section. The loading of the soil/structure system was an impulsive force provided by a 26kg mass (a beam to maintain plane strain conditions) dropping through 200mm onto a 100mm wide footing located at the soil surface. The centreline of the beam and footing coincided with that of the cylinder.

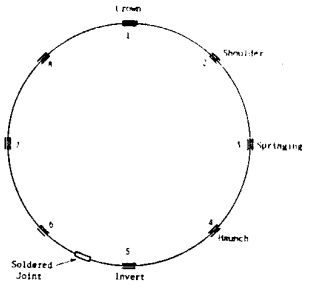

Figure 1 - Location of strain gauges

Circumferential strains in the cylinder wall were measured by 8 pairs of stain gauges positioned symmetrically around the middle segment, Fig. 1. In each pair of gauges one was located on the inside and the other on the outside of the cylinder wall. This configuration enabled measurement of hoop and bending strains from which hoop stresses and bending moments could be obtained.

Dynamic stresses at locations in the soil between the point of impact and the structure and adjacent to the structure were measured using miniature pressure cells.

3 NUMERICAL MODEL

A two dimensional non-linear hydrodynamic finite difference computer code describing the dynamics of continuous media was used in the validation exercise. In this code the conservation of mass, momentum and energy are expressed through differential equations which are solved with an explicit, centred difference, time integration method. Materials are described through an equation of state, where pressure is a function of density or internal energy, and a constitutive relationship. Spacial discretisation may be described through either a Lagrange processor, where the coordinate system is permitted to move, or a Eulerian processor, in which the coordinate system is fixed.

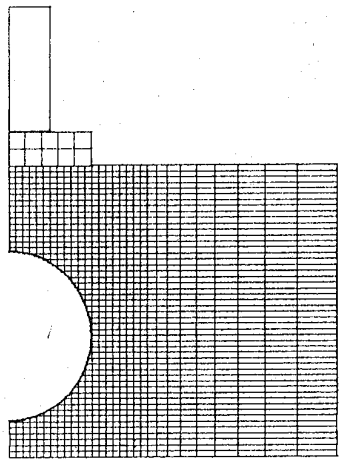

Figure 2 - Soil/cylinder model mesh

3.1 Discretisation and choice of material models

As has been described above, the experiment was devised to simulate plane strain conditions. This allowed planar geometry to be used for modelling; the geometry being symmetrical about the impactor centre line. Modelling the complete depth and width of the soil tank used for the model tests was impractical in terms of the size of mesh needed and, thus, the computer time required. Mesh boundary conditions were chosen to simulate a symmetrical loading condition and an extended medium. This was considered to be a satisfactory assumption, because in the experiments the boundaries of the tank were located at a great distance from the cylinder. A plot of the mesh showing the impactor, plate soil and cylinder components is presented in Fig. 2. A Lagrange grid description was used for both the impactor and plate, a Eulerian grid description being used for the soil. The cylinder, which had a thickness of only 0.127mm, was modelled using shell elements. The shell grid description assumes a biaxial stress state and is based on full bending theory.

The material behaviour of the brass forming the cylinder was modelled using a linear equation of state together with a Von-Mises failure criterion. Two models were used to describe the soil stress strain behaviour; the performance of each material model being assessed as part of the validation exercise. The simpler of the two models ("Linear") represented the soil using linear elasticity, whilst the more complex non-linear model ("Porous"), in which the stress/strain relationship was a function of soil density, permitted both recoverable and irrecoverable deformations. The failure criterion used in the Porous model was Mohr-Coulomb. Material parameters for use in the models for both brass and soil were initially obtained from monotonic loading laboratory tests. In addition, comparisons of the predicted and measured stresses and wave velocities in the free-field experiment were used to select the most appropriate parameters for the Porous soil material relationship used in the analysis of the soil/structure model.

4 VALIDATION OF CODE

4.1 Free-field analysis

The analysis of the free-field test had two primary objectives. The first was to establish the most suitable parameters for use in the Porous material model for sand. This was necessary because at the relatively low levels of in-situ stresses in the experiment the material parameters for the Porous model are highly sensitive to changes in stress. This problem would not be encountered at the levels of stress in a full scale prototype or geotechnical centrifuge model (in which at elevated levels of gravity prototype values of in-situ stresses are obtained) where the material parameters are less sensitive to changes in stress. A calibration exercise was therefore conducted to obtain the material parameters - within the range of values measured in single element laboratory tests - with which the analysis correctly predicted the dynamic stress at the level of the top of the structure in the soil/structure model, i.e. at a depth of 50mm.

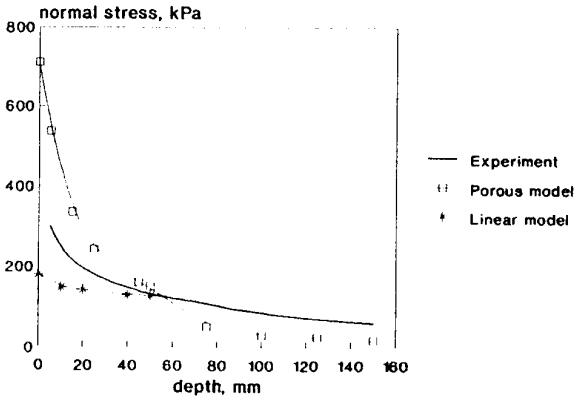

Figure 3 - Comparison of measured and predicted stress in free-field model

In Fig. 3 the values of pressure recorded at different depths in the physical model are plotted together with the values predicted using the Linear and Porous models in the finite difference analysis. The plot shows that although the Linear model (which used parameters obtained in laboratory element tests) correctly predicted the level of stress at a depth of 50mm, the value of

stress at the surface is under predicted. Conversely, for predictions with the Porous soil model, using material parameters chosen to obtain the correct stress at a depth of 50mm, the value of stress immediately beneath the point of impact at the surface of the sand is greater that measured in the model test. However, with depth the values predicted by the Porous model rapidly converge on the measured values and thereafter shows similar attenuation.

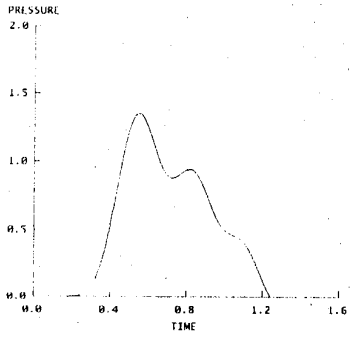

(a) Linear model

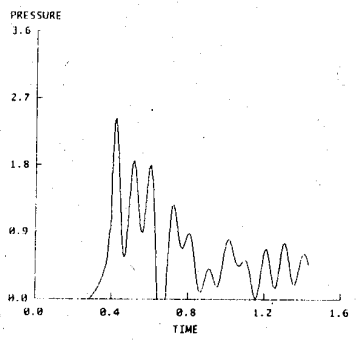

(b) Porous model

Figure 4 - Pressure history at a depth of 25mm

Having calibrated the soil model the second aim of the analysis of the free-filed test was to investigate the accuracy of the code in predicting the characteristics of the pressure pulse resulting from the impact of the mass on the plate located at the surface of the soil. The pulse duration was predicted to be 1.2ms and 1.6ms in analyses using the Linear and Porous soil models respectively. These values compare exceptionally well with the average value measured in the experiments of 1.22ms. The predicted pressure/time curves shown in Fig. 4 show slightly different characteristics. The plot obtained using the more complex Porous model indicates significant reduction in stress including, at some points, complete unloading, whereas the curve predicted using the Linear model is more continuous - and was found to more closely resemble the experimental curve. Variation in pressure resulted from the multiple impact of the dropping mass on the plate. The difference in the analytical results probably indicates that the Porous model, which allows irrecoverable strains to develop, did not permit sufficient rebound of the soil between impacts.

The propagation velocity in both analyses were also very similar, being 14.28 cm/ms and 15.15 cm/ms for analyses using the Linear and Porous models respectively. Although the predicted velocities were somewhat lower that the value of 23 cm/ms measured in the experiment they are of similar magnitude.

4.2 Soil/structure model analysis

The soil/structure model was analysed using both the simple Linear and the more complex Porous material models for the soil. The material parameters used in the latter model were those obtained from the calibration of the analysis (using the data of the free-field model test) to produce the correct level of stress at the depth of the structure.

A suitable parameter to assess the initial cylinder response was felt to be the maximum hoop strain. As has been presented above, the circumference of the buried cylinder was instrumented with strain gauges enabling hoop strains to

Location	Experiment μ strain	Predicted 1* μ strain	Predicted 2+ μ strain
CROWN	-190	-254	-140
SPRINGING	-120	-258	-144
INVERT	- 85	-257	-147

*Linear Model +Porous Model

Table 1 - Measured and predicted cylinder hoop strains

be measured. Measured and predicted maximum values of hoop strain at the crown, springing and invert of the cylinder are presented in Table 1. Both analyses predicted uniform hoop strains around the circumference of the cylinder which are of the same order of magnitude as those measured in the experiment. Hoop strains predicted by the analysis using the more complex

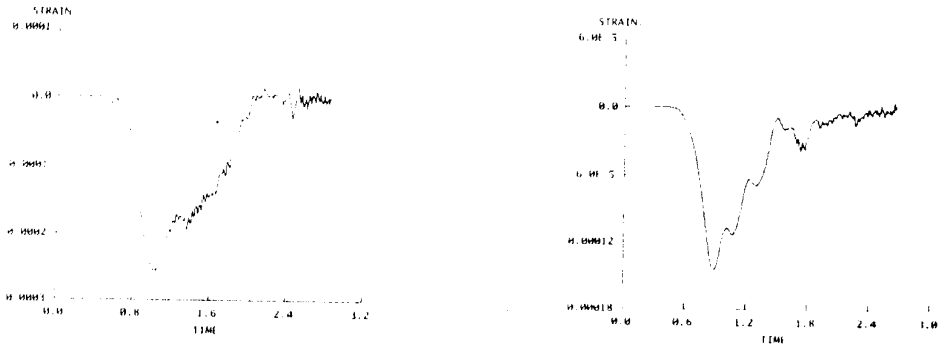

(a) Linear model (b) Porous model

Figure 5 - Predicted hoop strain history at cylinder springing

Porous soil model are very close to experimental values. Typical hoop strain/time curves for both analyses, Fig. 5, show almost identical behaviour; these also closely resembled experimental observations. As is shown in Table 1, in the experiment there was some variation in hoop strain around the cylinder circumference. This observation was more marked in the experiment used for the validation exercise considered herein than in others in the series of tests, [4], and probably resulted from small variations in soil density around the cylinder in this experiment.

At a depth of 50mm (i.e. the level of the crown of the cylinder in the soil/structure test) in the free-field test the dynamic stress was measured (and predicted) to be 130kPa. Measurements of the stress in the soil/structure model test indicated that 5mm above the structure the stresses were identical to those in the free-field experiment. In the analyses similar behaviour was predicted. At the boundary of the soil and the structure predicted stresses reduced to 42kPa in the analysis using the Linear model and 28kPa when the Porous model was used for the soil. This reduction in stress adjacent to the structure resulted from the deformation of the highly flexible cylinder.

5 CONCLUSIONS

The validation of a finite difference code has been conducted by comparing the soil stresses and structural strains measured in experiments of surface impulse loading of soil and soil/structure systems with values predicted by the code. The following conclusions may be drawn from the validation exercise.

1. At the levels of in-situ stresses encountered in the experiments the material parameters from the Porous soil model are highly sensitive to small changes in stress. Using the results of the free-field experiment, a calibration exercise was conducted to obtain the most appropriate material parameters for use in the analysis of the soil/structure model.

2. In general good agreement was obtained between the experimental observations and predictions obtained by the code using both soil material models. Predictions using the more complex Porous model were closer to measured values. However, the level of sophistication of these material models is not high and they may not be suitable for satisfactorily predicting the stress/strain behaviour of other soil types, such as saturated clay, or behaviour at higher rates of strain. It is proposed that a more sophisticated model be incorporated into the code.

Prototype stress conditions may be achieved in scale models tested using a geotechnical centrifuge. A programme of centrifuge tests of impulsive and blast loading of soil/structure systems is currently being conducted. The results of these experiments will be used in future validation exercises conducted by University of Wales College of Cardiff and the Royal Armaments Research and Development Establishment.

ACKNOWLEDGEMENTS

The numerical modelling described herein was carried out at the Royal Armaments Research and Development Establishment, Christchurch, U.K. The financial support of RARDE (Christchurch) for the research in dynamic soil/structure interaction at University of Wales College of Cardiff is gratefully acknowledged.

REFERENCES

[1] Stevens, D.J. and Krauthammer, T. (1991), Analysis of Blast Loaded, Buried RC Arch Response. I: Numerical Approach, J. Struct. Engrg., ASCE, 117(1), 197-212.

[2] Stevens, D.J., Krauthammer, T. and Chandra D. (1991), Analysis of Blast Loaded, Buried RC Arch Response. II: Application, J. Struct. Engrg., ASCE, 117(1), 213-234.

[3] Davies, M.C.R. (1989), Physical Modelling of Impact Loading of Buried Structures, in Structures Under Shock and Impact (Ed P.S. Bulson), Proceedings of the 1st Int. Conf. on Structures Under Shock and Impact, Cambridge, Massachusetts, Elsevier, Amsterdam, 431-442.

[4] Davies, M.C.R. (1989), Impact Loading of Buried Structures, Report, Contract No. 2072/043, Royal Armaments Research and Development Establishment, Christchurch, U.K.

EFFECTS OF CUSHION LAYER FOR UNDERGROUND STRUCTURE SUBJECTED TO IMPACT LOADINGS

Kazuo FUJIMOTO, Hiroshi YAMAGUCHI, Mitunori SAYAMA and Yasuhisa KUZUHA
4th Research Center, Technical R&D Institute, Japan Defense Agency
2 9 54 Fuchinobe, Sagamihara, Kanagawa, 229 JAPAN

ABSTRACT

The ground shock produced by projectile or bomb explosion near buried structures generally represents the dominant threat for undeground protective structures. This paper presents some laboratery experiment about the reducing of ground shock on the surface of structure . The experiments were performed by using many kinds of cushion material. As the results, the effects of cushion material may be available for reducing the ground shock from near burst of the underground structures.

INTRODUCTION

The underground protective structure must satisfy basic requirement to resist the high stress level developed in the surounding soil medium due to the explosion. The requirement for significantly higher hardness levels may lead to very heavy primary structure or deeply buried structure. In order to reduce the high stress level, an application of a cushion material seems one of advantageous method [1),2)] . The concept is the isolation of the underground structure from the free-field medium by putting the cushion layer between structural wall and explosion source.

This paper deals with the effects of cushion layer for redusing stress level by experiment results. There are some types of cushion materials ,i.e soft crushable material, relatively low elastic material and very low replosive coefficient. The experiments were carried out by using many kinds of cushion material, and two types of soil, i.e. compacted bentonite clay and dry sand.

TEST APPARATUS

Test apparatus to give the impact load by using falling weight is shown in Fig. 1. This loading system is composed of a guide tube, the falling weights, a falling weight holder, velocity measurement censors and vacuum apparatus.

The falling weights are from 30kg to 300kg of mass and 29cm in diameter. When the

impact load is applied to target, the falling weight is accelerated by the gravity acceleration only or atmospheric pressure by using vacuum system. In the case of using vaccum system, the bottom of the guide tube is covered with thin membrane and the inside of the tube is made vacuous. Therefore, the falling weight is accelerated by atomospheric pressure. Maximum velocity is about 80m/s with using most light weight of 30kgm. In this test, falling weight mass is 126kg and impact velocity is 14m/s.

Fig.2 shows the test container and arrangement of load cell, cushion layer and beam in the container. The specimen tested was a steel beam buried in compacted dry sand and bentonite clay. The water content of bentonite clay was 30% and soil layer was made by compacting under constant condition.

The shape of specimen is a box section of 28 mm height, 100mm in width, 500mm of span length

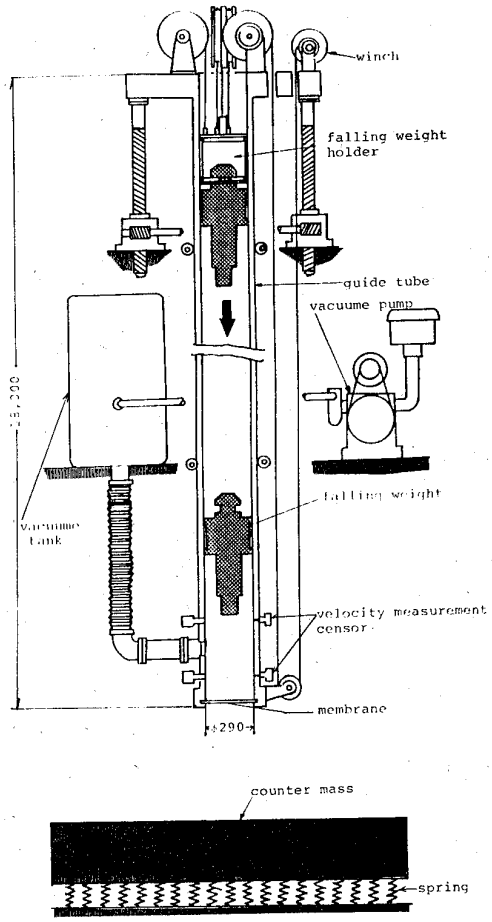

Fig.1 Falling weight impact loading facility

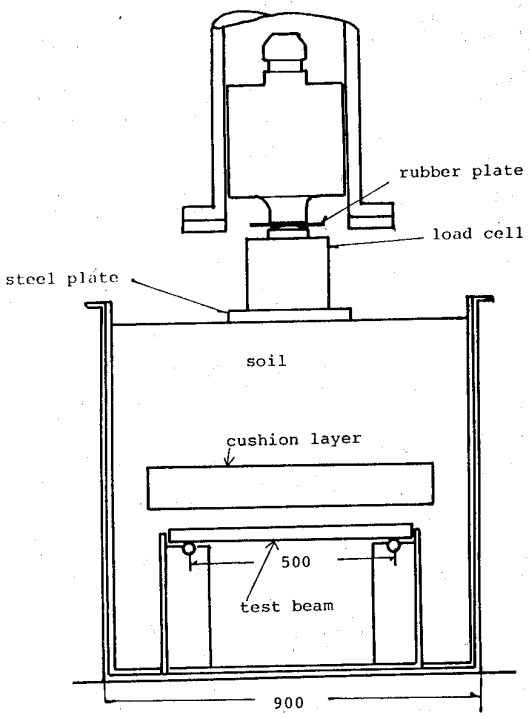

Fig.2 Schematic drawing of test set-up

and 3.2mm of the steel plate thickness. The moment of inertia is 10.43cm^2. As shown schematically in Fig.2, the cushion layer was buried in soil upside the steel beam, and the thicknesses of cushion layer were 100mm and 150mm.

TEST RESULTS

1. DIFFETENCE OF STRESS PROPAGATION CHARACTERITIC BETWEEN SAND AND CLAY

The stress history on the surface of beam can be varied by changing the mass of falling weight, impact velocity, and the depth of beam. Fig. 3 shows a comparison of the stress history of the results from

this loading system with a field test of a underground explosion of TNT 15lbs at distance of 2m from wall. As it is evident from Fig.3 that the loading system is available for application of almost same wave form to the test specimen.

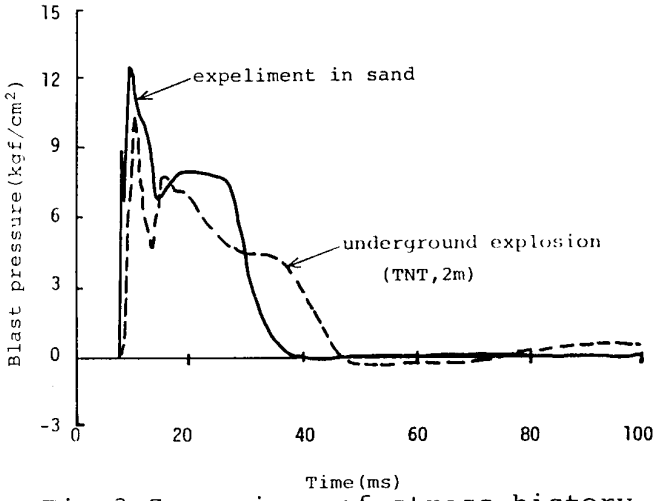

Fig.3 Comparison of stress history in field test with lab. test

The impact load on the surface of soil bin is applied by impacting falling weight through rubber plate on the load cell which is set up on a square steel plate of 350mm ×350mm with 35mm in thickness. The examples of experimental results of impact load are shown in Fig. 4. Generally, the maximum impact load applied on dry sand was greater than that of bentonite clay, however the shapes of wave form is not different remarkably between the dry sand and the bentonite clay. Usually it is difficult to measure the high level load because the load cell vibrates by itself due to wave propagation through load cell. In this tests, a rubber plate was set up on the top of load cell, in order to protect direct hit each other.

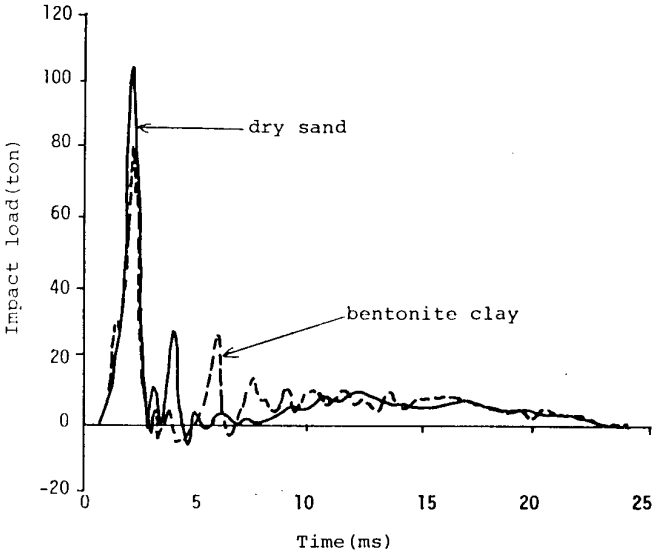

Fig.4 Impact load on soil surface

The medium soils were chosen for comparison of primary difference of characteristics of wave propagation through the dry sand and the bentonite clay. The experiments were carried out concerning the steel beam responce buried in dry sand and bentonite clay. Fig.5 shows stress histories at the middle of beam in the case of no cushion layer. It is apparent that there is noticable difference in the stress history between the dry sand and the bentonite clay. In the case of dry sand, the rising time is very fast and the sharp oscilations occur in the wave form, on the other hand, in the case of bentonite clay there are no sharp oscilations and the wave form is very smooth. A tendency of the displacement histories are almost same as the stress history as shown in Fig.6. The

stress displacement relationship at the middle of beam buried in the dry sand is quite distinct from that in the bentonite clay as shown in Fig. 7. It is apparent, as is also the case of stress hisory that the relationship is very complex due to the oscilation of stress history and displacement history. The factors affecting these phenomena could be as follows. (1) The seismic velosity of bentonite clay of about 80m/s is about half of it of dry sand. (2) The soil damping of bentonite clay is very larger than that of dry sand.

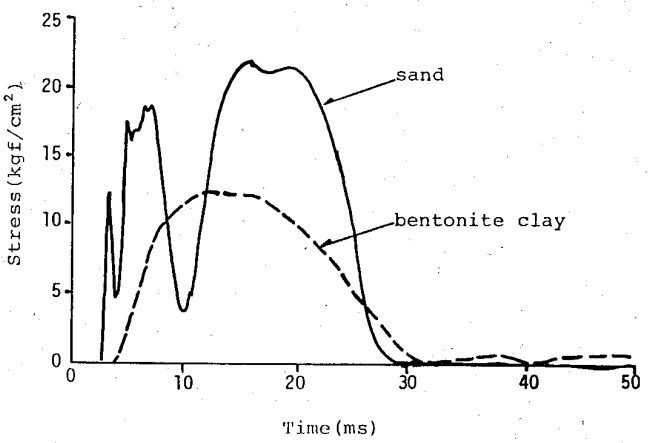

Fig.5 Comparison of stress history at the middle of beam in bentonite clay with dry sand

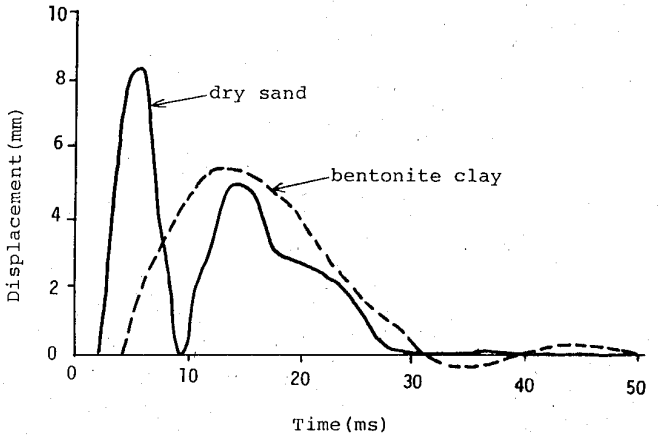

Fig.6 Comparison of displacement history at the middle of beam in bentonite clay with dry sand

2. EFFEXTS OF CUSHION LAYER

It is considered that the application of structural isolation materials may be useful for underground structure. There are some kinds of types of cushion material, i.e crushable material like a honeycomb, relatively soft elastic material like a foam and very low elastic material like a gell and so on. The cushion materials used herein are three types of material. Before the dynamic tests, some static tests were conducted in order to obtain the static load displacement properties as shown in Fig. 8. The crushable materials used herin were paper honeycombs. Three different strengrh paper

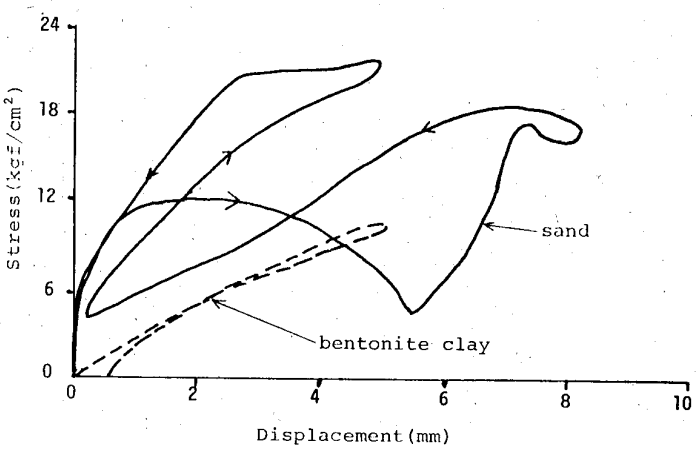

Fig.7 Comparison of stress displacement curves

honeycombs were used, which all deformed in essentially sustaining the constant compression strength, respectively. In the case of polyethyrene foam, the stiffness of material is very low at the start of loading, however the stiffness increase gradually with increasing of displacement.

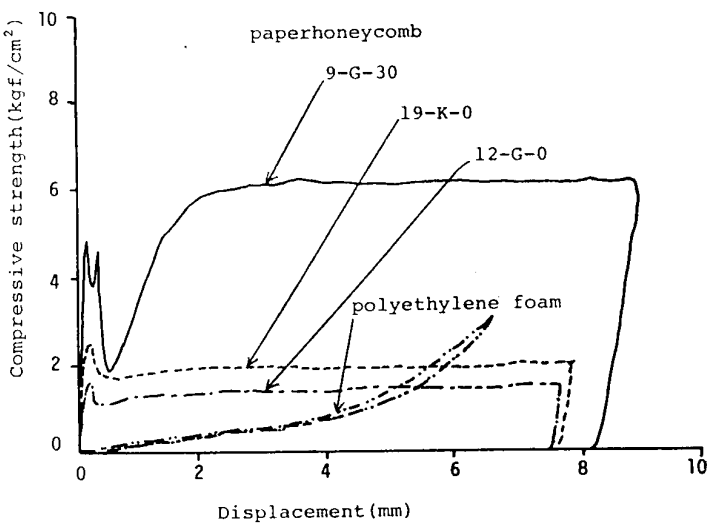

Fig.8 Statical characteristics of cushion material.

In order to compare the effects of the cushion layer, the stress histories at the middle of beam are shown in Fig.9. As it is evident from the figure, when the paper honeycombs were used for cushion layer, the rise times at the start are almost same as the case of no cushion, and the maximum stresses are almost same as the static compresssive strengthes, then the stresses are maintained the almost constant level until the stress or the deformation capasity vanishes. It is considered that the paper honeycomb begins the crushing at reaching compressive strength and the crushing continues until the subjected load becames less than the compressive strength . If the thickness of material is relatively thin, the material should be crush completely, then the stress should increase again.

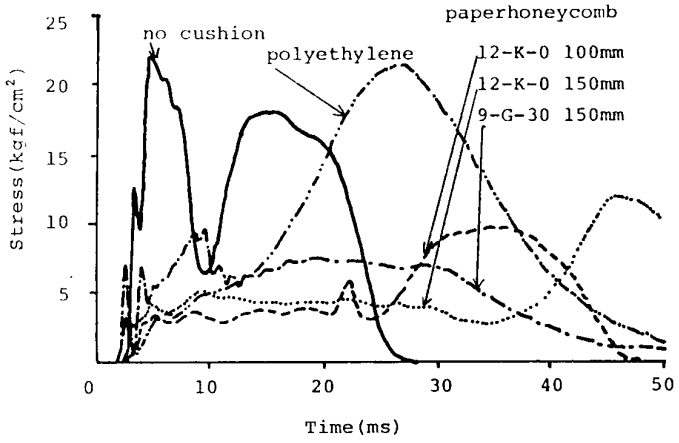

Fig.9 Difference of stress histories at the middle of beam.

On the other hand, in the case of polyethylene foam, it was found that the stress increases gradually, and the maximum stress appears after a while. The reason may be considered that the stiffness of material increase with deformation. As can be seen from Fig.9, the maximum stress used paper honeycomb is very low level.

Fig. 10 shows the strain histories at the middle of beam. It is apparent, as is also the case of the stress histories that there are noticable differences in the dynamic responses of beam with respective cushion layer. The strain history of using the polyethylene foam shows considerable delay in arrival of peak strain and the maximum strain is relatively high level. In the case of paper honeycomb, the maximum strains are

smaller than that of no cushion. The smallest strain is shown in paper honeycomb of 12-K-0 of 150mm in thickness. The maximum strain is about 1/3 of the maximum strain in the case of no cushion. As a results, the paper honeycomb of a suitable compresive strength and thickness may be usuful for reducing the ground shock from the ungerground explosion.

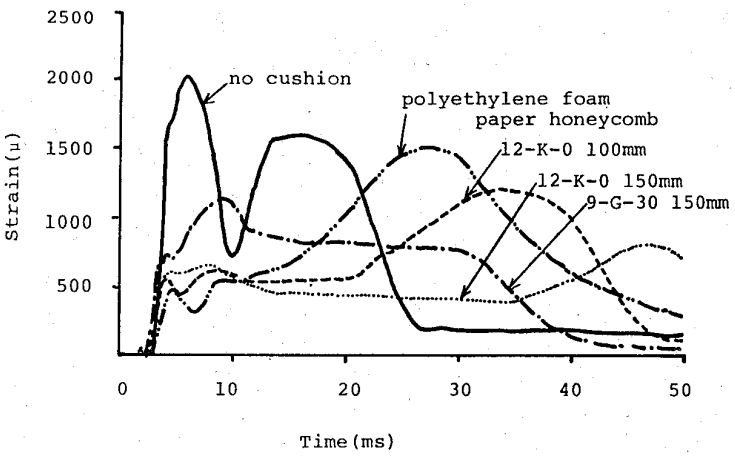

Fig.10 Difference of strain histories at the middle of beam

CONCLUSIONS

The use of cushion layer proved to be effective in reducing stress level within the limits of this experiments. The use of paper honeycomb of a suitable compressive strength and thickness seems to be effective in reducing ground shock from the underground explosion. Further study of the field explosion tests may be needed to determine the effectiveness of the cushion layer.

REFERENCES

1)Carl J. Constantino and Eban Vey:"Respnse of Buried Cylinders Encased in Foam", ASCE, Vol.95, No. SM5, Sept., 1969.

2)Henry s. McDevitt, Jr:"External Shock Mitigation for Buried Structure", Proc. of 4th Int. Symp. on the Interaction of Non-nuclear Munitions with Structures, April, 1989.

Jessberger, H.L., Prof. Dr.-Ing., Ruhr-Universität Bochum
Thiel, G., Dr.-Ing., Ruhr-Universität Bochum

Kurzfassung zum:

5. Internationalen Symposium
Interaktion konventioneller Waffen mit Schutzbauten

22.-26. April 1991
Bundesakademie für Wehrverwaltung und Wehrtechnik
Mannheim, FRG.

Thema:

Untersuchungen zum Einfluß der Baugrunddämpfung bei explosionsartiger Belastung auf die Verformungs- und Lastzustände von unterirdischen Bauwerken mit Hilfe einer geotechnischen Großzentrifuge.

Auf dem Gebiet der Bodendynamik sind bei höherfrequenter Lastbeanspruchung des Baugrundes insbesondere bei Wellenfortpflanzungsproblemen die Dämpfungseigenschaften des Bodens von Bedeutung. Diese energieschluckenden Dämpfungskapazitäten lassen sich aufspalten in einen Dissipationsanteil für den Boden selbst und in einen Anteil, welcher im allgemeinen als geometrische Dämpfung bezeichnet wird. Oft wurde versucht, diese Dämpfungseigenschaften in einfachen physikalischen Modellen zu erfassen. Hier bieten sich kleinmaßstäbliche Modellversuche an, welche aber wegen der ungünstigen Relation zwischen Explosionenergie und erfaßtem Bodenvolumen bzw. dem Volumen der erregten Struktur zu nicht wirklichkeitsgetreuen Ergebnissen führen, dies vor allem bei einer Modellmaßstabsreduzierung die kleiner ist als 1:n = 1:10, s.a. /1/, Murphy (1950).

Durch die Vergrößerung des allgemein wirkenden Schwerefeldes kann dieser Fehler der Modellskalierung mit einhergehender Erhöhung der Trägheitskräfte, die auf ein Volumenelement einwirken, behoben werden. Im Bereich der Bodenmechanik werden zur Erhöhung dieser Trägheitskräfte besondere Zentrifugen eingesetzt. Die vorgestellte Untersuchung über den Dämpfungseinfluß des Bodens bei Explosionsbelastung wurde an der Geotechnischen Großzentrifuge des Institutes für Grundbau und Bodenmechanik der Ruhr-Universität Bochum durchgeführt. In diesem Versuchsgerät können Modellmassen bis zu 2000 kg in einer Kreisbahn auf eine Geschwindigkeit von bis zu ca. 400 km/h beschleunigt werden; sie erfahren hierbei Kräfte bis zum 250-fachen ihres Eigengewichtes.

Durch eine derartige Versuchsmethodik kann sichergestellt werden, daß das Dämpfungs- und Steifigkeitsverhalten eines verkleinerten Bodenmodells und das des Prototypes bei Berücksichtigung der entsprechenden Modellfaktoren identisch ist, weitere Hinweise hierzu sind gegeben in /2/, /3/, /4/ und /5/.

Die vorliegende Untersuchung umfaßt die ingenieurmäßigen Fragestellungen im Zusammenhang mit oberflächennahen, explosionsartigen Erschütterungen und ihrer Auswirkungen auf ein sich in der Nähe befindliches Bauwerk. Die schockartige Belastung wurde durch Zünden von PETN-Detonatoren mit Ladungsdichten zwischen $1{,}46<\delta<1{,}56$ [g/cm^3] erzeugt. Nach Untersuchungen von Nielson /6/, (1983) und Gill /7/, (1985) ist für den Einsatz in kleinmaßstäblichen Versuchen im erhöhten Beschleunigungsfeld die Ladungsmasse proportional mit n^3 zu skalieren, wobei n der geometrische Faktor der Modellreduzierung bzw. der Erhöhung des Beschleunigungszustandes darstellt.

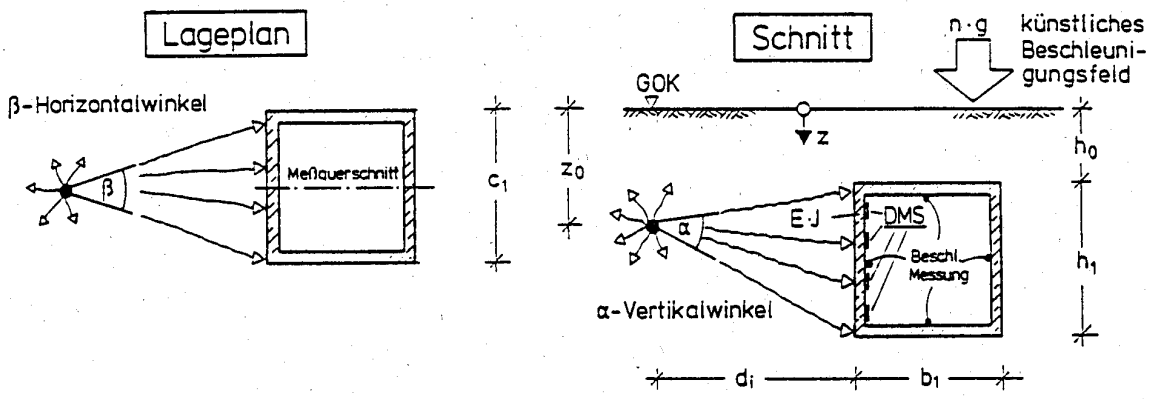

Bild 1 Anordnung eines Modellversuches im künstlich erhöhten Beschleunigungsfeld der Geotechnischen Großzentrifuge

Das im Boden eingebundene Bauwerk wird durch eine senkrecht stehende, im Boden eingebettete Wand repräsentiert, deren Eigenschaften an die Steifigkeits- und Lagerungsbedingungen von üblichen Betonbauwerken steifer Bauart angelehnt sind, siehe auch Bild 1. Der Abstand des Explosionsherdes von diesem Bauwerk wurde variiert, sodaß unterschiedliche theoretische geometrische Dämpfungen und Bodeneigendämpfungen im Hinblick auf das Betonbauwerk aktiviert werden.

Die auf die Wand für unterschiedliche Ranbedingungen wie Abstand, Energiedichte etc. auftreffenden Energieanteile wurden über Dehnungsmeßstreifen und Beschleunigungsmesser erfaßt und aufsummiert. Daneben wurden Freifeldbeschleunigungen im Boden in unterschiedlichen Abständen zum oberflächennahen Explosionsherd gemessen. Die Ergebnisse der Messungen sowie die Auswertung der Energiebilanzen werden vorgestellt.

Die theoretischen Ansätze für die unterschiedlichen Arten der Energiedissipation eines Lockerbodens werden mit den in den Versuchen ermittelten Werten verglichen und diskutiert. Für das eingebundene Betonbauwerk können in Abhängigkeit vom Lastfall Detonation und den unterschiedlichen geometrischen Bedingungen Bemessungsschnittgrößen angegeben werden.

Zusammenfassung:

Die geotechnischen Zentrifugenversuche eröffnen einen gangbaren Weg zur Verifikation der Belastung und Bemessung von im Boden eingebundenen Bauwerken ohne auf kostspielige 1:1-Prototyp-Versuche angewiesen zu sein. Skalierungsfehler wie sie an kleinmaßstäblichen Modellen im einfachen Schwerefeld auftreten werden bei Versuchen im erhöhten Schwerefeld vermieden. Damit besteht die Möglichkeit, realitätsnahe Systemantworten für hochschnelle dynamische Beanspruchungen zu erhalten und unter ingenieurmäßigen Aspekten auszuwerten.

Literatur:

/1/ Murphey, G., 1950. Similitude in Engineering, Ronald Press Co., N.Y., N.Y.

/2/ Güttler, U., Thiel, G. & Jessberger H.L, 1986. Simulation of earthquake loads in cyclic triaxial tests. Proc. Int. Conf. on Earthquake Prognostics, pp. 377-391.

/3/ Güttler, U., Thiel, G. & Jessberger H.L, 1987. Cyclic hardening of sand during earthquake events. Soil dynamics and liquefaction. Elsevier Publ., Amsterdam - Oxford - New York - Toky, pp. 107-122.

/4/ Thiel, G., 1988. Steifigkeit und Dämpfung von wassergesättigtem Feinsand unter Erdbebenbelastung. Schriftenreihe des Institutes für Grundbau, Wasser- und Verkehrswesen, Ruhr-Universität Bochum, Heft 14.

/5/ Thiel, G., Güttler, U., 1989. Cyclic hardening and liquefaction in sands - Triaxial and centrifuge investigations. Proc. Int. Conf. on Earthquake Resistant Construction and Design, ERCAD, Berlin.

/6/ Nielson, J.P., 1983. The Centrifuge Simulation of Blast Parameters. ESL-TR- 83-12, Tyndal AFB Fla.

/7/ Gill, J.J., 1985. Centrifugal Modeling of a Subterranean Structure Subjected to Blast Loading. M.S. Report, Univ. of Fla., Gainesville, Fla.

Investigation of the Effect of Soil Damping in Explosive-Type Loading on the Deformation and Load of Buried Structures by Means of a Large-Scale Centrifuge.

In soil dynamics damping properities of the soil are significant for higher-frequency loadings of the foundation soil, particularly in the presence of wave propagation problems. These energy-absorbing damping capabilities can be split into dissipation of the soil itself and a portion which is generally referred to as geometric damping. It has been tried frequently to include these damping properties in simple physical models. In this context, small-scale tests offer themselves as a solution. However, they will yield non-realistic results due to the unfavorable relationship between explosion energy and the affected soil volume and the volume of the excited structure, in particular where model scales are reduced below 1:n = 1:10, see Murphy (1950). This scale-related error can be eliminated by increasing the general gravitational field by means of an increase of the inertial forces acting on a volume unit. In soil mechanics, special centrifuges are used to increase these inertial forces. The present investigation on the damping effect of the soil under explosive loading was conducted in the large-scale centrifuge of the Institute für Grundbau und Bodenmechanik of the Ruhr University in Bochum. This apparatus allows acceleration of model masses up to approximately 2000 kg on a circular path up to approximately 400 km/h where they experience forces up to the 250-fold of their proper weight.

...

Such a test methodology ensures that the damping and stiffness response of a reduced soil model and the prototype are identical when appropriate model factors are considered.

The present investigation covers the engineering analysis of near-surface, explosive vibrations and their effects on a close-by structure. The shock-type loading was generated by means of PETN detonators with charge densities ranging from $1.46 < \delta < 1.56$ (g/cm^3). According to investigations conducted by Nielson and Gill (1985) the charge size is to be scaled proportionally with n^3 in small-scale tests with increased acceleration fields, where n is the geometrical factor of model reduction or the increase of the state of acceleration.

The structure embedded in the soil is represented by a perpendicular wall whose properties are similar to the stiffness and support conditions of common stiff-design concrete structures. The distance of the explosion from this structure was varied so as to activate various geometrical dampings and internal soil dampings with regard to the structure.

The energy portions hitting the wall under various conditions were measured by means of strain gages and accelerometers and added up. In addition free-field accelerations in the soil were measured at various distances from the near-surface explosions. The measurement results as well as the evaluation of the energy balances are presented.

The various theoretical approaches to assess the energy dissipation in a loose soil are compared with the test results and discussed. Design cross sections can be given for the structure embedded in the soil as a function of the detonation load and the various geometric conditions.

FOUNDATION SYSTEMS OF CIVIL DEFENCE SHELTERS AND PROTECTIVE STRUCTURES

R. Melamed - S. Schwarz (*)

Star Engineers Ltd. - Haifa, Israel

Abstract

The design of foundation systems of Civil Defence Shelters, as well as of other protective structures is not covered adequately in the professional literature, perhaps because a typical shelter is considered as a massive structure which is not sensitive to small soil displacements. Therefore, the usual foundation systems of Civil Defence Shelters consist of shallow foundations (continuous and/or raft foundation systems).

In cohesive soils, where shallow foundation systems are not suitable and/or economical, pile foundation systems should be used. Similar situations occur also in cases when the Civil Defence Shelter is part of a larger unprotected structure. In such cases the foundation system of the Civil Defence Shelter should be adapted to the foundation system of the unprotected structure, which in many cases consists of pile foundations.

In the absence of generally agreed upon design methods for pile foundation systems of Civil Defence Shelters, the article presents at this stage a practical design method and proposes possible directions for future development of analytical computation methods for determination of the forces, caused by conventional weapon effects, acting on pile foundation systems of Civil Defence Shelters, and/or other protective structures.

(*) Adjunct Senior Lecturer - Faculty of Civil Engineering - Technion I.I.T - Haifa, Israel

1) Introduction

Civil Defence Shelters intended to withstand the effects of near miss hits of conventional weapons are designed in most of the civil defence oriented countries according to regulations, standards and/or codes of practice relevant to such structures.

In spite of the dynamic nature of the loads expected to act on CD Shelters the various regulations usually adopt the quasi-static design approach, based on Limit States Design method [1]. There are certain of reasons for this aproach, such as:

a) Simplicity and easy adaptability to well known design methods used in ordinary civilian construction.

b) Reluctance of the authorities to disclose the reference threat and the defined protection criteria.

In relation to foundations of CD Shelters almost all of the regulations refer only to continuous strip and/or raft foundation systems. The loading of these foundations is defined in terms of the overall loading on the CD Shelter. This loading is in principle of distributed nature. Therefore, the design of such foundation systems may be carried out in a manner similar to the design of other structural elements of a given CD Shelter. However, reference to pile foundation systems of CD Shelters is very vague or non existent at all. The main problems in relation to pile foundations systems of CD Shelters can be condensed into the following subjects:

a) Realistic evaluation of the loads expected to act on the piles.

b) Determination of an adequate analysis model for evaluation of the piles response to the expected loads.

In the quasi-static approach adopted by many regulations, the design of a CD Shelter, including it's foundation system, should check the structure in two different types of limit states [2], namely:

a) Ultimate Limit State (ULS)

b) Serviceability Limit State (SLS)

In Ultimate Limit State two distinct types of loading combinations should be checked, namely:

a) Basic Loading Combinations

b) Accidental Loading Combinations

In Serviceability Limit State three types of loading combinations should be checked, namely:

a) Infrequent Loading Combinations

b) Frequent Loading Combinations

c) Semi-permanent Loading Combinations

The actions to be taken into account in analysis should be the characteristic loads defined by the relevant standards for loading of structures, multiplied by load factors (γf), load combination factors (ψi) and modifying factors (γn).

In Accidental Loading Combinations additional accidental loads should be considered as follows:

a) Loads due to weapon effects (groundshock, air blast, impact of fragments).

b) Collapse loads caused by failure of an unprotected superstructure and/or other nearby buildings.

In the quasi-static design approach these effects are represented by certain nominal values of loading, which are considered as additional static loads acting on the CD Shelters' structure. Since these loads are of accidental nature, they should not be multiplied by load factors and/or load combination factors. In addition, reduced factors of safety for strength of materials (γm) may be applied.

Due to the accidental nature of these loads, and the time difference between the action of these loads, there is no need to consider their simultaneous action in any load combinations.

2) Design principles of pile foundation systems in CD Shelters

The basic design requirements in relation to RC pile foundation systems of CD Shelters, designed to resist the effects of near-miss hits of conventional weapons were evolved in civil defence oriented countries, in which pile foundations are a neccessity, due to specific soil conditions [3]. These design requirements are based on many years of practical engineering experience. However, their theoretical substantiation is not always adequate. These design requirements can be summarized as follows:

a) The minimal distance between centres of two adjacent piles along the external perimeter of a CD Shelter should be 5.0m, to lessen the danger of simultaneous damage to two adjacent piles.

b) The diameter of RC piles should be 600 mm at least.

c) The minimum amount of longitudinal reinforcement of RC piles should be 0.8% of the gross area of the pile.

d) The diameter of the longitudinal reinforcing bars should be 12 mm at least.

e) The diameter of the helical stirrups of a RC pile should be 8 mm at least. The spacing of the helical stirrups in the upper part of the pile (2.0m) should be no more than 100 mm.

f) The concrete used in piles should be Grade 30 or Grade 40 concrete.

g) The connection between the pile and the CD Shelters' structure should be by means of an adequate pile head. The dimensions of the pile head should be defined in accordance with the diameter of the pile and should enable adequate anchorage in tension of the longitudinal reinforcement of the pile and of the start-up bars connecting the pile head to the CD Shelter's structure.

h) The resistance in bending and shear of the connection between the pile and the pile head, as well as between the pile head and the CD Shelter's structure should be no lower than the corresponding resistance of the pile itself.

i) The CD Shelter's structure should be designed in such a way, that it's overall stability will not be impaired, even if any one of it's peripheral piles will be destroyed.

j) The pile foundation system of a CD Shelter should be checked in Serviceability Limit States for settlement, deformations, etc., and in Ultimate Limit States for assesment of it's ultimate resistance and stability.

A typical RC pile used in CD Shelter construction is detailed in Fig. 1. The principles of load transfer in case of damage to one of the peripheral piles is shown in Fig. 2.

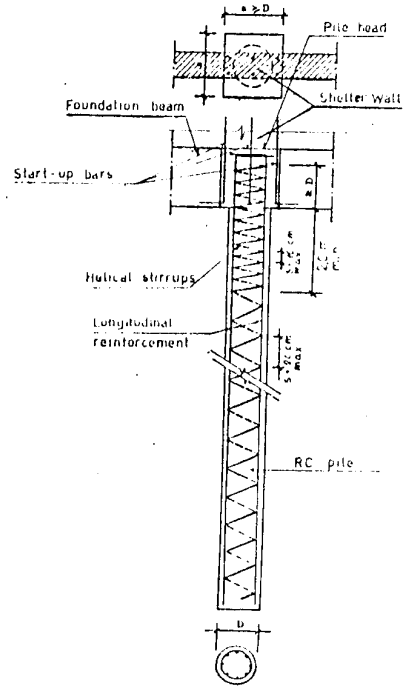

Fig. 1: Typical RC pile for CD Shelters construction

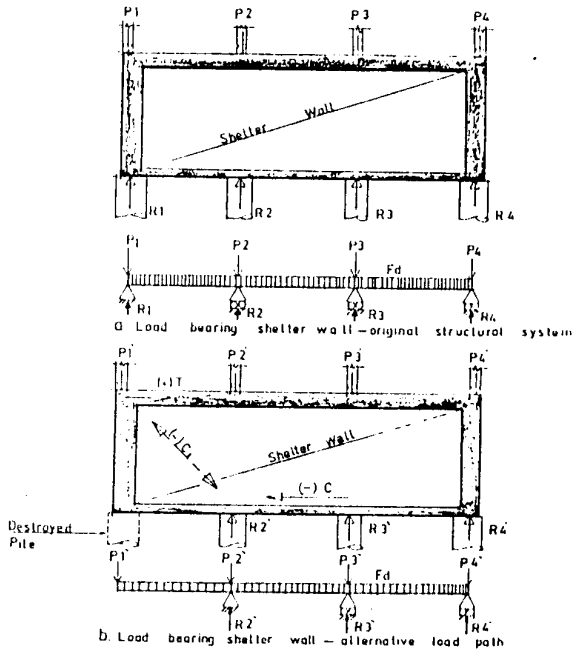

Fig 2: Alternative load path design procedure in pile foundations systems of CD Shelters

3) Design of RC piles against weapon effects

The analysis and design of pile foundation systems of CD Shelters according to the principles detailed in section 2 above is a time consuming task. In certain situations they may also cause an increase in overall construction costs of a given CD Shelter.

It may be possible to achieve a more reliable, and in certain cases a more economical design, if the loads caused by a near miss hit of a conventional warhead expected to act on the piles of CD Shelters are evaluated.

The effects of these loads may be evaluated with acceptable engineering accuracy by utilizing a two stage analysis model [3]. In the first stage of the analysis the relative movement between the pile and the CD Shelter at their connection point should be calculated, assuming that there is no physical connection between them. It may be assumed that the movement of the free pile caused by the ground shock is the same as the maximum soil displacement at the same distance from the explosion epicenter. The maximum displacement of the soil caused by an explosion depends on many factors, such as: type of soil, depth of explosion, confinment factor, distance from explosion epicenter, etc., [4,5,6]. Heavy, water saturated clays are characterized by high accelerations and small soil displacements, while in granular soils the accelerations are relatively much lower and the soil displacements larger. Burried explosions cause larger soil displacements than surface detonations, depending on depth of burrial and confinment factor, while larger distance from the epicenter results in smaller soil displacement.

Characteristic properties of different soils and formulae for determination of maximum soil displacements are detailed in the professional literature [4,5,6]. For actual design purposes the relevant soil properties should always be established on the basis of on-site soil investigations. Surface detonations of conventional weapons at near miss hit distances, for which the standard CD Shelters are usually designed, cause soil displacements of a few milimeters (5-10 mm) in clay, in comparison to few tens of milimeters (10-30 mm) in granural soils. However,burried explosions, even the partially burried ones, cause soil displacements larger by an order of magnitude (> 100 mm), mainly in granural soils.

Such displacements may cause failure of RC piles of CD Shelters. One widely used method for limiting this problem is the construction of an adequate horizontal RC surface slab, on, or just below the ground level, all around the CD Shelter. The aim of this slab is to ensure that the detonation will be in every case a surface one. This usually have a beneficial effect from protection point of view, not only on the pile foundation system, but also on other parts of the given CD Shelter.

Parallelly to evaluation of the expected soil displacements it is neccessary to calculate the expected overall movement of the CD Shelter due to air blast (in above ground CD Shelters) or groundshock (in underground CD Shelters). The difference between the expected soil displacement and the CD Shelter's movement is part of the basic input data for the second stage of the analysis.

Large CD Shelters, mainly those forming part of an other larger structure, are of such dimensions and mass, that the effect of a conventional weapon's explosion is localized to a relatively small part of the structure. Therefore the overall movement of the CD Shelter may be disregarded in the calculations.

In the second stage of the analysis the response of the individual pile is analysed, for a relative displacement at the pile-structure connecting point, equal and opposite to the relative displacement calculated in the first stage of the analysis. The response of the pile may be analysed by suitable computer codes, allowing analysis of structural elements supported by spring supports. In spite of the fact that in this type of analysis it is not possible to describe the actual time-dependent dynamic behavior of the pile foundation system of a given CD Shelter, it allows the evaluation of the maximum values of the bending moments and shear forces expected to act on it. In the first step of this stage the required length of the pile is calculated on the basis of the actual soil properties and the vertical loads expected to act on the pile, in a manner similar to analysis of ordinary pile foundations. Thereafter the analysis of the given pile is performed for the above mentioned horizontal displacements. In Fig. 3 the analysis results for a given typical 600 mm diameter, 10m long RC pile are presented.

The principal input data for this pile are as follows:

a) Pile diameter: D = 600 mm
b) Vertical design loads: NDmax = 500 KN; NDmin = 415 KN
c) Soil friction coefficient: μ = 50 KN/sqm
d) Modulus of subgrade reaction: K = 4000 KN/cu.m
e) Specific weight of soil: γ = 18 KN/cu.m
f) Seismic velocity: c = 1200 m/sec
g) Attenuation coefficient: n = 2.4

On the basis of these data the required length of the pile is evaluated as 10m, taking into account that the upper 2.0m of the pile are ineffective in vertical load transmission. The expected maximum horizontal soil displacement caused by explosion of a given conventional warhead was evaluated as 100 mm, taking into account partial burrial of the warhead.

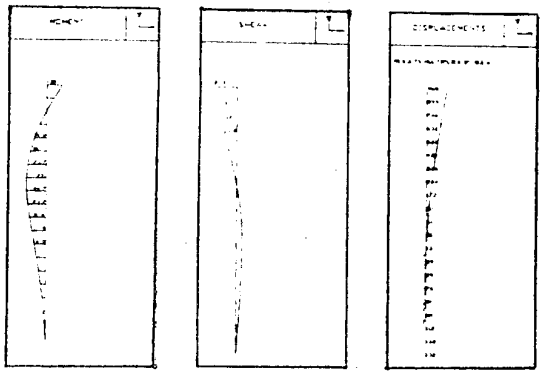

Fig. 3: Analysis results for a 600 mm diameter RC pile
a) Horizontal displacement
b) Bending moments
c) Shear forces

The analysis results presented in Fig. 3 form the basis for design of the RC pile, which is based on M-N interaction diagrams for circular RC sections [7]. A typical M-N diagram for circular RC sections is presented in Fig 4.

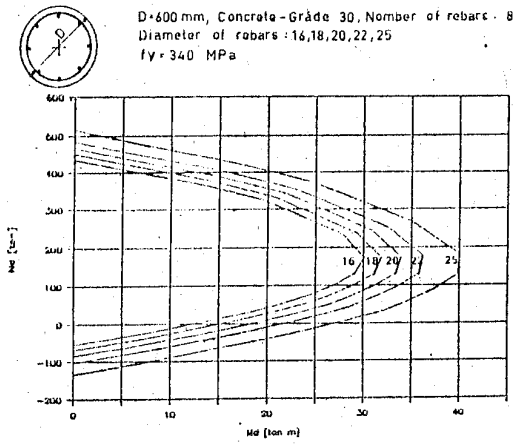

Fig. 4: M-N interaction diagrams for 600 mm diameter RC piles.

4) Conclusion

The proposed analysis model for design of pile foundation systems of CD Shelters and other protected structures enables straightforward design of these foundation systems, taking into account the weapon effects expected to act on them. This is an important step forward in comparison to the design methods used until now as described in section 2 above.

The advantages of the proposed analysis model can be summarized as follows:

a) Consideration of the horizontal loads expected to act on pile foundation systems of CD Shelters in case of a near miss hit of a criterion warhead.

b) Elimination of the requirement to design the piles in accidental loading combinations in which one of the piles is destroyed due to the criterion detonation.

c) Elimination of the requirement for design of CD Shelter walls as deep beams of large spans, due to the possible failure of any one of the peripheral piles.

An additional development in design of pile foundation systems of CD Shelters may be foreseen in possible full scale dynamic analysis of the piles, taking into account the actual horizontal stiffness of the piles on elastic supports as well as the actual dynamic loads caused by a near miss hit of a given conventional weapon.

Since the problem of pile foundation systems of CD Shelters is of great importance, it is advisable to perform scaled and even full scale tests to verify the accuracy of the proposed analytical model.

5) References

[1] Civil Defence Regulations - Specifications for construction of CD Shelters; IDF. July 1990 (Hebrew).

[2] CEB FIP Model Code 1990; First Draft; March 1990.

[3] R. Melamed, S. Schwarz: Foundation Systems of CD Shelters; Journal of the Association of Engineers and Architects in Israel, March 1990. (Hebrew).

[4] TM-5-855-1, Fundamentals of Protective Design for Conventional Weapons; July 1984.

[5] R. Crawford at.al.: Protection from Non-Nuclear Weapons; AFWF-TR 70-127, February 1971.

[6] W.E. Baker at al.: A Manual for Prediction of Blast and Fragment Loading on Structures, November 1980.

[7] Y. Gluck: Design of Structures for Earthquakes; Technion ITT - January 1990. (Hebrew).

TESTS ON THE INTERACTION OF CONTAINED EXPLOSIVES WITH A SMALL BURIED SHELTER IN SATURATED SAND

Harry J. van der Graaf

Delft Geotechnics
The Netherlands

Introduction

The protection of buried and unburied structures against conventional bomb impacts has been and still is an item of research for the Dutch ministry of Defence. Previous research was conducted to investigate experimentally the influence of vertical buried shock damping shields on the reduction of shock loads. These tests have been performed in loose saturated sand with the water table near the surface. The shock loads were measured below the water table. It was concluded that for large scaled distances ($\lambda > 6$ in SI units) the prediction formulas, which were generally used in the Netherlands, did not agree well with the field measurements. The prediction formulas are only valid for a limited range of scaled distances ($0.3<\lambda<4$). The scaled distances of interest in this series of field tests, were above the limited range. By extrapolation of the prediction formula for the scaled distance, the predicted level of the induced shock was some order of magnitude lower than measured.
However, the general relation between the scaled distance and the shock amplitude could be described in the same way as in the prediction formula. Based on these results it was concluded that for large scaled distances the characteristic parameters, e.g., attenuation coefficient and constant of the prediction formulas, had to be defined.

This paper presents the results and analyses of 58 explosion tests performed in loose saturated sand. The explosion tests are conducted on two test sites near Breda in the South of the Netherlands between May and September 1990. The explosive charges varied between 0.250 kg and 3.000 kg. The scaled distances varied between 2.0 and 90 in SI units.

Site and soil investigations

The test sites were located in the neighbourhood of a railway, a motorway, and houses. The test sites themself were previously used for cattle breeding.

In the previous research, a field investigation has been carried out. The results of these tests are reported by v.d. Broek (in Dutch) [1]. The soil conditions at both test sites consist of an horizontal loose sand layer, 12 m thick, on top of a clayey layer. In the sand layer some thin silty sand lenses are found. The sand layer is covered with a sandy layer of 1 m thickness with some humus components. At site 1 the phreatic water table was 1.3 m below ground level and at site 2 it was 2.4 m below ground level.

The cone penetration resistance of the sand layer varied between 3 and 10 MPa. The grain size distribution shows a poorly graded medium sand with an average grain size of 0.240 mm and a very small silt content of 4 %. The internal friction angle varied between 34° and 36°.

Shelter design

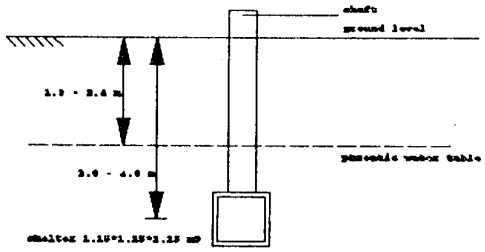

Figure 1. Section of the shelter and shaft

For the research into the effects of buried explosive charges on shelters, it was made use of a small cubical reinforced concrete shelter. The internal sizes of the shelter are 1.0*1.0*1.0 m^3 and the wall thickness is 0.075 m. On top of the shelter, a circular steel entrance shaft was mounted. The diameter of the shaft is 0.6 m and the length 4.0 m. The connection between the shaft and the shelter has been made watertight with a silicon lute.A cross section of the shelter is presented in Figure 1. At site 1 the centre of the shelter was installed into the sandy layer below the phreatic water table at a depth of 2.0 m. At site 2 the installation depth was 4.0 m below ground level. The shelter was installed by means of an small excavation and a temporary water table lowering. To avoid unwanted influences of the excavation on the shock behaviour of the shelter, the fill was compacted and flushed with water during the water pumping.

Instrumentation and data logging

The instrumentation in the shelter consisted of accelerometers in both horizontal and vertical direction connected to the walls and bottom.
In the soil the free field accelerations were measured with 3 cone penetration devices instrumented with vertical and horizontal accelerometers. The accelerometers are mounted behind the cone and friction sleave. At both sites the soil devices are installed at the depth of the centre of the shelter. The horizontal direction is pointing in the direction of the charges. The accelerometers are of the type Sundstrand AQ700 and AQ800. The maximum acceleration range has been fixed from -15 g to +15 g. The resonance frequency of the accelerometers is 470 Hz.

Horizontal excess soil pressures are measured by means off soil pressure meters fixed to the tip of cone penetration devices.
The pore pressure generation is measured by means of two cone penetration devices with pore pressure meters close to the cone. The pore water generation is measured at the depth of the centre of the shelter and at 8 m below ground level. The pore pressure meters are of the piezo-resistive type. The maximum range of the pore pressure meters is 200 kPa. The chamber in front of the piezo-resistive gauge and the filter are fully saturated, filled with silicon oil. The resonance frequency of the piezo-resistive pore pressure meter is above 500 Hz.

By means of an HP-300 computer a total of 12 signals from the accelerometers and the pore pressure meters are sampled at a rate of 3000 samples per second and digitally filtered at 300 Hz.

Charges and charge positions

The type of explosive used was Iremite. The material was available in units of 0.250 kg with a length of 0.25 m and a diameter of 0.03 m. Units of Iremite were tied together to create charges of 0.5, 0.75, 1.0, 1.25, 1.5, 2.0 and 3.0 kg. The ratio between length and diameter of the charges was such that a circular explosion behaviour could be assumed. The specific energy content of Iremite is 1400 kcal/kg and 1000 kcal/kg for TNT. This means that the TNT equivalent of Iremite is 1.4.

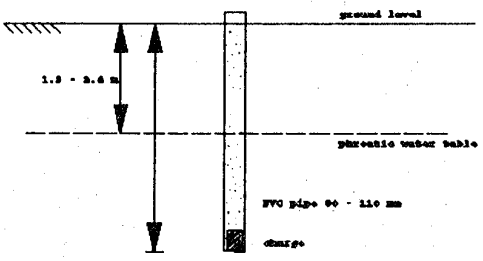

Figure 2. Position of PVC pipe and charge in the soil

The distance between the charges and the shelter and field instruments was varied over a wide range. At site 1 the distances of the charges were 10, 20, 30 and 40 m on opposite sides of the shelter. At site 2 the distance varied between 5 and 27 m from the shelter on the 4 sides of the shelter. By means of a water jet a grid of thin wall PVC pipes was installed into the ground at a depth of 4.00 m below ground level. Figure 2 presents the position of a pipe and charge in the soil. The internal diameter of the pipes was 80 mm and 110 mm. The charges were placed at the bottom of the pipes and the pipes were filled up with sand to ground level. In this way the charge was in full contact with the soil.
To prevent for launching of the pipes during the explosion the top of the pipes were covered with rubber mats.

According to [5] the required depth of the charge to realize a fully covered detonation can be expressed by:

$$d = \sqrt[3]{\frac{W}{0.055}} \qquad (1)$$

with the weight of the charge W in kg TNT and the depth d in metres. The Iremite charges are installed 3.75 m below ground level to ensure a full camouflet explosion.

Analyses of test results

The analyses of the measurements have been focused on the maximum amplitude readings of accelerometers, pressure meters and pore pressure meters. These amplitudes have been related to the scaled distance of the charges. The scaled distance λ is the ratio between the distance and the third root of the weight of the charge.

$$\lambda = \frac{R}{\sqrt[3]{W}} \qquad (2)$$

As this scaled distance is generally used in prediction formulas, the results could be compared with experimentally determined prediction formulas as proposed by Drake [2,3] and by the U.S. Army [4]. The general expressions of Drake's prediction formulas for the acceleration and pressure are:

$$a_0 * \sqrt[3]{W} = A * \lambda^{(-n-1)} \quad (3)$$

$$p = B * \lambda^{-n} \quad (4)$$

with a_0 = maximum acceleration [g]
W = weight of the charge [lb]
A = constant (A = 50*f*c) [ft/s]
B = constant (B = 160*f*ρ*c) [$\frac{lb^{2/3}s}{ft^4}$]
λ = scaled distance [ft/$lb^{0.33}$]
n = attenuation coefficient [-]

In US units the constant A and B depend on the camouflet factor f (f=1 for full camouflet depth) and the seismic velocity c in the soil. B also depends on the density of the soil. After transformation into SI units the constants A and B depend also on the attenuation factor n. At site 1, the seismic velocity of the first wave arrival was about 1300 m/s, and at site 2, about 1525 m/s. The validity of the prediction formula has been set to scaled distances between 0.8 and 10 in US units and 0.3 to 4 in SI units. Based on the material description for saturated sand with a small amount of air voids given by [4] the attenuation factor n is 2.25-2.5.

The results presented are expressed in SI units. By means of linear integration of the logarithmic amplitudes and of the logarithmic scaled distances, the attenuation factor n and the constant A have been determined.

Accelerations in the shelter

Figure 3 shows the maximum vertical accelerations in the shelter at site 1. The regression curve fits very well with the data. The scatter of the data is small. Figure 4 shows the linear regression curves for the attenuation of the vertical accelerations at both sites. Each curve is derived from one accelerometer. As can be seen from the graph the prediction formula of Drake does not fit for the scaled distances of the tests but under estimate the amplitudes to some extend. Both the attenuation factor n and the constant A are smaller. In Table 1 the mean values derived for n and the logarithmic of A are given. The mean acceleration level at site 2 is 3 to 6 times lower than at site 1. For both sites the average vertical acceleration level is 2.5 to 5.5 higher in magnitude than the horizontal acceleration level.

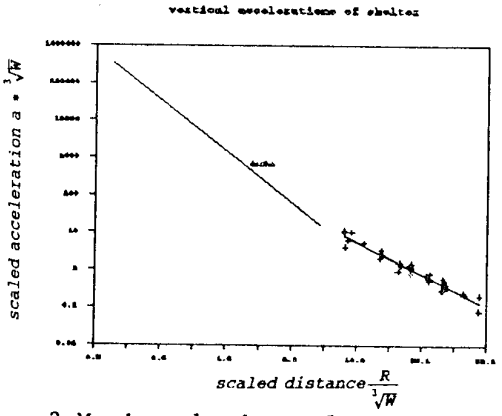

Figure 3 Maximum horizontal accelerations in the shelter at site 1

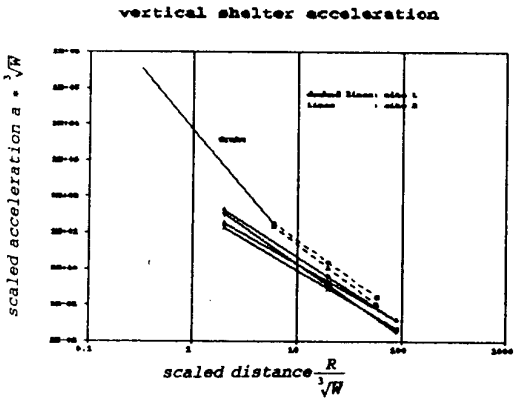

Figure 4 Attenuation of vertical acceleration in the shelter

accelerations	attenuation factor n	log(A) SI units	log(A) US units
Drake's formula	2.40	3.84	5.34
site 1 horizontal	0.89	2.20	3.05
site 1 vertical	1.09	2.79	3.77
site 2 horizontal	0.89	1.67	2.52
site 2 vertical	0.81	1.94	2.79

Table 1 Attenuation factor n and constant A for shelter acceleration at site 1 and 2.

Accelerations in the soil

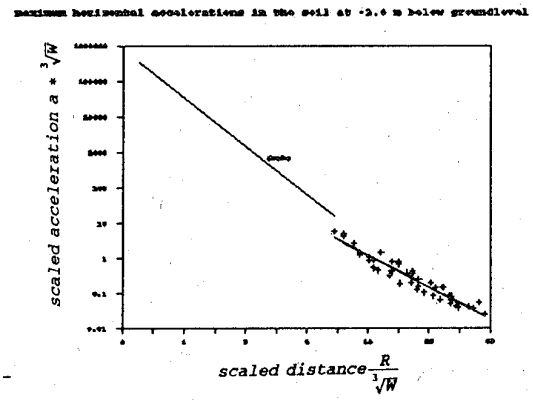

Figure 5 Maximum horizontal accelerations in the soil at site 1

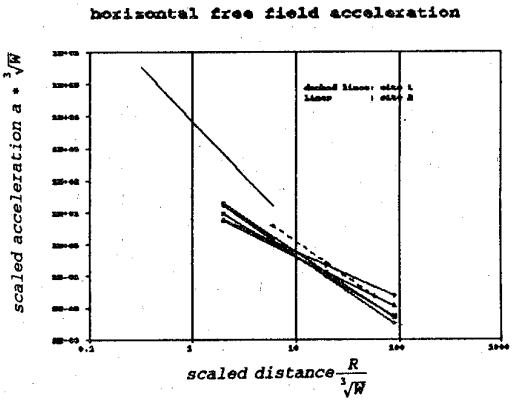

Figure 6 Attenuation of horizontal acceleration in the soil at site 1 and 2.

At site 1, the accelerations are measured at 2 m below ground level, and at site 2, at 4 m below ground level. In Figure 5 the maximum horizontal accelerations in the soil are shown. Again the scatter in the data is small. Figure 6 shows the results of linear regression curves for all horizontal accelerometers in the soil. The linear regression curves for the vertical accelerations are similar.
In Table 2 an overview is given of the mean attenuation factor n and A for horizontal and vertical accelerations in the soil.

accelerations	attenuation factor n	log(A) SI units	log(A) US units
Drake's formula	2.40	3.84	5.34
site 1 horizontal	1.27	2.33	3.45
site 1 vertical	1.38	3.02	4.12
site 2 horizontal	0.80	1.57	2.37
site 2 vertical	0.44	1.44	2.12

Table 2 Attenuation factor n and constant A for free field accelerations at site 1 and 2.

The vertical acceleration in the soil is a factor of 3.6 higher in amplitude than the horizontal acceleration although the horizontal acceleration is measured in the radial direction.

Soil pressures

excess horizontal soil pressure	attenuation factor n	log(B) SI units	log(B) US units
Drake,s formula	2.40	4.14	4.33
site 2 0.5 m - gl.	0.91	1.44	0.92
site 2 4.0 m - gl.	1.65	2.98	2.75

Table 3 Attenuation factor n and constant A for excess horizontal soil pressures at site 1 and 2.

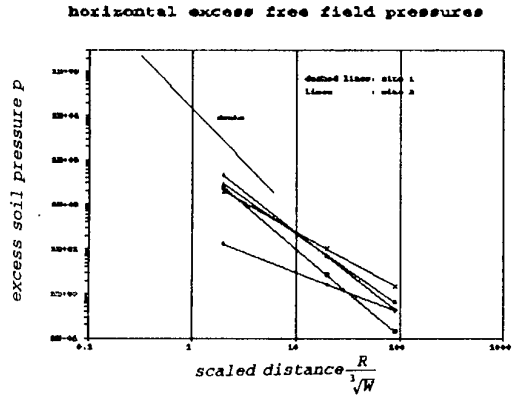

Figure 7 Attenuation of the excess soil pressure

The soil pressures are only measured at site 2 at 0.5 m and 4.0 m below ground level. Figure 7 shows the attenuation curves for each pressure meter. By comparing the curves for the pressures at 4 m below ground level with the curve derived by Drake, (see formula 4) it can be noticed that the prediction formula underestimates the pressure at smaller scaled distances with a factor of 8 in magnitude. The mean attenuation factor n and the constant B are presented in Table 3. There is a distinct difference between the pressures near the surface and pressures at 4 m below ground level. Due to a smaller mean attenuation factor n of 1.65, at larger scaled distances the prediction formula fits reasonably well. Near the surface, the pressures are much smaller due to boundary conditions. The attenuation factor is further reduced to n = 0.91.

Comparison between field and shelter behaviour.

In analyzing the time signals of the accelerometers the following characteristics can be noticed for horizontal and vertical accelerations. Two representative time signals of the vertical accelerations in shelter and soil are presented in Figure 8. As the distance between charge and accelerometer is small, the maximum acceleration appears earlier in the shock load signal. In this part of the signal the main frequency is about 180 Hz. After several peaks, in about 0.02 sec, the signal changes into a signal with a main frequency range between 25 and 30 Hz. Finally, the signal dominant frequency content changes to frequency between 6 and 8 Hz. In this final part of the signal the displacements will be generated. The low frequency signal reduces further to zero. The separation of the three parts can be seen better for larger distances between charge and accelerometer.
As can be seen from Figure 8, the accelerations in the soil compare reasonably well with the accelerations in the shelter. By analyzing the soil and shelter records, some differences can be noticed. At larger scaled distances, the horizontal acceleration amplitude of the first arrival has been reduced more in the soil than in the shelter. The peak amplitude occurs at the later arrival of the shear wave in the signal. The high frequencies in the signals of the shelter do not occur in the signals of the soil. For that reason these frequencies must correspond to the resonance frequencies of the walls and the shelter. From the time delay between the arrival of the first wave and the low frequency

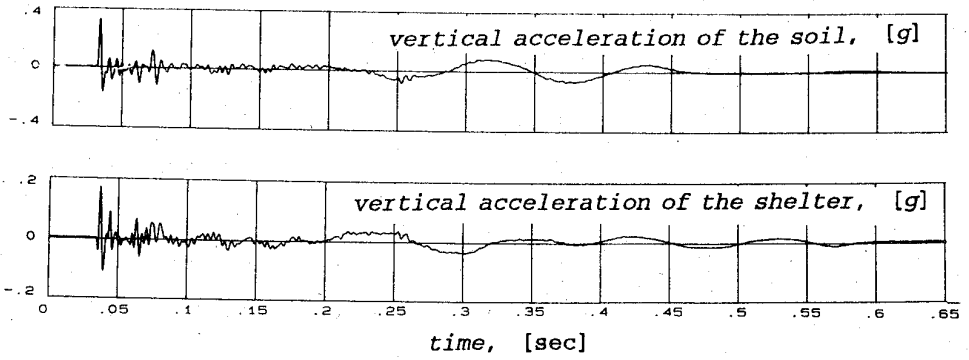

Figure 8 Vertical acceleration in soil and shelter at 2 m below ground level, charge 0.25 kg, distance 10m.

Rayleigh wave, the wave velocity of the Rayleigh was determined. The wave velocity of the Rayleigh wave varied between 180 and 220 m/s. With a frequency between 6 an 8 Hz the wave length of the Rayleigh is about 22 to 37 m.
The arrival time of the shear wave could not be established from the time signals, but if the generally accepted relation

$$V_R = 0.9 * V_S \qquad (5)$$

between shear wave and Rayleigh wave velocity is adopted the shear wave velocity is 200 - 240 m/s. As the frequency of the shear wave was 25 - 30 Hz the wave length of the shear wave has been 6 - 10 m.
The dominant frequency in the first arriving pressure wave is about 180 - 200 Hz. Combined with the wave velocity of 1300 - 1525 m/s the average wave length is 6.5 - 8.5 m. All three wave types, pressure wave, shear wave and Rayleigh wave, have a wave length an order of magnitude longer than the dimension of the shelter. The difference in shock loading on the front wall and the backside wall is minor compared to the overall load. Therefore the motion of the shelter has followed the motion of the soil.
The vertical motion, perpendicular to the radial motion is not expected to be important in a spherical radiation pattern. At a depth of 2 and 4 m below ground level the effects of the free field surface boundary condition is important. The vertical motion is directly related to the horizontal motions observed, as the radiation pattern tends to be more cylindrical than spherical. This may be the reason why the attenuation factor n in these tests has been lower than could be expected based on the predicting parameters of Drake.

Pore pressure generation

In a number of tests pore pressure changes have occurred during the shock loads. In tests with smaller charges or with charges at larger distances no pore pressure effects could be noticed. The peak pore pressure has always coincided with the first pressure wave arrival. After the shock waves no pore pressure generation has been measured. Figure 10 shows the variation of the ratio between the maximum change in the positive pore pressure and the effective vertical stress at 2 m and 8 m below ground level versus the scale distance of the charges. There is no strict relation found with the scaled distance, only a slight tendency can be noticed. The maximum ratio between pore pressure change and effective stress has, in some tests almost reached the

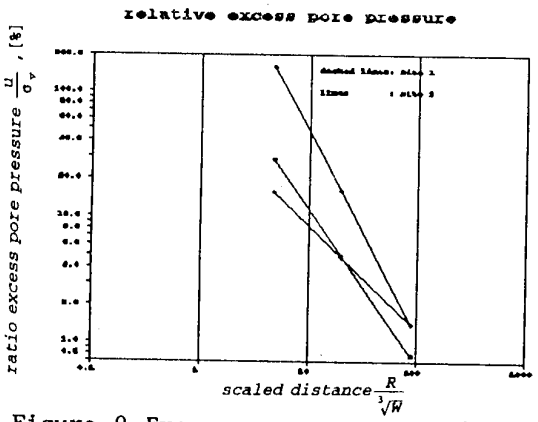

Figure 9 Excess pore pressure during the shock load

100 % which means a transient state of liquefaction. The duration of the high pore pressure change has been so short that the grains did not have the time to start rearranging. From the fact that no long term pore pressure generation has been measured it can be concluded that the distance between the charges and the pore pressure meters has not been small enough.

Conclusions

The prediction formulas of Drake appear to be valid qualitatively, but not quantitatively for large scaled distances. For large distances, the attenuation factor n and the constants A and B are smaller than the one obtained from Drake's original formulas. It is believed that the difference comes from the fact that, at large distances not only the pressure wave, but also the shear and Rayleigh wave play an important role.

Due to free field boundary conditions the vertical shock loads on the soil and the shelter are predominant. At short distances the vertical and horizontal shock loads are coupled. It was observed, as expected, that at large distances, with the presence of shear and Rayleigh waves the coupling between the vertical and horizontal shock loads changes.

The dimensions of the shelter are small compared to the three wave lengths. For this reason the observed differences between shock loads in the shelter and in the soil are small.

Literature

[1] c.v. van der Broek, E.J., "Schokdempende laagsystemen", Koninklijke Militaire Academie Breda, April 1988.

[2] Drake, J.L., "Ground Shock Treat to Buried Structures from Conventional Weapons", presented at the protective Design Symposium, 22-23 Sept. 1975, Brussels, Belgium.

[3] Drake, J.L., and C.D. Little Jr., "Ground Shock from Penetrating Conventional Weapons in the Interaction of Non-Nuclear Munitions with Structures", U.S. Air Force Academy, Colorado, May 1983.

[4] U.S. Army, "Fundamentals of Protective Design for Conventional Weapons, Technical Manual", Publication of Department of the Army, Washington D.C., november 1985, TM 5-855-1.

[5] Henrych, J., "The dynamics of explosions and its use", Amsterdam, 1979.

NUMERISCHE/EXPERIMENTELLE UNTERSUCHUNG DES DYNAMISCHEN VERHALTENS EINES FLUGZEUGSHELTERS DER 3. GENERATION INFOLGE EINER DETONATION IM BODEN

O. von Estorff, W. Pfrang, W. Bergerhoff
Industrieanlagen-Betriebsgesellschaft mbH
Einsteinstr. 20, D-8012 Ottobrunn

F. Glaser
Wehrtechnische Dienststelle 91 - 131
D-4470 Meppen

1. EINLEITUNG

Die Untersuchung von unterirdischen Detonationen und deren Einfluß auf naheliegende Strukturen stellt ein sehr komplexes Problem der Bauwerk-Boden-Interaktion dar. Während im Falle niedertransienter Anregungen und kleiner Amplituden davon ausgegangen werden kann, daß sich Bauwerk und Boden weitestgehend linear verhalten, siehe z.B. Wolf [1], Beskos [2], und Antes und von Estorff [3],[4], sind bei dem vorliegenden Problem eine Vielzahl zusätzlicher Phänomene zu berücksichtigen. Hierzu zählen insbesondere die Ausbreitung der Explosions-Schockwelle und das Phänomen großer Materialbewegungen aufgrund der Expansion der Detonationsprodukte. Zudem sind hochgradig nichtlineare Steifigkeiten und Trägheitsmomente der Strukturelemente, große Verschiebungen sowie eine Separation zwischen Bauwerk und Boden zu berücksichtigen.

Basierend auf umfangreichen Erfahrungen aus dem Bereich der dreidimensionalen Fluid-Struktur-Interaktion infolge Ansprengung, siehe z.B. Bergerhoff, Mohr, Pfrang und Scharpf [5], wurden bereits im Vorfeld der nachfolgend diskutierten Studien erste Untersuchungen zum Verhalten von Stahlbetonstrukturen unter hochtransienter Anregung durchgeführt [6],[7],[8]. Hierbei kam das Programmsystem DYSMAS [9] zum Einsatz, welches für Problemstellungen der Bauwerk-Boden-Interaktion zunächst erweitert werden mußte [10],[11]: im Gegensatz zum rein hydrodynamischen Verhalten eines Fluids, das durch seine komplexen Kavitationseigenschaften geprägt ist, waren im Bodenmaterial zusätzlich deviatorische Spannungen zu berechnen und vor allem Kompaktierungs- und Dekompaktierungseffekte in Abhängigkeit von der Bodenbeschaffenheit zu berücksichtigen. Die Validierung des Programmes erfolgte zum einen durch die numerische und experimentelle Untersuchung der Ansprengung einer Stahlbetonplatte [7], zum anderen durch Simulation einer Bodendetonation gegen einen kompletten Shelter der alten Generation [8].

In der vorliegenden Arbeit wird die Wirkung einer verdämmten Bodendetonation auf einen Flugzeugshelter der neuen Generation diskutiert. Von wesentlichem Interesse ist hierbei die Lokalisierung gefährdeter Bereiche des Bauwerks, sowie die Ausbreitung der Schockwellen in der Struktur. Auf der Basis aktueller Bedrohungs-

angaben wird die Detonation einer MK83 seitlich unterhalb des Fundamentes in Sheltermitte angenommen und die Übertragung der Anregung durch den Boden simuliert. Bezüglich der Ausbreitung von Luftstoßwellen durch das Ausblasbauwerk in den Shelter sei auf [12] verwiesen.

2. GRUNDLAGEN DER BERECHNUNG

Die wesentlichen Merkmale des eingesetzten Programmsystems **DYSMAS/ELC** [9], und insbesondere dessen Möglichkeiten bei der nichtlinearen Berechnung der Bauwerk-Boden-Interaktion, werden nachfolgend kurz zusammengefaßt:

Das System ist ein hybrider Finite Differenzen/Finite Elemente Berechnungscode bestehend aus den zwei unabhängig voneinander arbeitenden Prozessoren DYSMAS/E und DYSMAS/L, die mittels eines dritten Moduls, DYSMAS/C, miteinander gekoppelt sind. Durch die implementierte explizite Zeitintegration eignet sich das Programmsystem speziell zur Simulation von Vorgängen im Kurzzeitbereich. Hierbei können sowohl geometrische als auch physikalische Nichtlinearitäten berücksichtigt werden, was zur realistischen Abbildung der Phänomene im betrachteten Fall unbedingt erforderlich ist.

Der Berechnungscode **DYSMAS/E** basiert auf der sogenannten Euler'schen Betrachtungsweise und eignet sich daher vor allem für die Beschreibung von Problemen mit großen Materialbewegungen, wie sie bei Detonationen oder hydrodynamischen Problemen auftreten. In der vorliegenden Studie wurde daher die Detonation des Sprengstoffes, sowie die daraus resultierende Schockwellenausbreitung und die Gasblasenexpansion im Boden, mit Hilfe dieses Programmteiles simuliert. Hierbei wird das zu betrachtende Gebiet zunächst in einzelne Eulerzellen unterteilt. In jedem Zeitschritt werden dann, unter Berücksichtigung der Massen-, Impuls- und Energieerhaltung, die dynamischen Kenngrößen des bewegten Mediums in dem orts- und zeitfesten Gitter bestimmt. Unter Verwendung Finiter Differenzen erfolgt dann in jedem Zeitschritt z.B. die Ermittlung der Dichte oder Geschwindigkeit in jeder Zelle. Abgeleitete Größen, wie z.B. der Druck, ergeben sich anschließend aus der Lösung von speziellen, meist hochgradig nichtlinearen Zustandsgleichungen.

Für das Medium Boden als Dreiphasengemisch aus Festmaterial, Wasser und Luft ist die Bestimmung der Zustandsgleichung äußerst komplex. So müssen z.B. Kompaktierungs- und Komprimierungseigenschaften genauestens abgebildet werden, wobei deren Abhängigkeit von der Porosität (Wasser- und Luftanteil) bzw. vom Sättigungsgrad (Wasseranteil der Porosität) des real vorhandenen Bodens zu berücksichtigen ist. Das Verhalten des Materialgemisches wird durch die einzelnen Bestandteile beschrieben, ergänzt durch ein sogenanntes Schlupfkonzept [11],[14].

Im Programmteil **DYSMAS/L** wird das dynamische Verhalten einer mit Finiten Elementen diskretisierten Struktur numerisch simuliert. Der Code basiert auf einer Lagrange'schen Betrachtungsweise, bei der die Bewegungen einzelner Massenpunkte in einem materialgebundenen, mitgeführten Koordinatensystem beobachtet werden. Dies ermöglicht eine sehr genaue Bestimmung der Verzerrungen und Spannungen unter Einbeziehung der Deformationsgeschichte. Die Materialmodelle decken, über den linear elastischen Bereich hinaus,

plastisches Fließen, Bruch- und Nachbruchverhalten ab und es können z.B. Verfestigung und Dehngeschwindigkeitsabhängigkeit berücksichtigt werden.

Für die vorliegende Arbeit ist das in DYSMAS/L integrierte Betonmodell von besonderer Bedeutung. Die Fließ- und Versagensfläche wird im Hauptspannungsgraum durch fünf Parameter nach Willam und Warnke [13] beschrieben und hat die Form eines Paraboloids mit der Spitze im Bereich des hydrostatischen Zuges. Auf diese Weise werden die asymmetrischen Materialeigenschaften, hohe Druck- und geringe Zugfestigkeit, berücksichtigt. Die erforderliche Stahlbewehrung wird mit Hilfe von Membranelementen simuliert.

Das Bindeglied zwischen DYSMAS/E (Modellierung von Boden und Luft) und DYSMAS/L (Modellierung der Struktur) ist der Koppelmodul **DYSMAS/C**. Dieser steuert den gesamten Programmablauf und ermittelt die physikalisch relevanten Größen der Wechselwirkung. In jedem Zeitschritt wird die Kopplung über alle Elemente der Strukturberandung vorgenommen. Dabei wird entlang des Interfaces einerseits eine zeitvariable geometrische Randbedingung auf das umgebende Eulermedium (Boden, Luft) übertragen, andererseits stellen die Zustandsgrößen der Eulergebiete eine ebenfalls transiente Lastrandbedingung für die Struktur dar.

Bei Materialien wie z.B. dem Boden müssen, neben den Kräften aus hydrostatischem Druck, Anteile aus Deviatorspannung aus der dem Koppelrand nächstgelegenen Eulerzelle übertragen werden [11]. Bei Zugkraft wird generell ein Kontaktabriß angenommen und keine Kraft übertragen. Tangential zum Interface besteht zwischen Struktur und Medium ein Reibkontakt mit verminderter Übertragung der Tangentialkräfte.

3. SYSTEM UND DISKRETISIERUNG

3.1 Sheltermodell

Zwecks numerischer Simulation der Ansprengung mußte ein vollständig dreidimensionales Finite-Elemente-Modell des Shelters diskretisiert werden (siehe Bild 1). Aufgrund der vorgegebenen Geometrie und Lastanordnung war eine symmetrische Betrachtung des Systems nicht möglich.

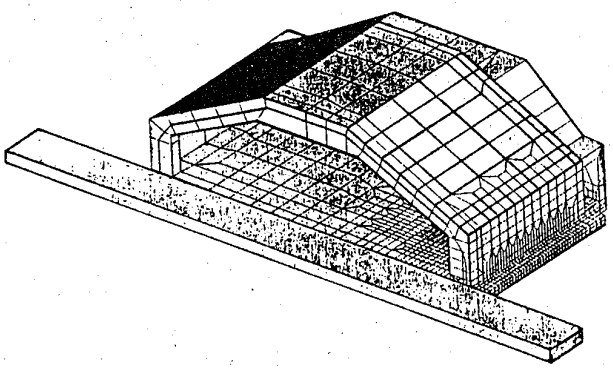

Bild 1: Finite-Element-Modell der Shelterstruktur (LAGRANGE)

Das FE-Modell (ca. 9000 Elemente und 7000 Knoten) wurde so angelegt, daß einerseits die globale Tragwirkung der Stahlkonstruktion des Shelters realistisch erfaßt wurde, andererseits auch lokale Phänomene möglichst genau abgebildet werden konnten. Das besondere Interesse galt den Längsfundamenten mit den Anschlüssen an die Außenwand bzw. an die Bodenplatte. Zudem wurde bei dem zu untersuchenden Shelter, abweichend vom Natokonzept, eine

Verjüngung der Bodenplatte im Mittelbereich vorgenommen, deren Standfestigkeit es zu beurteilen galt. Das gesamte Bauwerk ist ca. 15 m lang, 25 m breit und 8.5 m hoch. Es ist damit wesentlich kürzer als der reale Shelter was bei dessen Beurteilung hinsichtlich des dynamischen Verhaltens von Bedeutung sein wird.

Das Bauwerk wurde aus Stahlbeton (B 25, BSt 500/550) mit starren Anschlüssen zwischen den Fundamenten, der Bodenplatte und den Wänden erstellt. Da das Haupttor, einschließlich Fundament, durch Fugen von dem eigentlichen Shelterbauwerk getrennt ist, wurde es im Modell nicht explizit abgebildet, stattdessen fand lediglich das Torfundament (als Starrkörper) Berücksichtigung (Bild 1).

Neben den tragenden Systemkomponenten waren noch einige Einbauten und ein Flugzeugrumpf zu modellieren. Dieses geschah durch geeignete Feder-Masse-Systeme. An den Innenwänden erfolgte zudem im unteren Bereich die Diskretisierung eines Abplatzschutzes (Stahlblech, d = 4 mm) mit Scheibenelementen.

3.2 Boden-/Luftmodellierung

Im Bild 2 sind verschiedene Ansichten der Euler-Diskretisierung von Baugrund und Luft dargestellt. Die Ladung von 206 kg PETN-Sprengstoff wurde 4.25 m unterhalb der Geländeoberkante, in drei Metern Abstand von der Außenwand und mittig in Längsrichtung des Bauwerks positioniert. Der Nahbereich der Ladung wurde besonders fein diskretisiert (Bild 2). Die Zusammensetzung des anstehenden Bodens konnte aus früheren Versuchen [6] übernommen werden (62% Quarz, 14% Wasser, 24% Luft). Der Grundwasserspiegel wurde im Abstand von 3 m unterhalb der Geländeoberkante angenommen.

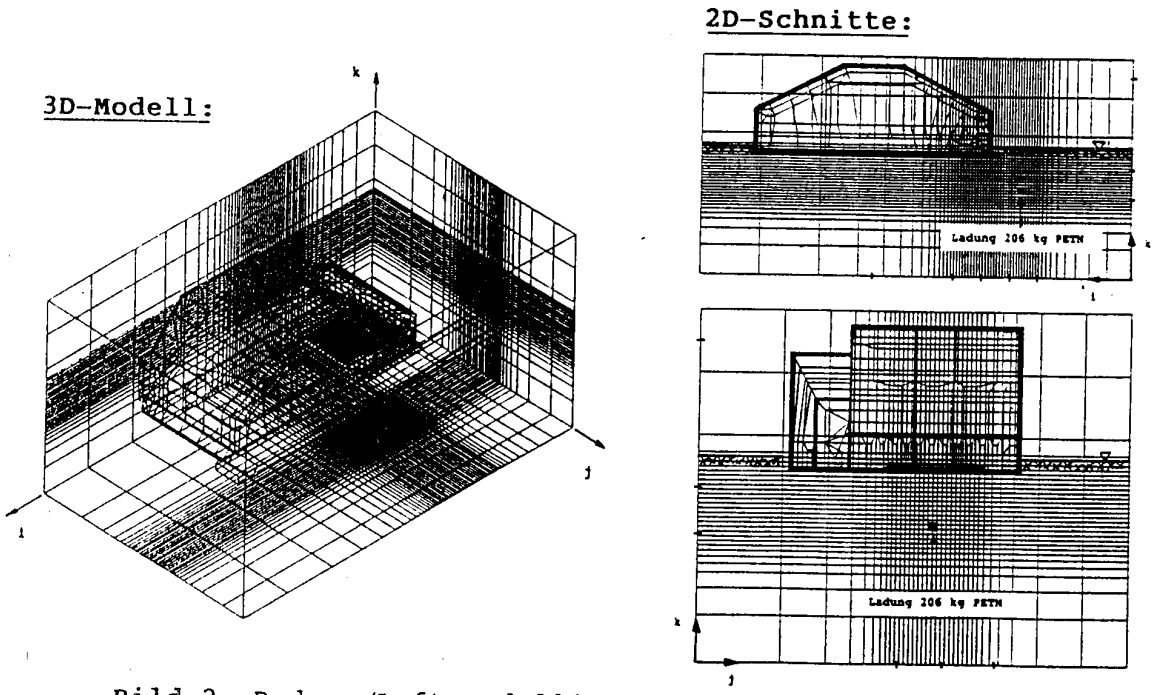

Bild 2: Boden-/Luft-Modellierung durch EULER-Zellen

4. ERGEBNISSE

Aufgrund der begrenzten Darstellungsmöglichkeiten im Rahmen dieser Arbeit werden nachfolgend im wesentlichen die globalen physikalischen Abläufe während des Ansprengvorganges diskutiert, wobei dem Vergleich der diesbezüglichen numerischen und experimentellen Aussagen eine besondere Bedeutung zukommt.

4.1 Vorgänge im Boden

Nach Zündung des Sprengstoffes kommt es zunächst zum Durchbrennen der Ladung. Es entsteht eine Gasblase, die sich schnell aufweitet und das Fundament nach ca. 100 ms erreicht. Bild 3 zeigt die Verteilung der Impulsdichte zum Zeitpunkt t = 100 ms. Deutlich zu erkennen ist die starke Aufwärtsbewegung des Boden/Luft-Gemisches und die starke Belastung des Shelterfundamentes durch das verdrängte Erdreich. Das Ausblasen der Detonationsprodukte steht unmittelbar bevor. Das zwischen Gasblase und Shelter befindliche Bodenmaterial wird in den momentan noch von der Gasblase ausgefüllten Trichter fallen, so daß das Längsfundament teilweise freigelegt wird. Diese Feststellung konnte durch das Experiment exakt belegt werden. Ebenfalls in sehr guter Übereinstimmung mit den Messungen war der jeweils ermittelte Durchmesser des entstehenden Kraters.

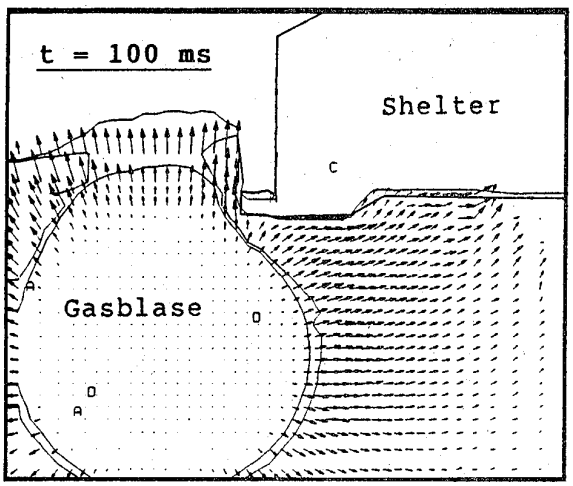

Bild 3: Vektorplot der Impulsdichteverteilung mit Materialkonturen

4.2 Bewegung der Struktur

Das globale Verhalten der Shelterbauwerks läßt sich anhand der in Bild 4 gezeigten vertikalen Verschiebung besonders gut erkennen. Es zeigt sich eine recht homogene Verteilung der Verschiebungen, deren Amplitude mit größer werdendem Abstand von der Detonation

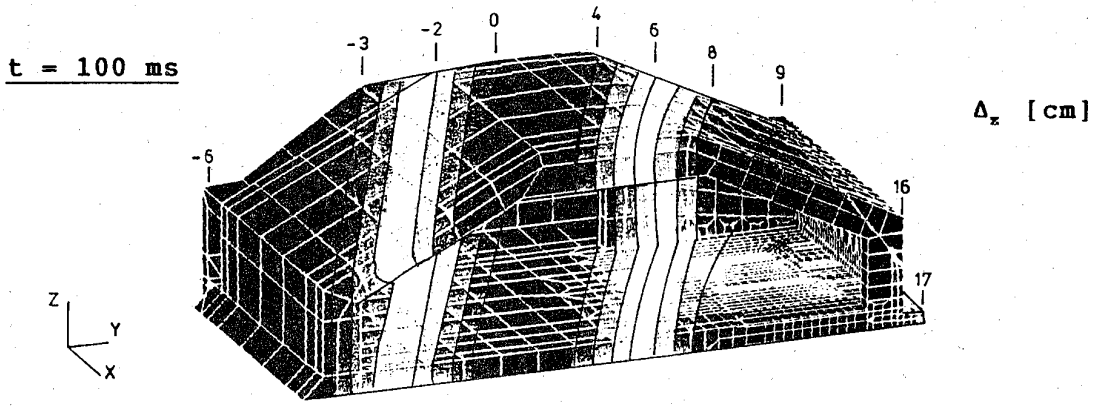

Bild 4: Vertikale Verschiebung des Shelters (Konturdarstellung)

deutlich abnimmt (max. Auslenkung zum betrachteten Zeitpunkt ca. 14 cm). Zudem ist eine Kippbewegung des Bauwerkes um eine schräg zur Mittelachse verlaufende Achse überlagert, d.h. der von der Ansprengung abgelegene Teil der Struktur drückt sich in den Boden, während der nahe gelegene Teil abhebt. Die maximal erreichte Geschwindigkeit des Systems von ca. 2 m/s ist nach 80 ms erreicht; die maximale vertikale Auslenkung (Längsfundament nahe der Detonation) kann mit 25-30 cm angegeben werden.

4.3 Beanspruchung der Struktur

Die Beanspruchung der Struktur wird zunächst anhand der Transienten der Vergleichsdehnung untersucht. Besonders kritisch ist der Bereich des Überganges zwischen den Längsfundamenten nahe der Detonation und der Bodenplatte (Verjüngung). In Bild 5 ist die Vergleichsdehnung für zwei diesbezüglich repräsentative Elemente der äußeren Betonschicht (oberhalb und unterhalb der Bodenplatte) dargestellt. Es zeigt sich, daß nach einer Zeit von t = 45 ms bzw. t = 30 ms Dehnungen erreicht werden, die im Bereich der Bruchdehnung des Beton B25 liegen, d.h. es muß mit Rissen gerechnet werden. Größere Schäden, z.B. herausgelöste Betonbrocken, sind jedoch nicht zu erwarten, da die Stahleinlagen in diesem Teil der Struktur während der gesamten Zeit im linearen Bereich bleiben. Das Auftreten von Betonrissen an dieser Stelle (siehe Bild 6: Bereich 2.5 ‰) wurde durch die Experimente bestätigt.

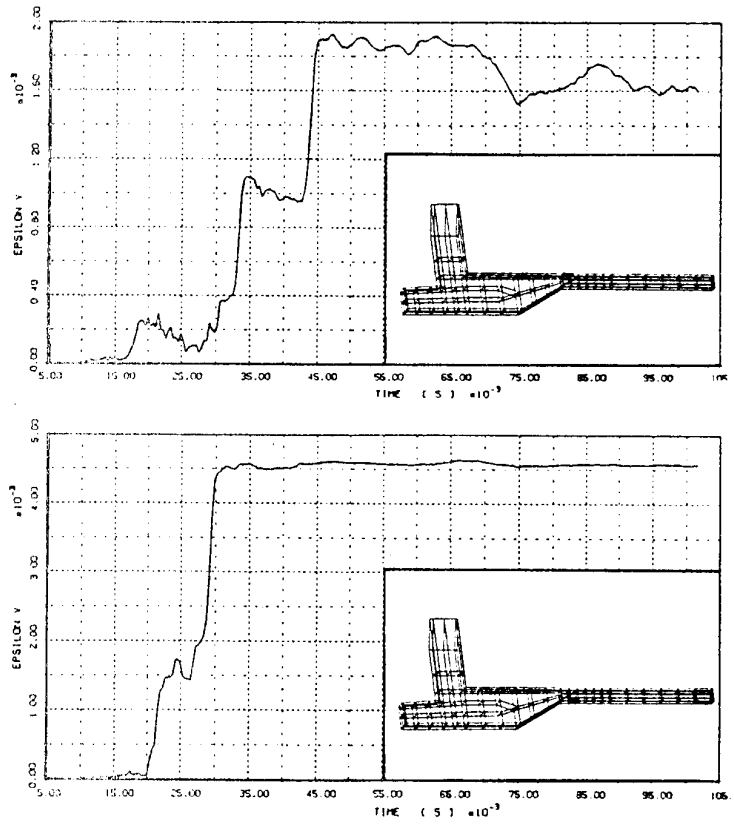

Bild 5: Transiente Vergleichsdehnung

Ein weiterer kritischer Bereich ist der auskragende Teil der Längsfundamente. Aufgrund der exponierten Lage und des geringen Abstandes zur Detonation treten an diesen Stellen hohe Lasten auf und es ist, in sehr guter Übereinstimmung mit dem Experiment, das Auftreten von Rissen festzustellen. Der Konturplot Bild 6 zeigt die rißgefährdeten Bereiche. Die beobachteten Schäden sind jedoch für die Funktion des Shelters nicht von Bedeutung.

Nahe der Detonation sind auch die Seitenwände des Bauwerks relativ hoch beansprucht. Das Abplatzen des Betons wurde hier jedoch durch die Stahlinnenverkleidung verhindert.

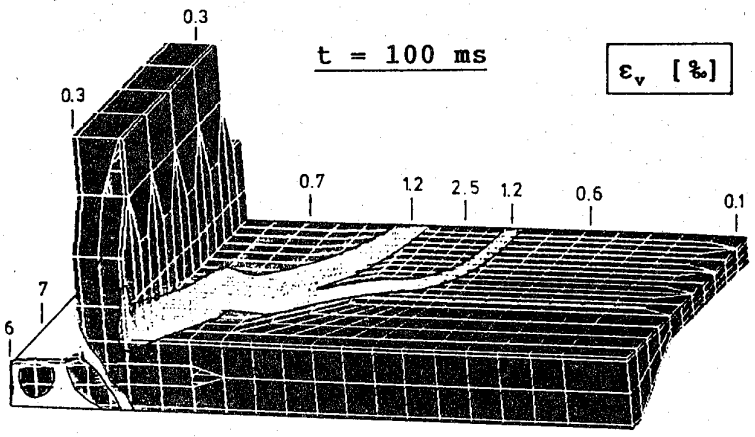

Bild 6: Globale Vergleichsdehnung (Konturdarstellung)

5. ZUSAMMENFASSUNG

Ein gekoppelter Euler/Lagrange-Algorithmus, realisiert im Programmsystem DYSMAS/ELC, wurde zur Untersuchung der Einwirkung von Bodendetonationen auf Flugzeugshelter der 3. Generation eingesetzt. Durchgeführte Vergleiche zwischen Rechung und Experiment machten deutlich, daß das vorgeschlagene Berechnungsverfahren in der Lage ist, insbesondere das globale Verhalten der angesprengten Shelterstruktur sehr gut zu simulieren. Mit dem Rechenprogramm DYSMAS/ELC steht somit ein Werkzeug zur Verfügung, welches in der Lage ist, zukünftig wertvolle Unterstützung bei der Entwicklung und Konstruktion von Schutzbauwerken zu leisten.

Obwohl die zugrundegelegte Schockbelastung aktuellen Bedrohungsangaben entsprach, zeigte sich das untersuchte Bauwerk als sehr resistent. Offensichtliche Schwachstellen in der Konstruktion konnten nicht festgestellt werden. An einigen exponierten Stellen führte die Beanspruchung zwar zum Versagen des Betons, die dabei auftretenden Dehnungen waren jedoch so gering, daß lediglich sichtbare Risse, nicht aber größere Schäden auftraten. Da zudem die Bewehrung, von geringen Plastifizierungen an einigen Stellen abgesehen, nur elastische Verformungen erfuhr, war die Tragfähigkeit der untersuchten Struktur in keiner Weise gefährdet.

Es sei abschließend betont, daß die hinsichtlich der Festigkeit des Probebauwerks gemachten Aussagen nicht ohne weitere detaillierte Untersuchungen auf das reale Shelterbauwerk übertragbar sind. Der Grund hierfür ist vor allem in den stark unterschiedlichen Gebäudeabmessungen (Längenverhältnis 1:3) zu sehen, durch die das dynamische Verhalten des Shelters, insbesondere das der Bodenplatte (Bild 6), und die komplexen, nichtlinearen Vorgänge bei der Ansprengung entscheidend beinflußt werden.

LITERATURVERZEICHNIS

/ 1/ **J.P. Wolf:** Dynamic Soil-Structure Interaction. Prentice-Hall, Inc., Englewood Cliffs, New Jersey (1985)

/ 2/ **D.E. Beskos:** Boundary Element Methods in Dynamic Analysis. Appl. Mech. Rev. **40**, 1-23 (1987)

/ 3/ **H. Antes, O. von Estorff:** Dynamic Response Analysis of Rigid Foundations and Elastic Structures by Boundary Element Procedures. Soil Dyn. and Earthquake Engng. **8**, 86-74 (1989)

/ 4/ **O. von Estorff:** Dynamic Response of Elastic Blocks by Time Domain BEM and FEM. Computers and Structures (in print)

/ 5/ **W. Bergerhoff, W. Mohr, W. Pfrang, F. Scharpf:** The Program DYSMAS/ELC and its Application on the Underwater Shock Shock Loading of Vessels. First Intercontinental Symposium for Maritime Simulation and Mathematical Modelling, Munich (1985)

/ 6/ **D. Krassin:** Überprüfung von Flugzeugschutzbauten aus wehrtechnischer Sicht. B-TF-2050, IABG, München (1986)

/ 7/ **W. Pfrang, W. Bergerhoff, H.J. Schittke, F. Glaser:** Die numerische Simulation einer verdämmten Bodendetonation. Int. Symposium "Interaktion konventioneller Munition mit Schutzbauten", Mannheim (1987)

/ 8/ **W. Pfrang, W. Bergerhoff, H.J. Schittke:** The Response of an Aircraft Shelter to a Buried Explosion - 3D Coupled Simulation. 4th Int. Symp. of the Interaction of Non-Nuclear Munitions with Structures, Panama City, FA (1989)

/ 9/ The Program Family **DYSMAS**. B-TF-V197/2, IABG, München (1986)

/10/ **D. Krassin:** Erweiterung der Kopplung in DYSMAS/ELC zur Abbildung der Vorgänge an der Interface bei 2D-Boden-Bauwerks-Interaktion. B-TF-V234, IABG, München (1986)

/11/ **W. Bergerhoff, D. Krassin:** Erweiterung der Kopplung in DYSMAS/ELC zur Abbildung der Vorgänge an der Interface bei 3D-Boden-Bauwerks-Interaktion. B-TF-V234, IABG, München (1987)

/12/ **B. Fießler, F. Glaser:** Numerische Simulation eines Luftstoßes gegen das Ausblasbauwerk eines Shelters. Int. Symp. "Interaktion konventioneller Munition mit Schutzbauten", Mannheim (1991)

/13/ **K.J. Willam, E.P. Warnke:** Constitutive Model for the Triaxial Behavior of Concrete Structures Subjected to Triaxial Stresses, Bergamo (1974)

/14/ **W. Bergerhoff:** Flugzeugshelter der 3. Generation, Verhalten bei einer Detonation im Boden. B-TF-2720, IABG, München (1990)

MODELING OF EXPLOSIVELY-FORMED CRATERS; ANALYSIS AND COMPARISON OF PROTOTYPE AND REDUCED-SCALE TEST EVENTS

John J. Gill, Major USAF, PhD
WL/NTESG, KAFB, NM 87117-6008
(505) 846-6471

ABSTRACT

Several techniques are being developed at the Civil Engineering Research Division, Kirtland Air Force Base, New Mexico, which permit the real time viewing of soil displacement in response to extreme loading rates such as those associated with blast loading. These techniques include the use of half-space containers with cast acrylic viewing windows which are suitable for testing in normal gravity and the high-gravity environment created by a geotechnical centrifuge. This paper presents the results of a series of explosive cratering tests conducted using these devices. Tests conducted on the Sandia National Laboratories centrifuge modeled scaled net explosive weights ranging from 227 kg (500 lbs) to 910 (2000 lbs) using a 5 gm (nominal weight) charge of C-4 explosive. Tests were conducted at gravity levels (g's) ranging from 26 to 42 g's. Scaled depth of burial in a sandy soil ranged from half buried to 4.8 meters (15 ft). The results of a one-gravity reduced scale test using a half-buried 4 gram spherical charge of C-4 explosive are included in the analysis. Model craters are compared with prototype events and predictions developed using AFWL-TR-70-127, Protection From Nonnuclear Weapons, and the CONWEP program developed by the Waterways Experiment Station (Ref. WES TM 5-855-1, Fundamentals of Protective Design for Conventional Weapons).

A STUDY OF CRATERING PHENOMENA FROM CONVENTIONAL WEAPONS USING SMALL CHARGES IN A HALF SPACE APPARATUS

Robert W. Henny, WL/NTE, KAFB, NM 87111

Results from field tests comparing cratering phenomena between a conventional bomb and an equivalent yield, uncased spherical HE charge were presented by the author at the 3rd International Symposium on the Interactions of Conventional Munitions with Protective Structures. To better understand the significant differences observed in their crater sizes and shapes as well as as permanent displacement fields, a half space apparatus was designed, built and prototyped. This half space apparatus, measuring 8 feet in diameter by 5 feet deep contains a large, specially designed window to allow direct, continuous visual documentation of particle motions during the entire cratering event. Three experiments using 5-gm charges were designed to simulate a series of well documented, buried 1000-lb HE spherical field tests. Resulting crater shapes were similar to the field events. More important, vector directions of particle motion data matched the field data reasonably well. Thus, we believe that this half space apparatus can be used to examine the kinematics of the cratering process in a wide variety of highly controlled geologic configurations. This devise should be very useful in better understanding and in extrapolating past field event data, including crater/structure interactions, as well as in improving the design and instrumentation placement for future field tests. Further, when used in conjunction with our companion centrifuge cratering studies, the examination of the kinetics of the cratering process and the attendant scaling issues is feasible.

* work funded by the Tri-Lab Program

DYNAMIC RESPONSE OF EMBEDDED CIRCULAR REINFORCED MICRO-CONCRETE SLABS - AN EXPERIMENTAL STUDY.

by

A. N. Dancygier, S. P. Shah, and L. M. Keer

Department of Civil Engineering
Northwestern University
Evanston, IL 60208

ABSTRACT

The response of circular reinforced concrete slabs embedded in a shallow depth and subjected to an external low impact was studied experimentally. Soil-structure interaction phenomena which affect the stresses acting on the structure and its response were considered to rationalize the physical mechanisms involved. The experimental setup consisted of a small scale model of the soil-structure system. The external impact was simulated by dropping a steel ball on a 12 in. diameter aluminum target plate which rested on the backfill surface of the soil which was 20-30 dry Ottawa sand. The structure was a vertical 6 in. diameter plexiglas cylinder which supported a circular slab roof made of reinforced micro-concrete. Records of the pressure acting on the roof of the structure were obtained and compared to reference free field records, along with the corresponding motion records. A study of those signals implies a pattern of the system response, which is demonstrated in a typical test. Analysis of the experimental results suggests that the initial portion of the impact, equal to that of the free field, acts on the structure until the response of the structure reaches a critical velocity. That initial impact, depending on the level of loading in the free field and on the speed of response of the structure, might be sufficient to cause a failure. The soil-structure interaction, driven by the velocity and the deflection of the structure and by the properties of the backfill, will cause the load to deviate from the free field, and in case of failure can determine its degree.

INTRODUCTION

The stresses acting on an embedded structure are dependant on the soil-structure interaction, such that the deflection of the buried structure affects the loads that act on it and those loads in turn are responsible for its deflection. Under static externally applied loading, the normal stresses that act on a relatively flexible structure decrease while the normal stresses at both sides increase. That case is called *positive arching* while the opposite case of a relatively rigid structure is *negative arching*[1,2,3]. Arching was found to occur at even shallow depths of burial (ratio of depth to structure span which is less than 1/2)[4,5].

For external loads that are not static, soil-structure interaction will still affect the stresses acting on the structure and its response, but the physical mechanisms do not consist only of arching. Under a typical external impact whose duration is the order of magnitude of the period of the structure, a pressure wave is generated that propagates into the medium. The soil-structure interface acts as a boundary that determines the stresses that act on it and that are responsible for the initial response of the structure. Since the development of arching depends on a sufficient displacement of the structure, to what extent the response of the structure under an external impact is affected by arching is not clear.

The problem was studied experimentally by a small scale model of a soil-structure system. The objective was to measure and record the motion response and the normal stresses acting on the structure under a low external impact, generated by impact of a steel ball dropping on an aluminum target plate, resting on the backfill surface. This experimental system enabled relative flexibility of varying the experimental parameters, such as the impact level or depth of burial, and provided test conditions that were relatively well defined. Thus, it was possible to perform repeated experiments under different external impact, with varying boundary conditions for the roof of the structure. Free field measurements of the

pressure at the roof level, under the various levels of impact were taken as a reference for the soil-structure test records. The pressure records over the roof of the structure, as measured at the center and over its edge, together with the velocity and displacement records of the roof, provided useful information on the mechanisms that are involved.

EXPERIMENTAL PROCEDURE

Experimental Setup. The experimental setup consisted of a small scale model of the soil-structure system (Fig. 1). The external impact was simulated by dropping a 4 lb. steel ball on a 12 in. diameter aluminum target plate. The target plate rested on the surface of the soil and generated a pressure impact wave beneath it, whose duration at the center was 0.3 to 0.5 millisecond with a peak of 1100 to 2000 psi, depending on the height of drop, H. The soil was 20-30 dry Ottawa sand, which with layered pouring and tapping enabled a relatively uniform density after each excavation and re-embedment of the model structure. The structure was a vertical 6 in. diameter plexiglas cylinder, supporting a circular slab roof. The wall and floor of the structure were 0.5 in. and 1.0 in. thick, respectively, and were buried at 2.5 in. under the target plate. The response of the circular slab, as the main structural element, was primarily being monitored. The slab specimens were made of reinforced micro-concrete, had thickness of less than 0.5 in. and a clear diameter span of 5 inches. The reinforcement consisted of spot welded meshes made of black annealed deformed wire of a 0.0348 in. diameter (#20 wire). Both the micro-concrete and the reinforcement were prepared according to the recommendations given by Cunningham, Townsend and Fagundo[6], who found this small scale design suitable for modeling reinforced concrete structures of larger scale. Two types of boundary conditions at the perimeter of the slab were used: a simple support was provided by holding the roof slab at three separate points located 120° from each other, while fixing the slab all around with a rigid aluminum cap restrained the slope of the slab at its perimeter (Fig. 2). Special attention was given to the measurement and recording devices of the loads and deflections of this small scale system: The relative deflection of the center of the roof was recorded. Acceleration measurements of the whole structure, which was thick enough to be assumed relatively rigid, were also taken. Normal pressure was recorded at the center of the roof, 2 in. from the center, and also 2.5 in. from the center in the simply supported case.

Test Plan. A typical example of the tests that were performed with restrained slab roof is described here (the simply supported case is not discussed). Under a 2.5 in. of backfill a 0.45 in. thick restrained roof slab was subjected to external impact. The height of drop of the steel ball impactor was gradually increased from 25 in. (denoted as the "H25" case) and the center displacement signal was examined after each drop for plastic deflection, indicating possible failure. Such indication was observed under external impact which was generated by dropping the impactor from a height of 90 in. (denoted as the "H90" case). Measurements of the normal pressure were recorded over the roof center and over its edge, 2 in. from the center. The compressive strength of the micro-concrete was 6500 psi. The reinforcement wires had a yield stress of 51 ksi, and were placed in an equal number for a compressive and tension ratio of 0.21% in each direction.

TEST RESULTS

The normal pressure records and the corresponding motion records of the restrained roof under the lower impact, H25 case (height of drop of the impactor was 25 in.), and under the highest impact, H90 case, are given in figures 3 and 4, respectively. Under an external impact generated by a drop of the impactor from 90 in. the roof failed. The plastic deformation of the slab center at t = 1.3 msec was minimal (about 0.004 inch at 1.3 msec in Fig. 4b), but the full displacement signal showed that the roof oscillated for about 2 more milliseconds with an average deflection of about 0.01 in.. These oscillations, however, had a relatively small amplitude and did not seem to affect at that time the normal pressure over the roof, which was decaying rapidly at t > 1.5 msec. Excavation of the structure revealed visible radial cracks at the bottom of the roof, but there was no catastrophic failure. No cracks were detected on top of the slab, indicating that the roof slab was not fully fixed at its supports. Free vibration measurements of the slab roof under the two boundary conditions showed, however, that the restrained slab had indeed a higher natural frequency, about twice as much as the simply supported roof.

DISCUSSION

Analysis of the normal pressure signal over the roof and the displacement and velocity signals shows that the pressure wave, generated at time zero under the target plate, reached the center of the roof at t = 0.15 to 0.18 msec, and hit the edge of the roof 10 to 50 μsec later (Fig. 3a and 4a). At about 0.2 msec both the pressure over the center and over the edge started to drop. Note that in comparison with similar free field reference signals recorded in Figs. 5 and 6, this drop was a deviation and was caused by the roof gaining

velocity immediately upon being hit. Therefore, it was concluded that for the first 0.05 to 0.1 msec the response of the roof was dominated by a mechanism typical to wave propagation in a medium with elastic boundary, where the velocity of the boundary affects the normal pressure acting on it. At about 0.25 msec, the pressure over the center kept dropping while over the roof edge again it rose and returned to the free field level (Figs. 5 and 6) although the edge was still moving downwards with a negative velocity (Figs. 3a and 4a). This part of the response indicates the development of arching identified by a decrease of the normal pressure over the more flexible central part of the roof and its increase over the stiffer edge, due to relative displacement of the center (Figs. 3b and 4b). In fact, the center displacement and velocity records of the two cases, H25 and H90, are similar in the first 200 μsec of the response, which explains the similarity in the load records. The difference in the absolute peak of the pressure over the roof center is due to the difference in the free field stresses of the two cases: the free field pressure 2.5 in. under the center of the target plate, at t = 0.2 msec was higher when the external impact was generated by a higher drop of the impactor. The pressure over the center in case H90 dropped to zero, but maintained a moderately higher minimum in case H25. In both cases the pressure record over the edge of the roof did not drop to zero during the first 700 μsec of the response. This indicates that while in case H90 the velocity of the roof was sufficient to cause detachment of its center part from the sand above it, in case H25 the roof remained in contact with the backfill.

At about 0.35 to 0.38 msec, and up to 0.58 msec in case H90, there was an increase of the normal pressure over the center of the roof, while the pressure over the edge slightly decreased below the level of the free field (Figs. 4a and 5a). Note that during this period of time the motion of the roof center was still downward (negative center velocities during t < 0.525 msec in Fig. 3a, and during t < 0.6 msec in Fig. 4a). The amplitude of the center velocity decreased at that time, and the velocity of the sand above this region perhaps again matched the velocity of the roof and reloaded it. It was also possible that due to the displacement of the edge of the roof (Figs. 3b and 4b) negative arching was developed over it, decreasing somewhat the pressure over the edge and increasing it over the center and over a region outside the structure (where the pressure was not recorded). Further analysis of the failure case, H90, shows that at t = 0.58 msec the velocity of the roof center became positive (Fig. 3a), indicating an upward motion, and the normal pressure over that part of the roof increased again in a similar, but opposite, manner to the decrease of the pressure at the beginning of the response of the structure, at t = 0.2 msec. The pressure over the center following t = 0.525 msec was different in case H25, where it did not show a third peak but continued to decrease monotonically. Note that while the amplitude of the velocity was near zero in the two cases, the displacement was much larger in case H90, causing a relatively sharp decrease of the pressure (at t = 0.58 msec in Fig. 4a) by arching.

Elastic analysis of the circular plate was performed to evaluate at what time of the response cracks were formed. A Poisson ratio of 0.15 was assumed, and two types of loading were considered: uniformly distributed load, and linearly distributed load with a maximum at the center. Furthermore, as no cracks were detected on the top surface of the slab, a simply supported scheme was used, even though the roof was restrained. Based on the compressive strength, and according to the ACI recommendations, and the recommendations by Cunningham, Townsend and Fagundo[6], the elastic modulus of the slab was evaluated to be equal to $33w_c^{3/2}f'^{1/2}_c = 4 \cdot 10^6$ psi (where w_c of micro-concrete is 130 pcf), and the static modulus of rupture was evaluated as $7.5f'^{1/2}_c = 600$ psi. Since loading and deflection were at a high rate, the dynamic modulus of rupture was assumed as 1100 psi[7]. The analysis indicates that at a center displacement of about 0.003 to 0.005 inch the elastic stress at the bottom of the slab reach the tensile capacity of concrete and further indicates that cracks must have started to form in the roof slab at a rather early time of the response at about 0.22 and 0.30 msec in cases H90 and H25, respectively (see Figs. 3b and 4b). Arching, which started to form at about that time, released the load over the center of the roof for about 150 μsec, preventing its total failure in the H90 case. Therefore, it can be concluded that from the time the roof was hit by the pressure wave, about 50 μsec elapsed until a sufficient velocity was developed to reduce the normal pressure and about 50 μsec more were required to develop sufficient displacement for arching. Nevertheless, if the external impact is high enough, during the first 50 μsec to cause large deformations of the structure, then the mechanisms described above can only affect the degree of failure but can not prevent it.

Note that the static ultimate capacity of a clamped slab, evaluated according to the yield line plastic theory (no horizontal support was provided to enable compressive membrane action) is $p_u = 12m_u/R^2 = 30$ psi, where R = 2.5 in. is the radius of the slab, and m_u is the ultimate moment capacity of the slab, which for $\rho_x = \rho_y = \rho = 0.21\%$ is $\rho d^2 f_y(1-0.5\rho f_y/0.85f'_c) = 15.73$ lb-in/in. The ultimate capacity for a simply supported circular slab is $p_u = 6m_u/R^2 = 15$ psi. Similar slabs tested under a uniformly distributed, static

and quasi-static load, with and without horizontal supports, had a capacity of 20 to 120 psi[8]. Evidently the dynamic peak of the impact was much higher than the static capacity, and even when taking into account the enhanced properties of the slab under impact loading, the fact that this load was applied for a relatively short time was the dominant reason that the slab sustained it. Therefore it seems that the portion of the free field impulse, acting on the structure until it decreases by the mechanisms described above, has an important effect on the response or even capacity of the structure. This result is also illustrated in Fig. 7, which shows the impulses over the center and over the edge of the slab in the two cases. The two curves have a similar shape, but while the initial impulse during the first 300 to 400 μsec in case H25 reaches a plato of 0.012 to 0.015 psi•sec, it is 0.038 psi•sec in case H90.

CONCLUSIONS

Records of the pressure acting on the embedded structure were obtained and compared to reference free field records, together with corresponding motion records. Study of those signals suggests a pattern of the system response, demonstrated in a typical test, and observed in others:

1. During an initial period of time, the pressure acting on the structure is equal to that of the free field. That period of time determines the initial impact acting on the structure, which when sufficiently long may cause failure.
2. The structure, acting as a relatively flexible boundary for the medium above it, gains velocity, which causes the pressure above it to decrease.
3. The displacement of the more flexible part of the structure triggers arching, which keeps the pressure decreasing over it, and increases the pressure over the stiffer supports.
4. A second, lower peak in the pressure above the center occurs when the velocity decreases. At that time the velocity of the backfill probably matches the velocity of the roof center and re-loads it.
5. Depending on the external impact and the response that it generates, a third peak may occur over the relatively flexible center when it bounces and its velocity changes sign.

ACKNOWLEDGEMENTS

The authors are grateful for the support from the Air Force Office of Scientific Research. They are pleased to acknowledge the program Manager, Director of Aerospace Science, Major Steven C Boyce. Special thanks are given to Dr. F.C. Townsend from the University of Florida and to Dr. P. Perdicaris from Case Western University who helped in deforming the wires used later as micro-reinforcement.

REFERENCES.

1. Davis, R.E., Bacher, A.E., "Concrete Arch Culvert Behavior - phase 2", Journal of Structural Division, ASCE, Vol. 98, No. ST11, Nov. 1972, pap. No. 9352, p. 2329.
2. Kiger, S.A., "Ultimate Capacity of Earth-Covered Slabs", Journal of Structural Engineering, Vol. 114, No. 10, Oct. 1988, p. 2343.
3. Kiger, S.A., Eagles, P.S., Baylot J.T., "Response of Earth- Covered Slabs in Clay and Sand Backfills", Technical Report SL-84-18 (AD-A 149 296), U.S. Army Engineer Waterways Experiment Station, Vicksburg, Miss., Oct. 1984.
4. Kiger, S.A., Getchell, J.V., "Vulnerability of Shallow-Buried Flat-Roof Structures; Report 1, Foam HEST 1 and 2", Technical Report SL-80-7-1, U.S. Army Engineer Waterways Experiment Station, Vicksburg, Miss., Sept. 1980.
5. Kiger, S.A., Getchell, J.V., "Vulnerability of Shallow-Buried Flat-Roof Structures; Report 2, Foam HEST 4", Technical Report SL-80-7-2, U.S. Army Engineer Waterways Experiment Station, Vicksburg, Miss., Oct. 1980.
6. Cunningham, C.H., Townsend, F.C., and Fagundo, F.E., "The Development of Microconcrete for Scale Model Testing of Buried Structures", Technical Report ESL-TR-85-49, Department of Civil Engineering, University of Florida, 1986.
7. Suaris, W. and Shah, S.P., "Properties of Concrete Subjected to Impact", Journal of Structural Engineering, Vol. 109, No. 7, July 1983, p. 1727.
8. Chen, Y.J., Chen, H.L., Dancygier, A.N., Shah, S.P., Keer, L.M., "Tests of Small Scale Reinforced Concrete Circular Slabs", ACI Structural Journal, V. 87, No. 6, November-December 1990.

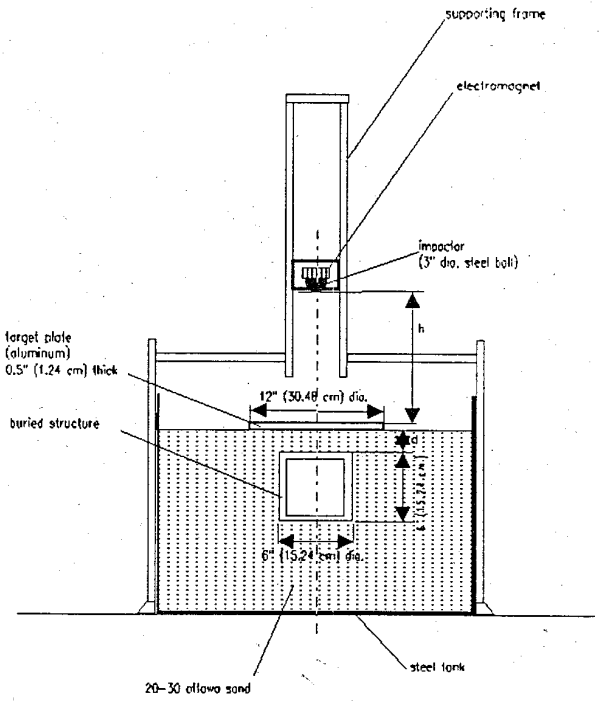

Fig. 1: Experimental set-up for a small scale model of a soil-structure system.

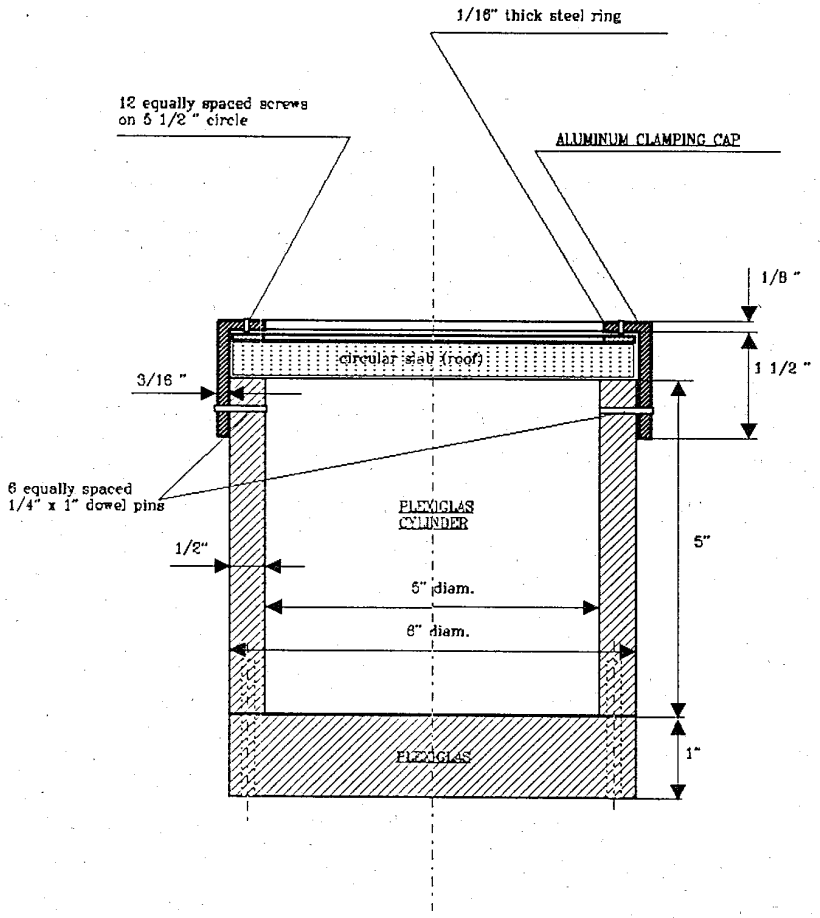

Fig. 2: Details of boundary conditions for the roof – clamped type.

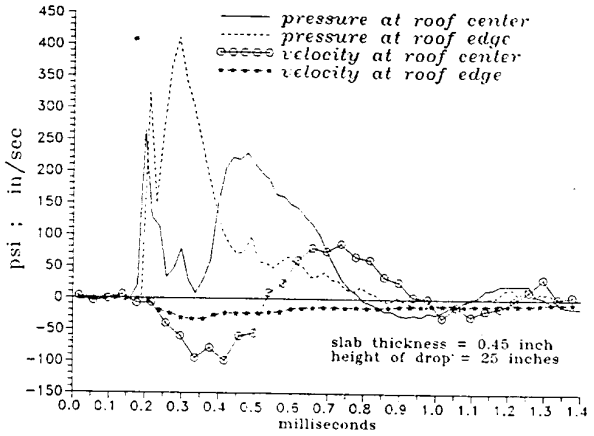

Fig. 3a: Response of a restrained roof buried under 2.5 inches of sand: Normal pressure and velocity distribution.

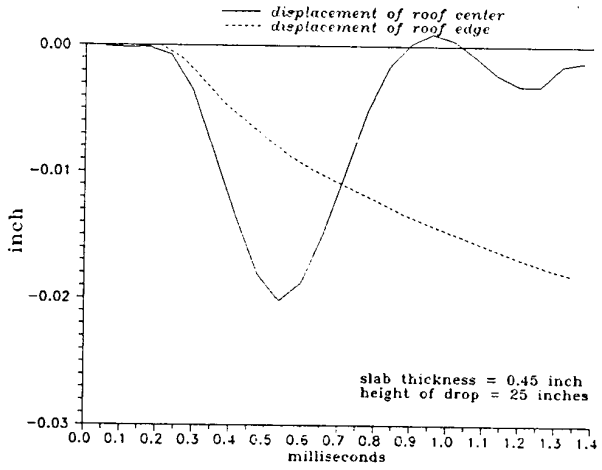

Fig. 3b: Displacement of a restrained roof buried under 2.5 inches of sand.

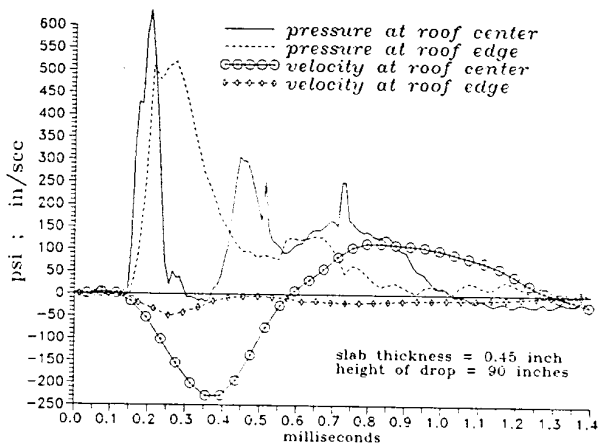

Fig. 4a: Response of a restrained roof buried under 2.5 inches of sand: Normal pressure and velocity distribution.

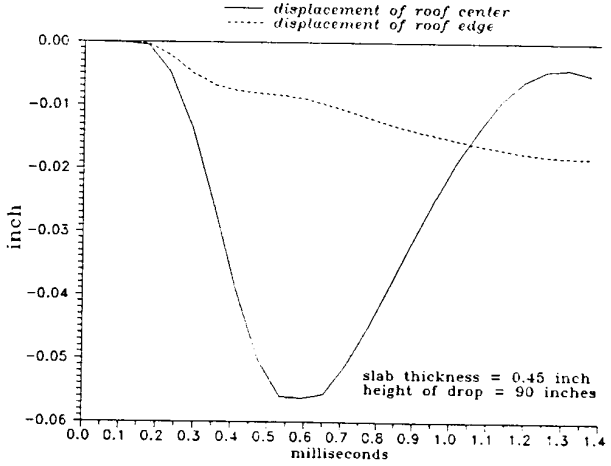

Fig. 4b: Displacement of a restrained roof buried under 2.5 inches of sand.

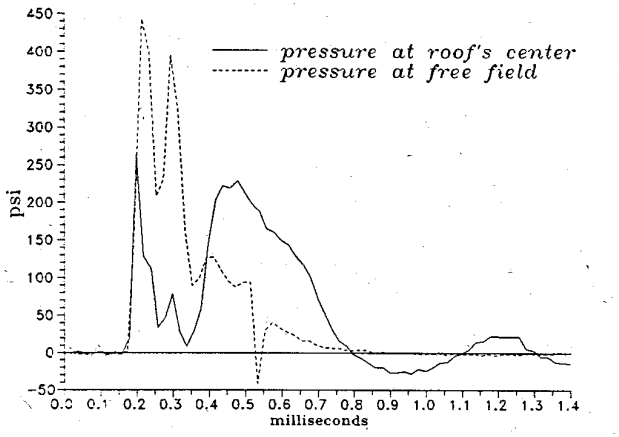

Fig. 5a: Normal pressure over the center of a restrained roof
(d = 2.5 inches; h = 0.45 inch; height of drop = 25 inches)

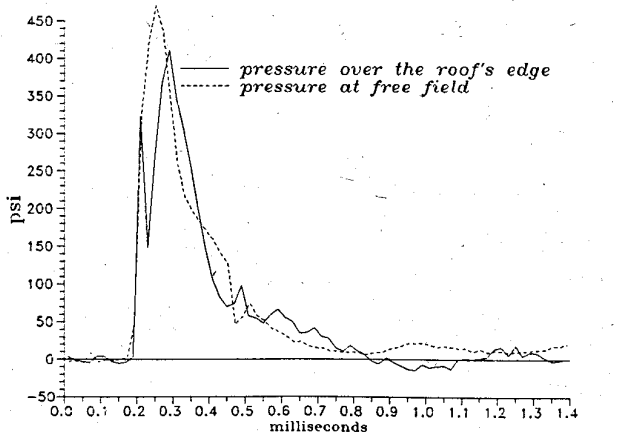

Fig. 5b: Normal pressure over the edge of a restrained roof
(d = 2.5 inches; h = 0.45 inch; height of drop = 25 inches)

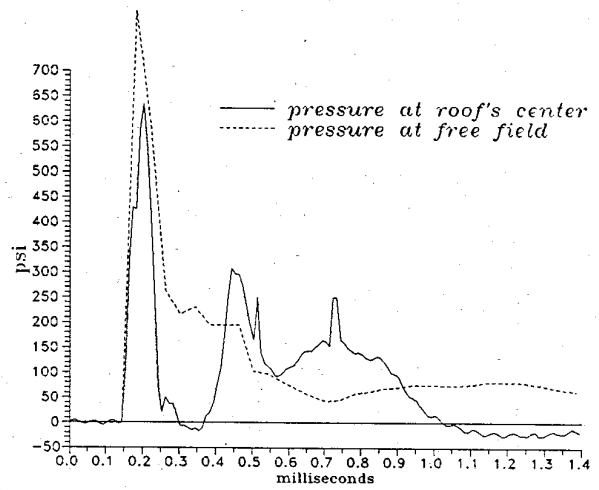

Fig. 6a: Normal pressure over the center of a restrained roof
(d = 2.5 inches; h = 0.45 inch; height of drop = 90 inches)

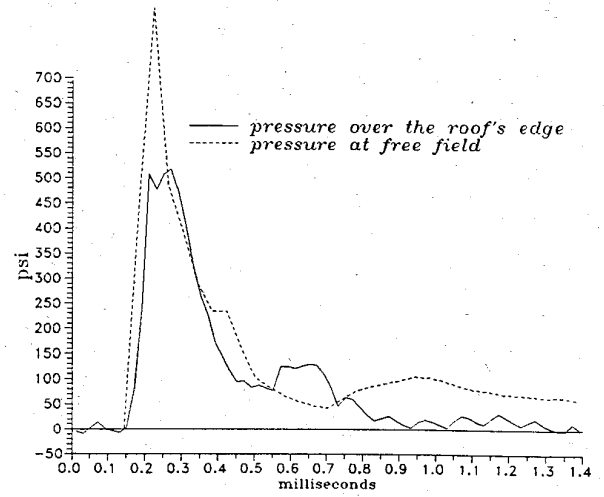

Fig. 6b: Normal pressure over the edge of a restrained roof
(d = 2.5 inches; h = 0.45 inch; height of drop = 90 inches)

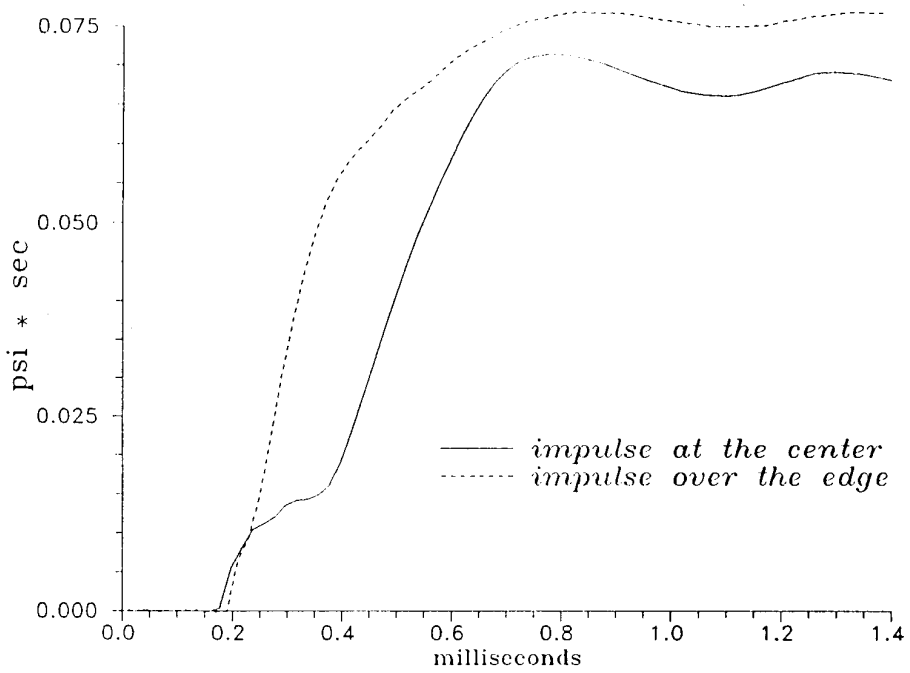

Fig. 7a: Impulse records over a restrained roof.
(d = 2.5 inches; h = 0.45 inch; height of drop = 25 inches)

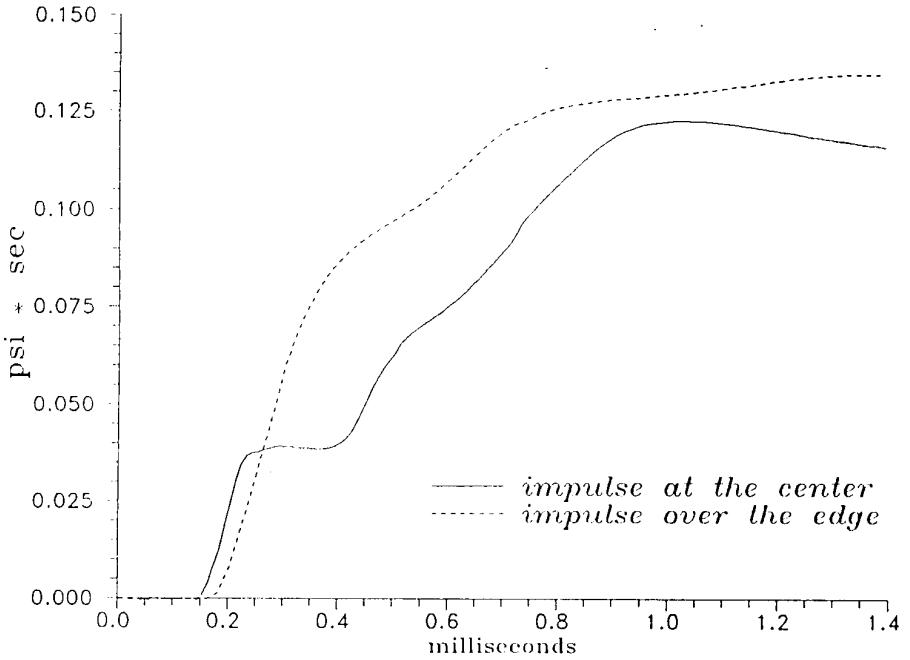

Fig. 7b: Impulse records over a restrained roof.
(d = 2.5 inches; h = 0.45 inch; height of drop = 90 inches)

Hydrocode Analysis of Ground Shock Environment From Buried Subscale Munition Tests in Wet Clay Backfill

Harold D. Zimmerman, Y. Marvin Ito,
California Research and Technology, Titan Corporation, Chatsworth, CA

Jon E. Windham
U.S. Army Engineer Waterways Experiment Station, Vicksburg, MS

Abstract

California Research & Technology (CRT) has supported the U.S. Army Engineer Waterways Experiment Station (WES) in developing methodology to evaluate cratering, ground shock, and loads transmitted to buried protective structures from conventional munitions. A series of detailed 1-D and 2-D hydrocode calculations of the near-source ground shock induced by the detonation of a 1/3-scale MK83 bomb buried in low air-filled-void wet clay, has been performed. These calculations are posttest simulations of instrumented field events, denoted CONWEB 1 and 2 (respectively a vertically and horizontally oriented charge), conducted in 1989 at Ft. Knox Kentucky. Close coordination between theoretical analysis and experiments is essential to validate the hydrocode results, aid in the interpretation of the experimental data, and understand in-situ constitutive properties.

As modeled, the test bed configuration consisted of a layered half-space, clay backfill overlaying in-situ clay. A steel jacketed cylinder of C4 explosive was placed vertically, centered at 5 ft depth. Hydrocode simulations allow graphical visualization of the explosive detonation and shock propagation. Peak values of calculated radial stress and velocity, along with selected waveforms are compared to their experimental counterparts. Both the 1-D spherical fully contained and 2-D cylindrical free-surface calculated waveforms and attenuations, tend to be in very good agreement with the measured experimental environment.

Computer-Programme

Computer Simulation

SABER-PC: A Ground-Shock Software Package for the PC

by

Stephen A. Akers
Research Civil Engineer
U.S. Army Engineer Waterways Experiment Station
3909 Halls Ferry Road, Vicksburg, Mississippi, USA 39180-6199

and

Jill Stelter
formerly of California Research & Technology, Inc.
20943 Devonshire Street, Chatsworth, California, USA 91311

ABSTRACT

A PC software package was developed to calculate the fully-contained, spherical, free-field, ground-shock environment produced by the detonation of buried conventional weapons. The software package includes menu-driven pre-processing programs to select soil types, explosive sources, and output stations; an explicit, large-strain finite element code to perform the ground-shock calculations; and a collection of plotting programs to post-process the results from single or multiple calculations. The purpose of this paper is to describe the features of the software package, give examples of the graphical output, and compare calculated results with measured field data.

NUMERISCHE SIMULATION EINES LUFTSTOSSES GEGEN DAS AUSBLASBAUWERK EINES SHELTERS

B. Fießler
Industrieanlagen-Betriebsgesellschaft mbH
Einsteinstr. 20
D-8012 Ottobrunn

F. Glaser
Wehrtechnische Dienststelle 91 - 131
D-4470 Meppen

1. Aufgabenstellung

Der Prototyp einer neuen Sheltergeneration wurde als Versuchsbauwerk bei der WTD 91 in Meppen erstellt.

Ein wichtiges Merkmal dieses Shelters ist die Gestaltung des Ausblasbauwerkes. Seine Aufgabe ist einerseits, die Flugzeugabgase möglichst ungehindert ins Freie gelangen zu lassen, und andererseits den Shelterinnenraum gegen Waffenwirkung von außerhalb zu schützen. So werden die Abgase im rückwärtigen Raum des Shelters durch eine große Öffnung nach beiden Seiten hin durch verhältnismäßig kleine Ausblasöffnungen hinausgeleitet. Zur Unterstützung der Ableitfunktion ist mittig an der Rückwand hinter dem Flugzeugstandort ein Leitblech montiert, das die Abgase zu den seitlich gelegenen Ausblasöffnungen hin umlenken soll. Diese Auslegung begünstigt natürlich auch einwärts gerichtete Strömungen, insbesondere die Einleitung von Luftstoßwellen, die von außen auf die Ausblasöffnung treffen.

So war das Ziel eines der verschiedenen, an diesem Prototypen durchgeführten Versuche, die Belastung im Shelterinnern als Folge einer seitlichen Bombendetonation zu klären. Hierzu wurde im Experiment drei Meter seitlich einer der beiden Ausblasöffnungen eine Bombe MK 83 mit der Spitze auf dem Boden stehend gezündet. Innerhalb des Bauwerkes waren fünf Druckaufnehmer verteilt.

Parallel zum Experiment wurde dieser Versuch numerisch mit Hilfe der bei IABG/TFF entwickelten und eingesetzten Codes DYSMAS/E (Fluiddynamik) und DYSMAS/ELC (Fluid-Struktur-Interaktion) simuliert. Die den beiden Codes zugrundeliegenden Methoden sind in [1] beschrieben.

Dieser Beitrag soll zeigen, inwieweit sich die Ergebnisse aus Experiment und Simulation bestätigen und darüberhinaus ergänzen und damit zum unfassenden Verständnis der physikalischen Vorgänge im Shelter beitragen.

2. Problembeschreibung

2.1 Bombe

Die im Experiment verwendete Bombe war vom Typ MK 83 mit 200 kg Sprengstoff Tritonal. Sie wird in der Simulation als Zylinder modelliert. Der "Encasement"-Einfluß des Stahlgehäuses wird durch eine vereinfachte Hohlzylinderform mit realistischer Massenverteilung berücksichtigt. Abb. 4 zeigt die Bombe in

einem Zustand kurz nach der Zündung. Die Bombe wird in der Mitte gezündet. Die Detonation erfolgt nach einem Abbrandmodell mit konstanter Detonationsgeschwindigkeit.

2.2 Shelter

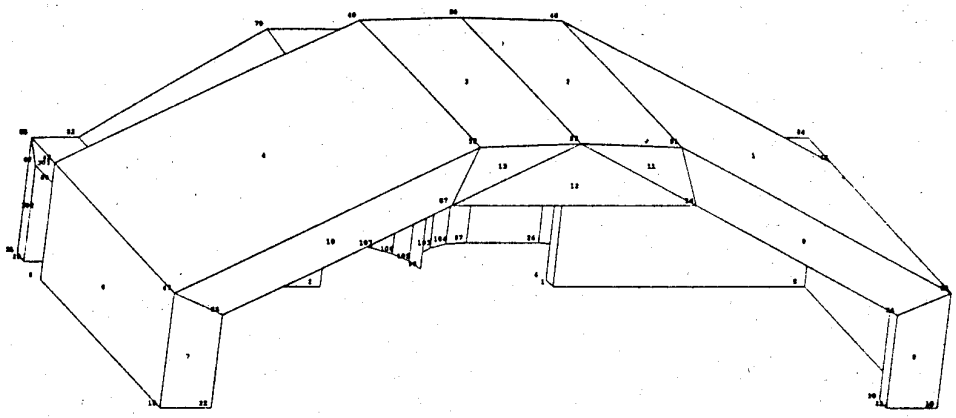

Abb. 1 FE-Diskretisierung des Shelters

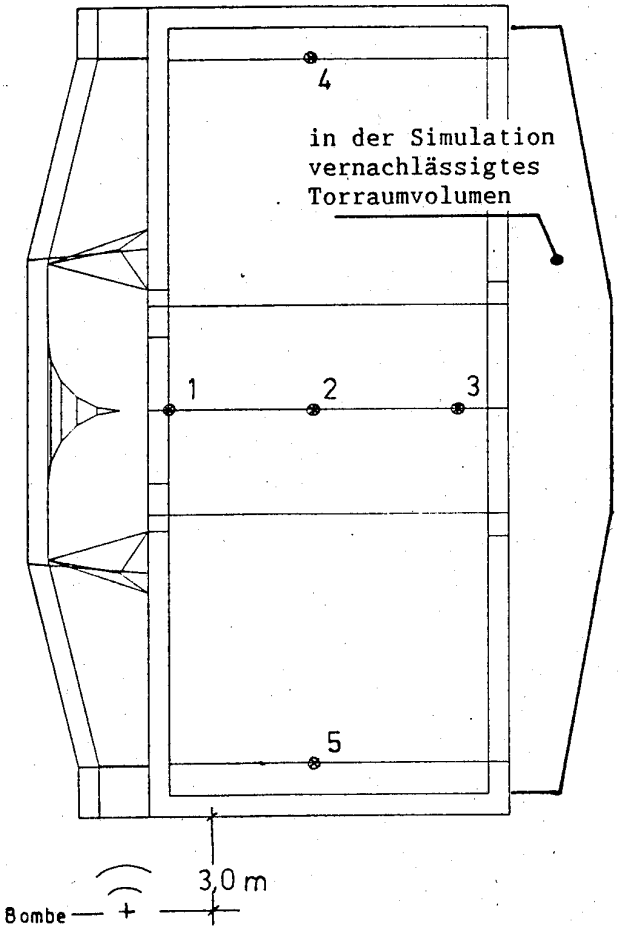

Abb. 2 Lageplan von Shelter, Bombe und Meßaufnehmern

Der Shelter wird im Rahmen einer gekoppelten 3D-Simulation mit DYSMAS/ELC durch eine FE-Diskretierung abgebildet. Eine Alternative hierzu wäre der Einsatz von "body-fitted coordinates". Ein derartig komplexes Modell wie das des Innenraumes des vorliegenden Shelters läßt sich jedoch mit dieser Methode praktisch nicht handhaben.

Die Oberflächen des Shelters werden als unverformbar und unverschieblich (starr) angesehen. Erschütterungen des Shelters, die ihrerseits wieder Wellen in der Luft anregen, werden durch die Modellierung des Shelters als Starrkörper nicht erfaßt. Diese Schwingungen mit geringen Schalldrücken liegen im akustischen Bereich und damit weit unterhalb des hier interessierenden Druckstoß-Levels, der sich mit diesem Vorgehen ohne störende Überlagerungen untersuchen läßt.

Abb. 1 zeigt die starre FE-Diskretisierung des Shelters. Sie besteht aus

insgesamt nur 107 Elementen, da die großen ebenen Flächen nicht wie etwa bei einer Festigkeitsuntersuchung fein aufgelöst werden müssen, sondern lediglich zur Abbildung der geometrischen Kontur dienen. Am Ausblasbauwerk ist eine der beiden seitlichen Ausblasöffnungen zu erkennen. In der Mitte der Rückwand des gleichen Bauteiles ist das Leitblech zu sehen. Boden und Torwand des Shelters werden durch starre, reflektive Eulerzellen geschlossen. Hierbei wurde, wie sich später herausstellte, fälschlicherweise der Torraum in der Diskretisierung eben abgeschlossen. Das durch die räumliche Schrägstellung der Tore nicht unerhebliche Torwandvolumen ging dadurch verloren (vgl. Abb. 2). Dieser Effekt zeigt sich in den Ergebnissen der Endphase der Berechnung, wie später gezeigt werden wird.

2.3 Boden

Der Boden unterhalb der Bombe (vgl. Abb. 4) wird in der Anfangsphase durch ein kompaktierbares Gemisch von Sand, Wasser und Luft modelliert. Damit soll die anfänglich hohe und daher relevante Energiedissipation in den Boden ermöglicht werden. Im späteren Verlauf der Simulation wird der Boden innerhalb und außerhalb des Shelters durch eine starre Platte gebildet.

2.4 Materialien

Während der Simulation werden bis zu sechs verschiedene Materialien teils gleichzeitig einbezogen.

Luft und verbrannter Sprengstoff sind während der ganzen Simulationszeit anzutreffen. Die Luft wird durch das Idealgas-Gesetz beschreiben, der verbrannte Sprengstoff durch die JWL-Zustandsgleichung.

In der Anfangsphase sind zusätzlich der unverbrannte Sprengstoff, der Stahl für das Bombengehäuse, sowie die Materialien Sand und Wasser als Fraktionen des Bodens zu berücksichtigen. Stahl wird durch die speziell für hochdynamische Zustandsänderungen von Metallen aufgestellte TILLOTSON-Gleichung beschrieben, der unverbrannte Sprengstoff, der Sand sowie das Wasser durch eine modifizierte TAIT-Gleichung.

2.5 Eulergitter

Zündung und Detonation der Bombe stellen extrem hohe Anforderungen an die Auflösung in der numerischen Simulation, weil die Zustandsgrößen im detonierenden Sprengstoff extrem steile Gradienten aufweisen. Ungenauigkeiten, die hier einfließen, pflanzen sich unvermeidbar über die ganze Simulation hinweg fort. Andererseits ist es weder möglich noch nötig, das gesamte Sheltergebiet mit der gleichen Auflösung zu überziehen, da einerseits nach heutigem Stand der Rechnertechnik weder Speicherplatz noch Rechenzeit verfügbar wären und andererseits zur Erfassung von Luftstoßwellen außerhalb des unmittelbaren Nahbereiches der Bombe eine geringere Auflösung völlig ausreicht.

Das angewandte Rezoning-Verfahren gestattet es, in zeitlicher Abfolge verschiedene Eulergitter mit degressiver Auflösung zu verwenden und damit das während der Simulation expandierende Beobachtungsgebiet jeweils vollständig zu erfassen. Beginnend mit der Zündung wird das höchstauflösende Gitter eingesetzt, das jedoch nur die unmittelbare Bombenumgebung erfaßt. Darin läßt sich solange simulieren, bis die Stoßwelle irgendeinen der Gitterränder erreicht. Der letzte Zustand wird in das nächstgröbere und größere Gitter über-

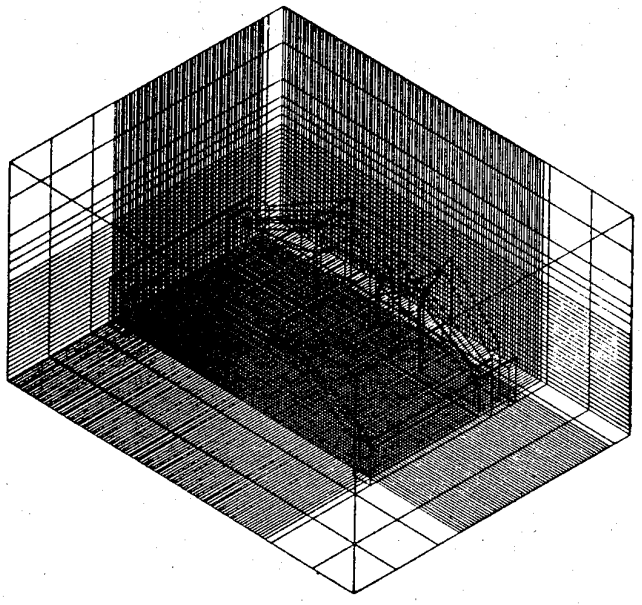

Abb. 3 Räumliche Ansicht des Shelters im letzten 3D-Euler-Gitter

tragen, wo die Simulation fortgesetzt wird, bis wiederum die Stoßwelle einen der neuen Ränder erreicht.

Solange die Stoßwelle den Shelter noch nicht erreicht hat, liegt innerhalb der Stoßfronten ein rotationssymmetrisches Problem vor, das den Einsatz von von 2D-Eulergittern erlaubt. Danach erfolgt der Übergang auf 3D-kartesische Eulergitter.

Insgesamt werden für die Simulation sechs Gitter benutzt, nämlich 2 axialsymmetrische für die Anfangsphase sowie vier 3D-kartesische Gitter für die weitere Simulation. Abb. 3 gibt einen räumlichen Eindruck der Diskretisierung des letzten Eulergitters wieder.

Die relevanten Zellabmessungen beginnen mit 1 cm im ersten axialsymmetrischen Gitter und wachsen über die Folge 2,12,12,24 und 24 cm bis zum sechsten Gitter an. In den vier 3D-Gittern werden jeweils zwischen 210000 und 220000 Zellen benutzt.

2.6 Meßpunkte

Abb. 2 zeigt Lage und Numerierung der fünf Meßaufnehmer im Sheltergrundriß. Die Aufnehmer befinden sich jeweils 1.80 m über dem Boden.

3. Darstellung der numerischen Simulation

Dieser Abschnitt zeigt einige Ergebnisse, die die komplexen physikalischen Vorgänge illustrieren. Sämtliche Zahlenwerte sind - soweit nicht anders angegeben - im cgs-System gegeben. Drücke sind demnach in µbar, Geschwindigkeiten in cm/s, spezifische Impulse in g/(cm·s) und spezifische Energien in $(cm/s)^2$ skaliert.

3.1 Detonation

Abb. 4 zeigt einen Zustand während der Detonation zum Zeitpunkt t=0.104 ms. Im mittleren Bereich, wo die Zündung erfolgte, ist der Stahlmantel bereits aufgeweitet, im Sprengstoff sind anhand der Konturlinien die nach oben und unten laufenden Detonationsfronten zu sehen. Außerhalb dieser Fronten ist der Sprengstoff noch undetoniert. Transienten der Drücke auf einem Radiusstrahl in Höhe der Bombenmitte finden sich in Abb. 5. In der Legende sind die Abstände von der Bombenachse angegeben. Demnach sind die Drücke in Abständen von 110 cm bis 220 cm dargestellt - ein Bereich, der meßtechnisch nicht zu-

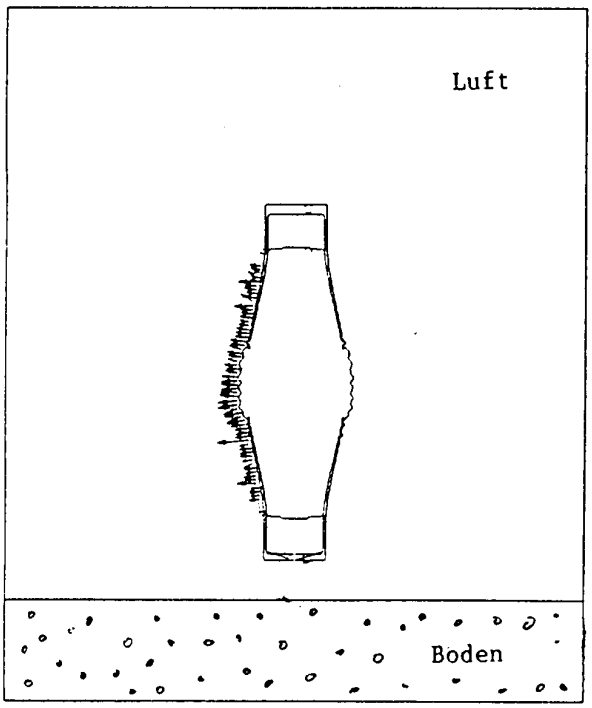

Abb. 4 Detonation der Bombe t=0.104 ms

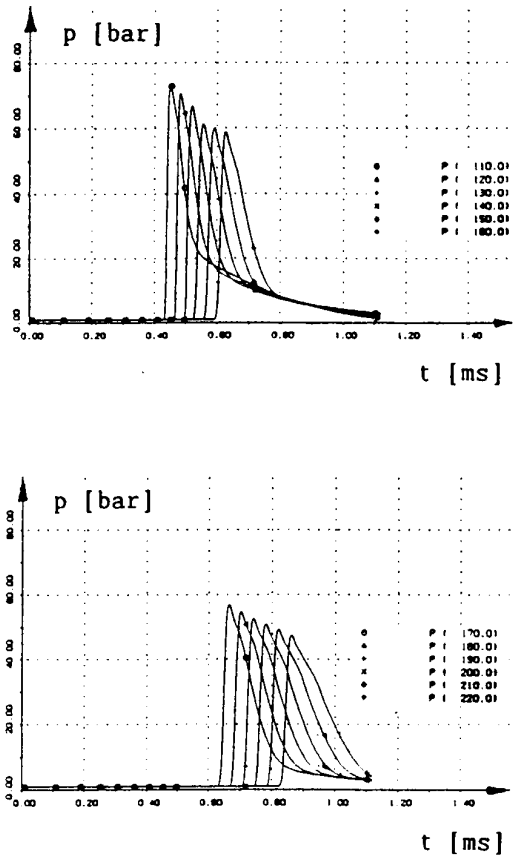

Abb. 5 Drucktransienten in Bombennähe Abstände 110 bis 220 cm

gänglich ist. Die Spitzenwerte fallen sehr rasch von ca. 73 bar bis auf ca. 47 bar ab. Der schwach ausgeprägte Knick direkt hinter der Druckspitze deutet den Durchlauf der der Stoßwelle dichtauf folgenden Gasblasengrenze an.

3.2 Stoßwelle im Bereich der Ausblasöffnung

Ab dem Zeitpunkt t=1.118 ms läuft die Simulation 3D-kartesisch. Zunächst sind vor allem die Effekte an und hinter der Ausblasöffnung von Interesse. In Abb. 6 ist ein horizontaler Schnitt in 180 cm Höhe über dem Boden zur Zeit t=3.721 ms wiedergegeben. Zu erkennen sind der Grundriß des Shelters in der Umgebung der Ausblasöffnung, die Gasblasenkontur sowie das Geschwindigkeitsvektorfeld, wobei die Länge eines Pfeiles der lokalen Geschwindigkeit v proportional ist.

Abb. 6 läßt erkennen, wie sich beiderseits der Ausblasöffnung eine reflektierte Front aufbaut. Es wird deutlich, daß die beiden Fronten vor der Ausblasöffnung aufeinandertreffen und die "rechte" Front als die stärker entwickelte die Strömung nach links abdrängt. Durch dieses Abdrängen löst sich die Strömung an der "linken" Kante der Shelterrückwand, und es entsteht hinter der Kante eine Umkehrströmung. Wichtig ist hier, daß die Reflexionsfronten offenbar einen "choking"-Effekt hervorrufen, wodurch die Strömung in das Bauwerk hinein abreißt.

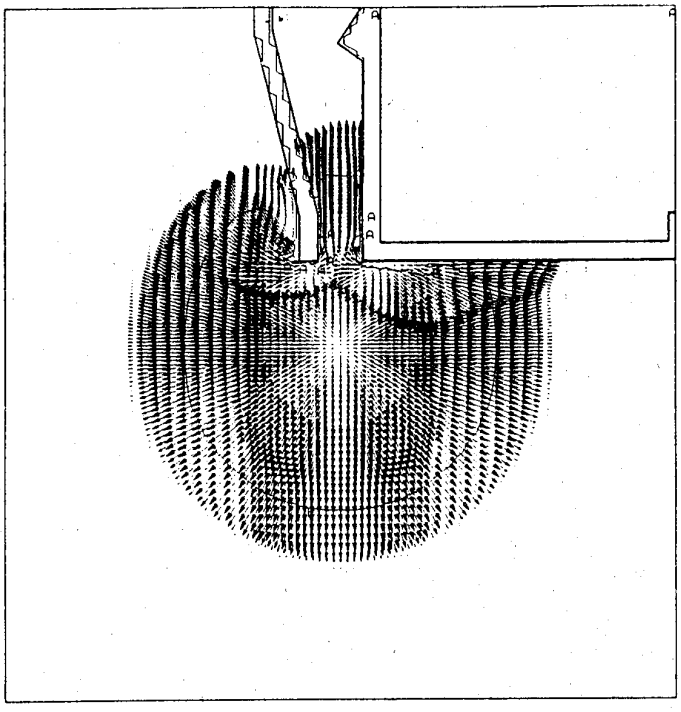

Da das Ausblasbauwerk sich nach innen erweitert, wirkt es wie der divergente Teil einer Düse; die Strömung muß hier - relativ zu einer Freifeldströmung - beschleunigt werden. Abb. 6 läßt diesen Effekt sehr gut erkennen.

Abb. 6 Geschwindigkeitsverteilung im Bereich der Ausblasöffnung; t=3.721 ms

3.3 Stoßwelle im Shelterinnenraum

Die folgenden Abbildungen zeigen die Verteilungen der spezifischen Impulse in zwei zueinander senkrechten Schnitten. Der obere Bildteil zeigt einen vertikalen Schnitt entlang dem Ausblasbauwerk (Abb. 7) bzw. in der Ebene der Meßpunkte 2, 4 und 5 (Abb. 8 und 9), der untere Bildteil jeweils einen horizontalen Schnitt in 1.80 m Höhe über dem Boden.

Die Abbildungen zeigen fortlaufend die Ausbreitung der Stoßwelle. Zu beobachten sind insbesondere die Umlenkung der Welle zuerst an der Lisene und danach am Leitblech sowie die Ablösung und Rückströmung hinter dem Leitblech. Im gegenüberliegenden Teil des Ausblasbauwerkes ist neuerlich ein "choking"-Effekt zu beobachten, der noch von der jenseitigen Lisene des Innentores verstärkt wird.

Die durch das Shelterinnentor in die Flugzeughalle hineinlaufende Welle weist unterschiedliche Charakteristiken auf. An der der Bombe abgewandten Seite behält die Welle ihre Stoßwelleneigenschaft. Sie verliert diese zunehmend zu der der Bombe zugewandten Seite hin, wo sie schließlich als einfache Druckwelle um die Torkante herum nach rückwärts gebeugt wird.

In der Flugzeughalle (Abbn. 8 und 9) wird die Welle zunächst von der schrägen Decke nach unten reflektiert. Eine weitere Reflexion entsteht ab etwa 36 ms an der Torwand auf - wegen des vernachlässigten Torraumvolumens hier früher als im Experiment. Schließlich entstehen Reflexionen an den Seitenwänden des Shelters, insbesondere an der der Bombe abgewandten Seite. Es wird deutlich, daß gerade auf der Seite des Meßpunktes 4 mit hohen Belastungen infolge der direkten Stoßwelle und der verschiedenen Reflexionen zu rechnen ist.

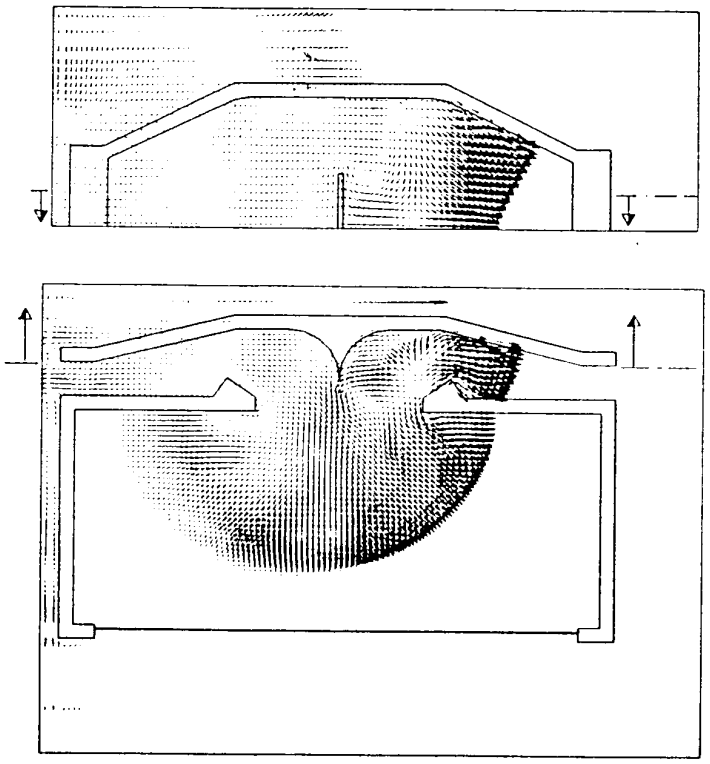

Abb. 7 Verteilung der spezifischen Impulse im Ausblasbauwerk; t=29.29 ms

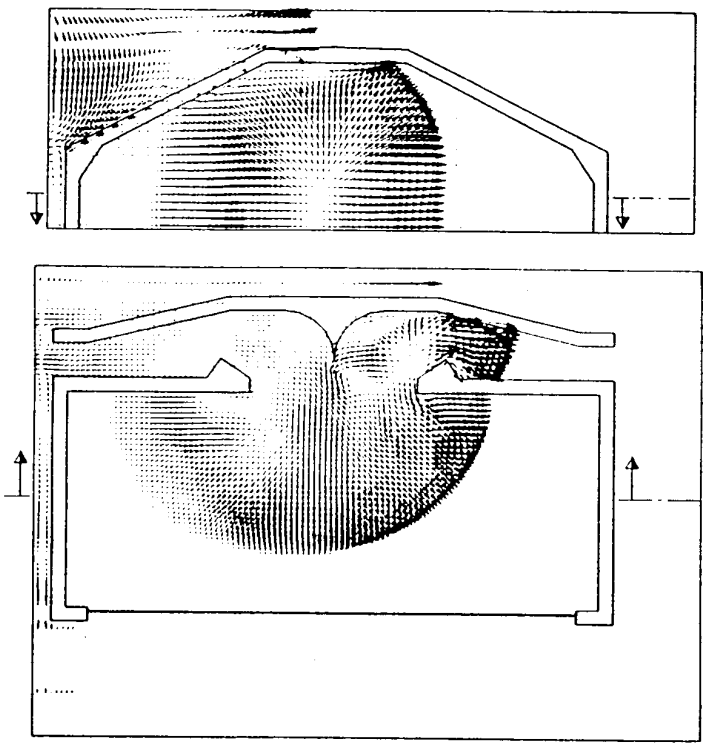

Abb. 8 Verteilung der spezifischen Impulse in der Flugzeughalle; t=29.29 ms

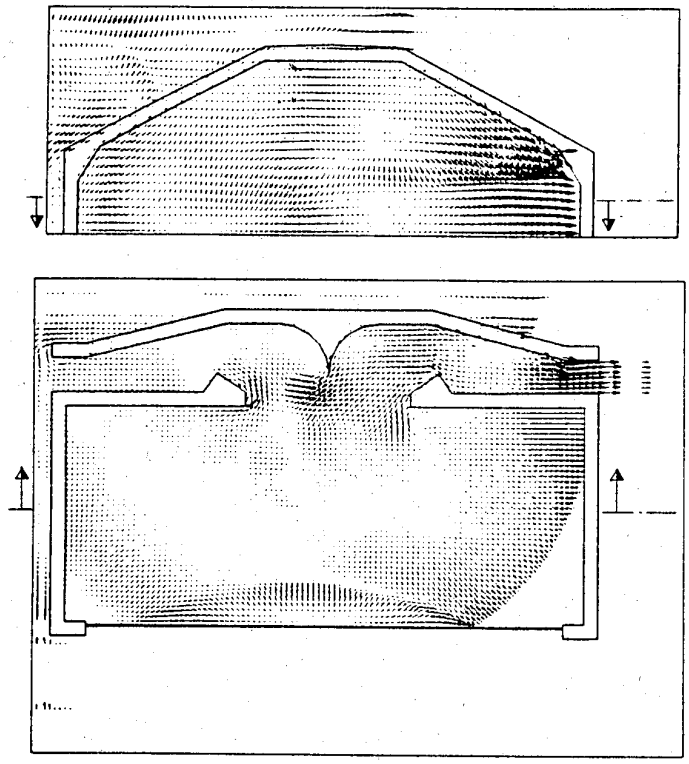

Abb. 9 Verteilung der spezifischen Impulse in der Flugzeughalle; t=42.37 ms

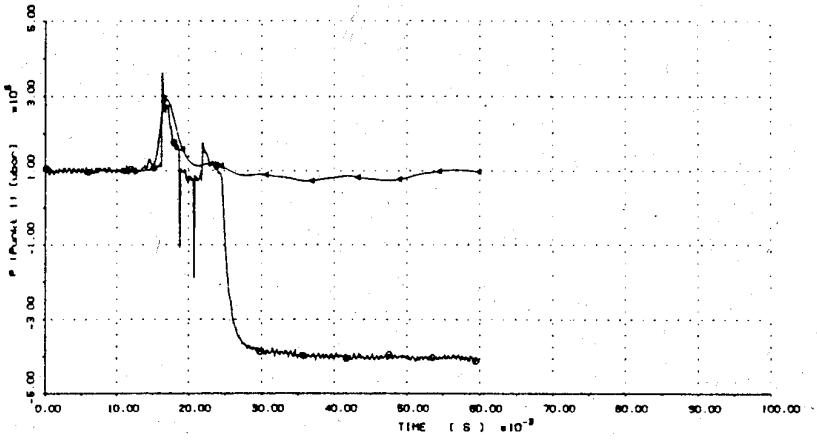

Abb. 10 Meßstelle 1: Drucktransienten aus Experiment und Simulation

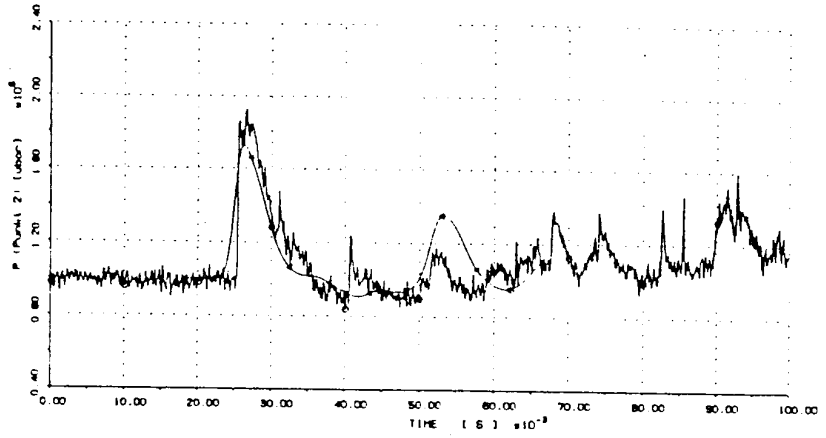

Abb. 11 Meßstelle 2: Drucktransienten aus Experiment und Simulation

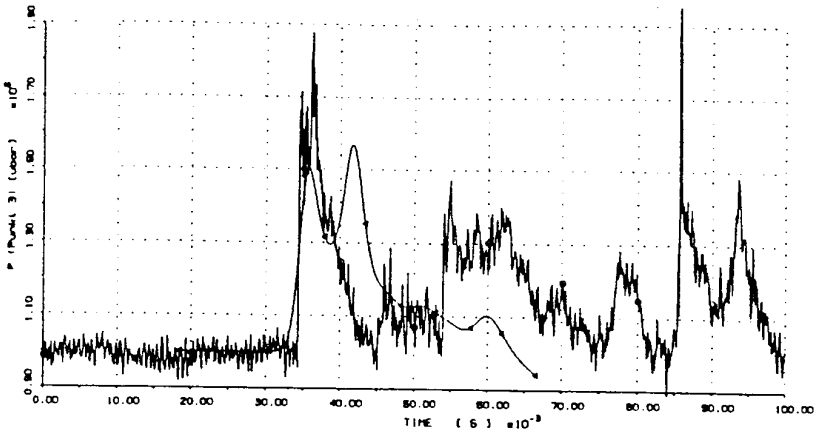

Abb. 12 Meßstelle 3: Drucktransienten aus Experiment und Simulation

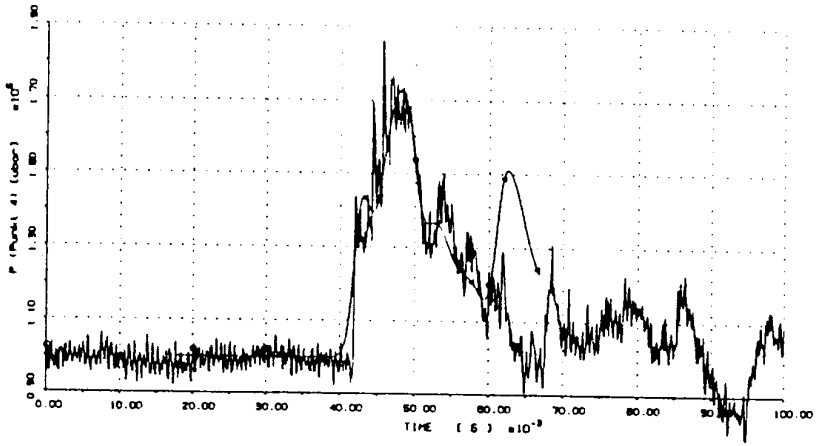

Abb. 13 Meßstelle 4: Drucktransienten aus Experiment und Simulation

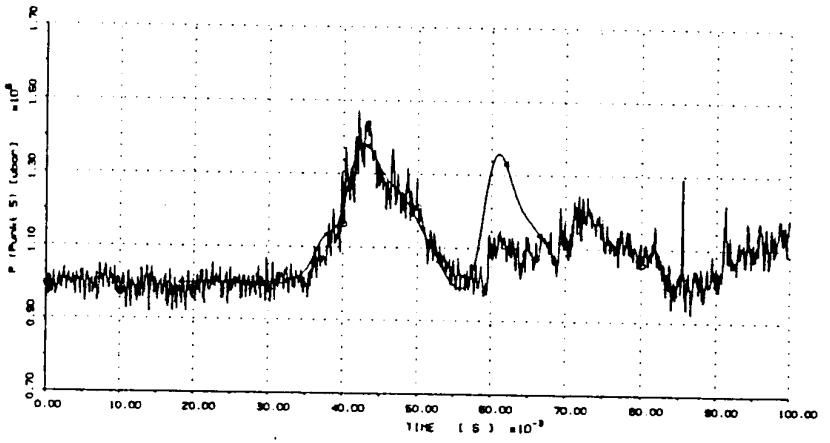

Abb. 14 Meßstelle 5: Drucktransienten aus Experiment und Simulation

4. Transienten an den Meßpunkten – Simulation und Experiment

Die Abbn. 10 bis 14 geben Druck-Transienten an den Orten der im Experiment installierten Meßaufnehmer sowohl aus der Messung als auch aus der Simulation wieder. Die Transienten der Simulation enden bei 66 ms und werden durch die "glatten" Kurven wiedergegeben. Die Kurven der Meßergebnisse entstanden aus jeweils ca. 32000 Meßwerten über der dargestellten Zeitspanne, die wegen der hier begrenzten Auflösung durch Mittelung auf je etwa 1500 Werte reduziert werden mußten.

Zur phänomenologischen Interpretation der einzelnen Druckverläufe können die Impulsverteilungen der Abbn. 7 bis 9 herangezogen werden.

Am Ort des Meßpunktes 1 ist lediglich eine Druckspitze von ca. 2.9 bar (bzw. 1.9 bar Überdruck) zu beobachten. Der Meßaufnehmer erfuhr frühzeitig erhebliche Störungen und fiel nach ca. 25 ms gänzlich aus.

Am Meßpunkt 2 sind die primäre Stoßwelle sowie die Reflexion von der Torwand zu unterscheiden. Dies ist ein Punkt, an dem auch das Flugzeug stehen würde. Eine Reflexion an der in der Simulation zu nahe stehenden Torwand bewirkt die frühe und hohe zweite Druckspitze des Simulationsergebnisses.

Solche verfrühten Reflexionen in der Simulation als Auswirkung der zu dicht angenommenen Torwand sind auch in den Transienten der Meßpunkte 3, 4 und 5 zu beobachten.

Die übrigen Meßpunkte zeigen deutlich die unterschiedlichen Reflexionen, wie sie aus den Impulsverteilungen (Abbn. 8 und 9) herauszulesen sind. Beispielsweise treffen am Meßpunkt 4 (Abb. 13) nacheinander die direkte Stoßwelle (t~43 ms), die Reflexion von der Decke (t~48 ms, vgl. Abb. 9), sowie die Reflexion von der Seitenwand ein (t~52 ms, vgl. Abb. 9). In der Druckspitze der Simulation bei t~62 ms am gleichen Meßpunkt überlagern sich die "echte" Reflexion aus der Ecke zwischen Seitenwand und Torwand und die verfrühte Reflexion von der Torwand.

5. Zusammenfassende Bewertung

Die Ergebnisse aus Experiment und Simulation können unter Berücksichtigung der durch die unterschiedliche Torwand verursachten Abweichungen als konsistent angesehen werden. Die Simulation vermittelt darüberhinaus mit Hilfe der freizügig wählbaren Darstellungen des Strömungsgebietes ein vertieftes Verständnis der gesamten Entwicklung der physikalischen Phänomene in ihrer Abhängigkeit von der geometrischen Konstellation. Daran anschließend gestatten weitere Simulationen die einfache und konsistente Analyse von Änderungen in den Randbedingungen, wie z.B. bauliche Modifikationen oder geänderte Bedrohung.

6. Literatur

[1] Pfrang W., Poth A., Schittke H.-J.
The Program Family DYSMAS
IABG-Bericht B-TF-V197/2, 1986

Kurzdarstellung ausgewählter APC-Rechenprogramme zur Ermittlung von Waffenwirkungsparametern und zum Standsicherheitsnachweis von Baustrukturen gegen Wirkungskomponenten

Ronald R. Kaufmann

Amt für Studien und Übungen
der Bundeswehr
Bereich Sonderaufgaben-Infrastruktur

Einleitung

Arbeitsplatzrechner (APC) sind in den letzten Jahren immer leistungsfähiger geworden und damit ein sehr gut nutzbares Werkzeug für schnelle und kostengünstige Berechnungen auch komplizierterer Vorgänge. Beim Fehlen von Anwendersoftware zum Lösen spezieller Einzelfälle kann hierfür ein Rechenprogramm unmittelbar am Arbeitsplatz erstellt und angewendet werden. Schnittstellenprogramme erweitern die Einsatzmöglichkeit des APC und erlauben beispielsweise gezielte eigene Auswertungen von Fremddaten oder die Beurteilung der Sicherheit von Bauwerken gegen Waffenwirkung, deren Entwurf von anderer Stelle übernommen, nach Überprüfung auf Waffenwirkungserfordernisse ggfs. verändert und dann zur weiteren Planung zurückübertragen wird.

Amt für Studien und Übungen der Bundeswehr - Bereich Sonderaufgaben-Infrastruktur - hat auf der Grundlage von Angaben in der Literatur, von Versuchsergebnissen und von fertigen Teilprogrammen APC-ablauffähige Rechenprogramme zur Ermittlung von Waffenwirkungsparametern nach Detonation konventioneller Waffen und zum Standsicherheitsnachweis von Baustrukturen gegen diese Wirkungskomponenten erarbeitet bzw. überarbeitet. Die Programme sind überwiegend in FORTRAN geschrieben. Nachfolgend erläutere ich kurz drei Programmfamilien aus den Bereichen Penetration von Projektilen, Luftstoßparametern in Stollensystemen und dynamische Plattenbemessung.

Penetration / Perforation von Projektilen

Die Programmfamilie zur Berechnung der Penetration von Projektilen besteht aus 3 Einzelprogrammteilen.

PERF berechnet das Eindringen von starren Projektilen in Stahlbetonziele. Wesentliche Waffenparameter sind Masse, Waffendurchmesser, Länge der Waffenspitze, Form der Spitze (Ogive, Halbkugel, Konus oder stumpf), Auftreffgeschwindigkeit und Auftreffwinkel. Beim Zielmaterial werden in die Rechnung für den Beton Festigkeit, Dichte, Durchmesser des maximalen Zuschlagkorns und der angenommene Winkel eines auf der Rückseite auftretenden Bruchkegels einbezogen; beim Stahl wird die Zugfestigkeit und der von einem

Bruchkegel geschnittene Bewehrungsprozentsatz berücksichtigt. Im Verfahren wird grundsätzlich ein üblich bewehrtes Betonbauteil unterstellt.

Die Perforationsberechnung erfolgt numerisch in zwei Teilen. Zunächst wird die Penetration des Projektils im Stahlbeton nach Bernard bestimmt. Einzelheiten hierzu können der Literatur (1) und (2) entnommen werden. Danach erfolgt die Berechnung der Bruchkegelhöhen eines endlichen Stahlbetonbauteils nach Herzog (Lit. 3). Diese Höhen ergeben sich aus der Interaktion zwischen Auftreffgeschwindigkeit und Festigkeit des Zielmaterials einschließlich der Bewehrungsanteile unter Einbeziehung der Projektilkopfgeometrie, der hieraus resultierenden Projektilverzögerung und somit der auftretenden Wirkkräfte. Bild 1 zeigt die Prinzipdarstellung während des Penetrationsvorganges. Der wirksame Nasenfaktor NSF als zusätzliche, die Penetration beeinflussende Größe wird in jedem Zeitschritt neu bestimmt. Für jeden Penetrationszeitschritt wird die optimale Kegelhöhe gerechnet. Das ist die Höhe, die bei jedem Zeitschritt den größten Wert unter Gegenüberstellung von wirkender Stoßkraft und Materialhaltevermögen im betrachteten Schnitt ausmacht. Aus den maximalen Werten der jeweiligen Penetrationsphasen errechnet sich dann unter Berücksichtigung des Auftreffwinkels die maximale Penetrationsdicke, die zum Schutz erforderlich ist. Mögliches Projektilabprallen bei schrägem Auftreffen wird untersucht. In Bild 2 sind Perforations- und Penetrationsweg sowie der Stoßkraftverlauf beispielhaft für ein auf eine Stahlbetonplatte mit definierter Geschwindigkeit auftreffendes großkalibriges Projektil dargestellt. Das Rechenergebnis ist in guter Übereinstimmung mit Ergebnissen aus Versuchen.

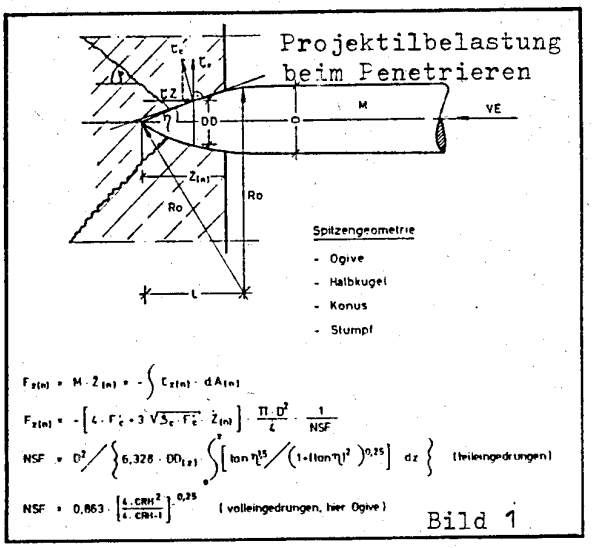

Bild 1

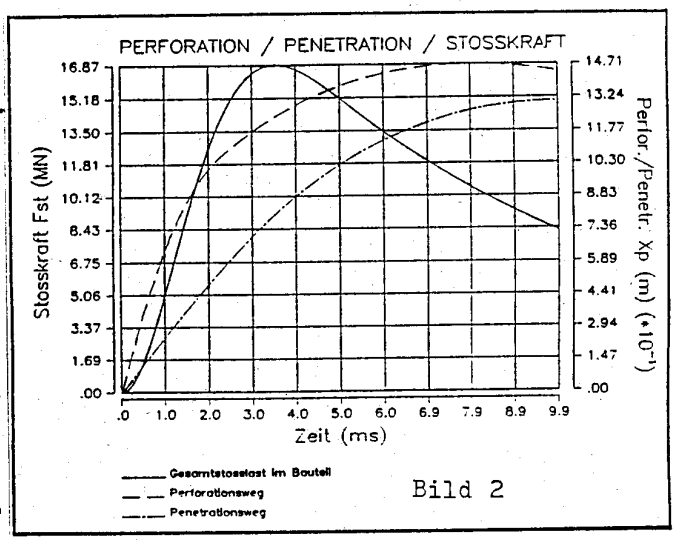

Bild 2

Das Folgeprogramm BERST prüft, ob während des Penetrationsvorganges zu irgendwelchen Zeitschritten die Materialfestigkeit der Projektilhülle auf Grund der auftretenden Verzögerungskräfte überschritten wird. Die hierzu erforderlichen Rechengrößen werden aus den Ergebnissen der Penetrationsberechnung mit PERF übernommen. Sie werden ergänzt durch Einzelangaben zu Geome-

trie, Festigkeiten und Massen sowohl der Projektilhülle als auch des Sprengstoffes. Die hüllenaussteifende Wirkung des Sprengstoffes über Reibungverbund wird im Programm berücksichtigt.

In Bild 3 sind einige die Rechnung bestimmende Größen angegeben, auf Einzelheiten soll hier nicht näher eingegangen werden. Untersucht wird jeweils der Projektilschnitt am Betonrand. An dieser Stelle werden die dort wirksamen Stoßkräfte den Materialwiderstandskräften gegenübergestellt.

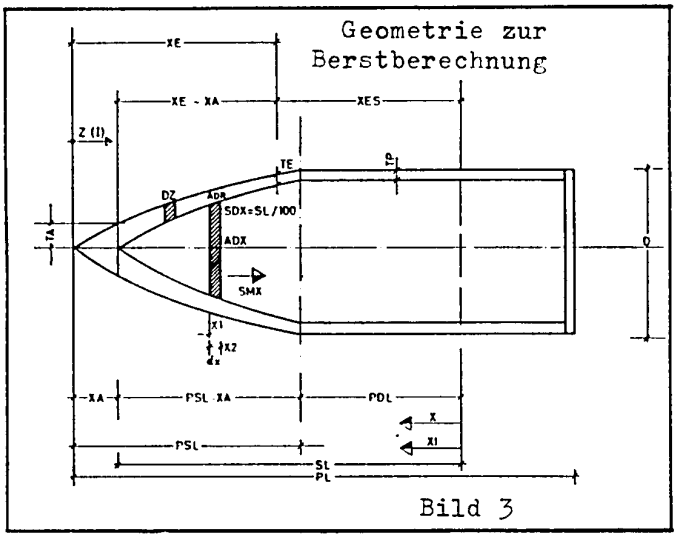

Bild 3

Die graphische Ergebnisdarstellung gibt die auftretende Gesamtstoßlast aus der Rechnung mit PERF an (Bild 4) und zeigt die Gegenüberstellung der wirksamen Stoßkräfte mit dem Berstlastvermögen des Projektils. Bei sonst unveränderten Ausgangswerten wurden im Beispiel zwei verschiedene Materialfestigkeiten des Projektils untersucht. Die Festigkeit von Material 2 lag ca. 40% über derjenigen von Material 1. Im Überschneidungsbereich dieser Berstlastkurve mit der wirksamen Stoßlast tritt Projektilhüllenversagen auf.

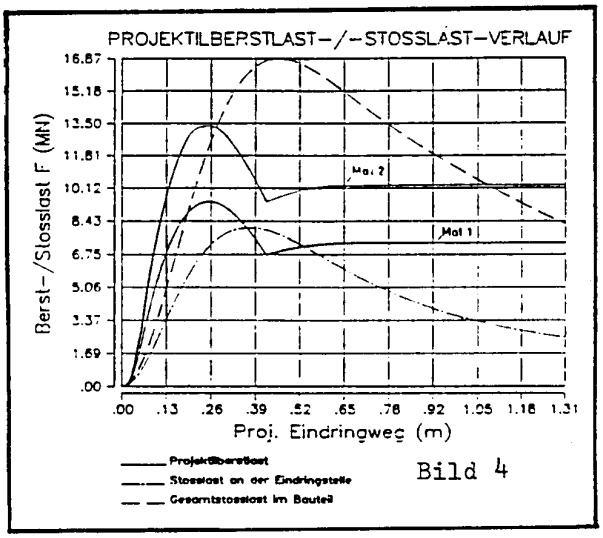

Bild 4

Zur Berechnung der Penetration in andere Medien steht ein weiterer Programmteil zur Verfügung. PEN berechnet die Penetration von starren Projektilen in Beton oder Fels oder Boden ebenfalls numerisch nach Bernard ergänzt durch Ergebnisse aus Berechnungen mit Hilfe der in der Literatur gebräuchlichen empirischen Penetrationsformeln. Geschichtete Ziele können durch iterativen Ansatz berücksichtigt werden, mögliches Projektilabprallen bei schrägem Auftreffen wird ebenfalls untersucht. In einem anderen Programmteil kann das Eindringen in Stahlplatten bzw. in Schichtziele aus Stahl und Beton berechnet werden.

Luftstoßparameter in Stollen

Zur Ermittlung aller Parameter von Luftstößen, die nach Detonation von konventionellen Ladungen im Eingangsbereich von Stollen entstehen und sich in das Stolleninnere fortpflanzen, sind im Auftrag unseres Amtes vom Ernst-Mach-Institut Versuche durchgeführt, Gesetzmäßigkeiten erarbeitet und diese in Programmform um-

gesetzt worden. In der Literatur war bislang für Stollensysteme nur das reine Druckverhalten als maßgebende Größe bei langandauernden Druckstößen beschrieben ohne Angaben zu Impuls und Wirkdauer, die im konventionellen Lastfall ebenfalls wesentliche Größen darstellen.

EMI hat bisher gerade offene und geschlossene Stollen, solche mit Abzweigungen und Stollen mit bestimmten Expansionskammersystemen untersucht. Letztere Arbeiten sind noch nicht abgeschlossen. Die mathematische Umsetzung der Versuchsergebnisse und die gefundenen Zusammenhänge sollen hier nicht vorgetragen werden. Hierzu verweise ich auf den Vortrag von Dr. Scheklinski-Glück anläßlich des letzten Symposiums in Panama City Beach, April 1989 (Lit. 5), den kürzlich von ihm gehaltenen Vortrag und Literatur (4) als Grundlage, worin die Verifizierung von Verfahren / Versuch aufgezeigt ist.

Das Programm LUSTO bietet die Möglichkeit, nach Näherungsformeln die Druckstoßverlaufsparameter an jedem definierten Ort in einem Stollensystem zu berechnen. Die Verlaufsform entspricht der Friedländerfunktion. Dies gilt auch bei zusammengesetzten Verläufen, z.B. bei der Überlagerung von einlaufender und reflektierter Welle bei geschlossenen Systemen für die jeweiligen Teilbereiche. Die Querschnittsform des Stollens hat auf das Verhalten der Stoßwelle keinen meßbaren Einfluß. Die Querschnittsfläche des Abzweigstollens kann zwischen dem 0.5-fachen bis 1.5-fachen des Hauptstollenquerschnitts liegen, ohne das Ergebnis zu verändern. Gültigkeitsbereiche sind angegeben und müssen eingehalten werden. Hinter dem Ort einer Abzweigung wird prinzipiell mit den gleichen Formeln weitergerechnet wie für einen einfachen Stollen. Eine Modifizierung besteht durch Einführung einer reduzierten Ladung. Die Reduktionsfaktoren sowie Hinweise und Beschreibungen für den Benutzer sind in das Programm eingearbeitet.

Mit dem Programm EK können Luftstoßparameter in Stollen mit Expansionskammern auf der Grundlage eines Systems von empirischen Näherungsformeln ermittelt werden. Die Parameter können an jedem Ort eines gegebenen Stollen-/Kammersystems berechnet werden, wenn die Kammer in Form eines Kubus oder Quaders ausgebildet ist. Da die gewählten Versuchsbedingungen Voraussetzung für die ordnungsgemäße Anwendung des Verfahrens ist, müssen auch hier die angegebenen Gültigkeitsbereiche eingehalten werden.

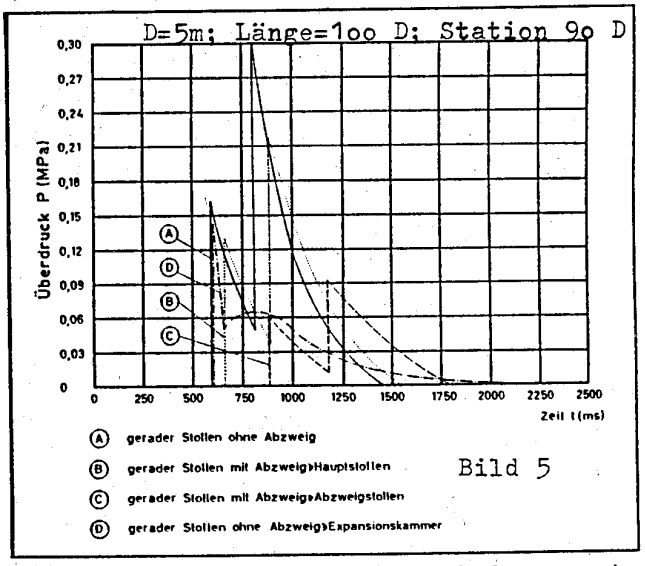

Bild 5

Der Druckstoß in der Kammer ist charakterisiert durch einen scharfen Spitzenverlauf dem ein nahezu parabelförmiger Druckaufbau folgt. Nach ca. 20% der gesamten positiven Druckdauer fällt dieser in Form der Friedländer-Funktion auf Umgebungsdruck ab. Eine Veränderung des

Kammervolumens hat gravierenden Einfluß auf Amplitude und zeitlichen Verlauf der Welle.

In Bild 5 ist als kleine Parameterstudie der Einfluß verschiedener Stollensysteme auf die Ergebnisse der Verlaufsformen dargestellt. In allen Fällen wurden geschlossene Systeme bei unveränderten Größen wie Stollendurchmesser, Stollenlänge und Ladungsmenge berechnet. Der im Beispiel betrachtete Ort liegt kurz vor dem Stollenende, so daß die Amplitude der rücklaufenden, reflektierten Welle in den Fälle A, B und C deutlich über derjenigen der einlaufenden Welle liegt. Kurve D zeigt den typischen Verlauf in der Expansionskammer.

Die so ermittelten Druckverläufe können als unmittelbare Belastungsgrößen für Bemessung von Bauteilen und zur Beurteilung der Wirksamkeit von Druckabschlüssen in Stollen- und Luftführungssystemen dienen.

Plattenbemessung

Als Instrument zur dynamische Bemessung von Platten (Lit. 6,9) nach der Methode der finiten Differenzen bei Detonation von Waffen inner- und oberhalb des Bodens möchte ich als dritte Programmfamilie die Programme PLALUF und PLABOD vorstellen.

Die Lösungsgleichung des Differenzenverfahrens soll im Bild 6 nur noch einmal in Erinnerung gerufen werden. Auf Einzelheiten zum Differenzenverfahren selbst möchte ich hier nicht eingehen zumal ausreichende Ansätze in der Literatur (z.B. Lit. 7) vorhanden sind. Die aufgezeigte Gleichung ist durch Einsetzen und Umformen so für das Programm aufbereitet (Lit. 8), daß die Bewegungsgrößen mit den örtlichen Momenten, der Masse und der zeitlich abhängigen Last gekoppelt berechnet werden. Aus den Bewegungen werden die Krümmungen bestimmt und in Verbindung mit den Steifigkeiten wiederum die Momente ermittelt. Dies geschieht für den ungerissenen (Zustand I) und den gerissenen (Zustand II) Querschnitt bis in den plastischen Bereich hinein. Neben den orthogonalen Momenten werden bei der Verformungsberechnung im ungerissenen Zustand die Drillmomente mit einbezogen.

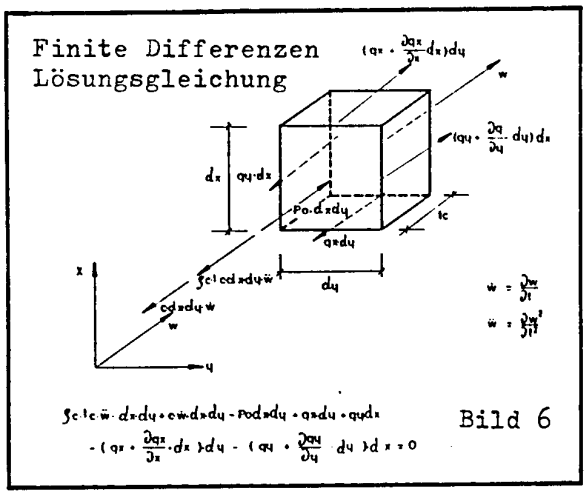

Bild 6

Bei der Formulierung des Programms sind zur Vereinfachung aber auch zur Behandlung von projektbezogenen Besonderheiten einige Vereinbarungen wie folgt getroffen worden

- es werden Rechteckplatten betrachtet, bei anderen Plattenformen müssen auf die Hauptmomente bezogene Umformulierungen erfolgen
- Knoten auf Auflagerrändern haben in z-Richtung die Verschiebung w = 0

- als Randbedingungen können beliebig gewählt werden
  + eingespannt
  + aufliegend frei drehbar
  + freier, ungestützter Rand
- die Bewehrungsnetze oben und unten sind orthotrop, jedoch homogen
- die statische Höhe wird in den Richtungen getrennt, jedoch oben und unten gleich angesetzt
- der Plattenteiler ist in den Richtungen x und y gleich
- die Interaktion Gesamtbauwerk - Platte wird vernachlässigt, da im konventionellen Lastfall die örtliche Wirkung maßgebend, die Gesamtmasse Bauwerk allgemein >> der Plattenmasse ist und somit in der Regel nur ein geringfügig günstigeres Plattenverhalten auftreten kann. Ergebnisse sind damit konservativ.

Die auf Grund der Vereinfachungen auftretende Fehlergröße liegt im Rahmen der Ungenauigkeiten, die sich z.B. aus den angenommenen Festigkeiten, dem Medium Boden und den Lastansätzen ergeben.

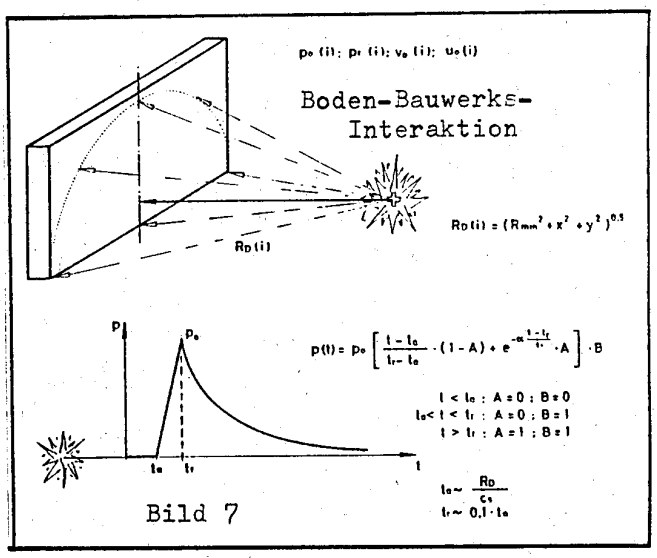

Bild 7

Die notwendigen Eingabedaten zum Programmablauf brauchen nicht gesondert aufbereitet zu werden, sondern können den Bauunterlagen unmittelbar entnommen und nach Menü eingegeben werden. Die Eingabe der Lastannahmen kann ebenfalls recht einfach erfolgen. Sowohl bei Detonation im Boden (Lit. 13) als auch auf dem Boden oder in der Luft (Lit. 10, 11) ist die Angabe des Detonationsortes in seiner Lage zur Platte sowie die Ladungsgröße ausreichend. Bei oberirdischen Detonationen kann dabei noch zwischen verschiedenen Ladungsformen (Lit. 12) unterschieden werden. Für jeden Knoten werden individuell alle Lastgrößen (Bild 7) unter Berücksichtigung von Reflektion, Winkeleinfluß, Randeinfluß etc. programmintern ermittelt. Als Option können extern Druck-Zeit-Verläufe als Belastung in Form von Stützstellen- oder Friedländerfunktionen auf Einzelknoten oder Knotenfelder bezogen eingegeben werden.

Boden-Bauwerks-Interaktion

Freefield

$$p_o = f \cdot \varrho_s \cdot c_s \cdot 48{,}77 \cdot (0{,}4)^n \cdot \left(\frac{R_D}{W^{\frac{1}{3}}}\right)^{-n} \quad [N/m^2]$$

$$v_o = \frac{p_o}{\varrho_s \cdot c_s} \quad [m/s]$$

$$v(t) = v_o \left\{ \frac{t - t_a}{t_r - t_a} \cdot \left[1 - A\right] + \left[1 - \frac{\beta (t - t_r)}{t_+}\right] \cdot e^{-\beta \frac{t - t_r}{t_r}} \cdot A \right\} \cdot B$$

$$u(t) = \frac{1}{2} \cdot \frac{p_o}{\varrho_s c_s} \cdot \left[\frac{(t - t_a)^2}{t_r - t_a} (1 - A) + (t_r - t_a) \cdot A + 2 \cdot (t - t_r) \cdot e^{-\beta \frac{t - t_r}{t_r}} \cdot A \right] \cdot B$$

Reflection Pressure

$$p_r = p_o + \varrho_s \cdot c_s \cdot v_o + \frac{\varrho_s \cdot c_s^2}{2 R_D} \cdot u_o$$

$$p_{r\perp} = p_r \cdot (\cos^2 \alpha + \lambda_s \cdot \sin^2 \alpha) \quad \text{where} \quad \cos^2 \alpha = \left(\frac{R_{min}}{R_D}\right)^2 ; \; \sin^2 \alpha = \left[1 - \left(\frac{R_{min}}{R_D}\right)^2\right] ; \quad \lambda_s = \frac{\nu_s}{1 - \nu_s}$$

Interaction Pressure

$$p = p_{r\perp} - \varrho_s \cdot c_s \cdot \frac{\delta w}{\delta t} - \frac{\varrho_s \cdot c_s^2}{2 R_D} \cdot w$$

Bild 8

Der formelmäßige Ansatz bei Detonation im Boden ist im Bild 8

wiedergegeben. Der Interaktion Bauteil - Boden wird im letzten Gleichungsansatz Rechnung getragen, in dem die aktive Last Pr mit der Bauteilbewegung über die Anteile Geschwindigkeit und Verschiebung gekoppelt wird.

Berechnet und ausgegeben werden die Bewegungsgrößen, die Momente, die Krümmungen (als wesentliches Maß für die Beurteilung der Biegebeanspruchung) und die Querkräfte (als Maß für die Schubbemessung). Für Verlaufsplots, Schockberechnungen und Darstellung der Netzverformung werden die erforderlichen Größen wie üblich abgespeichert und mit anderen Programmen separat weiterverarbeitet.

Unter Berücksichtigung einfacher Strukturen zeigten die Ergebnisse aus Rechnungen dieser Programme, aus solchen mit Programmen nach der Methode der finiten Elemente und aus Versuchen recht gute Übereinstimmung. Dies ist besonders bei einem Vergleich der Schockreaktionsspektren festzustellen.

Zusammenfassung

Die Präsentation sollte kurz anreißen, daß unter dem Aspekt der praxisbezogenen Anwendung von Rechenprogrammen viele Problemfelder der Waffenwirkung kostengünstig mit Hilfe des APC gelöst werden können. In den meisten Fällen ist besonders in Hinblick auf die Wirkung konventioneller Waffen auf Bauwerke die Untersuchung eines komplexen Bauwerks nicht notwendig, da es in der Regel nur zu örtlichen Beanspruchungen kommt. Die Genauigkeit leidet durch Einführung von Vereinfachungen allgemein ebenfalls nicht, da viele Eingangsparameter bereits nur Abschätzungen sein können und deshalb ein genaueres Verfahren das Ergebnis naturgemäß nicht verbessern kann.

Programme wie dargestellt können ebenfalls rasch veränderten Problemsituationen angepaßt werden, so daß sie zu einem flexiblen Instrument bei der Lösung von Waffenwirkungsberechnungen werden. Dabei ist es sehr hilfreich, relativ kurze, übersichtliche Programme mit gemeinsamen Bausteinen zu nutzen.

Literatur

(1) Bernard, R.S., Creighton, D.C., Projectile Penetration in Soil and Rock: Analysis for Non-normal Impact, USAEWES, TR-SL-79-15, Dec 1979

(2) Bernard, R.S., Depth and Motion Prediction for Earth Penetrators, USAEWES, TR-S-78-4, June 1978

(3) Herzog, M., Durchstanzen der Abschirmkuppel eines Reaktorgebäudes bei Flugzeugaufprall, Bauingenieur 53, 1978

(4) Gürke, G., Scheklinski-Glück, G., Mehlin, H.P., Ein Rechenverfahren zur Ermittlung von Luftstoßparametern in ...(geraden und rechtwinklig verzweigten)... Stollen ...(mit Expansionskammern)... bei der Detonation von Explosivstoffladungen im Eingangsquerschnitt / Stolleneingang, Ernst-Mach-Institut, Freiburg, E9/83, E6/86, E1/88, E19/89

(5) Scheklinski-Glück, G., Scale Model Tests to Determine Blast Parameters in Tunnels and Expansion Rooms from HE-Charges in the Tunnel Entrance, Proceedings of the Fourth International Symposium on the Interaction of Non-Nuclear Munitions with Structures, Panama City Beach, Fl., Apr. 89

(6) Timoshenko, S.P., Woinowsky-Krieger, S., Theory of Plates and Shells, 2nd Edition, McGraw-Hill Book Company, London, 23rd Printing 1982

(7) Ghali, A., Nevill, A.M., Structural Analysis, A Unified Classical and Matrix Approach, Chapman and Hall, London,1978

(8) Fricke, K.-L., Dynamische Beanspruchung einer Stahlbetonrechteckplatte, elasto-plastische Analyse, Konstruktiv Sozietät Dr.-Ing. K.-L. Fricke, Hannover, Sept. 1982

(9) Biggs, J.M., Introduction to Structural Dynamics, McGraw-Hill Book Company, New York, 1964

(10) Kingery, C.N., Coulter, G.A., Reflected Overpressure Impulse on a Finite Structure, Technical Report ARBRL-TR-02537, Ballistic Research Laboratory, Aberdeen, Md., Dec 1983

(11) Kingery, C.N., Bulmash, G., Airblast Parameters from TNT Spherical Airburst and Hemispherical Surfaceburst, Technical Report ARBRL-TR-0255, Ballistic Research Laboratory, Aberdeen, Md, April 1984

(12) Gürke, G., Scheklinski-Glück, G., mehrere Berichte über die Untersuchung der Blastparameter nach Detonation von Explosivstoffzylindern, Ernst-Mach-Institut, Freiburg, E6/82, V2/84, E12/85, E15/85, E16/85, E17/85, E18/85

(13) TM 5-855-1, Fundamentals of Protective Design for Conventional Weapons, HQ Department of the Army, Washington, D.C., Nov 1986

ABSTRACT

SURVIVABILITY ASSESSMENT METHODOLOGY

by: Capt. Diane Miller — Air Force Engineering and Services Center
Mr. William L. Hacker — Applied Research Associates, Inc.

The Effectiveness/Vulnerability Assessment in Three Dimensions (EVA-3D) computer code, which has been predominantly a blue on red analysis tool, has been upgraded to perform survivability assessments of domestic air base structures. The upgrades include the capability to model generalized shapes and above ground targets, as well as new concrete breach algorithms. These modifications are presented along with the practical application of the code to two air base facilities.

DYNA/NIKE Modeling of Shock Wave Interactions and High Explosive Effects on a Personal Computer

Michael J. Murphy
Hydrosoft International
1595 Cross Creek Place
Livermore, CA 94550

PC-based implementations of DYNA2D/DYNA3D and NIKE2D/NIKE3D are now being used to model problems previously relegated to mainframe and/or large mini-computers. A comprehensive conversion of the entire source code allows for running the same problems on the PC that were formerly run on the CRAY, VAX, or SUN. For example, a 16 Mbyte portable 486 system with VGA graphics and 200 Mbyte hard disk (currently avaiable in the US for less than $7000) can run a 48,000 element DYNA2D or DYNA3D problem at speeds that are 7 times faster than the VAX 11-780. Pre- and post-processing of the analysis using high resolution (800 x 600) color grahics monitors is as good or better than on the mainframe. High resolution (300 DPI) grey scale or color postscript files can be created and sent to HP or other compatible laser printers. Computational throughput for a 80486/33 MHz PC system is the same as for the latest generation SUN and DEC workstations while being about an order of magnitude less than for a typical timeshared CRAY. Benchmark comparisons for several computer systems are summarized in Table 1.

The paper will describe the modeling results of several example problems including a shaped charge, EFP, Taylor test, split hopkinson bar, and shock initiation of a High Explosive. A comparison of CPU times, "throughput" times, and modeling accuracy will be presented for several computer systems including the CRAY, SUN, DEC, and PC's.

COMPUTER	DP LINPACK	11-780 VAX MIPS
VAX 11-780	0.14	1.0
386/387-16MHz	0.16	1.1
386/387-20MHz	0.20	1.4
VAX 11-785	0.21	1.5
386/387-25MHz	0.26	1.9
SUN 3/160 w/FPA	0.41	2.9
386/387-33MHz	0.43	3.1
VAX 8600	0.49	3.5
VAX 8650	0.70	5.0
SUN 4/110	0.86	6.1
DECstation 2100	0.95	6.8
486-25 MHz	0.98	7.0
SUN SPARC-1	1.36	9.1
DECstation 3100	1.36	9.7
486-33 MHz (NCR)	1.44	10.3
CRAY 1S CFT	12.00	85.7

Table 1. Double precision LINPAC and VAX 11-780 MIPS Benchmarks

* Work performed under the auspices of the U.S. Department of Energy by the Lawrence Livermore National Laboratory under contract No. W-7405-ENG-48.

INBLAST--A New and Revised Computer Code for the Prediction of Blast Inside Closed or Vented Structures

Michael M. Swisdak, Jr.
Paul E. Montanaro
Naval Surface Warfare Center
10901 New Hampshire Avenue
Silver Spring, MD 20903-5000
301-394-1186

ABSTRACT

The computer code INBLAS was developed and published in the early 1970's to describe the blast produced by the reaction of energetic materials inside closed or partially vented structures. Since then, refinements have been made to several of the code algorithms. These changes have been collected into a new version of the code called INBLAST. This version is designed to run on a desk top personal computer. The code is briefly described. Sample problems (with emphasis on time-dependent burning) are presented and some results are compared with experimental data.

BACKGROUND

In 1972, Proctor[1] published the first version of a computer code designed to describe the phenomena associated energetic reactions inside closed structures. Since that original publication, many of the basic algorithms and concepts contained within the code have been improved and/or expanded and have become widely used in later versions of the same code or incorporated into other codes. In 1976, Ward and Lorenz of the Naval Surface Weapons Center (NSWC) developed a module for the program that allowed the use of time-dependent burning of the energetic material (rather than detonation). Other sections have become obsolete or superceded as new technology or information has become available. The best example of the latter are the sections of the code dealing with shock wave reflections within the chamber and the accompanying loading on the chamber walls. Waterways Experiment Station (WES) and their contractor Applied Research Associates (ARA) replaced the original shock calculations in INBLAS with more accurate shock reflection and superposition algorithms to form the BLASTINW code in the early 1980's[2,3,4].

The original code was designed and written to run on a main-frame computer. With the proliferation of both versions of the computer code and of desk top computers, the Department of Defense Explosives Safety Board (DDESB) deemed desirable to both update the original code and to produce a version which would run on a personal computer. This updated code could then become a benchmark against which future versions or variations of the code could be compared.

To accomplish this task, it was felt that the "best parts" of both the INBLAS code and the BLASTINW code should be combined and a new and improved code produced. This effort was undertaken by the Boeing Military Airplane Company (Mr. Richard Lorenz) under contract to the Naval Surface Warfare Center (NAVSWC). This task was accomplished in 1989. At that time, however, it was felt that the program was still not "user friendly." NAVSWC then began the task of developing an input module which, through a series of interactive screens, generates, runs, and displays the output of the INBLAST program.

DESCRIPTION OF THE CONFINED EXPLOSION GAS PRESSURE CALCULATION

The chemical reaction of the explosion/burning and mixing with the air in the closed structure creates the combustion products Al_2O_3, H_2O, CO, CO_2, C, Al, H_2, O_2, and N_2. A priority in the reaction is assumed as follows: (1) The aluminum in the energetic material reacts with oxygen to form the solid Al_2O_3; if there is insufficient oxygen, the remaining Al is treated as a solid. (2) The hydrogen has the next priority on the oxygen to form H_2O; again for insufficient oxygen, the remaining hydrogen is treated as H_2. (3) If there is an overabundance of oxygen in the energetic material and structure air, complete combustion occurs such that all carbon appears as CO_2 and the remaining oxygen not needed in any of the reactions appears as O_2. (4) If there is insufficient oxygen in the system after the Al_2O_3 and H_2O reactions, then CO and CO_2 are produced in quantities given by the following equations:

$$n(C) + m(O) \rightarrow a(CO) + b(CO_2) \qquad \text{for } m>n$$

$$a + b = n \qquad a = 2n - m$$

or

$$a + 2b = m \qquad b = m - n$$

where

- a = number of moles of CO produced
- b = number of moles of CO_2 produced
- n = number of moles of C
- m = number of remaining moles of O

and no O_2 exists in the final combustion products. (5) In the above equations, if $m<n$, no CO_2 will be formed or if $b = 0$, then CO is produced such that $a=m$ and solid carbon particles will appear in the combustion products in the amount n-m. (6) The nitrogen does not participate in the reaction and appears as N_2 in the final mixture. From the above calculations, the number of moles of component gases and solids that make up the final products in the closed structure can be calculated. Once these are known, the final pressure and temperature within the chamber can be calculated.

The following information is required to perform an INBLAST quasi-static pressure calculation:

(1) C-H-N-O content of the energetic material (already in program for many materials)
(2) Heat of formation of the energetic material (already in program for many materials)
(3) Weight of energetic material
(4) Volume of initial chamber
(5) Vent area of exit from initial chamber
(6) Volume of secondary chamber
(7) Vent area of exit from secondary chamber
(8) Ambient pressure and temperature

The time-dependent, volume burn module requires the following information in addition to the standard data required to run INBLAST:

(1) A table of pressure versus material consumption rate (determined from the burn rate parameters and the material density).
(2) A table of total burning area versus weight of material consumed.

With this information, pressure-time profiles in all chambers can be generated by the program.

The program allows for multiple chambers with energetic events possible in any of them. Each chamber may be vented to any other chamber or to an ambient reservoir. The equations governing the flow between the chambers are the appropriate ones for both supersonic and subsonic flow through a perfect nozzle. The ratio of the specific heats, γ, is not taken as a constant of 1.4--rather it is allowed to assume an appropriate value determined by the pressure, volume, temperature and mix of constituents of the gases exiting the chamber.

CODE DESCRIPTION & HARDWARE REQUIREMENTS

The program uses techniques and algorithms developed for the LAMB (Low Altitude Multi-Burst) computer code to predict the direct and multiple reflected shockwaves present after a detonation inside a closed chamber. For a description of these techniques, the reader is referred to References 2 and 3. Currently, the program is limited to rectangular geometries. Current work includes modifications to the code to enable it to handle cylindrical symmetries. The code has built into it over fifty energetic materials and compounds. These are shown in Table 1. These can be used in any combination, or new materials may be used. The input to the code is set up through the use of interactive menus. To use a new material, its composition (C-H-N-O balance), heat of formation, and TNT equivalence must be known.

The program is designed to run on any IBM-compatible machine using DOS 3.1 operating system (or higher) with 640 kilobytes of memory and a hard disk. The program supports CGA, EGA, and VGA color monitors. An IBM-AT (or faster) machine with math co-processor is not necessary, but its presence signifcantly decreases running time.

The code was described in more detail at the most recent Department of Defense Explosives Safety Board Seminar held in St. Louis, Missouri[5].

COMPUTATIONAL RANGE

The original version of the program (INBLAS) was demonstrated to accurately predict the confined gas pressures as a function of loading density (charge weight divided by chamber volume) over several orders of magnitude in pressure. This has not changed. In fact, the range has been extended even further. This comparison is shown in Figure 1. The computation is for TNT and was performed with this latest version of the code.

SAMPLE PROBLEM

Consider a volume which contains M1 propellant. This material is allowed to undergo time-dependent burning. The reaction products are allowed to vent to other chambers. Determine the pressure-time histories in each of the chambers.

M1 is one of the materials which is already built into the program. Thus, the only additional information which will be needed is a description of the actual physical characteristics of the propellant grain itself. These are shown in the following table:

Number of perforations:	1
Grain length:	0.2237 inches (5.68 mm)
Grain Outside Diameter:	0.0499 inches (1.27 mm)
Perforation Diameter:	0.0185 inches (0.47 mm)
Density:	0.0567 lb/in^3 (1.569 g/cm^3)
Burn Rate Coefficient:	0.00161 in/s-psi
Burn Rate Exponent:	0.741

Figure 2 is a schematic of the test arrangement for these computations. Two propellant weights were considered: 0.95 pounds and 2.3 pounds. The initial volume (chamber 1) is 3.29 ft^3 (0.0932 m^3); the volume of the secondary chamber is 0.73 ft^3 (0.0208 m^3). The initial vent area is 0.02182 ft^2 (20.3 cm^2); the secondary vent to the atmosphere is 0.08727 ft^2 (81.1 cm^2). At time zero, the vents between the chambers are assumed to open.

The results for this problem are shown in Figures 3 and 4.

DISCUSSION OF RESULTS

Both figures exhibit similar features. They show a relative slow rise to a peak value (corresponding to the time at which all of the material has been consumed) followed by an essentially exponential decay caused by venting to the atmosphere.

There appears to be competing processes between the rate of venting and the rate of consumption. Since the rate of consumption is extremely pressure dependent, at low pressures not much material is consumed. If the vent area is too large, the chamber does not pressurize sufficiently to dramatically increase the burn rate. When this occurs, lower pressures are obtained.

The use of burning propellant has been successfully used in the United States to provide long duration loading to closed or partially vented structures. The technique provides a long duration loading without an accompanying shock loading. This allows an easier interpretation of the structure's behavior.

REFERENCES

1. Proctor, James F., "Internal Blast Damage Mechanisms Computer Program," NOL TR 72-231, 31 August 1972.

2. Britt, J.R. et. al., "BLASTINW User's Manual," ARA 5986-2, Applied Research Associates, Inc., Vicksburg, MS, April 1986.

3. Britt, J. R. and Drake, J. L., "Blast Loads from Internal Explosions and Other Reflected Shock Waves," International Symposium on the Interaction of Conventional Munitions with Protective Structures, 9-13 March 1987.

4. Nelson, D. H. and Watt, J. M., "Analysis of Internal Blast Loads in Vented Chambers," Minutes of the Twenty-Third Explosives Safety Seminar, Volume II, 9-11 August 1988.

5. Swisdak, Michael M., Jr. and Montanaro, Paul E., "INBLAST--A New and Revised Computer Code for the Prediction of Blast Inside Closed or Vented Structures," Minutes of the Twenty-Third Explosives Safety Seminar, 28-31 August 1991.

TABLE 1 TABLE OF EXPLOSIVES

NUMBER	NAME	EQWT	EFORM	C	H	N	O	Al
1	TNT	1.00	-70.50	0.3702	0.0222	0.1850	0.4227	0.0000
2	TNETB	1.13	-307.10	0.1860	0.0170	0.2170	0.5800	0.0000
3	EXPLOSIVE D	0.85	-382.00	0.2926	0.0246	0.2276	0.4551	0.0000
4	PENTOLITE (50/50 PETN/TNT)	1.40	-237.10	0.2798	0.0239	0.1807	0.5155	0.0000
5	PICRATOL (52/48 EXPL D/TNT)	0.90	-238.50	0.3290	0.0240	0.2070	0.4400	0.0000
6	CYCLOTOL (70/30)	1.14	26.22	0.2254	0.0257	0.3193	0.4294	0.0000
7	COMPOSITION B	1.10	11.48	0.2513	0.0264	0.2983	0.4241	0.0000
8	RDX/WAX (98/2)	1.19	57.00	0.1760	0.0300	0.3710	0.4230	0.0000
9	COMPOSITION A-3	1.09	28.40	0.2233	0.0375	0.3428	0.3964	0.0000
10	TNETB/Al (90/10)	1.23	-276.40	0.1680	0.0140	0.1960	0.5220	0.1000
11	TNETB/Al (78/22)	1.18	-239.50	0.1460	0.0120	0.1700	0.4520	0.2200
12	TNETB/Al (72/28)	1.18	-221.10	0.1340	0.0110	0.1570	0.4180	0.2800
13	TNETB/Al (65/35)	1.23	-199.60	0.1210	0.0100	0.1420	0.3770	0.3500
14	TRITONAL (TNT/Al 80/20)	1.07	-53.68	0.2960	0.0178	0.1480	0.3382	0.2000
15	RDX/Al/WAX (88/10/2)	1.30	50.38	0.1600	0.0270	0.3330	0.3800	0.1000
16	RDX/Al/WAX (78/20/2)	1.32	43.76	0.1440	0.0240	0.2950	0.3370	0.2000
17	RDX/Al/WAX (74/21/5)	1.30	29.36	0.1630	0.0270	0.2800	0.3200	0.2100
18	RDX/Al/WAX (74/22/4)	1.30	33.28	0.1540	0.0260	0.2800	0.3200	0.2200
19	RDX/Al/WAX (62/33/5)	1.19	21.42	0.1430	0.0240	0.2350	0.2680	0.3300
20	TORPEX II (42/40/18 RDX/TNT/Al)	1.24	-3.57	0.2161	0.0203	0.2328	0.3507	0.1800
21	H-6	1.38	-17.48	0.2230	0.0259	0.2238	0.3171	0.2100
22	HBX-1	1.17	-25.40	0.2482	0.0265	0.2216	0.3336	0.1700
23	HBX-3	1.14	-25.30	0.2003	0.0221	0.1709	0.2566	0.3500
24	TNETB/RDX/Al (39/26/35)	1.24	-102.60	0.1150	0.0130	0.1840	0.3380	0.3500
25	ALUMINUM	0.00	0.00					1.0000
26	WAX	0.00	-392.00	0.8560	0.1440	0.0000	0.0000	0.0000
27	RDX	1.10	66.16	0.1621	0.0272	0.3782	0.4322	0.0000
28	PETN	1.27	-407.10	0.1898	0.0255	0.1772	0.6074	0.0000
29	TETRYL	1.07	16.26	0.2928	0.0176	0.2439	0.4458	0.0000
30	HMX	1.10	61.00	0.1621	0.0272	0.3782	0.4322	0.0000
31	OCTOL (HMX/TNT 75/25)	1.10	28.62	0.2135	0.0260	0.3303	0.4302	0.0000
32	PBXW-9 (estimated)	1.30	72.40	0.2050	0.0340	0.3480	0.4130	0.0000
33	MOTOR OIL	0.00	-400.00	0.8470	0.1410	0.0000	0.0000	0.0000
34	POLYISOBUTYLENE	0.00	-840.00	0.8600	0.1400	0.0000	0.0000	0.0000
35	DI-SEBACATE	0.00	-780.00	0.7300	0.1200			
36	AMMONIUM NITRATE (AN)	0.70	-1084.00	0.0000	0.0504	0.3497	0.5998	0.0000
37	IREMITE-60	1.00	-999.50	0.0000	0.0462	0.3029	0.5499	0.0330
38	NITROMETHANE	1.00	-442.00	0.1966	0.0495	0.2295	0.5244	0.0000
39	PBX-9404	1.20	0.80	0.1705	0.0281	0.3650	0.4364	0.0000
40	POLYSTYRENE	0.00	181.70	0.9226	0.0774	0.0000	0.0000	0.0000
41	WATER	0.00	-3792.00	0.0000	0.1119	0.0000	0.8881	0.0000
42	ANFO (94/6 AN/FO)	0.87	-1043.40	0.0515	0.0558	0.3289	0.5638	0.0000
43	COMPOSITION C-4	1.40	32.43	0.2185	0.0357	0.3444	0.4014	0.0000
44	NITROCELLULOSE (NC)(12%N)	0.50	-658.00	0.2646	0.0278	0.1260	0.5816	0.0000
45	NITROCELLULOSE (NC)(13.35%N)	0.50	-574.00	0.2529	0.0252	0.1345	0.5874	0.0000
46	NITROCELLULOSE (NC)(14.14%N)	0.50	-525.00	0.2425	0.0237	0.1414	0.5924	0.0000
47	NITROGYLCERINE (NG)	1.80	-390.00	0.1585	0.0222	0.1850	0.6343	0.0000
48	TATB (Triaminitrinitrobenzene)	1.00	-142.70	0.2790	0.0234	0.3255	0.3720	0.0000
49	CYCLOTOL (75/25)	1.14	32.89	0.2141	0.0260	0.3299	0.4300	0.0000
50	M1 PROPELLANT	1.00	-539.00	0.3039	0.0309	0.1265	0.5387	0.0000
51	LX-14	1.80	15.00	0.1824	0.0294	0.3626	0.4256	0.0000
52	NITROGUANIDINE (NQ)	1.00	-212.00	0.1154	0.0387	0.5383	0.3076	0.0000
53	FUEL OIL (FO)	0.00	-406.70	0.8591	0.1409	0.0000	0.0000	0.0000

FIGURE 1 COMPARISON OF MEASURED QUASI-STATIC PRESSURE WITH INBLAST COMPUTATIONS

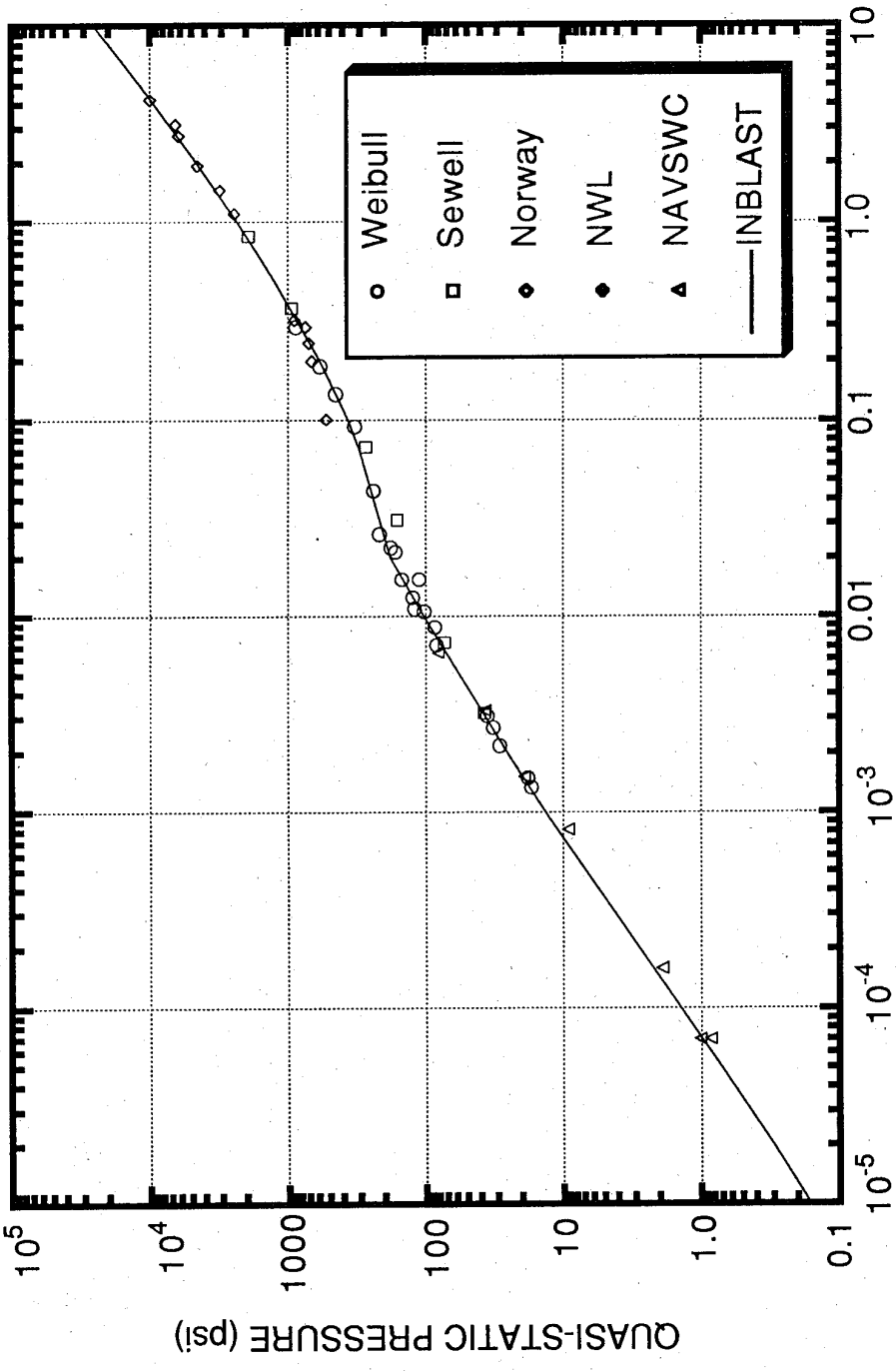

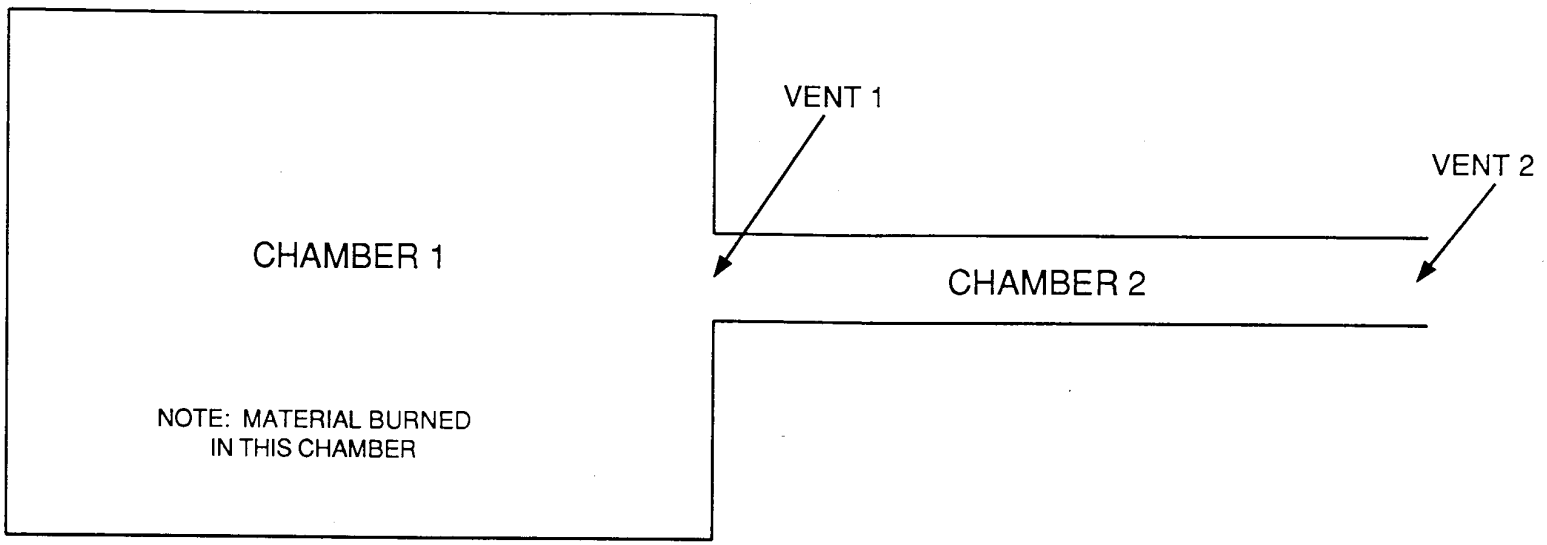

VOLUME OF CHAMBER 1: 3.29 CUBIC FEET
VOLUME OF CHAMBER 2: 0.73 CUBIC FEET
AREA OF VENT 1: 0.02182 SQUARE FEET
AREA OF VENT 2: 0.08727 SQUARE FEET

FIGURE 2 SCHEMATIC OF SAMPLE PROBLEM

FIGURE 3 TIME DEPENDENT BURNING OF 0.95 POUNDS OF M1 PROPELLANT

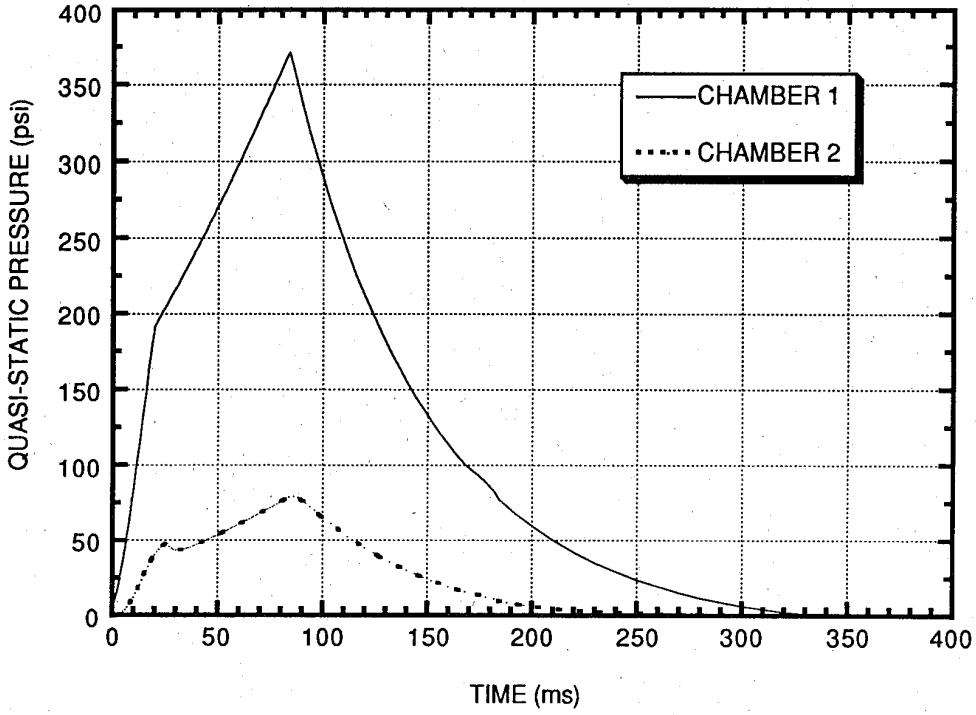

FIGURE 4 TIME DEPENDENT BURNING OF 2.3 POUNDS OF M1 PROPELLANT

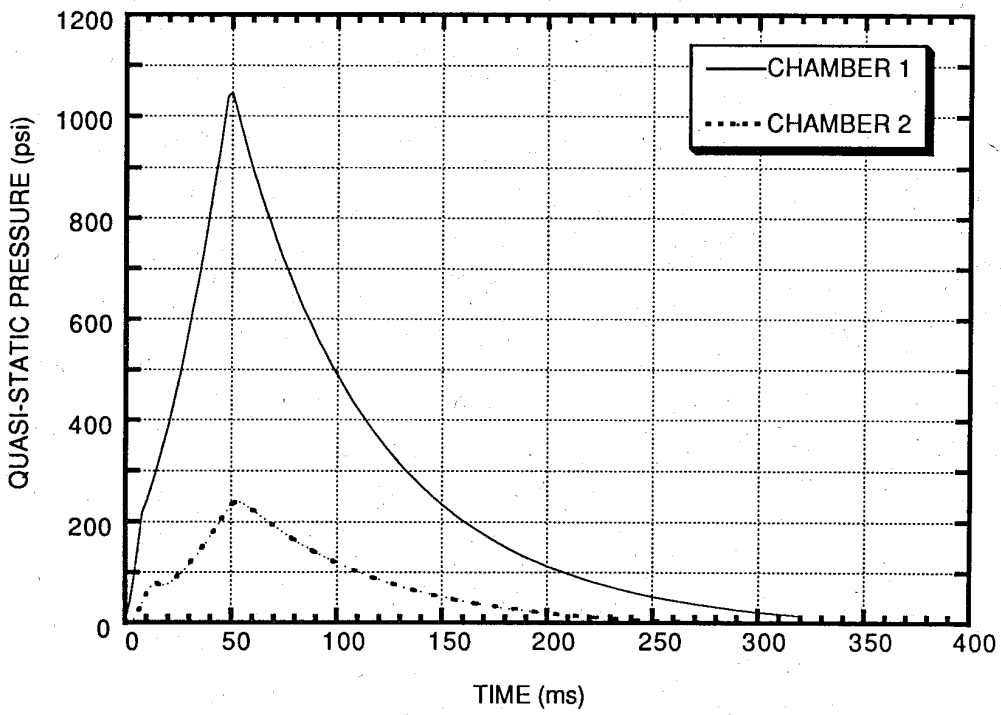

absichtlich
freigelassen

blank

A P.C. based program for blast load analysis and damage estimation

A.J. Watson, B. Hobbs, A.K. Chan, J. Peters, R. Westaway
Department of Civil and Structural Engineering
Sheffield University, England

ABSTRACT

The paper describes a P.C. based computer program which can carry out a vulnerability analysis of multi-storey, multi-bay buildings subjected to blast loading. The basic method of analysis used by the program is given and demonstrated by application to a single storey multi-bay industrial type building.

1.0 INTRODUCTION

This P.C. based program permits the prediction of structural damage to buildings of various hardness from explosions inside and outside the buildings, using a structural engineering approach. The building may be up to five storeys high as a framework of beams and columns, walls and floor slabs, forming a plan of 4 x 6 bays. Defining the building within the program is greatly facilitated by the ability to replace or modify building elements and to act on groups of elements. For example it is possible to load all the slabs on one floor level with the same occupancy load and it is also possible to copy a floor definition from one floor level to the next. The frame can be viewed isometrically following the basic definition of the frame. Frame definitions can be stored on disk and subsequently retrieved and edited.

The framework is defined using an interactive graphics editor with a built in stability checker to ensure that the building definition is always stable. Consequently, if a building element which supports other elements is removed in editing or by the blast, then all dependent elements are automatically removed. Using this facility the user is able to view the building graphically before and after the blast to assess the damage.

A vulnerability analysis of a single storey, multi-bay industrial type building under a single blast load is chosen to demonstrate the program in the limited space available here. The building has symmetric portal frames, fig. 1, which is typical of a modern industrial type building although the structural details can vary. It is clad with steel decking on the walls and roof and these are fastened to side rails and purlins which span between adjacent portal frames.

2.0 VULNERABILITY ANALYSIS

The vulnerability analysis developed here for buildings, identifies structural load paths through the building and the analysis is based on the conservation of energy.

2.1 Load paths

The structure of a building supports the loads and must be capable of transferring them to the foundations along a safe and serviceable load path. An interruption in the load path will cause progressive collapse to occur unless an alternative load path can be found. A load path is said to be interrupted when the member(s) in it no longer have the strength or stability to carry the loads. In blast loading this may occur because the members are subjected to loads of a magnitude or a direction which was not anticipated in the original design of the building.

An ability to identify the load path and its most vulnerable parts is essential in a vulnerability analysis. It is also necessary to consider the dynamics of the collapse because when a collapse is initiated it does not necessarily follow through to total destruction

2.2 Conservation of energy

The kinetic energy KE delivered from a blast wave to a building or an element of the building is given by:

$$KE = I_e^2/2M_e$$

where I_e = effective impulse; M_e = equivalent mass of the building or element.

I_e is defined as the area under the reflected overpressure-time curve of the blast wave up to the lesser of time t_c for the component or the duration of the positive blast pulse, time t_d. The time t_c is the time when the element would reach maximum deflection under steady state vibration, i.e. $t_c = T/4$ where T is the lowest natural period of the component. It has been assumed by Sewell & Kinney (1968) that under blast loading, t_c is the time when the resistance of the component starts to develop.

M_e is the mass of the element in the equivalent single degree of freedom system and is dependent on the condition of the structural element.

If the element is to survive the blast loading then the internal work done, or the energy absorbed by the element, must be equal to the KE supplied by the blast. Referring to an elasto-plastic resistance-displacement function, the work done during deformation is:

$$WD = R_e(X - 0.5X_e)$$

where R_e = maximum resistance; X = maximum displacement; X_e = elastic displacement limit

For most building materials, the work done in the elastic regime is generally small compared to that in the plastic regime and therefore WD can be approximated as R_eX.

Since the dynamic resistance R_e is generally in direct proportion to the dynamic yield stress, R_e is assumed to increase by the same ratio as the dynamic yield stress to its corresponding static value. Experimental results have indicated that the dynamic yield strength of concrete can be up to 140% of the static yield strength and for structural steel, up to 160%.

In the case where a plastic hinge is formed in the element, the work done by rotation of the hinge is:

$$WD = M_{pd}\theta$$

where M_{pd} = dynamic plastic moment resistance of the hinge; θ = rotation of the hinge

When the component has an axial extension, the work done is:

$$WD = F_{maxd}e$$

where F_{maxd} = maximum dynamic tensile force resistance of the component;
e = extension

Combining these work equations gives an energy balance equation:

$$\frac{I_e^2}{2M_e} = \Sigma(M_{pd}\theta + F_{maxd}e)$$

2.3 Blast pulse

Bode type equations for blast pulses generated by chemical explosions, Kinney and Graham (1985), are used to calculate the peak side-on overpressure p_o, the duration t_d and the impulse per unit area I/A at a distance D from an explosive charge, mass W and scaled distance $(D/W^{1/3})$. An impulse fraction factor $IFF = (I/A)/p_o t_d$ is calculated to facilitate the process of converting the blast pulse to an equivalent triangular pulse. A reflection coefficient of 1.65 was used to convert p_o to the peak reflected overpressure.

3.0 GENERAL PROCEDURE

The steps in the analytical procedure used in this program and the associated assumption are

Step 1: Find the first building element exposed to the explosive pressure
For external explosions this element is usually the 'skin' or cladding of the building and may be of secondary importance for the structural integrity of the building under gravity loads. It is generally in the form of a large panel and is visible from outside e.g. wall and roof cladding. This cladding is unlikely to be able to resist blast pressures for long but it will form part of the load path transferring blast pressures into the main structural frame or secondary support members. For internal explosions the first element could also be cladding or part of the main gravity loading bearing structure such as internal walls, columns or floors.

Step 2: Estimate the dynamic characteristics of this component

The parameters required are M_e, T, M_{pd} and F_{maxd} assuming adequate connections.

M_e and T can be calculated for the structural element from standard factors e.g. Biggs (1964). M_{pd} and F_{maxd} can be obtained from an analysis of the section of the element.

Step 3: Calculate the effective impulse I_e on this element

Assuming the details of the explosion (charge weight and distance) are known, the overpressure p_o, duration t_d, impulse per unit area I/A and the impulse fraction factor IFF are determined from the bode-type equations.

By comparing t_c and t_d, the effective impulse per unit area I_e/A is found and knowing the area A of the component, I_e is calculated.

In the case where an external explosion is close to the building, I/A will vary across the face of the building, but at present an average I/A is assumed to act on the whole surface area.

Step 4: Estimate the work done on this element

For a first approximation, it is assumed that the dynamic deformed shape is identical to that produced by static loading of identical form and acting in the same locations. The positions of the plastic hinges are found from the deformed shape and the axial extension e, in terms of the rotations θ of the plastic hinges, is obtained using the geometry of the element and assuming that it is fully anchored at the supports.

Step 5: Find the dynamic deformation of the element

The only unknown left in the energy balance equation is now θ. Using the assumption and information in Step 4, θ can be found and the deformation of the component can be quantified.

Step 6: Check conditions at supports and fasteners

If the element is not fully anchored to the supports then it will be disconnected when local failure occurs at the connections (i.e. shear, bearing or tensile fracture in the connectors or the element fractures at the connectors) before reaching its full strength capacity at sections where it has not been weakened by holes drilled for connectors. Because there are many possible failure modes and the total energy absorption at the joint is a complex matter, the condition at the support is best checked by an equivalent static load method.

Step 7: Repeat Step 2 to Step 6 for the next element in the load path including the last one

Step 8: Check residual strength of the building

Following the calculation of direct blast damage, the program then determines which elements will fail because their load path has been destroyed. The residual strength of the building is the remaining ability of those parts which have not collapsed, to support their self weight and any imposed load. Instability may occur more readily after part of the building has collapsed and the likelihood of progressive collapse is checked under self weight and any imposed loads which are still there. It is intended that ultimately the program will be able to calculate response to debris loading.

4. DAMAGE ANALYSIS

An intermediate bay of the portal frame building shown in fig. 1 is used as an example of the program application for an external explosion. The blast pressure is first applied to the steel cladding and then transferred along a structural load path, to the cladding rails and the stanchion of the structural steel portal frame. The program permits the explosion to occur at any location defined by prescribed coordinates.

In the limited space available in this paper, only the analysis for the portal frame is given here.

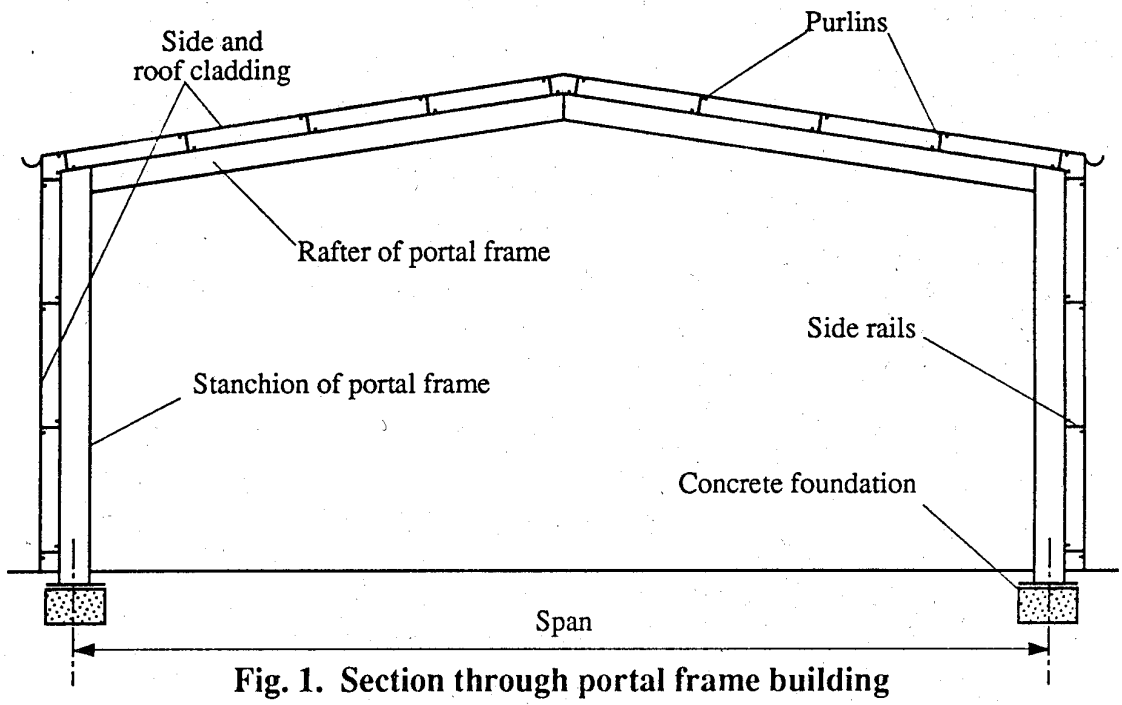

Fig. 1. Section through portal frame building

Portal Frame Analysis

Assuming the bay spacing is 5.0m and the eaves level is 6.0m above ground level, the loaded area carried by the frame will be 5.0 x 6.0 = 30.0m^2. The roof area is ignored assuming the roof is shallow enough so that the effect on the frame is small compared to the side.

Step 2: Dynamic characteristics

Natural period T = H/50 = 7/50 = 0.14s

Equivalent mass M_e

(a) Actual

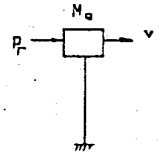

(b) Equivalent system

Frame equivalent system

Velocity at eaves = v = velocity of M_e = velocity of roof
Velocity of side at y above ground = vy/6
Mass of roof, M_R = 1647kg; mass of two sides, M_s = 1264kg
K.E. of equivalent system = $\frac{1}{2}M_e v^2$; K.E. of roof = $\frac{1}{2}M_R v^2$
K.E. of sides = $\frac{1}{2}\int_0^6 \frac{M_s}{6}\left(\frac{yv}{6}\right)^2 dy$

$$\therefore \frac{1}{2}M_e v^2 = \frac{1}{2}M_R v^2 + \frac{1}{2} \cdot \frac{1}{6^3} M_s v^2 \int_0^6 y^2 dy$$

$$M_e = M_R + \frac{1}{3} M_s = 1647 + 1264/3 = 2068\text{kg}$$

Dynamic resistance

section modulus = 774cm^3; yield stress = 250N/mm^2
$\therefore M_p = 250 \times 774 \times 10^3 \times 10^{-6} = 193.5\text{kNm}$
$\therefore M_{pd} = 1.55 \times 193.5 = 300\text{kNm}$

The moment offered by the pinned base is small and therefore ignored.

There is no extension in the frame, hence F_{maxd} is not calculated.

Step 3: Calculate I_e

$t_c = T/4 = 35\text{ms} > t_d$
I_e/A at D = 609Ns/m^2 and I_e/A at A = 703Ns/m^2
$\therefore$ average $I_e/A = \frac{1}{2}(703 + 609) = 656\text{Ns/m}^2$
$\therefore I_e = 656 \times 30 = 19680\text{Ns}$

Step 4: Work done

Assume a static load acting on the frame

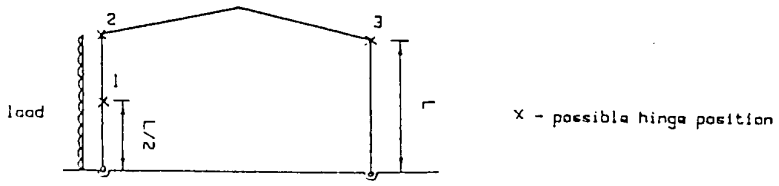

Possible hinge position

There are 3 possible hinge positions and the frame contains one redundancy. Therefore, there are two basic collapse mechanisms and the critical one is sway:

Mechanism	Rotation of hinge			$M_p\theta$	WD (by load) (WLθ)	critical W = $M_p\theta$/WD (M_p/L)
	1	2	3			
Sway 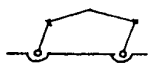		$-\theta$	$+\theta$	2	1/2	4

The WD is therefore:

$$WD = 2M_{pd}\theta$$

Step 5: Deformation

Since I_e = 19680Ns; M_e = 2068kg; M_{pd} = 300kNm
∴ from energy balance equation:
$19680^2/2 \times 2068 = 2 \times 300 \times 10^3 \times \theta$
i.e. θ = 0.156 rad. (8.94°) and deflection at eaves $\delta = 6 \tan\theta = 0.9437$m

Step 6: Support condition

The supports are assumed O.K. because the load acting on them is small.

Step 8: Residual strength

Assuming all the members in the bay are still attached to the frame, the loads applied to the deformed frame are:

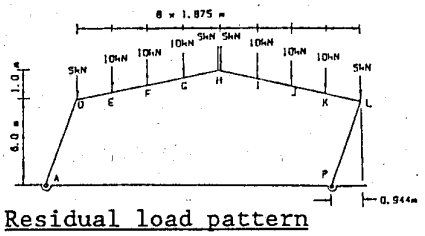

Residual load pattern

(a) Cut frame at H and calculate free bending moment M

M_A = 187.8kNm

Similarly, the free bending moments at the other locations are calculated.

(b) Determine salient reactant moments MR

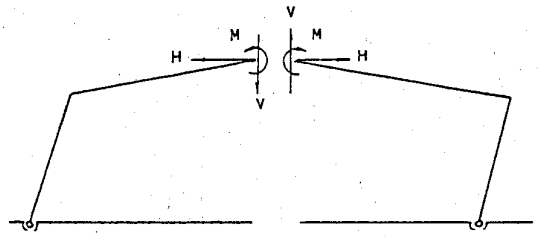

Reactant diagram

$MR_A = 8.444V - 7H$

Similarly the reactant moments at the other locations are calculated.

(c) Let M_{pc} = collapse moment and assume hinges form at G and L.

∴ at A : $M_A + MR_A = 0$
$\Rightarrow 187.8 + 8.444V - 7H - M = 0$
at G $\Rightarrow 9.4 + 1.875V - 0.25H - M = -M_{pc}$
at L $\Rightarrow 150 - 7.5V - H - M = +M_{pc}$
at P $\Rightarrow 112.2 - 8.444V - 7H - M = 0$

Solving

$V = -4.48kN$, $H = 9.05kN$
$M = 86.64kNm$, $M_{pc} = 87.91kNm$

Hence the reactant moments can be evaluated and since the $|$free BM + reactant BM$| < |M_{pc}|$ at all points the mechanism with hinges at G and L is the critical one.

$\therefore$ Unless the residual strength of the frame is less than M_{pc} (= 87.9kNm), the deformed frame will not collapse.

5. CONCLUSIONS

This damage analysis method yields an estimate of the severity of damage related to the blast distance and type of explosion. By repeating this analysis procedure, the relationship between extent of damage and the location of the explosion can be determined and displayed as isodamage contours.

The program can be used where exact structural and material data may not be available. Although the energy balance equation does not include all the absorbed energy the method provides a reasonable alternative to finite element or finite difference procedures and equivalent single or multi-degree of freedom model analyses. It will operate on any IBM PC or compatible microcomputer fitted with a graphics adaptor.

ACKNOWLEDGEMENTS

This work is funded by the US Government through the Denver Research Institute, Denver, USA. The assistance and co-operation from Mr. M. Keith and Mr. L. Ullyatt is very gratefully acknowledged.

REFERENCES

Biggs, J.M. Introduction to Structural Dynamics, McGraw Hill, 1964.
Kinney, G.F., Graham, K.J. 'Explosive Shocks in Air', Springer-Verlag, 1985.
Sewell, R.G.S., Kinney, G.F. 'Response of Structures to Blast: A New Critrion' Annals of the New York Academy of Sciences, Vol. 152, Article 1, pp. 532-547, October 1968.

PENETRATION OF A RIGID PROJECTILE INTO A SEMI-INFINITE LAYERED MEDIUM

David Z. Yankelevsky*

ABSTRACT

An analytical model had been developed to study the normal penetration of a rigid projectile into various soils. The model is based on the spherical cavity expansion theory applied to thin discs of the target material. With several simplifying assumptions the response is solved analytically to yield the interaction pressure and the discs' response. The contribution of all discs being in contact with the projectile to its motion is carried out numerically.

The projectile shape may be defined by its specific shape (cone, ogive, etc.) or by its coordinates. The model is implemented in a computer program on a PC which follows the projectile motion through the target, provides information on targets' reponse, calculates the interaction pressure distribution at any time, etc. The computation of a complete penetration event is carried out within seconds. The model had been compared with test data, empirical and analytical equations and computer codes; the results will be shown in the paper.

A unique advantage is obtained from the model which is semi-analytical and semi-numerical. General criteria and results were obtained for the interaction pressure distribution shape, cavitation criteria, etc. Further simplification of the analytical expression led to similarity with existing penetration formulae and the physical background for their constants has been determined. The effect of various parameters had been studied and the nose shape "constant" has been found to increase with increasing the impact velocity, as observed in high velocity tests.

The model has been extended to treat layered targets and includes other materials as well.

---

* Faculty of Civil Engineering & National Building Research Institute, Technion - Israel Institute of Technology, Haifa 32000, ISRAEL.

Druck in Tunneln/Detonation im Innern

Pressure in Tunnels/Internal Detonation

Experimentelle Untersuchung der Ausbreitung konventioneller Luftstösse in Tunnelsystemen

Eduard Binggeli, Bernard Anet

AC-Laboratorium, CH-3700 Spiez

Zusammenfassung

Die Zielsetzung dieser im Modelmassstab durchgeführten Untersuchung lag in der experimentellen Ermittlung der Ausbreitungscharakteristiken von Luftstössen in einem Tunnel, wenn konventionelle Ladungen im Bereich 100 bis 1500 kg TNT in unmittelbarer Umgebung des Portals, ausserhalb des Tunnels, im Abstand von 4 bis 12 m detonieren.

1. Einleitung

Die Sicherstellung des Schutzes vor den Auswirkungen nuklearer und konventioneller Waffen ist die Grundaufgabe der modernen zivilen und militärischen Schutzbauten in der Schweiz. Wurden bisher solche Schutzbauten vornehmlich nach nuklearen Belastungskriterien bemessen, muss heute, in Berücksichtigung der fortschreitenden Entwicklung hochpräziser konventioneller Waffensysteme, auch dem konventionellen Nah- oder Direkttreffer vermehrt Beachtung geschenkt werden.
Detaillierte Kenntnisse über die Belastungscharakteristiken konventioneller Waffen, insbesondere im Nahbereich, sind somit unabdingbar.

Für die in der vorliegenden Arbeit untersuchten Fälle - Tunnel-Eingangskonfigurationen und Tunnelsysteme - liegen über die Ausbreitung langdauernder, nuklearer Luftstösse Daten vor. Im Gegensatz dazu hat eine Literaturdurchsicht gezeigt, dass für die kurzzeitigen Luftstösse konventioneller Explosionen nur sehr wenige Daten verfügbar sind [2],[3],[5]. Eine mögliche Ursache hierfür liegt sicher in der Vielfalt der Anordnungen, die einer systematischen Erfassung entgegenläuft, aber auch im ausgesprochen dreidimensionalen Charakter solcher komplexen Luftstossausbreitungen.

Obschon hochentwickelte Computercodes (HULL,SHARC,..) in der Lage sind, 3-dimensionale Ausbreitungsprobleme zu behandeln, sind sie äusserst kostspielig, arbeitsintensiv und nur auf verhältnismässig einfache Konfigurationen 'sicher' anwendbar. Zur Validierung solcher numerischen Berechnungen sind Versuchsdaten zudem unerlässlich.

Der experimentelle Weg über **Modellversuche** zur Untersuchung spezifischer Eingangs- und Tunnel-Konfigurationen stellt somit eine effiziente Alternative dar.

2. Zielsetzung

Anhand von Modellversuchen sind die Luftstoss-Belastungscharakteristiken (Spitzenüberdruck und Impuls) innerhalb eines Tunnels zu bestimmen, wenn Detonationen konventioneller Explosivstoffe (TNT) in unmittelbarer Umgebung von typischen Tunnel-Eingangskonfigurationen stattfinden.

Innerhalb dieser Versuchsreihe wurden neben den Sackstollen-Konfigurationen auch der gerade Stollen (Explosionspunkt im Stollen) sowie diverse konkrete Tunnelanordnungen experimentell untersucht.

3. Theoretische Betrachtungen

Das Einlaufen eines sich vom Explosionsort sphärisch ausbreitenden Luftstosses in einen Tunneleingang ist ein komplexes, 3-dimensionales Beugungsphänomen.

Der gesamte Einlaufprozess wurde deshalb in drei verschiedene Bereiche aufgeteilt und in der Folge auch separat behandelt (siehe Fig 1).

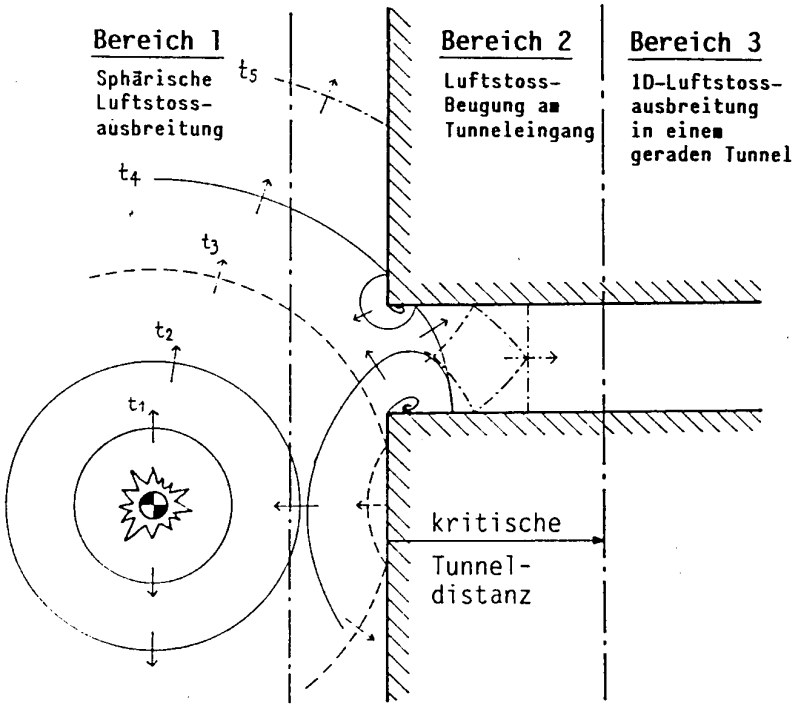

Fig 1: Schematische Darstellung der Beugungsphänomene beim Einlaufen eines Luftstosses in einen Tunnel.
t1 bis t5: verschiedene Beobachtungszeiten für die Stossfront

Im Bereich 1 herrscht die annähernd ungestörte halbsphärische Ausbreitung.

Bereich 2 ist die Zone der Wechselwirkung des Luftstosses mit dem Tunnel-Eingang, welche durch komplexe 3-D Beugungseffekte mit Wirbelbildungen an den Kanten des Tunneleinganges etc gekennzeichnet ist. Die vom Reflexionsgebiet ausserhalb des Tunnels nachströmende Luft verstärkt den einfallenden Luftstoss im Tunnel.

Reflexionen an den Tunnel-Seitenwänden bewirken ein Aufsteilen der Stossfront innerhalb einer bestimmten Distanz. Diese zur 'Stabilisierung' des Luftstosses erforderliche Distanz wird als die **kritische Tunneldistanz** bezeichnet und stellt für die nachfolgenden Untersuchungen einen wichtiger Parameter dar.

Im anschliessenden **Bereich 3** findet eine nahezu 1-D Luftstossausbreitung statt.

4. Versuchsanordnung

Aus verschiedenen, aber vorallem aus praktischen Gründen wurde ein **geometrischer Modellmassstab von 1:30** gewählt.

Fig 2 zeigt die Versuchsanordnung inkl der eingesetzten Messstellen. Der Tunnel-Querschnitt ist halbkreisförmig. Die 'unendliche' Felswand, welche den Tunneleingang umgibt, wurde als senkrecht angenommen. Sämtliche Modellladungen wurden ausserhalb des Tunneleinganges zur Detonation gebracht.

Die 1:1 Ladungen, welche für diese Versuchsserie modelliert wurden, lagen zwischen 100 kg und 1500 kg TNT. Die 1:1 Abstände des Explosionsortes (nachfolgend als Nullpunkt bezeichnet) variierten zwischen 4 m und 12 m, der Winkel α zwischen 0° und 90° im 30°-Intervall. Der Referenzpunkt, auf welchen sich sämtliche Distanzen und Winkel beziehen, liegt genau im Zentrum des Tunneleinganges (vgl Fig 2).

Fig 3 vermittelt die Kaliber, Abstände und Winkel der untersuchten Konfigurationen sowohl für den **1:1 Fall** (Originalmassstab) als auch für den **Modellmassstab 1:30.**

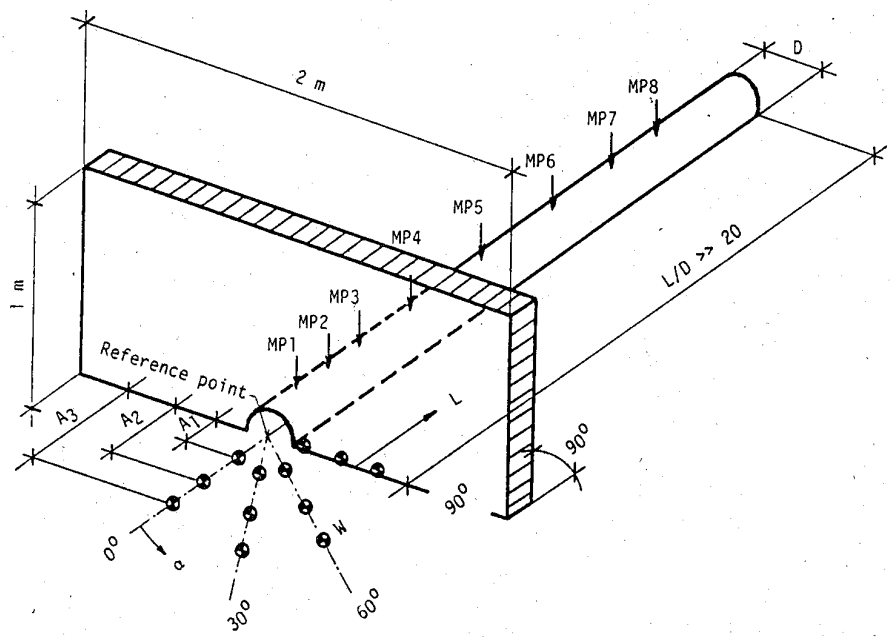

Fig 2: Modell-Versuchsanordnung

Mass / Distanz	1:1 [m]	1:30 [m]
A1	4	0,133
A2	8	0,267
A3	12	0,4

Mass / Distanz	1:1 [kg]	1:30 [g]	Mass / Distanz	1:1 [kg]	1:30 [g]
W1	100	3,7	W4	750	27,8
W2	250	9,25	W5	1000	37,0
W3	500	18,55	W6	1500	55,6

Fig 3: W, A und α im Originalmassstab (1:1) sowie im Modellmassstab (1:30)

5. Versuchsprogramm

Ingesamt wurden über 200 Versuche à je 8 Messstellen durchgeführt. Jede Anordnung wurde zwecks Ueberprüfung der Reproduzierbarkeit mindestens 3 mal untersucht.

6. Auswertung der Versuchsergebnisse

Vorerst galt es, die über 1600 gemessenen Druck-Zeit-Verläufe zu ordnen, dann auszuwerten und anschliessend zu interpretieren. Dieser ohnehin schon schwierige Schritt wurde durch das Fehlen einer theoretischen Problembeschreibung zusätzlich noch erschwert.
Aus diesem Grunde wurde eine computerunterstützte, **halbempirische Auswertetechnik** entwickelt, welche erlaubt, einzelne Datensets untereinander zu vergleichen und dadurch Hinweise über mögliche physikalische Zusammenhänge zwischen den involvierten Parametern (Kaliber, Nullpunkt, Winkel, etc) zu gewinnen.

Dieses Auswerteverfahren wurde insbesondere für den Spitzenüberdruck in den Bereichen 1 und 3 angewendet, d.h.:

a) im **Bereich 3** (1-D Luftstossausbreitung in einem geraden Tunnel) um mögliche halb-analytische Ausdrücke zur Beschreibung des Druckabbaus herzuleiten und die kritischen Tunneldistanzen zu bestimmen.

b) im **Bereich 1** (annähernd ungestörte halbsphärische Ausbreitungsverhältnisse) die Daten derart auszuwerten und darzustellen, dass für ein gegebenes Kaliber und einen an der kritischen Distanz im Tunnel definierten Druck die Koordinaten der möglichen Nullpunkte ausserhalb des Tunnelportals gefunden werden können.

Die komplexen 3-D Wechselwirkungen im **Bereich 2** liessen von vornherein kaum Hoffnungen auf eine Erfassung vernünftiger Zusammenhänge zwischen den involvierten Parametern zu. Aus diesem Grunde wurde der Bereich 2 in einer ersten Phase der Auswertung nicht untersucht.

7. Ausgewertete Resultate

In Anbetracht des Umfanges des Datenmaterials können in diesem Beitrag nur typisch repräsentative Resultate gezeigt werden. Für die Gesamtheit der Resultate wird auf den Schlussbericht [6] verwiesen.

Sämtliche aufgeführten Modell-Resultate wurden auf den **1:1-Originalmassstab rückskaliert.**

7.1 Druckabbau im Tunnel (Bereich 3)

Eine Untersuchung des Datenmaterials anhand der in der Einleitung erwähnten halbempirischen Auswertemethodik zeigte rasch, dass der Abbau des Spitzendruckes entlang der Tunnelachse mit einer mathematischen Formel der Art

$$p_s = a \cdot (L/D)^{-b} \qquad (1)$$

beschrieben werden kann.

Eine weitere Parameter-Studie zeigte, dass der **Exponent b** in erster Linie durch das **Kaliber W** und die **Distanz A** (vgl Fig 2) bestimmt wird. Der Einfluss des Einfallswinkels α auf b ist nämlich so gering, dass dieser vernachlässigt werden konnte.
Fig 4 zeigt den Exponent b für sämtliche Kaliber W in Abhängigkeit der Nullpunkt-Distanz A.
Der **Koeffizient a** der Gl (1) scheint die Komplexität des Beugungsphänomens am Tunnelportal zu widerspiegeln. Seine Abhängigkeit zu den anderen Versuchsparametern liess sich nicht auf eine einfache Form reduzieren, sodass dieser direkt aus dem experimentellen Datensatz gewonnen werden musste.

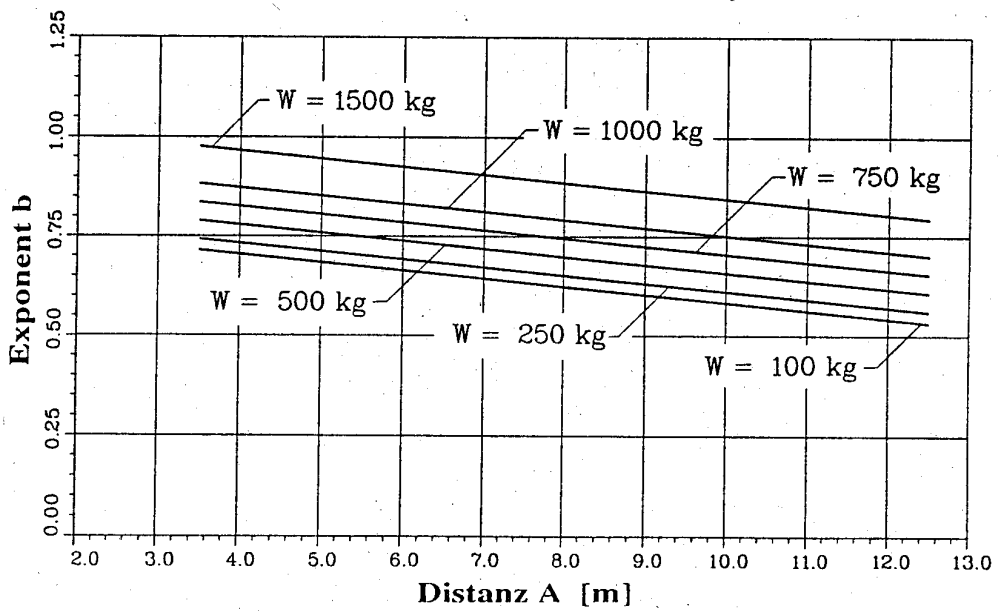

Fig 4: Druckabbau im Tunnel; Exponent b in Abhängigkeit der Nullpunkt-Distanzen A für alle Kaliber W

Die daraus resultierenden Ausgleichskurven sind in Fig 5 dargestellt. Die Korrelationskoeffizienten zu den eingetragenen Messdaten liegen durchwegs bei 0.9 und höher. Dabei repräsentiert jedes Symbol den aus drei identischen Versuchen gemittelten Spitzenüberdruckwert. Die Standardabweichungen sind ebenfalls eingetragen.

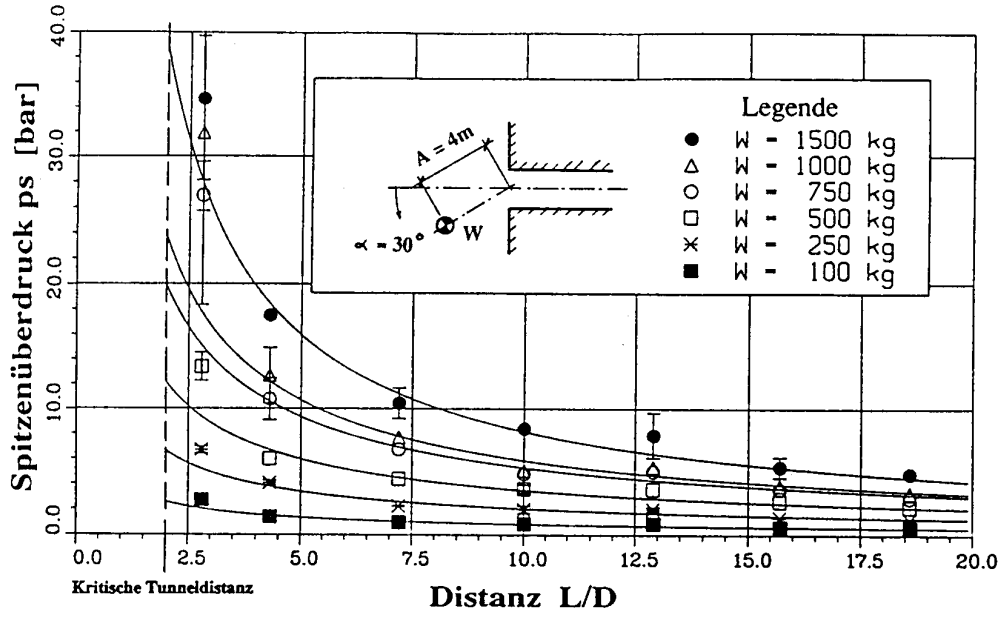

Fig 5: Abbau des Spitzenüberdruckes im Tunnel für verschiedene Kaliber W. (A = 4 m; α = 30°)

Da die Kurven eine unerwartet gute Korrelation sogar für die Daten ab L/D ≈ 2 zeigen - der Entschluss zur vorläufigen Vernachlässigung des Bereiches 2 wird dadurch unterstützt -, wurde die kritische Tunneldistanz im Tunnel auf L/D = 2 festgelegt. **Sämtliche nachfolgenden Auswertungen stützen sich dabei auf diesen Wert.**

7.2 Nullpunkt-Koordinaten ausserhalb des Tunnels

Basierend auf den Ausgleichskurven in Fig 5 kann der Spitzenüberdruck p_s im Tunnel bei der kritischen Distanz (L/D = 2) in Abhängigkeit des **Nullpunktabstandes A**, des **Kalibers W** sowie des **Winkels α** dargestellt werden (Fig 6). Fig 7 zeigt eine Auswahl von vier verschiedenen Kalibern mit den entsprechenden Koordinaten X und Y ($A = \sqrt{X^2+Y^2}$). Diese Nullpunkt-Kurven erlauben, den 'Einsatzpunkt' (Nullpunkt) vor dem Portal für das jeweilige Kaliber W zu bestimmen, welches zum Erreichen eines bestimmten Spitzenüberdruckes bei der kritischen Distanz im Tunnel (L/D = 2) erforderlich ist.

Eine mathematische Beschreibung dieser Kurven liegt noch nicht vor.

Ablesebeispiel: W = 1500 kg, A = 5,8 m (X = 5 m, Y = 3 m), α = 30°

=> $p_{(L/D=2)} \approx 25$ bar

Der Abbau des Spitzenüberdruckes im Tunnel wird dann anhand der Ausgleichskurven in Fig 5 bestimmt.

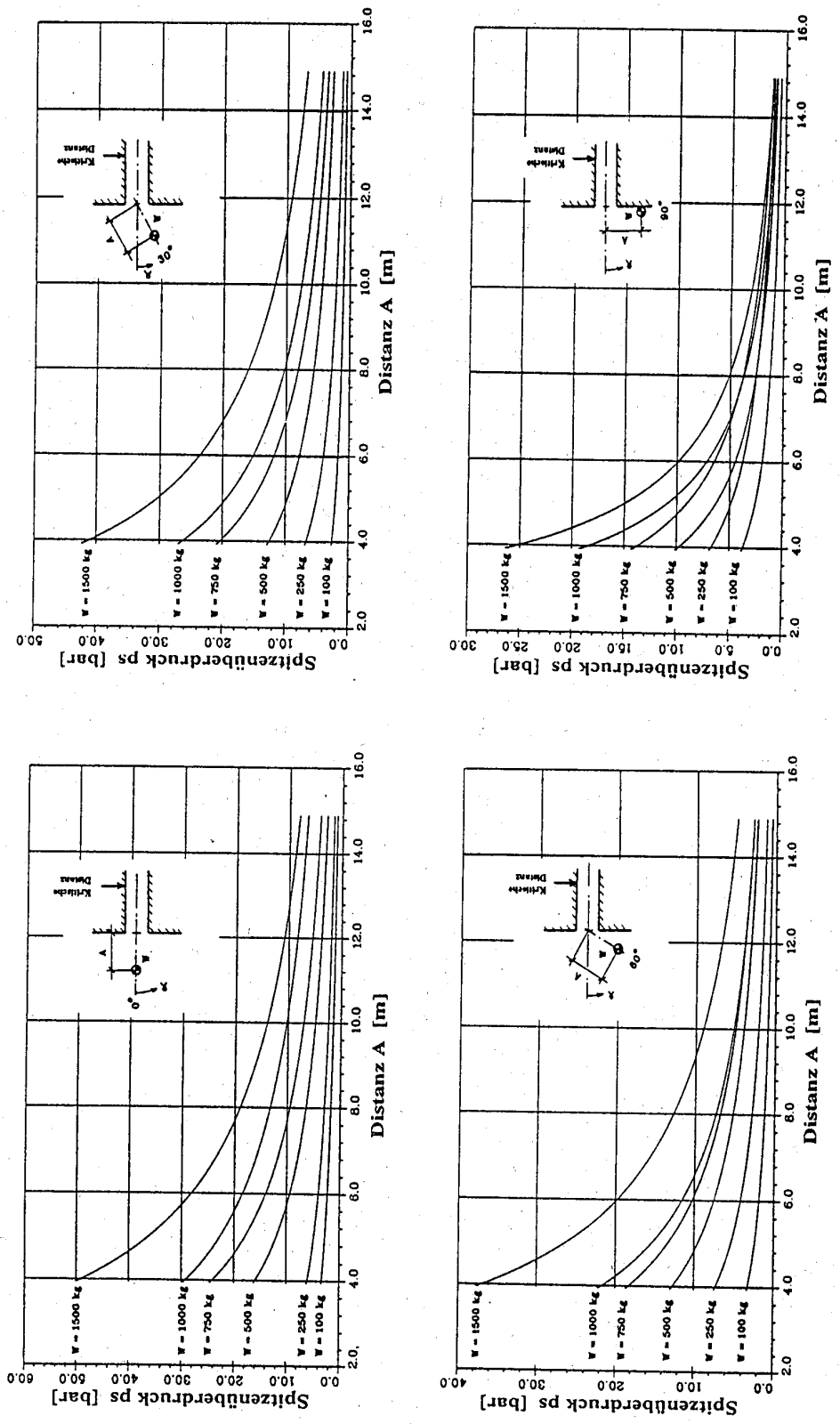

Fig. 6: Spitzenüberdruck bei der kritischen Tunneldistanz (L/D = 2) in Abhängigkeit des Nullpunktabstandes A für alle Kaliber W und Winkel α

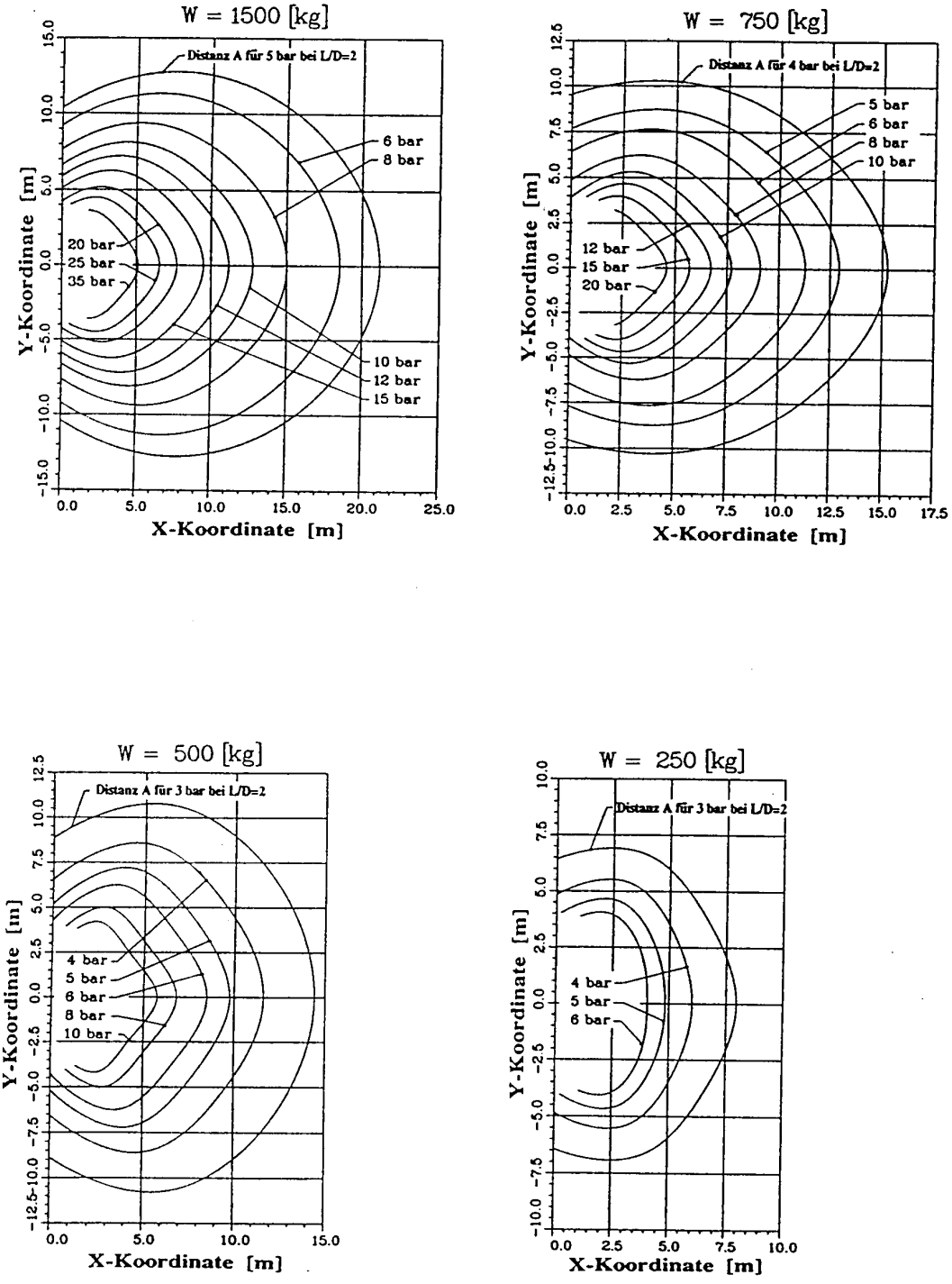

Fig. 7: Beispiele von Nullpunkt-Abständen

8. Schlussbemerkungen

Die vorliegenden Daten zeigen, obwohl die Auswertung noch vorläufigen Charakter aufweist, dass sich über den experimentellen Weg die gegebenen Zielsetzungen innerhalb einer vernünftigen Zeitspanne erreichen lassen. Die computerunterstützte Auswertemethode ermöglichte eine einfache und auf praktische Anwendungen bezogene Beschreibung der Luftstossausbreitungscharakteristik sowohl ausserhalb wie auch innerhalb des Tunnels.

Zur Abschätzung der Belastungscharakteristiken für andere Kaliberwerte bzw bei anderen Tunnelabmessungen müssen letztere zunächst auf den Originalmassstab der vorliegenden Versuchsreihe (Tunneldurchmesser D = 7 m, vgl Fig 2) skaliert werden. Die gewünschten Daten lassen sich dann anschliessend durch Inter/Extrapolation der Kaliberwerte bestimmen.

Der Schlussbericht [6] zu dieser experimentellen Untersuchung, welcher sämtliche Anordnungen behandelt (vgl Kapitel 2) wird voraussichtlich ab Ende 91 verfügbar sein.

Die Autoren sprechen Herrn Fritz Binggeli für die sorgfältige Durchführung der Versuche und für die gewissenhafte Zusammenstellung des Datenmaterials den besten Dank aus.

Referenzen

[1] Glasstone, S. and Dolan, J.J.
The Effects of Nuclear Weapons, 1977

[2] Baker, W.E.
Explosions in Air, 1973

[3] Little, C.D.
Airblast Attenuation in Entranceways and Other Typical Components of Structures, 1984

[4] Anet, B. and Binggeli, E.
Model Scale Experiments for the Investigation of Air Blast Loading on Structures. Proceedings MABS 10, 1987

[5] Skjeltorp, A.
One-Dimensional Blast Wave Propagation, 1968

[6] Binggeli, E. and Anet, B.
Experimentelle Untersuchung der Ausbreitung konventioneller Luftstösse in Tunnel und Tunnelsystemen
Bericht ACLS 9106

COMPUTER CODE SPIDS/SHOCK PROPAGATION IN DUCTING SYSTEMS UTILIZING A PC COMPUTER

R.H. Fashbaugh, Ph.D.
Mechanical Engineering Department
University of Nevada, Reno
Reno, NV 89557

The computer code SPIDS is used for calculation of shock wave propagation in a system of air ducts. The source of the shock waves can be a surface or air nuclear burst, a conventional high explosive detonation which occurs outside the entrance of a ducting system, or a conventional high explosive detonation inside the ducting system. Each duct in the system can have ten branches up to a total of 1000 branch ducts possible for the entire system. The equation of state for real air is used which is valid up to 24000 K. Duct inlet losses and wall friction losses are included through empirical relations.

Included with the SPIDS code is a pre-processing microcomputer program which is used to generate an input file for this code. The wave shape parameters for a nuclear wave and empirical junction loss factors for various types of duct junctions are included in this pre-processing program.

Also included with the SPIDS Code is a post-processing microcomputer program which allows plotting of the output parameters of SPIDS on the computer screen or on an external plotter. Seventeen plots in all are available included in which are pressure, temperature, and dynamic pressure as a function of location in a given duct, or these parameters as a function of time at a given location in a duct.

INTRODUCTION

This paper describes the structure and use of the computer code SPIDS which has been developed for predicting shock wave propagation in a system of air ducts [1]. The source creating the shock wave that propagates over the entrance to the ducting system can be a surface or air nuclear burst or a conventional high explosive detonation; a multiple shock front of known waveform shape can also be specified at the system entrance. The conventional high explosive detonation can also be internal to the ducting system. The ducting system configuration is shown in Fig. 1 and can be a main air duct with up to ten ducts branching from it. Each of these branch ducts can have up to ten ducts branching from them; and further, up to ten branch ducts from each of these branches is possible. Each of the ducts in the system can have one change in cross section area. The computer program is a one-dimensional variable area hydrodynamic solution which includes friction effects at the duct wall. A centered finite-difference scheme is utilized in a Lagrangian formulation which includes pseudo-viscosity to remove shock front discontinuities [2.]. An equation of state for real air up to a temperature of 24000 K, the temperature corresponding to a shock wave overpressure of approximately 30,000 psi, is included [3]. Nine types of duct inlet junctions are available. The shock wave losses at these junctions are included empirically.

A pre-processor microcomputer program is available which greatly simplifies the writing of an input file for SPIDS. A post-processing microcomputer program is also available which provides either spatial or temporal plotting of the SPIDS output variables such as pressure and temperature. The output can be plotted either on the microcomputer CRT or an external plotter. Both of these programs are written in the Turbo Pascal language for an IBM-AT, or compatible, computer utilizing a menu, user friendly, style of programming.

COMPUTER PROGRAM SPIDS DESCRIPTION AND USE

The basic structure of the SPIDS computer code and the input and output variables are described briefly below. Also presented are explanations of the various code options. The detail input and output variables and formats is given in Ref. 1. The computer code is written in Microsoft Fortran and consists of a main control program with auxiliary subroutines. Table 1 is presented to outline the structure of SPIDS and provide the basic function of each subroutine.

TABLE 1. SPIDS Subroutine Structure.

Subroutine Name	Function
SPIDS	Controls main logical flow and reads input data.
BDY2	Specifies a rigid closed end or open end at a duct exit.
DATEXP	Specifies duct inlet losses using experimental data.
EQST	Controls equation of state subroutine acquisition.
EQS3	Equation of state for real air; T < 24,000°K.
FIT	Real air equations used in EQS3.
GENR	Initializes problem; establishes zones in a duct and initial pressure, density, and velocity.
GEOM	Calculates cross-sectional area and zone volume.
HEBDY	Specifies motion of interface at duct inlet for a high explosive wave input.
HTEMP	Calculates compressibility factor Z for real air.
HYDR	Computes hydrodynamic motions for all zones in the duct.
LINT	Interpolation subroutine; used when reading files as inputs to branch ducts.
NUBDY	Specifies motion of interface at duct inlet for a nuclear wave input.
OUT1	Prints overpressure, velocity, etc., in each zone in a duct at specific times.
OUT3	Prints time history of overpressure, velocity, etc., at up to ten locations in a duct.
REZEN1	Adjusts zones at duct entrance for mass inflow or outflow.
REZEX1	Adjusts zones at duct exit for mass outflow.
TIMEST	Calculates time step.

The following SPIDS characteristics are illustrated through Table 1: a duct inlet boundary condition can be the specification of either a nuclear shock wave or a high explosive shock wave; a duct exit boundary condition can be a rigid closed end or open to the atmosphere; duct inlet losses are accounted for empirically, using experimental data [4,5] with nine junction types possible; the equation of state is for real air at temperatures to 24000 K [3]; mass inflow or outflow is calculated at a duct entrance and at a duct exit; flow variables such as pressure, temperature, and dynamic pressure are output for each finite difference zone at desired calculation cycles; and a time history of pressure, temperature, and dynamic pressure can be output at up to ten desired locations in a duct. The time history of pressure, temperature, and dynamic pressure can be written to a file for points in a duct where branch ducts are located; these files are then used as input files to describe the input wave for a branch duct calculation.

The calculation of the propagation of a shock wave in a system of ducts is done sequentially. For example, considering a main air duct with one branch duct, the shock propagation in the main duct is calculated and the time history of pressure, temperature, and dynamic pressure is saved on a computer file at the location of this branch duct. This file then serves to specify the pressure, temperature and dynamic pressure at the inlet of the branch duct and the shock propagation in this branch duct can be calculated. This procedure can be used for any number of branches but only ten branches can be specified for any specific duct. This procedure poses some limitations in the SPIDS code. For instance, reflected shock waves in branch ducts that propagate from a branch duct entrance back into a main duct cannot be accounted for; when using the code, one should therefore record the pressure time history at a branch duct entrance so that any significant reflected shock waves can be detected. In the case of high explosive shock waves it is the authors experience that a reflection from a duct closed end is attenuated substantially by rarefaction and wall friction effects when the wave reaches the duct inlet, i.e., the reflected wave has usually a much lower overpressure than the initial shock wave. Another limitation also is that the losses of a shock wave as it passes by a branch duct is not accounted for which, of course, yields a conservative shock wave prediction; Ref. 1 shows an approximate method for accounting for shock wave losses due to passing a branch junction for exponential waves.

A high explosive input wave is approximated by a step overpressure at the wave front followed by an exponential decay which can be with or without a negative phase. Inputting a series of five pressure waves is possible. The relationship that is used for the pressure wave is:

$$P_s = P_a + P_{so}\ e^{-B_1\tau}(1 - A_1\tau) \qquad (1)$$

where

$$\tau = \frac{t}{D_p}$$

t = time
P_a = ambient pressure
D_p = duration of positive pressure phase
P_{so} = shock peak overpressure
A_1, B_1 = wave constants.

If the constant A_1 is zero the wave will have no negative pressure phase, B_1 is taken as one, and D_p then becomes the initial slope time intercept of the wave, t_i.

A classical nuclear blast wave at the inlet to a main duct can be specified in the form of Ref. 6. Either a surface burst or an air burst at a given slant range can be specified [7]. The relationship for pressure, for the nuclear wave is given below.

$$P_s = P_a + P_{so}\left[A_1 e^{-B_1\tau} + A_2 e^{-B_2\tau} + A_3 e^{-B_3\tau}\right](1-\tau) \tag{2}$$

where

$\tau = (t - t_s)/D_p$
t = time from detonation
t_s = shock arrival time
D_p = duration of positive pressure phase
P_{so} = shock peak overpressure at $t = t_s$

The quantities A_1, A_2, A_3, B_1, B_2, and B_3 are constants for which values are given in Refs. 6 and 7. In addition to a relationship for the surface pressure (P_s), relationships for the dynamic pressure (Q_s) and the temperature (T_s), are required.

$$Q_s = Q_{so}\left[A_4 e^{-B_4\omega} + A_5 e^{-B_5\omega}\right](1-\omega)^2 \tag{3}$$

$$T_s = T_{so}\left(\frac{t}{t_s}\right)^{B_6} \tag{4}$$

where

$\omega = (t - t_s)/D_u$
D_u = duration of positive velocity phase
Q_{so} = peak dynamic pressure
T_{so} = shock temperature at $t = t_s$

A blast wave from a high explosive detonation within a system of ducts is determined empirically using the scale model test data described in Ref. 8. The shape of the blast wave is determined, using the exponetial form (1), from the overpressure, P_{so}, the wave impulse, I, and the wave positive duration, D_p. These parameters have the form,

$$P_{so} = C_1\left(\frac{Q}{V_t}\right)^{n_1}$$

$$I = C_2\left(\frac{Q}{A_j}\right)\left(\frac{Q}{V_t}\right)^{n_2} \tag{5}$$

$$D_p = C_3\left(\frac{Q}{A_j}\right)\left(\frac{Q}{V_t}\right)^{n_3}.$$

Q is the charge quantity, V_t is the volume swept by the blast wave and A_j is the duct area. The coefficients and exponents C_1, C_2, C_3, n_1, n_2, n_3 depend upon the blast chamber geometry. Relations (5) are the scaling relationships for the problem [8].

Simulation of a duct entrance, such as the side-on type entrance shown in Fig. 1, is achieved by evaluating the flow losses from point s outside the entrance to point e inside the entrance through the use of experimental data reported in Ref. 4 and Ref. 5. This flow loss is measured by the entropy increase from point s to point e. Assuming that the compressibility factor Z, gas constant R, and ratio of specific heats γ do not change significantly from point s to point e, this entropy can be expressed in terms of static variables as

$$Se - Ss = ZR \ln\left[\left(\frac{T_e}{T_s}\right)^{\frac{\gamma}{\gamma-1}}\left(\frac{P_s}{P_e}\right)\right] \tag{6}$$

and this entropy change in terms of stagnation variables is

$$Se - Ss = ZR \ln\left[\left(\frac{T_{te}}{T_{ts}}\right)^{\frac{\gamma}{\gamma-1}}\left(\frac{P_{ts}}{P_{te}}\right)\right] \tag{7}$$

In the above equation, T_s, P_s, T_e, and P_e are static temperatures and pressures at points s and e, respectively, and T_{ts}, P_{ts}, T_{te}, and P_{te} are stagnation temperatures and pressures. Equating relationships (Eqs. 6 and 7) yields a desired relation for the duct entrance static pressure, P_e, in the form

$$P_e = P_s\left(\frac{P_{te}}{P_{ts}}\right)\left[\left(\frac{T_e}{T_{te}}\right)\left(\frac{T_{ts}}{T_s}\right)\right]^{\frac{\gamma}{\gamma-1}} \tag{8}$$

In this relationship, γ is evaluated at point s. The stagnation pressure ratio can be expressed by the relation

$$\frac{P_{te}}{P_{ts}} = A(2) \quad \exp \quad (-A(1)M_s) \tag{9}$$

where M_s is the flow Mach number at point s, and A(1) and A(2) are empirical constants determined from the experimental data of Ref. 4 and Ref. 5. A plot of this experimental data for the side-on entrance is shown in Fig. 2, which shows the linear relationship between log (P_{te}/P_{ts}) and M_s.

The value of the empirical constants A(1) and A(2) in Eqn. 8 depends upon the geometrical configuration at the duct entrance, e.g., a side-on entrance, a T-junction, or a Y-junction, etc. Table 2 presents the values of A(1) and A(2) for the possible junctions.

Table 2. Duct Inlet Type and Parameters

Type of Inlet	Value of loss coefficient A(1)	A(2)
No inlet loss	2.3026	1.00
Surface side-on	1.1398	1.24
Surface face-on	-0.1400	1.30
T-junction, side transmission	1.2296	1.14
T-junction, through transmission	0.3408	0.99
T-junction, reverse transmission	0.5699	1.07
45 Degree Y-junction	0.6102	1.00
Cross-junction, side transmission	1.1997	1.02
Cross-junction, through transmission	0.2600	0.93
Surface side-on, 50 deg. air burst	0.6102	1.52
Surface side-on, 60 deg. air burst	0.5089	1.61
Surface side-on, 70 deg. air burst	0.3401	1.61
Surface side-on, 80 deg. air burst	0.1200	1.56
Surface side-on, 90 deg. air burst (same as surface face-on)	-0.1400	1.30

Shock wave attenuation due to viscous friction at the walls of a duct is calculated. A friction factor for a smooth wall used in the calculations is determined by the flow state in each finite difference zone. The Reynolds number is calculated in each zone and the friction factor for the zone is determined from the relation

$$f = 0.176(Re)^{-0.27}(Pr)^{0.48} \tag{10}$$

The Reynolds number is defined in this application as $Re = \rho Du/\mu$, where ρ is the air density, u is the flow particle velocity, μ is the absolute viscosity, and D is the duct diameter. The parameter Pr is the pressure ratio across the initial shock wave at the duct inlet. The values of the coefficient and exponents were determined by comparing the computer code pressure attenuation predictions to the experimental shock tube data reported in Ref. 9 for smooth wall ducts. A comparison of the SPIDS code prediction of peaked shock wave attenuation with the experimental data is given in Fig. 3.

A constant value of friction is used in the program for ducts with rough walls. The friction factor depends upon the roughness of the wall and is a function of the wall roughness ratio which is the ratio of average wall protrusion height to duct diameter, ϵ/D. There is considerable variation in the data for friction factors for rough wall ducts as noted in Ref. 5. The equation that is used for the friction factor in terms of $\sqrt{\epsilon/D}$, which is the variable used in some references, using Ref. 10 data, is

$$f = 0.016 + 0.00491\sqrt{\epsilon/D} + 0.258(\sqrt{\epsilon/D})^2 \tag{11}$$

The SPIDS code will predict shock wave pressure change due to the change in the cross section area of a duct. A comparison of this prediction with experimental data for an area increase is presented in Fig. 4. The predictions are compared with shock tube data [11] and the full scale data of the DIAL PACK [12] experiment where the wave source is a 500 ton TNT explosion in air. This comparison shows that the code adequately predicts shock attenuation due to an area increase in a duct.

MICROCOMPUTER BASED PRE-PROCESSOR AND POST-PROCESSOR PROGRAMS

Two microcomputer programs have been written to simplify and reduce the work required to utilize the SPIDS computer code when analyzing a problem concerned with shock wave propagation

in ducts. A pre-processing program that generates the SPIDS input files and a post-processing program that creates plots from the a SPIDS output file are described in this section. Both of these programs are written in the Turbo Pascal language and are compatible with an IBM-AT microcomputer. The pre-processing program is named SPIDS1 and the post-processing program is named SPIDS2. Both programs are written in an interactive menu style.

The SPIDS1 program generates an input file for computer code SPIDS. The program is divided into three primary operations: 1) problem editing, 2) microcomputer data file control, and 3) terminating or quitting the input data file program and return to the computer operating system. A 'pull down' menu is activated when one of the above selections is made. This program greatly simplifies the use of the SPIDS code. All nuclear parameters of Ref. 6 and Ref. 7 are 'built into' the program as well as the junction loss parameters. For illustration of SPIDS1, the duct geometry selection screen is presented in Fig. 5.

The SPIDS2 program processes the output file of the computer code SPIDS. The program is divided into four primary operations: 1) name file to process, 2) plot on the computer screen, 3) plot on an external plotter, and 4) quit and return to the operating system. A "pull down" menu is activated when one of the above selections is made. Two curves or a single curve can be plotted on the computer screen. The curve options that are available are as follows: overpressure, temperature, dynamic pressure, and a shock location index versus time at given locations or versus location in the duct at given calculation cycles (or times); the impulse growth versus time at the given locations, which is on the same graph as overpressure when using a plotter; maximum values of overpressure, temperature, and dynamic pressure versus location in the duct for the time of the computation; the time the maximum values of overpressure, temperature, and dynamic pressure occur versus location (for shock arrival time); and the value of maximum impulse versus location and the inlet pressure versus time. Any of these curves can be plotted by an external plotter.

CODE OUTPUT EXAMPLE

The capability of the SPIDS code is illustrated through an example. The example is the shock wave from a conventional high explosive propagating into an air intake shaft (Fig. 6). The shock wave overpressure inside the system side-on entrance is 1650 psi and the wave initial slope time intercept is 0.287 milliseconds. A selected SPIDS output curve plotted using the SPIDS2 post-processing program is given in Fig. 7. Fig. 7 shows the pressure time history in the main duct at the location of the branch duct. The figure shows the initial shock wave and the shock wave reflected from the end of the main shaft.

CONCLUSIONS

The SPIDS computer code can be used to calculate the propagation of blast waves in systems of air ducts of constant or variable cross section. Branched ducts may be analyzed by sequential application to each branch and branch inlet losses are included empirically. Peak overpressures of reflected waves which follow the primary wave in a branch are somewhat higher than the real case because some energy losses of the reflected wave at the branch inlet junction are neglected. However, all losses in the primary wave are included at a branch inlet. Blast wave attenuation due to friction at walls is included through a variable wall friction factor with the friction factor relation determined empirically through experimental shock tube data.

ACKNOWLEDGMENT

The development of computer code SPIDS was sponsored by the U.S. Army Corps of Engineers, Omaha District under contract numbers DACA4588P0121, DACA4587PO153, and DACA4582M2881.

REFERENCES

1. R.H. Fashbaugh and J.W. Muran, "Shock Propagation in Ducting Systems," U.S. Army Corps of Engineers, Omaha District, contract report DACA4588PO121, June, 1990.
2. R.D. Richtmyer and K.W. Morton, Difference Methods for Initial-Value Problems, pp. 288-388, Interscience Publishers, 1957.
3. F.R. Gilmore, "Equilibrium Composition and Thermodynamic Properties of Air to 24,000 K," Rand Corp. Research Memorandum RM-1543, Aug. 1955.
4. Ballistic Research Laboratory Shock Tube Staff, "Information Summary of Blast Patterns in Tunnels and Chambers," BRL Memorandum Report No. 1390, Mar. 1962.
5. A.R. Kriebel et al., "Air Blast in Tunnels and Chambers," DASA 1200-II Supplement 1, Oct. 1972.
6. H.L. Brode, "A Review of Nuclear Explosion Phenomena Pertinent to Protective Construction," Rand Corp. Report No. R-425-PR, May 1964.
7. R.E. Crawford et al., "The Air Force Manual for Design and Analysis of Hardened Structures," AFWL-TR-74-102, Oct. 1974.

8. "Underground Ammunition Storage I, Test Programme, Instrumentation and Data Reduction," A. Skjeltorp, T. Hegdahi and A. Jennsen, Tech. Note No. 80172, Norwegian Defense Construction Service, September 1972.
9. G.A. Coulter, "Attenuation of Peaked Air Shock Waves in Smooth Tunnels," BRL Memorandum Report No. 1809, Nov. 1966.
10. G.A. Coulter, "Attenuation of Shock Waves in Roughened Tunnels," BRL Memorandum Report No. 1903, Jan. 1968.
11. H.R. Bredfeldt et al., "Measurement of Shock Wave Attenuation in Various Duct Components - Phase II and III," Stanford Research Institute Report No. C-0096, July 1968.
12. D.E. Williams and R.H. Fashbaugh, "High Explosive Field Test of a Hardened Air Entrainment System," NCEL Technical Note N-1181, Oct. 1971.

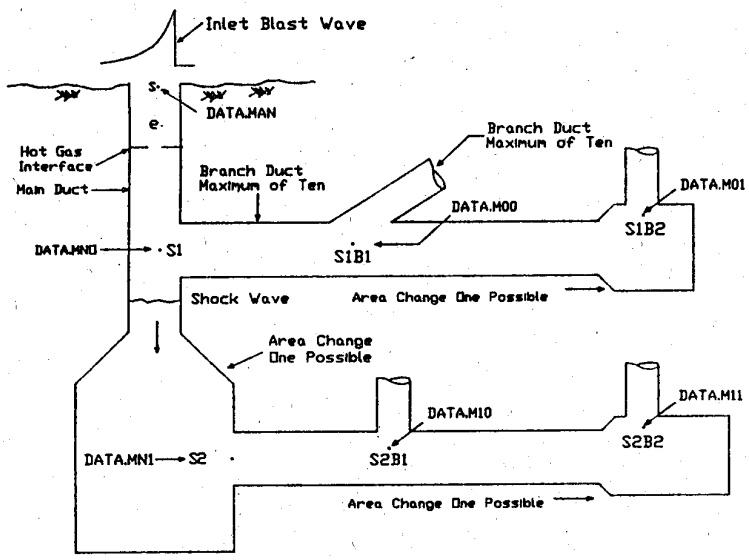

Fig. 1. Sketch of an example ducting system from [1].

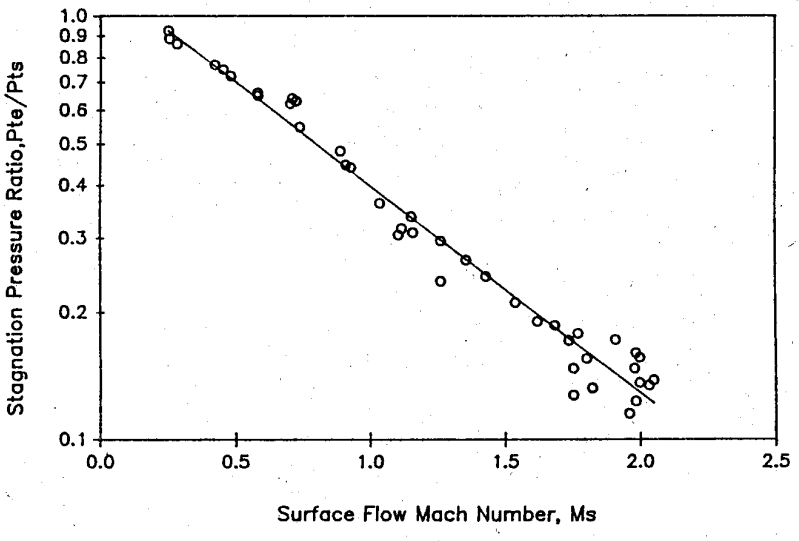

Fig. 2. Stagnation pressure loss versus surface Mach number for side-on entrance.

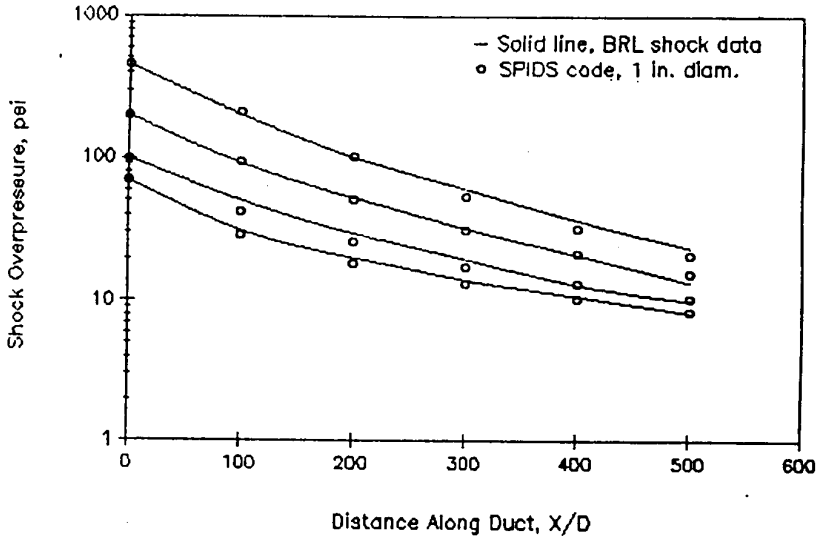

Fig. 3. Shock wave attenuation, computed results compared with data; smooth wall.

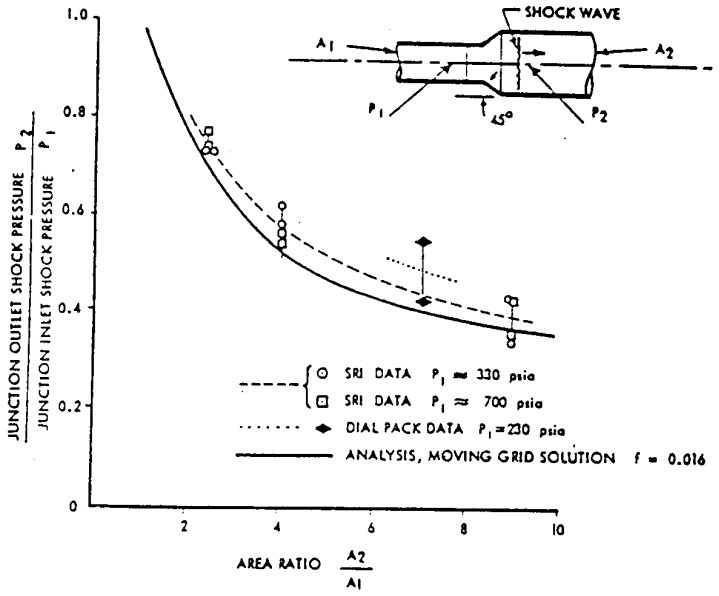

Fig. 4. Effect of area change on shock pressure.

Duct selection - Total ducts: 2

Current branch	: Main			Inlet Zone Size	: Default	
Entrance	: Surface side-on			Altitude	: 0.00	
Length	: 56.00	Diameter	: 9.84	Exit	: Closed	
Roughness	: 0.0000	Zones	: 100	Cycles	: 3000	
Taper Start	: 43.00	End	: 46.00	End Dia.	: 21.65	

Zone data stored every 100 cycles, format : simplified
Time data stored every 10 cycles, format : simplified

Branch point	Location	Type	Plot time history data
1	1.00	No Junction	Yes
2	7.00	No Junction	Yes
3	13.00	No Junction	Yes
4	20.00	No Junction	Yes
5 active	36.00	T - Side	Yes
6	43.00	No Junction	Yes
7	44.50	No Junction	Yes
8	46.00	No Junction	Yes
9	50.00	No Junction	Yes
10	55.00	No Junction	Yes

Active Function Keys

1:Abort 3:Exit 5:Help 6:Edit Alt FN: Goto N

Shock Propagation in Ducting Systems - Input Program

Fig. 5. Duct selection computer screen in SPIDS1.

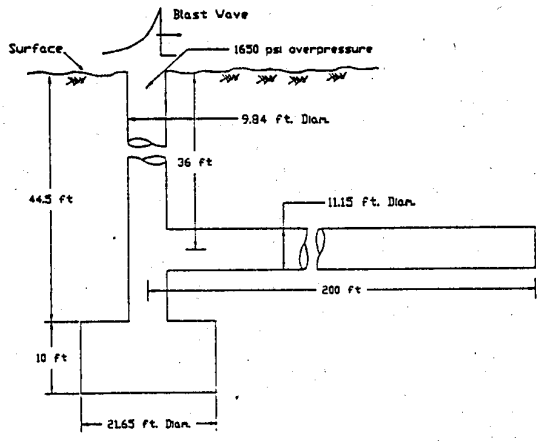

Fig. 6. Typical air intake shaft.

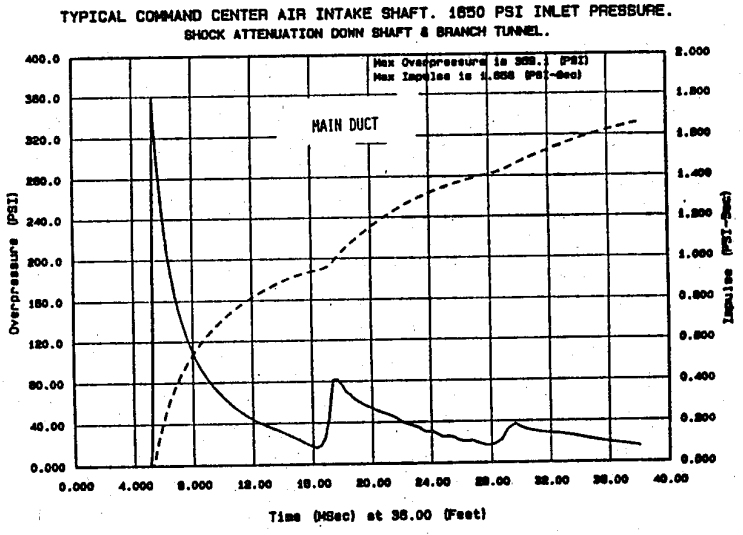

Fig. 7. Pressure time history plot in a main duct from SPIDS2.

Experiments to validate the structural behaviour of a new laboratory for ballistic research

W.P.M. Mercx and J. Weerheijm

TNO Prins Maurits Laboratory
P.O. Box 45
2280 AA Rijswijk, The Netherlands

ABSTRACT

Very recently, a new laboratory for ballistics came into service, which offers new experimental possibilities for the TNO Prins Maurits Laboratory. In the fully closed facility, projectiles with a calibre of 76 mm can be fired from a firing room, through a tunnel into a target room. The target room is designed for a combined amount of explosives of both projectile and target of 25 kg TNT. Two very large blast dampers, filled with shingle, are placed on top for a slow release of the overpressure.

The demand of the high explosive resistance led to a rather unique construction of the target room. As specific experience was lacking, a number of assumptions were made on the structural behaviour of the facility subjected to the complex and extreme dynamic load.
The dynamic load of the structure was determined with experiments on a scale 1 : 6,3 of the target room.

To obtain certainty whether or not the facility fulfilled the requirements, it was decided that experiments should be carried out with an amount of explosives up to the design limit, before the building was put into service. This offered also the unique opportunity to check the assumptions for the structural behaviour. Therefore, a total of 27 strain gauges were welded to the steel reinforcement at critical sections, during construction.

The paper will give a brief overview of the lay-out of the facility. The experiments will be described and the results of the measurements will be discussed, especially:

- the internal pressure measurements with regard to the scaled tests and the design loads
- the strain measurements with regard to the assumed overall dynamic behaviour, the transition of the cylindrical shapes side-walls to the hemispherical head wall and the internal labyrint walls meant for pressure reduction
- the displacement measurements with regard to the connection of the target room and the tunnel
- the external pressure measurements with regard to the noise levels in the vicinity of the facility and the proper functioning of the blast dampers.

Parameterstudien zum Luftstoß in Expansionskammern und Zuführungskanälen

G. Scheklinski-Glück
Ernst-Mach-Institut, Freiburg

Kurzfassung

Ein aus Modellversuchen empirisch abgeleitetes System von Näherungsformeln erlaubt die Berechnung der Blastparameter Druck, Impuls und Druckdauer sowie kompletter Druck-Zeit-Verläufe in einer Expansionskammer und den Zuführungskanälen, wenn im Eingangsbereich eine konventionelle Ladung detoniert. Die Studie dient zur ingenieurmäßigen Bemessung von Druck- und Ventilationsabschlüssen. Im vorliegenden Teil wird die in früheren Versuchen auftretende Fixierung des Verhältnisses von Kammervolumen zu Stollenquerschnitt von 1000 m^3 zu 10 m^2 auf beliebiges Kammervolumen erweitert. Damit wird die aufwendige Untersuchung generalisiert und erlaubt Parametereinfluß-Studien verschiedenster Baugeometrien und Belastungsfälle, um die Druckbelastung zu minimalisieren oder, für bestehende Anlagen, exakt zu berechnen.

1. Einleitung

In einer vorausgegangenen Untersuchung [1] wird der prinzipielle Druck-Zeit-Verlauf in einer Expansionskammer durch eine Parabel mit anschließender Exponentialfunktion (s. Bild 1) beschrieben. Bild 2 zeigt die Güte des gewählten Approximationsmodells am Vergleich mit einer typischen Meßkurve. Es wurden verschiedene Kammerformen (Würfel, lange flache Quader, kurze hohe Quader) mit gleichem Volumen untersucht, auch Kammern mit zwei Zuführungskanälen (s. Bild 3).

In der vorliegenden Studie wird die Ableitung der empirischen Formeln für Kammern mit dem doppelten oder dreifachen Volumen bei einem Zuführungskanal beschrieben.

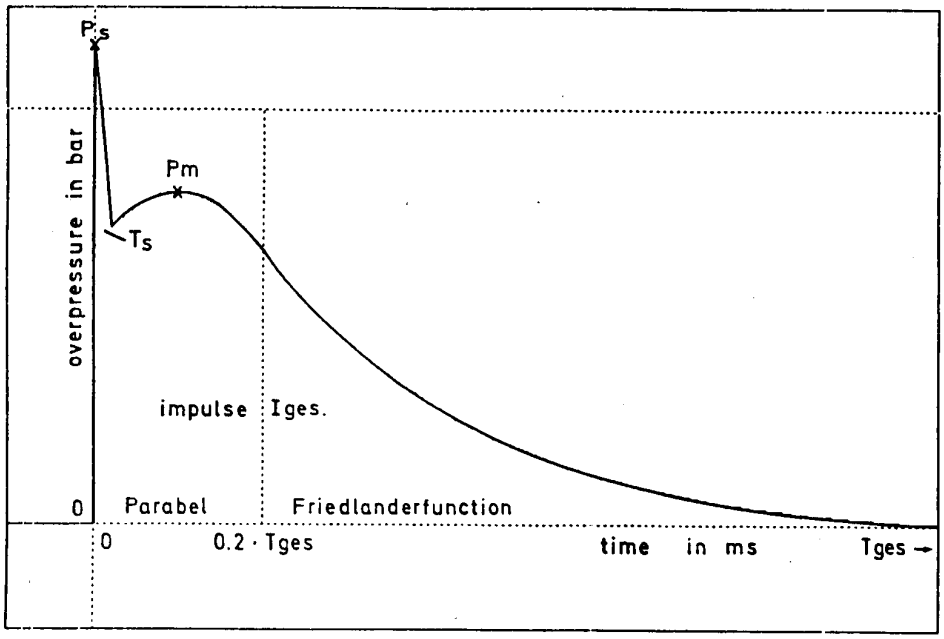

Bild 1
Prinzipieller Druck-Zeit-Verlauf in der Expansionskammer. Approximation durch eine Parabel mit anschließender Exponentialfunktion

Principle pressure-time history inside an expansion chamber. Approximation by a parabola and annexed Friedlander function

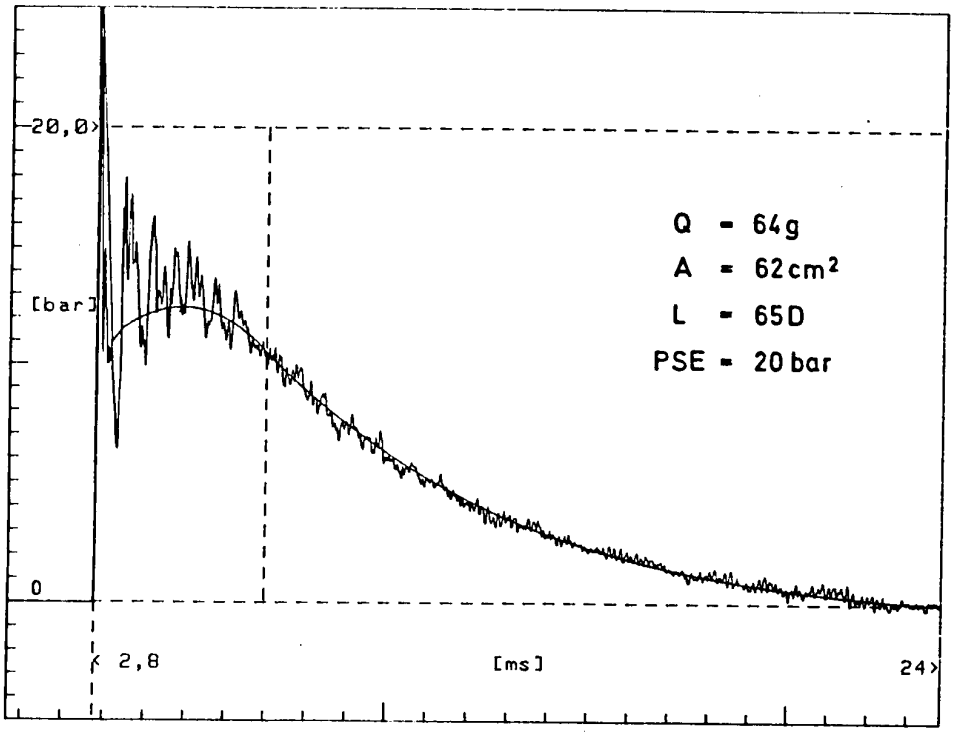

Bild 2
Typische Druck-Zeit-Meßkurve in einer Expansionskammer im Vergleich mit der aus Näherungsformeln berechneten glatten Kurve

Comparison of measured and calculated pressure-time histories inside a chamber

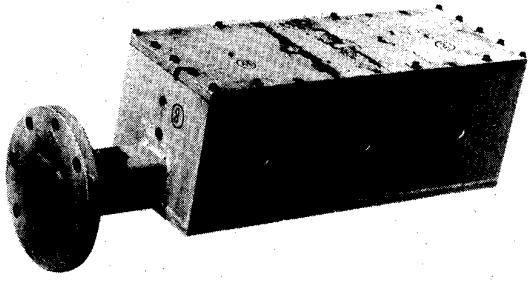

Quader mit dreifachem Volumen (V11)

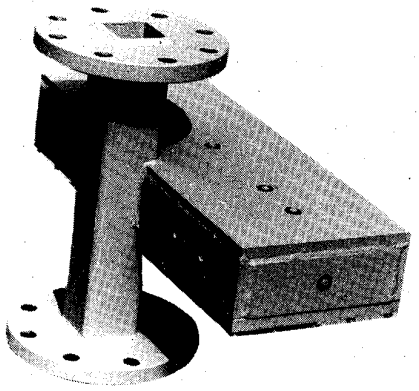

Quader kurz, flach Stollen seitlich (V10)

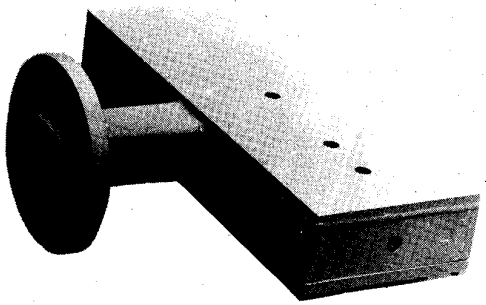

Quader kurz, flach (V9)

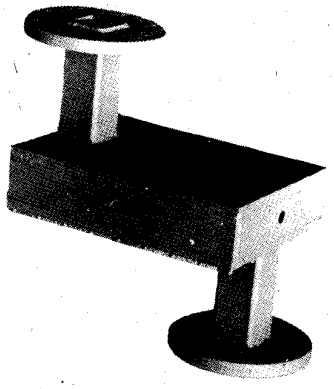

Quader lang, flach mit zwei Stollen (V8)

Modelle der untersuchten Expansionskammern

Bild 3

2. Ableitung der Näherungsformeln für beliebiges Volumen

Bild 4 zeigt den maximalen Fülldruck Pm (vgl. Bild 1) über der skalierten Ladung Q/D^3, mit Q = Lademenge und D = Tunneldurchmesser. Für jede der drei verwendeten Ladungen wird der Druck am Kammereingang (PSE) durch die entsprechende Tunnellänge auf PSE = 20 bar, 50 bar, 80 bar und 100 bar eingestellt. Für die vier PSE-Werte ergeben sich vier parallele Gerade in der gewählten doppellog Darstellung

$$Pm = A \cdot (Q/D^3)^{0.576} \qquad (1)$$

wobei 0.576 die Steigung der Geraden ist.

Das untersuchte Kammervolumen beträgt 1000 m^3 bei einem Stollenquerschnitt von 10 m^2. Je vier weitere Geraden zeigen die Ergebnisse für 2000 m^3 (2 x Vol.) und 3000 m^3 (3 x Vol.). Alle Geraden haben die Steigung von Gleichung (1).

Die Achsenabschnitte A1 bis A4 hängen jeweils vom Kammereingangsdruck PSE ab. Dies ist in Bild 5 dargestellt. Es ergeben sich drei parallele Geraden für einfaches, doppeltes und dreifaches Volumen mit der Gleichung

$$A = F\,(Vol.) \cdot PSE^{0.415} \qquad (2)$$

Der Achsenabschnitt F hängt von der Kombination Kammer-Volumen und Stollenquerschnitt ab.

Durch die Einführung des dimensionslosen Parameters

W/T = Wandfläche des volumengleichen Kubus / Tunnelquerschnitt
= $(\sqrt[3]{Vol.})^2$ / $D^2/4 \cdot \pi$

gelingt schließlich die Formulierung des Volumen-Einflusses (s. Bild 6).

Die drei untersuchten Volumina betragen 1000, 2000 und 3000 m^3. Bei einem Tunnelquerschnitt von 10 m^2 ergibt sich für den "Volumen-Parameter" W/T:

1 x Vol.: $W/T = (\sqrt[3]{1000\ m^3})^2 / 10\ m^2 = 10$
2 x Vol.: $W/T = (\sqrt[3]{2000\ m^3})^2 / 10\ m^2 = 15.9$
3 x Vol.: $W/T = (\sqrt[3]{3000\ m^3})^2 / 10\ m^2 = 20.8$

Bild 4
Zur Ableitung empirischer Formeln:
Mittelwerte der Meßergebnisse für den Fülldruck in Abhängigkeit von der skalierten Ladung (Kammer mit Volumen V, 2 x V und 3 x V)

Development of empirical formulae:
Max. pressure in the chamber versus scaled charge for a chamber with volume V, 2 x V and 3 x V

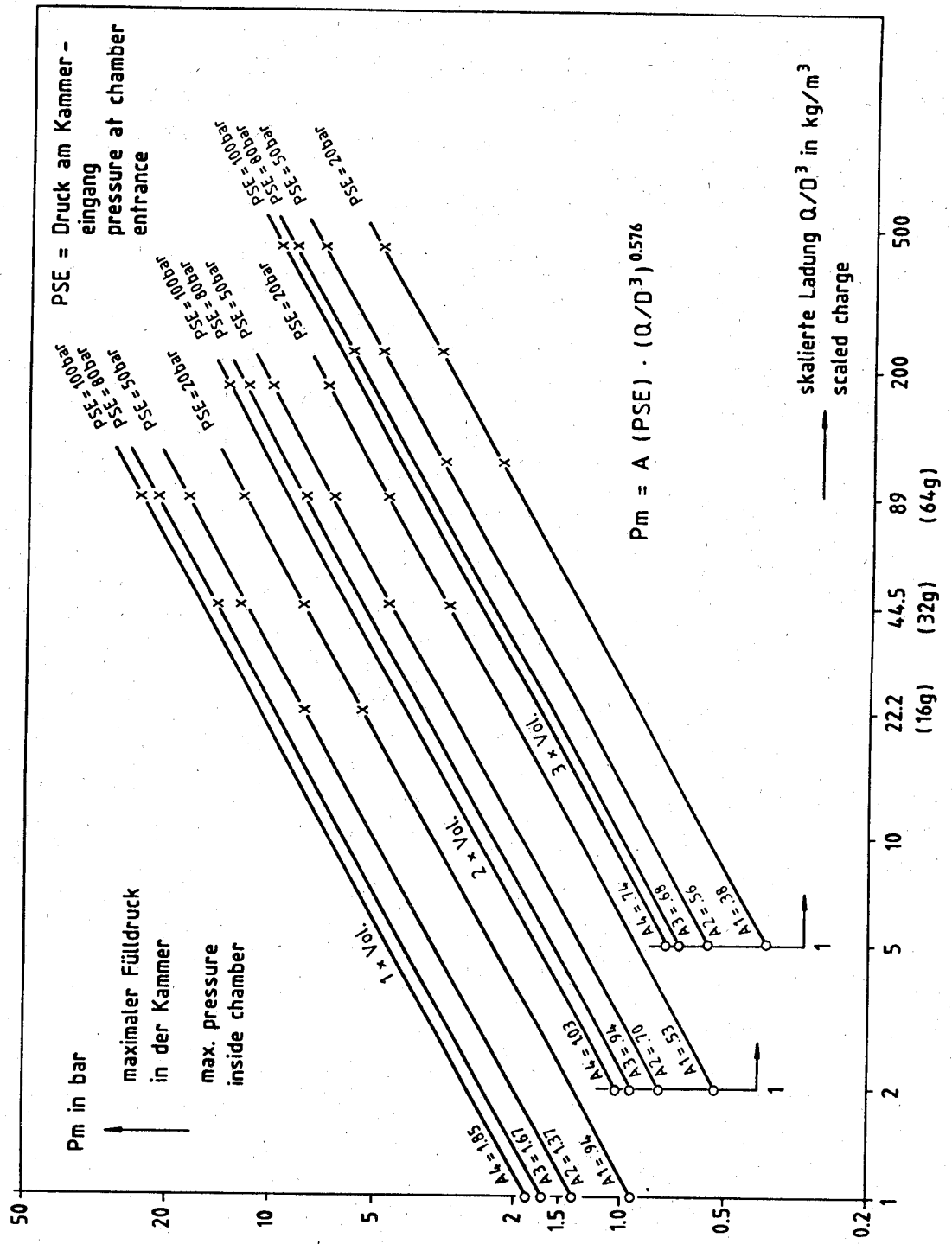

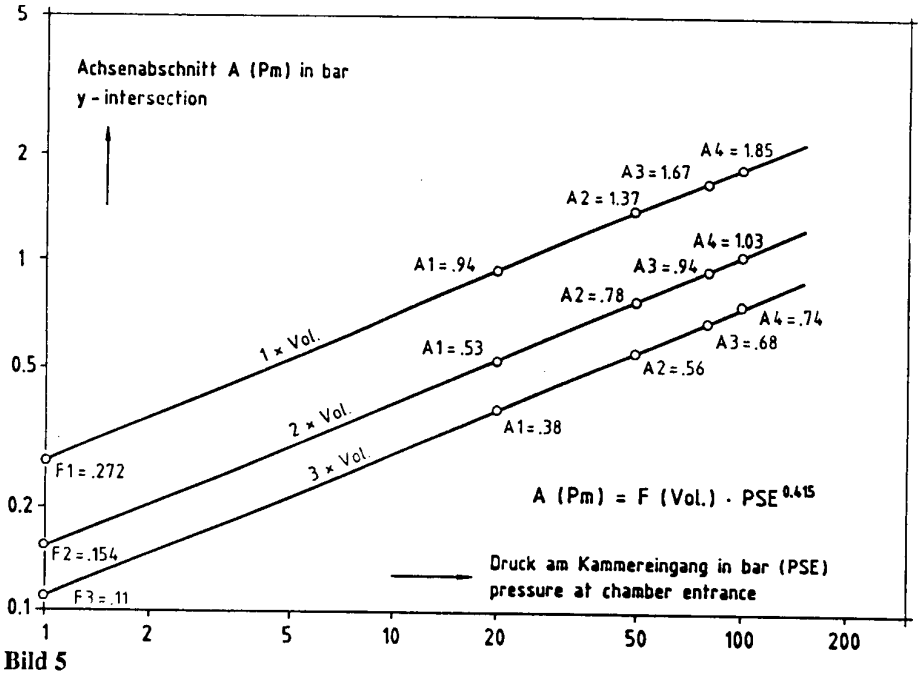

Bild 5
Zur Ableitung empirischer Formeln:
Achsenabschnitt A (Pm) aus Bild 1 gegen Kammereingangsdruck PSE für Kammern mit Volumen V, 2 x V und 3 x V

Development of empirical formulae:
y-intersection A (Pm) versus entrance pressure PSE for a chamber with volume V, 2 x V and 3 x V

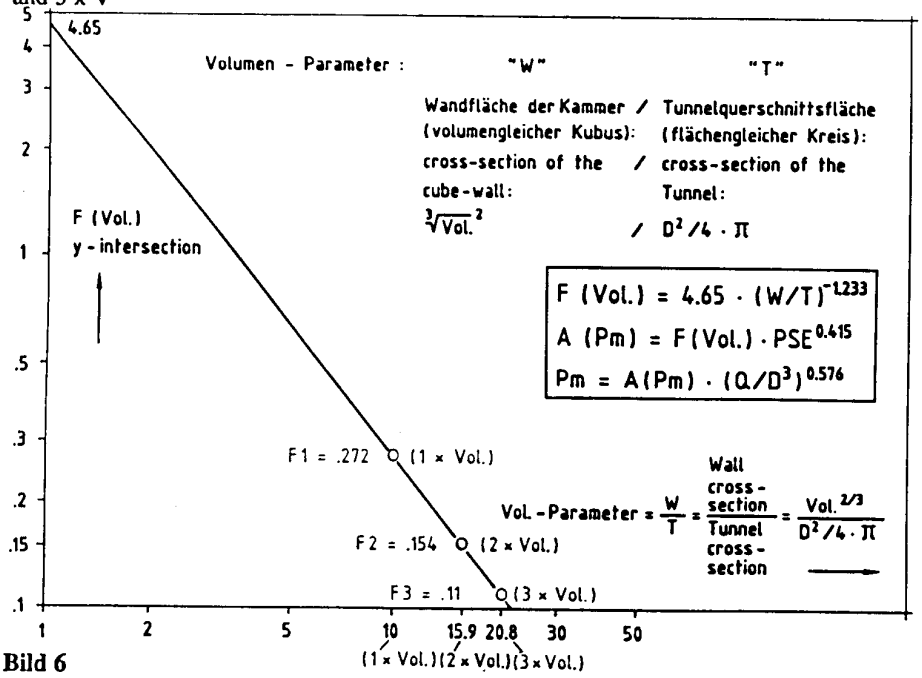

Bild 6
Zur Ableitung empirischer Formeln:
Einführung eines dimensionslosen Parameters für den Sprung der Fläche vom Stollenquerschnitt auf die Kammerwand am Eingang. Damit wird das Kammervolumen (des volumengleichen Kubus) an den Stollenquerschnitt (des flächengleichen Kreises) gekoppelt und frei wählbar gemacht.

Development of empirical formulae:
A dimensionless parameter for the jump in cross-section from the tunnel to the chamber wall allows to create a formula for any volume.

Über W/T ist in Bild 6 die unbekannte Größe F (Vol.) aus Gleichung (2) dargestellt.

Es ergibt sich

$$F\,(Vol.) = 4.65 \cdot (W/T)^{-1.233} \tag{3}$$

Durch Einsetzen von Gleichung (3) in (2) und (1) ergibt sich eine empirische Näherungsformel für den Fülldruck in der Kammer

$$Pm = 4.65 \cdot (W/T)^{-1.233} \cdot PSE^{.415} \cdot (Q/D^3)^{.576} \tag{4}$$

Die Formeln für die Druckdauer Tges und den Impuls Iges (s. Bild 1) ergeben sich auf ähnliche Weise und lauten

$$Tges = 8.4 \cdot (W/T)^{1.16} \cdot D \cdot PSE^{-.255} \cdot (Q/D^3)^{.32} \tag{5}$$

$$Iges = 16.6 \cdot D \cdot PSE^{.14} \cdot (Q/D^3)^{.85} \tag{6}$$

3. Gültigkeitsbereich

Für einen vorgegebenen Stollendurchmesser D ist die skalierte Ladung Q/D^3 gültig von 1 bis 100 [2]. Das Kammervolumen berechnet sich nach Abschnitt 2 aus dem Parameter W/T, wie die folgende Tabelle zeigt.

Tunnelquer-schnitt in m^2	Tunnel Ø in m	skalierte Ladung $Q/D^3 = 1$ von kg		skalierte Ladung $Q/D^3 = 100$ bis kg	Kammervolumen $W/T = 10$ von m^3		Kammervolumen $W/T = 20.8$ bis m^3
3	1.95	7.5	-	750	165	-	500
10	3.57	45	-	5000	1000	-	3000
20	5.05	128	-	12000	2800	-	8500
50	7.98	500	-	50000	11000	-	33000

4. Parameterstudien

Ein BASIC-Programm ist verfügbar [2], welches auf der Basis der obigen Näherungsfunktionen die Blastparameter berechnet und an jeder interessierenden Stelle im Stollen-/Kammersystem den Druck-Zeit-Verlauf konstruiert. Der Gültigkeitsbereich ist in Abschnitt 3 gegeben. Mit Hilfe des Programms können Parameterstudien durchgeführt werden, um zu testen, wie die Druckbelastung variiert für

- verschiedene Ladungen (bei fester Stollen-/Kammerkonfiguration)
- verschiedene Stollenquerschnitte
- verschiedene Stollenlängen und rechtwinklige Verzweigungen
- verschiedene Kammervolumen

Für den letzten Fall zeigt Bild 7 ein Beispiel. Der in die Kammer einlaufende Druckstoß wird von PSE = 20 bar auf 5,6 bar durch die Wellenexpansion in einer 1000-m^3-Kammer reduziert; bei 2000 m^3 erfolgt Reduktion auf 3,2 bar und bei 3000 m^3 auf 2,2 bar.

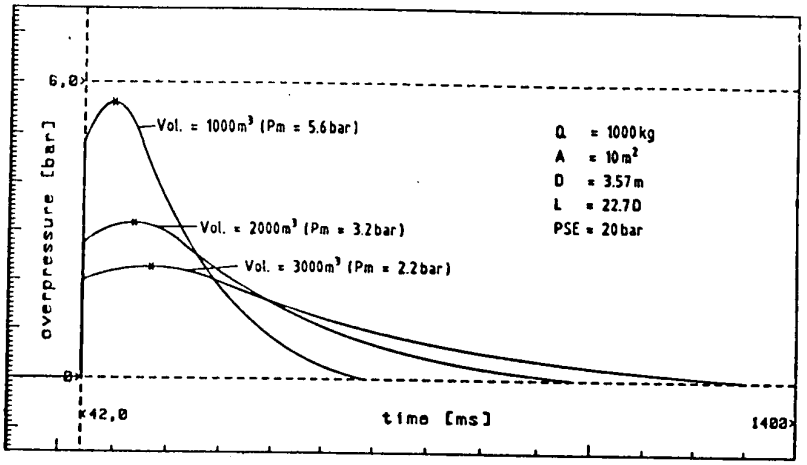

Bild 7
Parameterstudie:
Einfluß des Kammervolumens auf den Druck-Zeit-Verlauf in der Expansionskammer. Der Zugangstunnel hat 10 m^2 Querschnittsfläche (ϕ D = 3.57 m) und ist 22.7 D lang. Im Tunneleingang detonieren 1000 kg, die Druckwelle am Kammereingang hat 20 bar Spitzenüberdruck.

Parameter study:
Effect of the chamber volume on the pressure-time history inside a chamber. The tunnel cross section is 10 m^2, the tunnel length 22.7 D. The charge size is 1000 kg.

5. Literatur

[1] Scheklinski-Glück
Scale Model Tests to Determine Blast Parameters in Tunnels and Expansion Rooms from HE-charges in the Tunnel Entrance
Proceedings of the Fourth Intern. Sympos. on the Interaction of Non-nuclear Mun. with Structures, 1989

[2] Scheklinski-Glück, Mehlin
Ein Rechenverfahren zur Ermittlung von Luftstoßparametern in Stollen mit Expansionskammern bei der Detonation von Explosivstoffladungen im Stolleneingang.
Bericht E 19/89 des Ernst-Mach-Instituts, Freiburg, Germany

Druckstoßventile

Blast Valves

ANALYTICAL STUDY OF PASSIVE AIRBLAST ATTENUATION VALVES

Quentin A. Baker, Wilfred Baker Engineering, Inc.
Dr. Wilfred E. Baker, Wilfred Baker Engineering, Inc.
Dr. Christoph Y. Tuan, Wilfred Baker Engineering, Inc.

This analytical study addressed the feasibility of a passive airblast attenuation device for protection of personnel and equipment in protective structures from conventional weapon attack. The requirements imposed on the device were that it have no moving parts, reduce blast pressure and impulse by at least two orders of magnitude, and not restrict normal airflow more than currently available active blast valves. Such a device is attractive because of its potential as a low-cost low-maintenance item.

The literature was reviewed for references relating to airblast attenuation and flow loss through vents or restrictions of various configurations. Passive airblast valves were then analyzed to predict blast attenuation, flow loss performance and structural response. Devices considered were composed of common structural components, including nested and side-by-side angles of zees, louvers, interlocking I-beams, and perforated plates.

More data were available for shock losses through perforated plates and single orifices than for other configurations. This data base allowed complete design of an attenuation device consisting of a series of orifice plates with offset holes. A prototype design has been built and tested in a simulated above ground hardened structure, and provided excellent blast attenuation. Other configuarations will be analyzed more thoroughly and tested in an ongoing project.

Blast Valves - Unnecessary Expense or Vital Components in Structure Hardening

Ann-Sofie L.E. Forsberg

FortF - Royal Swedish Fortifications Administration
S-63189 Eskilstuna Sweden

ABSTRACT

In the art of fortification blast valves have major applications. Openings in a defence structure are potential weak points. To obtain a balanced hardening of a structure it is essential that the openings provide protection at the same level as the rest of the installation.

Whether there is a threat of nuclear (long duration) blast or blast from conventional weapons - which might be of short or long duration depending e.g. on geometry - there exists a great number of valves for different applications and protection levels.

The Research Department of FortF applies special test procedures for valves using a high-explosive driven shock tube. Varying the charge yield and the distance between charge and object facilitates modelling of the impinging shock wave within certain limits. For some testing applications the tube is open in the rear end resulting in a suction phase succeding the overpressure as in a real case.

The paper describes different kinds of blast valves and their applications for protective structures and gives examples of testing procedures.

Paper prepared for presentation at The International Symposium on Interaction of Conventional Munitions with Protective Structures, April 22-26 1991 in Mannheim, Germany.

THE BLAST WAVE

Introduction •

When a charge detonates in air, a glowing gas-cloud is created. It expands rapidly to a maximum, after which it immediately starts to decrease. The space-demanding gas-cloud during the expansion exposes the mass particles of the sorrounding air to a powerful shock followed by a suction phase. The shock is transmitted through the air like a wave motion with a steep front, i.e. a blast wave.

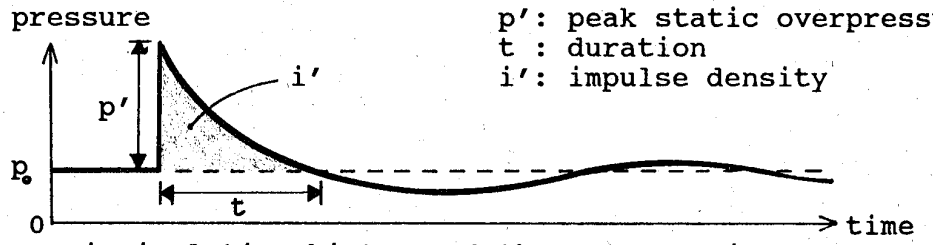

Principal time history of the pressure in a measuring point that is passed by by a blast wave.

Long Duration Blasts from Conventional Weapons

In principal, nuclear weapons give rise to long duration blast waves, while short duration blasts emanate from conventional weapons. Conventional weapons, however, can also be the cause of blast waves of considerable duration, depending on the surrounding geometry.

When a blast wave is allowed to expand freely in three dimensions its peak pressure, p', and impulse density, i', decrease while the duration increases with the distance from the burst point.

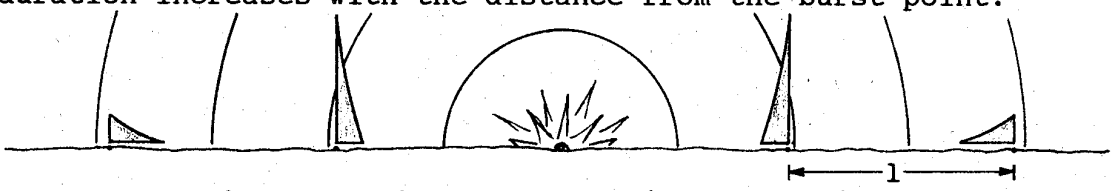

Change of the blast wave in a free field

If the expansion of the blast is limited, for example to two dimensions (between two walls) or to one dimension (in a tunnel), the pressure will decrease more slowly and the duration increase faster than in free expansion.
In this way also conventional weapons can cause blasts with long duration. The effect is even more pronounced in a tunnel with an area reduction.

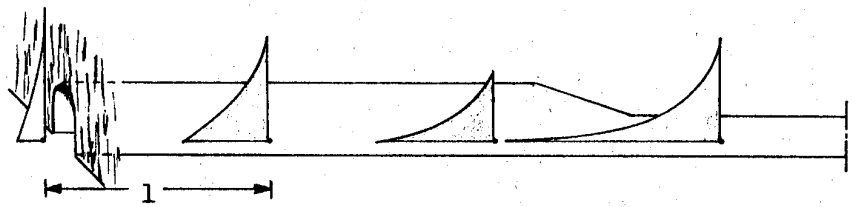

Change of the static blast wave in a tunnel with area reduction

Example of Blast Loads against Barriers in a Tunnel

The magnitude of the load on a barrier depends on its location in the tunnel.

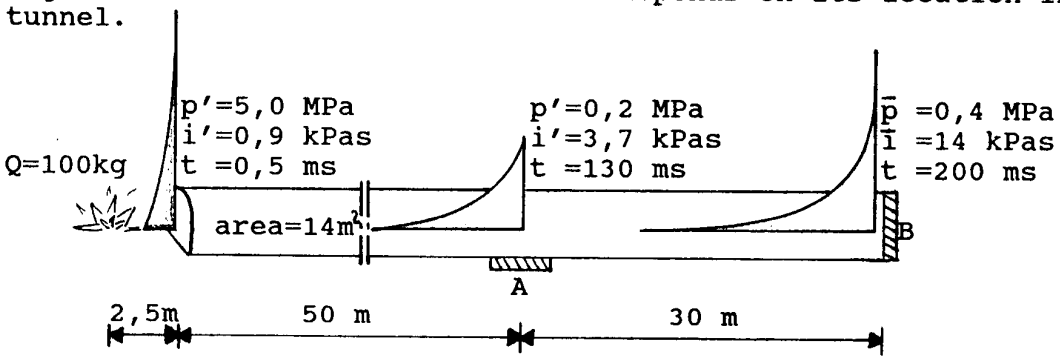

Barrier A is exposed to the side-on pressure, p',while B is exposed to the fully developed reflexion pressure, $\bar{p}$.

The impulse density, i'= 3,7 kPas, that barrier A is exposed to can be compared with the fact that fans and filters inside an air-intake can stand up to only hundreds of Pas.
To prevent damage to vulnerabel equipment inside the structure, it is obviously necessary to attenuate the blast before it passes through the openings.

A protective structure can not be stronger than its weakest point, and to obtain a balanced hardening it is essential that the openings provide protection at the same level as the rest of the installation.

Attenuation of the Blast

As the example above shows, it is possible to avoid reflexion load against a barrier if the tunnel is extended to pass by the barrier in to a so-called blast-pocket. Another method is to let the tunnel continue all the way out of the rock. Then the blast will blow straight through without being reflected.
Also an area enlargement in front of the barrier will attenuate the blast.

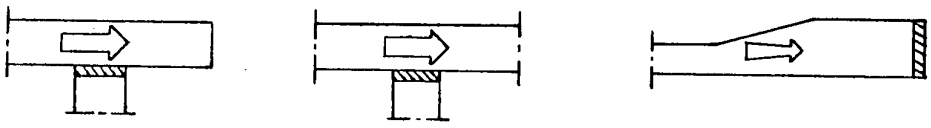

Blast-pocket *Blow through* *Area enlargement*

A considerable part of the passing blast wave will penetrate air intake and exhaust openings and might destroy expensive air handling equipment inside, if they are not provided with some sort of blast attenuation device.
In order to reduce the incident pressure on weak points in a barrier, different designs for so-called grid-effects can be used.

Grid-effects occure when a blast wave impinges against a wall with pervading holes. The wave turns partially reflected and the peak pressure immediately behind the wall comes to be lower than the incident pressure.

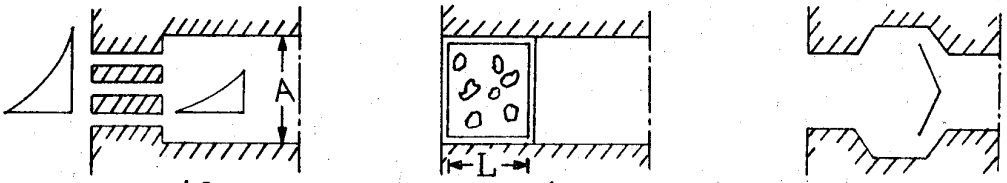

A **grid** consists of a wall with many pervading holes. The pressure reduction over it depends on the ratio between the total hole area A_g and the cross-section area A. A reduction of the A_g/A-value lessens the peak pass-through pressure.

A **rockfilter** functions as a grid, but the total hole area is considerably smaller. The pressure reduction here depends on the filter length L and the rock size average, d. An increasing L/d-ratio lessens the peak pass-through pressure.

Grids and rockfilters accomplish a good blast attenuation if the blast wave has short duration. At long durations the pressure in the space behind can become pumped up to a considerable size.

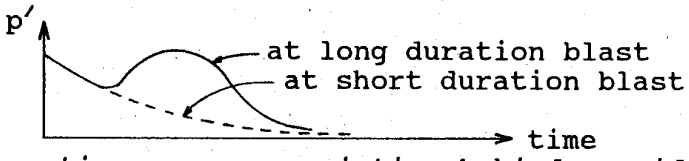

Schematic pressure variation behind a grid

A blast activated **valve** attenuates the incident blast wave in two different manners. During the initial part of the loading, a pressure reduction occures caused by the grid-effect. Meanwhile the closing components start to move, and when the valve closes, the remainder of the incident blast wave will become shut out. At a high peak pressure, rapidly closing valves only require some milliseconds to close.

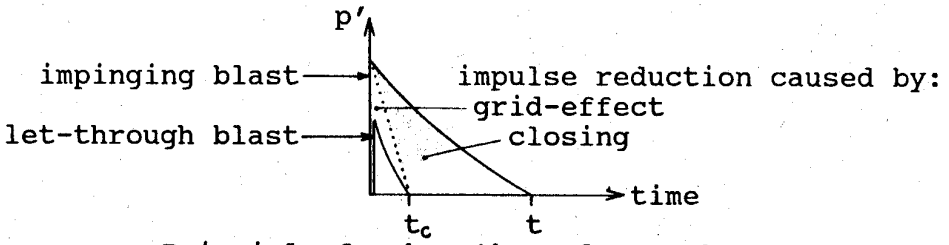

Principle for how the valve works

At **short durations** blast, a good protection can be provided by a grid or rockfilter. A rapid closing valve, though, gives better protection since it shuts out a part of the blastwave.
At blast durations near the closing time, however, the valve is not much more effective than a grid.

At **long duration** blast, a valve is superior to other attenuation devices, while cutting off most of the blast. A grid or rockfilter, however, can contribute to reduce the front pressure.

BLAST VALVE

Several different types of valves and concepts have been developed at FortF through the years. Reference /1/ and /2/ contain testresults for some recently studied valves. Experiences have also been achieved from many tests of valves by different manufacturers, e.g. /3/. The scope of this paper is for a number of reasons limited to principals, and it is focused on blast activated valves since this type can be used for a vast number of applications.

The closing component of the valve often consists of a disc. In other designs tubes or rectangular strips of spring steel are used to close the valve. One advantage with a tube-valve is that it can provide a greater air flow per unit area than a disc-valve.

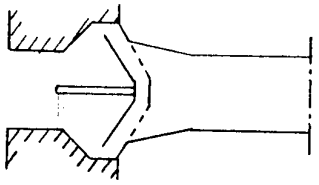

disc-valve

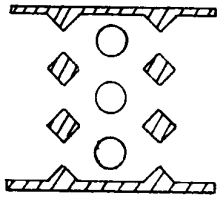

tube-valve

The disc or tubes are held in the ventilating position by springs. An incident blast exposes these components to a force to close against the housing. The disc / tube may close both inwards - during the overpressure phase of the blast -, and outwards - during the following suction phase. The springs return them to ventilation position after the passage of the blast wave.
A major advantage of blast activated valves is that they cause only a momentary interruption of the air supply. The disadvantage is that a part of the blast wave passes through the valve while it is closing. Light materials can facilitate rapid closing.

Head Criteria that Guide the Principal Design of a Valve

Desired **air flow** capacity at a certain pressure drop over a valve guides the size of it. Large flow capacity requires large slits and therefore big valves.
The disadvantage of a bigger valve that allows a big air flow is that it also lets through a bigger part of the blast wave. There are two reasons for this. A big slit creates less grideffect than a small one, and the reduction of the peak pressure is hereby smaller. The other cause is that bigger closing components give longer closing time, t_c.

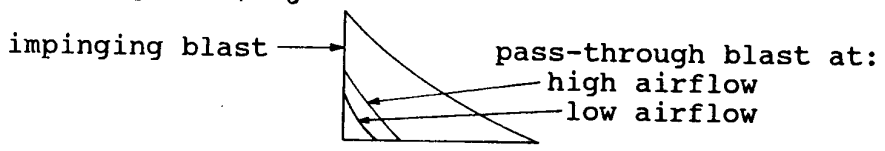

Pass-through blast, depending on airflow capacity of the valve

The desired **protection level** guides the choice of material for the valve, especially for the closing components. At high incident pressures a strong material is needed. A stroger material often means that the closing components become heavier and close more slowly. To achieve a high protection level one may, consequently, have to accept a bigger pass-through impulse.

The choice of material, however, does not only depend on the front pressure. The duration of the blast is also very important. A short **duration** blast contains less impulse density during the closing time of the valve than a long duration blast does.

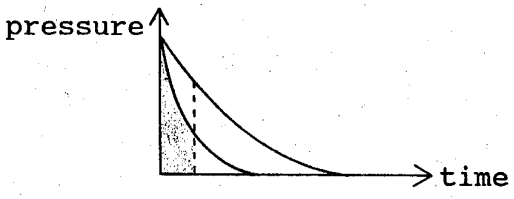

Impulse contents at different blast durations

When the closing components hereby are subjected to a lower average pressure during its closing, the hit velocity against the housing and thereby the deformations will be smaller. This makes it possible to change to a weaker and thereby often lighter material in the disc or tubes, which results in a shorter closing time and thereby a smaller let-through impulse.

Valves are Vital in Structure Hardening

Even at blast **durations about as long as the closing time**, valves are useful. Since the slit is decreasing all the time, the let through impulse will be smaller than at a plane hole.
In combination with a peak pressure reducing grid in front of the valve the protection level can be reduced. A lighter disc lessens the closing time and at least some parts of the incident blast will now be shut out.

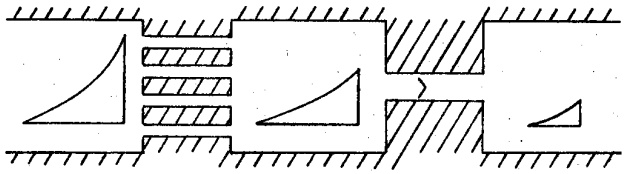

Attenuation combination at short duration blast

A damping chamber might be used behind the valve, big enough to attenuate the passing through impulse to an acceptable level.

At a **long duration** blast, the valve is irreplaceable, since a major part of the blast is shut out by it.
In combination with a weaker rapid closing valve behind it, the blast is reduced even more.

There exists a great number of valves for different applications and protection levels.
Whether there is a threat of nuclear (long duration) blast or blast from conventional weapons - which might be of short or long duration depending e.g. on geometry - valves can be used to reduce the penetrating part of the wave and thereby protect vulnerable equipment inside a structure.

The **cost** for the protective devices should be studied together with the costs for the equipment to be protected.

TESTING PROCEDURES

When a valve is to be tested against blastwaves, it can be done either with a full-scale test, or it can be done in a simulator, usually a shock tube.

Full-Scale Test

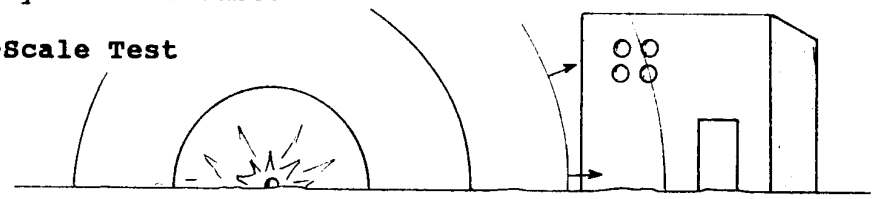

The advantage with a full-scale test compared to a test in a simultor is the possibility to test the conditions in the real case, e.g., also other weapon effects than blast waves, such as ground shocks and debris that might occur simultaneously.

Interesting full-scale tests have been made in the USA in order to compare different types of valves with plain holes /4/.
A problem in interpreting the results from such a test is that the magnitude and the angle of incidence of the blast front may differ between the valves and the holes. Besides, an obliquely loaded valve closes less effectively than a straightly loaded one.
Results from a full-scale test have direct application to the particular structure tested with the particular valves etc. To translate the results to other structures may imply major difficulties, however.

Shock Tube

A shock tube gives a possibility to test a single valve.
The blast waves can be produced by letting compressed air penatrate a membrane. Varying the blast pressure is attained by using membranes of different materials and varying thicknesses. Another method to produce blast waves is to detonate a charge inside the tube. By varying the charge yield and the distance between charge and object the impinging blast can be modified.

Since the charge detonates in the middle of the cross-section of the tube, the blast wave has a right angle of incidence. The valve will therefore be subjected to a straight incoming load, the magnitude of which only depends on the charge yield and distance. Comparisons between different valves can therefore be more reliable than at a full-scale test.
In the tube a substantial part of the created blast energy is utilized, while in a full-scale test only a minor part is used. Hence, tube tests can be made at low costs.

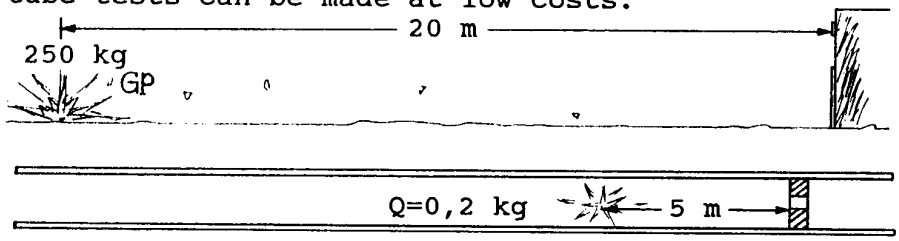

A free field blast effect simulated in a shock tube.

Standardized Testing Method

As shown in the beginning of this paper, the expanding blast wave is always changing. One test can give rise to completely different results, depending on how the measuring is made.
To make comparisons between test results possible, FortF has developed a standardized testing method.

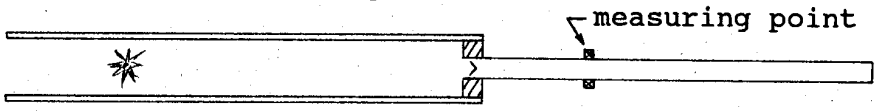

The tests are executed in a high-explosive driven shock tube.
At the calibration of the tube, the pressure-time history of the impinging wave was been determined at different charge yields and different distances.This is the incident pressure stated in the results at valve testing.
The let-through pressure is registrated in a tube with the same cross-section as the valve, five diameters behind. At this distance the blast wave is found to be stabilized and the propagation mainly one-dimensional. The length of the tube behind the measuring point is choosen big enough to prevent any attenuation wave from the tube opening to disturbe the measurements during the most interesting part of the laps.

CONCLUSIONS

This paper is to point out that reducing blast waves often is a necessity when hardening structures. This can be made by passive or active methods. Passive methods - a hole,grid, or rockfilter - can be used at blast waves with very short duration, as at small conventional charge in open geometry.
Active methods, as a rapid closing valve, are often necessary to protect from big conventional charges in limited geometries, and, naturally, to protect from nuclear blast.
It is important to define what is to be protected and what it can withstand.
A balanced hardening of the structure should always be aimed at, as the protection level of the structure is lessened or even ruined by any weak points that might exist.
When comparing different kinds of pressure-reducing devices it is important to make the studies systematically.

In my vision all concerned should have a standardized testmethod for valves, making comparisons between tests made at different times and in different simulations a very straight-forward procedure that will facilitate the use of correct data for optimal design of blast protection.

REFERENCES

1.Karlén, A, Blast load test of FortF/F tube valve 800x452. FortF Research Department Report C7:89, 1989. (In swedish)
2.Karlén, A, Development of anti-blast valve ø350 M/70 to anti-blast valves M/80 and M/83. FortF Research Department, Report A1:85,1985. (In swedish)
3.Karlén, A, Comparative tests on rapid-closing anti-blast valves. FortF Research Department, Report 104:9, 1971.
4.Weathersby,JH, U.S. Army Engineer Waterways Experiment Station. A private communication with Bengt Vretblad, FortF, 1989.

PASSIVE BLAST ATTENUATORS - A POSSIBLE ALTERNATIVE TO ACTIVE BLAST VALVES?

J. Hasler

LUWA Ltd, Filters and Shelter Equipment, SWITZERLAND

Abstract

At the last Symposium, in Panama City in April 1989, WES (Waterways Experimental Station) presented test results comparing the performance of blast valves from two manufacturers with that of an open hole. The valves were exposed to pressures both acting as normal blast valves and also with their closing elements held in the open position. The conclusion that the pressure and impulse behind the various arrangements did not show significant differences created doubt in the minds of the designers and the military authorities.

Can static attenuators, explosion protection devices without moving parts, replace conventional blast valves?

Many possible solutions are compared culminating in the development and build of two prototype attenuators also using experience from previous tests. These two units were subjected to field tests by WES on behalf of DNA. (Defence Nuclear Agency).

In parallel, we also performed series of tests in a shock wave tube at the laboratory of the Swiss Group of Armaments in Spiez at various pressures and duration of blast load. As a result of this, modifications were made and further tests carried out with one particular design of attenuator. Combinations of attenuators and blast valves were also included in the test series.

We present the results of these very extensive tests and outline the features of the resulting passive attenuator in this paper.

Background

It is generally accepted that chicanes can significantly reduce the pressure resulting from a very short duration blast but have little effect on the impulse.

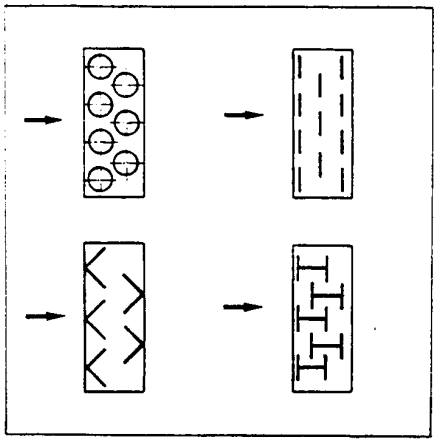

Fig. 1. Different chicane principles

The test results presented by WES cannot be considered to be conclusive since they are based on very few tests but nevertheless they indicate interesting avenues for investigation.

Therefore the WES approach has suggested to us that we reanalyse previous test results with particular reference to short duration blast loads. Hence we are able to consider possible designs in order to build static attenuator prototypes.

Tests can then be carried out to determine the operating envelope of these devices.

Objective

From the above, it was apparent that an attenuator should be capable of both replacing and of being combined with, our conventional blast valve. Consequently, the face dimensions, the modular system and the fixing details of the blast valve had to be design parameters of the attenuator.

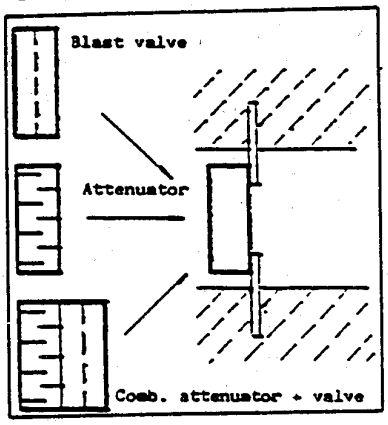

Fig. 2. Modular blast protection devices

We set out to determine the following information:

- Behaviour of blast attenuators, blast valves and combinations of both when subjected to very short duration blasts.

- Confirmation of results in field and laboratory tests.

- Appropriate range of application, in relation to technolgy and cost.

- Whether a bypass could be incorporated in the attenuator to initiate movement of the blast valve spring prior to the arrival of the main blast wave, when the two units are used in combination.

- Development of an anchor frame to allow the installation of the attenuator or valve, either singly or in combination, without modification to the frame. The decision on which combination of elements may be made after completion of the civil works.

Procedure

How to get valid answers in reasonable time and with acceptable costs?

We therefore derived the following programme:

- Repeat the WES field tests with reliable data using our blast valve.

- Analyse the previous work using inlet devices in front of the blast valve.

- Derive from this a design for prototypes of passive blast attenuators.

- Construct two different ply-wood models to determine pressure drop/flow characteristics in normal ventilating mode.

- Manufacture two different steel prototypes. Carry out extensive blast wave tube rig tests in April 1990 and field tests at White Sands in June 1990.

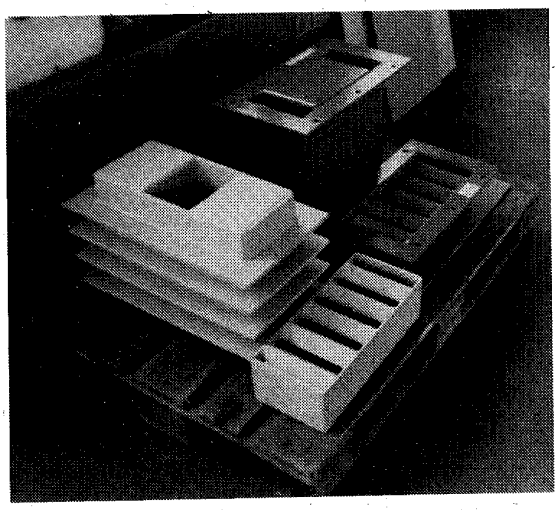

Fig 3. Two different prototypes

- Analyse these results to come up with further refinements to the design.

- Produce new aluminium prototypes. Test these to confirm performance and to determine the effective performance envelope.

- Analyse these final results. Apply for patents, set-up manufacturing methods, prepare technical documentation.

Test Programme

In addition to the tests at White Sands, the GRD (Swiss Group of Armament) have carried out on our behalf three extensive test series on their blast wave tubes to help determine the utility of passive blast attenuators. All test results have been recorded on computerized print-outs using state of the art instrumentation.

A) The first test series was made in September 1989 using the larger blast tube and consisted of 45 shots with blast loads of 11-44bar (150-630 psi) with pressure durations of 5 ms and 10 ms. The objective was to repeat the tests presented by WES in 1989. The following were tested:

- Active blast valve with baffle plate.

- Blast valve with baffle plate but with the valve springs fixed in the open position.

- Open hole only with baffle plate and without blast valve.

As opposed to the field tests which produced single point results which were difficult to interpret, the laboratory tests enabled us to repeat results where necessary and so allowed us to compare the relative performance of the active and passive attenuators more closely. Consequently, we were able to understand what was happening and so derive a more effective design of passive attenuator.

B) The second series of tests was aimed at refining the design of two different prototype passive attenuators and at determining their performance alone and in combination with active blast valves. 130 shots with blast pressures of 10 bar to 70 bar (140-990 psi) and blast load times of 2-10 ms were carried out.

These tests were carried out on the GRD small research blast wave tube to utilise its ability to simulate very short duration high pressure blasts.

C) The third series of tests was intended to define the final performance envelope of the type 'AA' attenuator - the result, after some modification, of the previous two series of tests. We tested both aluminium and steel prototypes to determine relative strength. 30 shots were carried out using the larger blast tube at the GRD.

Test Results

The first test series demonstrated that the blast valve with permanently open springs and baffle plate attenuates pressure relatively effectively. However, with pressure durations greater than 10 ms the let through impulse becomes critical (figure 4). The blast valve casing without springs and the open hole, both with baffle plate, proved to be of little value (figure 5).

The second test series with both the prototype attenuators, the type F blast valve, and the combination of the blast valve with either attenuator demonstrated that the Type F blast valve has excellent attenuation properties with very short duration blasts.

The tests also confirmed the validity of the formulae for our blast valves presented at the last seminar in Panama City, Florida in April 1989 (figure 6).

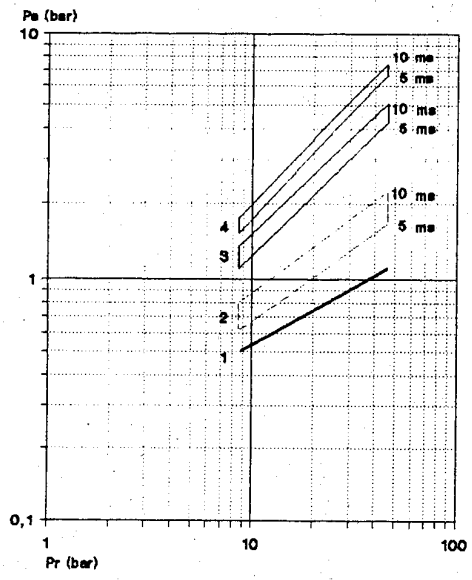

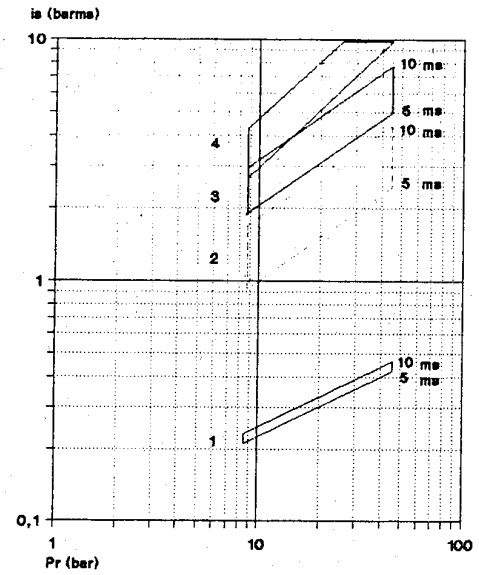

1) EPV-F 2) EPV-F with blocked springs
3) EPV-F without springs 4) Open hole

Fig. 4 & 5 Pressure impulse behind blast protection device

$$P_s = 0{,}158\ P_r^{0{,}539}$$

$$i_s = 0{,}077\ P_r^{0{,}394}\ t_p^{0{,}104}$$

Fig. 6. Trend pressure/impulse behind F-Valve

The data presented in figures 7,8,9 & 10 show that the Type AS prototype attenuator has slightly better performance than the type AA. However, since the much higher manufacturing cost, the larger space requirements and the higher pressure drop in normal ventilating mode of the type AS were more significant, we therefore concentrated on the type AA design. In particular, in the relevant pressure duration range of 2-5 ms this attenuator gave very good results.

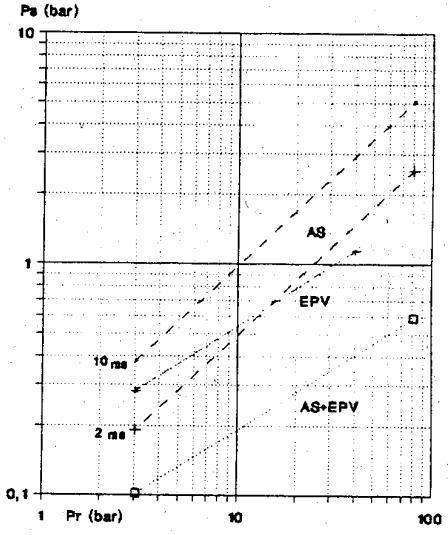

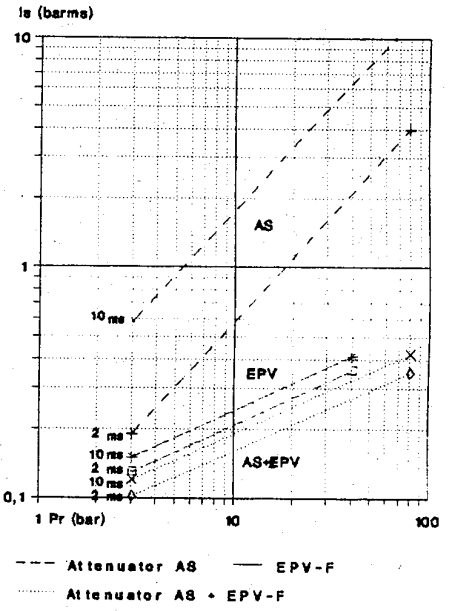

Fig. 7 & 8 Pressure/impulse behind attenuator AS and EPV-F

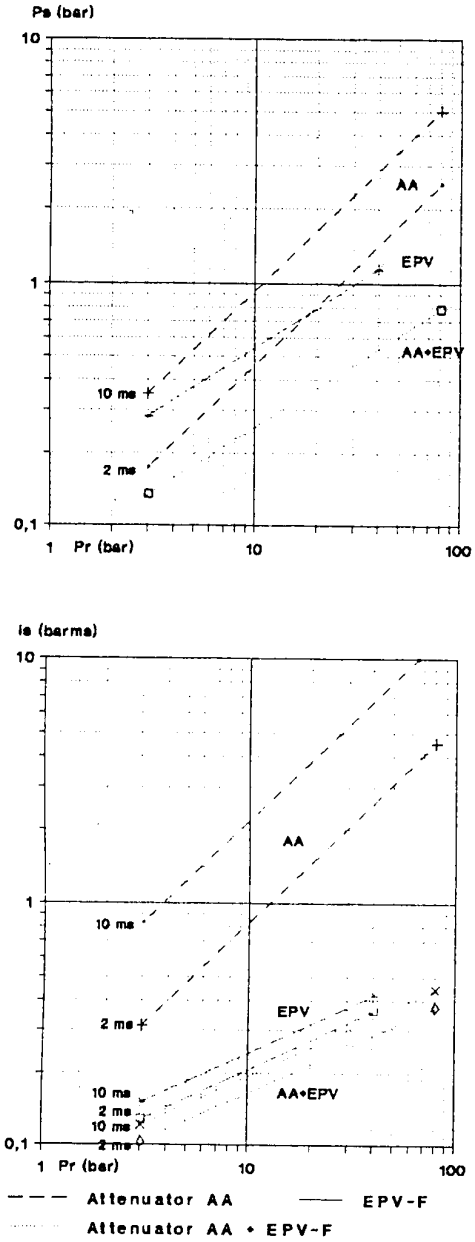

Fig. 9 & 10 Pressure/impulse behind attenuator AA and EPV-F

The combination of the blast valve with the attenuator gave excellent results and proved extremely effective against longer duration high pressure waves.

Another attractive way to demonstrate the effectiveness of blast attenuators and blast valves is shown in figure 11. It plots let through impulse and reflected let through impulse against reflected incident pressure.

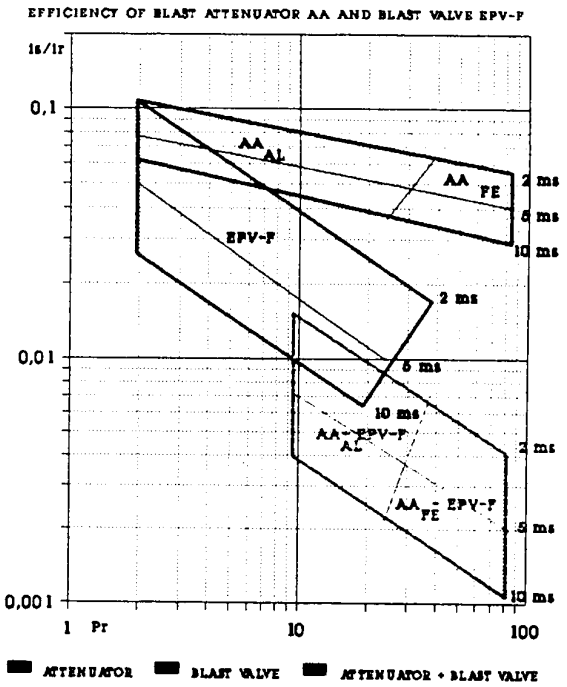

Fig. 11. Efficiency of blast attenuator AA and blast valve EPV-F

Practical Applications

What then are the criteria to be considered when deciding what form of blast attenuation should be incorporated into a design?

In order to select the most effective blast protection device we should take into account:

- the peak pressure and duration of the blast wave.

- the volume and shape of the area behind the blast protection device.

- the distance between the blast protection device and any sensitive equipment and personnel.

- the level at which equipment and personnel would suffer damage from let through pressure and impulse.

For a given incident pressure and pressure duration, the let through pressure and impulse behind the blast protection device can be read off (figure 12).

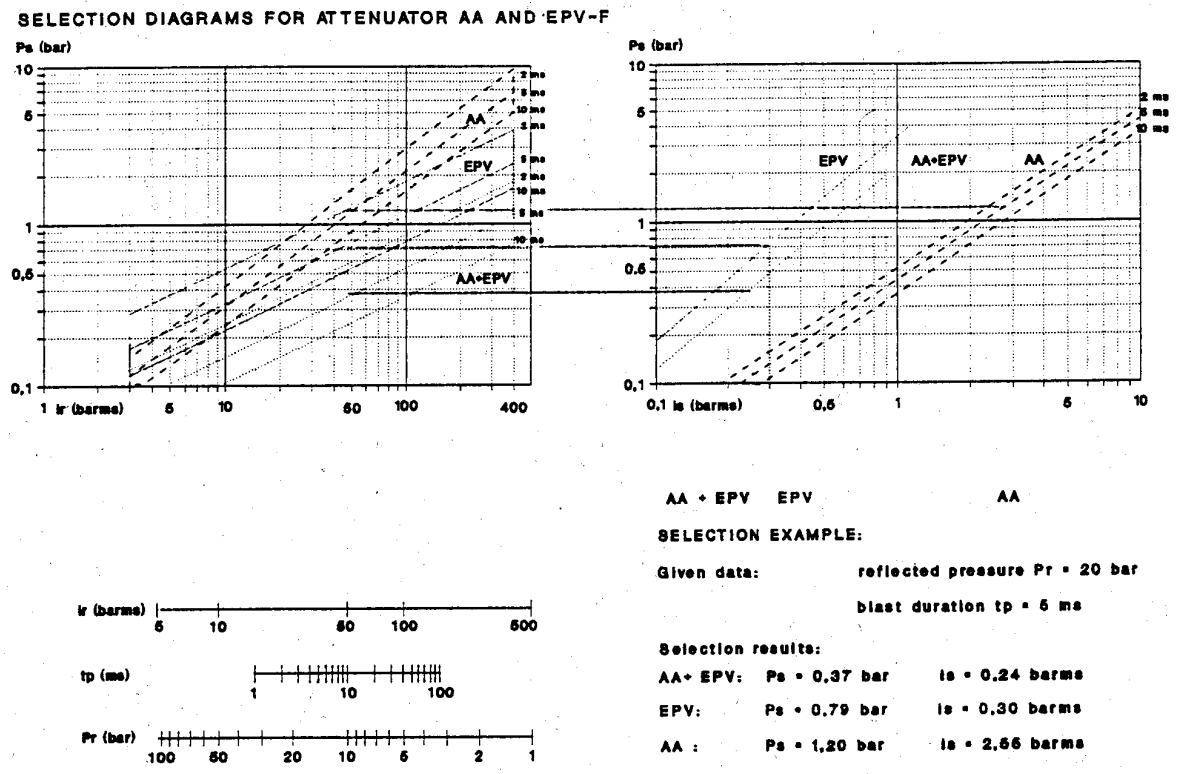

Fig. 12. Selection diagrams for attenuator AA and EPV-F

Depending on the equipment and lay-out behind the blast protection device either the attenuator, the blast valve or a combination can be selected. This chart enables the designer to select the optimum protection device for his particular application. As far as we are aware, such a diagram has not previously been published.

Summary

This extensive test programme has suggested a number of interesting conclusions. First, blast attenuators can be used as an alternative to active blast valves. However their application is advisable dependant on a short pressure duration (2-5 ms) and specific geometry behind the attenuator. Second, installation of attenuators in front of blast valves will give impressive security against high blast pressures with short and long duration (figure 13). Bypass holes in the attenuator reduce the effective closing time of the associated F-type blast valve.

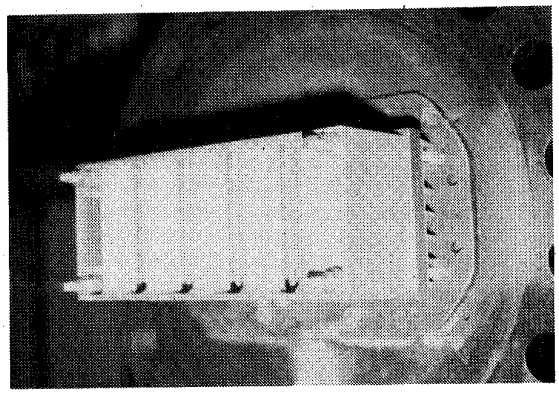

Fig. 13 Test combination attenuator AA with blast valve F

The passive attenuator "AA", with international patents pending, evaluated in these tests gives a hardened facilities design engineer a unique blast protection system either in place of or in combination with the conventional blast valve. All situations, from low to very high protection levels can now be easily covered.

The type AA attenuator optimised for airflow, cost and attenuation, gives the design engineer a broad range of solutions and, due to the standardised size of the attenuator and blast valve, allows subsequent modifications should potential threats change. A common anchor frame allows installation of the blast valve and attenuator either singly or in combination at any time.

The White Sands field tests have shown that Dr. Baker's attenuator design gives higher attenuation than our Type "AA". However, the high pressure drop in normal ventilating mode, the high manufacturing cost - much higher than that of the conventional blast valve- and the large space requirements of that design persuaded us to follow our path.

We are convinced that the type AA attenuator gives the optimum solution to the problem of attenuating blasts in all respects (figure 14).

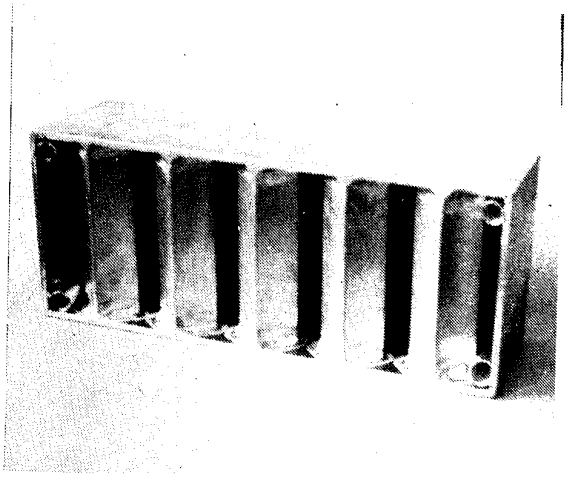

Fig. 14 Attenuator AA

Applied abbreviations

P_r = incident reflected pressure bar
i_r = incident reflected impulse (bar ms)
P_s = let through pressure (bar)
i_s = let through impulse (bar ms)
t_p = duration of incident pressure (ms)
ms = milliseconds

Acknowledgement

We appreciate very much the help and professional assistance of the following organizations during our research and test work for attenuators.

- Basler & Partner, Consulting Engineers, Switzerland.
- DNA Defence Nuclear Agency, U.S.A.
- WES Waterways Experimental Station, U.S.A.
- Dr. Baker Engineering, U.S.A.
- GRD, Test Laboratory of Swiss Group of Armament.

An Experimental Study of Airblast Attenuation Devices

Randy L. Holmes, Paul W. Graham, and Gayle E. Albritton

U.S. Army Engineer Waterways Experiment Station
3909 Halls Ferry Road
Vicksburg, Mississippi 39180-6199

for

The Fifth International Symposium

on

Interaction of Conventional Munitions

with

Protective Structures

Bundesakademie fuer
Wehrverwaltung und Wehrtechnik
Mannheim

Federal Republic of Germany
April 22-26, 1991

ABSTRACT

This paper compares test data for active airblast valves and passive airblast attenuation devices subjected to conventional weapons effects. Existing semihard and protective facilities utilize active airblast valves to restrict airblast passage into their intake and exhaust systems. Active airblast valves are associated with high initial and maintenance costs and are designed for nuclear weapon airblast threats rather than conventional weapons airblast threats.

Previous tests sponsored by the Defense Nuclear Agency (DNA) have indicated problems with these active airblast valves when subjected to high peak pressures associated with conventional weapons. During tests, many active airblast valves have failed, consequently; jeopardizing the mission of the facility.

The development of passive airblast attenuation devices against conventional weapons effects is a requirement, which has not been properly addressed in the past. Passive airblast attenuation devices have the advantage of relatively low initial cost and minimal or no maintenance cost, and can be designed for any loading that the structure can survive.

The objectives of this study are to develop, proof test, and document the performance of passive airblast attenuation devices subjected to conventional weapons effects.

To study airblast attenuation devices, the DNA and the North Atlantic Treaty Organization (NATO) have jointly funded three high-explosive tests, DIPOLE BLADE (DP) Events 1, 2, and 4. Data were obtained during these tests

to evaluate passive attenuation devices' effectiveness to decrease peak airblast pressures to acceptable levels. The devices were installed in a test building to model intake and exhaust systems in semihard and protective facilities.

Each test consisted of a reaction structure and four instrumented expansion chambers. These chambers housed two passive airblast attenuation devices and two active airblast valves. The reaction structure had a reinforced concrete floor slab, replaceable steel columns, beams, shear walls, and perimeter walls. The expansion chambers were positioned and attached atop the reaction structure.

Each expansion chamber was instrumented to record airblast pressure in front of and behind the passive airblast attenuation devices and active airblast valves. The front and rear walls inside the expansion chambers were also instrumented in order to monitor airblast. Airblast pressure is attenuated primarily by the airblast passing through the body of the passive airblast attenuation device or the active airblast valve and then expanding inside the expansion chamber.

The test environment for DP1 was generated by detonation of a rocket with a burst near the building, just outside the expansion chamber tunnel. The test environments for the remaining tests were generate by detonation of a GP bomb located at a stand-off distance in front of the reaction structure.

Test data indicate that the passive airblast attenuation devices are very effective in reducing the peak airblast pressure and peak airblast impulse to acceptable levels for both intake and exhaust systems in semihard and

protective facilities. Passive attenuation devices are more effective in reducing the peak pressure and peak impulse from conventional weapons than active airblast valves.

This paper will present the active data obtained from these three tests, and compare the effectiveness of the passive attenuation devices and active airblast valves used during this test series.

Eigenschaften von Material

Material Properties

The Use of Shotcrete for Expedient Repair of Bomb-Damaged Structures

Mark Anderson, Ph.D., P.E.

Applied Research Associates, Inc.
Tyndall Air Force Base, Florida

ABSTRACT

Shotcrete, or pneumatically applied concrete, is presented as a method for the expedient repair of structures in a post-attack environment. A general overview of shotcrete is presented which includes a brief history, as well as describing the advantages and disadvantages of the two main processes, dry-mix and wet-mix. The engineering properties of shotcrete, particularly those which relate to rapid structural repair, are discussed. The advantages and disadvantages of admixtures and special shotcrete mixtures as they relate to expedient structural repair are discussed. The use of automated shotcrete equipment is discussed, and a conceptual view of a Mobile Automated Shotcrete Expedient Repair Vehicle (MASERV) is presented. A successful field demonstration of the feasibility of shotcrete use for expedient structural repair is described.

BACKGROUND

Expedient repair of critical structures is a military concern, because missions may depend on base recovery capability. In a postattack environment, both personnel and equipment must be protected from damage suffered during the attack and from subsequent attack(s). With this in mind, two major goals of expedient repair for structures emerge, structural repair and sealing protection. Expedient repair for structural rehabilitation should recover sufficient structural capability to stabilize the structure and minimize the propagation of damage. Sealing protection is a less obvious, but equally important reason for expedient repairs in the postattack environment. Simple weather conditions, such as rainfall, could be a threat to some mission-critical equipment. Other, more severe, weather conditions could also threaten mission-critical personnel. In addition, chemical and/or biological intrusion, either by accident or by design, cannot be ruled out as a threat in the postattack environment. Shotcrete is a very attractive alternative, because it can meet both of the goals of expedient repair simultaneously.

OVERVIEW OF SHOTCRETE

Shotcrete is a general term for mortar or concrete pneumatically projected, or gunned, at high velocity onto a surface. Shotcrete was introduced in the early 1900s, under the trade name Gunite [1]. Several proprietary names have been used for various mixtures which have been grouped under the general heading of shotcrete. The term, shotcrete, was first coined by the American Railway Engineering Association in the early 1930s and was adopted in 1951 by the American

Concrete Institute to describe the dry-mix process. Shotcrete is now the accepted term for both wet-mix and dry-mix processes [2].

Although conventional concrete can be molded into any shape by placement in a form, shotcrete has the added advantage of using only a backup surface as a light form, or even no form. For example, shotcrete may be shot against the softest type of insulation material without serious damage to, or compaction of, the soft material [3]. In new construction, shotcrete is well adapted for thin, lightly reinforced sections. Common uses include roofs, walls, canal linings, tunnel linings, swimming pools, prestressed tanks, thin overlays over structural materials, repair of concrete deteriorated by fire or earthquake, rock slope stabilization, and refractory linings for fireproofing. Shotcrete has properties similar to conventional concrete with the same mix proportions [2]. The major advantages of shotcrete are the convenience of application and the high degree of bonding which can be achieved. Shotcrete is generally economical, compared to conventional concrete, for layer thicknesses greater than 3 inches (8 cm) [4].

SHOTCRETE PROCESSES

The two common processes of producing and placing shotcrete are known as the dry-mix process [5] and the wet-mix process [6]. The two shotcrete processes differ primarily in the way mix water is added. In the dry-mix process most (or all) of the mix water is added to the mixture by a water ring (or rings) at or near the nozzle. In the wet-mix process, the mixture is produced in a batch, with mix water added before transporting the shotcrete material.

The minimum equipment for a dry-mix process shotcrete operation is the gun, an air compressor, material hose, air and water hoses, nozzle, and a water pump (if needed). There are two main types of dry-mix process shotcrete guns, chamber guns and rotary guns. A typical shotcrete rotary gun is illustrated in Figure 1. Transport of dry-mix process shotcrete is done pneumatically, with the dry particles suspended by compressed air. A single venturi-type nozzle, typical for dry-mix shotcrete, is shown in Figure 2. Special nozzle types, such as the premixing "hydromix" nozzle, are also available. Accelerating admixtures may be added using either dry (added to feed bowl) or wet (added to nozzle water) accelerator dispensers.

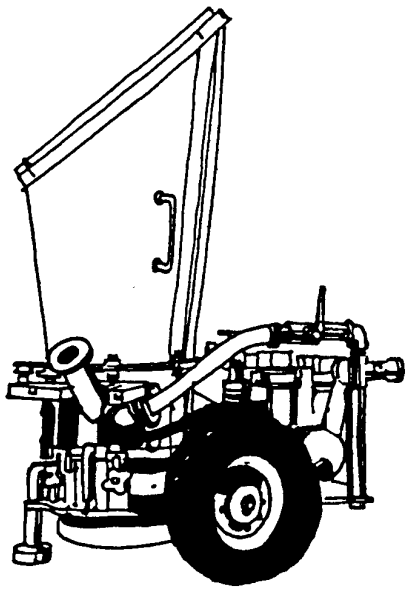

Fig. 1. Typical Shotcrete Rotary Gun

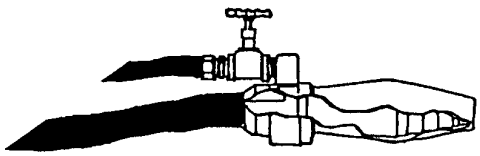

Fig. 2. Typical Shotcrete Nozzle

The major advantages of dry-mix process shotcrete are: (1) schedule flexibility, (2) little or no waste material, (3) high early strengths, and (4) highest ultimate strengths. Because dry-mix process shotcrete does not begin hydration until it reaches the nozzle, its use can be suspended almost instantaneously.

This gives the operator a great amount of flexibility in scheduling. Similarly, this flexibility minimizes waste material. However, one of the strongest selling points for the dry-mix process is the success this process has with accelerating admixtures. With the addition of accelerators, it is possible to achieve very high early strengths (3 ksi (21 MPa) compressive strength can be easily achieved in 8 hours). The dry-mix process is also the method which has achieved the highest ultimate strengths. Very high strengths (more than 10 ksi (69 MPa) compressive strengths at 28 days) have been reported. However, high early strength and high ultimate strength appear to be mutually exclusive, and care must be used when designing the mix to insure that all strength requirements are met.

There are several disadvantages of the dry-mix process, including: (1) the need for experienced crew, (2) dust generation, (3) particle rebound, and (4) inadequate mixing. The major disadvantage of the dry-mix process is the need for an experienced crew. A poor or distracted nozzle operator can quickly produce a layer of poor quality material. Generation of dust continues to be a problem, although new dust collectors have helped. Rebound of particles, particularly large particles, is a greater problem for the dry-mix process. Not only is waste a problem, but also as the larger particles rebound, the ratios of cement to aggregate and fine aggregate to coarse aggregate increase, changing the properties of the material. Inadequate mixing can lead to localized areas of too high and/or too low water/cement ratios for proper strength gains, as well as increased rebound.

Mix design for wet-mix process shotcrete is similar to that for dry-mix process shotcrete, but allows much more control over the mix proportioning of the delivered material. Although a finer mix with relatively high slump is typical, wet-mix process shotcrete may have up to 40% coarse aggregate, and be gunned in a zero slump mix with up to 3/4 inch (2 cm) aggregate. There are two methods of delivering wet-mix shotcrete, pumping and pneumatic feed. Pumping may be achieved using either a positive displacement (piston) pump or a squeeze pump, and both require the injection of compressed air at the nozzle to break up and spray the material. The velocity of impact is often reduced for the pumping method (reducing the level of compaction). Delivery rates for pumping range from 1.5 to 12 cubic yards (1 to 9 cubic meters) per hour. The pneumatic gun uses a set of mixing paddles to push wet concrete to the material feed valve. Alternating slugs of wet concrete and compressed air are sent through the material hose to the nozzle, where additional compressed air must be added to create a high-velocity impact. Liquid accelerators are typically used with wet-mix process shotcrete, and are generally less effective because the wet concrete has already begun to hydrate.

The major advantages of wet-mix process shotcrete include: (1) accurate batching, (2) thorough mixing, (3) reduced duties on the nozzle operator, and (4) high overall production. The addition of mix water away from the nozzle can produce a very consistent mix with properties which can be predicted accurately. By delivering a steady stream of uniformly mixed shotcrete material at a consistent slump, the nozzle operator can concentrate on the proper placement of material, which can result in a significant improvement in the quality of *in situ* shotcrete. The wet-mix process also has the potential for high overall (project) production rates, since concrete batch plants can be used to produce large quantities of premixed concrete for subsequent delivery.

The major disadvantages of wet-mix process shotcrete include: (1) low delivery velocities, (2) low schedule flexibility, (3) waste material, (4) lower early strengths, and (5) mechanical problems. Low delivery velocities result in lower compaction, which may in turn reduce

strength. Since the concrete is wetted before delivery at the nozzle, there is reduced flexibility in scheduling. Similarly, waste material can be a problem, since it is generally better to have too much material than too little material. In general, the wet-mix process does not produce early strengths comparable to those produced by the dry-mix process. Mechanical problems, most notably clogging of lines, are a major difficulty for the wet-mix process.

SHOTCRETE PROPERTIES

Shotcrete has similar properties to cast-in-place concrete formed at the same water/cement ratio and density. However, the density of shotcrete *in situ* tends to be higher than cast-in-place concrete of similar design, particularly when placed by the dry-mix process. The density of shotcrete is related to the exit velocity of particles at the nozzle [7], but the relationship has not been well characterized. Similarly, the void content and permeability of shotcrete are lower than for cast-in-place concrete of similar design. Based on actual performance studies (*e.g.*, [8]), shotcrete is very durable when subjected to severe freeze-thaw conditions, the opposite of the expected behavior for a concrete with low void content. This phenomenon has been attributed to the low permeability which provides sealing.

Compressive strength is the most common method of indexing shotcrete quality, although flexural strength is also used. The preferred method of determining shotcrete strength is by the use of core samples or beam samples taken from the *in situ* shotcrete. However, this method may be impractical in many applications, either due to difficulty in obtaining cores or in the potential structural damage which could result from the sampling. The next most preferred method utilizes a field prepared slab. A frame is placed next to an area being gunned with shotcrete and is gunned at the same time, usually to a depth of 3 or 4 inches (8 to 10 cm). Samples may be obtained from the slab, or the slab itself may be tested. A method which is often used for quality control involves gunning a standard size concrete cylinder into a mesh form. Ease of specimen preparation is the only advantage of this method, because the specimens formed by this method are not representative of the *in situ* shotcrete.

Shotcrete for expedient repair situations would often be in a planar configuration. Fernandez-Delgado, *et al.* [9], reported on the failure mechanisms of shotcrete in planar configurations, based on large-scale slab tests, as shown in Figure 3. These results are directly analogous to the case of a shotcrete-repaired breach which is subsequently loaded (*e.g.*, by a bomb or a fragment). Figure 3(a) illustrates a diagonal tension, or punching, failure which occurs when bonding is strong. Figure 3(b) shows an adhesion failure, which is controlled by the condition of the underlying bond interface. Figure 3(c) illustrates the third common failure mechanism for planar configurations, which is a bending, or flexural, failure. This type of failure depends on the flexural strength of the shotcrete.

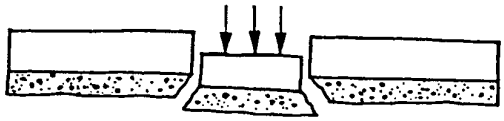

(a) punching failure

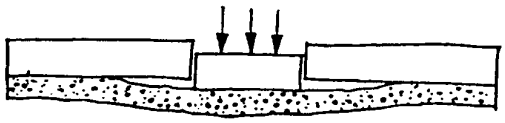

(b) bonding failure

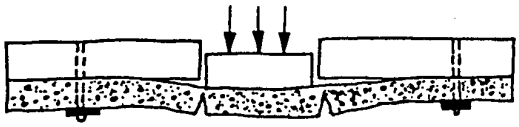

(c) flexural failure

Fig. 3. Typical Failure Modes

An examination of the primary failure mechanisms shows that the most important properties for shotcrete used in expedient repairs are not related to compressive strength, but to tensile strength and ductility. Testing to determine suitability of shotcrete designs or mixes for expedient repair purposes should, therefore, concentrate on tensile/flexural properties rather than relying on compressive strength as the primary index parameter.

HIGH EARLY STRENGTH SHOTCRETE

The potential for high early strength is a strong selling point for shotcrete as an expedient repair material. It is often possible to achieve both rapid setting and high early strength with the addition of a suitable accelerating admixture.

Accelerating admixtures may be classified physically as either wet or dry, but functionally as either organic or inorganic. The chemical nature of the admixture has a controlling effect on properties and performance of the *in situ* shotcrete. Nearly all accelerators currently available are of the inorganic type, and typically induce well-known chemical reactions [10] which lead to a reduction in ultimate strength. However, newer organic accelerators, often proprietary and very expensive, do not change the basic cement/water reaction, so there is no significant strength penalty [5].

SPECIAL SHOTCRETE MIXTURES

Special shotcrete mixtures include regulated-set cement shotcrete, latex shotcrete, polymer shotcrete, and fibrous shotcrete. The first three types share two major disadvantages for expedient repair: (1) difficulty in long-term storage, and (2) difficulty in intermittent use. Of all special shotcrete mixtures, fibrous (steel fiber reinforced) shotcrete has the greatest potential for expedient repair purposes. Numerous examples of the successful use of fibrous shotcrete mixtures for structural rehabilitation can be found in the literature (*e.g.*, [11,12]). The following quotes [13] are typical of conclusions from those who have used fiber-reinforced shotcrete. "The addition of steel fibers to shotcrete makes it almost an ideal material for concrete repair and renovation." "... steel fibers make shotcrete a tenacious material." "Steel fiber shotcrete resists far greater impact and shock ... than plain shotcrete." "Because of its increased resistance to blasts and shocks, ... fiber shotcrete is highly recommended for military structures." In a state-of-the-art report, the American Concrete Institute [14] concluded that fiber reinforcement in shotcrete generally improves material properties including ductility, toughness, flexural strength, impact resistance, fatigue resistance, and compressive strength. Although other fiber types are available, steel fibers are the most commonly used for shotcrete. Figure 4 shows typical data for tensile strength tests on shotcrete both with and without fiber reinforcement.

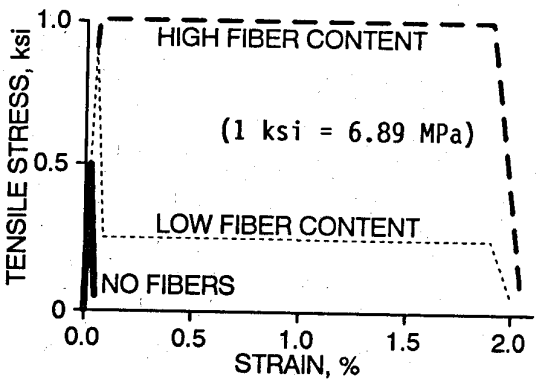

Fig. 4. Fibrous Shotcrete Tensile Strength (Typical)

A typical unreinforced shotcrete specimen will fail quickly after the first cracking, showing a relatively low ultimate tensile strength (typically 400 to 500 psi (2.8 to 3.4 MPa) and complete failure at a very low strain level (typically less than 0.1% strain). By the addition of a small amount of steel fibers, the stress required to induce

cracking is increased, thereby increasing the ultimate strength. More important, the specimen retains a significant residual strength even after the initial cracking (typically 200 to 300 psi (1.4 to 2.1 MPa)) which is directly related to the pull-out strength of the steel fibers. Strain without failure occurs until the fibers actually pull out of the cement binder matrix (typically at about 2% strain), therefore producing a ductile material. With a high fiber content, the concrete does not crack until the pull-out strength of the fibers has been exceeded (typically at about 1000 psi (6.9 MPa)). This means that even though the ultimate strength is increased, the ductility is retained.

Existing equipment with little or no modifications can be used for the application of steel-fiber shotcrete, when special fibers are used. These have deformed ends and are glued together to reduce balling. In addition, specialized equipment is available for the addition of fibers and the application of fibrous shotcrete [14].

AUTOMATED EQUIPMENT

The use of automation in the shotcrete process has numerous advantages. The two most important advantages of automated shotcrete equipment are: (1) the nozzle operator can be relieved of much of the repetitive functioning typically associated with shotcrete application, allowing most of his concentration to be put on delivering top-quality shotcrete, and (2) measures to improve safety in hazardous situations can be easily implemented. The most common use of automation has been in tunnel linings (*e.g.*, [15]). However, many of the advantages of automated rotary tunneling systems have been incorporated into more general purpose automated equipment [16,17], which is commercially available.

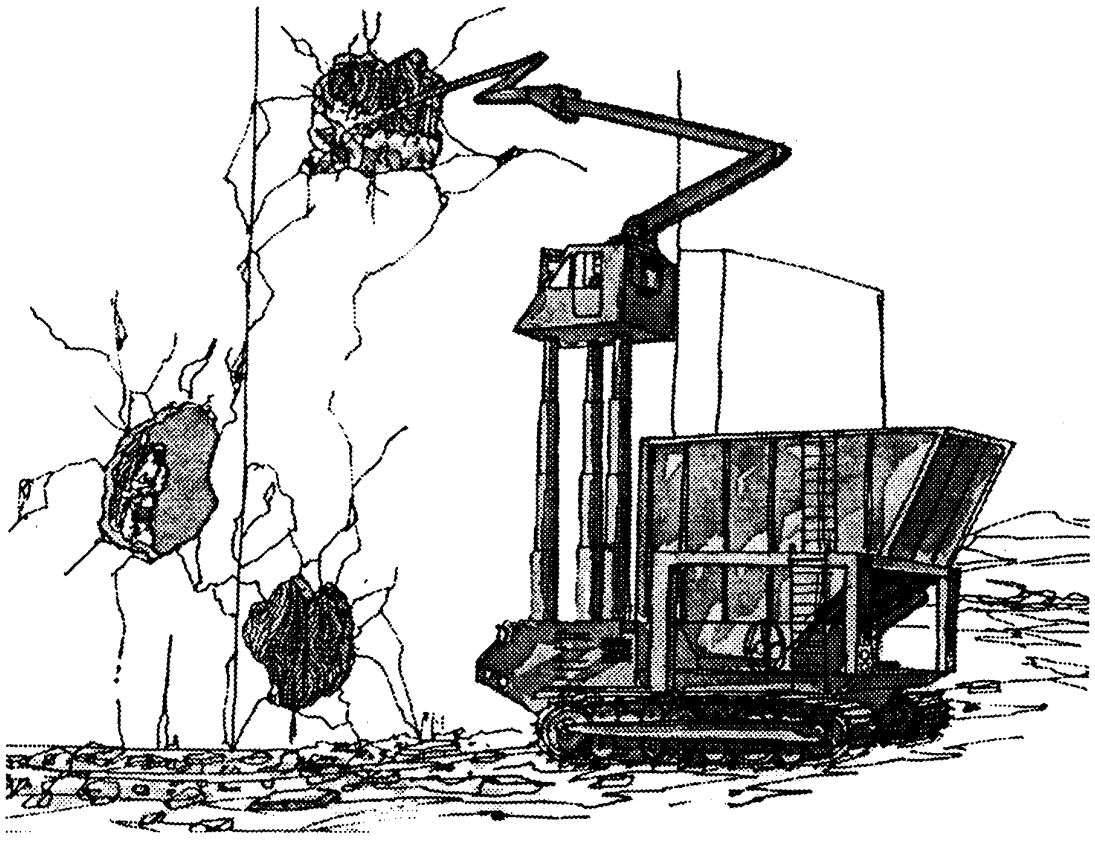

Fig. 5. MASERV (Mobile Automated Shotcrete Expedient Repair Vehicle) Concept

THE MASERV CONCEPT

Figure 5 illustrates a concept, developed by the author, of an advanced repair vehicle called MASERV (Mobile Automated Shotcrete Expedient Repair Vehicle). The MASERV concept includes all of the automated functions of commercially available robotic shotcrete machines, with some additional advanced features. The MASERV is track-mounted and armored for use in a postattack environment. It can carry large volumes of materials and has a highly versatile robot arm attached to a cab which can be hydraulically lifted to allow repairs on upper floors of structures. The concept illustration includes repair workers equipped with chemical garb who are working inside the building to provide backing material for the shotcrete spraying. While the MASERV concept is clearly more advanced than the equipment currently available, it is likely that some version of this vehicle (with many of the capabilities shown) could be built almost immediately if funding were available.

FIELD DEMONSTRATION

In February, 1990, a field demonstration of the feasibility of shotcrete use for expedient repair of bomb-damaged structures was performed for the Air Force Engineering and Services Center by Applied Research Associates, Inc. personnel [18]. For the demonstration, a preblended high early strength fibrous shotcrete mix was utilized. The preblended material consisted of Portland cement, silica sand, pea gravel, steel fibers, microsilica, and an accelerator. The preblended mix was designed to provide a compressive strength of 1 ksi (7 MPa) at 8 hours, when used in the dry-mix process. The feasibility test consisted of spraying shotcrete onto several 4 foot by 4 foot (1.2 m by 1.2 m) panels. The panels were tested for compressive strength by the Windsor probe and by breaking cores taken from the panels. The compressive strength data is shown in Figure 6, and a strength curve fit to the data is shown in Figure 7. The strength curve shows that the ultimate compressive strength is about 3.5 ksi (24 MPa). More importantly, the strength was well above the required 1 ksi (7 MPa) at 8 hours.

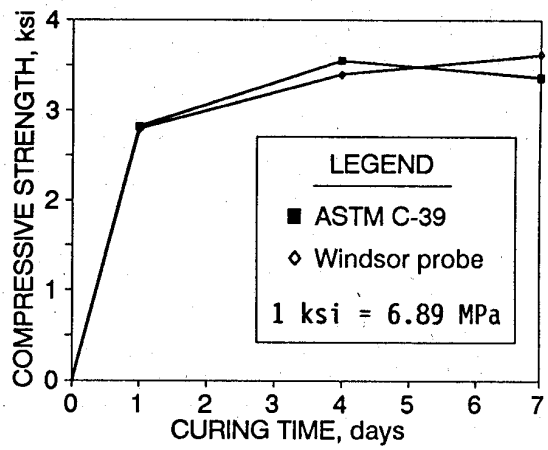

Fig 6. Field Demo Strength Data

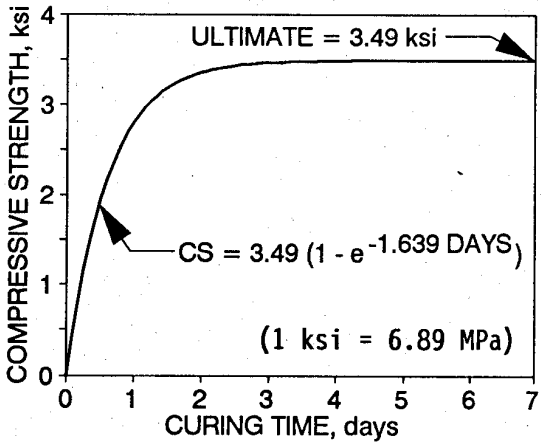

Fig. 7. Field Demo Strength Curve

CONCLUSIONS

Shotcrete is a material which appears ideal for expedient structural repair. A primary advantage is the potential for use of locally available materials commonly used for Portland cement concrete, rather than having a stockpile of material ear-marked for expedient repair. In general, shotcrete can provide rapid repairs for structural

and sealing protection in a postattack environment. Automated equipment is available which allows shotcrete to be used in remote areas. Shotcrete, particularly when used with steel fibers, is very resistant to tensile/flexural failure and penetration. Based on the results of a successful field demonstration, it is concluded by the author that shotcrete can be used as an expedient replacement for any proposed (cast-in-place) conventional concrete repair.

REFERENCES

1. Miner, G. M., "Use of Shotcrete from the Standpoint of the Owner," ACI Publication SP-45, Detroit, MI, 1973.

2. *Guide to Shotcrete*, ACI Publication 506R-85, Detroit, MI, 1985.

3. "Air-Inflated Forms Cut Cost of Drainage Structure," *Public Works*, Vol 118, No 7, July, 1987.

4. Reading, T. J., "Shotcrete as a Construction Material," ACI Publication SP-14, Detroit, MI, 1966.

5. Crom, T. R., "Dry-Mix Shotcrete Practice," ACI Publication SP-14, Detroit, MI, 1966.

6. Hoffmeyer, T. A., "Wet-Mix Shotcrete Practice," ACI Publication SP-14, Detroit, MI, 1966.

7. Glassgold, I. L., "Shotcrete Durability: An Evaluation," *Concrete International, Design and Construction*, Vol 11, No 8, August, 1989.

8. Reading, T. J., "Durability of Shotcrete," *Concrete International, Design & Construction*, Vol 3, No 1, January 1981.

9. Fernandez-Delgado, G., *et al*, "Structural Behavior of Thin Shotcrete Liners Obtained from Large Scale Tests," ACI Publication SP-54, Detroit, MI, 1977.

10. Schutz, R. J., "Properties of Shotcrete Admixtures," ACI Publication SP-54, Detroit, MI, 1977.

11. Scanlon, J. M., "Recent Research on Shotcrete by the US Army Corps of Engineers," ACI Publication SP-54, Detroit, MI, 1977.

12. Morgan, D. R., "Steel Fiber Shotcrete for Rehabilitation of Concrete Structures," *Transportation Research Record 1003*, Washington, DC, 1984.

13. Ramakrishnan, V., "The Role of Superplasticized Fiber Reinforced Concrete and Fiber Shotcrete in the Rehabilitation of Bridges," *Proceedings*, Conference on Rehabilitation of Buildings and Bridges, NSF, Washington, DC, 1981.

14. *State-of-the-Art Report on Fiber Reinforced Shotcrete*, ACI Publication 506.1R-84, Detroit, MI, 1984.

15. Monaghan, D. A., *et al*, "Remote Shotcrete Lining of Raised Shafts," ACI Publication SP-54, Detroit, MI, 1977.

16. Alberts, C. and Kramers, M., "Swedish Shotcrete Equipment and Developments in Fibrous Shotcrete," ACI Publication SP-54, Detroit, MI, 1977.

17. Alberts, C., "Use of Remote Controlled Spraying Nozzle," ACI Publication SP-45, Detroit, MI, 1973.

18. Muszynski, L. C., *et al*, "Fibrous Shotcrete for Expedient Repair of Structures," Gulf Coast Division, Applied Research Associates, Inc., Tyndall Air Force Base, FL, 1990.

FRACTURE MECHANICS MODEL FOR CONCRETE UNDER HIGH LOADING RATES

T. Krauthammer and D. Chandra

Penn State University, University Park, Pennsylvania, U.S.A.

INTRODUCTION

A reliable material model for concrete should represent its brittle nature, and its strain rate sensitivity. It is reasonable to assume that these phenomena are related to internal fracture processes, and the material model should include such considerations. Since cracks are present in the concrete body (either in micro- or in macro-scale), they should be taken into consideration appropriately while developing a representative damage function. Ilankamban and Krajcinovic (1987) assumed a damage function depending on the orientation of a plane through a certain point in the concrete body. However, instead of a continuously variable orientation vector, they assumed a variable that was restricted to have discrete values depending upon the most probable orientations of the damage surfaces. They restricted their theory to small deformation and homogeneous temperature distribution, and employed a stress tensor and the Helmholtz free energy for deriving their solution.

The algorithm chosen by Fanella and Krajcinovic (1988) is based on the assumption that the pre-existing microcracks are located on the aggregate-cement interface and have an isotropic distribution. Depending upon various stages of crack evolution, the approach was modified to obtain the limiting values of compressive stress for the corresponding evolution stages. Thereafter, they derived the expression for overall compliance tensors for various stages mentioned earlier, assuming that the total strain tensor could be expressed as the sum of the elastic strain tensor and the inelastic strain tensor. The inelastic strain component was subdivided further into the inelastic strain tensor corresponding to the stage when crack size increased from an initial size to a critical value and the inelastic strain tensor due to opening of the kinked cracks.

Localization instability and spurious mesh sensitivity (particularly in the domain of strain softening) while dealing with finite element methods must be addressed. The nonlocal continuum/damage plasticity model developed by Stevens and Krauthammer (1989) can be used for overcoming these problems. Its validity and merit were demonstrated by Stevens and Krauthammer (1989) who applied it successfully for analyzing reinforced concrete beams subjected to high amplitude impulsive forces. Using their hybrid code (combined finite element and finite difference approach) Stevens and Krauthammer (1991) and Stevens, Krauthammer and Chandra (1991) analyzed successfully buried reinforced concrete arches subjected to blast loads. The damage parameters based on the work by Ilankamban and Krajcinovic (1987) and by Fanella and Krajcinovic (1988) can be conveniently merged into the nonlocal continuum/damage plasticity model developed by Stevens and Krauthammer (1989) that also contains a damage parameter in its formulation. The issue of strain rate sensitivity, however, requires further attention.

Increase in concrete strength due to high loading rates is a well-known phenomenon. Higher strength magnification, by a factor of 2 or more, can be achieved by a strain-rate in the range of 10^2-10^3/sec, as discussed by Malvern (1984) and by Curbach (1987). This phenomenon is not fully understood, and the lack of a rational and reliable explanation could result in either unsafe or possibly also uneconomical structures. The amount of experimental work performed in this loading range is very limited. Moreover, most tests are performed under uniaxial stress or strain conditions, and out-of-plane or radial stresses or strains are not recorded.

Usually, four techniques have been used for investigating strain rate effects on the compressive behavior of concrete in the strain rate range from 10^{-6} to 10^{3}/sec. Drop hammer test devices and hydraulic driven uniaxial devices are similar in that uniaxial impact or shock loads are applied to cylindrical test specimens. The validity of the results from these tests has been called into question by Hughes and Watson (1978) and Hegemier and Read (1985). Since most brittle solids undergo dilatancy during failure, the material must accelerate in the radial direction while unloading; this creates a confining pressure on the material that is not yet failed. Concrete, being a frictional material, has higher strength under confinement and, therefore, the strength increases observed in the drop-hammer test and the hydraulic test may be entirely due to radial inertia effects and not to any true rate dependence of the material itself. In the Split Hopkinson Pressure Bar (SHPB) test apparatus, an applied stress wave is initiated by the impact of a cylindrical striker bar onto a short cylindrical specimen of the same diameter as the bar; the amplitude of the stress wave is proportional to the velocity at which the striker bar impacts the incident bar while the duration is a function of its length. It was concluded by Malvern et al. (1986) that there was unfortunately some uncertainty in knowing what value of stress to associate with the average strain in the rising portion of the stress-strain curve due to some non-uniformity in stress along the length of the 3-inch specimen. Also, for strain rates near 10^{2}/sec, the maximum stress of unconfined specimens was approximately twice the static strength. While the yield stress (not the maximum stress) was 30% larger than the static ultimate strength, it appeared to be independent of the strain rate at yield, and this enhanced dynamic yield strength could not be attributed to inertia confinement. The fourth test approach is the explosively driven triaxial test at the Stanford Research Institute (Gran et al., 1987). Although, they used the same mix that had been used in the specimens tested by Malvern et al. (1986), they made their specimen of different size (diameter to axial length ratio as 1:2) than that used by the SHPB group. There were some differences in the results of these two groups, however, the differences could not be explained by radial inertia effects.

Based on the results of these and other tests, attempts were made to define empirical relationships between dynamic stress enhancement (in tension and compression) and strain rate usually with a least square approach, such as by Dilger, Koch and Kowalczyk (1984), Bischoff and Perry (1986), and Soroushian et al. (1986, 1986).

STRAIN RATE EFFECTS AND CONSTITUTIVE FORMULATION

There have been five approaches for modelling constitutive behavior of concrete that include strain rate effects, as follows.

1. Dynamic enhancement factor approach: The static material properties are increased by a "dynamic enhancement factor" (for example, Schumacher 1983).

2. Classical plasticity approach: The ultimate strength varies with loading rates, as attempted by Soroushian and Sim (1987).

3. Viscoplastic approach: Similar to the elastic/viscoplastic theory by Perzyna (1966), wherein viscous-like behavior was introduced by means of a time-rate flow rule employing a plasticity yield function. It was used by Nilsson (1983) for the steel sphere impacting a suspended concrete rod. Also, Mould and Levine (1987) proposed a Perzyna type approach using a Cap model that incorporated all three invariants.

4. Fracture mechanics approach without thermodynamic consideration: Considering the brittle nature of concrete which leads it to a stage of fragmentation prior to failure, it is not inappropriate to assume that a body of concrete goes through a process of fracture prior to failure. As a consequence, several formulations exist relating those parameters with other mechanical parameters of concrete that determine the constitutive laws for it. Furthermore, the loading rate (either in terms of stress or strain rate) has always played a key role in those formulations. Since, there are two major domains in fracture mechanics, linear elastic fracture mechanics (denoted henceforth by LEFM) and elasto-plastic fracture mechanics (denoted henceforth by EPFM), all such formulations have been stemmed into either one or the other of the two major streams, depending upon which state (elastic or plastic) the concrete is considered to attain under certain loading conditions.Two trends are observed in the application of LEFM to concrete fracture process.

    a. Macro Level LEFM: Concrete is assumed as an elastic homogeneous isotropic material. The size of the concrete element and the crack therein should be greater than certain minimum values depending upon the concrete grade in order to apply LEFM. The order of specimen dimensions is generally one meter (Reinhardt 1986). Sih and Chen (1970) solved the problem of a finite strip with a semi-infinite crack, the faces of the strip were moved by an instantaneous displacement which was kept constant. It was found that the ratio $K_I/K_{I,v=0}$ varied almost linearly starting with a value of

unity for v=0 to a value of zero for v equal c_R, the Rayleigh wave speed for the material (K_I is the stress intensity factor for a particular constant crack propagation velocity v, and $K_{I,v=0}$ is the stress intensity factor for the static condition when the crack is not propagating, i.e., v=0 and c_2 is the propagation velocity for a shear wave). Kipp et al. (1980) derived an expression for dynamic stress concentration factor $K_I(t)$ for a penny-shaped crack. They extended the concept of static K_I to a dynamically varying stress intensity factor by introducing an arbitrary stress-time relation. The result was a relation which predicted that the fracture strength of the material was directly proportional to the applied strain rate raised to the power of 1/3, and they derived an expression for the approximate size of the concrete fragments generated after the failure.

b. Micro Level LEFM: LEFM has been applied to concrete at a micro level with several assumptions and idealizations. In the approach taken by Zieliński (1984), concrete was idealized as a particulate composite consisting of spherical aggregate particles varying in size, dispersed and embedded within the cement matrix. It was considered as a fictitious material with equidistant and regular flaws that are physically due to pores in the hydrated cement paste and the shrinkage and thermal cracks around the large aggregate grains (Reinhardt 1986). It was assumed that the fracture surface is a planar surface in a macro scale and the undulations and irregularities in the micro scale do not affect the overall fracture mechanics behavior of concrete. The plane section of the cracked surface was assumed to form partially through the matrix and partially through the fractured aggregate particles. Under very slowly increasing tensile loading the crack would grow along relatively weaker matrix-aggregate interface and penetrate through the matrix. Whereas, under rapidly increasing tensile load, the time in which fracture occurs is extremely short. The effect of strain relief in the zones surrounding the propagating crack does not have much influence on the response of the material in the zones remote from the crack. Thus, the cracks under rapidly increasing load are forced to develop along shorter paths of higher resistance penetrating through the tougher aggregates instead of just growing around them.

Since there is very little plasticity involved in a body of concrete undergoing fracture (concrete is more like glass in this respect) there is not much justification for the application of EPFM. What is found in practice is the modification of LEFM formulations taking into account the nonlinearity of concrete behavior under the assumed plastic deformations. Application of EPFM in that manner has been proved to be successful for static loading where concrete is considered mainly as a strain-softening material (Reinhardt 1986). The strain field around the crack tip causes much higher stress than the tensile strength of concrete. As a consequence, a process zone develops ahead of the crack tip which is treated as a part of the crack (Dugdale 1960 and Barenblatt 1962) where cohesive stresses tend to close the crack. The governing parameters are the tensile strength and stress crack opening relationships. It is understood that EPFM is not a good method for assessing the tensile strength of concrete; but it is a good tool to judge the behavior of a cracked concrete element. In the approach by John and Shah (1987) for modelling the rate effects on Mode I fracture (tensile crack growth), the crack tip opening displacement (CTOD) was assumed to be rate dependent. Although CTOD is the result of plastic deformation of the material at the zone of crack tip, their model was developed using an equivalent CTOD which is based on LEFM. The reason for this was to get rid of size dependency of K_{Ic} (if calculated otherwise) which in turn is the result of the crack extension before the peak loading occurs. Hence, their approach was primarily based on LEFM and the plasticity was represented by the nonlinear analysis. Based on these findings and observations, it seems to be reasonable that one could employ laws of thermodynamics for incorporating strain rate effects into constitutive formulations.

5. Fracture Mechanics Approach with Thermodynamic Consideration: In order to apply principles of thermodynamics to the fracture process of concrete, it should be considered on an atomic level (Reinhardt 1986). If energy is supplied from the external environment to the system of atoms, then the atoms can overcome their energy barrier (which is also defined as activation energy) more easily. This external energy can be introduced to the system as mechanical, thermal, or chemical energy. Mihashi and Wittmann (1980) used this approach to predict the loading rate influence on the strength of concrete. They assume that the fracture of concrete may be caused by a series of local failure processes in the phase which consists of a crack of hydration products of cement and interfaces between cement and aggregate. The concrete consisted of a group of elements linked in series. Each element contains a circular crack whose length depended on the pore sizes of hardened cement paste (for the prediction of rate influence, the absolute value of crack length was not important). After calculating the mean value of probability of fracture during a time interval, a relation between stress rate and tensile strength was developed. Similarly, Lindholm et al. (1974) applied rate theory to predict the rate and temperature influence on the strength under multi-axial loading.

RECENT DEVELOPMENTS

The following observations are made on the algorithms described above for modelling high loading rate effects on constitutive behavior of concrete: They are limited by idealistic assumptions and because of scanty experimental data they still need rigorous verifications, and none of these algorithms is complete in the sense that they attack the problem from different points of view and put emphasis on different aspects of concrete behavior separately ignoring totally or partially the interaction between the parameters governing those aspects. In other words, the current state-of-the-art in modelling rate effects in concrete is at a very preliminary state. It is evident that some parameters are state variables while the others are input/output variables. Curbach (1987) performed both numerical and experimental investigations of the issue of strain rate effects on a concrete specimen under impulsive tension. He noted a distinctly different stress distribution along the crack line depending on the load rate. Under short duration dynamic loads, the stresses were enhanced as compared to the cases of lower load rates. Based on his findings, he introduced an additional correction to the strength enhancement factor that is proportional to the stress rate, to the cracked distance and inversely proportional to the crack tip velocity. In his tests, Curbach (1987) found that the crack tip velocity was between 400 to 500 m/s, below the Rayleigh wave speed.

In order to gain a better insight of the phenomenon of strength enhancement under high loading rates, a model analysis was performed in this study, with a similar approach as employed by Curbach (1987). A rectangular, 20 inches by 10 inches, strip of 4000 psi concrete was analyzed by the finite elements method. It represented one quarter of a plate with a 1 inch central through crack subjected to a remotely applied transient tension, with different increasing loading rates, acting over a short region symmetrically spaced about the crack's center line. A plane strain condition was imposed, as shown in Figure 1.

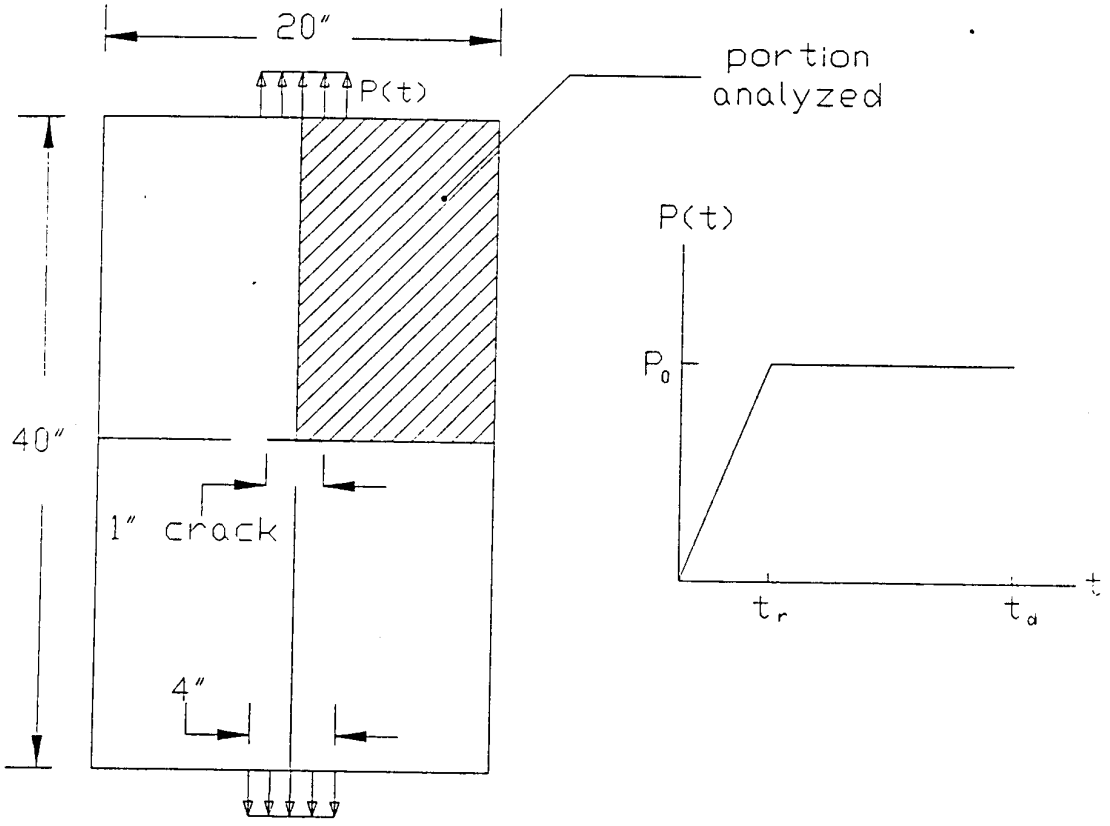

Figure 1 Numerical Model

The finite element model employed two types of elements: 2D isoparametric solid elements and control elements. In order to include the defects in the present investigation, the crack was introduced in the model and the stage for its development was set in the following manner: Assuming that the existing crack would propagate through the concrete material along a direction projected by the plane of crack flank, spring-damper elements were introduced along that projected crack direction with their longitudinal axes perpendicular to the crack direction. One end of those elements was attached to the main body of the model and the other end was fixed. These elements had a special capability that they would be active as long as their elongation was within a predefined limit. However, if the elongation exceeded that limit, the element would become inactive (i.e., fail).

Two interesting trends were observed. First, the stress at the tip of the propagating crack was always higher than the failure stress imposed on the spring-damper elements, as shown in Figures 2 and 3 for a loading rate of $1.45*10^6$ psi/s. However, this was observed to be more pronounced when the load was applied at a higher rate. Second, it was found that at a stress rate higher than $1.45*10^6$ psi/s, the stress level at the anticipated crack plane never exceeded 20 percent of the 510 psi failure stress, as shown in Figure 4 for a loading rate of $1.45*10^8$ psi/s. That means that the initial crack was not elongated any further, and the failure was somehow hindered by the oscillating action of the material along the projected crack plane. One may recall that Reinhardt (1986) and Freund (1972) pointed out that when the crack tip velocity increased, approaching the Rayleigh wave speed for the material, the stress intensity factor at the crack tip decreased, approaching zero.

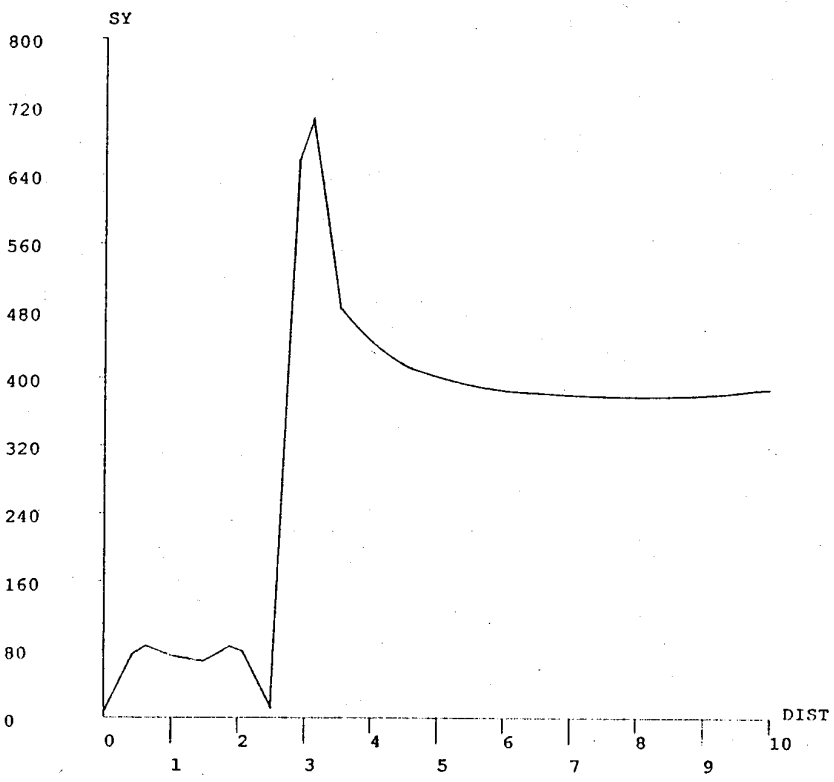

Figure 2 Stress Distribution at 1.4 ms

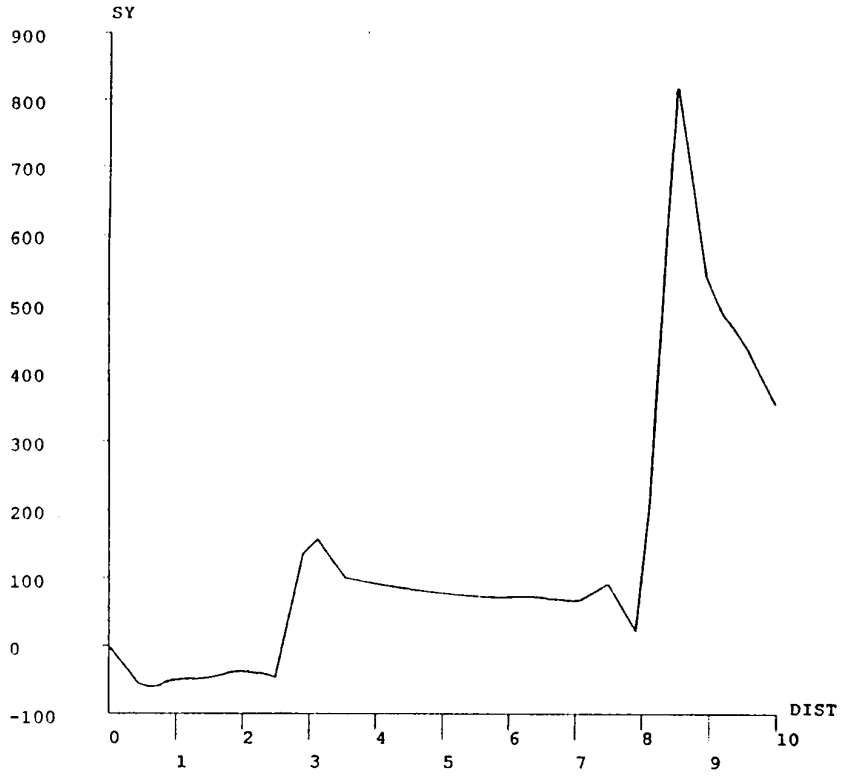

Figure 3 Stress Distribution at 1.46 ms

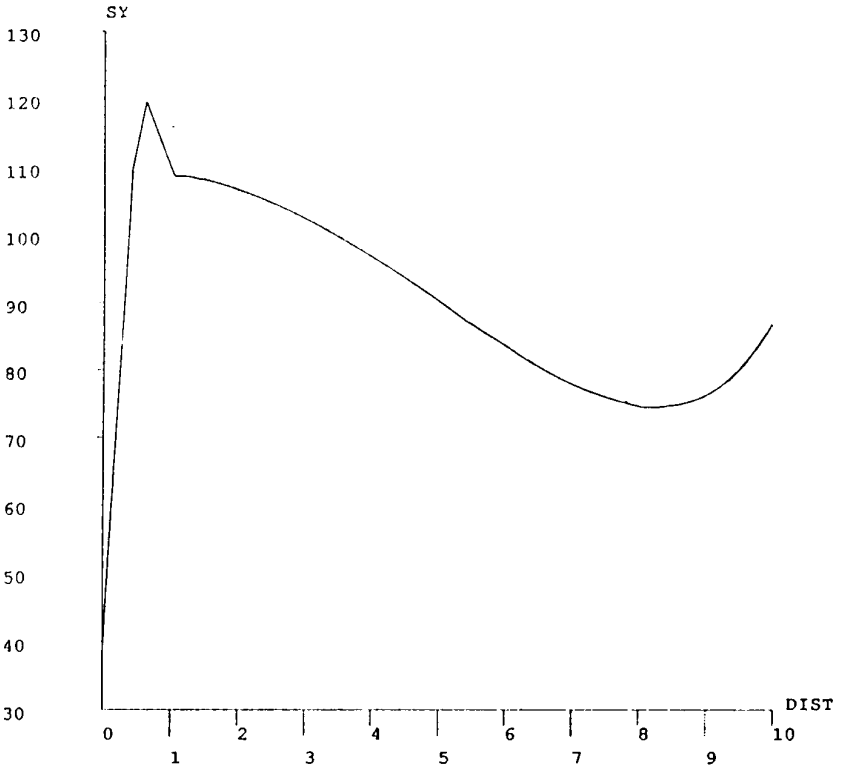

Figure 4 Stress Distribution for High loading Rate at 0.186 ms.

It is quite evident that this issue of strength enhancement cannot be resolved by consideration of radial inertia effects, as noted by Hughes and Watson (1978) and by Hegemier and Read (1985), nor from the point of view of size effects (Bažant 1986). Those effects might play some role under certain circumstances, however, it is most probable that some other mechanical and thermodynamic aspects of the material play important roles in determining this phenomenon. The present study is continuing along this direction, and the anticipated model will be incorporated into the fracture nonlocal continuum/damage plasticity model, described earlier.

REFERENCES

Barenblatt, G.I., "The Mathematical Theory of Equilibrium Cracks in Brittle Fracture", Advances in Applied Mechanics, Vol. 7, 1962, pp. 55-129.

Bažant, Z., "Mechanics of Distributed Cracking", Applied Mechanics Review, ASME, Vol.39, No. 5, May 1986, pp. 675-705.

Bischoff, P.H., and Perry, S. H., "Compressive Strain Rate Effects of Concrete", Mat. Res. Soc. Symp. Proc., Vol. 64, 1986, pp. 151-165.

Curbach, M., "Festigkeitssteigerung von Beton bei hohen Belastungsgeschwindikeiten", Dr.-Ing. Dissertation, Instituts für Massivbau und Baustofftechnologie, Universität Karlsruhe, 1987.

Dilger, W.H., Koch, R. and Kowalczyk, R., "Ductility of Plain and Confined Concrete Under Different Strain Rates", ACI Journal, Title No. 81-11, 1984, pp. 73-81.

Dugdale, D.S., "Yielding of Steel Plates Containing Slits", J. Mech. Phys. Solids, Vol. 8, 1960, pp. 100-104.

Fanella, D., and Krajcinovic, D., "A Micromechanical Model for Concrete in Compression", Engg. Fracture Mechanics, Vol. 29, No. 1, 1988, pp. 49-66.

Gran, J.K., Florence, A.L. and Colton, J.D., "Dynamic Triaxial Compressive Experiments on High-Strength Concrete", ASCE 6th Annual Structures Congress, Orlando, Florida, 1987.

Hegemier, G.A., and Read, H.E., "On Deformation and Failure of Brittle Solids: Some Outstanding Issues", Mech. of Mat., No. 4, 1985, pp. 215-259.

Hughes, B.P., and Watson, A.J., "Compressive Strength and Ultimate Strain of Concrete Under Impact Loading", Mag. Conc. Res., No. 30, 1978.

Ilankamban, R., and Krajcinovic, D., "A Constitutive Theory for Progressively Deteriorating Brittle Solids", Int. J. of Solids and Structures, Vol. 23, No. 11, 1987, pp. 1521-1534.

Ingraffea, A.R., and Gerstle, W.H., "Nonlinear Fracture Models for Discrete Crack Propagation", Application of Fracture Mechanics to Cementitious Composites, ed. S.P. Shah, Martinus Nijhoff Publishers, Dordrecht, The Netherlands, 1985.

John, R., and Shah, S.P., "Effect of High Strength and Rate of Loading on Fracture Parameters of Concrete", Proceedings, RILEM-SEM Int. Conf. on Frac. of Con. and Rock, Edited by S. P. Shah and S. E. Swartz, Houston, Texas, 1987.

Kipp, M.E., Grady, D.E., and Chen, E.P., "Strain-rate Dependent Fracture Initiation", Int. J. Fracture, Vol. 16, 1980, pp. 471-478.

Lindholm, U.S., Yeakley, L.M., and Nagy, A., "The Dynamic Strength and Fracture Properties of Dresser Basalt", Int. J. Rock Mech. Min. Sci. & Geomech., Abstr. 11, 1974, pp. 181-191.

Malvern, L.E., Tang, D., Jenkins, D.A., and Gong, J.C., "Dynamic Compressive Strength of Cementitious Materials", Mat. Res. Soc. Symp. Proc., Vol. 64, 1986, pp. 119-138.

Malvern, L.E., "Experimental and Theoretical Approaches to Characterization of Material Behavior at High Rates of Deformation", Proc. of the 3rd Conf. on Mechanical Properties at High Rates of Strain, 1984, Institute of Physics, London.

Mihashi, H. and Wittmann, F.H., "Stochastic Approach to Study the Influence of Rate of Loading on Strength of Concrete", HERON, Vol. 25, No. 3, 1980.

Mould, J.C. and Levine, H., "A Three-Invariant Viscoplastic Concrete Model", in Constitutive Laws for Engineering Materials: Theory and Applications Edited by C.S. Desai et. al., Elsevier Science Publishing Co., 1987, pp. 707-716.

Nilsson, L., "On Wave Propagation and Fracture in Concrete Structures", in Recent Advances in Engineering Mechanics and Their Impact on Civil Engineering Practice, Vol. 1, Edited by W. F. Chen and A. D. M. Lewis, ASCE, New York, New York, 1983, pp. 972-976.

Perzyna, P., "Fundamental Problems in Viscoplasticity", Recent Advances in Applied Mechanics, Vol. 9, 1966, pp. 244-368.

Reinhardt, H.W., "Strain Rate Effect on the Tensile Strength of Concrete as Predicted by Thermodynamic and Fracture Mechanics Models", Cement-Based Composites: Strain Rate Effects on Fracture, MRS Symposia Proceedings, ed. S. Mindess and S.P. Shah, Vol. 64, 1986, pp. 1-14.

Schumacher, J.V., "Nonlinear Structure Analysis for Fragility Estimates (NONSAFE)", TRW Defense Systems Group Report to the Air Force Weapons Laboratory, Kirtland AFB, New Mexico, 1983.

Sih, G.C., editor, Dynamic Crack Propagation, Noordhoff International Publication, Leyden, 1972.

Soroushian, P., Choi, K.B., and Alhamad, A., "Dynamic Constitutive Behavior of Concrete", ACI Journal, Title No. 83-26, 1986, pp. 251-259.

Soroushian, P., Choi, K.B., and Fu, G., "Tensile Strength of Concrete at Different Strain Rates", Mat. Res. Symp. Proc., Vol. 64, 1984, pp. 87-92.

Soroushian, P. and Sim, J., "Strain Rate Effects on the Dynamic Response of Reinforced Concrete Elements to Impulsive Loads", International Symposium of Interaction of Conventional Munitions with Protective Structures, Mannheim, West Germany, 1987, pp. 538-556.

Stevens, D.J., and Krauthammer, T., "Nonlocal Damage Plasticity Model for Impulse Loaded RC Beams", ASCE, Journal of Structural Engineering, Vol. 115, No. 9, September 1989, pp. 2329-2347.

Stevens, D.J., and Krauthammer, T., "Analysis of Blast-Loaded, Buried Arch Response Part I: Numerical Approach", Journal of Structural Engineering, ASCE, Vol. 117, No. 1, January 1991, pp. 197-212.

Stevens, D.J., Krauthammer, T., and Chandra, D., "Analysis of Blast-Loaded, Buried Arch Response Part II: Application", Journal of Structural Engineering, ASCE, Vol. 117, No. 1, January 1991, pp. 213-234.

Zieliński, A. J., "Model for Tensile Fracture of Concrete at High Rates of Loading", Cement and Concrete Research, Vol. 14, pp. 215-224, 1984.

STRAIN-RATE EFFECTS ON COMPRESSIVE TESTING OF FOAM

S. T. KUENNEN

C. A. ROSS

AIR BASE STRUCTURAL MATERIALS BRANCH

ENGINEERING AND SERVICES LABORATORY

HQ AIR FORCE ENGINEERING AND SERVICES CENTER

TYNDALL AIR FORCE BASE, FLORIDA 32403-6001

J. W. TEDESCO

DEPARTMENT OF CIVIL ENGINEERING

AUBURN UNIVERSITY

AUBURN, ALABAMA 36849

ABSTRACT

Polyurethane foams of variable density were tested quasistatically using a standard material test machine and dynamically using a split-Hopkinson pressure bar (SHPB). Yield stress, plateau stress, and compaction strain were all found to be both density and strain-rate dependent. Complete dynamic stress-strain curves may be produced using thin foam specimens and a SHPB.

INTRODUCTION

Generally, the effect of increasing load or strain-rates in material tests results in increased yield strength and ultimate strength. This effect is present in most all materials with the exception of work hardened aluminum and very high strength steel. The internal mechanism(s) which contribute to this phenomenon are not fully understood but experimental data are available for many materials.

Strain rate effects have also been observed in foams. Strain rate effects of small (0.38 - 0.5 inch, 10-13 mm dia) foam specimens of low density, 0.05 to 0.24 g/cc, are reported in References [1] and [2]. These data show increases in yield strength and plateau stress with increases in strain rate. (See Figure 1). Data of rigid polyurethane foam show the yield strength and plateau stress are linear with log of strain rate and the slope of the stress-log strain rate curve increases with increasing foam density.

The importance of strain-rate effects in foams to be used as shock mitigators lies in the necessity of knowing details of the stress-strain curve when calculating the energy absorption capability of the foam. Several parameters, as shown in Figure 1, may change with increased strain-rate. The increase of yield strength and plateau stress was observed in References [1] and [2]. Little or no increase in elastic modulus appears at the higher strain rates. However, the effect of strain-rate on the "lock-up" or compaction strain was not given in either reference. In energy absorption of shock mitigators the absorption process is effective up to compaction or "lock-up" strain. If the compaction strain is reduced to a low value, then the foam may become detrimental rather than an asset in mitigating the shock.

The objective of this study was to determine the effectiveness of the split-Hopkinson pressure bar (SHPB) to produce details of the stress-strain curve at high strain-rates.

The low strain-rate data of this study were obtained using a standard material test machine. All tests at the lower strain rates were run under a load control mode and the strain was calculated using the displacement output and the specimen length. The strain rate was determined at the plateau stress for all specimens including the higher strain-rate tests.

The split-Hopkinson pressure bar (SHPB), described in Reference [3], is best suited for test of materials which deform plastically. A very basic assumption of the SHPB is that several wave reflections must occur in the specimen in order to achieve uniformity of stress along the specimen length. This means that the initial stresses, which is the elastic portion of the response, are a result of nonuniform loading and will not represent a true elastic modulus of the material.

All SHPB tests were performed using the 51 mm diameter Air Force Engineering and Services Center SHPB at Tyndall AFB, Florida [4]. Specimens of the same diameter as the SHPB were tested using a 0.653 m striker which results in a 257 microsecond pulse length.

The procedure for changing the strain rate of the test is either change specimen length or increase the incident stress by increasing the impact velocity of the striker bar. Both methods were used for the foam tests. It was found that a specimen length of 3.2 mm (0.13 in) and an incident pressure of approximately 220 MPa were necessary in order to have sufficient energy to produce the compaction strain in the specimens. In addition, it was determined that foam stresses less than 0.3 MPa were masked by noise of the instrumentation system.

RESULTS AND DISCUSSION

Tests were performed on several kinds of foams and of various densities. The data reported here is limited to that of Table 1. Four different densities of polyurethane (General Plastics FR 3700 Series) rigid unicellular foam were tested and compared to a lower density, lower strength phenolic foam.

TABLE 1 - COMPRESSIVE FOAM PROPERTIES

Foam	Density	Comp. Strength at 15% Strain			Exp. Strength Ratio
		Manuf.	Exp. Static *	Exp. Dynamic **	Dynamic/Static
	g/cc	MPa	MPa	MPa	
Phenolic	0.10	No Data	0.9	1.1	1.2
Polyurethane	0.16	2.5	2.0	3.0	1.5
Polyurethane	0.22	4.3	4.4	7.0	1.6
Polyurethane	0.30	7.0	6.8	12.0	1.7
Polyurethane	0.48	14.7	19.0	38.0	2.0

*Static strain-rate 1.0E-3/S to 1.0E-2/S

**Dynamic Strain-rate 2.0E+3/S to 3.0E+3/S

The foam that was tested, normally used in the aircraft industry, was chosen for its good quality control and uniformity of properties across the sheet. It would not be an economical shock mitigation material.

Stress-strain diagrams for the compressive tests are given in Figures 2 to 6. All curves show the typical yield, plastic plateau and followed by the compaction or lock up strain. All specimens were tested parallel to the foam rise. The specimens were cut from a single block and final machined in a machine shop lathe. All specimens were of circular cross-section of nominal 50.8 mm diameter and flat ended.

Manufacturer's data show the polyurethane foams to have a density dependent modulus of elasticity. But, due to problems associated with nonuniformity of stress in the SHPB at the low dynamic strains, there is no basis to predict a strain-rate dependent modulus. The assumption in

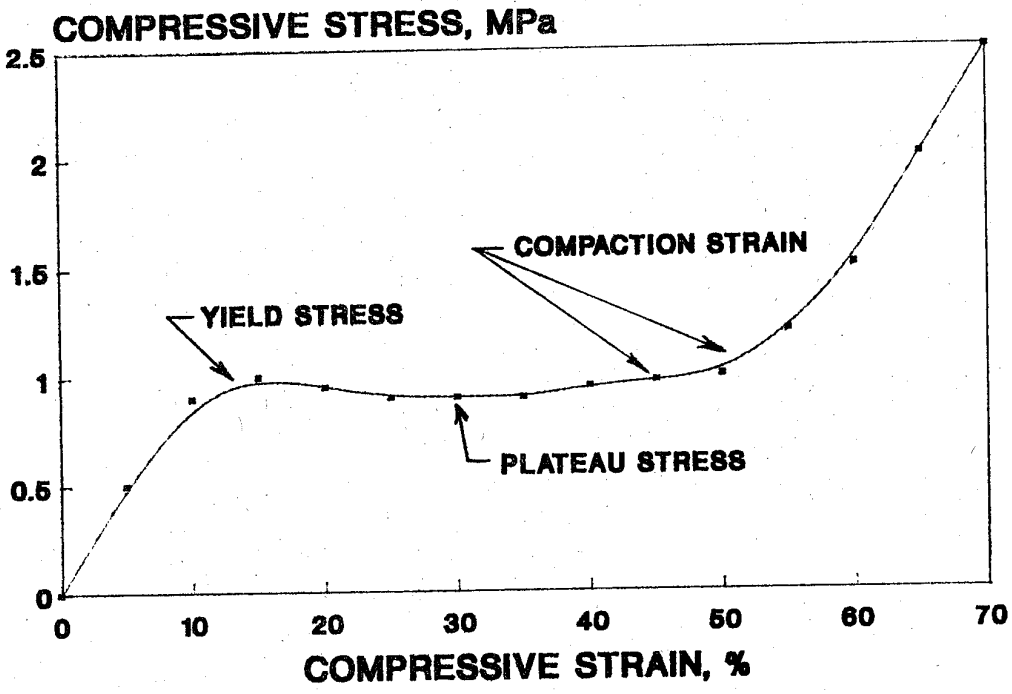

Figure 1. Typical Stress-Strain Curve for Shock Mitigating Foam

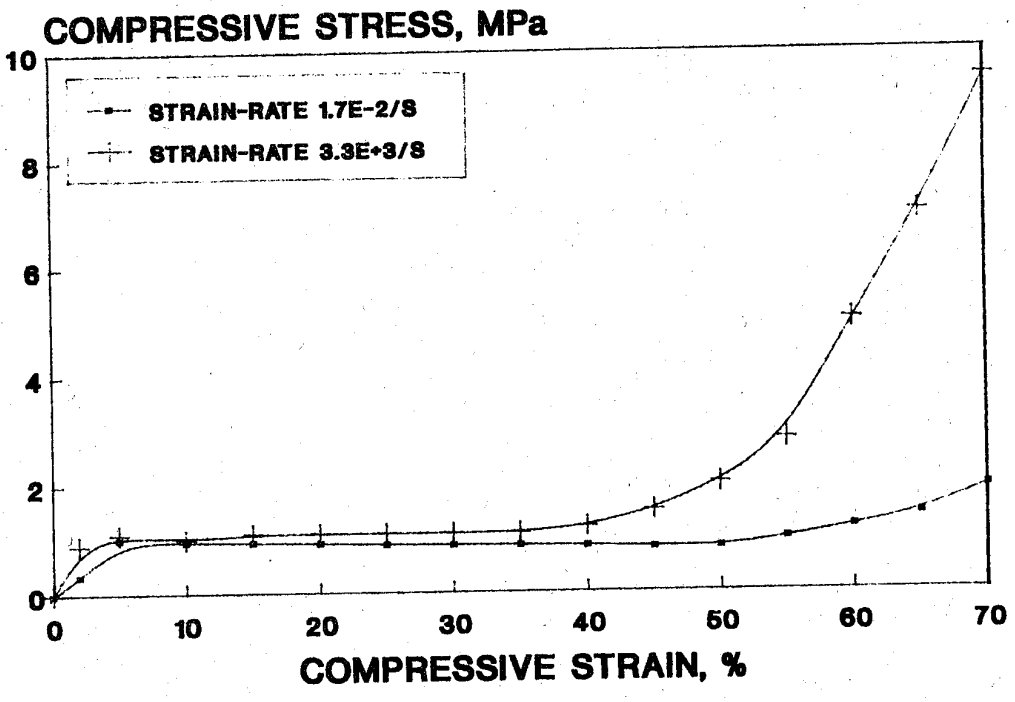

Figure 2. Stress-Strain Curve for Phenolic Foam. Density = 0.1 g/cc.

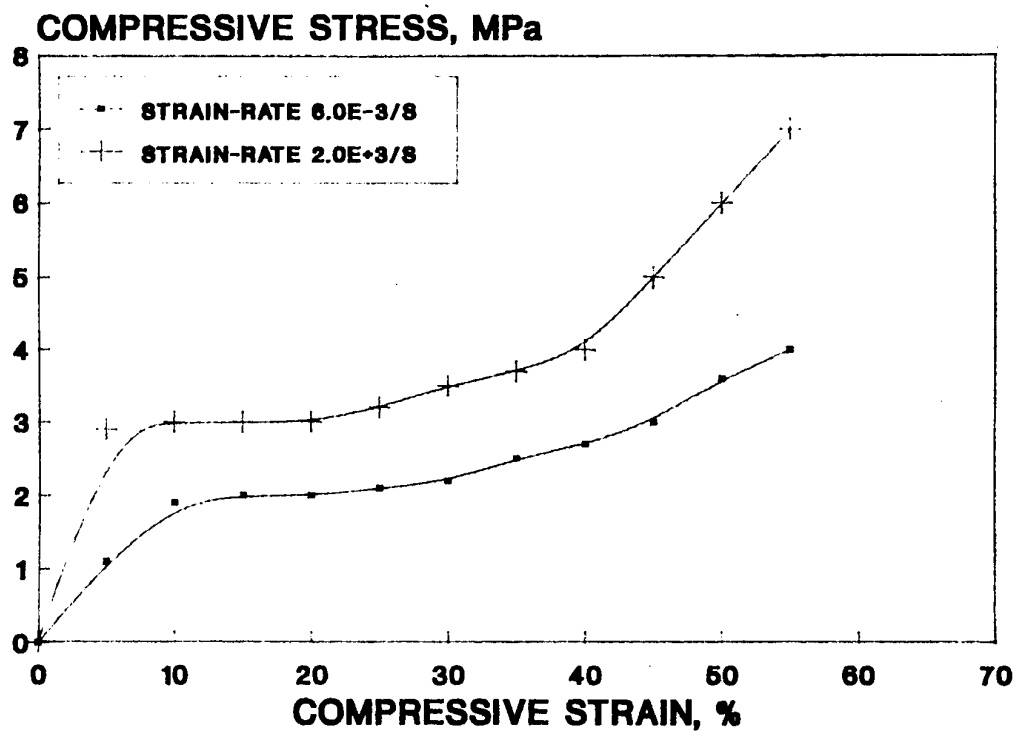

Figure 3. Stress-Strain Curve for Polyurethane Foam. Density = 0.16 g/cc.

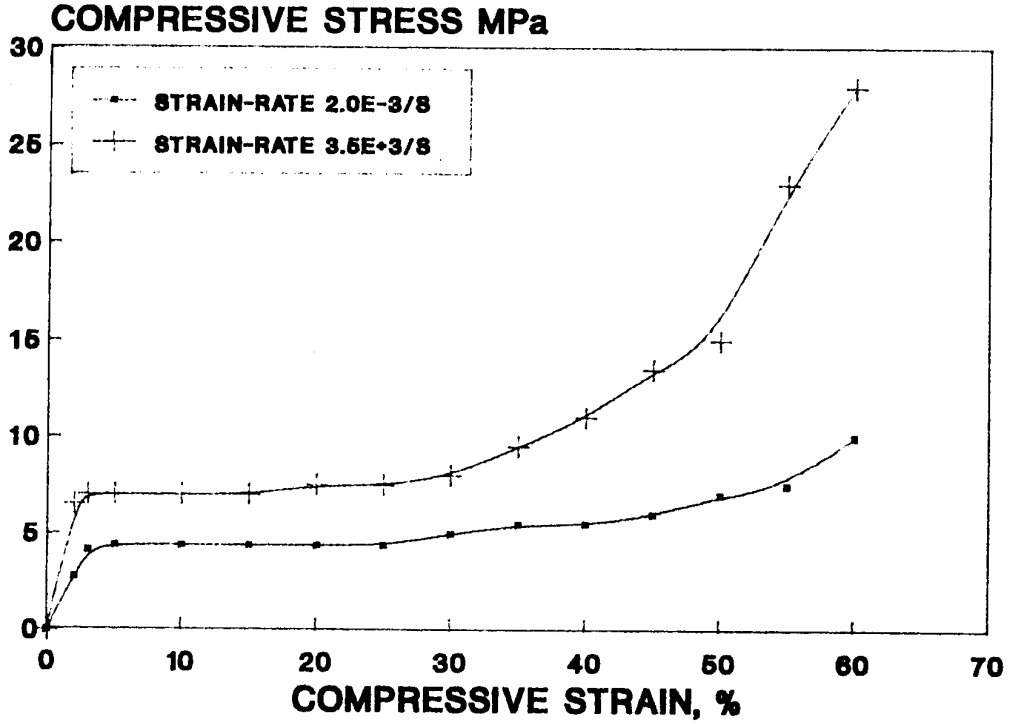

Figure 4. Stress-Strain Curve for Polyurethane Foam. Density = 0.22 g/cc.

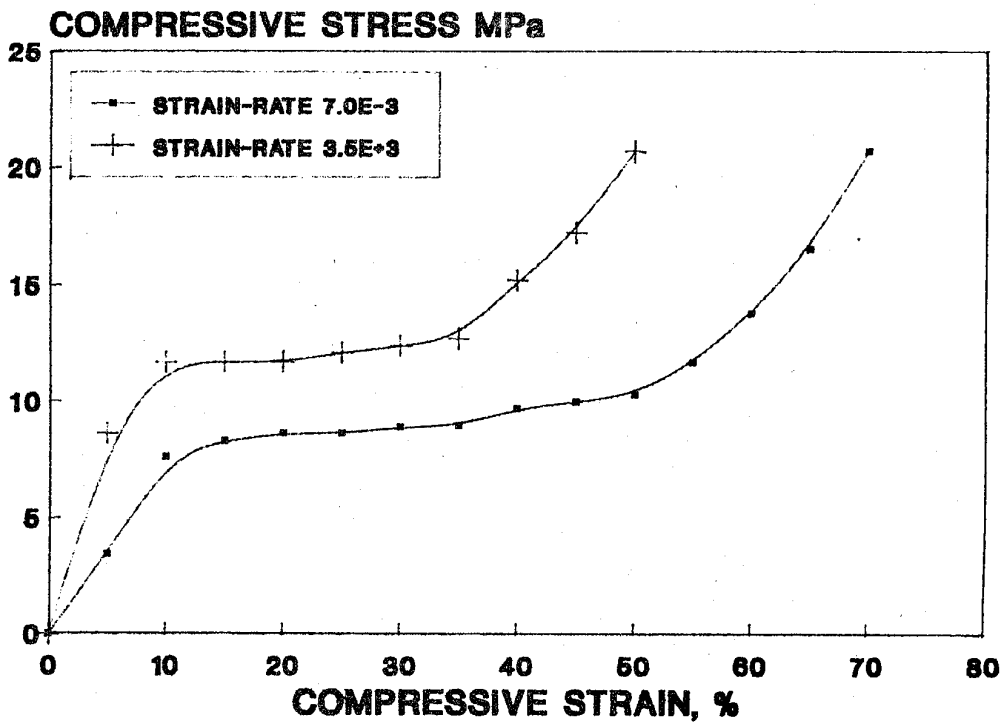

Figure 5. Stress-Strain Curve for Polyurethane Foam. Density = 0.30 g/cc.

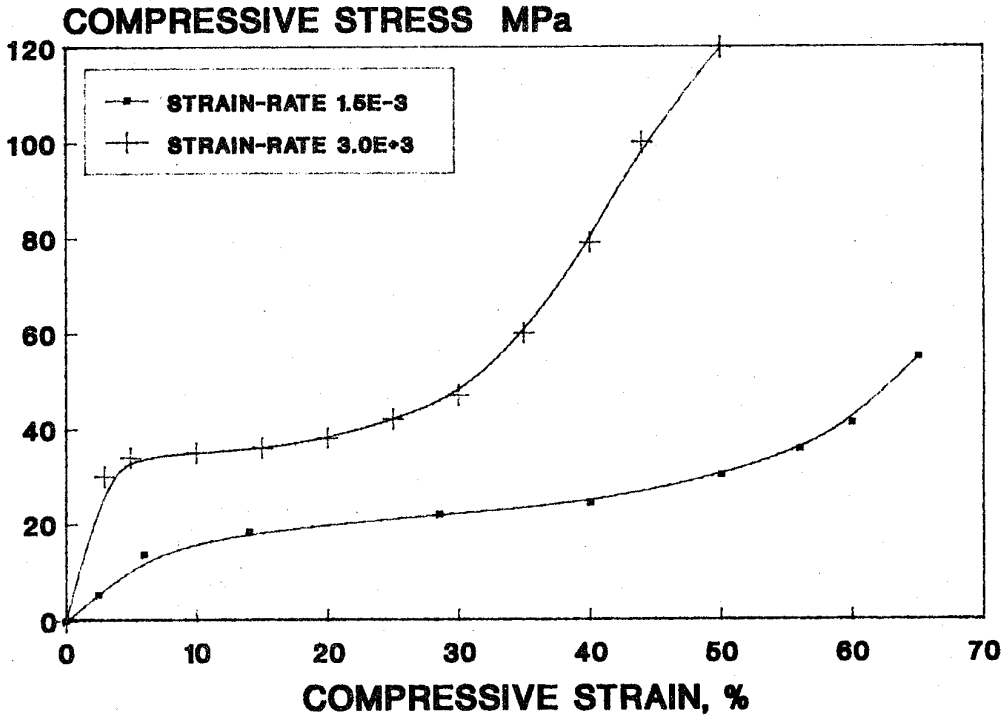

Figure 6. Stress-Strain Curve for Polyurethane Foam. Density = 0.48 g/cc

Reference [1] is that the elastic modulus is strain-rate independent. The yield stress and plateau stress are found to be density and strain-rate dependent and in qualitative agreement with data of References [1] and [2]. The compaction strain or tendency toward compaction, as shown in Figures 2 to 5, is very nebulous but does show a tendency to occur at lower strain as the strain-rate increases. Although not easily defined, a measure of this decrease was chosen at a point where there appeared a 50 percent increase above a plateau stress, measured at 15 percent strain. Since this quantity is probably both density and strain-rate dependent, there is insufficient data here to quantify a dependency. However, since energy is absorbed as long as the material is not compacted or locked, it is important to account for reduced compaction strain at high strain-rates. For the data given here a reduction of 10 to 30 percent in the compaction strain is discernible at strain rates above 1000/sec. Further tests are recommended to better describe the plateau stress and compaction strain as functions of density and strain rate.

CONCLUSION

Yield stress, plateau stress, and compaction strain are found to be both density and strain-rate dependent in polyurethane foams. Using thin specimens the complete dynamic stress-strain curves may be found using a split-Hopkinson pressure bar. Additional tests are needed to better describe the plateau stress and define, relative to this stress, an onset of the compaction strain.

REFERENCES

1. Hinckley, W.M., and Yang, J.C.S., Analysis of "Rigid Polyurethane Foam as a Shock Mitigator," Naval Ordnance Laboratory White Oak, Silver Spring, MD 20910 NOLTR-73-162 August 1973, p 50.

2. Hoge, K.G.. and Wasley, R.J., "Dynamic Behavior of Various Foam Materials," Applied Polymer Symposia, No 12, pp 97-109, 1969.

3. Nicholas, T. "Material Behavior at High Strain-Rates," Chapter 8 of Impact Dynamics, ed. Zukas, J.R., John Wiley and Sons N.Y. pp 180-332, 1982.

4. Ross, C.A., "Split Hopkinson Pressure Bar Tests," HQ AFESC/RDCM, HQ AF Engineering and Services Center, Tyndall AFB, FL 32403-6001, ESL-TR-88-82, p 80, March 1989.

ACKNOWLEDGEMENT

All tests were performed in the Engineering and Services Laboratory, Headquarters Air Force Engineering and Services Center, Tyndall Air Force Base, Florida. Samples of foam were furnished by the General Plastic Manufacturing Company, Tacoma, Washington.

EXPERIMENTELLE UNTERSUCHUNGEN ZUM DYNAMISCHEN TRAGVERHALTEN VON SONDERFASERBETON - SIFCON

Chr. Mayrhofer

Fraunhofer-Institut für Kurzzeitdynamik
Ernst-Mach-Institut
Institutsteil Wintersweiler
Am Klingelberg 1
7859 Efringen-Kirchen 6

KURZFASSUNG

Militärische Schutzeinrichtungen, die einen hohen Schutzgrad aufweisen müssen, erfordern hochfeste Werkstoffe. Mit SIFCON und speziellen Faserbetonen liegen Baustoffe vor, die neben hohen Festigkeitswerten auch das für dynamische Beanspruchungen notwendige duktile Verhalten aufweisen. Durch die Bildung plastischer Gelenke wird vor allem das Energieaufnahmevermögen gesteigert. Damit lassen sich im Vergleich zu Stahlbeton selbst bei stark bewehrten Konstruktionen äußerst günstige dynamische Lastfaktoren erreichen. Mit den ermittelten maßgebenden Einflußgrößen auf die Biegezug-, Druckfestigkeit und das Arbeitsvermögen sind die Auswirkungen auf die dynamische Tragfähigkeit erfaßbar.

EINLEITUNG

Durch die multidirektionale Faserverteilung entsteht ein weitestgehend homogener Werkstoff, der gegenüber Stahlbeton ein isotropes Verhalten zeigt. Der damit verbundene bessere Gefügezusammenhalt reduziert bei Stoßbelastungen die Gefahr von Abplatzungen und das Penetrieren von Bauteilen. Die hohe Energieabsorptionskapazität sowie das Dämpfungsvermögen infolge innerer Reibung lassen günstige Einsatzmöglichkeiten bei dynamischen Beanspruchungen erwarten.

Bei Faserbeton ist der Fasergehalt V_f (Volumen-%) ein wichtiger Parameter für die Materialeigenschaften. Aus Gründen der Verarbeitbarkeit ist bei konventionellem Faserbeton der maximale Faseranteil auf $V_f = 2 - 3$ % begrenzt. Die damit bereits erreichten guten Ergebnisse (/1/, /2/) waren durch noch höhere Faseranteile weiter zu verbessern. Dazu wurden unterschiedliche Faserlängen und Fasergemische verwendet, bei denen mit entsprechenden Anteilen an kurzen und langen Fasern sowohl Mischprobleme (kurze Fasern lassen sich gut einmischen) als auch eine verminderte Plastizität (nur lange Fasern garantieren ein duktiles Verhalten) ausgeschlossen werden sollte. Mit dieser Maßnahme konnte der Fasergehalt bis auf $V_f = 5$ % gesteigert werden. Als Zuschlagstoffe kamen die Korngruppen 0/4 und 0/8 zur Anwendung.

Noch größere Fasermengen (maximal 20 %) sind nur mit SIFCON (Slurry Infiltrated Fiber Concrete) möglich, dem kein Zuschlag, sondern nur Zementleim beigegeben wird. Dadurch liegt ein anderer Werkstoff vor, der mit "Faserzement" zu bezeichnen ist.

Ziel der Arbeiten war, an kleinen Probebalken die Wirkung der Parameter Zuschlagstoff, Faserabmessung, Fasergeometrie und Faseranteil auf die charakteristischen Materialeigenschaften

Biegezugfestigkeit,
Druckfestigkeit und
Arbeitsvermögen

zu erfassen. Dabei fanden auch Besonderheiten bei den Probekörperabmessungen in Verbindung mit den Laststellungen (Schubschlankheit) Beachtung sowie Kombinationen mit Stahlbeton und SIFCON bzw. Faserbeton, die vor allem der Bildung plastischer Gelenke dienten. Die Ermittlung des dynamischen Tragverhaltens erfolgte an Platten.

VERSUCHSDURCHFÜHRUNG

Mit Ausnahme der Untersuchungen zum Einfluß der Schubschlankheit (λ = a/d) wiesen die Balken die Abmessungen $l \cdot b \cdot d = 600 \cdot 100 \cdot 100$ mm^2 und die Platten $l \cdot b \cdot d = 1250 \cdot 750 \cdot 75$ mm^3 auf. Der Aufbau der "Verbundkonstruktion" Stahlbeton/SIFCON zur Unterstützung einer Gelenkbildung in Balkenmitte ist nachfolgend aufgeführt:

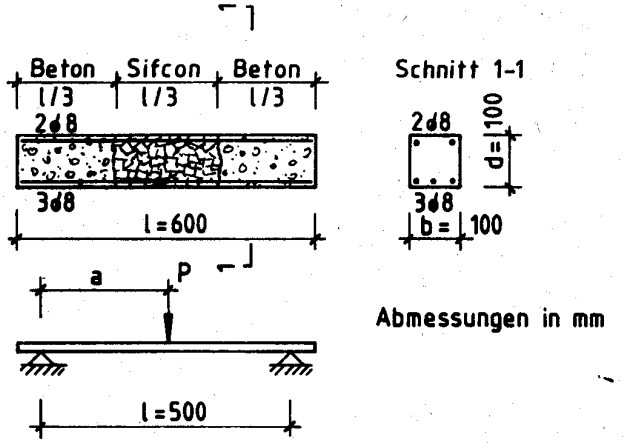

Abb. 1: SIFCON-verstärkter Stahlbetonbalken

Das verwendete Tragsystem entsprach einer zweiseitigen, drehbaren Lagerung, bei der bei den Balken eine Einzellast und bei den Plattenbeanspruchungen eine flächenhafte Belastung aufgebracht wurde. Bei der dynamischen Versuchsdurchführung kam der quasistatische Beanspruchungsfall (Drucksprung, Belastungsdauer/Eigenschwingdauer $\rightarrow \infty$) zur Anwendung. Diese ungünstigste Belastung (unterer Grenzwert) bildet die Basis bei der Nachweisführung über die Anwendbarkeit des Rechenmodells des Ein-Massen-Schwingers, mit dem außerdem die Zusammenhänge von Druck-Zeit-Verläufen kurzer Einwirkungszeiten bestimmt wurden.

Bei Faserbeton konnte wegen der hohen Faseranteile ($V_f \leq 5$ %) dem Beton nur gerade Fasern (OL) beigemischt werden. Hingegen waren bei SIFCON davon abweichende Faserformen einsetzbar (Abb. 2).

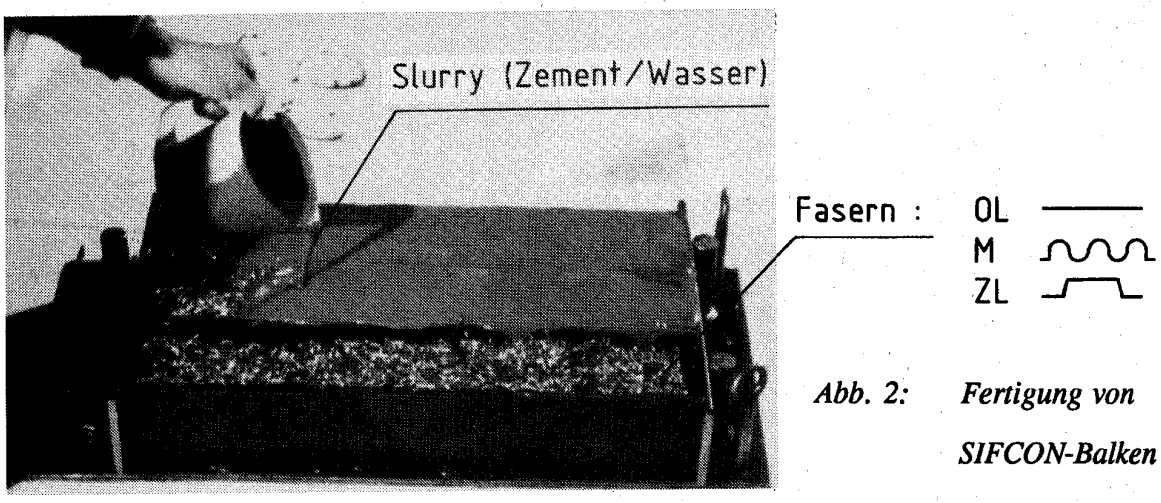

Abb. 2: Fertigung von SIFCON-Balken

ERGEBNISSE

Für gleichartige Fasergerüste (einstufig, Faser OL) ist in den Abbn. 3 und 4 die Wirkung des Faseranteils V_f und des Verhältniswertes Faserlänge zu Durchmesser (l_f/d_f) für Faserbeton und SIFCON auf die Werkstoffeigenschaften dargestellt. Die Biegezugfestigkeit von Faserbeton wird danach von den beiden Parametern V_f und l_f/d_f gleichermaßen beeinflußt, während bei SIFCON der Faseranteil unbedeutend ist und die Biegezugfestigkeit im Grunde nur vom l_f/d_f der Faser geprägt wird. Darin besteht ein ganz wesentlicher Unterschied zwischen SIFCON und Faserbeton. Außer der Dominanz von l_f/d_f ist bei SIFCON noch die Faserform entscheidend auf das Festigkeitsverhalten (Tab. 1, 2).

Wie die Bilder der Abbn. 3 und 4 des weiteren zeigen, ist die Wirkung von V_f und l_f/d_f auf andere Materialeigenschaften durchaus unterschiedlich. So bleibt die Druckfestigkeit bei Faserbeton von V_f und l_f/d_f praktisch unberührt. Bei SIFCON ist hingegen eine Abhängigkeit von diesen beiden Größen feststellbar. Bezüglich der Duktilität (Arbeitsvermögen, Plastifizierung) dominiert hingegen bei beiden Werkstoffen der Einfluß von l_f/d_f gegenüber dem Faseranteil.

Die großen Verformungseigenschaften von SIFCON und die Fähigkeiten zur Gelenkbildung gehen aus der Abb. 5 hervor.

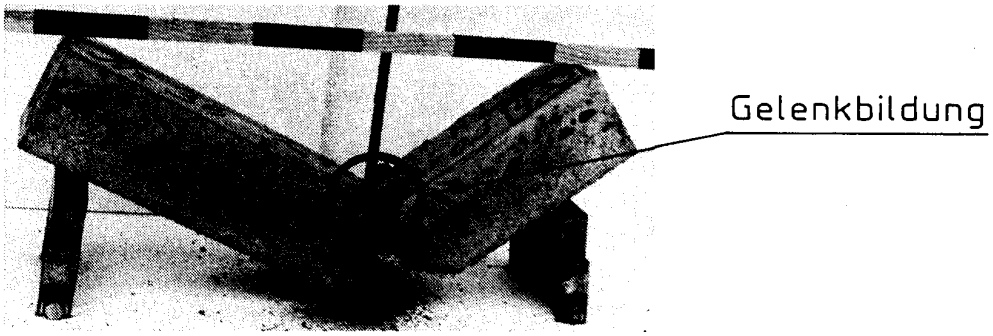

Abb. 5: Bruchzustand eines SIFCON-Balkens

In diesem hohen Energieaufnahmevermögen besteht generell der Hauptvorteil. Dies gilt im besonderen für Faserbeton, bei dem die Faserzugabe - selbst bei $V_f = 5$ % - nur die Duktilität, nicht aber die Biegezug- oder Druckfestigkeit entscheidend erhöht. In Abb. 6 sind dazu die Materialkennwerte von Faserbeton auf die von unbewehrtem Beton bezogen.

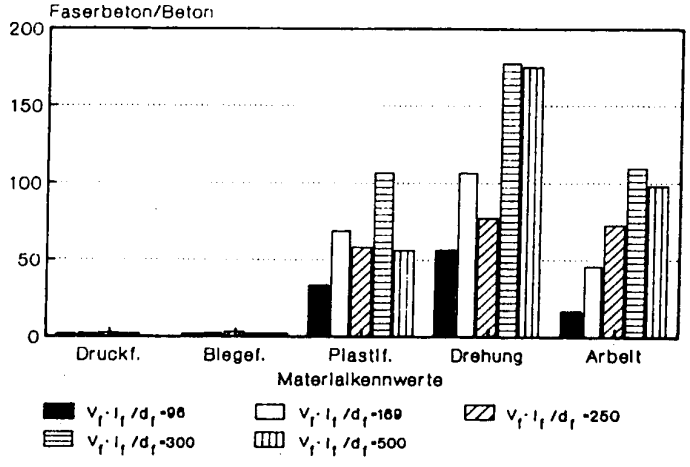

Abb. 6: Steigerungsfaktoren der charakteristischen Materialkennwerte von Faserbeton im Bezug zu unbewehrtem Beton für verschiedene Werte von $V_f \cdot l_f/d_f$

Neben der drastischen Steigerung der Verformungsenergie (Plastifizierung, bezogene Drehung, Arbeitsvermögen) geht aus Abb. 6 auch noch ein gewisser Sättigungsgrad hervor. Dies bedeutet, daß eine Verbesserung der Materialeigenschaften mit zunehmendem $V_f \cdot l_f/d_f$ nur bis zum Erreichen eines gewissen Grenzwertes eintritt und darüber hinausgehende Anteile - wegen Verdichtungs- und Verarbeitungsschwierigkeiten - eine Verschlechterung zur Folge haben.

Die Verwendung mehrstufiger Fasergemische (maximal drei abgestufte l_f/d_f-Verhältnisse) wirkt sich lediglich auf die Verarbeitbarkeit günstig aus und führt zu keinen beachtenswerten Änderungen der Werkstoffeigenschaften (Abb. 7).

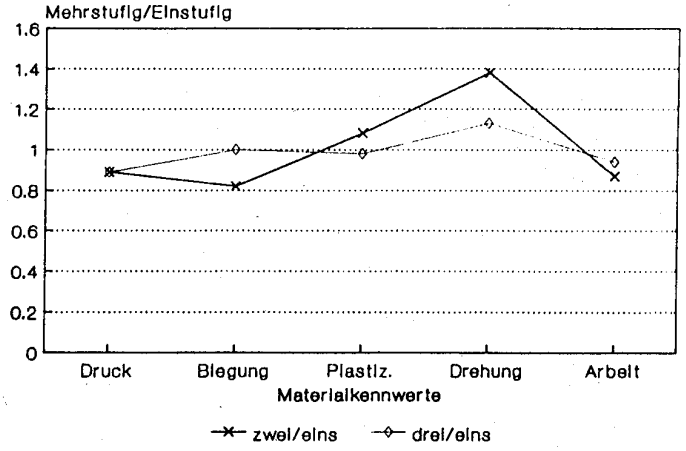

Abb. 7: Einfluß von Fasergemischen im Vergleich zu einstufigen Faseraufbauten auf die Materialeigenschaften von Faserbeton

Mit SIFCON war außer der Erhöhung der Energieaufnahme (2fach höher als bei Faserbeton) auch noch bei der Biegezug- und Druckfestigkeit ein bedeutender Zuwachs registrierbar. Maximal wurden erreicht:

Faserbeton - $\sigma_{BZ} = 11$ N/mm^2, $\beta_W = 70$ N/mm^2
SIFCON - $\sigma_{BZ} = 29$ N/mm^2, $\beta_W = 92$ N/mm^2

Bei der Beurteilung der Biegezugfestigkeitswerte sind jedoch die geometrischen Verhältnisse der Probekörper zu beachten. Im besonderen werden bei SIFCON in der Literatur häufig extrem hohe Festigkeitswerte benannt, die aufgrund der Laststellung und Balkenstärke nicht mehr dem Lastfall Biegung entsprechen, sondern Schubbeanspruchungen zuzuordnen sind. Den Einfluß der Schubschlankheit $\lambda` = a/d$ auf die Biegezugfestigkeit von SIFCON zeigt für verschiedene Faseranteile die Abb. 8. Daraus folgt, daß ähnlich wie bei Stahlbeton erst für etwa $\lambda` > 5$ keine Auswirkungen der Schubschlankheit auf die Biegezugfestigkeit mehr bestehen. Dabei ist zudem der Fasergehalt zu berücksichtigen.

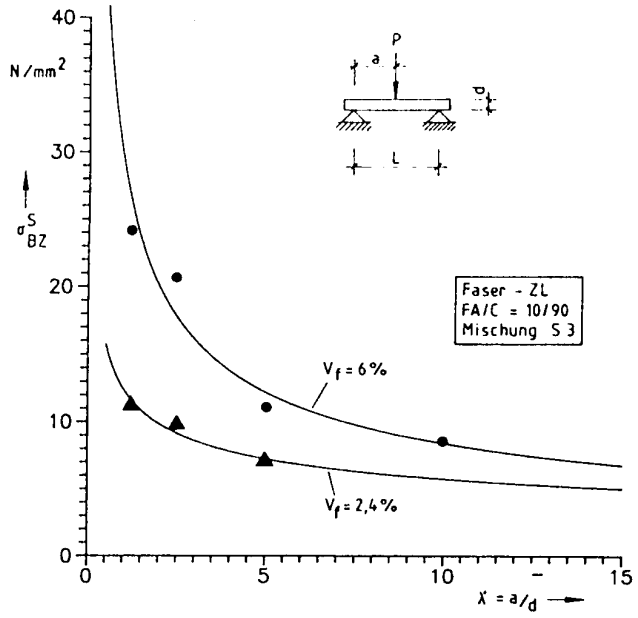

Abb. 8: Auswirkungen der Schubschlankheit auf die Biegezugfestigkeit von SIFCON

Stahlbetonkonstruktionen neigen mit zunehmendem Bewehrungsgrad zu einem Sprödbruchverhalten und zur Reduzierung der Rotationsfähigkeit. Mit Ergänzungen durch Faserbeton oder SIFCON (Abb. 1) kann dieses für dynamische Beanspruchungen ungünstige Verhalten nachhaltig verändert werden. Nach der Abb. 9 nimmt das bezogene Drehvermögen $\theta \cdot d$ ($\theta = 4 \cdot x_{Br}/L$) der auf Schub versagenden Balken trotz der hohen Bewehrungsanteile infolge Faserbeton und SIFCON zu.

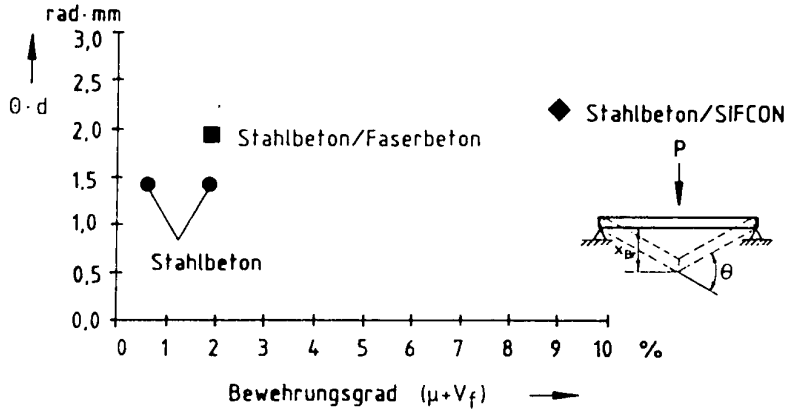

Abb. 9: Rotationsverhalten von mit Faserbeton und SIFCON verstärkten Stahlbetonbalken bei Schubversagen

Mit den durch Fasern verstärkten Stahlbetonbalken läßt sich außer dem größeren Drehvermögen auch noch die aufnehmbare Belastung steigern, die im Verhältnis zu Stahlbeton folgende Erhöhungen mit sich bringt:

1,3fache bei Stahlbeton/Faserbeton
1,7fache bei Stahlbeton/SIFCON

Um die an kleinen Balken gewonnenen Ergebnisse auf eine breitere Basis zu stellen, fanden zusätzlich Versuche an Platten mit größeren Stützweiten statt. Das daraus resultierende Rotationsverhalten der ausschließlich betrachteten SIFCON-Konstruktionen mit Biegeversagen ist in der Abb. 10 aufgeführt und gleichartigen Stahlbetonplatten gegenübergestellt. Damit ist auch für biegeweichere Bauteile in Verbindung mit größeren Rißweiten die Wirksamkeit von SIFCON im Zusammenhang mit der Bildung plastischer Gelenke bestätigt.

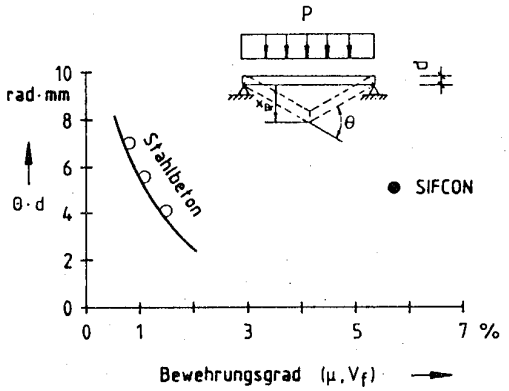

Abb. 10: Vergleich des Drehvermögens von biegebeanspruchten Platten aus Stahlbeton und SIFCON

Das statische und dynamische Last-Verformungsverhalten von SIFCON-Platten enthält die Abb. 11. Über den daraus ermittelbaren dynamischen Lastfaktor $\lambda = p_d/p_s$ (abhängig von V_f) und Berechnungen auf der Grundlage des Modells des Ein-Massen-Schwingers konnte als Zerstörungskriterium gefunden werden, daß die untersuchten Platten beim 3fachen der elastischen Durchbiegung (normierte Größe $x_E = 1/\lambda$) zu Bruch gehen. Mit diesem Kriterium und den in Abb. 11 bestimmten statischen Widerstandskennlinien läßt sich das in Abb. 12

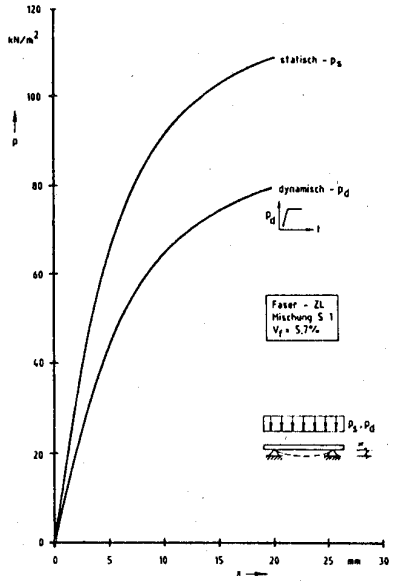

Abb. 11: Statische und dynamische Lastverformungskennlinien zweiseitig gelagerter SIFCON-Platten ($l \cdot b \cdot d = 125 \cdot 75 \cdot 7{,}5$ cm^3)

angegebene Druck-Impuls-Diagramm entwickeln. Damit sind Aussagen über aufnehmbare Druck- und Impulswerte möglich, die nicht experimentell untersucht wurden. Für den Grenzbereich einer quasistatischen Belastung (Belastungsdauer >> Eigenschwingdauer) wird eine maximale Bruchlast von $p_d \doteq 70$ kN/m^2 maßgebend und im Impulsbereich ein für die Zerstörung erforderlicher Mindestimpuls von $I \doteq 460$ kN/m$^2 \cdot$ ms.

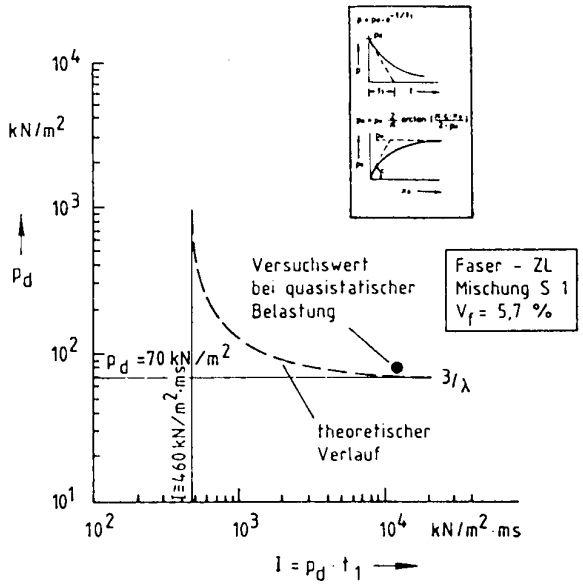

Abb. 12: Druck-Impuls-Diagramm für zweiseitig gelagerte SIFCON-Platten ($l \cdot b \cdot d = 125 \cdot 75 \cdot 7{,}5\ cm^3$)

ZUSAMMENFASSUNG

Bei Faserbeton nimmt selbst bei hohen Faseranteilen (V_f = 5 %) im Vergleich zu unbewehrtem Beton im wesentlichen nur das Arbeitsvermögen zu. Demgegenüber wird mit SIFCON auch bei der Biegezug- und Druckfestigkeit ein deutlicher Festigkeitszuwachs erreicht. Während für das Festigkeitsverhalten von Faserbeton das Produkt $V_f \cdot l_f/d_f$ ausschlaggebend ist, tritt bei SIFCON der Einfluß von V_f in den Hintergrund. Die Materialeigenschaften von SIFCON werden durch das l_f/d_f-Verhältnis der Faser und der Faserform geprägt, wobei abgewinkelte Faserenden die günstigsten Ergebnisse liefern.

Fasergemische (abgestufte l_f/d_f-Verhältnisse) haben gegenüber einstufigen Faseraufbauten nur Vorteile bei der Verarbeitung (problemlose Verteilung), nicht aber bei den Materialkennwerten.

Einflüsse der Schubschlankheit auf die Biegezugfestigkeit sind bei SIFCON erst für $\lambda' > 5$ bis 10 (in Abhängigkeit von V_f) ohne Bedeutung. Bei kleineren λ' Werten sind vergleichende Betrachtungen von Biegezugfestigkeiten nur für gleiche Schubschlankheiten möglich.

Durch die Zugabe von Fasern (Faserbeton, SIFCON) läßt sich das Rotationsvermögen von stark bewehrten Stahlbetonkonstruktionen erhöhen und ein Sprödbruchverhalten verhindern. Mit SIFCON ist auch bei hohen Faseranteilen ein günstiges dynamisches Tragverhalten erreichbar (große λ-Werte).

LITERATUR

/1/ Mayrhofer, Chr.:
Voruntersuchungen zum Verhalten von bewehrten und nicht bewehrten Faserbetonplatten unter dynamischer Belastung
E 16/80, Ernst-Mach-Institut, Freiburg i. Br., Nov. 1980

/2/ Hülsewig, M., Mayrhofer, Chr.:
Endballistisches Verhalten von plattenförmigen Objekten aus Faserbeton bei punkt- und flächenhafter Belastung
E 4/82, Ernst-Mach-Institut, Freiburg i. Br., März 1982

Faser-bezeich-nung	Faseranteil V_f [%]	Faseranteil $V_f \cdot l_f/d_f$ [%]	Misch-rezept	Biegezug-festigkeit $\sigma_{BZ}^{f,b}$ [N/mm²]	Druck-festigkeit $\beta_w^{f,b}$ [N/mm²]	Arbeits-vermögen $A^{f,b}$ [kN·cm]	bezogene Drehung $\theta^{f,b} \cdot d$ [rad·mm]	Plastifizierungsgrad $\bar{\beta}^{f,b}$ [-]
OL-1	3,0	96	B 3	6,6	49,2	36,4	34,0	33,8
OL-2	4,0	250	B 3	11,2	70,4	160,4	46,4	58,7
OL-3	3,0	300	B 3	8,5	50,5	241,0	106,7	106,8
OL-3	5,0	500	B 3	7,7	-	216,3	105,2	56,4
OL-3	2,1	210	B 4	6,3	49,5	168,9	88,4	63,1
OL-4	3,0	169	B 3	6,0	42,0	100,3	64,0	69,7

Tab. 1: Versuchsergebnisse - Faserbeton (einstufig)

Faser-bezeich-nung	Faseranteil V_f [%]	Faseranteil $V_f \cdot l_f/d_f$ [%]	Misch-rezept	Biegezug-festigkeit σ_{BZ}^{s} [N/mm²]	Druck-festigkeit β_w^{s} [N/mm²]	Arbeits-vermögen A^{s} [kN·cm]	bezogene Drehung $\theta^{s} \cdot d$ [rad·mm]	Plastifizierungsgrad $\bar{\beta}^{s}$ [-]
OL-1	11,3	362	S 1	5,6	14,0	28,0	16,9	13,0
OL-3	4,6	460	S 1	14,2	68,4	347,6	90,3	47,3
OL-3	5,8	580	S 1	16,5	75,3	432,1	80,5	40,7
OL-4	4,6	259	S 1	5,7	39,3	59,2	32,0	31,3
OL-4	8,4	473	S 1	9,0	71,5	139,8	69,7	33,3
OL-4	11,3	636	S 1	10,2	68,9	161,9	77,7	41,4
M-1	8,4	462	S 1	10,5	52,7	291,8	82,1	41,9
M-1	11,3	622	S 1	10,3	66,8	337,5	100,9	62,7
M-2	6,7	436	S 1	9,0	51,0	392,3	119,1	61,8
M-3	6,7	503	S 1	11,1	43,7	473,3	108,9	51,1
M-4	8,4	504	S 1	13,2	57,3	393,9	91,8	26,4
M-4	10,7	642	S 1	12,8	68,9	471,0	117,6	39,7
ZL	5,3	318	S 1	18,1	65,5	196,9	25,3	17,0
ZL	6,9	414	S 1	22,5	80,1	330,8	47,5	25,5
ZL	8,4	504	S 1	28,8	78,8	391,6	64,7	24,8
ZL	9,6	576	S 1	23,4	92,3	410,5	52,8	21,4

Tab. 2: Versuchsergebnisse Sifcon (einstufig)

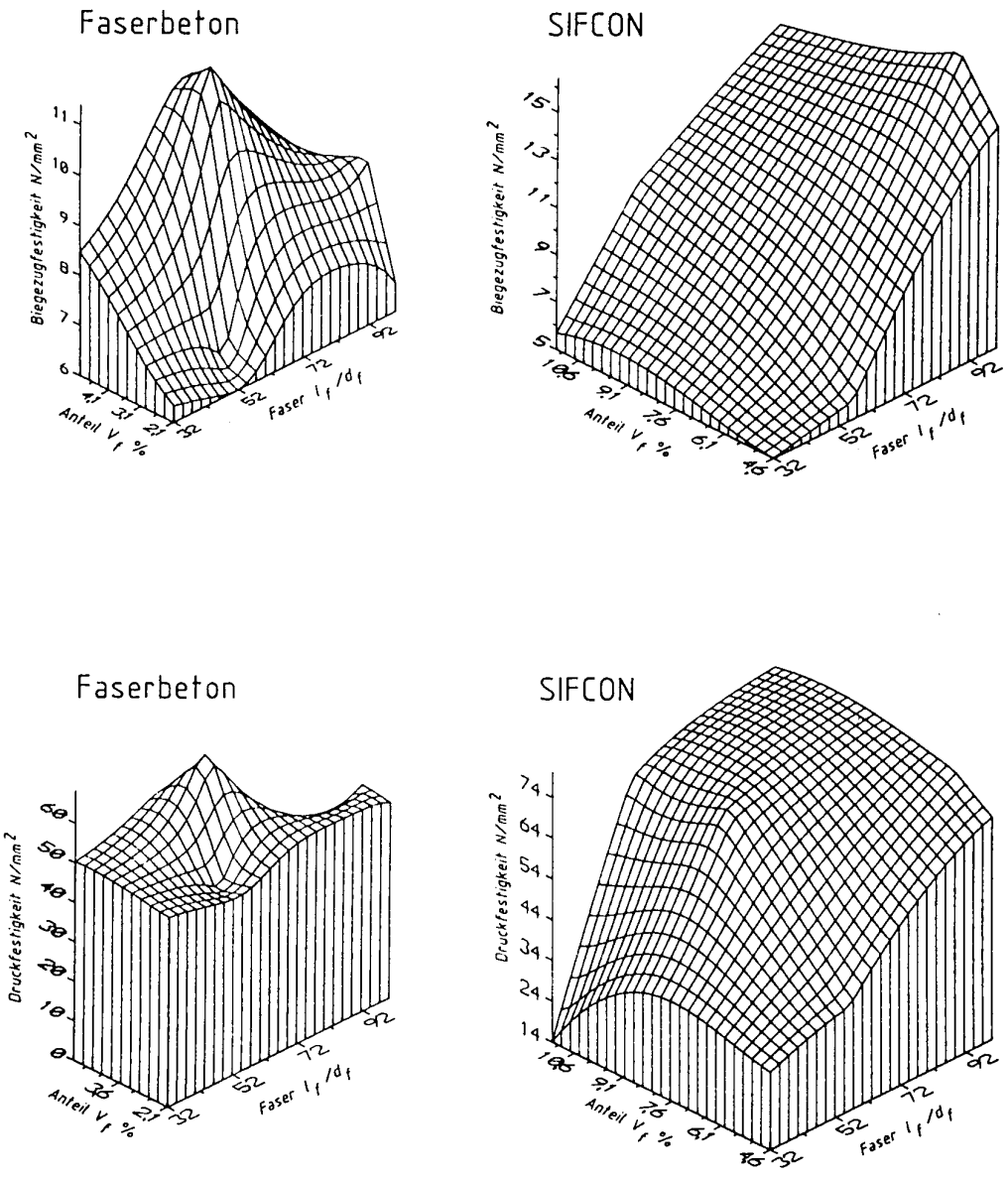

Abb. 3: Einfluß der Faser (V_f, l_f/d_f) auf das Festigkeitsverhalten von Faserbeton und SIFCON (gerade Faser - OL)

$$\text{Arbeitsvermögen } A = \int_{x=0}^{x=x_{Br}} P(x) \cdot dx$$

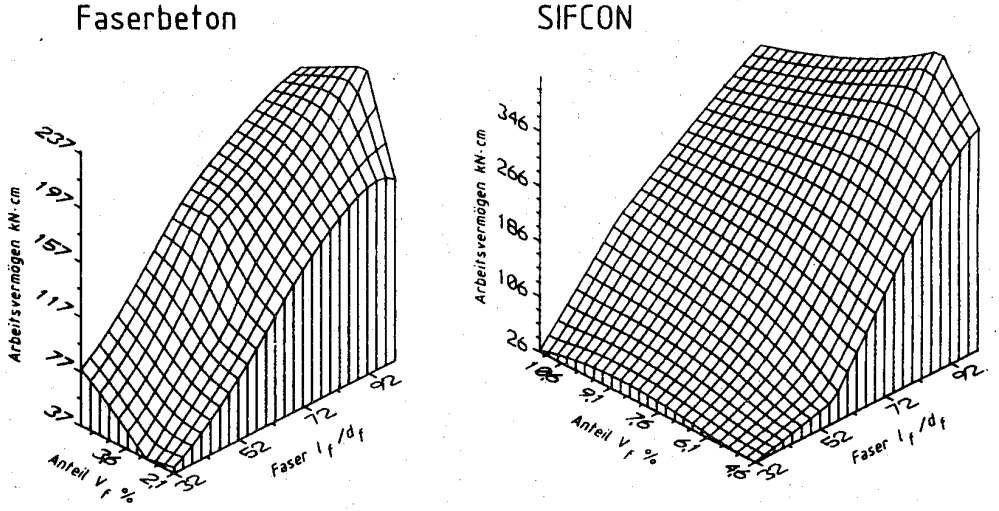

$$\text{Plastifizierung } \bar{\beta} = {}^{x_{Br}}/_{x_E}$$

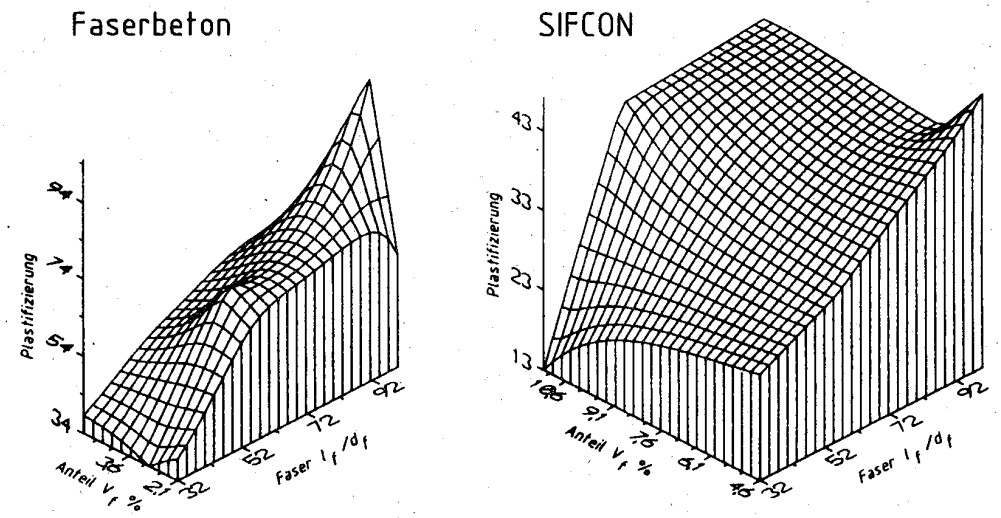

Abb. 4: Einfluß der Faser (V_f, l_f/d_f) auf die Duktilität von Faserbeton und SIFCON (gerade Faser - OL)

FIBROUS SHOTCRETE FOR EXPEDIENT REPAIR OF STRUCTURES

L.C. Muszynski
M.A. Rochefort
APPLIED RESEARCH ASSOCIATES
GULF COAST DIVISION
TYNDALL AFB, FL

ABSTRACT

The scope of this study was to identify, test, evaluate, and recommend construction materials, equipment and techniques for the expedient repair of conventional weapons damage to structures in PACAF and USAFE in a postattack environment.

Air Base Structures and Weapons Effects Branch (RDCS) requested the services of the Air Base Structural Materials Branch (RDCM) to develop an expedient repair system that can be applied in different environments under a wide variety of environmental conditions and develop a minimum of 13.8 MPa compressive strength in 1 hour.

Applied Research Associates has accomplished this task by developing a shotcrete material that meets the environmental operating requirements, the environmental storage requirements, the performance requirements, and the reliability requirements.

This shotcrete material is based on a high early strength cement which has produced 34.5 MPa compressive strength concrete in the laboratory. Operating conditions for the shotcrete equipment have been evaluated and shotcrete produced in the field has attained 1 hour compressive strengths of up to 27.6 MPa.

INTRODUCTION

Air Force Engineering Services Center/Air Base Structures and Weapons Effects Branch (AFESC/RDCS) is investigating materials and methods for expedient repair of structural facilities (ERSF) at air bases after an attack. The purpose of ERSF is to: 1) make damaged structures, which are mission-critical to an airbase, safe for use, or allow entry into the structure so critical equipment and resources can be removed; 2) make damaged structures more resistant to subsequent attacks; 3) minimize entry of chemical and biological agents into the structure; and 4) minimize environmental effects, such as rain, wind, frost, or fire from entering the structure.

The developed repair system would have to meet environmental operating requirements, environmental material storage requirements, material performance requirements and reliability requirements. In order to meet these requirements (1) the material must be functional under the following conditions: an ambient thermal environment of -26 to 49°C, a rainstorm of 2.5 cm per hour or equivalent snowfall, day or night, and in the presence of

chemical and biological agents. The materials must have a storage life of 3 years at temperatures between 10° and 32°C with no humidity control, and the material must provide structural integrity to the facility and attain the design compressive strength of the structure in 1 hour after placement.

LABORATORY TESTING

Product development and evaluation was initiated based on the results of a preliminary investigation using a fiber reinforced microsilica shotcrete product from Ocean Construction Services, LTD., Vancouver, Canada. The initial goal was to develop a repair system similar to the Ocean fiber reinforced microsilica system with its enhanced shooting characteristics and physical properties and have a minimum of 13.8 MPa compressive strength in 1 hour.

High early strength cements were pre-evaluated as to their appropriateness as an expedient repair material. A calcium fluoroaluminate cement was eliminated due to its inability to gain strength below 10°C. Historically, magnesium phosphate and gypsum cements have been efficient rapid rapair materials, but in this case were NOT recommended by their manufacturers as a dry-process shotcrete material. The reasons include water sensitivity, and flow characteristics, i.e., rheology.

Blended cements can be altered by additions of 12 percent silica fume to be able to produce thick layers of shotcrete using the dry-process method.(2) Unfortunately, this particular blended cement was not able to be accelerated by the Scamper 16®(3) accelerator, so further work with this system was delayed.

The calcium sulfoaluminate cement not only developed high early strength but the set time was accelerated using the Scamper 16® admixture. Therefore, this cement was used as a basis for developing an expedient repair material.

The calcium sulfoaluminate cement system that was investigated consisted of a grout, which is described as a dry blend of calcium sulfoaluminate cement and quality sand. The product contains no chlorides and when mixed with water produces a uniform, nonshrink mortar.

Initial set times of potential cement systems incorporating the shotcrete accelerator, Scamper 16®, were performed according to ASTM C-403. The results indicate that this blended cement was responsive to Scamper 16® and calcium sulfoaluminate cement with and without silica fume appears to be very responsive to the solid accelerator. The laboratory screening results were developed by varying the aggregate content, silica fume content, fiber content and accelerator dosage.

FIELD TESTING

The object of the field testing part of this study was to develop shotcrete equipment operating parameters that would allow successful build up of shotcrete layers, strength gain, and material uniformity.(4) These parameters include flow rate of material, water flow rate, and the rotating speed of the rotor which determines the output capacity of the equipment.

Another area of interest is the effect of different nozzle/tip assemblies on the physical properties of the shotcrete repair material. Eleven shotcrete tests were performed in order to develop information regarding the relationship between material strength development and shotcrete operating conditions. High speed photography was implemented in order to measure particle velocities of the material exiting through three different nozzles.

Shotcrete tests simulating hot-weather and cold-weather environments were also performed with the expedient repair material formulation.

1. MATERIALS

a. USAF Expedient Repair Material (XPR) System

The XPR expedient repair material system, developed in the laboratory, is a dry-blended pre-packaged system whose formulation can be found in Table 1. The formulation is equivalent to 8 sacks of cement per cubic yard of shotcreted material. The silica fume content is 12 percent by weight of the cement and the steel fiber content is 1.6 percent by volume of the concrete composite. The water-to-cement ratio is based on the total water required per total amount of cement and dry densified silica fume.

2. EQUIPMENT

a. Dry-Process Shotcrete Equipment

The dry-process shotcrete process investigated in this study was leased from Master Builders Technologies, Shotcrete Division. The machine was a MEYCO Piccola 020, an air motor operated machine with a capacity of 3.5 cubic yards per hour.

b. Nozzle Bodies and Tips

The nozzle bodies and tips evaluated in this study include the standard Hamm style, the Spirolet, the Double Bubble, and the Hydro-Mix Nozzle. The Hamm nozzle body is composed of a metallic nozzle and considered by most as the standard in the shotcrete industry. The Spirolet nozzle is composed of a polyurethane body with "rifling" in the barrel. This would appear to provide greater velocity and a tighter shot pattern. The "double bubble" nozzle is composed of a flexible elastomer and is shaped like an old fashioned coke bottle. The flexible nozzle can be manually bent to direct the exiting material into tight places. The hydro-mix nozzle is actually a predampening device attached prior to the nozzle and tip. The operator can control the amount of "prewet" the dry material receives and can control the amount of mix water at the dry-process nozzle. This predampening nozzle reduces the dust associated with dry-process shotcrete operations and assures better mixing of the predampened material at the nozzle.

3. RESULTS

a. Material Properties

One foot square boxes 25 cm in depth and 2 foot square boxes 25 cm in depth were shotcreted in the field. Cores were taken approximately 30 minutes after shotcreting and tested at 1 hour.

Highlights of the eleven shotcrete tests include 1 hour compressive strengths of 24.8 MPa, over 27.6 MPa when using hot water, and 1 hour compressive strengths using a non-destructive test method, the Windsor probe, of 26.2 MPa.

b. Operating Parameters

The parameters relating to the operating conditions of the shotcrete equipment are described by the schematic in Figure 1. The operating conditions were optimized to properly match the flow rate of dry material to the

corresponding flow rate of water, i.e., water-to-cement ratio, both of which being dependent on air flow through the discharge chamber, main line pressure measured in psi.

c. Particle Velocities

The particle velocities versus nozzle type results can be found in Table 2. They correspond with the literature values for velocities determined by high speed photography.(5) Figure 2 illustrates the high speed photographic test set-up and Figure 3, the high speed particles in motion.

ENVIRONMENTAL TESTING

1. HOT WEATHER

One can concede that shotcreting in Florida during the months of June and July could be defined as "hot-weather concreting." We accelerated the hot weather conditions somewhat by exposing the dry materials to ambient conditions for several hours prior to testing and heating the mix water to 57°C.

The average 1 hour compressive strength was 26.2 MPa and the average Windsor probe reading resulted in a compressive strength value of 23.8 MPa.

2. COLD WEATHER

Since a large "cold room" environmental chamber was not available for a full scale field test for "cold-weather shotcreting," we evaluated the cold weather effectiveness of the material system in the laboratory.

The dry materials were refrigerated until they reached an equilibrium temperature of 1.1°C. At a water temperature of 1.7°C, no strength was developed in 1 hour. The water temperature was raised to 48.9°C and the 1 hour compressive strength of the 15 by 30.5 cm cylinder was 33.2 MPa.

The relationship between the compressive strength and time up to 7 days in a cold-weather environment is shown in Figure 4. The dry material was mixed with the water at varying temperatures and cured at 1°C prior to testing at 1 hour, 1 day, and 7 days.

ECONOMICS

An economic analysis of the very high early strength XPR expedient repair shotcrete system is given in Table 3. These numbers do NOT reflect the costs associated with purchasing the individual materials in bulk or bulk packaging such as "super-sacks."

FIELD DEMONSTRATION

A field demonstration involving the repair of a specific area of a damaged hardened structure at Tyndall AFB was completed in December 1990. A door opening in the hardened structure was used to simulate a wall replacement. The door area measured approximately 2.1 m in height and 1.4 m in width. Number 4 reinforcing rods were placed at 30.5 cm intervals around the door, Figure 5. Plywood backing was placed behind the repair area and braced with 2 x 4's. Three 20.3 cm long repair depth indicator rods protruded from the plywood backing toward the door front. The prepackaged shotcrete material is continuously fed from a concrete bucket to the shotcrete nozzle by compressed

air, and water is metered to the nozzle by a water drum - drum pump and flowmeter arrangement. The shotcrete material is then pneumatically conveyed at high velocities toward the repair area, Figure 6.

Figures 7, 8, and 9 illustrate the repaired door section, the conventional weapon with an explosive equivalent weight to 204.5 Kg of TNT, and the bomb standoff distance of 15.25 cm, respectively. Figure 10 illustrates the survivable repair after detonation. Some visible spalling was apparent on the front of the repair and some penetration of bomb fragments was visible but there was no perforation. A small crack was observed on the back face of the repair area but there was no evidence of spalling.

SUMMARY

A very high early strength construction material was developed as a material for the expedient repair of structural facilities. The method investigated in this program was that of pneumatically conveying such a material which is called shotcrete. The dry-mix process was the preferred method of shotcreting because 1) it allows the use of a very fast setting system and 2) it reduces the amount of equipment and waste required for such an operation. The dry-mix process is described as one in which the dry material is passed pneumatically through a hose to a nozzle. The water is pumped directly to the nozzle and the metering and mixing takes place in the nozzle body and the mixture is ejected through the nozzle tip toward the repair target. The pneumatically placed material sets in less than 2 minutes and has exhibited strength gains up to 27.6 MPa in 1 hour.

A door opening in the NATO hardened structure at Tyndall Air Force Base, Florida was shotcreted with the newly developed expedient repair material. The repair was 20.3 cm in thickness and it withstood the blast pressure and fragmentation effects of a 455 Kg bomb at a 15.25 m miss distance. To this date NO durability testing has been performed on this material.

REFERENCES

1. Read, D.L., and Merkle, D.H., "Field Demonstrations of Expedient Repair of Structural Facility Systems," Applied Research Associates, September 1990.

2. Hardy BBT Ltd., "A Report on Evaluation of Pyrament Dry-Mix Shotcrete," 23 October 1989.

3. Technical Bulletin, Scamper 16® Shotcrete Accelerator, Surecrete, Inc., Seattle, Washington, USA.

4. "State of the Art Report on Fiber Reinforced Shotcrete," ACI Committee 506, Concrete International, December 1984.

5. Glassgold, I.L., "Shotcrete Durability: An Evaluation," Concrete International, ACI, August 1989, pp. 78-85.

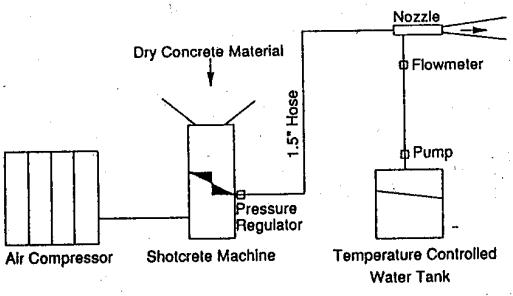

Fig 1. Schematic of Shotcrete Equipment

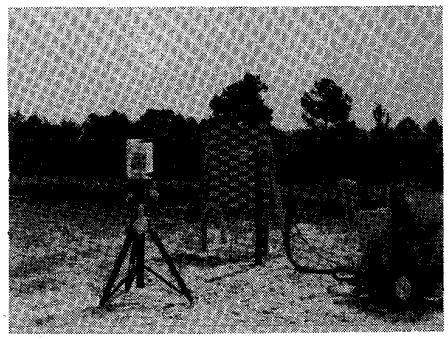

Fig 2. Test Set-up for High Speed Photography

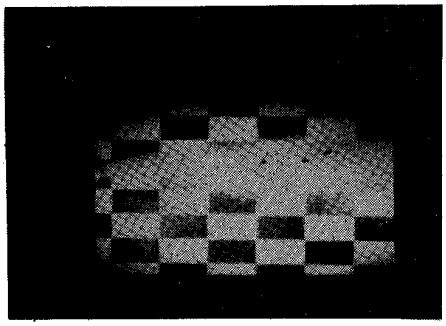

Fig 3. High Speed Shotcrete Particles

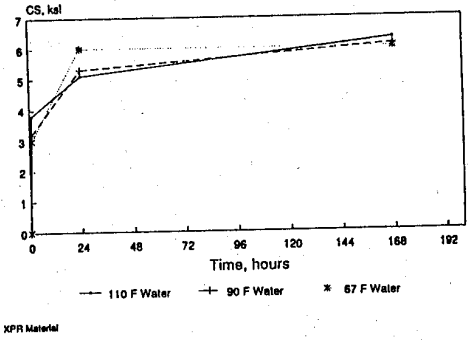

Fig 4. Compressive Strength vs. Time

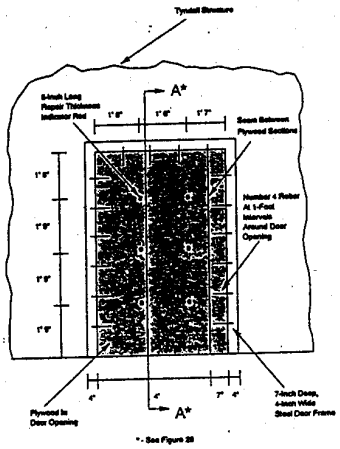

Fig 5. Front View of Shotcrete Wall Replacement

Fig 6. Shotcreting Damaged Area of Structure

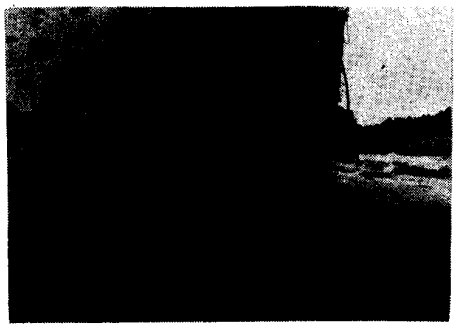

Fig 7. Finished Door Repair

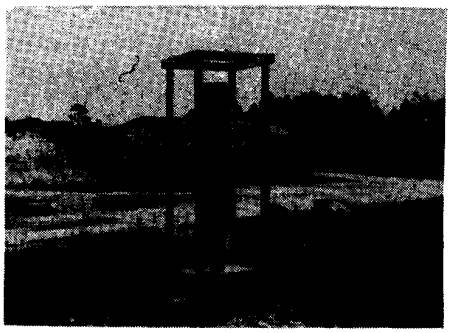

Fig 8. Conventional Weapon

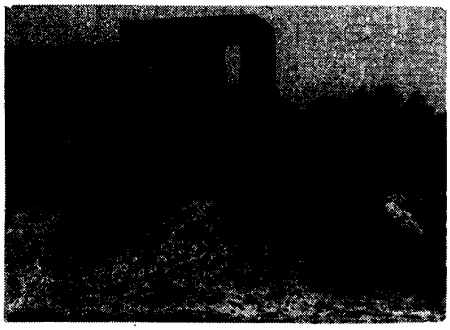

Fig 9. Weapon Location at Standoff

Fig 10. Door Repair After Detonation

TABLE 1. INGREDIENTS USED IN DRY-BLENDED PRE-PACKAGED XPR SYSTEM PER 50 POUND BAG

Material in bag	Weight in pounds
Calcium sulfoaluminate cement	24
Coarse Aggregate (3/8 in. max.)	24
Dry densified silica fume	1.4
Steel fibers (1-inch in length)	3.0
Scamper 16 accelerator	0.25
Total weight per bag	52.65
Physical Properties:	
Unit weight of dry material	121 lbs/cu.ft.
Equivalent cement sack content	8 sacks/cu.yd.
Water required	4.5 lbs
Water/cement+silica fume ratio	0.35

TABLE 2. PARTICLE VELOCITIES VS. NOZZLE TYPE USING HIGH SPEED PHOTOGRAPHY

Nozzle Type	Avg. Particle Velocity ft./sec.	Standard Deviation	Film Speed frames/sec
Hamm	231.13	2.74	5300
Double Bubble	172.04	4.83	7000
Spirolet	285.35	3.52	8000

Shotcrete Operating Conditions:

Main Line Pressure = 60 psi

Rotor rpm = 8

Flow rate of dry material (from Figure 18) = 109 lbs./min.

Flow rate of water = 1.1 gal./min.

TABLE 3. ECONOMIC ANALYSIS OF THE XPR EXPEDIENT REPAIR SHOTCRETE SYSTEM

Materials	Amount/Bag	Cost/Lb.	Cost/Bag
Calcium Sulfoaluminate Cement	24	$ 0.195	$ 4.68
3/8 in. gravel	24	$ 0.006	$ 0.14
Microsilica	1.4	$ 0.38	$ 0.53
1 in. Steel Fibers	3.0	$ 0.36	$ 1.08
Scamper 16	0.22	$ 0.75	$ 0.17
Total Weight/bag	52.6		
Material Cost/bag			$ 6.60
Packaging Cost			$ 2.10
Total Cost/bag			$ 8.70

MATERIAL MODELLING FOR HYDROCODE ANALYSIS OF CONCRETE RESPONSE TO EXPLOSIVE LOADING

A J Sheridan
Royal Aerospace Establishment, Farnborough, Hants. GU14 6TD, UK.
A D Pullen
Imperial College, London, SW7 2AZ, UK.
S H Perry
Trinity College, Dublin, Ireland.

ABSTRACT

When concrete structures are subjected to rapid and severe compression and deformation, as is the case with close-in explosions and high velocity impact/penetration, the concrete material can behave in an almost fluid like manner. Computer modelling of such events requires the use of 'hydrocodes' - which comprise finite element or finite difference formulations of the material continuum equations for conservation of mass, momentum and energy. Codes used by the RAE and Imperial College include DYNA2D/3D and AUTODYN. The properties of the material elements in such codes are generally quantified by an equation of state (governing behaviour in pure compression) and a strength model (determining the amount of shear that can be supported). For concrete, the equation of state should include a non-linear load curve - incorporating initial elastic deformation followed by plastic compaction of the pore structure and progressive strain hardening - together with a family of unload reload curves. The strength model should ideally provide shear and compaction yield criteria, as functions of mean effective stress, or pressure.

The paper presents techniques - developed by RAE Farnborough's Missile Technology and Countermeasures Department and Imperial College's Concrete Structures Section - for producing concrete material data for use in hydrocodes. Static triaxial data can be reliably generated for both concrete and soil in uniaxially loaded Steel Jacket Cells - which have been demonstrated to achieve much higher stress states than more traditional triaxial devices. A Hoek-type cell has also been specifically developed to permit lateral strains to be monitored and controlled - and will allow a more detailed analysis of material failure at the lower stresses. Dynamic properties have been sought, through the analysis of transients measured by a variety of gauges cast into the concrete. However, these have not proved reliable, due to a variety of noise sources associated with the gauges being close to the detonating charge. Proposals are presented for tests aimed at allowing dynamic enhancement factors to be determined which can be applied to the static triaxial data - and the method of tuning the dynamic enhancement factors will be demonstrated from hydrocode predictions.

CONCRETE MODEL

The concrete model quantifies the properties of elements of concrete which are small in relation to the size of the structure and assumed to be homogeneous and isotropic. The aim is to fully characterize the strain rate dependent triaxial behaviour of concrete, under all states of compaction, dilation and shear - for application to finite element and finite difference hydrocodes.

Equation of state:
This represents the degree of compaction imposed on the concrete as a function of the average applied stress (pressure). It is frequently expressed as a pressure/volumetric strain relation. The important features of the equation of state for concrete hinge on its non-linearity (figure 1). After initial elastic compaction the concrete crushes and then gradually stiffens as the stress distribution within the solid constituents readjust and permit higher stresses to be supported (strain hardening). The subsequent non-linear unloading response generally reveals a considerable degree of permanent plastic compaction. The pressure/volumetric strain relation must also allow for the representation of partial unload/reload and tensile failure.

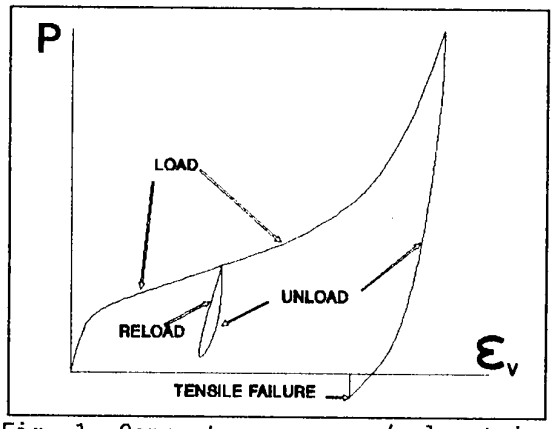

Fig 1 Concrete pressure/volumetric strain

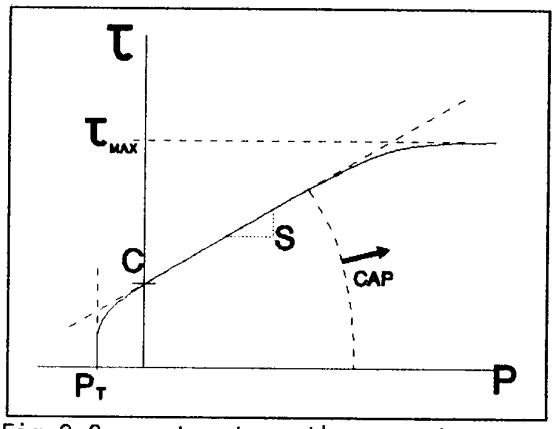

Fig 2 Concrete strength parameters

Yield Strength:
This is the main property of a solid that distinguishes it from a fluid. The failure envelope - for shear yielding - is generally expressed as some representation of the shear stress that can be supported as a function of the applied pressure (figure 2). Provided the concrete stress state lies beneath the failure envelope, it behaves elastically - defined by its shear modulus G. The essential features are the cohesion C, which is the shear strength under conditions of zero confinement, the hardening slope S, the maximum shear stress τ_{MAX}, and a tensile pressure cutoff $-P_T$.

Further to this, the model might incorporate the means for a more precise evaluation of the elastic and plastic components of strain, associated with compaction yielding, by incorporating a moving CAP curve.

Failure criteria:
Perhaps the most important property of concrete, when not considered as a steel reinforced element, is its low tensile strength. The simple tensile pressure cutoff provided by the the strength model is certain to be an over simplification. In practice, it would be expected to be dependent on the maximum principal tensile strain in relation to the the maximum compaction imparted in the direction of that strain component.

Strain rate effects:
One of the most important strain rate effects observed in material and structural testing is that associated with inertia. For example, in standard cube or cylinder crushing tests, the concrete specimen dilates laterally during axial compression. If the rate of compression was increased in relation to the rate of dilation, an enhancement in the maximum achievable load would be expected.

Hydrocodes can make use of material elements that are small enough that such effects are automatically accounted for. The strain rate effects that are sought are those due to the increase in internal energy associated with achieving a given strain state, under dynamic loading, in relation to that under static loading.

Whilst research is primarily directed at developing techniques for direct measurement of dynamic properties, a fall back option has been focussed on the production of dynamic enhancement factors, which can be applied to static data.

STATIC MATERIAL DATA

Whilst hydrocode predictions of the dynamic response of concrete under conventional weapons loads would obviously require the use of dynamic materials properties, static data is much more readily produced and analysed. A number of laboratory test methods are being investigated in the current research programme - aimed at a complete triaxial characterization of the behaviour of concrete and its constituents.

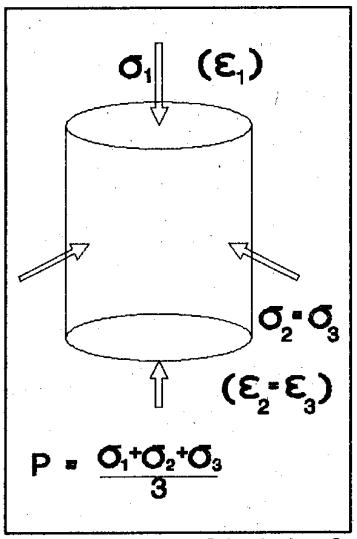

Fig 3 Cylindrical stress/strain components

Steel Jacket Cell:
A cylindrical specimen (figure 3) is end loaded such that the lateral strain is significantly less than the axial strain ($\epsilon_2=\epsilon_3<<\epsilon_1$). In practice this is achieved by use of a "Steel Jacket Cell" (SJC), developed at Imperial College (refs. 1,2,3). The specimen is confined circumferentially by a hollow steel cylinder or jacket, the inner surface of the steel cylinder being separated from the specimen by only a very thin double-liner of polythene sheet, to reduce friction. Concrete specimens are cast directly into the jacket. Soil specimens are prepared in bulk and compacted into the jacket to the required density. (Only reworked soil has been tested to date.)

Parameters measured are the applied end load, the platen to platen displacement, together with the steel jacket axial and hoop strains. Stress and strain states are then calculated from the test data. To date these tests have only been used to measure the non-linear compression up to peak load and the subsequent non-linear unloading. Future tests will also investigate the unload/reload behaviour.

It is also possible to calculate the shear stress as a function of pressure. The curve starts from zero shear at zero pressure, and both increase together until the failure envelope is reached. This is then followed up to the maximum shear and shows some degree of softening prior to unloading. It is believed that this softening has not been observed in other triaxial tests on concrete - and validation and further extension of this curve will be a major component of future research. Whilst the cohesion cannot be determined directly from this test, an approximate value can be found by extrapolating the hardening slope back to zero pressure.

Hoek Cell:
The Hoek cell (ref. 4) was originally developed in the 1960's at Imperial College. In it, a cylindrical specimen is loaded such that the lateral stresses ($\sigma_2=\sigma_3$) are held constant - where the radial stress component (σ_3) is maintained by a reservoir of hydraulic fluid, acting on it via a flexible membrane. The axial strain ϵ_1 (and hence σ_1) is increased until specimen failure is achieved.

Starting from zero stresses, the reservoir is slowly pressurised. A micro-computer monitors a pressure transducer in the reservoir's hydraulic system and instructs a similar system to drive the axial ram until the calculated axial stress matches the radial stress. This process continues until a pre-determined specimen pressure is reached. The reservoir pressure (and hence the radial stress in the specimen) is then held constant, while the ram drives the platens together at a constant rate, increasing the axial stress component (σ_1) until a peak value is achieved.

The experiment is repeated for a range of radial stresses. The resulting (σ_1;σ_3) pairs of stress values at failure are used to calculate a relationship between shear stress and pressure at failure, and hence determine the shear strength characteristics of the material. Again, this test is unable to directly measure the cohesion.

Tests to date have made use of a rig using a single action jack (push only) - and this has shown inadequate sensitivity at low stress. A new device has recently been built which utilizes a double action jack (push and pull) and has a 100 ton capacity over a 150mm stroke.

A further development of the Hoek cell will utilize the advantages of the SJC. It is planned to use a thin steel jacket - between the specimen and the sealing membrane - to provide a greater degree of lateral strain control. This will enable more detailed analysis of compaction yielding for a CAP model.

The results of the Hoek cell have been compared with the SJC and indicate a much weaker response. The precise reason for this has not yet been positively identified. However, it is suggested that it may be due to differing mechanisms of failure associated with each - whilst cracks are able to develop in the Hoek cell, no cracks have been evident in sectioned SJC specimens. Currently, the Hoek cell analysis may be based on either of two estimates of the maximum principal stress σ_1 - one based on constant area, the other on constant volume - it may be more appropriate to use the compaction curve from the SJC test to calculate the area over which the end load is applied. One of the possible sources of error, in the Hoek cell, is that any significant lateral deformation might drive an instability with respect to the structural integrity of the specimen. It also has to be recognised that the SJC is a relatively new test device, with very limited data at present, and in need of substantially more research to complete its validation. It is expected that the thin steel cylinder modification to the Hoek cell will help clarify the analysis.

Shear and Tensile Tests:
To determine the shear modulus G and cohesion C, concrete specimens can be tested in simple shear, or torsion. Finite element analysis will be used to assess existing techniques for measuring shear and tension, or to design new methods for evaluating these properties for not only concrete, but also rock and soil.

DIRECT MEASUREMENT OF DYNAMIC PROPERTIES

One of the most important tasks in the current research programme is the development of experimental techniques for direct measurement of the dynamic properties of concrete, rock and soil.

Transient analysis:
This involves casting sensors into concrete targets and subjecting them to contact high-explosive loads. The transients produced by the gauges are recorded and analysed to generate materials data. The ideal test would involve direct simultaneous measurement of stress and strain - from which dynamic stress-strain

relations can be produced. However, a suitable stress transducer - for which survivability and sensitivity are compatible - has not yet been positively validated. Alternatively, it is possible to perform a Lagrangian analysis on strain or velocity transients. Some degree of success has been achieved by this technique, but only up to strain values that are at least an order of magnitude lower than those that can be produced by the static tests.

Due to the low maximum stress-strain state that can be measured by transient analysis, all future transients will only be used for validation of hydrocode simulations.

Split Hopkinson Bar:
A 75mm diameter device is currently being developed at RAE, Farnborough. This is expected to be capable of generating dynamic concrete stress-strain data beyond that currently available from the transient analysis, but will still be limited by the strength of the component bars.

High-Speed Photography:
This has been used to observe the response of small concrete specimens to contact high-explosive detonation (figure 4). Tests to date have used a camera with a framing rate of approximately 36,000 per second, and are directed at preliminary development of the test procedures. Within the next year it is planned to acquire a camera with a minimum framing rate of 10^6 per second - and this should permit the evaluation of Hugoniot values (shock velocity, particle velocity) for concrete, rock and soil. Further to this, specimens will be produced for the evaluation of dynamic tensile strength - as determined from the velocities of multiple spall fragments.

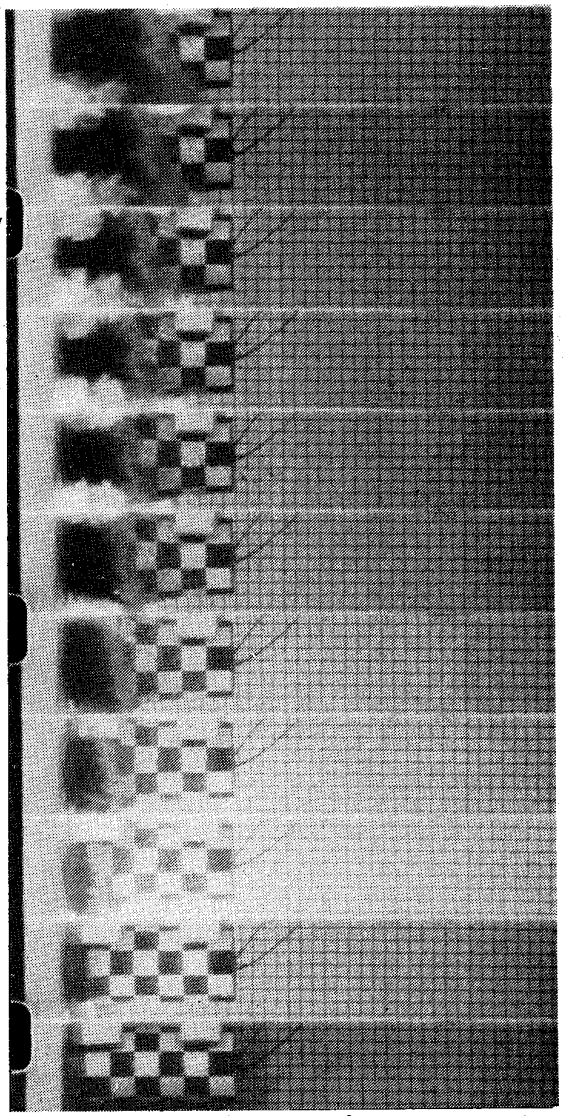

Fig 4 HE interaction concrete cylinder (high-speed photos.)

INDIRECT EVALUATION OF DYNAMIC PROPERTIES

Because of the high degree of confidence in the static materials tests - for concrete, rock and soil - and the difficulty experienced in generating the equivalent full set of dynamic parameters, directly from experimental data, a fall back option is also being pursued. This involves the use of hydrocodes to design a set of experiments that can be individually tuned to provide a sensitivity to specific material properties - i.e., equation of state, strength in compaction, shear or tension. The objective is to determine the dynamic enhancement factors that should be applied to each of the static material parameters. It is hoped that application of the correct enhancement factors would provide complete agreement between hydrocode simulations and experimental results. Again, high speed photography would be

used for analysis of the experimental response. This component of the research only started at the end of 1990, but the following examples demonstrate early success in the application of this technique.

Concrete compression:
The aim was to develop a test method that, under hydrocode simulation, was sensitive to the correct evaluation of the the dynamic enhancement factor for the equation of state - but was insensitive to the enhancement factor for other concrete properties (i.e., under shear and tension). The only situation in which shear would not be present, is when the specimen is subjected to a uniform pressure wave over its entire surface - which would not be practical. It is recognised, therefore, that the shear criteria will have some influence on the result; the aim was just to minimize it.

The configuration investigated first was an explosively end loaded concrete cylinder (figure 5). The steel plate, between the explosive and target, served two purposes: to reduce the flash picked up by the high speed camera, and prevent the ingress of explosion products into the concrete. The radial velocity of the target point predicted by the hydrocode simulation (figure 6) indicated that, whilst this configuration was sensitive to the dynamic enhancement factor applied to the equation of state, it was even more sensitive to the yield criteria. Consequently, it was recognised that this test had only limited value from the point of view of data production, but was considered appropriate as a datum and to assess the requirements of the instrumentation (the resultant high speed photographic images are presented in figure 4).

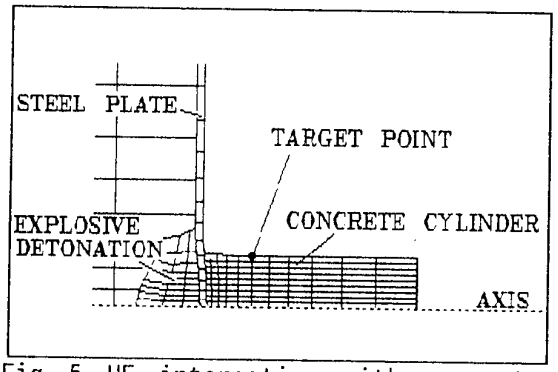

Fig 5 HE interaction with concrete cylinder (AUTODYN plot)

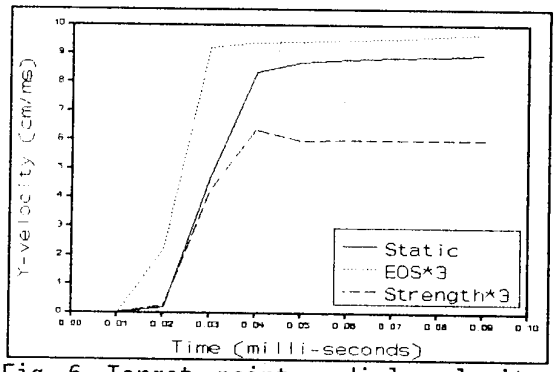

Fig 6 Target point radial velocity (AUTODYN results)

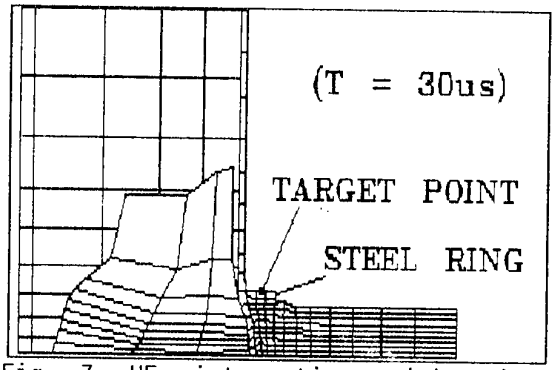

Fig 7 HE interaction with ring confined concrete (AUTODYN plot)

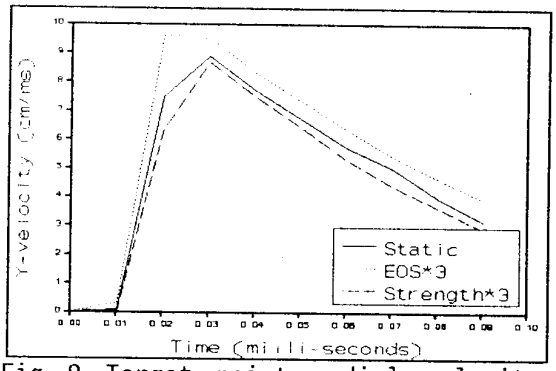

Fig 8 Target point radial velocity (AUTODYN results)

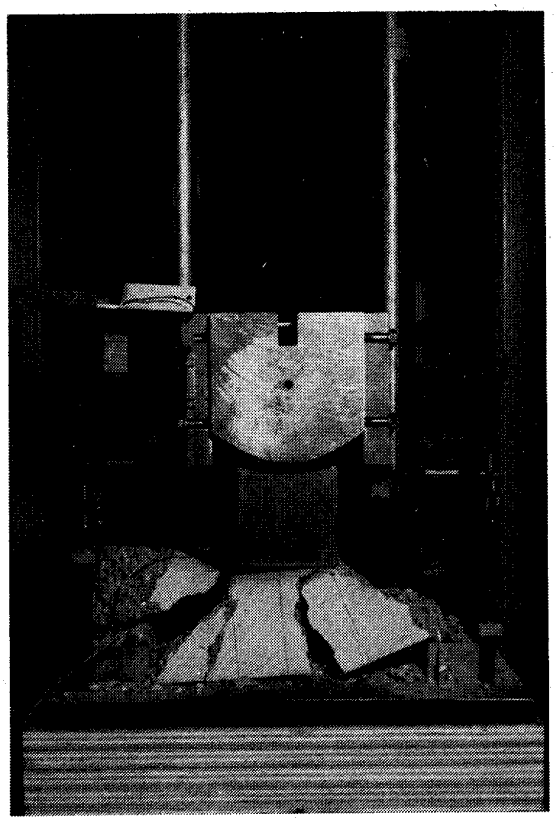

Fig 9 Impact rig for concrete shear

It was found, using hydrocode predictions, that confinement of the concrete (figure 7), in the region closest to the explosive load, provided the desired sensitivity to the dynamic enhancement factors. It can be seen in figure 8 that the radial velocity of the confining ring was significantly less sensitive to the dynamic enhancement factor applied to the yield criteria.

Concrete shear:
The aim was to develop a test method that, under hydrocode simulation, exhibited greatest sensitivity to the dynamic enhancement factor applied to the yield criteria. The initial configuration investigated was the impact of a dropped weight onto a 50cm long concrete bar, of 10cm square cross section (figure 9).

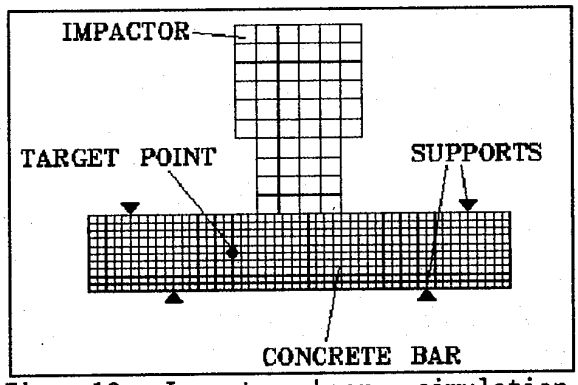

Fig 10 Impact shear simulation (AUTODYN plot)

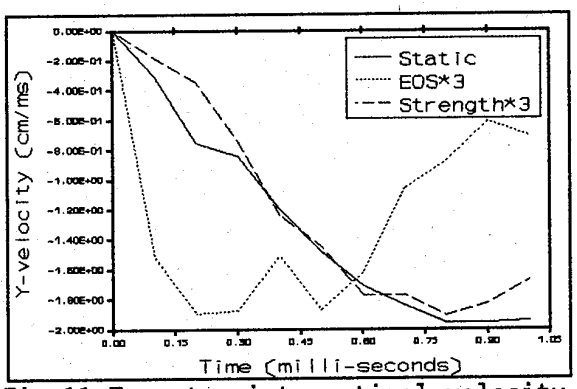

Fig 11 Target point vertical velocity (AUTODYN results)

The hydrocode simulations (figure 10) used plane symmetry and were found to be considerably more sensitive to the yield criteria than the equation of state - as desired. The sensitivity is demonstrated in figure 11, which shows that the displacements of the target point was very similar in the cases where static and enhanced EOS properties were used - but were significantly different in the case when an enhancement factor of 3 was applied to the yield criteria. However, it is likely that this test, in its present form, may have been even more sensitive to the concrete tensile strength. Hydrocodes will be used still further to identify configurations that allow the shear and tensile enhancement factors to be separated out.

CONCLUSIONS

This research has produced a number methods whereby static triaxial data can be generated, for concrete, rock and soil, with a high degree of confidence. Whilst the primary aim of future research is to develop methods for the direct measurement of the corresponding dynamic properties - from the analysis of electronically measured transient and high speed photographic records - the need for a fall back position has been deemed prudent. Initial results from this part of the study have demonstrated the validity of such an approach.

ACKNOWLEDGEMENTS

The authors would like to acknowledge the support of Dr J B Newman and his staff at the Imperial College Concrete Structures Laboratory, Mr M Wightman and the staff of the RAE Ball Hill Range, for their contributions to this research. The research was supported by the Ministry of Defence (Procurement Executive) under Research Agreement No. 2037/375.

REFERENCES

1. M D Kotsovos, S H Perry - Determination of the Stress-Strain Relationships for Confined Concrete. Final Report to RAE Farnborough, May, 1984.

2. M D Kotsovos, S H Perry - Behaviour of Concrete subjected to Passive Confinement. Matériaux et Constructions (RILEM), Vol.19, No.112, July, 1986.

3. A J Sheridan - Response of Concrete to High Explosive Detonation. PhD thesis, University of London, 1990.

4. E Hoek and J A Franklin - A Simple Triaxial Cell for Field and Laboratory Testing of Rock. Trans. Inst. Min. Metall. London, Section A, Vol 77, 1968, pp22-26.

IMPACT RESISTANCE AND TOUGHNESS OF POLYMER-MODIFIED STEEL FIBER REINFORCED CONCRETE

By

Parviz Soroushian, Ph.D., P.E.
and
Atef Tlili

Civil Engineering Department, Michigan State University
East Lansing, Michigan 48824 - U.S.A. -

ABSTRACT

The effects of latex modification and/or steel fiber reinforcement on the impact resistance, and flexural strength and toughness of concrete materials were investigated. Two levels of latex content and two different fiber volume fractions were considered. Latex modification was particularly effective in increasing the impact resistance of plain concrete. Flexural strength was also increased in the presence of latex, but the flexural toughness of plain concrete did not receive major benefits from latex modification. Steel fibers were effective in increasing the impact resistance, and flexural strength and toughness of concrete.

The combined action of steel fibers and latex polymers produced the best performance characteristics. In the case of impact resistance and flexural toughness, the joint effects of latex and steel fibers were more than additive, indicating a positive interaction between the two. Latex modification seems to make concrete matrices more compatible with steel fibers. The increase in fiber-to-matrix bond in the presence of latex also seems to enhance the reinforcement properties of steel fibers in concrete.

INTRODUCTION

Ordinary concrete suffers from relatively low flexural strength, toughness and impact resistance. Steel fiber reinforcement and polymer modification each can partly overcome some of these problems. Steel fibers enhance the ductility and energy absorption capacity, flexural strength, and impact resistance of concrete. Latex modification, on the other hand, improves the impermeability as well as strength and ductility characteristics of concrete.

Latex polymers in the presence of steel fibers provide a better bonding between fibers and the concrete matrix due to the formation of a monolithic polymer film that surrounds the fibers, fills the smaller voids, and links the cementitious environment to the fibers. As a result, the formation of much of the microcracks that tend to take place along the fiber-matrix interface is prevented. In addition, the resistance of fibers against pull-out action is further enhanced, resulting in improved flexural strength and toughness characteristics and impact resistance.

The study reported herein is concerned with the assessment of the advantages associated with the joint use of steel fibers and latex polymers in concrete materials. This paper specifically deals with the effects of steel fiber reinforcement and/or latex modification on the impact resistance, flexural strength and toughness characteristics of concrete materials. The hypothesis here is that the improved adhesion capacity and ductility of concrete matrices incorporating latex polymers make them more compatible with steel fibers.

BACKGROUND

This section reviews the test data reported in the literature on the effects of latex modification and steel fiber reinforcement on the impact resistance and flexural behavior of concrete materials. The impact resistance of concrete materials is an important factor in the design of systems such as concrete overlays on industrial floors and airfield pavements. Latex, due to its film formation action inside the concrete matrix gives the material some microcrack arresting properties which can potentially lead to improvements in the impact resistance of concrete.[1] Further test data are needed for verifying the latex modification effects on the impact resistance of concrete. Steel fiber reinforcement has also been shown in various investigations[2] to significantly improve the impact resistance of concrete.

Latex modification of concrete provides the material with higher flexural strengths.[3] This increase in flexural strength can be attributed to the microcrack-arresting action of polymers in concrete, and also to the bonding they provide between the matrix and aggregates. Improvements of workability through latex modification (which reduce water requirements for achieving similar workability in latex-modified concrete) is another factor contributing to flexural strength in latex-modified concrete. Previous test results[4] have indicated that, at a polymer/cement ratio of 0.20, Styrene Butadiene, Saran, Acrylic and PVA latexes provide flexural strengths of the order of 2, 3, 1.4, and 3 times, respectively, that of plain mortar after 28 days of dry curing at 50% relative humidity.

Steel fibers have been found to increase the first-crack and ultimate flexural strengths of concrete.[2] They also make major contributions to the ductility and toughness (represented by the area under the flexural load-deflection curve) of the material. Steel fibers, with their desirable pull-out performance, are especially effective at relatively large deformations and crack widths.

EXPERIMENTAL PROGRAM

The mix proportions selected for the latex-modified steel fiber reinforced concrete (LMSFRC) mixtures with different latex and fiber contents are presented in Table 1. The cement in all these mixes is regular type I, the coarse aggregate is crushed limestone with a maximum particle size of 13 mm. (1/2 in.); the fine aggregate is natural sand with gradation satisfying the ASTM C-33 requirements; the latex is BASF Styrofan 1186 Styrene-Butadiene dispersion (see Table 2 for properties); the steel fibers are hooked-end with a length of 30 mm. (1.18 in.) and a diameter of 0.5 mm. (0.0197 in.). The air-entraining agent (used only in the unmodified mixtures) was Naphtalene-based.

Table 1. Mix Proportions for Experimental Work.

V_f (%)	Styrenene Butadiene L/c (%)	w/c	Slump mm. (in.)	Vebe Time (sec.)	Air Content (%)
0	0	0.43	152 (6.0)	-----	5.5
0	10	0.32	190 (7.5)	-----	4.5
0.75	0	0.45	127 (5.0)	6.5	6.5
0.75	10	0.34	152 (6.0)	5.0	5.0

V_f = fiber volume fraction;
L/c= latex-cement ratio, by solids weight;
w/c= water-cement ratio, by weight;
s/c=2.5=sand-cement ratio, by weight; and
st./c=1.5=stone-cement ratio, by weight.

Table 2. Properties of Styrene Butadiene Latex.

Typical Properties	
Toatal solids (wt. %)	47
Specific gravity	1.01
pH (25 C)	10
Surface tension (mN/m)	38
Weight/volume , lb/U.S.gal. (kg/l)	8.3 (1.01)

It is worth mentioning that water content was adjusted in different mixtures, depending on the latex and fiber contents, for achieving a desirable level of workability (represented by a Vebe time of 7 to 9 seconds for fibrous mixes and a slump of 76 to 127 mm, 3 to 5 in., for plain mixes). The air content was also adjusted in unmodified mixtures by varying the dosage rate of air-entraining agent in order to achieve air contents of 4.5 to 6.5%.

Three cylindrical specimens 152 mm. (6 in.) in diameter and 63.5 mm. (2.5 in.) in height were prepared for impact tests from each of the 4 mixes of Table 1. They were moist-cured inside their molds under wet burlap coated by a polyehtylene sheet for the first 24 hours and then demolded and cured in air until the test age of 28 days. The impact resistance test is performed by repeatedly dropping a 4.5 kg (10 lb) hammer on a hard steel ball supported on the cylinder from a height of 457 mm. (18 in.).[5] The number of blows required to cause the first visible crack and the ultimate failure represents the impact resistance of the material. Ultimate failure is assumed to occur when the cracks open sufficiently so that the pieces of concrete are touching three of the four positioning lugs on the base plate. In addition, for each mix, three 102x102x356 mm. (4x4x14 in.) prismatic flexural specimens were prepared. They were all moist-cured inside their molds under wet burlap coated by a polyethylene sheet for the first 24 hours and then demolded and cured in air until the test age of 28 days. The flexural specimens were tested following the ASTM C-1018 and the Japanese Concrete Institute procedures (JCI-SF) by four-point loading on a span of 305 mm. (12 in.). A computerized data acquisition system was used for load and deflection measurements, and also for the processing of the flexural test results.

EXPERIMENTAL RESULTS

The raw test data obtained along with the derived conclusions based on statistical analyses of the test results are presented in this section.

Impact Resistance

The impact resistance test results obtained for the mixes of Table 1 are given in Table 3 and Fig. 1.

Table 3. Impact Resistance Test Results for Mixes of Table 1.

Vf (%)	L/c (%)	Number of Blows to First Crack	Number of Blows to Failure
0	0	29	33
		25	28
		32	35
0	10	232	233
		503	503
		50	53
0.75	0	60	106
		190	247
		154	264
0.75	10	900	1065
		395	530
		148	278

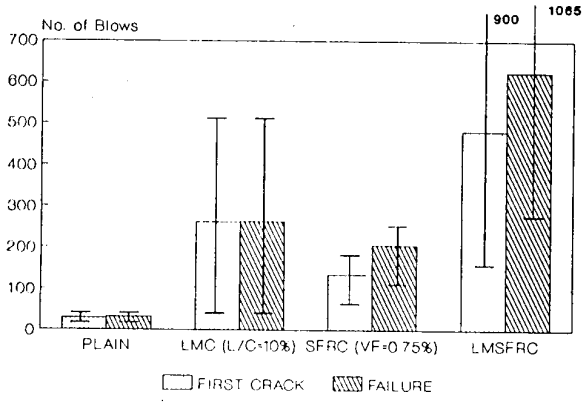

Figure 1. Impact Resistance Test Results.

From Table 3 and Fig.1 it can be seen that latex addition increases the impact resistance of plain concrete by an average of 800%. Steel fiber reinforcement increases the impact resistance by an average of 370%. Combined use of latex polymers and steel fibers leads to major improvements in impact resistance, causing 1500% increase over plain concrete.

When both steel fibers and latex are added to the plain concrete matrix, the improvements in impact resistance are superior. This indicates that there is an effective interaction between the steel fibers and the latex, which possibly results from the improved fiber-to-matrix bonding in the presence of latex polymers, and also from the increased compatibility of steel fibers and the matrix resulting from the reduced brittleness of the matrix incorporating latex.
It is also interesting to note that when fibers are missing from the matrix, even in the presence of latex, there is only a small difference between the first crack and the failure impact resistance. This indicates that fibers, but not latex, can provide the material with post-cracking integrity.

In order to statistically investigate the effects of latex modification and steel fiber reinforcement on impact resistance, one-way analyses of variances were conducted. A one-way analysis of variance (ANOVA) performed for the cases of unmodified and latex modified plain concretes (Vf=0%) indicated that the effects of latex content on the impact resistance of plain concrete are significant with about 15.2% chances of error in this statement. A similar one-way ANOVA performed for the cases of unmodified and latex modified SFRC (Vf=0.75%) resulted in very similar conclusions, with about 15.3% chance of error in stating that there is a latex effect on the impact resistance at Vf=0.75%.

Similar analyses were performed to investigate the effects of steel fiber reinforcement at constant latex content on the impact resistance of the concrete matrix. For the case of unmodified concrete (latex-cement ratio, L/c=0%), the one-way ANOVA showed that fiber addition has a significant positive effect on the impact resistance, with only 2.6% chance of error in this statement. At a constant L/c of 10%, the corresponding one-way ANOVA revealed that there is about 24.6% chance of error in stating that there is a fiber effect on impact resistance of concrete at a latex-cement ratio of 10%.

It is worth mentioning that the scatter in impact resistance test results is relatively large. This leads to conditions where, in spite of the large differences in average values of impact resistance for different mix proportions, the chance of error in stating that such a difference exists sometimes exceeds 15%.

Flexural Performance

The average flexural load-deflection curves for the four mix compositions considered in this investigation are presented in Fig. 2. The improvements resulting from latex modification and steel fiber reinforcement, and the desirable joint effects of latex and steel fibers, are obvious in this figure. The flexural strength and toughness (defined as the area underneath the flexural load-deflection curve up to a flexural deflection equal to the span length divided by 150) test results obtained for the mixes of Table 1 are shown in Table 4.

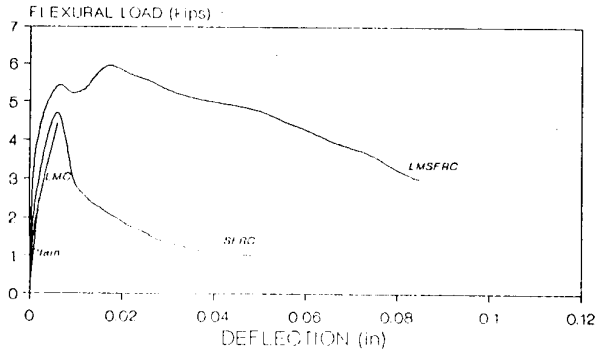

Figure 2. Average Flexural Load-Deflection Relationships.

Table 4. Flexural Strength and Toughness Test Results.

Vf (%)	L/c (%)	Fexural Strength (ksi)	Flexural Toughness (k-in)
0	0	0.420	0.00003
		0.467	0.00005
		0.522	0.00002
0	10	0.880	0.0046
		0.868	0.0058
		0.775	0.0034
0.75	0	0.893	0.254
		0.869	0.207
		0.881	0.231
0.75	10	1.018	0.339
		1.235	0.425
		1.126	0.382

Flexural Strength: From Table 4 and Fig.3 it can be seen that latex addition (L/c=10%) increases the flexural strength of plain concrete by about 87%, while steel fiber reinforcement (Vf=0.75%) increases it slightly more by about 92%. When plain concrete is both modified with latex polymers and reinforced with steel fibers, the improvements in flexural strength are more significant (an increase of about 150% over plain concrete).

A factorial analysis of variance performed on the above results confirmed the significance of the effects of latex polymers, steel fibers, and their interaction, at 5% level of significance. The relative significance of the effects of fibers and latex, and their interaction, on the flexural strength, as indicated by the factorial analysis of variance, is presented in Table 5.

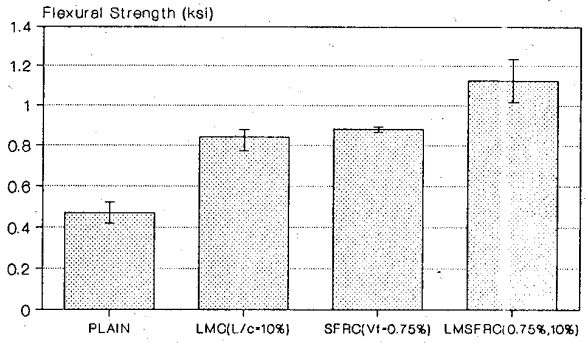

Figure 3. Flexural Strength Test Results.

Table 5. Factorial Analysis of Variance of Flexural Strength Test Results.

Factor	Importance
Steel fibers	**
Latex	**
Interaction	*

"**" very Important

"*" important

Flexural Toughness: Steel fiber reinforcement is observed in Table 4 and Fig.4 to have positive effects on the flexural toughness of concrete, while the improvements in toughness resulting from latex modification are relatively small. Latex modification, however, is highly effective in improving toughness characteristics in the presence of steel fibers.

A factorial analysis of variance confirmed that the effects of latex and steel fibers on flexural toughness, as well as their interaction, are important at 5% level of significance (see Table 6).

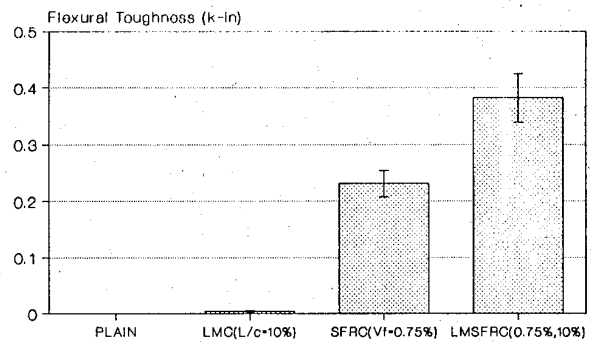

Figure 4. Flexural Toughness Test Results.

Table 6. Factorial Analysis of Variance of Flexural Toughness Test Results.

Factor	Importance
Steel fibers	**
Latex	**
Interaction	**

"**" very Important

"*" important

The significant improvements in flexural toughness of SFRC resulting from latex modification (noting that latex has relatively small effects on the flexural toughness of plain concrete) can be attributed to the improvements in fiber-to-matrix interfacial bond characteristics by latex polymers.

SUMMARY AND CONCLUSIONS

Experimental results regarding the effects of steel fiber reinforcement and/or latex modification on the impact resistance and flexural strength and toughness characteristics of concrete are reported.

From the generated test results it was concluded that:
(a) Latex modification or steel fiber reinforcement increase the impact resistance of the concrete matrix, with superior impact strengths obtained when steel fibers and latex polymers are used simultaneously, indicating an effective interaction between latex and steel fibers resulting from the improved bonding between the fibers and the latex-modified mixtures;
(b) The separate actions of latex polymers and steel fibers in concrete lead to improved flexural strength of concrete. The combined action of latex modification and steel fiber reinforcement leads to highest flexural strength values; and
(c) Steel fiber reinforcement is effective in increasing the flexural toughness (area underneath the flexural load-deflection curve) of concrete. While latex modification has relatively small effects on the flexural toughness of plain concrete, it is capable of significantly improving the toughness characteristics of SFRC. These improvements can be attributed to the positive effects of latex modification on the fiber-to-matrix interfacial bond characteristics and pull-out behavior.

ACKNOWLEDGEMENTS

Financial support for the performance of this research was provided by BASF Canada, Inc. and the Research Excellence Fund of the State of Michigan. These contributions are greatfully acknowledged. The authors are also thankful to Dr. Kar Lok form BASF Canada, Inc. and Dr. Lawrence T. Drzal from the Composite Materials and Structures Center of Michigan State University for their encouragement and technical support.

REFERENCES

1- Concrete Admixtures Handbook, Chapter 7, Noyes Publications, 1984, page 398.

2- Soroushian, P. and Bayasi, Z., "Mechanical Properties of SFRC," Concrete Seminar Proceedings, Michigan State University, February 1987.

3- Soroushian, P. and Aouadi, F., "Latex-Modified Concrete: State-of-the-Art," Department of Civil and Environmental Engineering, Michigan State University, E. Lansing, August 1988.

4- ACI Committee 548, "State of the Art, Polymers in Concrete," American Concrete Institute, Detroit, Michigan, 1977.

5- ACI 544.2R-89

STRAIN RATE EFFECT ON DYNAMIC RESPONSE OF REINFORCED CONCRETE PLATE UNDER IMPACT LOADING

Hiroshi Yamaguchi and Kazuo Fujimoto

Fourth Research Center, Technical Research and Developement Institute,
Japan Defense Agency
Fuchinobe 2-9-54, Sagamihara, Kanagawa 229, Japan

ABSTRACT

Presented is a stress-strain relationship defined by the tangent shear and bulk moduli for concrete considering the strain rate effect under high triaxial stresses. The tangent shear and bulk moduli are expressed as functions of the octahedral stress and strain, and the rates of increase of the initial elastic moduli and the failure stress due to the strain rate effect are taken into account. For the verification of the presented model, the finite element analyses of reinforced concrete members subjected to impact loadings have been carried out, and it is confirmed that the presented model is valuable for the evaluation of the strain rate effect on the dynamic response of reinforced concrete members.

1. INTRODUCTION

On the responses of reinforced concrete structures subjected to impact loadings, the characteristics of material may significantly depend on the strain rate effect. This effect characterized by the increases of the elastic moduli and the failure stress, has been studied extensively. However, most studies have been limited to rapid uniaxial behaviors. Concerning the dependence of triaxial behaviors of concrete on the strain rate, experimental informations seem to be not sufficiently. And so most stress-strain relationships of concrete considering the strain rate effect have been derived on the basis of uniaxial tests alone. In the reinforced concrete structres desingned to resist impact loadings, concrete is confined by heavy reinforcements in three directions, which causes rapid triaxial stresses to build up. The objectives of this paper are to propose a stress-strain relationship for concrete considering the strain rate effect and to verify the validity of the finite element analyses by using the proposed model by comparison with experimental results.

2. IMPACT LOADING TESTS OF REINFORCED CONCRETE PLATE

As the verification tests of the analytical approuch by using the proposed model, the impact loading tests are carried out. The experimental specimen has a circular geometory(300mm in diameter and 40mm in thickness) and is reinforced with rectangular steel mesh(mild steel 2.6 ϕ , @10mm)on the side of rear face to impact(Fig.1). The concrete mixture is based on a water-cement ratio of w/c=70%, a mix grading of c:s=1: 3.5 and a maximum sand size of 5.mm. The impact loadings are generated by dropping a hummer(30kg in weight) from the two stages of height(20cm and 40cm) and are applied on the loadcell with rubber plate(3.mm in thickness) placed on the center of the specimen(Fig.2). The specimen is fixed in circumference by the steel rings, and is called H20 or H40 corresponding to the height of a hummer. The displaement data are obtaind by integrating the acceleration data measured by piezo type accelerometer put on the center of rear face of the specimen

3. STRESS-STRAIN RELATIONSHIP CONSIDERING STRAIN RATE EFFECT

Authors previously have reported[1], the stress-strain relationship which is based on

the incremental isotropic model for concrete defined by the tangent elastic moduli on the basis of the rapid triaxial tests under high compression. But this model is available for concrete under compression stress only, so the modified model which can represent the behaviour under tension stress is proposed .

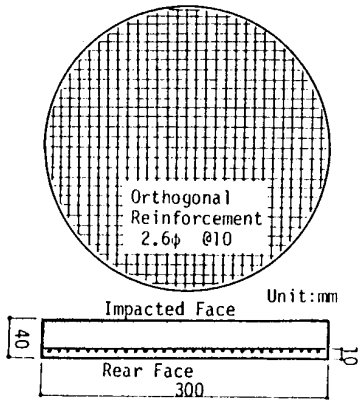

Fig.1 Specimen

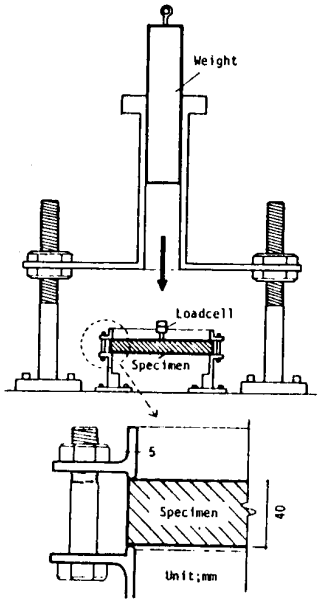

Fig.2 Loading Setup

Table 1 summarizes the formulation of the proposed model. The tangent elastic moduli are considered the dependences on both the hydrostatic pressure and deviatoric stress. The dependence on the hydrostatic pressure, which is represented by the rates of decrease of the tangent elastic moduli with the octahedral normal strain ε_{oct}, is given by the empirical equations(Eqs.3-4). In order to express the dependence of the deviatoric stress, it is assumed the existence of continuous curves which link the stress points of the equal rate of decrease of the tangent elastic moduli with increasing deviatoric stress on the octahedral stress plane. The curves, called the equivalent decreasing rate curves, are uniquely defined by a parameter ϕ_d ($0 \leqq \phi_d \leqq 1$). The rates of decrease of tangent elastic moduli should be related to the valiation of the deformation behaviours under triaxial loading. So the shapes of the equivalent decreasing rate curves are analogous to the failure curves(Figs.7-8), and the function forms of these curves are determined by fitting to the test data(Eqs.9-11). Then the good correlation between ϕ_d and the rates of decrease of tangent elastic moduli obtaind from test data. Therefore these relations between ϕ_d and the rates of decrease of tangent elastic moduli are given by Eqs.5-6, which represent the dependence on the deviatoric stress.

The strain rate effect is manifested mainly in the increases of the initial elastic moduli and the failure stress. The strain rate effect on the initial elastic moduli is obtaind as empirical equations (Eqs.16-22).

The increase of the failure stress is already considered by introducing the above parameter ϕ_d which is defined by using the expanded failure curves(Eqs.7-8) with the octahedral shear strain rate. The expanded failure curves are defined by using increased compressive and tensile strengthes(F_{cd} and F_{td}) with the octahedral shear strain rate(Eqs.12-15, in which F_c and F_t are static compressive and tensile strengthes, respectively). Note that the tensile strength ratios given by Eqs.14-15 are derived on the test data of rapid uniaxial tension by Zielinski[2] , and the shapes of the failure curve and the equivalent decreasing rate curves in tension region are simply defined as straight lines in consideration of continuities to these curves in compression region.

Namely, the tagent elastic moduli are given by multiplying the initial elastic moduli (KO and GO) by the rates of decrease of the tangent elastic moduli with

increasing hydrostatic pressure and with increasing deviatoric stress, and also by the rate of increase of the tangent elastic moduli with increasing strain rate (Eqs.1-2), and these rates are given by the current values of the octahedral normal stress σ_{oct}, the octahedral shear stress τ_{oct}, the octahedral noral strain ε_{oct}, the octahedral noral strain rate $\dot{\varepsilon}_{oct}$ and the octahedral shear strain rate $\dot{\gamma}_{oct}$.

Table 1 Formulation of proposed model

《 Tangent bulk modulus 》

$$K^t=K0\cdot k(\dot{\varepsilon}_{oct})\cdot\alpha_V(\varepsilon_{oct})\cdot\alpha_D(\phi_d) \quad \cdots(1)$$

《 Tangent shear modulus 》

$$G^t=G0\cdot g(\varepsilon_{oct},\dot{\gamma}_{oct})\cdot\beta_V(\varepsilon_{oct})\cdot\beta_D(\phi_d) \quad \cdots(2)$$

《 Rate of decrease of tangent elastic moduli 》

$$\alpha_V(\varepsilon_{oct})=a_1\cdot\exp(a_2\cdot\varepsilon_{oct})+a_3\cdot\exp(a_4\cdot\varepsilon_{oct}) \quad \cdots(3)$$

$$\beta_V(\varepsilon_{oct})=b_1\cdot\exp(b_2\cdot\varepsilon_{oct})+b_3\cdot\exp(b_4\cdot\varepsilon_{oct}) \quad \cdots(4)$$

《 Rate of decrease of tangent elastic moduli 》

$$\alpha_D(\phi_d)=a_5+a_6\cdot\phi_d+a_7\cdot\phi_d^2+a_8\cdot\phi_d^3+a_9\cdot\phi_d^4 \quad \cdots(5)$$

$$\beta_D(\phi_d)=b_5+b_6\cdot\phi_d+b_7\cdot\phi_d^2+b_8\cdot\phi_d^3+b_9\cdot\phi_d^4+b_{10}\cdot\phi_d^5+b_{11}\cdot\phi_d^6+b_{12}\cdot\phi_d^7 \quad \cdots(6)$$

《 Failure curves 》

$$\tau_{oct}/F_{cd}=f_d(\sigma_{oct}/F_{cd})$$

For $\sigma_{oct}\leqq 0$.(compression region)

$$f_d(\sigma_{oct}/F_{cd})=f_1/\exp(f_2\cdot\sigma_{oct}/F_{cd})+f_3 \quad \cdots(7)$$

For $\sigma_{oct}>0$.(tension region)

$$f_d(\sigma_{oct}/F_{cd})=f_o+m\cdot\sigma_{oct}/F_{cd} \quad \cdots(8)$$

$$f_o=f_1+f_3,\ m=(\sqrt{2}\cdot F_{td}/F_{cd}-3\cdot f_o)/(F_{td}/F_{cd})$$

《 Equiavalent decreasing rate curves 》

$$\tau_{oct}/F_{cd}=\Phi(\phi_d,\sigma_{oct}/F_{cd}) \quad \cdots(9)$$

For $\sigma_{oct}\leqq 0$.(compression region)

$$\Phi(\phi_d,\sigma_{oct}/F_{cd})=\phi_d\left[\frac{(1+c)^2}{(\phi_d+c)}-(1+c)\right]d^{-\frac{\sigma_{oct}}{F_{cd}}+t}+1]\cdot f_d(\sigma_{oct}/F_{cd}) \quad \cdots(10)$$

For $\sigma_{oct}>0$.(tension region)

$$\Phi(\phi_d,\sigma_{oct}/F_{cd})=\phi_d\left[\frac{(1+c)^2}{(\phi_d+c)}-(1+c)\right]d^{t}+1]\cdot f_o+m\cdot\sigma_{oct}/F_{cd} \quad \cdots(11)$$

《 Compressive strength ratio (F_{cd}/F_c) 》

For $\dot{\gamma}_{oct}\geqq 24.4\times10^{-6}$/sec

$$F_{cd}/F_c=u_1+u_2\cdot\log(\dot{\gamma}_{oct})+u_3\cdot[\log(\dot{\gamma}_{oct})]^2 \quad \cdots(12)$$

For $\dot{\gamma}_{oct}<24.4\times10^{-6}$/sec

$$F_{cd}/F_c=1. \quad \cdots(13)$$

《 Tensile strength ratio (F_{td}/F_t) 》

For $\dot{\gamma}_{oct}\geqq 24.4\times10^{-6}$/sec

$$F_{td}/F_t=[u_4+u_5\cdot\log(\dot{\gamma}_{oct})+u_6\cdot[\log(\dot{\gamma}_{oct})]^2] \quad \cdots(14)$$

For $\dot{\gamma}_{oct}<24.4\times10^{-6}$/sec

$$F_{td}/F_t=1. \quad \cdots(15)$$

《 Rates of increase of initial bulk moduli 》

For $\dot{\varepsilon}_{oct}\leqq -4.06\times10^{-6}$/sec

$$k(\dot{\varepsilon}_{oct})=k_1+k_2\cdot\log(-\dot{\varepsilon}_{oct})+k_3\cdot[\log(-\dot{\varepsilon}_{oct})]^2 \quad \cdots(16)$$

For $\dot{\varepsilon}_{oct}>-4.06\times10^{-6}$/sec

$$k(\dot{\varepsilon}_{oct})=1. \quad \cdots(17)$$

《 Rates of increase of initial shear moduli 》

$$g(\varepsilon_{oct},\dot{\gamma}_{oct})=g_1(\dot{\gamma}_{oct})-\varepsilon_{oct}\cdot g_2(\dot{\gamma}_{oct}) \quad \cdots(18)$$

For $\dot{\gamma}_{oct}\geqq 24.4\times10^{-6}$/sec

$$g_1(\dot{\gamma}_{oct})=g_{11}+g_{12}\cdot\log(\dot{\gamma}_{oct})+g_{13}\cdot[\log(\dot{\gamma}_{oct})]^2 \quad \cdots(19)$$

$$g_2(\dot{\gamma}_{oct})=g_{21}+g_{22}\cdot\log(\dot{\gamma}_{oct})+g_{23}\cdot[\log(\dot{\gamma}_{oct})]^2 \quad \cdots(20)$$

For $\dot{\gamma}_{oct}<24.4\times10^{-6}$/sec

$$g_1(\dot{\gamma}_{oct})=1. \quad \cdots(21)$$

$$g_2(\dot{\gamma}_{oct})=0. \quad \cdots(22)$$

《 Parameters of Eqs.3-22 》

$a_1=0.8812, a_2=0.7832\times10^3, a_3=0.1188,$
$a_4=-0.5518\times10^2, a_5=1., a_6=-0.3133\times10,$
$a_7=0.1071\times10^2, a_8=-0.1658\times10^2, a_9=0.9012\times10$
$b_1=0.5541, b_2=-0.2221\times10, b_3=0.4459,$
$b_4=0.8563\times10^3, b_5=1., b_6=-0.9260\times10,$
$b_7=0.6769\times10^2, b_8=-0.2730\times10^3, b_9=0.6110\times10^3$
$b_9=0.6110\times10^3, b_{10}=-0.7601\times10^3,$
$b_{11}=0.4910\times10^3, b_{12}=-0.1284\times10^3$
$f_1=-7.435, f_2=-0.1113, f_3=7.640$
$c=0.02, d=0.4, d=1/30$

$u_1=0.1021\times10, u_2=-0.5076\times10^{-1}, u_3=0.2583\times10^{-1},$
$u_4=0.8267, u_5=0.2987\times10^{-1}, u_6=0.4379\times10^{-1}$
$k_1=0.1009\times10, k_2=-0.2875\times10^{-1}, k_3=0.2362\times10^{-1}$
$g_{11}=0.1032\times10^{-1}, g_{12}=-0.4673\times10^{-1},$
$g_{13}=0.1684\times10^{-1}, g_{21}=-0.2187\times10, g_{22}=-0.5189,$
$g_{23}=0.1510\times10$

The caluculated results of uniaxial tensile loading by using the proposed stress-strain relationship show a satisfactory agreement with the test data by Hatano[3] (Fig.3).

Concerning the stress-strain relationship of reinforcement, the elastic moduli are regarded as to be not affected by the strain rate effect [4]. On the other hand, the yield sress increases with increasing strain rate, which is given by empirical equations(Eqs.23-24 in which σ_y is the static yield stress and σ_{yd} is increased yield stress with uniaxial strain rate ($\dot{\varepsilon}_1$).

For $\dot{\varepsilon}_1 \geq 22.5\times10^{-6}$/sec:

$$\sigma_{yd}/\sigma_y = y_1 + y_2 \cdot \log(\dot{\varepsilon}_1) + y_3 \cdot [\log(\dot{\varepsilon}_1)]^2 \quad \cdots\cdots\cdots(23)$$

For $\dot{\varepsilon}_1 < 22.5\times10^{-6}$/sec:

$$\sigma_{yd}/\sigma_y = 1. \quad \cdots\cdots\cdots(24)$$

in which $y_1=0.9905, y_2=0.1153\times10^{-2}, y_3=0.6725\times10^{-2}$.

As for bond behaviours. perfect bond is assumed. Cracking of concrete is based on the criterion of maximum principal stress.i.e., when maximum principal stress exceeds the increased tensile strength (F_{td}), a crack is assumed to develop in the plane normal to the direction of the maximum principal stress. After cracking, the stress normal to crack direction is reduced to zero linearly over ε_{c1}(strain normal to crack direction).

$$\sigma_1 = F_{td}\left(1 - \frac{\varepsilon_{c1}-\varepsilon_{cr}}{20\cdot\varepsilon_{cr}}\right) \quad \cdots\cdots\cdots(25)$$

in which ε_{cr} is strain at cracking.

Residual shear resistance of cracks due to aggregate interlock is also considered by using a constant shear reduction factor β_G (=0.2).

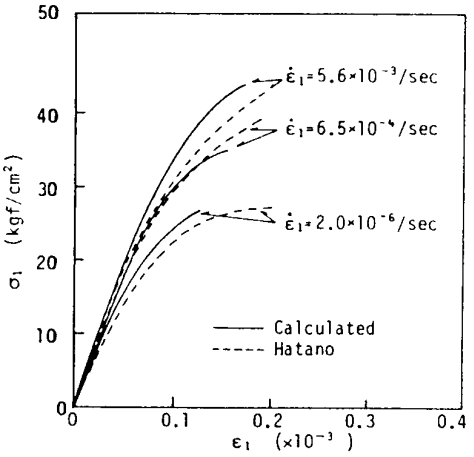

Fig.3 Stress-strain curves under uniaxial tension

4. FINITE ELEMENT ANALYSES

For the verification of the proposed stress-strain relationship, the finite element analyses of reinforced concrete plate subjected to impact loadings by using the proposed models are carried out. In the analyses, the linear quadrilateral element in axisymmetric stress is used for modeling of the specimen, and the reinforced concrete region is treated as an equivalent element which has stiffness including both concrete and reinforcement. Fig.4 shows the fineite element mesh for calculation. Cracks are allowed to form at each one direction in radial plane and in circumferential plane on axisymmetoric coordinates. Concrete is assumed to be orthotropic to crack axis for post-cracking, and the stress-strain matrix is changed to be provided that stress normal to crack direction is set to zero linearly over ε_{c1}.

Figs.5-6 show the actual applied impact loads and the simplified applied impact loads for calculation. Damping effect is needed for numerical stability of presented analysis, so the damping matrix is determined by the Rayleigh damping (damping coefficient=5%). The mass matrix is a constant mass matrix. The solution of the equation of motion is the Newmark β (β=1/4) method and the time increment of step by step solution is determined on basis of the minimum length of element.

Table 2 shows the material parameters for the calculation. Note that the calculations without the strain rate effcet are conducted by using the proposed model setting standard static strain rates, i.e., $\dot{\varepsilon}_{oct}=-24.0\times10^{-6}$/sec, $\dot{\gamma}_{oct}=-4.06\times10^{-6}$

/sec and $\dot{\varepsilon}_1 = 2.25 \times 10^{-6}$/sec in Eqs.12-24.

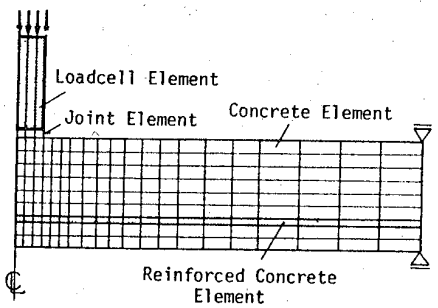

Fig.4 Finite element model

Table 2 Material properties

Concrete	KO=1.07x10^{5}kgf/cm^2,GO=1.01x10^{5}kgf/cm^2, F_c=240kgf/cm^2, ρ=2.25g/cm^3
Reinforcement	E_s=2.10x10^{6}kgf/cm^2,P_s=0.17, ρ=7.80g/cm^3
Loadcell	E_s=2.10x10^{6}kgf/cm^2,ν=0.3, ρ=71.7g/cm^3

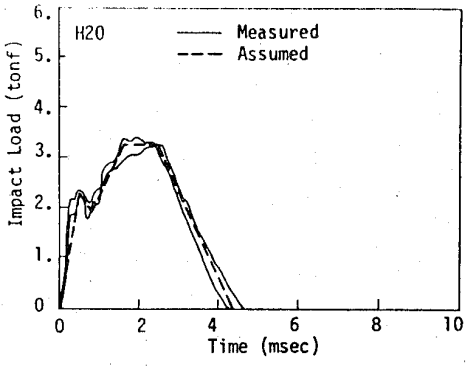

Fig.5 Impact load-time curves(H20)

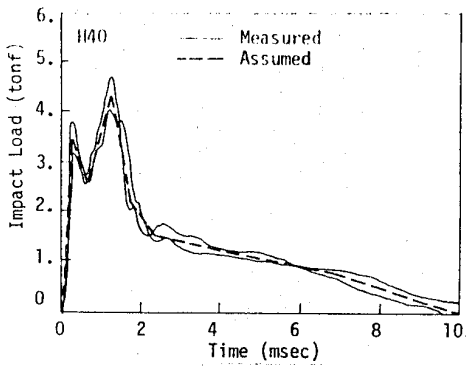

Fig.6 Impact load-time curves(H40)

5. CALCULATED PREDICTIONS AND COMPARISON WITH TESTS

Figs.7-8 show the displacement-time curves at the center of rear face of plates. In the calculated displacement-time curves, the initial stiffnesses increase and the maximum displacements decrease due to the strain rate effect. And so the calculated results with the strain rate effect show a reasonable agreement with the experimental ones rather than the calculated ones without the strain rate effect.

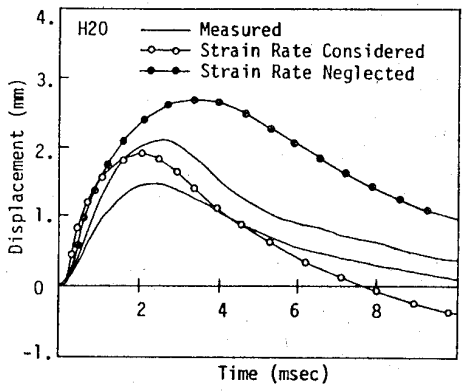

Fig.7 Displacement-time curves(H20)

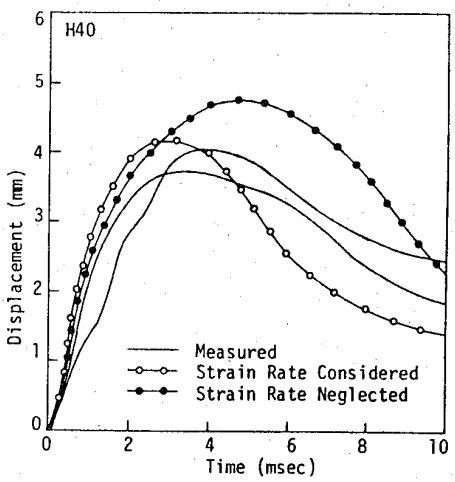

Fig.8 Displacement-time curves(H40)

Fig.9 shows the calculated deflection modes magnified by one fifth times at the maximum displacement. In the calculated deflection without strain rate effect, concrete gives way on the impact face, and swells around the impact face. On the other hand, concrete of the impact region is strengthened due to the high strain rate, so that the local deflections do not obviously occur in the calculation with the strain rate effect.

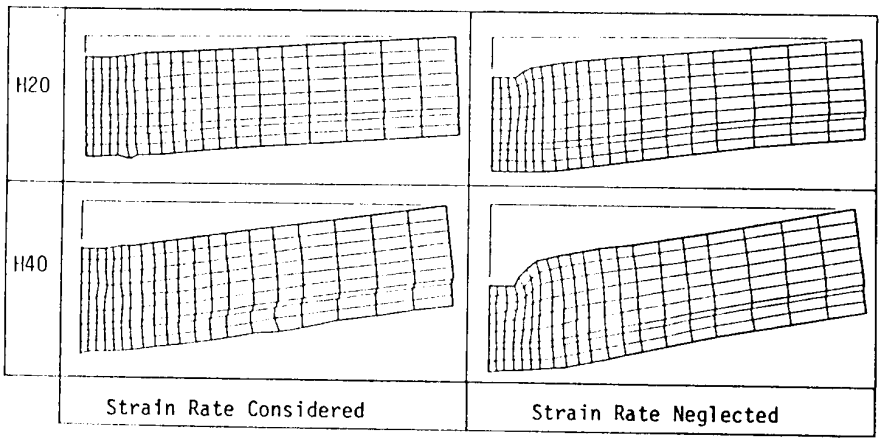

Fig.9 Deflection modes

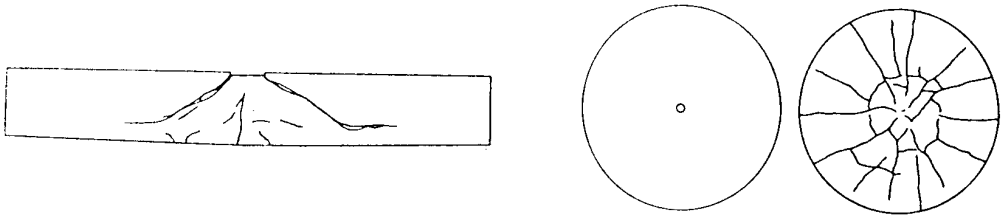

Fig.10 Cracking patterns(experiment)

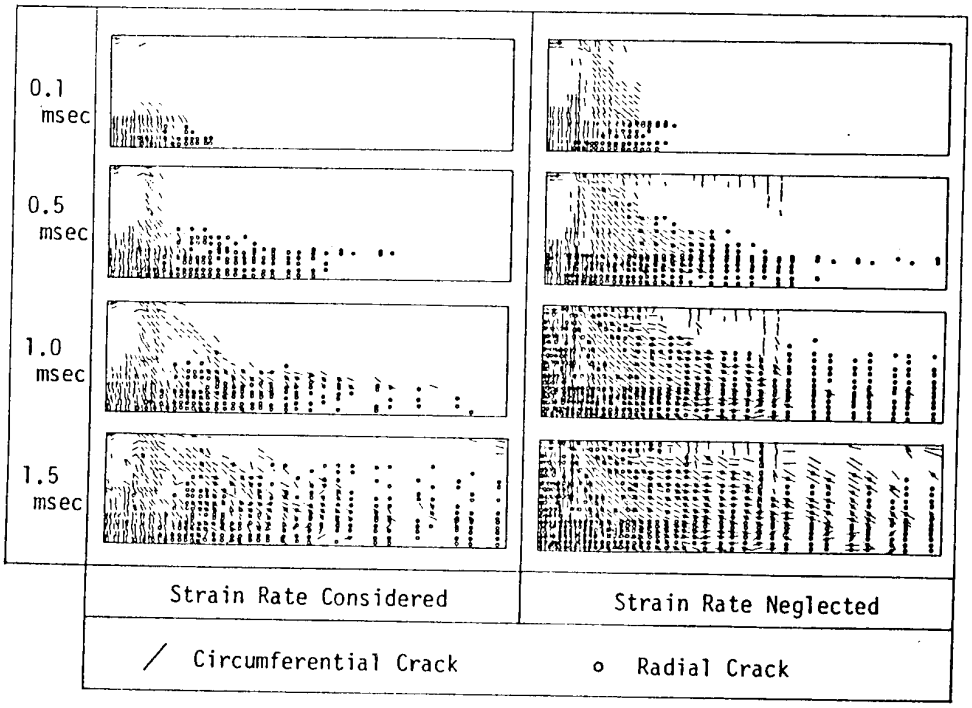

Fig.11 Cracking patterns(calculated)

Fig.10 shows the experimental crack patterns of the specimen H40, and Fig.11 shows the calculated crack patterns in time sequence. In the experiment, only a penetration due to impact is observed on the impact face and the shear cracks develope from the edge of impact face to the direction of reinforcements in the sectional plane. Also, tensile cracks occur on the rear face. In the calculation with the strain rate effect,

there is the decreasing trend on the occurrence of cracks as compared with the calculated ones without the strain rtae effect. Especially, in the calculation without the strain rate effect, the tensile cracks occur near the impact face, which are not observed in the experiment.

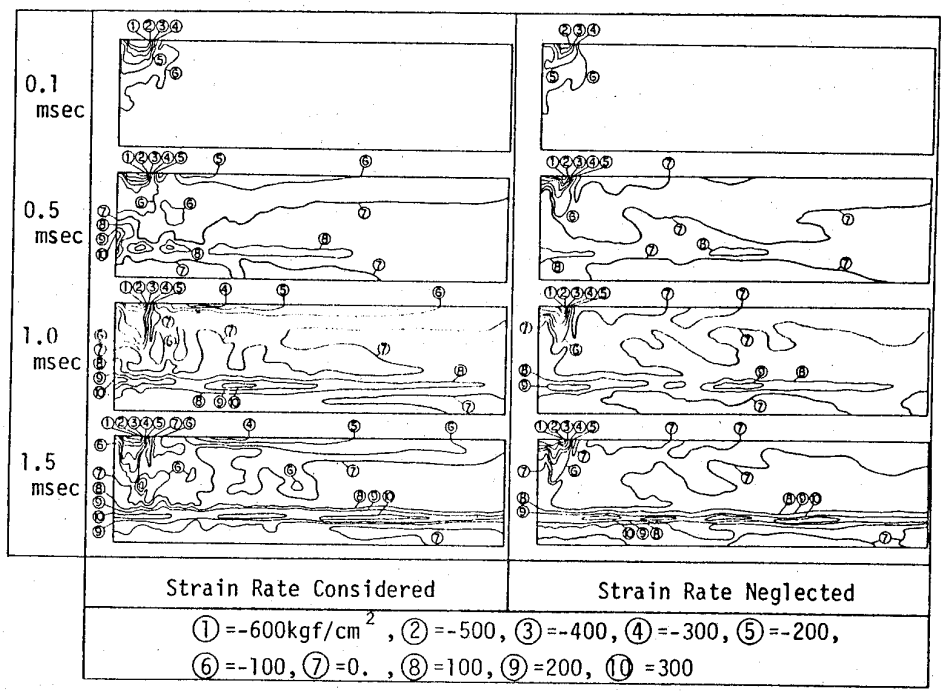

Fig.12 Contours of mean normal stress

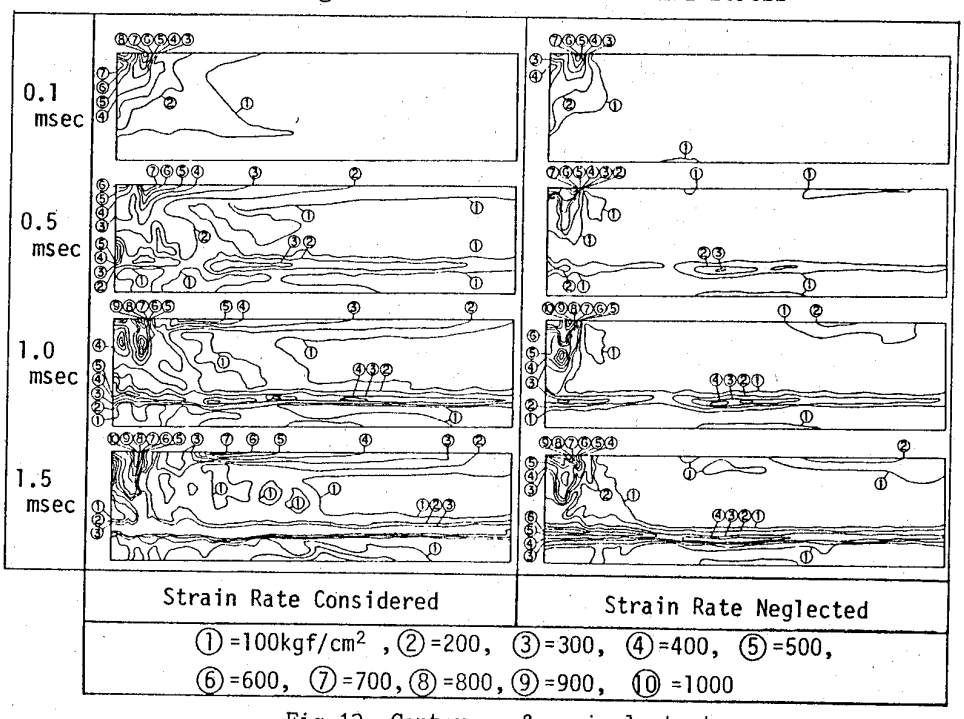

Fig.13 Contours of equivalent stress

Figs.12-13 show the contours of mean normal stress(= σ_{oct}) and equivalent stress(=3 $/\sqrt{2}$ τ_{oct}) in the calculation of the specimen H40 in time sequence. It is confirmed that high stresses are build up at impact region, which are made possible by using the proposed analytical approach considering the strain rate effect on the basis of high

triaxial compression tests. The mean normal stress on the impact face in the calculation with the strain rate effect is greater than the one without the strain rate effect soon after impact (at 0.1msec, the contour line① is showed), and the compression regions spread widely at later times (at 0.5-1.5msec, the contour lines ④ -⑥ are showed). The distribution of the contour lines of equivalent stress is similar to the one of the mean normal stress. Namely, the high mean normal stress and high equivalent stress are develope due to the strain rate effect, so that the stiffness of specimen increases, the displacement decreases, and especially the local deflection on impact region is restricted (see Figs.9-10.) due to high strain rate.

6. CONCLUSION

The stress-strain relationship of concrete considering the strain rate effect, which can adequately predict the behaviors under rapid triaxial compression and also under rapid tension, is proposed. The proposed model is available for the evaluation of the strain rate effect on the dynamic response of the reinforced concrete members subjected to impact loading.

References

1) Yamaguchi,H.,Fujimoto,K.,and Nomura,S.,"Strain Rate effect on Stress-Strain relationship of Concrete",Fourth International Symposium on the Interaction of Non-nuclear Munitions with Structures,Vol.1,Panama City Beach,Florida,USA,April 17-21,1989,pp.290-295.

2) Zielinski,A.J.,Reinhardt,H.W.,and Kormeling,H.A.,"Experiments on Concrete under Uniaxial Impact Tensile Loading",Materiaux et Constructions,Vol.14,No.80,1981,pp.103-112.

3) Hatano,T.,"Dynamic Behaviour of Concrete under Impulsive Tensile load",Technical Report No.C6002,Central Research Institute of Electric Power Industry,Tokyo,1969,pp.1-14.

4) ACI Comittee 439 "Effect of Steel Strength and of Reinforcement Ratio on the Mode of Failure and Strain Energy Capacity of Reinforced Concrete Beams",ACI Journal 1969,pp.165-172.

Eigenschaften von Waffen

Weapons-Characteristica

Measured Parameters of the Airblast Loading of generic Models from Shock Tube Tests and Comparisons with SHARC-Code Calculations

W. Heilig

Fraunhofer-Institut für Kurzzeitdynamik
Ernst - Mach -Institut
Freiburg im Breisgau, Germany

Abstract:
The paper deals with methods for determining the loading functions of obstacles hit by blastwaves. Such functions provide the input data of structural response codes in order to perform vulnerability analyses of the objects. Loading functions can be obtained experimentally on the basis of pressure measurements using gages. They also result from code calculations, a technique applied recently. Numerical simulations using the code SHARC will be presented in the paper and partly compared to experimental data available, thus validating the code. Comparisons with the von Neumann Theory which can be used for an approximate calculation of loading functions are given additionally.

Introduction:

In order to perform numerical vulnerability analyses of objects hit by blastwaves knowledge about the surface loading function is necessary assuming the obstacle to be a "rigid body". The resulting loading function provides the input data for a structural response code. This procedure is "State of the Art" unless a genuine Fluid-Structure Interaction Program is applied which are mostly not available. Therefore methods to determine loading functions have to be developed. They can be determined exprimentally by measuring the pressure on the surface of the obstacle using gages. An example of a vulnerability analysis with NASTRAN as the structural response code and with the help of an experimentally determined loading function is demonstrated in [1]. However, as codes come up loading functions are calulated more and more frequently, thus substituting expensive experiments which for the present problem can be performed as model tests only and which, in any case, do not supply all paramaters of interest.

For a long time the von Neumann Theory (VNT) [2] was used to calculate loading functions approximately. It is an analytical one and easily to handle. Many of the reflection factors mentioned in the literature are derived from it. Its boundary conditions are seldom met in the experiment it nevertheless yields values which partly agree with the measurements and partly not. The latter especially holds for the so-called von "Neumann

Paradox of weak Mach reflection". The reason for it actually is a violation of the boundary conditions in spite of other objections; that could be shown with the aid of code calculations.

The most efficient way to calculate loading functions is to apply codes which according to the problem base on the Finite-Difference- or the Finite-Element-Method as numerical schemes. Recently in the Ernst-Mach-Institut the Finite-Difference code called SHARC rendered good services to this end. Two examples will be presented in the following.

1. Shock Loading of plane Walls

a) Phenomenology:

The shock loading of an inclined plane wall (wedge) becomes a very simple process if the edge effects are neglected. Then it is two-dimensional and it furthermore provides an elementary understanding of the phenomena of shockwave reflection which finally are the physical background for the loading. These phenomena can be demonstrated best by shock tube runs in connection with a visualization technique and, if possible, with a direct measurement of the pressures using gages and performed simultaneously to visualization. Shadow-schlieren - or interference records demonstrate that two essential modes which the incident shock produces during reflection have to be distinguished.

At a steep wedge the plane incident shock undergoes a regular reflection (RR), the pattern of which consists of two shocks, the incident and the reflected one (Fig. 1). Its intersection point travels on the wall by what the RR is characterized. The reflected shock emanates from the wall and extends as a partly curved shock in the upstream direction.

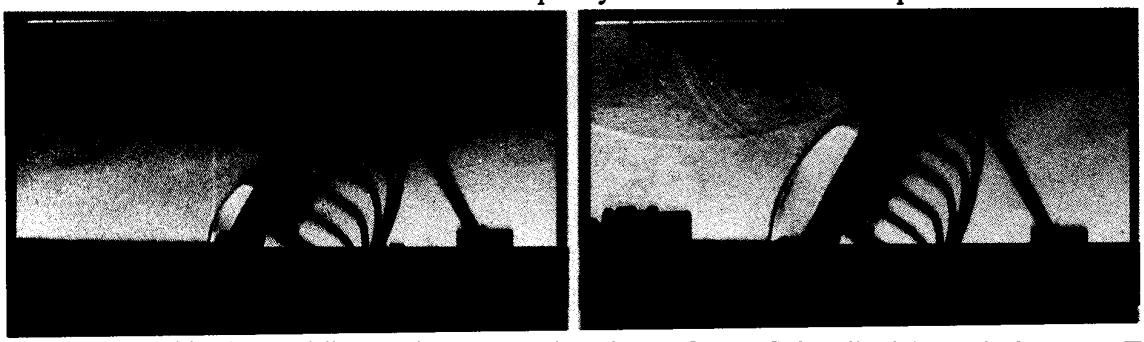

Fig. 1 *Shadow-schlieren pictures made using a Cranz-Schardin 24-spark Camera. Two different time instants of the phase of regular reflection (RR) are shown; incident shock Mach number M_O = 1.84, wedge angle θ_W = 60 deg. (#11 150). Note the gage's cables at the rear of the surface.*

The second reflection pattern called irregular reflection (IR) arises at a flat wedge . It is recognizable by a newly created shock, the Mach shock being joined to the incident and the reflected shock at a point called triple point which travels in the free flow field (Fig. 2 a). Another line, which is a discontinuity for density and for the tangential components of the velocity and is therefore not a shock, leaves the triple point, extends to the

wall and curls up there. It is called slipline. The pattern in Fig. 2 a) is called single Mach reflection (SMR) and is a special type of IR. - If a stronger incident shock hits the wedge of Fig. 2 a) the pattern of Fig. 2 b) arises. It is called double Mach reflection (DMR). Its prominent feature is that a kink appears in the contour of the reflected shock, from which

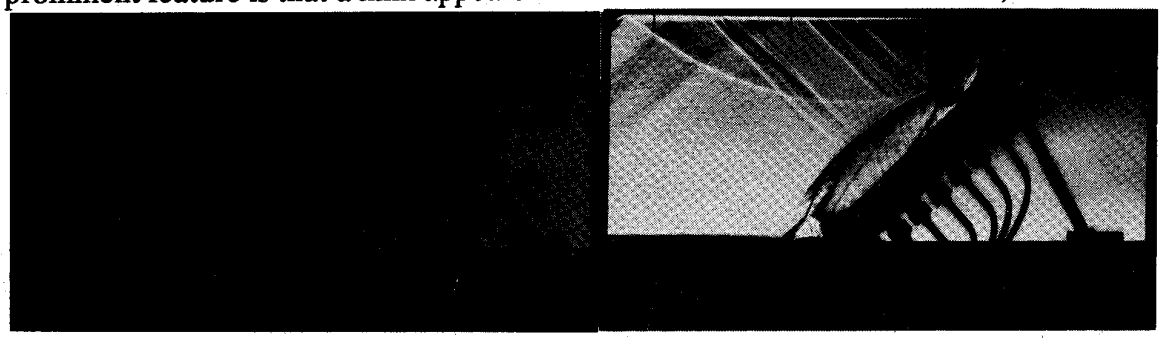

Fig. 2 *Shadow-schlieren pictures showing a time instant of the phase of irregular reflection, each.*
a) Left : Single Mach refl.(SMR); M_O = 1.26; θ_W = 34 deg. (#11 205)
b) Right: Double Mach refl.(DMR); M_O = 3.36; θ_W = 44 deg. (#11 143)

another shock travels towards the slipline, and apparently another line being a second slipline travels towards the wall. An analysis of the discontinuities leaving from this kink leads to the insight that it plays the role of a second triple point, and leading to the denomination DMR. For an incident shock of moderate strength a less sharp kink can be generated and the pattern then is called complex Mach reflection (CMR).
If shock tube runs with incident shocks of equal strength are performed but with wedges whose inclinations are different from run to run either RR or IR appears. Therefore a "limiting wedge" must exist for a certain incident shock strength.

b) SHARC-Simulations

In the following SHARC-simulations of the phenomena mentioned will be shown. It is important to point out which parameters of the process to be simulated enter the code. Only the speed of the incident still undisturbed shock, i.e. its shock Mach number M_O, serves as initial value besides the state parameters of the ambient region, and, additionally, the wall inclination as boundary condition has to be communicated to the code. As these data must also be adjusted in the shock tube run the code actually simulates it. Using isopycnics Fig. 3 shows the SHARC-simulated RR of an incident shock with Mach number M_O = 3.36 at a wedge with angle Θ_W = 52°. Note that the frame of reference has been chosen so that the wall is horizontal. The upper inset of Fig. 3 shows the trend of the density along the wedge surface from what the loading function can be derived. In Fig. 4 another SHARC simulation is shown with the same M_O but now with Θ_W = 51.5°. Its is very striking that within the interval of 1/2° of wall inclination (in which

the "limiting wedge" must lie) the pattern changes from RR to DMR. Note especially the trend of density along the wall which behind the first shock shows quite a different feature to that of Fig. 3.

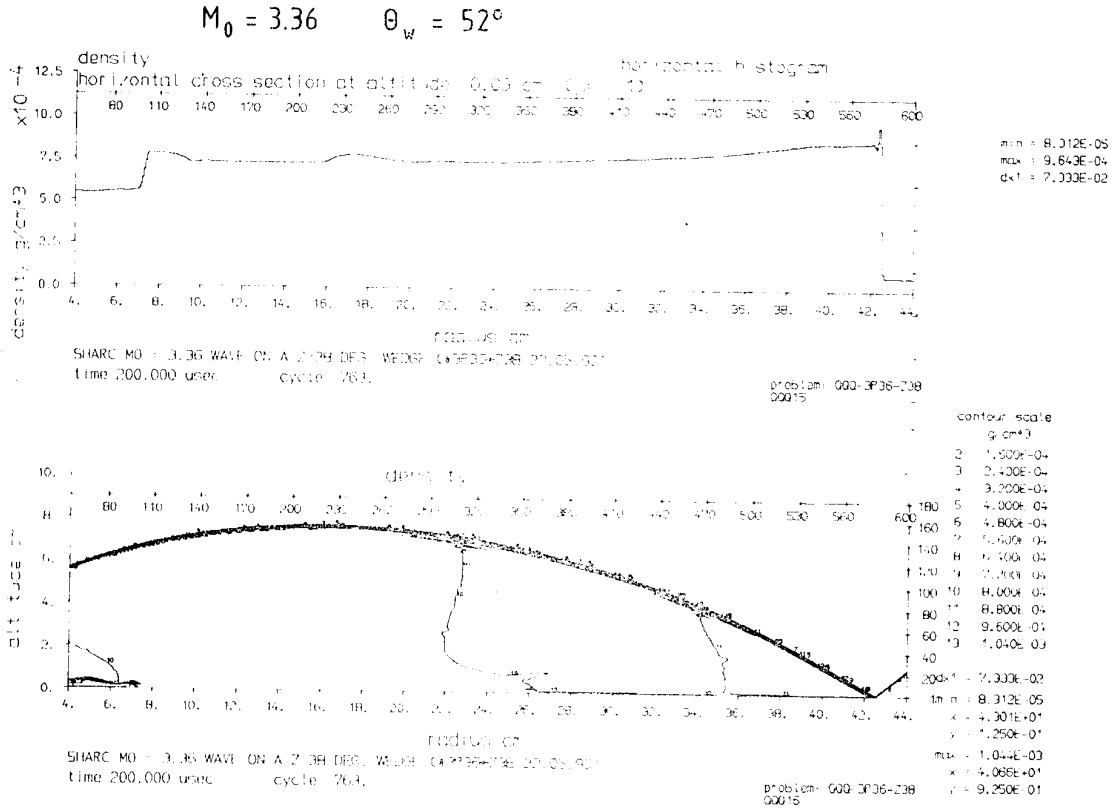

Fig. 3 *SHARC Code results of an inc. shock with M_O = 3.36 reflecting at a wedge with angle θ_W = 52 deg at time 200 μsec. after start. Frame is rotated so that the wedge surface is horizontal. Upper inset: Trend of density on the surface and along it. Lower inset: Isopycnics with contour levels at the right indicate that RR occurs.*

In Fig. 5 measured values of the front reflected pressure (i.e. pressure right behind the reflected shock in the phase of RR and pressure right behind the Mach shock in the phase of IR) picked up by gages are plotted versus the wedge angles for several shock tube runs performed all with approximately the same incident M_O = 1.26. Note that the trend of pressure exhibits a maximum at a wedge angle which is very close to the value of the "limiting wedge". We realize that SHARC excellently reproduces the measured data, a fact which can be considered as a validation of the code. - The solid lines in Fig. 5 indicate the results of the VNT. Good agreement prevails in the phase of RR (left branch) but a total failure of the VNT exists in the phase of IR (right branch). That is the demonstration of the "Paradox" mentioned above which is due to the violation of the boundary conditions of the VNT by the experiment. Therefore the VNT can only be

considered as an approximate theory if it is applied to shock loading processes. Consequently we must conclude that the calculation of the simplest process of shock loading of plane walls needs a numerical procedure as it was foreseen in the early paper

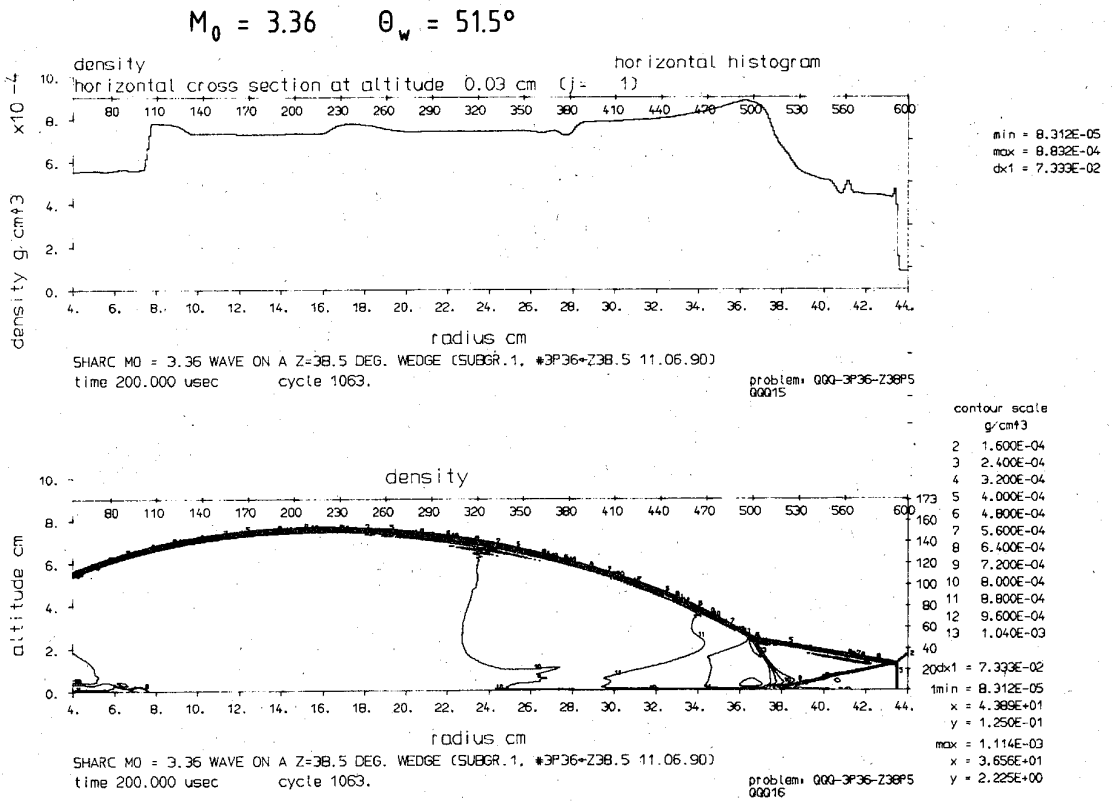

Fig. 4 *See legend of Fig. 3 with, however, θ_w = 51.5 deg. Instead of a RR pattern a fully developed DMR pattern appears. The density-distance curve clearly shows a trend different from that in Fig. 3, especially the "second peak" can be seen.*

of [3]. In the next section we will present a method to determine the loading of a non-plane obstacle experimentally.

2. The Loading of a cylindrical shaped Body

The mainly experimental determination of the loading function of a half cylinder as another generic model will be described in this section. Shadow-schlieren pictures (Fig. 6) indicate that both phases of reflection, RR as well as IR, appear one after another during the same run in which, also, the pressure is measured. In order to cover the entire surface by gages two runs were made with the cylinder being turned about its vertical axis. In both runs the incident shock Mach number was kept constant.

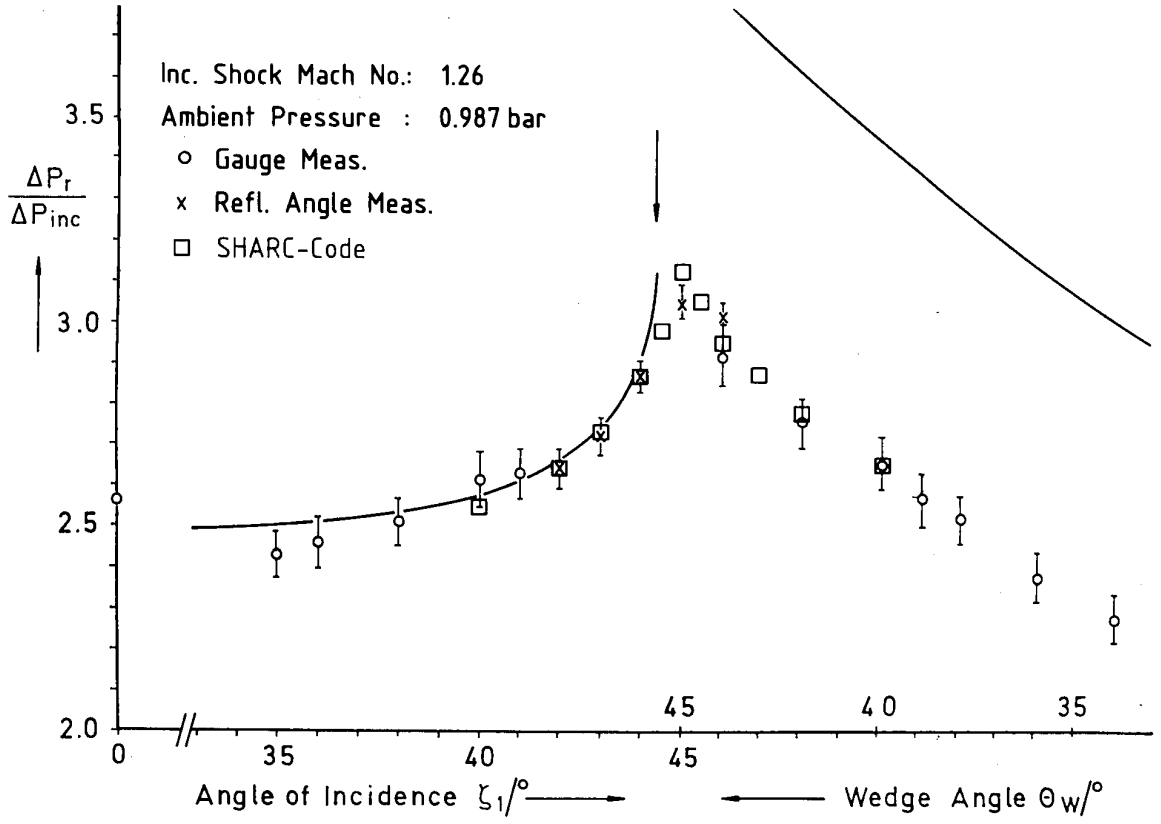

Fig. 5 *Two types of experimental pressure data for incident shocks with averaged M_O = 1.26. Solid lines represent the VNT, left branch for RR; right for IR (SMR, here). Note the large deviation of the VNT from the measured data in the IR regime called "von Neumann Paradox of weak Mach Reflection". Box symbols represent SHARC data.*

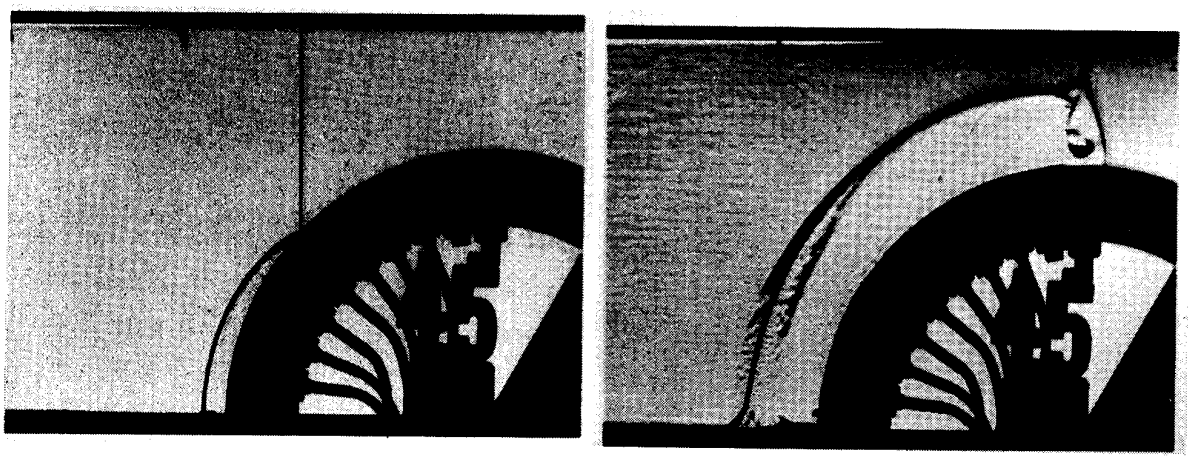

Fig. 6 *Two time instants of the RR- and IR-phase, each of the shock wave reflection at a half cylinder. M_O = 3.36 (#11 345).*

After magnifying the signal of a gage being hit by the engulfing shock and after digitizing this signal it appears as a pressure-time curve that can be plotted on a chart. The total loading on the obstacle at a fixed time-instant t', when e.g. the shock just hits the gage with the center angle η_0, must be composed by all the pressure-time curves at time instants earlier than t'. The appropriate procedure yields a pressure function $P(\eta)$. The x- and y-components of the force on the body, i.e. drag and lift are then given by

$$(1) \qquad K_x(\eta_o) = r \cdot l \cdot \int_o^{\eta_o} P(\eta) \cdot \cos\eta \cdot d\eta$$

$$(2) \qquad K_y(\eta_o) = r \cdot l \cdot \int_o^{\eta_o} P(\eta) \cdot \sin\eta \cdot d\eta$$

from which the unsteady drag coefficients result in the form of

$$(3) \qquad C_d(t) = \frac{K_x(\eta_o)}{0.5 \cdot \rho \cdot u^2 \cdot A} \; ; \qquad A = r \cdot l$$

(r, l: radius, length of the cylinder, ρ: density, u: velocity behind the incident shock).

In Fig. 7 the $C_d(t)$ curves obtained by the procedure described above are shown. They show a maximum lying near the zenith of the cylinder. The evaluation procedure was

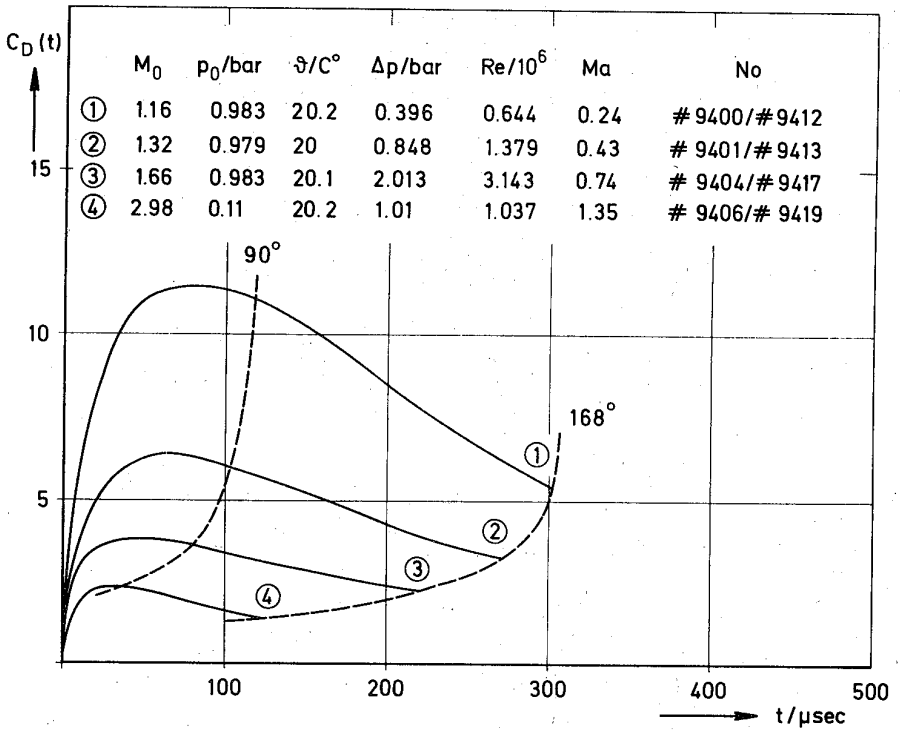

	M_0	p_0/bar	ϑ/C°	Δp/bar	Re/10^6	Ma	No
①	1.16	0.983	20.2	0.396	0.644	0.24	#9400/#9412
②	1.32	0.979	20	0.848	1.379	0.43	#9401/#9413
③	1.66	0.983	20.1	2.013	3.143	0.74	#9404/#9417
④	2.98	0.11	20.2	1.01	1.037	1.35	#9406/#9419

Fig. 7 *Time-dependent drag coefficients $C_d(t)$ during the loading of a cylinder with diameter 0.1 m by different strong incident shocks.*

stopped before the body was totally engulfed by the travelling shocks. It nevertheless shows how one has to proceed in principle. It also gets understandable that the procedure can essentially be approved if reliable code calculations can be performed. Fig. 8 shows first calculations of the shock reflection process at a cylinder with the help of SHARC. The comparison of the result with the visualization encourages to persue this way.

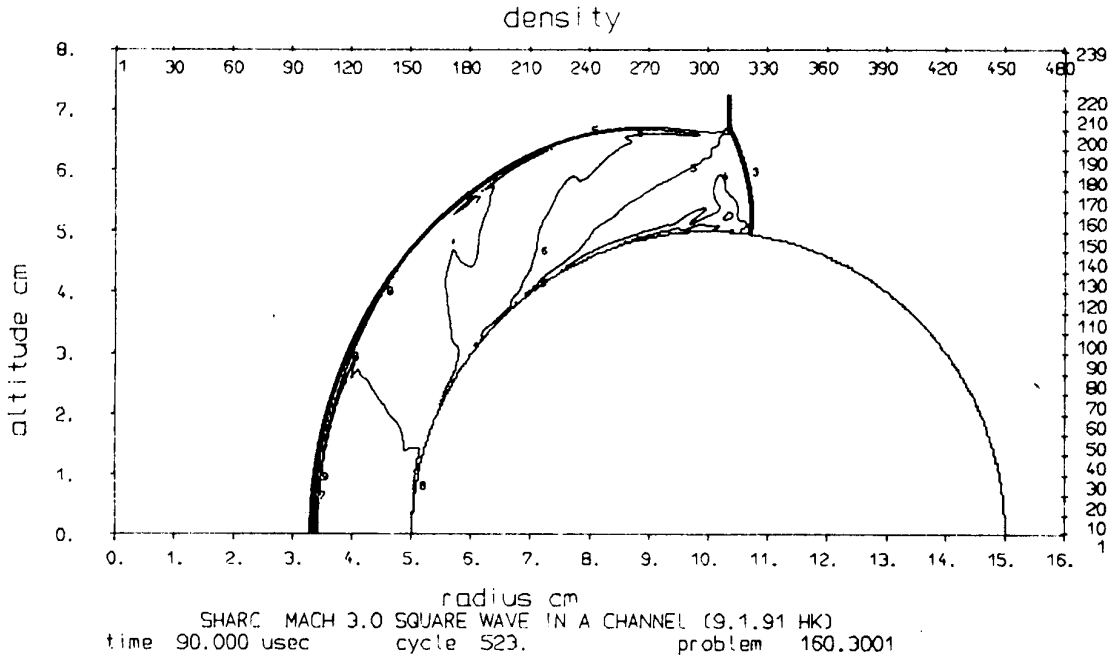

Fig. 8 *SHARC-Simulation of the loading of a cylinder by a shock with M_O = 2.12.*

3) Conclusions

We demonstrated that numerical simulation of the shock wave loading applying an appropriate code evidently enables us to determine loading functions in a relatively easy way avoiding high expenditure for experimental work. However, it is also apparent that further work in validating the code remains to be done. This can be achieved by comparing the numerical results to measured data ensuring in this way that the code is a reliable tool for relevant tasks.

Literature:

[1] T.K. Wheless, Nastran Analysis Comparison to Shock Tube Tests, Wright-Patterson Air Force Base, Ohio 45433, 1984

[2] J. von Neumann, Coll. Works, Vol. 6, Pergamon Press, 1966

[3] D.M. Jones, P.M.E. Martin, and C.K Thornhill, Proc. Roy. Soc. London, A209,238,1951

ENHANCED BLAST MUNITION EFFECTS PROGRAM

ABSTRACT

Enhanced Blast Munitions (EBM) has taken on world wide interest. Currently the Office of the Undersecretary of Defense for Research & Engineering, Office of Munitions, is sponsoring a program funded by the Balance Technology Initiative program to conduct research on new energetic materials and their effect on targets. Research in the development of new energetic and safe EBM fuels, solids, and slurries are being conducted by Sandia National Laboratories and by the Naval Weapons Center. The Weapons Laboratory is characterizing the blast and associated environments generated by the new energetic materials under development. Questions which need to be addressed are what are the airblast waveforms generated from these new materials, what are the effects of cloud formation around structures, and what is the response of an air base structure to these environments? The Weapons Laboratory has constructed an EBM test bed at Kirtland AFB, NM, to address some of these EBM concerns.

Preliminary investigations have revealed the Enhanced Blast Munitions are capable of generating devastating blast over extended ranges. The considerable lethality imposed by these weapons places Air Force assets in serious jeopardy. There is an urgent need to better understand enhanced blast explosives and their effects on protective structures in an effort to response to (defeat) this potential threat.

The Weapons Laboratory conducted a series of tests during FY89 to characterize the airblast environment generated by propylene oxide. Propylene oxide is the baseline fuel which the new fuels under development are being compared to in terms of energies and airblast environments. Sixty-four permanent in-place instrumentation channels were fielded to measure the airblast environment produced by propylene oxide. Two large scale tests were performed in this series. A single 1000 kg canister of propylene oxide was detonated and airblast environment recorded in each test. Add-on targets such as a tank, radar dish, and radar van were placed near the cloud edge to visually see the effects from an EBM.

EBM experiments against US Army Ballistic Research Laboratory M-60 tanks has been completed. Two M-60 tanks were exposed to an EBM environment inside the cloud and on the cloud edge to obtain data on the survivability of these systems to an EBM environments. Propylene oxide was the fuels used in the experiments. A total of two experiments were conducted on the M-60 tanks.

Analytical models were developed using existing hydrodynamic codes to predict the blast environment generated by an EBM. In the past, the only model that existed was an empirical model which was based on different fuels, size of charges, and detonator locations. This model was not adequate for detailed analysis purposes such as determining the response of air base systems to EBM effects.

In addition to the M-60 tank experiments, the FY90 Weapons Laboratory EBM planning are (1) possible EBM experiments on the Army's M-1 tanks, (2) characterize the effects of new nitrate fuels for the Naval Weapons Center, and (3) characterize new fuels for Sandia National Laboratories which are more energetic, much safer to handle, and not as toxic as propylene oxide. The program on the Army's tank experiments are joint efforts between the Weapons Laboratory and the US Army Ballistic Research Laboratory and sponsored by the Joint Live Fire Program. In addition, the Weapons Laboratory has submitted proposals to other agencies to address the loads and effects of air base systems.

Stan Lokaj, Phillips Laboratory (AFSC), Kirtland AFB, NM, USA

The Design and Evaluation of Shaped Charges Using Codes Developed for Micro-Computers

Mr. Mark E. Majerus
Dr. Ronald E. Brown

California Research & Technology, Inc.
A Subsidiary of The Titan Corporation
5117 Johnson Dr.
Pleasanton, CA 94588

1. INTRODUCTION

Hydrocodes and analytical codes are used extensively in the design of shaped charges and for estimating penetration performance. Hydrocodes typically use a finite element or a finite difference scheme to solve the differential equations of the physics and engineering models. These programs generally contain tens of thousands of lines of programming and require large amounts of computer memory. The high-end microcomputers and work stations are just reaching the computational capacity required to execute these codes in a timely manner. As a result, there are only a few hydrocodes such as AUTODYN, ZEUS, and DYNA2D, that are available for these computers (References 1, 2).

The setup and execution of these hydrocodes is still a time consuming process that does not lend itself well to the design and evaluation of shaped charges. Rather, analytical models have been established which model the collapse process of a shaped charge liner and the hydrodynamic erosion process of the jet. In the past, these models have been run on main frame computers. BRIGS and BASC are two common analytical models (References 3, 4). This paper will discuss two interactive and user friendly models developed at CRT, and their adaptation to run on a microcomputer system.

2. MICROCOMPUTER SELECTION

In the United States, there are generally two families of microcomputers widely used in the scientific community: IBM PCs and compatibles and the Apple Macintosh series. Each seems to have its loyal following. One should not merely download a mainframe code to a microcomputer, compile it and run it in the same manner as one did on the mainframe. To do so would be ignoring some of the advantages offered by microcomputers. High resolution graphics and user friendly interfaces can make most codes simpler to use and results easier to interpret . All of the codes to be discussed herein are setup for the Macintosh II computer. This system is the author's personal preference based on the ease of programming a user friendly interface. Although a 486 PC may run a problem faster, the complexity of generating a simple user interface has not been fully examined for this particular application. Since our codes run rather quickly (5 to 15 seconds) the higher computational speed of a 486 PC system does not offer a clear advantage.

To design and evaluate a shaped charge two types of analytical models are required. A jetting model is used to determine the jet characteristics based on the explosive, liner and confinement configurations and basic material properties. A penetration model uses the calculated jet and estimates its performance against a specific target. The general approach for the adaptation of each of these codes is discussed in the remainder of this paper.

3. SHAPED CHARGE JETTING CODE

The jetting code developed at CRT is CSCJ-M. In this code there are two phases of calculations. In the first phase, the problem geometry is determined. An input file defines the liner material, explosive, initiation site and the confinement geometry. These characteristics usually are fixed during a design effort. To insure that all the designers use the same properties, as well as to save time from looking the values up, the material properties are stored in a library and are retrieved during the code execution. The key feature that is changed in a design effort is usually the liner contour. For most modern applications, simple cones do not produce the jets required to defeat advanced armor, therefore, complex geometries are used.

Defining a liner contour is rather tedious in most hydrocodes. The location of each node has to be calculated and placed in a specific format in a input deck. To simplify this process, CSCJ-M offers the user two choices: geometric equation generation or interactive screen design. In the geometric equation generation, the user in a separate input file defines the explosive/liner interface contour by a series of equations. A contour can be described as a hyperbola, circle (or arc), parabola or a host of other geometrical shapes, see Figure 1. Furthermore, the contour can be described as a combinations of these forms; however, one must be cautious and assure that each intersection has a smooth transition of the liner angle, alpha (see Figure 2) so as to avoid sharp transition in the jet should this be undesirable.

In the interactive screen design approach, the user draws on the computer screen the liner contour to be examined. With the use of a mouse, the user may select any number of points within the confinement dimensions. A bezier curve is then fitted to these points. By moving any one of these points or adding points, the curve can be modified as desired.

The liner thickness profile may also be generated by either method. At this point, there is enough information to describe the liner. The liner is broken into a discrete number of mass points, in most cases approximately 50. The first phase of the code, generates these mass points and writes a file that describes the liner contour and thickness contour. This file may be directly imported into AutoCAD for generating fabrication drawings.

The second phase of the program takes the described geometry and material properties and computes the liner collapse and resulting jet. The collapse of each of these points is determined by a modified Pugh-Eichelberger-Rockstoker jetting theory (References 5, 6). The subroutines in this code permit the calculation of the time-dependent pressure that is exerted on a liner by the explosive detonation, the acceleration of the liner and the geometry at collapse. Liner material strength is included in the calculation. Each mass point collapses at a unique velocity and orientation. The time and location of impact on the central axis is determined as well as the mass partition into the jet and the slug. This phase of the code is relatively unchanged from the mainframe analytical model.

The microcomputer graphics become handy once again. The key jetting characteristics can be immediately viewed as the calculation is finished. As shown in Figure 3, the calculated liner contour, jet mass, jet velocity, and the flow velocity (critical in determining jet stability) are plotted to the screen during the program's execution. Another useful feature is the ability to overlay previous designs results at the same time in different colors. This allows one to determine the effect that various changes in the liner, initiation, or confinement have on liner collapse and jet formation (including resultant jet characteristics). These comparisons allow one to expediently determine the key parameters to modify and improve.

There are drawbacks to using an analytical model. It may not be possible to evaluate multi-material liners, non-uniform confinement, asymmetrical designs and complex detonation wave fronts. In spite of these weaknesses, this type of code is useful for most design efforts and is fairly accurate. A pre-test jetting calculation of a complex liner geometry in a boat-tailed confinement is compared to a reduced flash x-radiography result in Figure 4.

Two other features are possible with a code and setup similar to the one at CRT. First, since the collapse location, time, velocity and mass are known for each jet point (based on the liner mass points) it is possible to generate "computer flash x-radiographs" of the jet at various times. The MERGE subroutine, which produces these computer jet images, is useful in determining if and when the jet may compress or "ball up" or if there are regions of large velocity gradients and little mass that will cause the jet to neck-down and particulate early. The computed jets can also be visually compared to a experimental radiograph or an image-enhanced radiograph. CRT has developed a semi-automated PC-based system for radiograph image enhancement and data analysis (Reference 7).

4. SHAPED CHARGE JET PENETRATION CODE

Developed at CRT, MAJIC, a Multi-Dimensional Armor and Jet Interaction Code, is used to study the mechanisms and performance of shaped charge jets. The code is rather unique in the fact that it can use either calculated jets as from CSCJ-M or experimentally determined jets. The jetting properties recorded with flash x-radiography and reduced on our PC image analysis system allow full three-dimensional characterization of the jet. This characterization of each jet particle includes pitch, yaw, tumbling rates, dispersion rates, individual particle breakup time, as well as the particle mass and axial velocity. The jet description for the penetration calculation may also use a combination of experimental and calculated jet properties.

The code is setup in a modular format where new penetration models can easily be added as a new subroutine. Current routines include models for hydro-dynamic erosion, penetrator and armor strength, compression, target motion (including reactive armor and transverse motion), hole growth and attack obliquity.

Many of the routines use look-up tables. For instance, with compressive targets either experimental data or hydrocode runs can be used to determine the net effect on the penetration of a single jet particle. In this case, there is a strong dependence on impact velocity. We, therefore, construct a table that relates this effect on penetration. This

allows us to quickly estimate the effect during a design iteration without getting mired with the physics of the compression process.

A similar approach is taken with the reactive armor model. Again, the user has a choice of experimental data, a Gurney velocity approach, or hydrocode results to use in a lookup table. Obviously, experimental velocity data is preferred; however, it is usually not available or not enough data points are known. One could use a Gurney velocity type of approach; however, the effects of acceleration are ignored and these effects are usually important during the early jet/target interaction process. Using a hydrocode, one can determine the plate response to the explosive sandwich detonation. The acceleration, velocity, and even bowing can be modeled in a lookup table to provide hydrocode level of resolution in an analytical penetration model.

The code itself operates on one jet particle at a time. The first particle is advanced to the target and the appropriate penetration routines are called. The penetration depth is recorded as well as the hole diameters (two-dimensional hole profile). Specific active target response can be invoked whether it be elastic hole growth, flyer plate acceleration, or transverse motion, during this time and until the next particle reaches hole bottom. Between the impact times, the whole jet is moved forward. The individual particle velocities are used to move the particle axially and the dispersion and tumbling rates are applied to complete the three-dimensional characterization of the jet. Before the next particle penetrates, each remaining jet particle is examined to see if it has interacted with any of the target (i.e., reactive armor, transverse motion or hole collapse). If an interaction has occurred, the particle and target are updated according to the appropriate model.

During the penetration process, some of the jet particles run into particles preceding them. This phenomena is evident as bulbous jet tips on flash x-radiographs. MAJIC treats this with a momentum averaging approach to consolidate the mass.

The penetration process is a loop through the above described steps until the jet is expended. Due to the high level of modeling of the jet and target response, we have been able to eliminate the usual "fudge factor" of a minimum penetration velocity, Umin (Reference 8). We have demonstrated this approach to be accurate within 2% for a highly complex multiple material target and multiple material jet.

Again, the use of high resolution microcomputer graphics is extremely valuable in the penetration code. Since the three-dimensional nature of the jet and the target is known, it can be displayed during the calculations. We obtain a series of simulated flash x-radiographs of the penetration process which highlights the key penetration characteristics, see Figure 5. These pictures provide understanding to which portions of the jet are effective and where the jet should be improved.

5. SUMMARY

Although these analytical approaches do not completely model the physics of the shaped charge jet formation and penetration process, they can offer insight to the mechanisms that are key to design improvements. Considering the price, speed and availability of relatively fast and easy to use microcomputers, this insight is a too good to pass up. A useful design approach is to perform the design interations with these models and a final verification with a hydrocode. Having the liner design code, the penetration code, the image analysis code and the CAD/CAM code all on the same system provides the designer a highly effective design tool.

6. REFERENCES

1 AUTODYN, Copyright Century Dynamics Inc., 903 Paramount Rd, Oakland, CA 94610

2 Murphy, M., "Description of a PC-based Coupled 'PER' Teory/Finite Element Method for Calculating Shaped Charge Jet Characteristics," 12th International Symposium on Ballistics, San Antonio, TX, October 30 - November 1, 1990.

3 BRIGS, Copyright Brigs Co., 2668 Petersborough St, Herdon, VA 22071

4 Harrison, J.T., "Improved Analytical Shaped Charge Code: BASC," BRL Techincal Report No. ARBRL-TR-02300, March 1981.

5 Pugh, E., Eichelberger, R. and Rostoker, N., "Theory of Jet Formation by Charges with Lined Conical Cavities," *Journal of Applied Physics*, 23 (5) 1952.

6 Chou, P.C., Carleone, J., Hirsch, E., Flis, W.J. and Ciccarelli, R. D., "Improved Formulas for Velocity, Acceleration, and Projection Angle of Explosively Driven Liners", *Proceedings*, 6th International Symposium on Ballistics, Orlando, FL, October 27-29 1981.

7 Lystad, H.A., Majerus, M.E., Bakowsky, T. and Brown, R.E., "Automated Data Reduction from Flash-Xradiographs of Jets from Lined Shaped Charges," 1989 Flash Radiograph Topical Symposium, Welches, OR, 14-18 August, 1989.

8 DiPersio, R., Simon, J. and Merendino, A. B., "Penetration of Shaped Charge Jets into Metallic Targets," BRL-R-1296, September 1965.

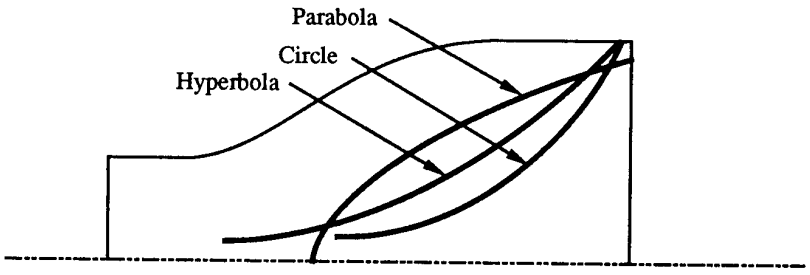

Figure 1. Examples of geometric shapes as liner contours.

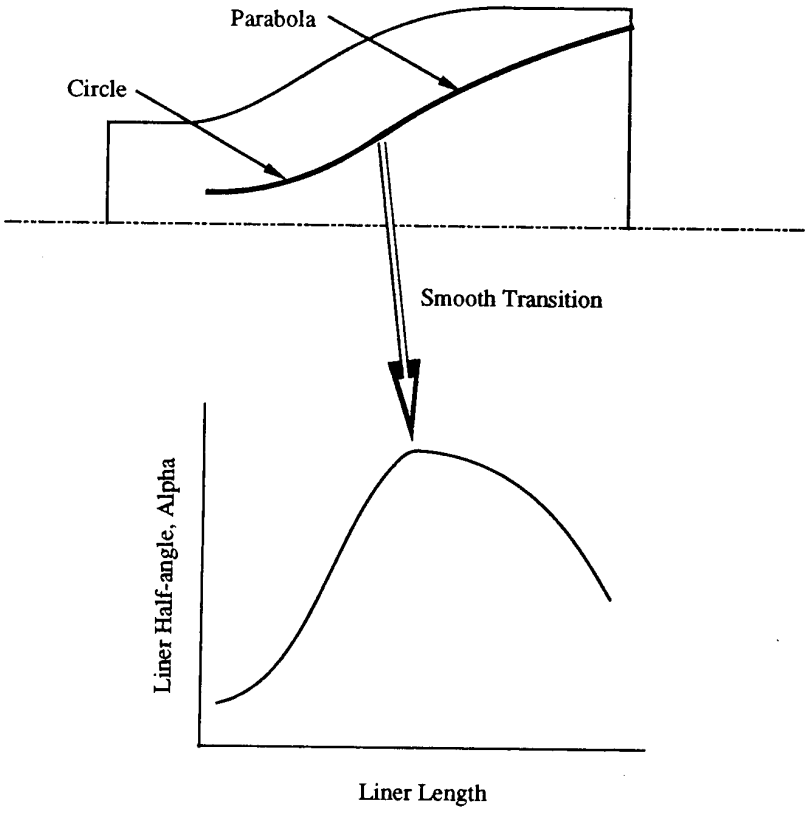

Figure 2. A combination of geometric shapes to generate a complex liner form.

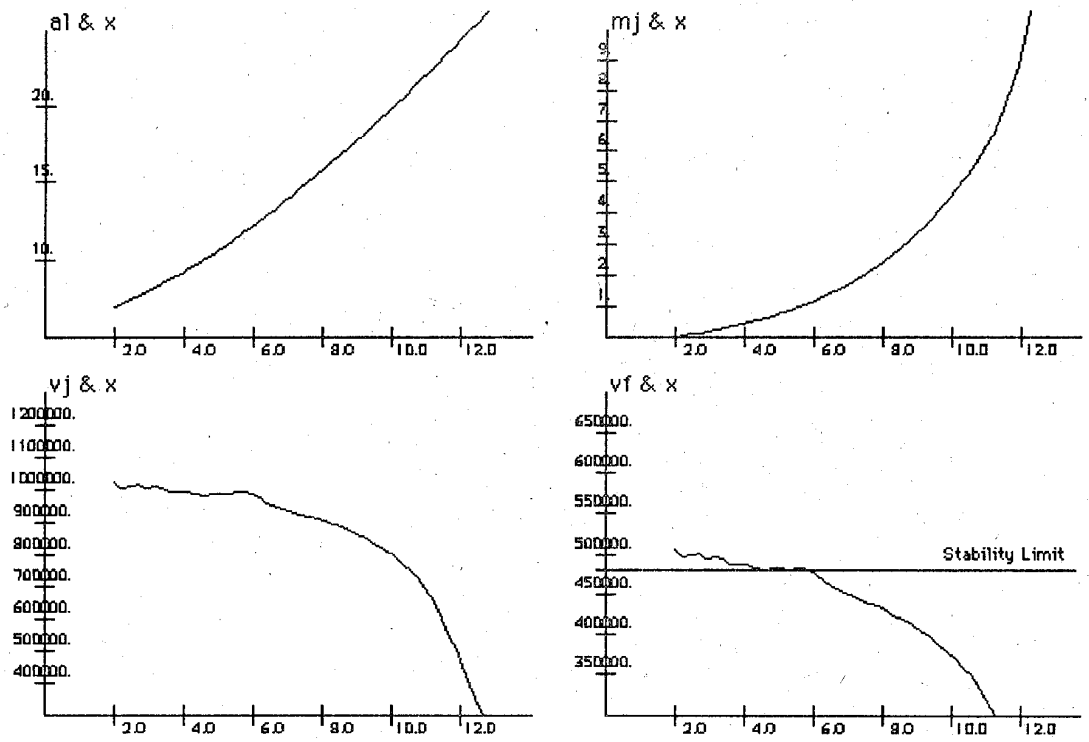

Figure 3. Typical computer screen showing key jetting characteristics of current design.

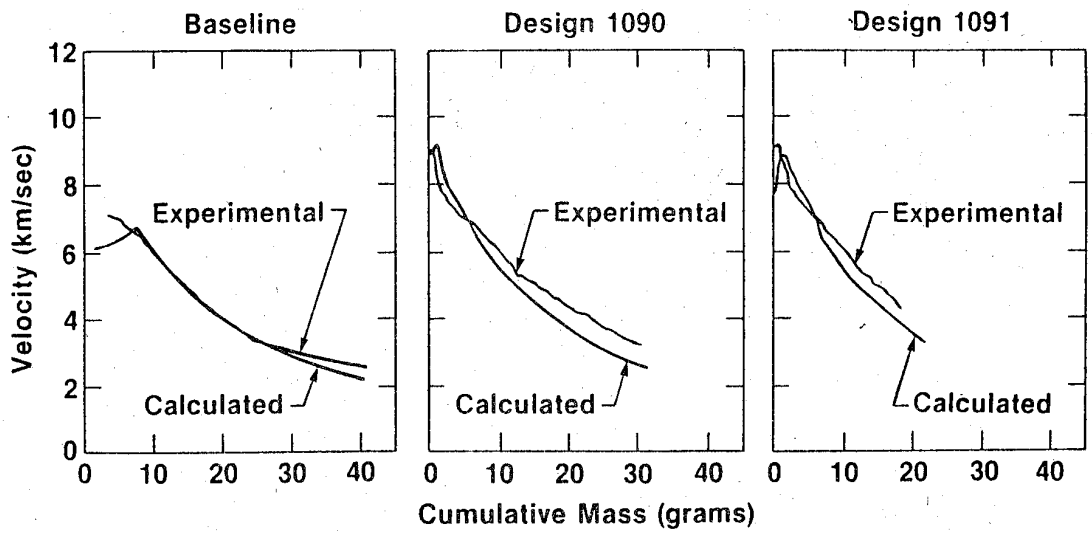

Figure 4. Comparison between prediction and experiment.

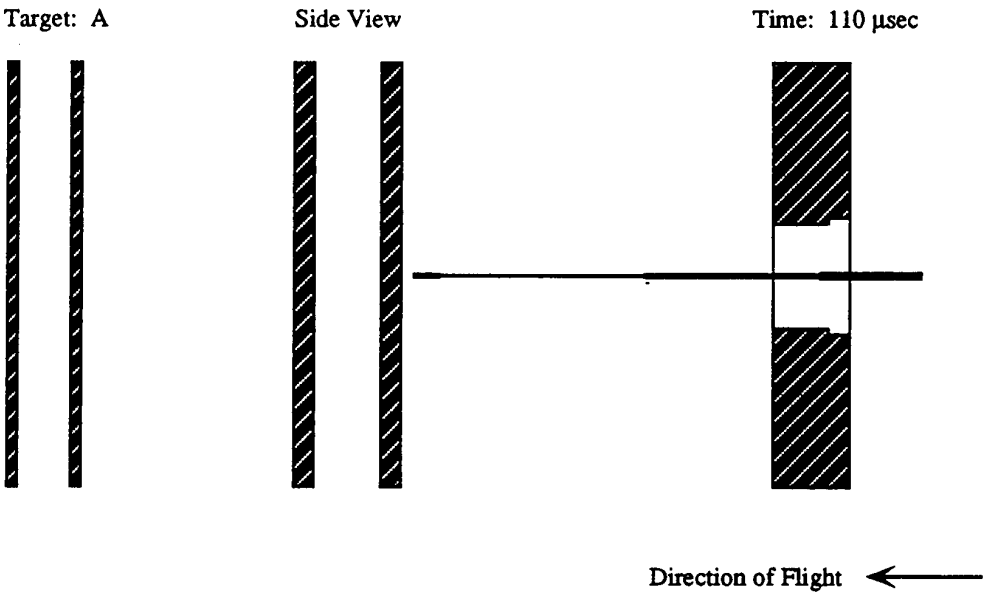

Figure 5a. Computer screen image from MAJIC which shows the jet penetrating the first plate and almost reaching the second plate at 110 μsec.

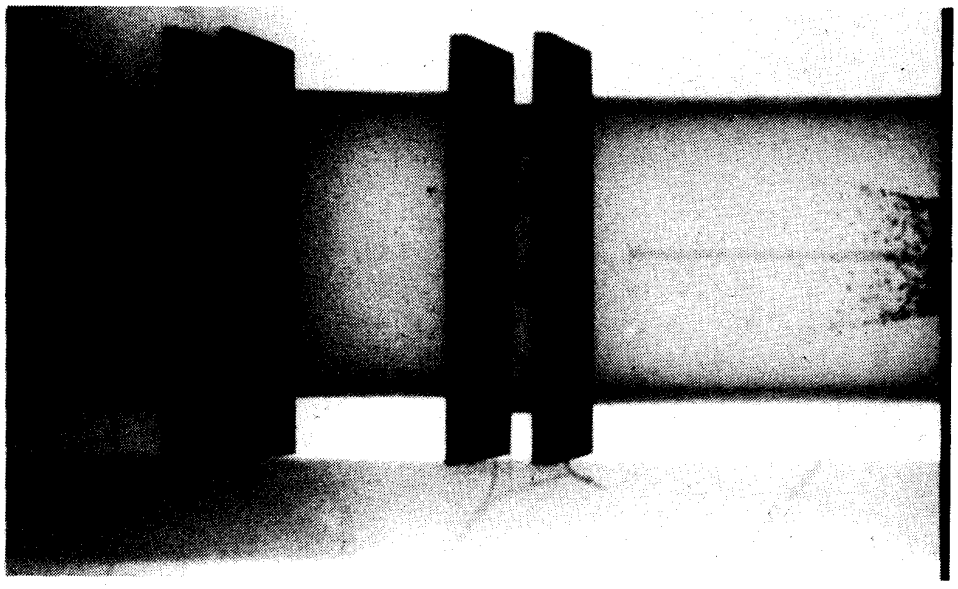

Figure 5b. Flash radiograph image also shows the jet penetrating the first plate and almost reaching the second plate at 110 μsec. The edge of the first place is just to the right of the film as evident by the spall cone. The plates appear as trapezoidal prisms due to the x-ray head and film alignment.

Munitionssicherheit

Munition Safety

SCALE MODEL ANALYSIS OF AN AMMUNITION PLANT

R. Bourgois, G. Naeyaert, B. Reymen, P. Joos

Royal Military School - Department of Civil Engineering
Brussels - Belgium

1. INTRODUCTION

The construction of ammunition plants becomes more and more critical in small countries. Respect of the commonly used safety distances is not always possible, requiring special protection measures in certain cases.

The classic solution was impossible in the involved case where an old plant was to be replaced by a modern one in a factory near a small village and so an alternative solution was suggested. This alternative solution consists of a main building with a series of independent cells with lateral blow-out walls, built between two earthen berms and covered by a large concrete roof, intended to resist the effects of blast and to protect the surroundings from fragments.

This paper presents first the general problems of ammunition plants in small countries and exposes the possible solutions.

Afterwards the scale model tests are discussed. The scale model is realized in reinforced microconcrete. Different transducers are installed on the model. The scale model test gives a lot of interesting information, showing the feasibility of the proposed solution and suggesting some structural modifications.

2. GENERAL PROBLEMS

In the early part of our century, the implantation of ammunition or explosives factories was not a serious problem. The population was rather limited, concentrated in villages or cities and the industry was localized in the vicinity of cities, waterways and railways.

The ammunition arsenal of the Belgian Army has been housed in the former fort of *Zwijndrecht* of the old fortification ring of Antwerp since 1919. Through the years the inhabited part of the village has been considerably extended.

In the scope of the modernization of the arsenal a new pyrotechnical workshop is planned requiring, in accordance with **NATO Standards**, a minimum safety distance of 270 m to neighbouring buildings. **UK Standards** permit shorter distances provided that screening traverses are used.

Another, more expensive, solution consists in the construction of the walls of the workshop with suppressive shields, minimizing the safety distances.

Using the *UK idea*, the Military Construction Service (JSI-KGC) studied a series of alternative buildings, of which one was selected.

3. PROPOSED SOLUTION

The selected solution consists principally of a building divided into cells **(fig.1)**, originally designed for 50 kg of high explosives or 200 kg of propellants. The outer walls are manufactured with frangible panels (blow-out walls). The different cells are separated by protective walls.

The projection of fragments is hindered and the blast is deflected by two earthen berms and a thick reinforced concrete roof plate, supported by columns.

In the final design an explosive charge of **80 kg of TNT** a cell was used.

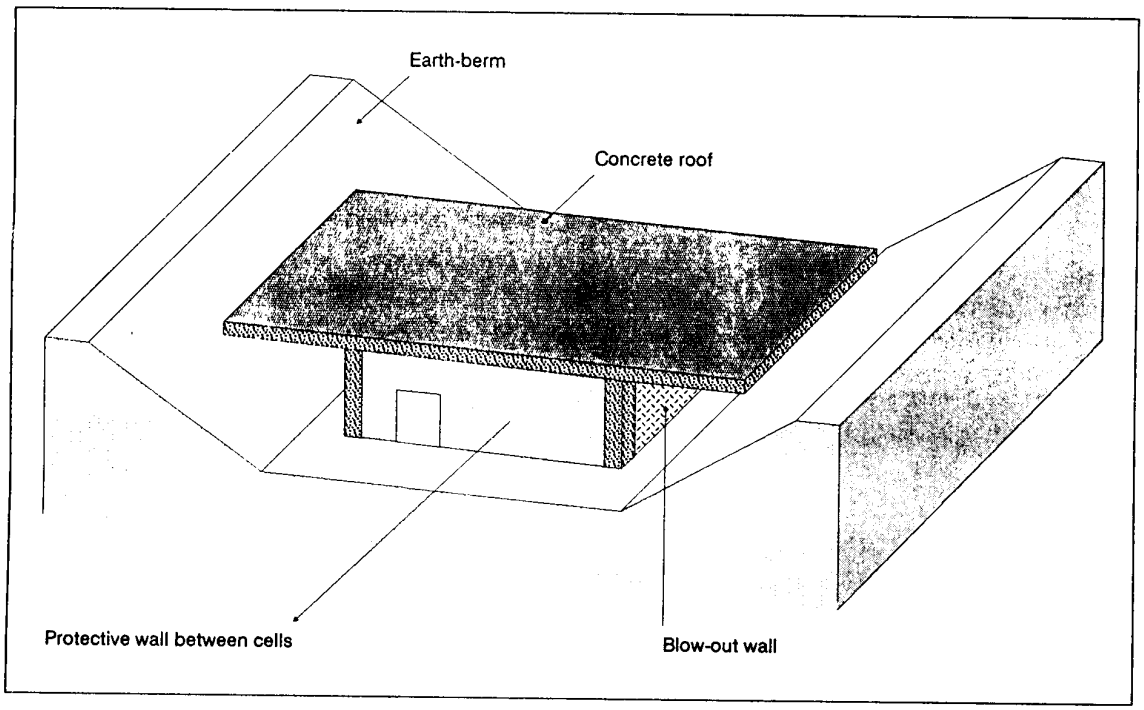

Figure 1: View of the implantation of a single cell

4. EXPERIMENTAL PROGRAMME

a. General considerations

On demand of the **Military Construction Service**, a scale model test programme was planned, with the following two objectives:

- verification of the general draft;
- control of the roof-slab.

In a preliminary calculation of the construction, the cell was considered as a fully vented cubicle ($A/V^{2/3} = 1{,}06 > 0{,}6$ [1]), simplifying the calculation of the pressures on the roof and the walls, the gas pressure pulse being small in this case. It is also accepted that the charge is a single uncased one, exploding in the centre of the cell.

b. Scale model

The preliminary calculations give a 50 cm total thickness of the roof slab with two layers of orthogonal reinforcement, consisting of 5⌀25 mm bars/m in both directions. The compressive strength of the concrete is $R'_{wk} = 20\ N/mm^2$ and the steel is a BE 500-quality ($R_{ak} = 490\ N/mm^2$).

The value 1/15 of the scale factor **(fig.2)** is based on considerations like quantity of explosive, dimensions of the model, composition of the microconcrete and manufacturing of the reinforcement. The columns supporting the roof are realized in steel instead of concrete. The protective walls between the cells are not studied.

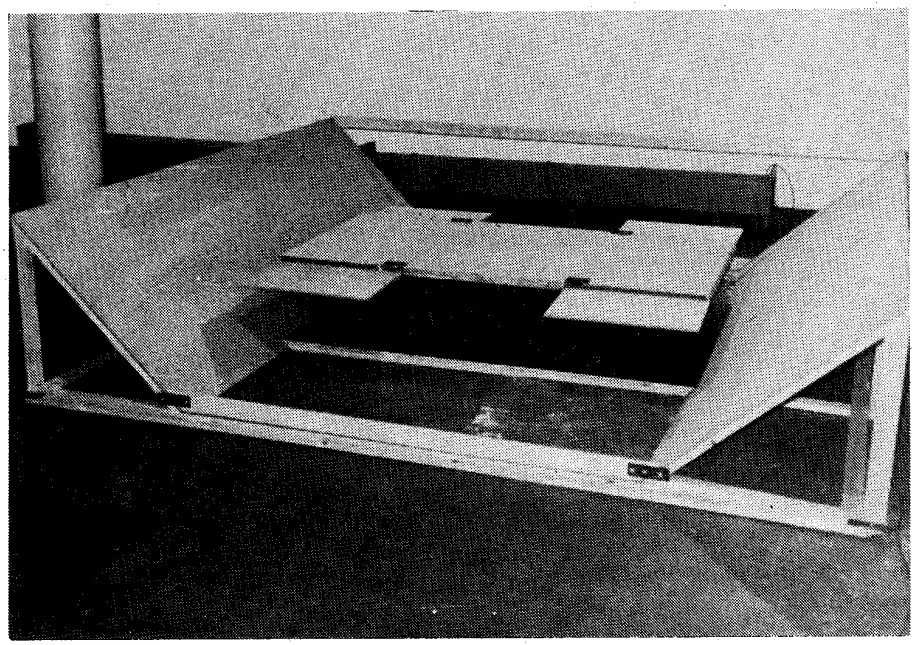

Figure 2: Scale model of an independant cell

The earthen berms are made with plywood, modifying only slightly the reflected pressures. The roof at the outside of the cells has been broadened to limit the spilling of the outcoming blast.

c. Microconcrete and reinforcement

The composition of the microconcrete is based on an article of *M. Kavyrchine* [2], with some modifications for practical and logistic reasons. It has been studied previously in our laboratory [3]. The actual mix is given in **fig.3**; it is a rather stiff concrete, giving some problems for scale models with a high density of reinforcement. This was avoided in our application by the use of a shaking table.

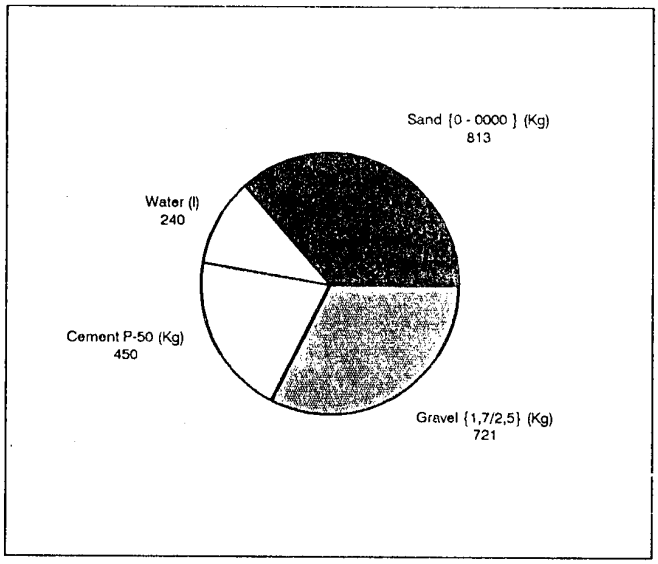

Figure 3: Composition for 1 m^3 micro-concrete

The reinforcement steel wire ⌀1,7 mm, indented to produce moderate surface deformations in order to obtain a better adhesion, was annealed and afterwards pulled to straighten it, finally giving the mechanical properties of steel BE 500.

The manufacturing of the reinforcement is very time-consuming, but it has to be done very carefully in order to simulate correctly the ultimate behaviour of the slab.

d. Instrumentation

The instumentation is rather limited (**fig.4**) and consists of two pressure transducers in the earthen berms, a blast pencil in an open outer-wall and some strain gages on the upper side of the slab.

The measurements are done with digitizing oscilloscopes and treated afterwards with a PC. This PC also controls the automatic execution of the test.

e. Explosive

Cylindrical charges are manufactured with Compound B and an electrical detonator MAT303 is inserted centrally.

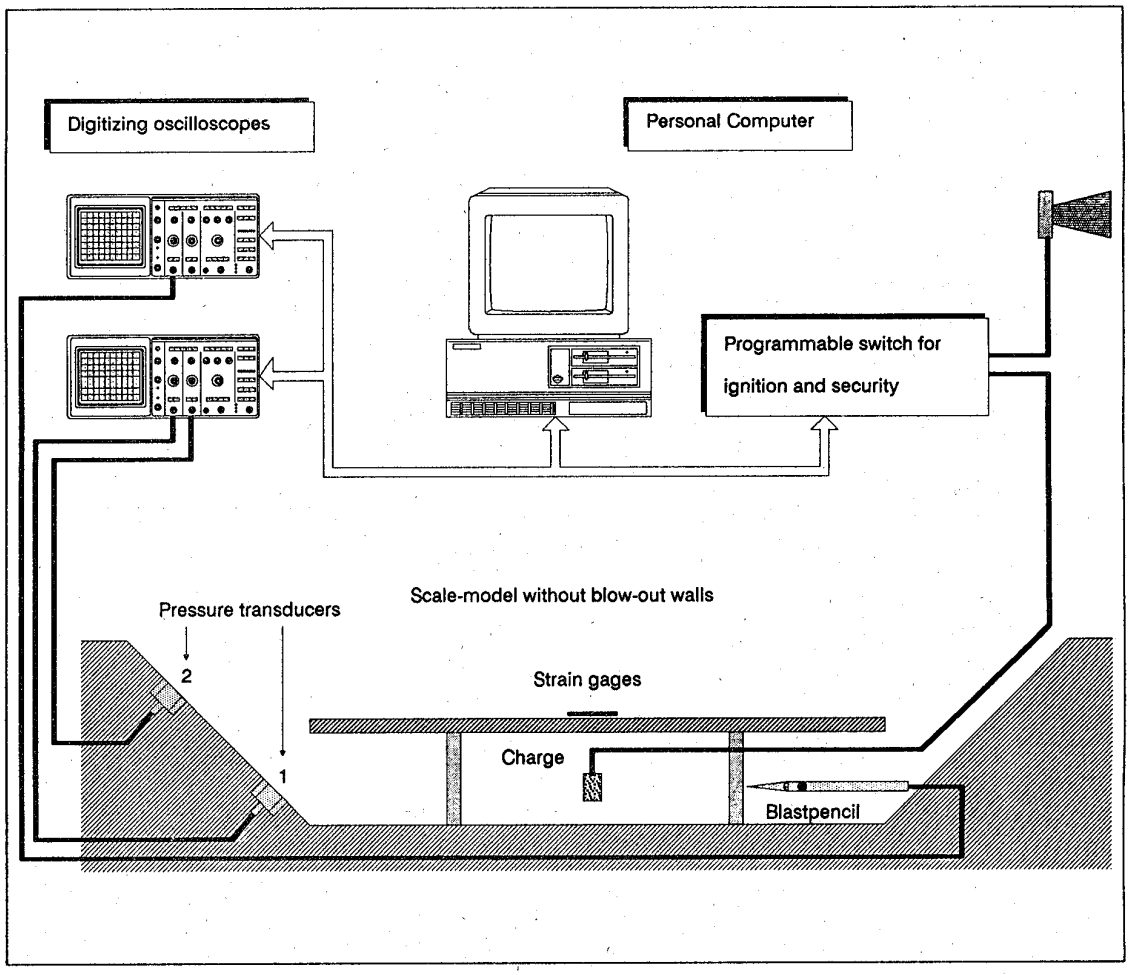

Figure 4: Measurement equipment

5. TEST RESULTS

a. General description

21 tests have been done with small charges (4,65 g simulating 21 kg TNT), in order to avoid early damage of the slab and to have in this way the possibility to perform several configurations of the transducers.

The last two tests (Nr.22 and 23) with charges of 11,1 and 17,7 g respectively (corresponding to 50 and 80 kg TNT) were intended to check the slab in extreme conditions.

b. Pressure measurements

The pressure transducer Nr.1 gives very reproductive results (**fig.5**; errors: 20% on pressure, 10% on time), with a good correlation to the calculated peak pressures. The successive peaks can be related to successive reflexions.

Pressure transducer Nr.2 gives considerably lower results than pressure transducer Nr.1, demonstrating the benefit of the earthen berms.

The results of the blast pencil are not very good in comparison to the theoretical values. This is probably due to the overall dimensions of the pencil with regard to the model.

c. Strain gage measurements

Strain gage measurements were only performed during the first tests, due to cracks beneath the gages. These cracks had been expected and were confirmed by the measurements. These measurements are not particularly useful with this type of experiments.

6. SUMMARY

The performed test programme confirms the feasibility of dynamic scale testing of concrete structures, but the procedure is time-consuming and costly.

The manufacturing of microconcrete is not a real problem.

The tests confirm the theoretical design of the plant and the measurements themselves guarantee the correct execution of the tests.

ACKNOWLEDGEMENT

The authors acknowledge their sincere gratitude to *Mr Verbruggen* of the Laboratory for Strength of Materials of the **Royal Military Academy**, Brussels for the realization of the scale model and to several students for their assistance during the research programme [3], [4].

BIBLIOGRAPHIE

[1] **"Blast environment from fully and partially vented explosions in cubicles"**, *W.A. Kegnan, J.E. Tancreto,* Conference Concrete for hazard Protection, Edinburgh, 1987

[2] **"Etudes structurelles en microbéton"**, *M. Kavyrchine,* Annales de l'Institut Technique du Bâtiment et des Travaux Publics, Nr.384, pp 70-92, 1980

[3] **"Experimenteel onderzoek van explosie-effekten op schaalmodellen"**, *J. de Spiegeleer, F. Goetynck,* Internal Report KMS, 1988

[4] **"Drukmetingen bij explosies op schaalmodellen van gebouwen"**, P. Joos, Internal Report KMS, 1989

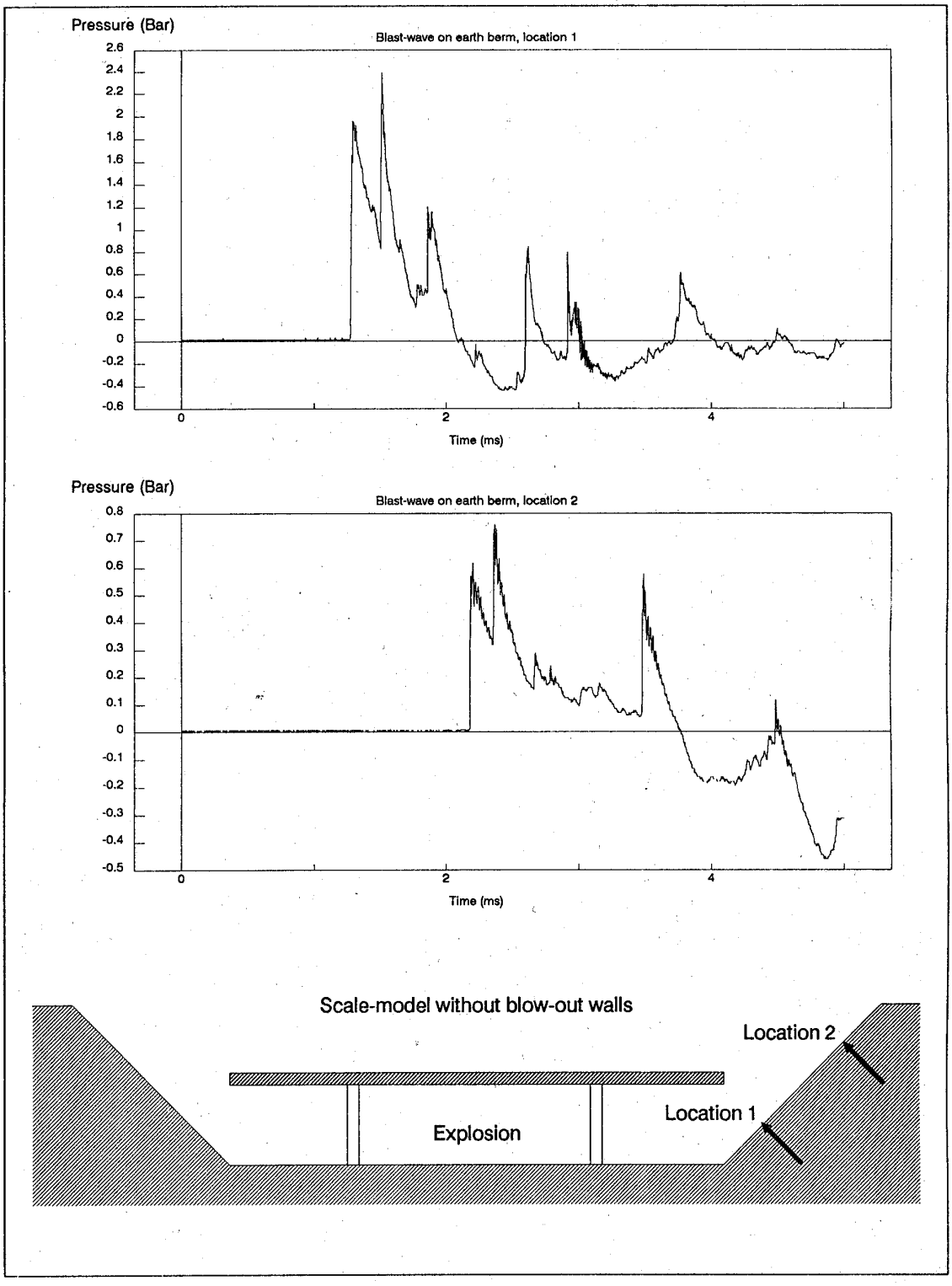

Figure 5: Blast at two different locations during a test

Splittermassenverteilung der Trümmer von gesprengten Flugzeugsheltern

Manfred Held

Messerschmitt-Bölkow-Blohm GmbH
8898 Schrobenhausen - Deutschland

Zusammenfassung

Mit der aufgezeigten Formel kann bei Optimierung der Ausgangsmasse die Massenverteilung der Trümmer der mit einer Innendetonation gesprengten Flugzeugshelter sehr gut beschrieben werden.

Einleitung

Zumindest in der offenen Literatur findet man praktisch keine Formeln für die Beschreibung der Massenverteilung von Trümmern von Gebäuden, wie sie z.B. bei der Innendetonation von mehreren Bomben in einem Flugzeug-Unterstand auftreten.

Dies liegt sicherlich in erster Linie daran, daß nur sehr wenig qualifizierte Versuche mit einer umfangreichen Auswertung der Massenverteilungen von derartigen Trümmern vorliegen. Der Autor bekam sehr gewissenhaft ausgewertete Versuchsergebnisse der ausgezeichnet geplanten Modellsprengungen von Flugzeugunterständen <1> um nachzuprüfen, ob die Massenverteilung dieser Trümmer auch mit der von ihm aufgestellten Formel beschrieben werden können.

Im folgenden wird aufgezeigt, daß mittels der Formel nach HELD, mit der sowohl die Splittermassenverteilungen der sogenannten natürlichen Splitter von Sprenggeschossen als auch die von Sekundärsplittern sehr gut beschrieben werden können (<2> bis <5>), auch die experimentell erfaßten Massenverteilungen von Trümmern von Sprengungen von Flugzeugunterständen gut dargestellt werden können.

Verteilungsfunktionen

Die Weibull-Verteilung <6> findet in der Technik für viele Probleme eine vielfältige Anwendung. Die Verteilungsdichte der 3-parametrischen Weibull-Verteilung lautet:

$$F(x) = 1 - e^{-\left(\frac{x}{\delta}\right)^{\lambda}} \quad , x > 0 \qquad (1)$$

$N(m)$ kumulierte Splitteranzahl, d.h. Anzahl aller Splitter, deren Massen größer oder gleich einer vorgegebenen Splittermasse m ist.

n kumulative Splitteranzahl, beginnend vom schwersten Splitter an.

M_x, λ_x, B sind Konstanten.

Während die Formel nach RRS keinen Bezug zur Splitteranzahl hat und die Formel nach MOTT eine bestimmte Splitteranzahl N_0 voraussetzt, ist dies bei der Formel nach HELD nicht notwendig. Es können noch beliebig viele feine Splitter, auch wenn diese nichts wesentliches mehr zu der Gesamtmasse M_0 beitragen, hinzugefügt werden.

Beschreibung der Massenverteilungen mit der HELD-Formel

Im folgenden soll das Auswerteverfahren von Massenverteilungen nach der HELD-Formel (<3> bis <5>) dargelegt werden, welche bei richtiger Anwendung in hervorragendem Maße die Massenverteilungen von natürlichen Splittern von allen untersuchten Sprenggeschossen, auch mit verschiedenen Sprengladungsfüllungen, wie von Sekundärsplittern, nach einer Zielplatte oder auch nach mehreren Schotten, sehr gut beschreibt. Die einfache Gleichung hierfür lautet:

$$M(n) = M_0 \left(1-e^{-Bn^{\lambda}}\right) \qquad (7)$$

Diese Gleichung ist schematisch in Fig. 1 wiedergegeben.

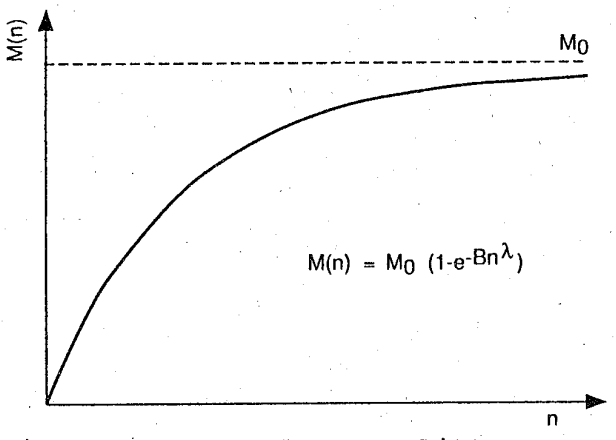

Fig. 1 Summe der Splittermassen, über der kumulativen Splitteranzahl n (vom größten Splitter angefangen).

Zur leichteren Bestimmung der Werte B und λ wird zweckmäßig die Gleichung (9) nochmals logarithmiert, so daß in einem logarithmischen Diagramm aus dem Durchstoßpunkt bei $n = 1$ bzw. $\log n = 0$ die Konstante $\log B$ auf der Ordinate direkt abgelesen und aus der Steigung der Geraden der Exponent λ bestimmt werden kann (Fig. 2).

Die Ermittlung der Konstanten B und λ der Gleichung (7) erfolgt am einfachsten dadurch, daß man den e-Term der Gleichung (7) separiert:

$$\frac{M_0 - M(n)}{M_0} = e^{-Bn^{\lambda}} \qquad (8)$$

und dann die Gleichung (8) mit dem natürlichen Logarithmus delogarithmiert.

mit den 3 Parametern

δ : Skalierungsparameter
λ : Formparameter
μ : Lageparameter

Die 3-parametrige Weibull-Verteilung (1) wird zu einer 2-parametrigen Verteilung vereinfacht, wenn der Lageparameter μ gleich 0 gesetzt wird, was gleichbedeutend ist mit der Transformation auf eine neue Variable $x - \mu$:

$$f(x) = \frac{\lambda(x-\mu)^{\lambda-1}}{\delta^{\lambda}} \cdot e^{-(\frac{x}{\delta})^{\lambda}}, \quad x > 0 \qquad (2)$$

Aus (2) ergibt sich die 2-parametrige Weibull-Verteilung durch Intergration:

$$f(x) = \frac{\lambda x^{\lambda-1}}{\delta^{\lambda}} \cdot e^{-(\frac{x}{\delta})^{\lambda}}, \quad x > 0 \qquad (3)$$

Die 2-parametrige Weibull-Verteilung (3) findet man in einigen Arbeiten über Splittermassenverteilungen auch unter der Bezeichnung ROSIN - RAMMLER - SPERRLING - Verteilung (RRS), die auf Anwendung der Beschreibung von Korngrößenverteilungen bei Mahlvorgängen zurückgeht. Die Verteilung der "Splittermassen" wird auch manchmal als RRS-Verteilung bezeichnet.

In Verbindung mit der Splitterbildung und der Splittermassenverteilung hat die Weibull-Verteilung (3) seit MOTT (siehe <6>) Eingang in die Splitterballistik gefunden. Häufig spricht man deshalb für diese spezielle Anwendung von der MOTT-Verteilung. Mit ihr wird üblicherweise die Verteilung der "Splitteranzahl" beschrieben.

Von Held <4> wurde aufgrund der Auswertung von Röntgenblitzaufnahmen und damit der Erfassung auch von kleineren und feineren Splittern ein experimenteller Ansatz für die Erfassung der Splittermassenverteilung als Funktion der Anzahl gewählt.

Im folgenden sind diese 3 Formeln zum Vergleich gegenübergestellt.

RRS : $$M(m) = M_0 \, e^{-(\frac{m}{m_R})^{\lambda_R}} \qquad (4)$$

MOTT: $$N(m) = N_0 \, e^{-(\frac{m}{m_M})^{\lambda_M}} \qquad (5)$$

HELD: $$M(n) = M_0 \, (1 - e^{-Bn^{\lambda_H}}) \qquad (6)$$

Die einzelnen Größen haben hierbei folgende Bedeutung:

M_0	Gesamtmasse der Splitter
$M^0(m)$	kumulierte Splittermasse, d.h. Summe der Massen aller Splitter, deren Masse größer oder gleich einer vorgegebenen Splittermasse ist.
$M(n)$	kumulierte Splittermasse, d.h. Summenmasse der Splitteranzahl n beginnend vom größten Splitter an.
m	bedeutet die Masse des n-ten Splitters.
N_0	gesamte Splitteranzahl.

$$\ln \frac{M_0 - M(n)}{M_0} = - Bn^{\lambda} \tag{9}$$

$$\log \left(- \ln \frac{M_0 - M(n)}{M_0}\right) = \log \left(\ln \frac{M_0}{M_0 - M(n)}\right) = \log B + \lambda \cdot \log n \tag{10}$$

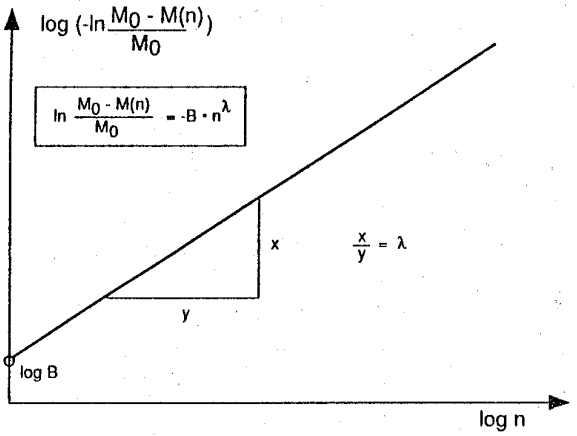

Zu diesem Zwecke ist M (n) vom größten Splitter an mit der entsprechenden kumulativen Splitteranzahl n zusammenzustellen. Die Größe ist jeweils von der gesamten Splittermasse M_0 abzuziehen und durch M_0 zu dividieren. Die entsprechenden Logarithmen können dann in ein Log-Log-Diagramm eingetragen werden.

Fig. 2 Log-Log-Diagramm für die leichte Bestimmung der Konstanten B und λ.

Durch Differentiation der Gleichung (7) nach n ergibt sich die Gleichung (11) für die Splittermasse m des n-ten Splitters:

$$m = \frac{d\,M(n)}{dn} = M_0 B \quad \lambda n^{\lambda-1} \; e^{-Bn^{\lambda}} \tag{11}$$

Die Ausgleichsgerade nach Formel (10) in den doppellogarithmischen Diagrammen gibt häufig nicht gut die experimentell gegebenen Meßpunkte wieder. Die Masse M_0 aller gefundenen Splitter ist nicht die Ausgangsmasse, bzw. stellt zumindest nicht die "optimale" Gesamtmasse für die Beschreibung einer optimalen Splittermassenverteilung dar.

Unter Verwendung der mit der Masse M_0 der gefundenen Splitter zuerst ermittelten Konstanten B und λ läßt sich aber eine optimale Masse $M_{0,Best}$ berechnen:

$$M_{0,Best} = \frac{M(n)}{1 - e^{-Bn^{\lambda}}} \tag{12}$$

Mit Hilfe dieser neuen Gesamtmasse $M_{0,Best}$ werden nun neue Konstanten B_B und λ_B ermittelt:

$$M(n) = M_{0,Best} \cdot (1 - e^{-B_B \cdot n^{\lambda_B}}) \tag{13}$$

Dieser Prozess wird mehrfach wiederholt, bis keine Verbesserung bzw. Änderung mehr auftritt <7>.

Massenverteilung von Trümmern von Flugzeugunterständen

In <1> werden die Massenverteilungen von Trümmern (Debri-Mass-Distribution) von 5 Modellversuchen von Flugzeugunterständen wiedergegeben, wobei in den Tabellen die Gewichtsklassen mit den dazugehörigen Splittenanzahlen, wie die Gesamtmasse ohne und mit einem Sieb, ausgewertet angegeben sind. In Fig. 3 ist beispielweise von Tabelle 4-28 für das Modell 1 wiedergegeben.

WEIGHT INTERVAL (LBS) W1 - W2	WITHOUT SIEVE DATA NUMBER	TOTAL WEIGHT	WITH SIEVE DATA NUMBER	TOTAL WEIGHT
.25 - .35	0	.00	234	73.37
.35 - .45	31	13.67	3374	1365.94
.45 - .55	2	.93	1294	615.95
.55 - .65	1	.55	59	33.95
.65 - .75	33	21.87	66	44.14
.75 - .85	4	3.22	50	40.15
.85 - .95	40	35.27	677	601.20
.95 - 1.05	0	.00	717	727.08
1.05 - 1.15	38	41.84	1401	1412.66
1.15 - 1.25	1	1.23	1044	1239.70
1.25 - 1.35	47	62.13	692	896.25
1.35 - 1.45	2	2.78	529	736.70
1.45 - 1.55	62	95.68	298	445.44
1.55 - 1.65	1	1.61	25	39.31
1.65 - 1.75	3	5.16	40	67.99
1.75 - 1.85	96	169.36	101	178.40
1.85 - 2.25	267	565.55	307	643.49
2.25 - 2.75	315	798.05	325	825.06
2.75 - 3.25	340	1011.48	342	1017.65
3.25 - 3.75	404	1412.13	408	1425.58
3.75 - 4.25	259	1051.65	260	1055.62
4.25 - 4.75	250	1124.14	250	1124.14
4.75 - 5.75	386	2028.23	388	2039.25
5.75 - 6.75	241	1515.13	244	1534.53
6.75 - 7.75	251	1819.89	262	1901.24
7.75 - 8.75	136	1126.12	136	1126.12
8.75 - 9.75	161	1490.10	161	1490.10
9.75 - 10.75	99	1013.62	99	1013.62
10.75 - 12.75	179	2093.33	179	2093.33
12.75 - 14.75	146	1998.09	146	1998.09
14.75 - 16.75	95	1491.29	95	1491.29
16.75 - 18.75	99	1752.39	99	1752.39
18.75 - 20.75	61	1204.03	61	1204.03
20.75 - 22.75	72	1563.89	72	1563.89
22.75 - 24.75	47	1119.02	47	1119.02
24.75 - 26.75	39	1004.29	39	1004.29
26.75 - 28.75	31	861.15	31	861.15
28.75 - 30.75	29	864.65	29	864.65
30.75 - 32.75	21	663.59	21	663.59
32.75 - 34.75	24	811.57	24	811.57
34.75 - 36.75	15	537.38	15	537.38
36.75 - 38.75	26	977.77	26	977.77
38.75 - 40.75	9	354.94	9	354.94
40.75 - 42.75	19	796.53	19	796.53
42.75 - 44.75	12	527.19	12	527.19
44.75 - 46.75	13	591.72	13	591.72
46.75 - 48.75	7	335.76	7	335.76
48.75 - 50.75	8	396.02	8	396.02
50.75 - 52.75	8	414.91	8	414.91
52.75 - ****	269	45864.77	269	45864.77
	TOTAL NB. 4699	TOTAL WEIGHT 81635.69	TOTAL NB. 15013	TOTAL WEIGHT 89918.92

NOTE: 1 LB = 0.454 kg

Fig. 3 Tabelle 4 - 28 für das Modell 1 aus <1>.

Er erfolgte eine Auswertung aller angegebenen Daten mit der HELD-Formel, wobei für eine gute Beschreibung der Trümmer-Verteilung eine Massenoptimierung sehr zweckmäßig ist.

Fig. 4-links zeigt die Auftragung des Logarithmus des Massenverhältnisses über der kumulativen Splitteranzahl mit der gegebenen Ausgangsmasse M_0 von 37.029 kg. Wie dieses Diagramm aufzeigt, stimmt offensichtlich die Ausgangsmasse nicht, so daß sich ein gekrümmter Kurvenzug für die Beschreibung der Splitterverteilung ergibt. Die daraus bestimmte Ausgleichsgerade kann die Splittermassen als Funktion der kumulierten Anzahl nicht beschreiben (Fig. 4-rechts).

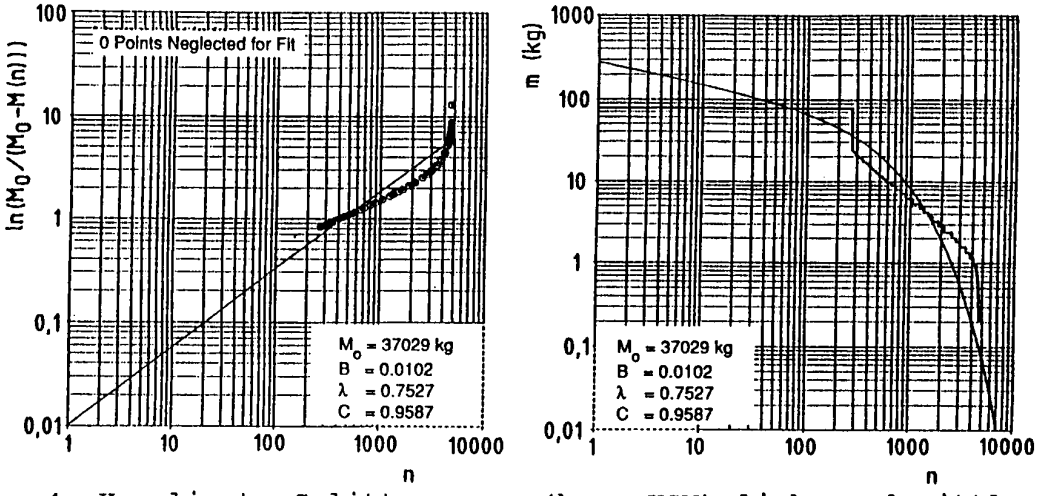

Fig. 4 Kumulierte Splittermasse (kurz KSM) links und mittleren Splittermasse (kurz MSM) über der kumulierten Splitteranzahl.

Führt man jedoch eine Optimierung der Masse M_0 nach dem voran aufgezeigten Optimierungsprozeß durch, dann erhält man eine Ausgleichsgerade, die hervorragend die experimentellen Meßergebnisse mittelt. Hierzu ist die Gesamtmasse von 37.029 kg auf 40.502 kg also um 8,6 % zu erhöhen (Fig. 5-links). Mit den nun gewonnenen Konstanten B = 0.0641 und λ = 0.4312 kann die experimentell gegebene Splitterverteilung in hervorragendem Maße beschrieben werden, wie jetzt auch Figur 5-rechts aufzeigt.

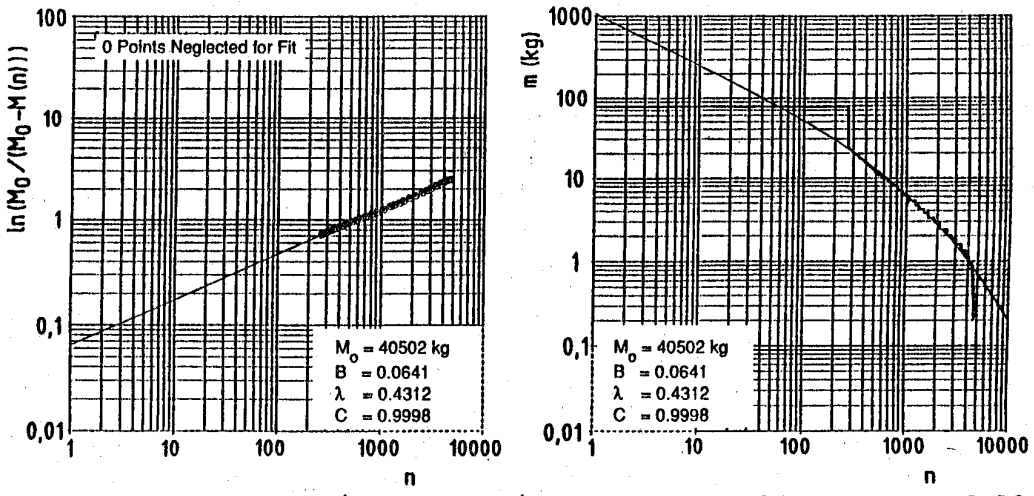

Fig. 5 KSM und MSM Diagramme mit Massenkorrektur von Modell 1 ohne Sieb.

Bei den gesiebten Daten ist die Massendifferenz für die Optimierung etwas geringer, da auch hier die Ausgangsmasse M_0 von 40.796 kg nicht optimal ist (Fig. 6). Durch die Korrektur der Ausgangsmasse um etwa 4 % wird eine optimale Anpassung an die Massenverteilung erreicht (Fig. 7).

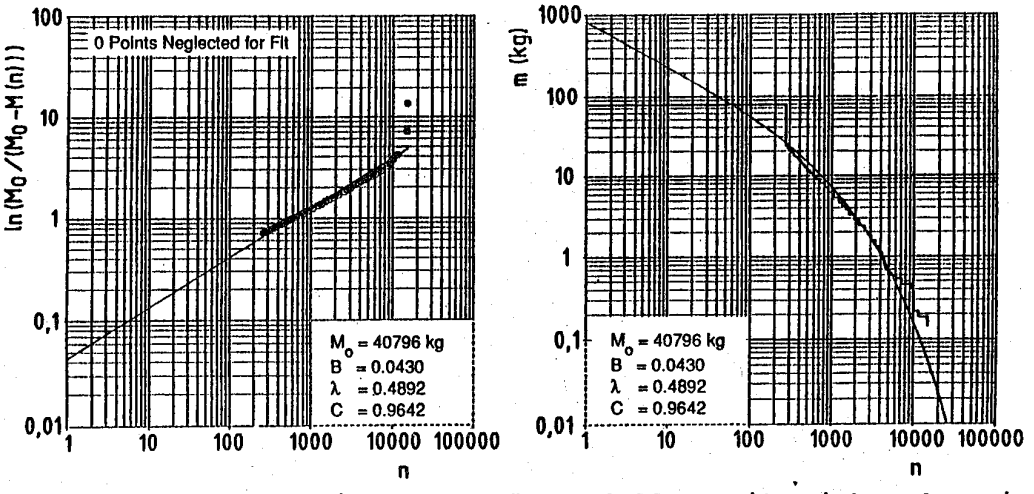

Fig. 6 KSM und MSM Diagramme für Modell 1 mit Sieb, ohne jede Massenkorrektur.

Bei den kleineren Splittermassen liegt bei der Massenverteilung aller Siebdaten offensichtlich ein Auswertefehler vor, der zu einer Abweichung der Ausgleichskurve von den Splittermassen in den Klassen im Bereich von 1 kg bis 0,2 kg führt.

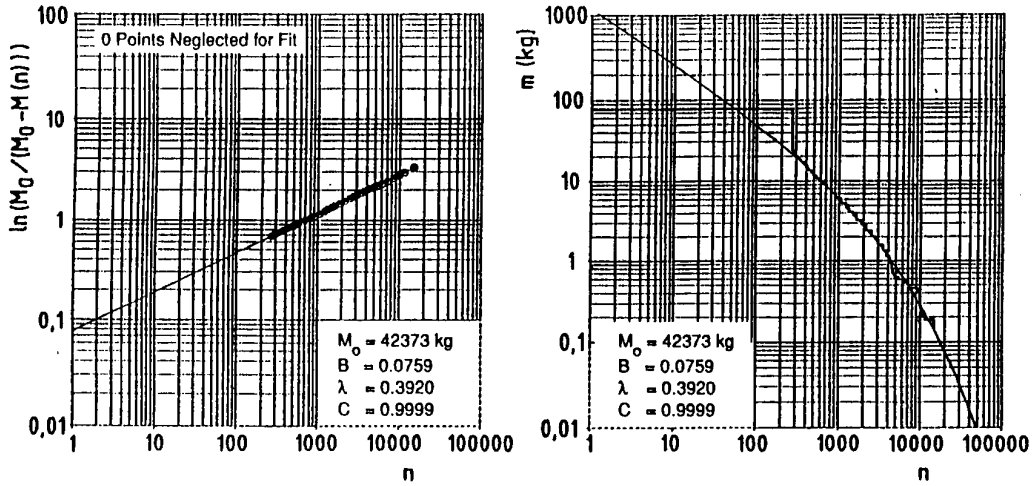

Fig. 7 KSM und MSM Diagramme für Modell 1 mit Sieb mit Massenkorrektur.

Auf die Wiedergabe aller Auswertungen für die weiteren Modellversuche 2 - 5 soll hier aus Platzgründen verzichtet werden. Der Vergleich der Splittermassen über die kumulierte Splitteranzahl bei jeweils optimaler Gesamtmasse $M_{0,Best}$ für alle vorliegenden Auswertungen - ohne und mit Sieb - zeigen doch auf, daß sie recht wenig voneinander abweichen (Fig. 8).

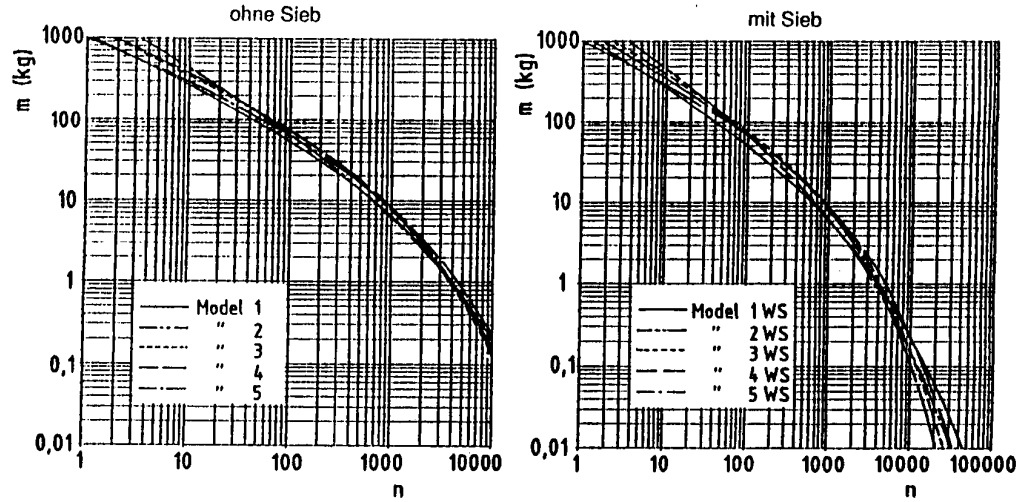

Fig. 8 Vergleich der Splittermassen über der kumulierten Anzahl für die Modellversuche 1 bis 5 ohne und mit Sieb ausgewertet.

In der folgenden Tabelle sind die Summenmassen M_0 laut Tabelle bzw. die korrigierten Massen $M_{0,Best}$ für optimale Splittermassenverteilung mit den Konstanten B und λ mit den Korrelationskoeffizienten C für die Werte Ohne-Sieb- bzw. Mit-Sieb-Daten wiedergegeben. Die mit Sieb gewonnenen Daten zeigen generell geringere Korrektur der Gesamtmasse als ohne Sieb.

Tabelle

Modell	M_0	$M_{0,Best}$	B	λ	C
1	37.020	40.502	0.0641	0.4312	0.9998
2	47.880	51.541	0.1363	0.3588	0.9999
3	50.582	52.874	0.0615	0.4608	0.9999
4	47.933	51.903	0.0602	0.4403	0.9999
5	41.975	44.859	0.0459	0.4932	0.9998
1	40.796	42.373	0.0759	0.3920	0.9999
2	50.644	51.461	0.1330	0.3630	0.9999
3	52.657	53.532	0.0665	0.4448	0.9999
4	50.891	51.763	0.0583	0.4458	0.9999
5	43.811	44.338	0.0404	0.5164	0.9998

Die in der Tabelle aufgeführten Werte für die einzelnen Modellsprengungen mit den Ausgangswerten für M_0 bzw. den geänderten $M_{0,Best}$-Werten durch den Optimierungsprozeß bzw. die entsprechenden Werte für λ und für B, bzw. deren Änderungen bei der Optimierung sind graphisch in Fig. 9 zusammengefaßt.

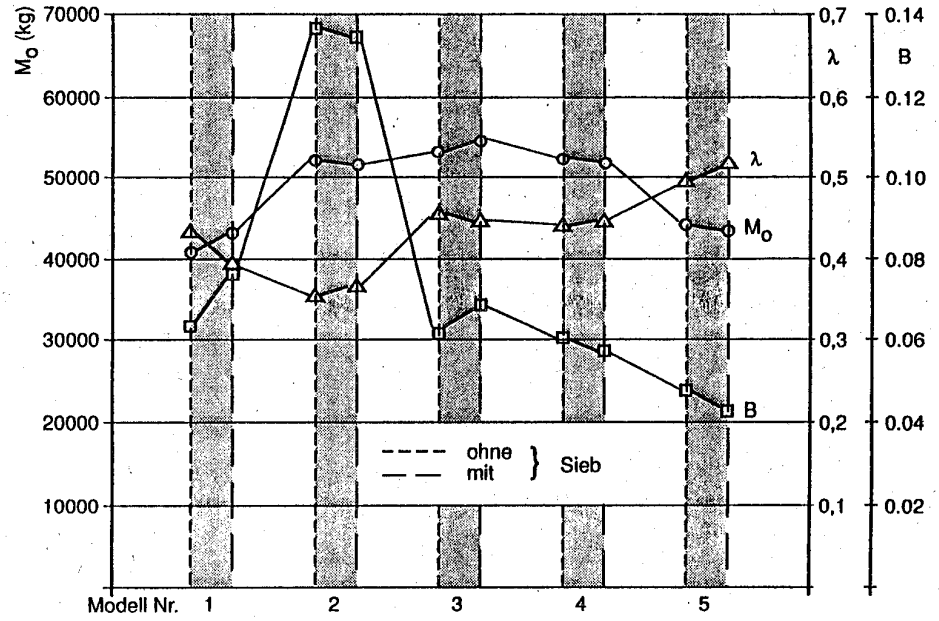

Fig. 9 Die Massen M_0 und die Konstanten B und λ für die Beschreibung der Splittermassenverteilungen der Modell-Tests, ohne und mit Sieb.

Zusammenfassung

Neben der Beschreibung der Massenverteilung von natürlichen Splittern eines Sprenggeschosses oder auch von Sekundärsplittern nach einer oder auch mehreren Schotten, kann die Gleichung nach HELD auch die Massenverteilung der Trümmer eines Flugzeugunterstandes sehr gut beschreiben.

Die beiden hierzu notwendigen Konstanten, Skalierungsparameter B und Formparameter λ, können zumeist mit hoher Aussagesicherheit, Korrelationskoeffizienten nahe 1, ermittelt werden, insbesondere wenn die vorgegebene Gesamtmasse M_0 auf eine die Splittermassenverteilung am besten beschreibende "Beste Masse $M_{0,Best}$" abgeändert wird.

Literatur

<1> J.M. Ward, M.M. Swisdak, P.J. Peckham, W.G. Soper, R.A. Lorenz
"Modeling of Debris and Airblast Effects from Explosions inside Scaled Hardened Aircraft Shelters".
NSWC TR 85-470, 1985

<2> M. Held
"Splitterballistik"
Explosivstoffe 15, 265 - 274, 1967; 16, 49 - 55; 73 - 78, 1968

<3> M. Held
"Berechnung der Splittermassenverteilung von Splittermunition"
Explosivstoffe 16, 241 - 244, 1968

<4> Oerlikon-Taschenbuch
6.2.1.3. "Splittermassenverteilung"; Seite 210 - 216, 1981

<5> M. Held
"Consideration to the Mass Distribution of Fragments by Natural-Fragmentation in Combination witz Preformed Fragments"
Propellants and Explosives 1, 20 - 23, 1979

<6> R. Heiser
"Gesetze für die Massen- und Formverteilung von natürliche Splittern"
Handbuch der Munitionswertung BWB - WM VI 2, 203 - 312, 1979

<7> M. Held
"Fragment Mass Distribution of HE-Projectiles"
Propellants, Explosives, Pyrotechnics, in Publication

FRAGMENT AND DEBRIS HAZARD EVALUATION PROJECT

A. G. Papp, S. L. Young, D. D. Barker
Mason & Hanger - Silas Mason Co., Inc.
Risk Management Department
P. O. Box 30020
Amarillo, TX 79177

ABSTRACT: On November 27, 1990, the Department of Defense Explosive Safety Board accepted the results of the Fragment and Debris Hazard Evaluation Project. Formal acceptance of this methodology by the Board represents a culmination of over two years of research and testing to establish a flexible, explosive operations facility siting tool.

The project was initiated because the DoD change in siting criteria (1987) was considered too broad for the relatively small quantities of explosives processed in DOE operating facilities. Impacts on DOE sites of this criteria change were increased real estate requirements, facility modifications to contain the explosive effects, and as a last resort, submission of Exemption Requests to continue operations.

The research program was developed and implemented around DOE specific facilities and explosive operations. The project was coordinated with the DOE and DoD Explosive Safety Boards, representatives from each of the DOE sites and a Technical Advisory Committee that consisted of technical experts in the fields of blast design and research from across the country.

INTRODUCTION: The Department of Energy (DOE) Explosives Safety Manual, DOE/EV/06194-5, requires that the DOE and its contractors use the fragment/debris hazard siting criteria outlined in the Department of Defense (DoD) "Ammunition and Explosive Safety Standards", DOD 6055.9, for determining safe separation distances for explosives facilities. This has caused great concern at existing DOE facilities for a number of reasons. Some of the now required separation distances exceed current site boundaries and distances between structures at these facilities because the original siting was based on blast overpressure protection alone. The threat of costly expansion of plant real estate or hardening of some structures has prompted the DOE safety community to question the applicability of the broad ranged DoD fragment separation criteria for siting DOE structures housing, in many cases, small quantities of high explosives (HE).

The need to provide safe clearance for hazardous debris generated by accidental explosions or detonations of energetic materials was not disputed. However, development of more specific criteria to supplement the quantity-distance tables for combinations of the structure and explosives types found at DOE facilities was determined to be cost effective. The goal was to have facilities comply with criteria without compromising the intended safety. These new criteria needed to be established by a careful examination of the structures and explosives present at DOE facilities, a study of existing data on fragmentation of these explosive configurations, and sub-scale or full scale testing of combinations of structure and explosives types.

PROJECT APPROACH: Southwest Research Institute of San Antonio, Texas was contracted to prepare a Safety Assurance Plan for the project. This plan was necessary to ensure that the project would culminate in a method for determining safe separation distances which would be approved by the DoD Explosives Safety Board (DDESB).

The Safety Assurance Plan was developed in 1987 and served as the foundation and guidelines over the life of the project. The plan included sufficient analytical and experimental investigations to address and satisfy the concerns of the DOE. The plan included assembly of existing data and technologies; development and use of predictive computer models and hazard analysis to define the worst case situations; identification of areas of low confidence in hazards prediction; and the use of testing increase the confidence level of the predictive model.

The specific tasks of the Safety Assurance Plan were as follows:

1. Establish of Current Database and Fragment Hazard Technologies
2. Collect Information on Structures and Explosive Configurations for DOE Facilities
3. Identify Structures of Similar Construction
4. Identify Explosives of Like Assembly
5. Establish Structure/Explosives Groups of Similar Hazard
6. Define Explosion Accident Scenarios and Maximum Credible Explosion (MCE)
7. Develop and Use Predictive Computer Model to Analyze Structure/Explosives Groups for the MCE
8. Identify Level of Confidence for the Data, Technology and Results of the Analysis of the Various Structure/Explosives Groups
9. Develop Small Scale Test Requirements and Perform Testing
10. Refine Predictive Model and Receive Approval of Method from DOE Headquarters and Department of Defense Explosives Safety Board (DDESB).

The project flow is identified in Figure 1 which includes milestones involving DOE review or approval. DDESB briefings were conducted frequently to ensure that the final criteria developed would be approved. In the following paragraphs, each of the accomplished items (1-10) are briefly described.

1. ESTABLISHMENT OF CURRENT DATABASE AND FRAGMENT HAZARD TECHNOLOGIES:
   The first step in obtaining modification of the DOE Explosives Safety Manual was to collect existing data and debris hazard prediction methodologies in the form of related reports and published papers to prevent repetition of efforts. Data on hazards from explosives fragmentation and the breakup of structures which already existed, and were applicable to DOE facilities was used as extensively as possible. To establish the current database, computer aided literature searches were conducted to locate pertinent documents. The resulting abstracts were reviewed, and relevant reports were obtained and examined for addition to the debris hazard database. In addition to the computer aided searches, fact gathering efforts by DOE safety personnel and Southwest Research Institute (SwRI) personnel were compiled and included in a summary of the existing fragment/debris hazard prediction database.

2. COLLECTION OF INFORMATION ON STRUCTURES AND EXPLOSIVE CONFIGURATIONS FOR DOE FACILITIES:
   Each of the DOE facilities were examined to determine the various types of structures (construction materials, characteristics such as frangible walls, vented roofs, or reinforced concrete walls and roofs, operations conducted, etc.) and the types of explosives processed. A general form letter requesting information on the structures and explosives was sent to each facility with an explanation of the nature of information needed and the reason for requesting it. Visits to the DOE sites by the project team were accomplished to gather additional information. It is important to note that the combination of structure types and explosives types dictated quantity-distance at a site, not just the quantity of HE contained in a certain area.

3. IDENTIFICATION OF STRUCTURES OF SIMILAR CONSTRUCTION:
After information on all the DOE facilities was collected, structures of similar construction were grouped together. A group consisted of several different sizes of buildings with similar structural characteristics. For example, one group included buildings similar to earth covered assembly bays with blast doors which failed under internal load and "hinged roof" construction. Operations conducted within buildings in a group could differ and the potential explosion hazard may or may not have been similar. The various structure types were grouped with explosives types to determine appropriate siting criteria.

4. IDENTIFICATION OF EXPLOSIVES OF LIKE ASSEMBLY:
Information collected on explosive configurations processed or handled at each DOE facility was grouped by configuration (casing, characteristics, shape) and explosive quantity similarities. Groups of explosives representing "worst case" hazards were selected since the variations in explosives and, thus, number of groups were very large.

5. ESTABLISHMENT OF STRUCTURE/EXPLOSIVES GROUPS OF SIMILAR HAZARD:
The structure categories and explosives groups identified following the facility data collection were combined into groups of similar hazard. Quantity-distance criteria and model development were based on these structure/explosives groups, not just on HE quantity, to reflect true separation distances from debris hazards. These groupings were used to determine the types of facilities to be analyzed and the component types to be tested.

6. DEFINITION OF EXPLOSION ACCIDENT SCENARIOS AND MCE:
The facility data collection was used to define explosion accident scenarios and the MCE for each structure/explosives group. Items considered include operations conducted, the potential for sequential or simultaneous detonation, and the possible explosion site(s) within a structure. The MCE defined for each group was used in a hazard analysis to establish appropriate quantity-distance relationships for that group.

7. USE OF PREDICTIVE COMPUTER MODEL TO ANALYZE STRUCTURE/MUNITION GROUPS FOR MCE:
A debris/fragmentation hazard refinement analysis was conducted for the MCE of each structure/explosives group using a predictive computer model and other available data. The data needed as input to the analysis consisted of building breakup, debris throw, and debris distribution. This information came from existing data obtained by the literature search, the facility data collection, and computer modeling. The breakup of a structure and debris characteristics were predicted based on the quantity and configuration of the explosive(s) involved in the MCE and the construction of the building. Predictions of the blast loads inside the structure enabled estimates of not only whether building breakup occurs, but also debris/fragment trajectories and maximum debris/fragment hazard distances.

8. IDENTIFICATION OF LEVEL OF CONFIDENCE OF THE DATA, TECHNOLOGY, AND RESULTS FOR THE ANALYSIS OF THE VARIOUS STRUCTURE/EXPLOSIVES GROUPS:
Approval of new quantity-distance criteria based solely on the analyses of the structure/explosives groups required identification of a level of confidence in the input data, the prediction methodologies, and the resultant missile maps and safe separation distances. Prediction of building breakup and debris throw had a low confidence level since specific data on the breakup of the structural components was not available. Accuracy of the prediction methodologies for blast loading, debris/fragment velocities, maximum clearance distances, etc. was dependent on comparisons with existing test or accident data available. Since very little data existed on the structural components, debris size, and initial velocity, component testing was required to verify the predictive method and establish an acceptable confidence level.

9. SMALL SCALE TEST REQUIREMENTS AND TESTING:
Since the hazard refinement analysis did not result in a high degree of confidence, scale testing was required. The testing was in the form of structural component tests in which only a portion of a building, such as a wall, was modeled to examine its response to a blast load. The majority of tests were performed on small scale components to reduce costs. A limited number of full scale tests were

conducted to validate the small scale results. Attention was directed toward careful modeling of material characteristics and structural strength in order to accurately duplicate dynamic response and structural breakup. Tests were performed to verify specific debris/fragment characteristics, such as maximum range. The inadequacies of the hazard analysis for each structure/explosives group determined the type of small scale testing necessary to "fill in the gaps". Over 50 small and full scale tests were accomplished to quantify debris characteristics and provided the basis for the component predictive model.

10. REFINEMENT OF PREDICTIVE MODEL AND FINAL ACCEPTANCE:
The predictive model was refined using debris sizes and initial velocities obtained during the scale test phase. Modifications to the predictive model were made to address the structure and explosive groups found within the DOE complex. The final product resulted in a flexible, quantitative method to predict building debris-throw for DOE facilities. DoD accepted the technique and incorporated the method into the DoD 6055.9-STD, which provides statute authority under federal law.

MODEL LIMITATIONS: The predictive model provides conservative estimates of maximum and hazardous building debris distances which can be expected following an internal detonation of bare explosives. The model is based largely on curve-fits to data collected from small scale and full scale tests. Use of the model outside the limits of the test data should be done with considerable care. Such extrapolation should be done on a case-by-case basis using sound engineering judgment.

The model is limited to use for charge weights equal to, or less than, 250 pounds TNT equivalent. It may be used for buildings with multiple charges (totaling no more than 250 pounds) if the combined impulse on a component from all charges is conservatively calculated.

Scaled charge standoff is limited to 0.5 $ft/lb^{1/3}$ or greater. The minimum standoff (unscaled) is 1.5 feet. The minimum standoff limitation is primarily intended to prevent the model from use in situations involving small charges nearly in contact with the wall.

The model is valid for building debris only and is not intended to predict dispersion of primary and secondary fragments in contact or in close proximity to the charge. Use of the model for highly confined buildings is restricted to configurations with relatively lightweight vent panels. Fragments from buildings which have no venting or that have reinforced vent panels may not be correctly predicted by the model. In these situations, the large quasistatic pressures vented through relatively narrow hinge lines propels the fragments at much higher velocities than would be produced in a vented condition.

The model is intended for use in situations in which maximum fragment velocities are less than 1000 ft/sec. Above this limit, drag forces on the debris differ significantly from those assumed in the model. The exception to this is debris produced by the breakup of corrugated metal walls or roofs. Velocities greater than 1000 ft/sec. were produced in the tests for this type of fragment and were accounted for on the model.

COMPUTER PROGRAMS: Three computer codes, SHOCK, FRANG, and MUDEMIMP, are required to use the model. SHOCK is a program written by the Naval Civil Engineering Lab (NCEL) in Port Hueneme, CA. It is a modification of the program PAIMPRES developed by Ammann and Whitney to produce the pressure and impulse curves for cubicles in ARLCD-SP-84001, Vol. II. SHOCK predicts reflected pressure and impulse loads on surfaces caused by incident and reflected waves. The program allows for calculation of loads at a point, average loads over a reduced area, or averaged over the entire surface.

FRANG is a program written by NCEL to calculate gas pressure loads in a room caused by an internal explosion. The program accounts for the effects of venting on the duration of the load based on the mass of the vent panel.

The MUDEMIMP code was also written by NCEL to simulate multiple debris impacts. The code was modified during this project to change the debris density calculations and to account for debris roll in determining hazardous debris distances.

SHOCK and FRANG are designed to run on a personal computer (PC). MUDEMIMP was originally developed on a VAX. A PC version has been developed however it currently does not contain the graphics routines necessary to produce the plots of input variables and fragment densities. The PC version does however produce a data file containing the information necessary to produce a fragment density histogram. This data can be imported into a spreadsheet to produce the desired plots.

SUMMARY OF RESULTS: An analytical model has been developed to predict hazardous building debris distances for accidental high explosive detonations within buildings constructed of various materials. The model was specifically developed for DOE to provide an approved method for determining safe siting distances for explosive loading conditions and building construction types most common to DOE facilities. However, it can be used to predict maximum hazardous debris distances using similar loading conditions in any building constructed of reinforced concrete, masonry (clay tiles or concrete masonry units), lightweight components such as corrugated metal, or a combination of one or more of these materials. Thus, the model will be equally useful to members of the DoD explosive safety community. Verification and refinement of the model have been accomplished using data from an extensive test program funded by DOE. The end result of the program is a flexible, component based predictive model, verified with data, which can be used to safely site explosive handling buildings according to predicted hazardous debris distances instead of using broad-ranged debris safety criteria which are based solely on explosive amounts.

The debris-safe siting criteria outlined in DoD 6055.9-STD state that the minimum distance for protection from hazardous fragments will be that distance at which fragments, including debris from structural elements of the facility or process equipment, will not exceed a hazardous fragment density of one hazardous fragment per 600 square feet. It further states that if this distance is not known, the distances of 670 and 1,250 feet will be used unless one can show by analysis or testing approved by the DDESB that a lesser distance meets the criteria. The model described in this paper provides an approved procedure for conducting such an analysis for building debris. The siting criteria have been modified to include the use of the model by specifically referencing a DDESB technical paper on the model as an example of an approved analysis. Primary fragments and fragments from process equipment must also be considered when analyzing a building for safe siting distances. Methods for analyzing debris distances for these fragments are not contained in the model.

This model will greatly aid in the reduction of siting distance for many existing and new explosive handling facilities, especially those using relatively small quantities of explosives. It is noted in some cases, such as close-in loading in highly confined buildings, a distance larger than 670 or 1,250 feet can be predicted by the model. Test data in areas such as this are extremely limited, therefore, methods were developed which are conservative, especially in the prediction of roll distance. However, to what degree the results would be overly conservative is not known. DDESB will approve the use of the default distances in cases, outside the range of the supporting test data, where the model predicted hazardous distance exceeds the applicable default distance, since those distances are based on a predetermined level of risk which have been accepted by DDESB.

The authors would like express appreciation to SwRI for their outstanding research and development work on the project and for their commitment to produce a valuable siting tool which will be used for many years to come.

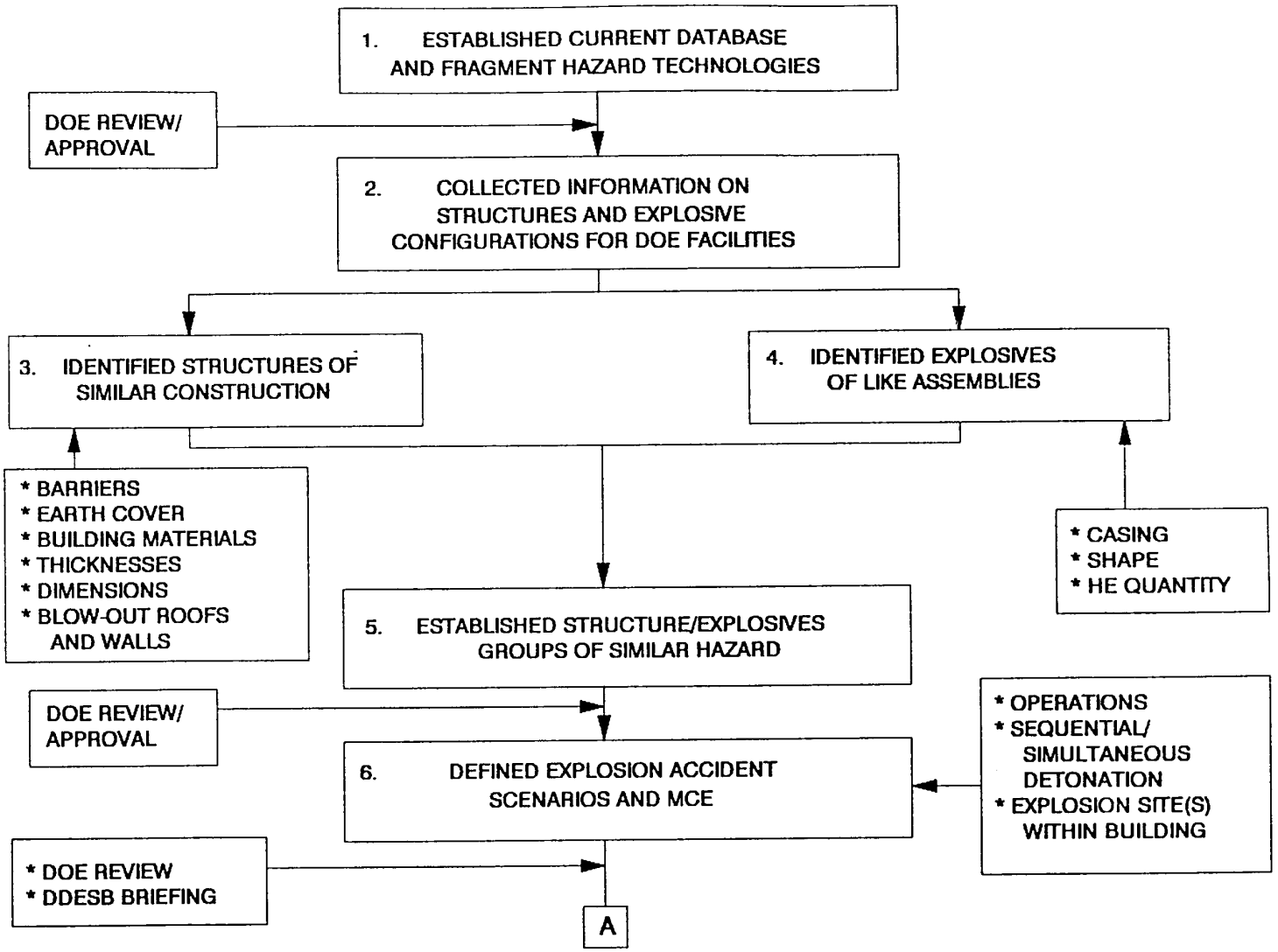

FIGURE 1. FRAGMENT AND DEBRIS HAZARD EVALUATION PROJECT SUMMARY

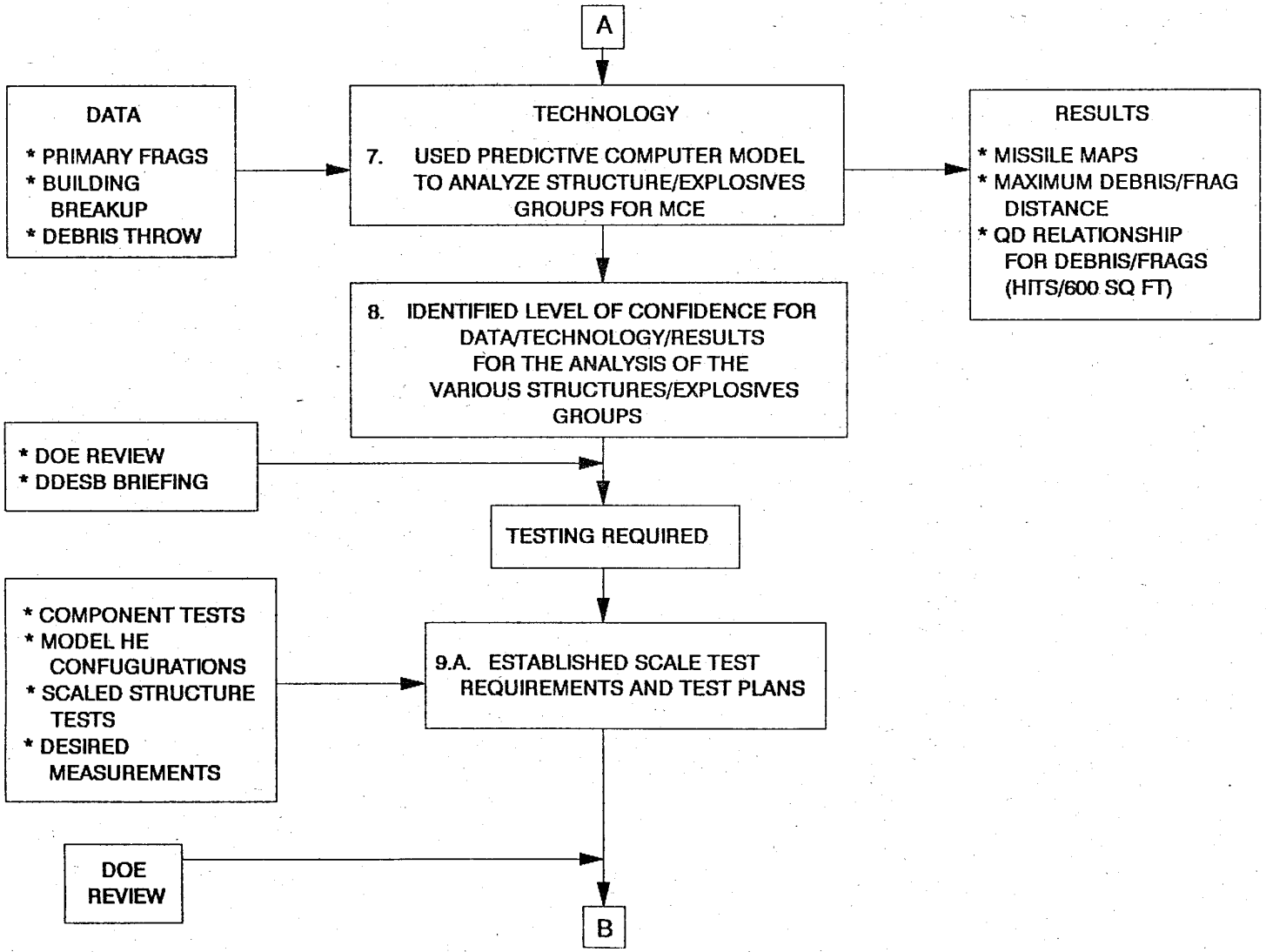

FIGURE 1. FRAGMENT AND DEBRIS HAZARD EVALUATION PROJECT SUMMARY (CONTD.)

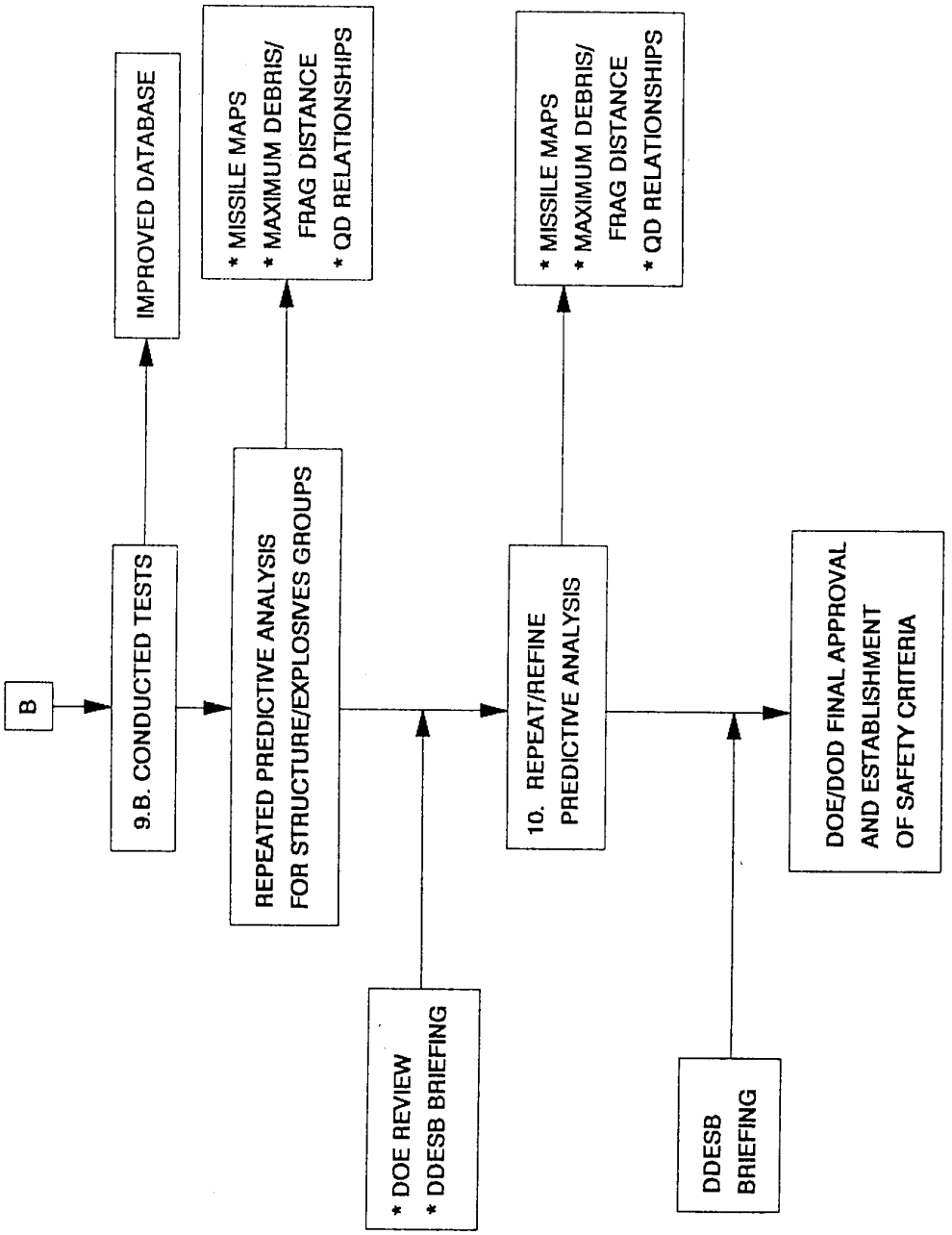

FIGURE 1. FRAGMENT AND DEBRIS HAZARD EVALUATION PROJECT SUMMARY (CONTD.)

IDENTIFICATION OF WALL CONCEPTS TO PREVENT SYMPATHETIC DETONATION IN MUNITIONS STORAGE MAGAZINES

Capt Glen J. Pappas, P.E., member ASCE
Shock Physics Division, Phillips Laboratory, Kirtland AFB

The containment of explosions from stored munitions is a challenge that has always existed. The difference now is that as excess munitions return from Europe this difficult challenge must be addressed. To reduce spacing requirements of munitions storage magazines (MSM) in order to meet the storage demand from our excess overseas munitions, cell walls may be used to separate one stockpile from another, if they can be designed to prevent sympathetic detonation. This paper analyzes fragment perforation and blast loading on MSM cell wall designs from the detonation of a high explosive stockpile. Wall thickness and construction costs for various materials were determined and compared.

1.0 INTRODUCTION

The construction presently used in Naval MSM does not include cell walls. The Maximum Credible Event (MCE) which results from the wall-less construction calls for MSM spacing which is too large according to the Navy's current needs. The Shock Physics Division of the Phillips Laboratory (PL/NTE), along with many other DOD and non-DOD organizations, was tasked by the Naval Civil Engineering Laboratory (NCEL) to identify MSM cell wall concepts, which will prevent sympathetic detonation, such that the MCE can be reduced. The following objectives were to be achieved: (1) the determination of material types and thicknesses required to prevent fragments from perforating at terminal speeds in excess of 457 m/s, (2) the development of design parameters which control cell wall motion (the walls must remain in position for the length of time required to stop or sufficiently slow the fragments), and acceptor munition kinetic trauma under airblast loading (kinetic trauma is, in this report conservatively assumed to occur when a cell wall impacts the acceptor munitions

stockpile at speeds greater than, or equal to, 76 m/s. = 250 ft/s, as opposed to the criteria given for a munition impacting a wall), and (3) cost versus wall thickness comparisons. Materials which were able to withstand the fragment and airblast threats by meeting or exceeding the criteria, and whose material and construction costs were deemed to be reasonable as compared with other alternatives, were recommended for full scale testing. This paper documents (1) NCEL's preliminary criteria, (2) how the objectives were achieved, (3) the results, and (4) conclusions and recommendations.

The analysis was limited to readily available materials, particularly, common building materials. This provided adequate flexibility in the selection of materials to analyze, yet put a 'ceiling' on the material and construction costs.

Various experts from both the DOD and industry were consulted about: (1) the prevention of sympathetic detonation, and (2) the wall materials and construction techniques required to prevent sympathetic detonation. Because the problem at hand is quite unique, those consulted were only able to provide general insight.

2.0 INTERPRETATION OF THE CRITERIA

NCEL provided MSM preliminary criteria and the threat environment that are used to evaluate several types of materials for potential use as walls in MSM. Many of the criteria were intended merely to guide the initial studies. It was necessary to make assumptions where MSM dimensions and other information was lacking; these assumptions are indicated in this paragraph. MSM length is 61 m, with 5 m cell spacings, and 2 m at each end of the magazine serves as aisle space. Cells are separated longitudinally from one another with cell walls and transversely separated via a wall which is the length of the MSM. A 0.75 m cell wall thickness was assumed in order to determine the number of cell walls in an MSM; this provides a standard upon which the construction cost estimates for the cell walls are based. The width and height of the cell walls is 3.7 m and 2.4 m, respectively. The explosives in the 4536 kg event are assumed to be H-6 ('worst case'). The event is assumed to occur via a chain reaction beginning with the munition located in the center of the stockpile. The cell wall airblast load of 172 MPa is assumed to occur through pressure build-up as the chain reaction progresses from the center of the munition outward. The airblast load is given as an instantaneously applied load with

a 0.005 s linear decay. The perimeter of the stockpile is assumed to be the point from which the airblast and fragment began to travel toward the wall (0.6 m is the space between the stockpile and the cell walls). The stockpile height is 2.1 m. The threat fragment given is a 0.13 m mild steel cube, weighing 0.016 kg, with an initial velocity of 2530 m/s (the fragment threat is given as just one threat fragment; the airblast load acting on the cell wall does not contain fragments).

3.0 STUDY OF MATERIALS SUBJECTED TO THE FRAGMENT THREAT

EPHULL 122 (the 2D version) Eulerian hydrodynamic code was used to perform the fragment penetration analysis. This code has been used and validated extensively for problems involving high impacts (ballistic through hypervelocity). The code can accommodate several materials and includes (1) equations of state (EOS) for porous media, (2) a Mie-Gruneisen model for metals and other solids, (3) a Jones-Wilkins-Lee (JWL) EOS for detonation products and (4) an air EOS based in tabular data. The constitutive relations contain options for purely elastic, elastic-plastic, and simple fracture material response. All problems were run with the failure mode on. EPHULL simulates failure by placing air in a zone that has exceeded a stress limit.

The purpose of the hydrocode calculations was to determine the velocity and penetration characteristics of a cubical fragment through various types of media. Because the purpose of this project was to look at many types of materials and determine only their stopping capability, no in-depth analysis of the stress wave propagation and material breakup was necessary.

Because a cubical projectile can only be exactly modelled in three dimensions, and since 3D calculations are both expensive and time consuming, it was believed that a "twin-cone" simulation in cylindrical coordinates would suffice. The only decision then was whether to go with the cubical cross section or the cubical mass of the projectile. In a calculation using the 0.013 m edge twin-cones into concrete, and another using the 0.016 kg twin-cones into concrete, the velocity and penetration profiles changed. The indication was that the added mass of the twin-cone was offset by the additional friction of the larger surface area. Therefore, most of the calculations were run with the 0.013 m edge, although its weight was only about 0.012 kg.

The cell size for these calculations depended on the individual problem. If the target was thin, a fine grid size would be used. As the thickness of the target grew, the grid became more coarse. The finest cell size was 0.0005 m square, and the largest was 0.002 m square. This made it possible to keep the computational grid between 12,000 and 25,000 cells. For a 3 or 4 material problem, this kept the run times on the CRAY-2 at cost effective levels, and still provided accurate calculations. The run times for the calculations varied from 10 minutes to 2 hours of CRAY-2 time.

4.0 STUDY OF MATERIALS SUBJECTED TO THE AIRBLAST THREAT

For each material, the acceleration of a square meter of cell wall area was determined from Newton's Second Law: $a = F/m$

a = acceleration (m/s^2); and is the unknown variable

F = force (MN); obtained by taking a unit wall area (m) and multiplying by the airblast pressure (172 MPa - (172 MPa/ 0.005 s)t); t is time from 0.0 - 0.005 s

m = mass (kg); obtained by multiplying the unit weight of one square meter of wall (kN/m) by the wall thickness; gravity is then divided out

Cell wall acceleration values are obtained as time t varies from 0.0 - 0.0005 s. In the determination of wall acceleration, the cell wall was assumed to be free-standing (unconnected) and friction between the floor and the cell wall was neglected. When the $a = F/m$ expression is integrated values of velocity and displacement are obtained. Wall displacement and airblast time-of-arrival were compared with the fragment time-of-arrival, with the time for the fragment to stop or slow to below the critical speed, and to the 0.6 m distance between the wall and the acceptor stockpile. These quantities were determined as follows:

Airblast Time-Of-Arrival (TOA)(pg 3-11, /1/: TOA is determined via cube root scaling. The 0.6 m distance between cell wall and the edge of the stockpile (the point from which the 172 MPa originates) is a key datum point in this analysis. The other key datum was the H-6 high explosive. The 4,536 kg of H-6 was converted to a TNT equivalent of 5,897 kg. The TOA determined is 0.00013 s.

Fragment TOA: determined by dividing the fragment travel distance (0.6 m) by the fragment initial velocity (2530 m/s). The TOA is 0.00024 s.

Fragment Time To Stop Or Slow To A Speed Less Than 457.2 m/s: determined using the EPHULL hydrocode.

A comparison of the values of the various parameters was used as the basis as to whether or not a cell wall material was worthy of being carried on to the last phase of analysis; the cost versus wall thickness comparison is described in paragraph 5.0.

If a material was unable to perform to criteria in either the fragment perforation or airblast loading analyses, then the material was dropped from consideration at this point. A summary of the materials selected and their performances are contained in paragraph 6.0.

It would be desirable if the cell walls could be connected such that they would not move as quickly under the action of the airblast. The wall materials chosen as wall candidates could then be used with smaller thicknesses thereby saving space and, perhaps, money. The problem is that 172.4 MPa applied to 8.9 m^2 (3.7 m x 2.4 m) of wall area yields a load of over 156,500,000 kg. If this load is divided by the 6.1 m of connection length available, one is left with designing a connection to withstand over 25,500,000 kg/m! Realizing that this is not practical economically or physically, the next concept is to use any reasonably strong, standard type of connection, in order to obtain any reduction in the motion of the wall.

5.0 CONSTRUCTION COST ESTIMATES

Cost versus wall thickness comparisons were completed for all of the materials which successfully performed in the fragment perforation and airblast loading analyses. This comparison was made in order to assist in the decision process as to which materials should be recommended for full scale testing. The assumption was made that space and money would be the determining factors for NCEL in their decision as to which materials to select for testing and eventual use.

The cost estimates are based upon a 20-cell MSM with 2.4 m x 3.7 m cell

walls; the thicknesses of the cell walls are based upon the largest thickness given by the fragment or airblast analyses. In every case, the largest thickness was that required to prevent cell wall kinetic trauma from occurring. The estimates are also based upon: material and labor costs which assume a large quantity purchase (e.g., $500,000), present (1990) dollar value, and overhead and profit.

6.0 RECOMMENDED CELL WALL DESIGNS

1. A 0.84 m wall composed of sand and a plywood and wood stud container will work. It was assumed that the wall would pulverize before reaching the stockpile so the thickness needed to keep the wall velocity less than 76 m/s was considered to be excessive and 0.84 m was deemed to be satisfactory. Wood may propagate fire; further analysis/testing is required.

2. A magnetite-based concrete wall, 2 m thick, will perform well. Magnetite is a naturally occurring iron-oxide mineral which would substitute for conventional concrete aggregate. A magnetite wall may also be a good candidate; further analysis should be done. The reader is reminded that in both of the recommended cell wall designs, the thicknesses given are extreme due to the conservative assumption made regarding cell wall kinetic trauma.

7.0 CONCLUSIONS

1. For a passive system, the mass required to prevent cell wall kinetic trauma and to maintain wall position long enough to stop or slow the threat fragment, calls for a wall thickness greater than that required considering fragment penetration.

2. The airblast arrives at the wall face before the fragments arrive.

3. Connection of the cell walls to remain in place under airblast loading is not feasible.

4. The materials with the highest unit weights perform the best in preventing fragment perforation and in resisting the movement caused by the airblast.

5. The materials with the highest units weights tend to be expensive.

8.0 RECOMMENDED FUTURE EFFORTS

1. Time of arrival for the airblast was obtained via a chart in which there was no provision for a standoff distance of 0.6 m. Testing needs to be done to add these 'close in' data points.

2. The effect of wall friction on the rigid body, overturning, and rotational motions of the wall needs to be determined. Friction was neglected here.

3. A connection scheme of even very limited capacity would mitigate wall motion. The details and cost of cell wall connections should be examined.

4. The loading caused by multiple fragment impacts needs to be examined. Wall loading in this report considered airblast only.

9.0 REFERENCES

1. Fundamentals of Protective Design for Conventional Weapons, TM 5-855-1, Headquarters, Department of the Army, Washington, DC, November 1986.

2. Crawford, Robert E., L. Rosenberg, L. Wilson, H. Schreyer, Protection from Nonnuclear Weapons, AFWL-TR-70-127, Air Force Weapons Laboratory, Kirtland Air Force Base, NM, 1970. Distribution limited to U.S. Government and associated contractors.

3. A Manual for the Prediction of Blast and Fragment Loadings on Structures, United States Department of Energy, Albuquerque Operations Office, Amarillo Area Office, Pantex Plant, Amarillo, TX, November 1980.

4. Protective Construction Design Manual, ESL-TR-87-57, Air Force Engineering and Services Center, Engineering and Services Laboratory, Tyndall Air Force Base, FL, November 1989.

Penetration

Eindringleistung und Sprengwirkung eines Pentrators gegen Runway - Ziel

Hans-Dieter Ackermann
Stefan Langer
MBB Deutsche Aerospace, Schrobenhausen

Einleitung

Die vorgestellten Arbeiten wurden 1987 und 1988 im Rahmen einer Experimentalstudie durchgeführt. Untersucht wurde die Machbarkeit und das Verhalten von kinetischen Penetratoren, die als Streumunitionen aus einem vertikal anfliegenden Behälter im schallnahen Bereich abgesetzt werden sollten. Neben Versuchen zur Eindringleistung und Sprengwirkung des Wirkteiles wurde im Unterauftrag ein zeitprogrammierbares Zündsystem entwickelt, welches bei vollscharfen Versuchen erfolgreich eingesetzt werden konnte. Dimensionsvorgaben kamen aus System- und OR-Betrachtungen; die Auftreffbedingungen aus aerodynamischen Simulationen und Toleranzabschätzungen.

Versuchsmusterbeschreibung

Vom Konzept her handelte es sich um einen flügelstabilisierten kinetischen Penetrator. Es wurde davon ausgegangen und in Versuchen gezeigt, daß der Flügelkasten bei der Zieleindringung sich von der Penetratorstruktur trennt. Dies wurde simuliert, indem der Treibspiegel exakt die Masse des Flügelkastens hatte und die Verbindung der konstruktiven operationellen Lösung entsprach. Im weiteren wird dieses Teil nicht mehr berücksichtigt.

Skizze 1

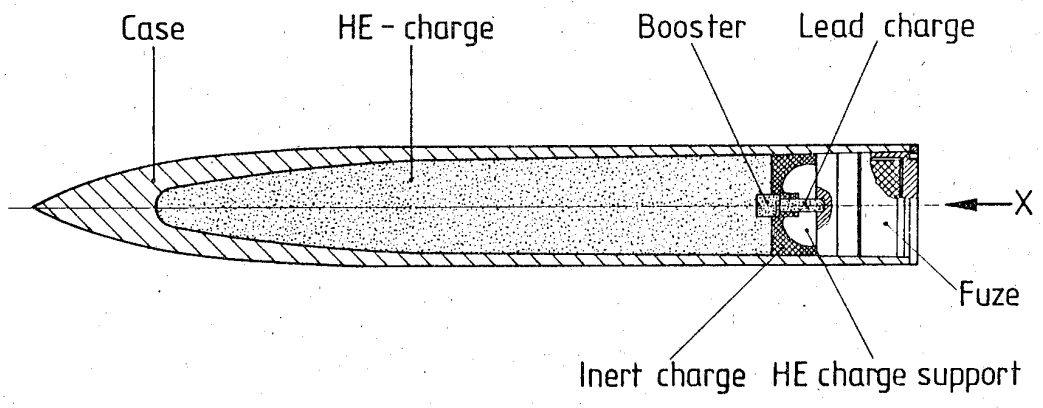

Daten des Versuchsmusters:

Durchmesser:	*82 mm*
Länge:	*720 mm*
Gesamtmasse:	*11,60 kg*
Sprengstoff:	*Masse 2,15 kg, Hexogen, Kunststoffgebunden, Aluminiumhaltig*

Versuchstechnik

Es sollten die auf der WTD-91 vorhandenen Runwayziele vertikal unter 20° Nato beschossen werden. Zur Beschleunigung der Penetratoren wurde eine rückstoßfreie Davis-Kanone benutzt, die in ein Dreibein eingebaut war.

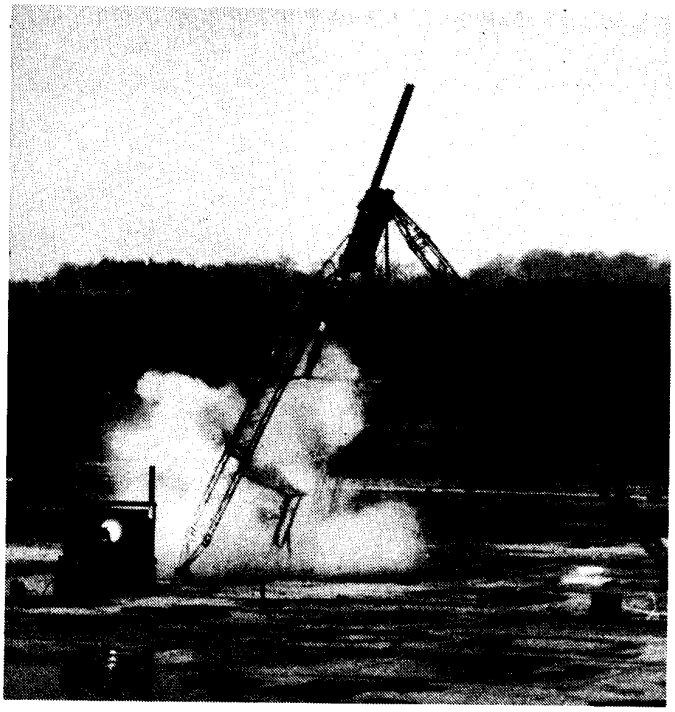

Bild 1
Versuchsaufbau während eines Schießeinsatztes

Das verfahrbare Dreibein wurde zum Beladen mit dem Ausstoßrohr flachgelegt.

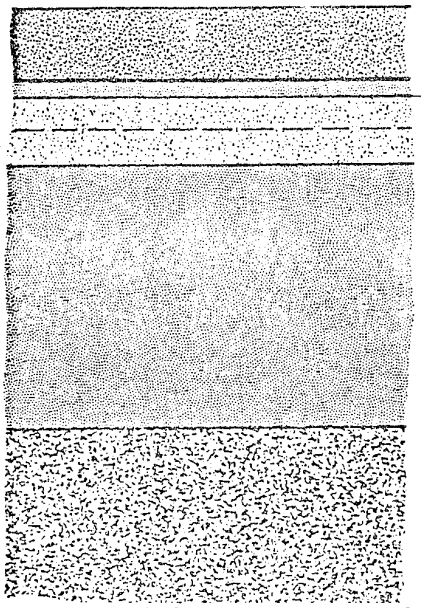

Skizze 2
Zielaufbau

Die Versuche wurden 1988 auf der WTD91 gegen das zu dieser Zeit spezifizierte Startbahnziel durchgeführt. Skizze 2 zeigt schematisch einen Schnitt durch den Aufbau.

Betonplattengröße	*4 x 5 m²*
Betonqualität	*B35*
Aktuelle Druckfestigkeit	*58 N/mm²*

Ermittlung der Eindringleistung

Als Voraussetzung für die geplanten vollscharfen Versuche wurden Tests durchgeführt mit inerten Penetratoren und Zündsystemen. Verifiziert werden sollte dabei die Eindringleistung des Penetrators und die Strukturintegrität während des Eindringvorganges sowie die Schockbeständigkeit des verwendeten Sprengstoffes. Die gewählten Auftreffbedingungen entsprachen den aus den theoretischen Simulationen errechneten Worst-Case-Bedingungen. Die verwendete Winkeldefinition 20°/+2° ersehen Sie aus Skizze 3. Darin ist auch dargestellt, wie der Schußkanal nach Aufprall auf das Ziel abknickt und dann einen Winkel von ungefähr 27° zur Normalen einnimmt. Zur Simulation des Attack-Winkels wurden die Penetratoren im Treibspiegelsystem des Beschleunigungsrohres schräg eingebaut.

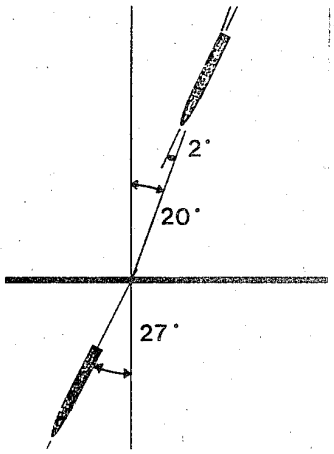

Skizze 3

Obliquitywinkel: 20°
Attackwinkel: +2°
(+ bedeutet "nose up")

Eindringleistung

Skizze 4

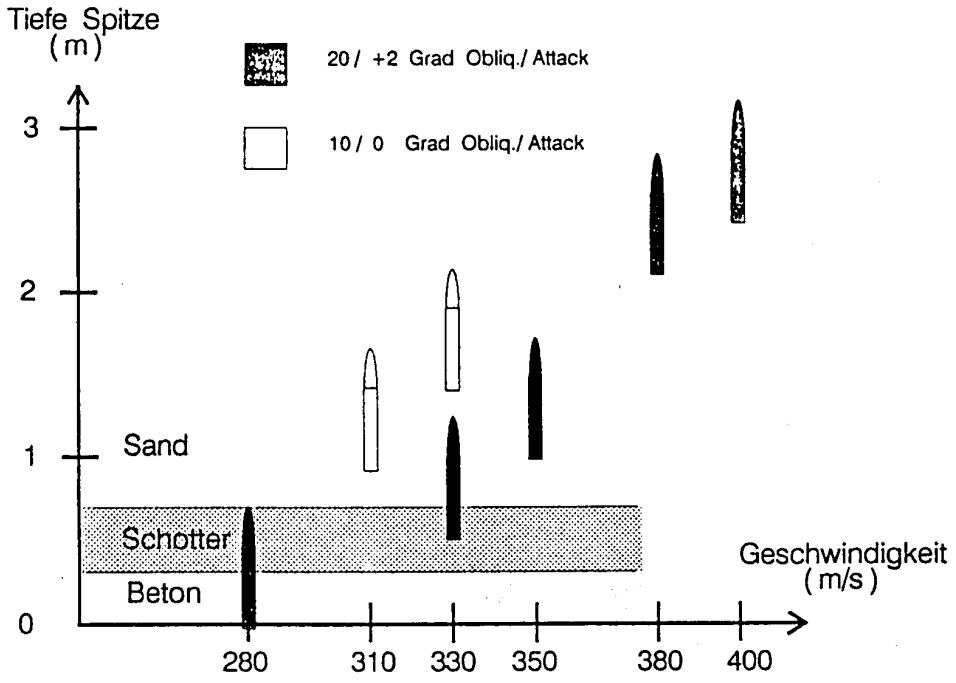

Skizze 4 zeigt die unter zwei Auftreffbdingungen ermittelten Eindringleistungen über der Geschwindigkeit. Auffallend ist die starke Abhängigkeit der Endtiefe von den Auftreffbedingungen. Beim Durchdringen des Betons erfährt der Penetrator eine starke Biegebeanspruchungen und Wechselwirkungen der Hülle mit dem Betonkrater. Nach Bergung des Versuchsmusters weist dieses starke Schleifspuren und plastische Verformungen auf.

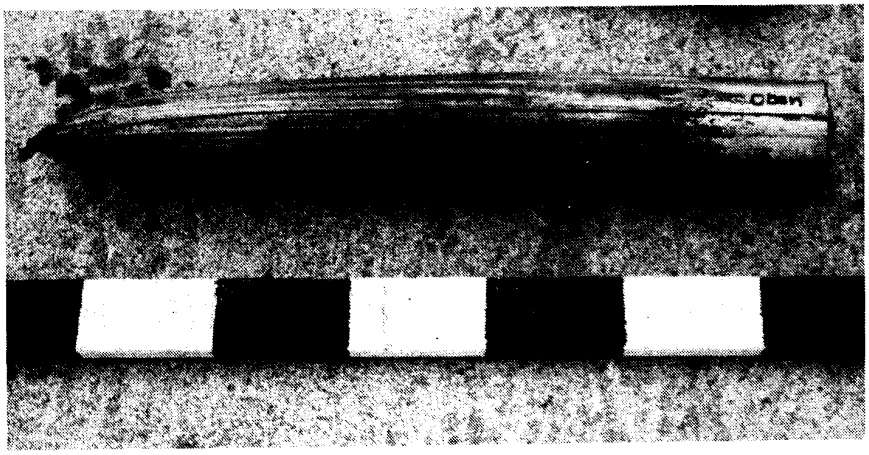

Bild 2
Versuchsmuster nach Verschuß

Insbesondere erwähnenswert ist der sogenante " Tailslap-Effekt". Gemeint ist damit ein peitschenartiges Ausschwingen des Hecks des Penetrators, unmittelbar bevor dieses in die Betonoberfläche eintaucht. Dabei schlägt das Heck hart gegen den Beton an, wodurch die Struktur und das Zündsystem gefährdet werden.

Penetration und Sprengleistung

Aus den Ergebnissen der Vorversuche wurde beschlossen, die vollscharfen Wirkversuche unter 10°/0° und mit einer Auftreffgeschwindigkeit von 310 m/s durchzuführen. Verschiedene Sprengtiefen (DOB) wurden dadurch realisiert, daß dem Zündsystem entsprechende Zündverzögerungszeiten (ab Impact) programmiert werden konnten. Durchgeführt wurden drei vollscharfe Schießversuche (Test Nr. 3, 4, 6) mit unterschiedlichen Verzögerungszeiten und ein statischer Sprengversuch (Nr. 5) zur Überprüfung der Zielreaktion bei exakt bekannten DOB. Tabelle 1 gibt einen Datenüberblick.

Tabelle 1

Cratering Tests/Sept 88/WTD 91 Meppen Range
Cratering Comparison - KERP, 12 kg

Test-Nº	3	4	6	5
	S 21171	S 21172	S 21173	D 53336
Test type	dyn.	dyn.	dyn.	static
fuze delay	6.6 ms	7.7 ms	9.1 ms	——
DOB	65cm (estim)	70cm (estim)	75cm (estim)	66cm
crater type	open	open	cavity	open
-max crater diam/surface	2.7 m	2.2 m	0.6 m	2.9 m
-crater diam/30cm depth	1.2 m	0,9 m	0.15 m	1.2 m
-crater depth	1.0 m	1.1 m	0.8 m cavity	1.0 m
max. upheave	≈ 2.5 cm	≈ 2.5 cm	≈ 4.0 cm	≈ 2.5 cm

Bei der Schadensbegutachtung werden die Durchmesser und Flächen des offenen Kraters und der angehobenen Betonoberfläche (Upheave) bewertet. Dabei gilt es, einen reparaturzeitoptimierten Kompromiß zu finden. Die statische Sprengtiefe DOB = 66 cm war aus Vorversuchen als guter Wert für den kombinierten Schaden bekannt. Beim Schießversuch Nr. 3 wurde die statische Sprengtiefe in eine Zündverzögerungszeit umgesetzt, um das theoretische Zeit-Eindringtiefenmodell zu verifizieren. Bei dieser Sprengtiefe tritt noch keine Kavernenbildung auf, sondern ein maximaler offener Krater. Bei den Versuchen 4 und 6 wurde durch eine längere Zündverzögerungszeit die Sprengtiefe erhöht. DOB = 70 cm bedeutet, daß der Ladungsschwerpunkt exakt in der Trennebene Gravel zu Sand liegt. Wie aus dem Kraterschnittbild zu ersehen, tritt dabei reduzierte Kraterbildung und eine beginnende Kaverne unterhalb der Betonplatte auf. Liegt der Ladungsschwerpunk nochmals tiefer, d.h. 5 cm unter der Schotterschicht Sand, tritt praktisch keine Kraterbildung mehr auf, sondern es bildet sich eine beachtliche Kaverne mit deutlich erhöhtem Upheave der Betonplatte.

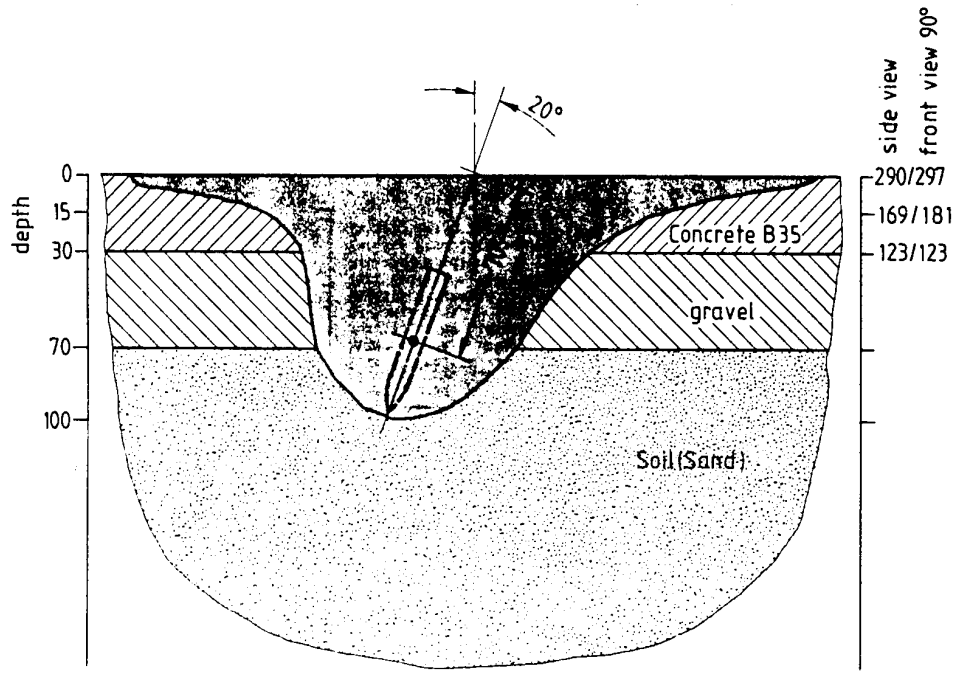

Test Nr. 5: Standsprengung mit DOB = 66cm

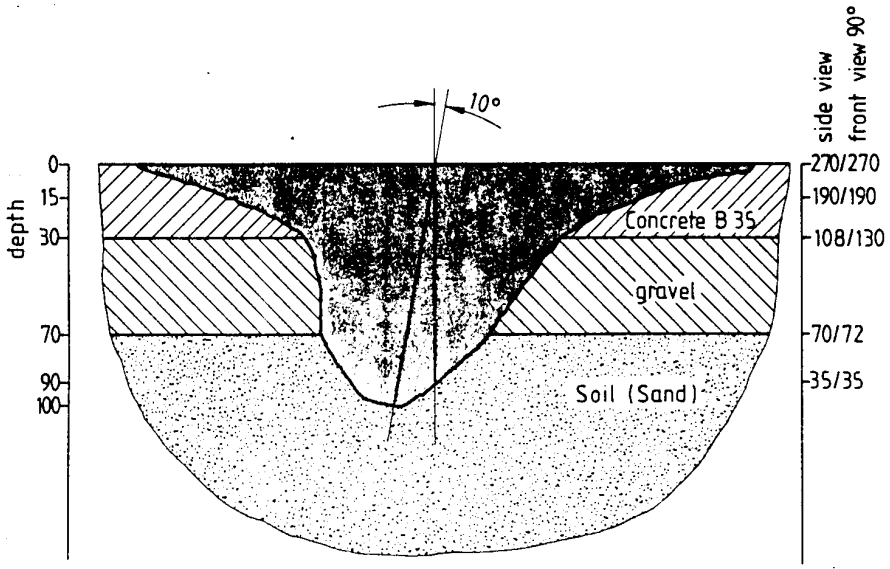

Test Nr. 3:Schießversuch *DOB = 65cm*

DOB = Depth of Burst
Betonoberfläche bis Schwerpunkt Sprengladung

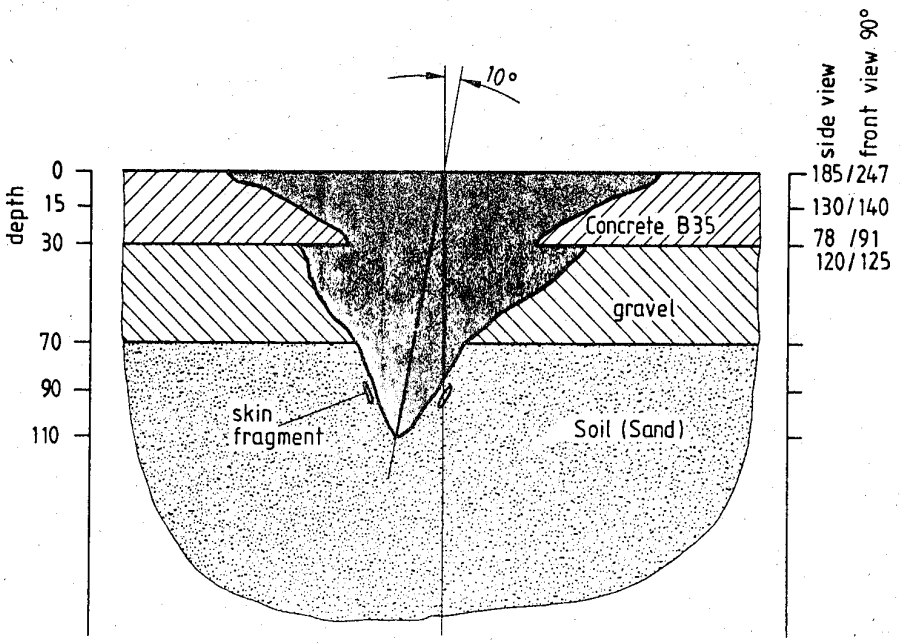

Test Nr. 4. Schießversuch *DOB = 70cm*

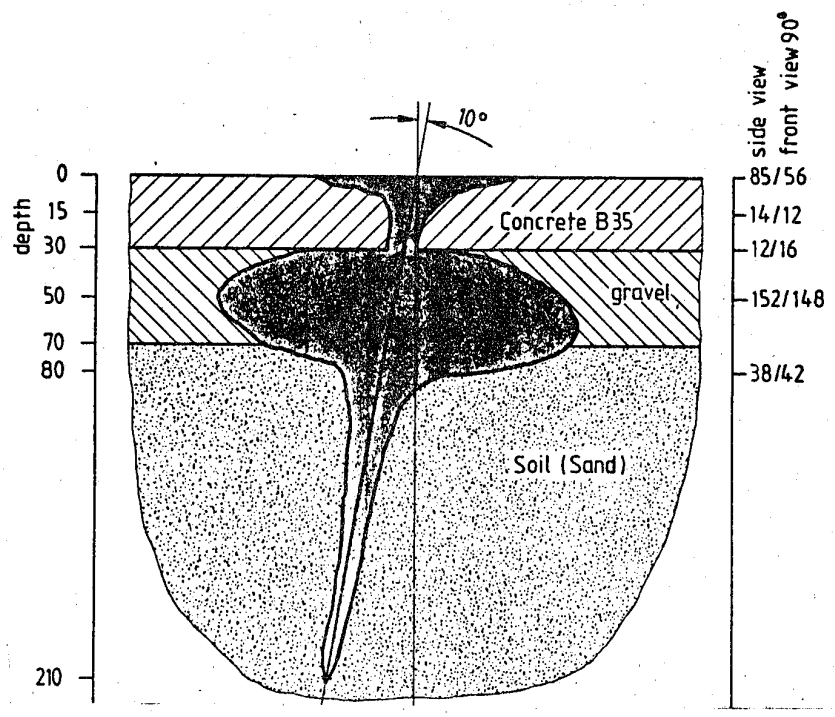

Test Nr. 6: Schießversuch *DOB = 75cm*

Skizze 5

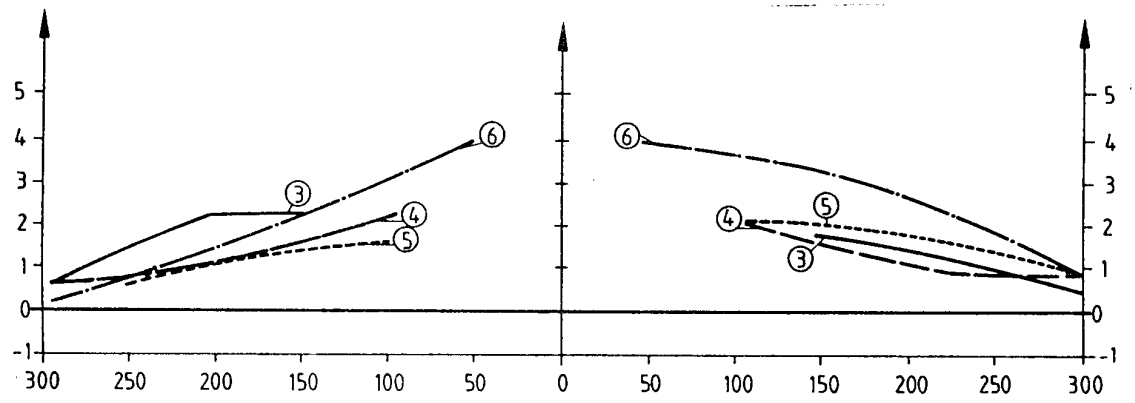

Darstellung des mittleren Upheaves im Querschnitt bezogen auf den Aufschlagpunkt.
Eine taktische Bewertung der Schäden wird an dieser Stelle nicht gemacht.

Schlußbemerkungen

1. *Es wurde gezeigt, daß die Übertragbarkeit von Standsprengdaten auf einen dynamischen Fall gegeben ist.*

2. *Die Versuche zeigen die erzielbare Bandbreite der erreichbaren Schadenskombination eines Penetrators mit ca. 2 kg Sprengstoff gegen Standard-Runwayziele.*

HIGH VELOCITY PROJECTILE PENETRATION INTO CEMENTITIOUS MATERIALS

William F. Anderson, Alan J. Watson and Jeffrey Peters
Department of Civil and Structural Engineering
University of Sheffield, UK.

ABSTRACT

This paper describes instrumentation developed to examine in real time the events which occur when small arms rounds impact and penetrate mortar and concrete targets. Results from preliminary tests are given and discussed in conjunction with data from previously published work.

INTRODUCTION

Numerous predictive equations, mostly empirical, have been published for projectile penetration into different materials. These usually relate the depth of penetration of the projectile to its mass, size and shape, impact velocity and projectile and target material properties. Inherent in all these equations is the assumption that if impact is normal to the target surface then the penetration will continue along the line of the projectile flight so long as the material is homogeneous. However, most construction materials, such as concrete, are not homogeneous, although if the projectile is orders of magnitude larger than the aggregate size, the concrete may be considered to act as a homogeneous mass. This is not the case with small projectiles, such as small arms rounds, impacting concrete or similar heterogeneous materials.

During studies to optimise fibre reinforced concretes for sprayed application (1) and rock polymer composites (2,3) for rapid construction or upgrading of protective structures, impacted targets were sectioned to examine and quantify the damage. It was found that rarely did the projectile continue through the material along the line of its original flight path. In extreme cases the projectile was found to have come to rest having turning through 180° so that it was pointing towards the impact face. In a number of targets the hardened steel core of an armour piercing bullet was found to have broken, possibly as a result of the stresses applied to it as it tried to change direction rapidly within the target.

Post test inspection of targets has shown damage to consist of an impact face spall crater, a projectile burrow and, depending on the thickness and nature of a target, a back face scab as shown in Figure 1. It has been noted that projectile deviation appears to start at the bottom of the impact face spall crater. Tentative explanations have been put forward for the formation of these features based on post test examination of specimen damage.

However, it is unlikely that the damage features are produced independently and a complex sequence of events occurs. For example, the impact face spall crater is probably produced partly by bursting as the projectile initially penetrates the target surface and partly by tensile failure as the compressive stress wave generated at impact is reflected as a tensile wave from the back face of the target. The projectile while decelerating will be penetrating through a zone of material which is being

subjected to a complicated stress regime as stress waves are reflected from the specimen boundaries. A fundamental study to examine the real time events which occur during impact and penetration has been initiated and the first stage has been the development of reliable methods of measuring and recording transient data.

TEST ARRANGEMENT

The projectiles being used are 7.62 armour piercing (AP) bullets with a bullet length of 33.3mm and a mass of 9.60 - 9.90g. They have a hardened steel core with length 23.8mm, diameter 6.10mm and a mass of 3.74g. These are fired from a 7.62mm proof barrel attached to a pressure housing incorporating a breech, firing pin, bolt and trigger mechanism with safety catch. The arrangement is mounted on a rigid steel frame bolted to the range floor. Firing is carried out by activating an 11.4 kgf solenoid with 18mm stroke length which is linked to the trigger. The solenoid is activated from a remote control room by a firing box with arming key either manually by pressing an off-biased switch or automatically by a high speed camera when it is ready to photograph the event.

Twenty metres down range the target is held in a rigid frame with edge support only. Mortar and concrete targets 450mm square and 125mm thick are being tested. In addition to conventional square targets, circular targets 450mm in diameter and 125mm thick are being tested to assess the influence of different stress wave fields on the events.

INSTRUMENTATION

Initial studies are concentrating on examining the deceleration of the projectile during penetration of the target. In these studies it is essential to know the projectile velocity prior to impact, the moment of impact on the front face of the target and the times after initial impact at which the projectile reaches various positions within the target.

Velocity measuring device

To ensure that the projectile flight is not disturbed during velocity measurement a non contact device is required. The reliability of inexpensive conventional collimated light beam systems which trigger a timer is suspect because the light beam is not completely extinguished, so a new low cost laser based system has been developed. In addition to high accuracy and a 100% success rate it was specified that the new measuring system should be low cost, easy to set up and check and, most importantly, should be able to accommodate deviations of the projectile from the anticipated flight path.

Laser based velocity measurement rigs have been used to measure the exit velocity of projectiles from devices such as gas guns. This system requires accurate positioning so that it is certain that the laser beam will be broken by the projectile. The accuracy of standard 7.62mm AP projectiles 20m downrange from the barrel is such that the success rate for this type of system would be very low. The new laser based system which has been developed allows a deviation of the projectile of between 15 and 20 times the diameter of the projectile but still gives full extinction of the beam as the projectile passes.

The principle of the laser triggering device is shown in Figure 2 and consists of a nominal 0.8mW Helium Neon laser, two front silvered mirrors (25mm x 75mm and 25mm x 100mm) fixed to adjustable mounts fitted on a flat dural sheet and a detector. The mirrors are aligned parallel to each other and the laser pointed to strike one at an angle of about 2°. As shown in Figure 3 the reflections form a triangular grid with an edge spacing of $2H \tan \Theta$ where H is the separation of the mirrors and Θ is the angle of incidence of the laser beam. The central band of the grid has a spacing of $H \tan \Theta$.

The detector output requires as high a slew rate as possible so that consistency in the triggering of the timer can be obtained between tests. This is achieved by use of an optoschmitt device which incorporates power supply conditioning components, an amplifier and a schmitt trigger in a single T0-18 device. As the projectile breaks the laser beam the optoschmitt output voltage drops.

However the ogive shaped nose of the bullet and the laser grid pattern mean that it is impossible to detect exactly when the tip of the nose breaks the laser plane. This problem is overcome by triggering a timer when the flat rear face of the bullet clears the laser plane giving a positive voltage jump as the laser path is re-established.

Two plates with laser trigger systems fitted are mounted 950mm apart on a tubular steel frame bolted to the range floor just uprange of the target. From the time it takes for the projectile to pass between these triggers the pre-impact projectile velocity is determined.

Impact detector

In order to establish the instant of projectile impact on the front face of the target as a time base reference, a trigger has to be stuck to the impact area of the target. One form of trigger (Type I) consists of two sheets of aluminium kitchen foil separated by an air gap a few millimeters wide. When the projectile perforates the front aluminium sheet a contact is made with the second sheet completing a circuit. Another form of trigger (Type II) consists of an array of bundles of optical glass fibres glued to the target impact area. If light is passed through the fibres it will be extinguished when a bundle of fibres is broken. This can be recorded photographically as described in the next section.

Embedded detectors

Initial attempts to estimate deceleration by monitoring the discharge on perforation of capacitance gauges, consisting of a 0.1mm thick brass plates separated by a sheet of paper, embedded at different positions within the target have been described by Anderson et al (1). Problems with these were that they were difficult to keep in position during concrete casting, they formed planar discontinuities within the concrete and, although relatively thin, they undoubtedly affected the projectile deceleration as it perforated them.

In an attempt to develop a less disruptive way of monitoring what happens within the target as the projectile impacts and penetrates, arrays of optical glass fibres have been cast within mortar and concrete targets at different distances from the impact face. The fibres are used in thin bundles of 20-30 fibres each fibre being 40mm diameter. Because the glass fibres are of a material similar to the aggregate, it is suggested that instrumented targets will behave in a similar way to non-instrumented targets.

Initial trials used optical fibres cast within mortar targets in which there is little deviation of the projectile during penetration. During preparation of the specimens stainless steel hypodermic tubes (2.65mm o.d., 2.00 mm i.d.) are positioned in the mould and the mortar or concrete cast and vibrated around them. Three metre long bundles of fibres are threaded through the tubes, the tubes carefully withdrawn from the mould and the concrete vibrated further. During impact testing one end of each bundle of optical fibres is fed into a box with reflective sides and illuminated by butting up to a 600W bulb. The fibres have a relatively low shear resistance and are easily broken by the passage of the projectile thus interrupting light transmission through them.

The large number of fibre bundles included in the target would require a large number of optoelectronic devices and recording channels if they were to be monitored electronically. To overcome this limitation, a photographic technique, shown diagrammatically in Figure 4, has been developed to record the extinction of the light passing through the fibre bundles.

A 16mm high speed camera has been modified to run in pseudo-streak mode by optically bypassing its framing prism and projecting the light transmitted by the fibres through a standard 50mm camera lens directly onto the film which is moving at a framing rate of 3000 frames per second. At this speed, using a film analyser, timing with a resolution of 1μs may be obtained.

When the Type I impact detector fitted to the front face of the target is impacted it completes the circuit for a flash gun with a propagation delay time of 63 μs $\pm$ 2 μs . This flash pulse is guided to the camera array by a separate bundle of fibres, as shown in Figure 4, so that the moving film is

marked and this acts as a datum. When the Type II impact detector is used the extinction of the light from the front face fibre bundle as recorded on the film acts as a datum. This datum is used for measurement of the timings to the extinction of light through other bundles of fibres. After testing the specimens are sectioned to record the position of each bundle of fibres and hence estimate the deceleration of the projectile through the target.

TEST RESULTS

Velocity measurement

The new laser based velocity measuring device has worked with a 100% success rate and for the 7.62 AP projectiles used has recorded velocities ranging from 851 m/s to 867 m/s

Embedded detectors

When the high speed film is developed it shows a series of lines representing the light from each of the bundles of optical fibres. This may be viewed frame by frame with a film analyser. The lines terminate as each bundle of fibres on the front face and within the target is broken. Representation of this is shown in Figure 4. By relating the time at which the lines terminate to the datum, and knowing the distance between each fibre bundle, it is possible to draw a fibre depth - time plot as shown in Figure 5.

DISCUSSION

To aid understanding of the mechanisms involved when a small arms round impacts and penetrates cementitious materials work has concentrated on developing a non intrusive method for recording times of events within the target.

From the data given in Figure 5 it is possible to estimate velocities. The plots for mortar targets (Tests 1 and 2) indicate an initial linear portion up to a depth of approximately 40mm into the target. The average velocity over this portion works out at 1000m/s, which is faster than the projectile impact velocity of approximately 860m/s. When the projectile impacts the specimen a compressive stress wave travels through the target with a velocity whose order of magnitude is about 3600 m/s. The impact causes cracking to the mortar and Yoshiki et.al.(4) has suggested the theoretical limit of brittle crack propagation velocity, c, in steel is

$$c = 0.25\, C_0 \sqrt{\frac{(1 - \nu)}{(1 + \nu)(1 - 2\nu)}}$$

where C_0 = stress wave velocity in a long rod of material
ν = Poisson's ratio

Assuming that this relationship also holds for concrete with a Poisson's ratio of 0.16 and C_0 of 3600m/s then the theoretical crack velocity is 928m/s.

It is therefore suggested that bundles of fibres in the front part of the target are being broken by cracking in advance of the projectile. At a depth of around 50mm, which is about the depth of the spall crater measured in the post test inspection, the average velocity is below that of the projectile in flight and since the shock wave and crack velocities are in excess of the projectile velocity it appears that beyond depths of about 40mm to 50mm the fibre bundles must have been broken by the penetrating projectile forming its burrow. Some deceleration occurs around the bottom of the spall crater and the projectile continues to penetrate forming a burrow with an average velocity between 50mm and 80mm of 545 m/s. Thereafter rapid deceleration stops the projectile within the next 15-20 mm.

Also plotted in Figure 5 are results (Tests V3 and V4) obtained by Armstrong (5) using brass sandwich capacitance gauges to monitor 7.62 AP penetration of concrete with maximum aggregate size

of 10mm. These detectors will not be discharged by crack propagation so the velocities obtained are actual projectile velocities. The intrusive nature of these detectors will have caused retardation of the projectile and the detectors are likely to reinforce the concrete so that less cracking could occur at the front of the target. The calculated velocities are therefore lower than for the mortar targets but it is interesting to note that there is also little velocity reduction in the spall crater zone and rapid deceleration as the bullet comes to rest.

CONCLUSION

Although the technique is still being refined and current interpretation is somewhat speculative the potential of optical glass fibres as non disruptive devices for detecting transient events in cementitious materials is clearly demonstrated.

ACKNOWLEDGEMENTS

The authors would like to express their thanks to the Science and Engineering Council and the Ministry of Defence (RARDE, Christchurch) who are jointly funding this work under Grant Number GR/F 20735.

REFERENCES

1. ANDERSON, W.F., WATSON, A.J. and ARMSTRONG, P.J. 'Fibre reinforced concretes for the protection of structures against high velocity impact.' Proc. Int. Conf. on Structural Impact and Crackworthiness, Imperial College, London, 1984, Vol. 2, pp 687-695.

2. ANDERSON, W.F., WATSON, A.J., JOHNSON, M.R. and McNEIL, G.M. 'Optimisation of rock/polymer composites to resist projectile penetration.' Materials and Structures, Vol 16, 1983, No. 95, pp 343-352.

3. ANDERSON, W.F., WATSON. A.J. and GALLAGHER, A.J. 'Use of rock/polymer composites as protective materials.' Proc. 4th Int. Symp. on the Interaction of Non-Nuclear Munitions with Structures.' Panama City Beach, 1989, Vol 1, pp 80-85.

4. YOSHIKI, M., KANAZAWA, T. and ITAGAKI, H. 'An analysis of the brittle fracture propagation.' Proc. Soc. for Exp. Stress Analysis, XXIII Part 2, 1966.

5. ARMSTRONG, P.J. 'Projectile penetration into fibre reinforced concrete.' Ph.D Thesis, University of Sheffield, 1987.

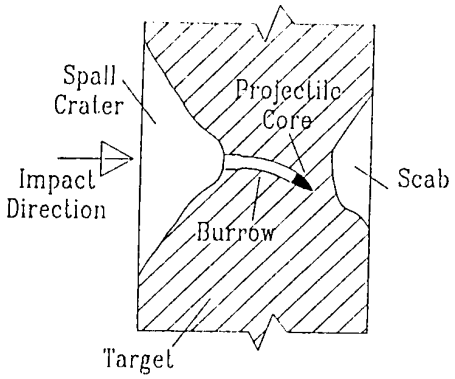

Fig. 1 Typical Damage

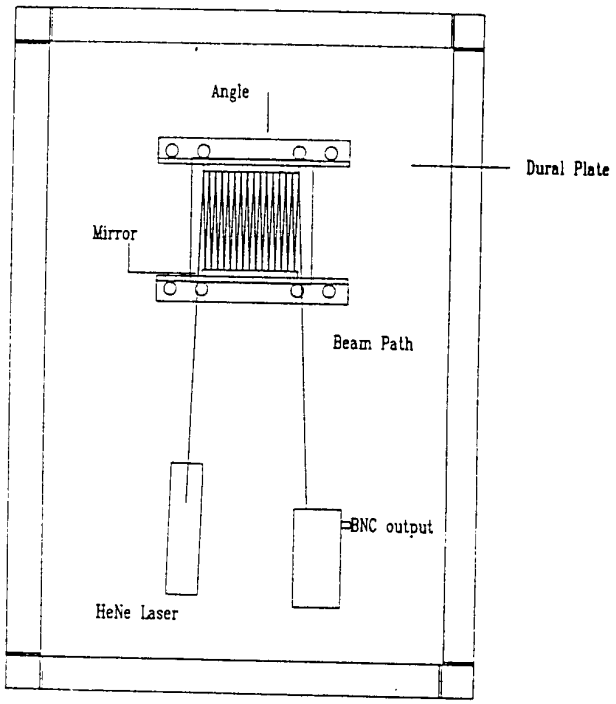

Fig. 2 Laser Triggering Device

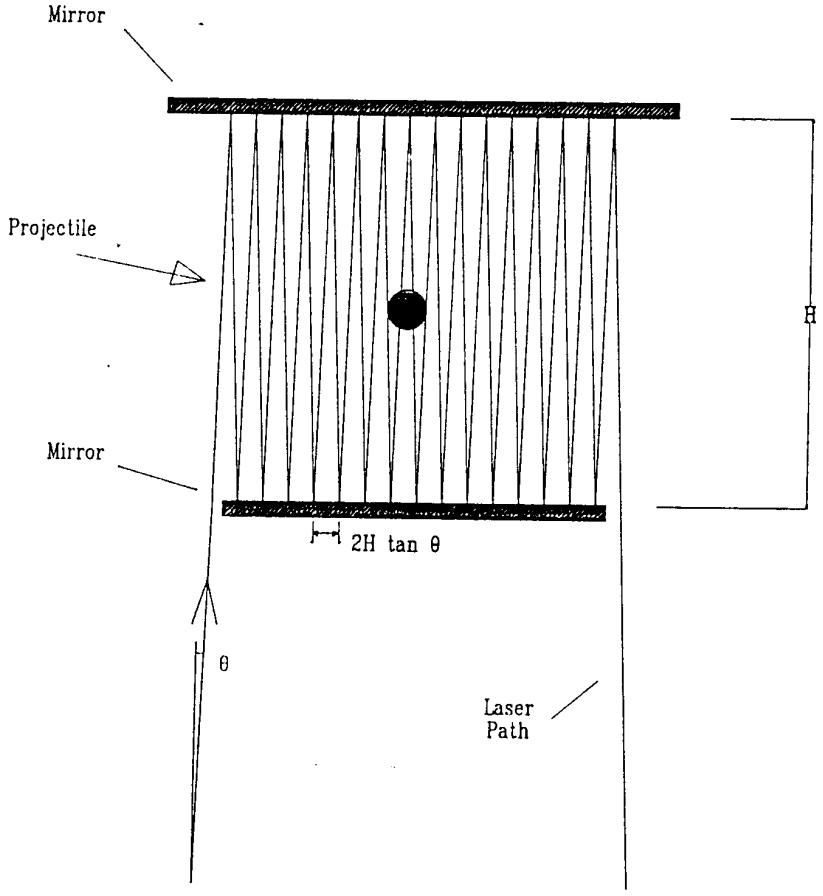

Fig. 3 Principle of Laser Triggering Device

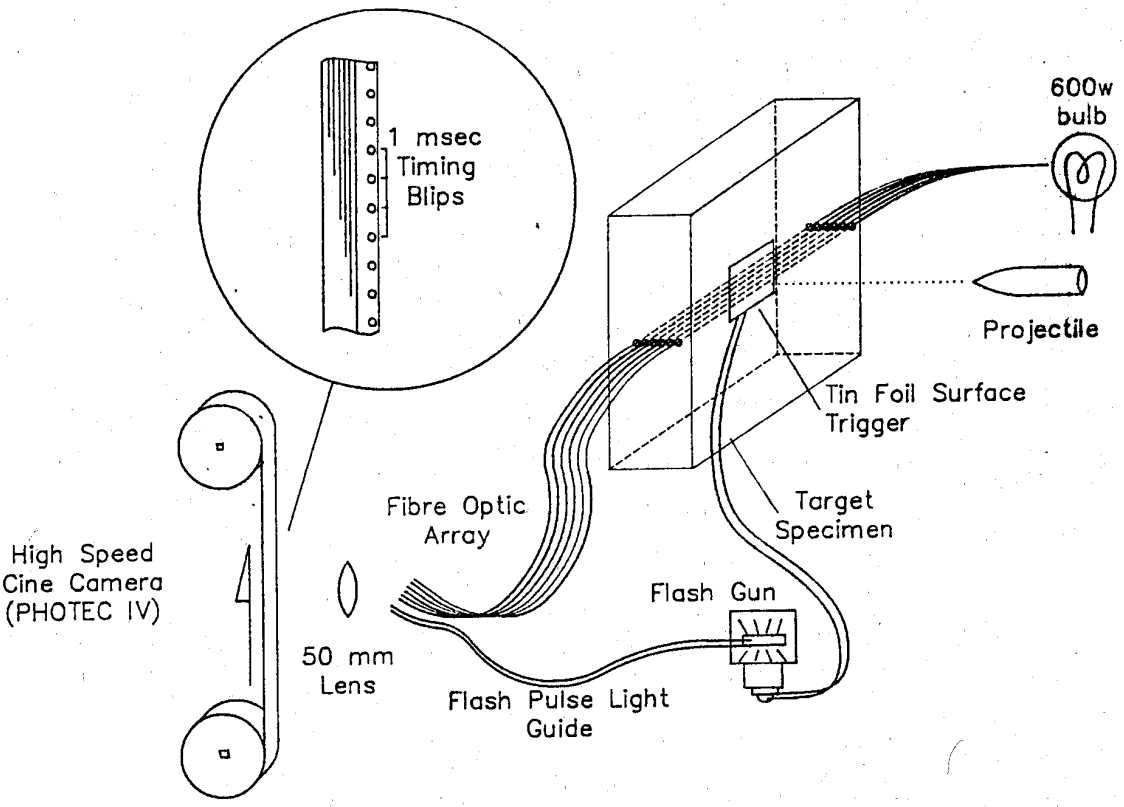

Fig. 4 Use of Embedded Fibre Optic Detectors

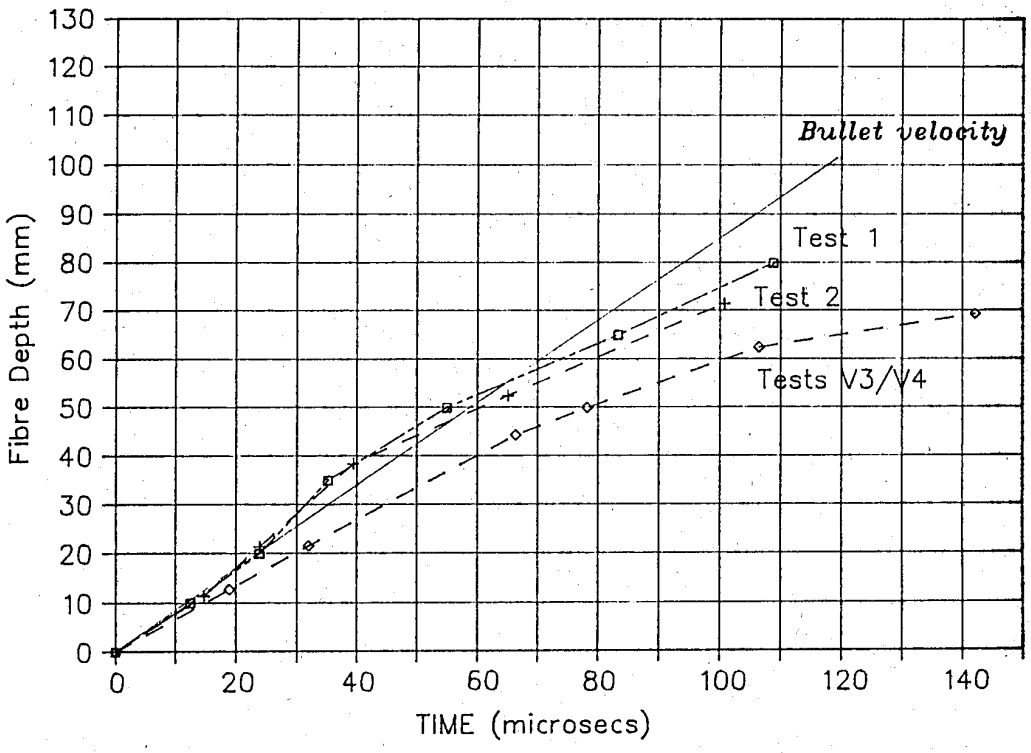

Fig. 5 Detector Depth Time Plot

EFFECTIVENESS OF STEEL BARS FOR INDUCING YAW IN THE FLIGHT PATH OF A SUBSCALE ARMOR-PIERCING PROJECTILE

by

James D. Cargile and Toney K. Cummins

Research Civil Engineer and Civil Engineer
U.S. Army Engineer Waterways Experiment Station
3909 Halls Ferry Road, Vicksburg, Mississippi, USA 39180-6199

ABSTRACT

Yaw angles of several degrees can cause a projectile to break up or deflect, or reduce its penetration depth when it impacts a hard target. Fourteen subscale tests were conducted to investigate the use of steel bars to induce yaw into the flight path of an armor-piercing (AP) projectile traveling with a velocity of approximately 365 m/sec. The tests investigated the effect of bar ductility, bar size, connection type, multiple impacts, spacing between two additive impact bars, and travel distance after bar impact on the induced yaw. The bar ductility and connection type did not affect the induced yaw. Impact with two closely spaced bars (additive impact) effectively doubled the induced yaw (relative to a single bar impact). Decreasing the bar diameter from 0.25 to 0.10 calibers (bar diameter/projectile diameter) decreased the induced yaw by a factor of about four.

Five subscale penetration tests were conducted on two yaw-inducing screens to investigate the concept's application as a component of a protective system. One screen consisted of three layers of 0.25 caliber bars and one screen consisted of nine layers of 0.10 caliber bars. The layers of bars were orthogonally alternated to induce yaw in two planes. After going through the yaw-inducing screens, the AP projectiles impacted concrete targets. In two tests with the 0.25 caliber bar screen and one with the 0.10 caliber bar screen, the projectile broke upon impact with a concrete target; the yaw at impact was at least 20 degrees. All five tests had penetration depths significantly less than a baseline test with no yaw-inducing screen.

SCALED UNDERGROUND COMPUTER CENTER TEST AND ANALYSIS

John A. Collins, Air Force Armament Laboratory, Eglin AFB, FL
Martin J. Schmidt, Air Force Armament Laboratory, Eglin AFB, FL
Frank A. Maestas, Applied Research Associates, Inc., Albuquerque, NM
John C. Galloway, Applied Research Associates, Inc., Albuquerque, NM
Larry L. Brown, Denver Research Institute, Denver, CO
James A. Keller, Denver Research Institute, Denver, CO

ABSTRACT

A scaled test program was conducted by Denver Research Institute (DRI) for the Air Force. The objective of the test effort was to validate methodology embodied in the computer code Effectiveness/ Vulnerability Analysis in Three Dimension (EVA-3D) developed by Applied Research Associates (ARA). ARA performed the pre and post analysis.

The test article, a scaled underground computer center (SUCC), was built and placed in the DRI test facility. An instrumented projectile was fired at the article. Twenty-four tests were performed. This paper provides the results of the first seventeen tests and the analysis effort performed thus far.

INTRODUCTION

Conventional penetrating weapons are being designed for increased depth of penetration into targets. Existing methodology has yet to be validated for the realistic multiple impacts/perforations that can result. Three-dimensional changes in the weapon terradynamics are predicted by the Effectiveness/Vulnerability Assessment in Three-Dimensions (EVA-3D) code. The weapon terradynamics were determined from SUCC test data and compared to calculational results; and where necessary EVA-3D modified. This paper provides the results of this effort.

BACKGROUND

This section provides background information on EVA-3D and the test article.

1. EVA-3D

Effectiveness/Vulnerability Assessment in Three Dimensions (EVA-3D) is a Monte Carlo based computer code that:

- Samples the delivery statistics which are specified as input parameters;
- Performs weapon trajectory calculations for the specified target;
- Determines the burst points based on the trajectory calculations and the specified fuze option;
- Calculates various weapon effects;
- Evaluates kill by comparing the produced environment to the components capacity; and
- Accumulates statistics

References 1 and 2 provide a detailed discussion of the methodology incorporated in EVA-3D, however, pertinent terradynamic capabilities will be discussed here.

Three-dimensional weapon terradynamics is accomplished in EVA-3D by one of two options. The first option uses the results of Sandia National Laboratories (SNL) computer code Simplified Analytical

Model for Penetration with Lateral Loading (SAMPLL) to predict changes in trajectory angle, angle of attack, and failure of a weapon as it travels through a target. SAMPLL is a two-dimensional code that calculates, as a function of time, the distribution loads on a weapon, translational and rotational motion, and the weapons's structural response to the applied load (Reference 3). For a specific weapon, SAMPLL results are obtained for various concrete slab thicknesses, weapon trajectory angles, weapon angle of attack and impact velocities. These results are analyzed, distilled, and the resulting critical parameters placed in a block data structure within the EVA-3D computer code. Thus, when a weapon impacts a given concrete section, the appropriate values for change in trajectory angle and angle of attack are interpolated from the data structure.

The second option available to treat weapon behavior in EVA-3D is a time marching curvilinear trajectory module. This module is a slightly modified version of the computer code PENCO-3D developed by Mr. Dan Creighton, Waterways Experiment Station (WES). The PENCO-3D module in EVA-3D Version 1.3 calculates the penetration of a rigid non-spinning axisymmetric weapon into various target media. It is used to track weapon behavior (trajectory angles, angle of attack, angular acceleration, angular velocity and velocity) through the concrete, soil, and air mediums within the target. The PENCO-3D module uses empirically based equations to calculate the resistance to penetration and the resulting force on the projectile itself. The forces acting on the rigid body projectile are used to determine the projectile trajectory. The resistance pressure for soil is a function of the weapon nose shape, weight, and velocity and the material penetrability number (S number). The resistance pressure for hard mediums is based upon a cavity expansion approximation and is a function of the same weapon properties described above and the density and yield strength of the material.

The cavity expansion model used in EVA-3D was adapted from the techniques developed by Dr. Michael Forrestal, Sandia National Laboratories (Reference 4). The loading stress on each element of the projectile is:

- **CONCRETE (from LUK and Forrestal, SNL 1987)**

$$\sigma_n = Y (A + B V_n^2)$$

where A = 2.81 for linear locked hydrostat (vol. stain = .04)

$$B = \frac{\rho}{Y_n^2} \left[\frac{3Y}{E} + .04 \left(1 - \frac{3Y}{2E}\right)^2 + .10\right]$$

$$\gamma = \left[\left(1 + \frac{Y}{2E}\right)^3 - .96\right]^{1/3}$$

ρ is density
Y is yield strength
E is Young's modulus
V_n is the normal velocity component of the element

- **REINFORCING BARS**

$$\sigma_s = \sigma_n + 3Y$$

- **FRICTION**

$$\sigma_t = n \sigma_n$$

where n is a coefficient of friction.

The force on an element F_i, is

$$F_i = n (\sigma_s + \sigma_n) \, dA_i$$

where dA_i is the incremental area of the element

If reinforcing bars are not in contact with the element then σ_s is zero. It should be noted that the equation is for loading stress due to the reinforcing bars, σ_s, is extremely elementary.

TEST ARTICLES

Test articles are comprised of three precast reinforced concrete units stacked on each other. Each unit is 140" x 140" square with 8" thick outside walls. There are two rooms associated with each unit separated by a 4" interior concrete wall. The units have a 28 day concrete compressive strength of 5,000 psi. Figure 1 provides a plan view of the units. Reinforcing bars (No. 4) were placed at 6" centers.

The test articles were stacked together and placed on 24" of sand over a 9" concrete slab. A steel cylinder surrounded the article and sand backfilled around and above the article. Figure 2 provides a sketch of the cross-section of the test article. The entire assembly is then placed in the test facility. Figure 3 is a photograph of the DRI test facility.

The test facility is comprised of a steel tower 66' high. The tower is connected to the side of a hill with a steel walkway. A 105 mm howitzer is anchored above the tower and positioned to fire vertically. The gun does have the capability of firing projectiles at non-normal trajectories.

TEST EFFORT

The impact conditions for the testing program were varied according to the following parameters:

Initial Velocity	796, 928, 1125 fps
Trajectory Angle	90°, 80°, 70°
Angle of Attack	0°

Several tests were run with the projectile ricocheting off the interior of structure.

The projectile was a generic penetrator with the following characteristics:

Length	25.8 in
Diameter	3.35 in O.D.
Weight	35 lbs

A single axis accelerometer was located in the aft section of the penetrator. An ENDEVCO 7270A-200k piezoresistive accelerometer was included in the instrument package. WES designed and manufactured the packages.

TEST RESULTS

The location and path of the weapon were noted on each test. The instrument package within the penetrator was downloaded to obtain acceleration, velocity, and distance time histories.

Pre-test predictions were made using the PENCO EVA-3D module for each of the tests before the test occurred. Table 1 provides the test condition and the pre-test prediction. Table 1 also provides the difference on the final location of the projectile between the prediction and actual test location. Two differences are presented; one that includes the air voids and one that deletes the air.

Figure 4 provides the path of the projectile through the test article for the various tests. Note that paths are not straight for those tests where there was normal impact conditions. The projectile's path was altered due to the impact of the reinforcing bars in the concrete. Figure 5 is a photograph of the ceiling of the top test unit on TTF3. The deformation of the reinforcing bars can be seen in the photograph.

Although the final position of the projectile was predicted with reasonable accuracy, the effects of the reinforcing bars on the lateral loading of the projectile was not included. Modifications to the stress algorithms in EVA-3D were deemed necessary. These modifications are discussed in the paper entitled "Effect of Rebar on Penetration".

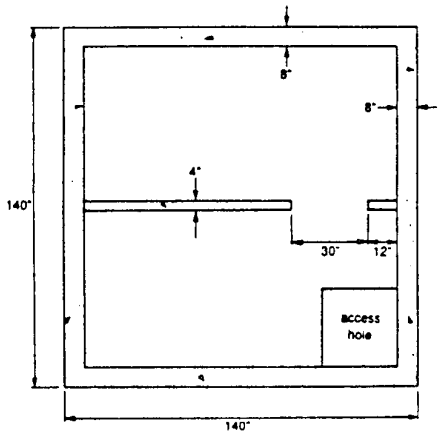

Figure 1. Plan View of Test Unit

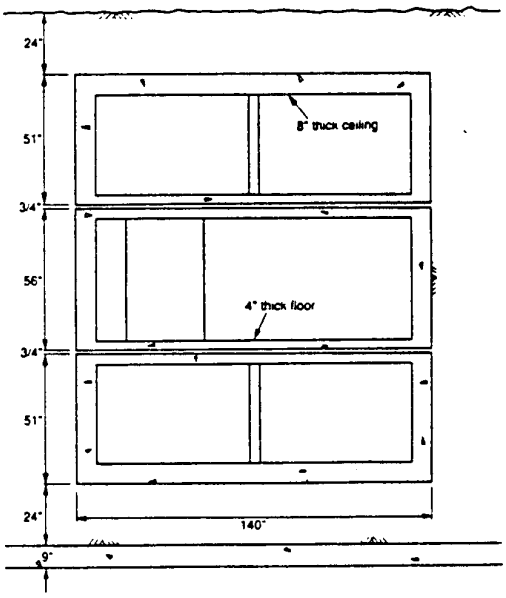

Figure 2. Section of Test Article

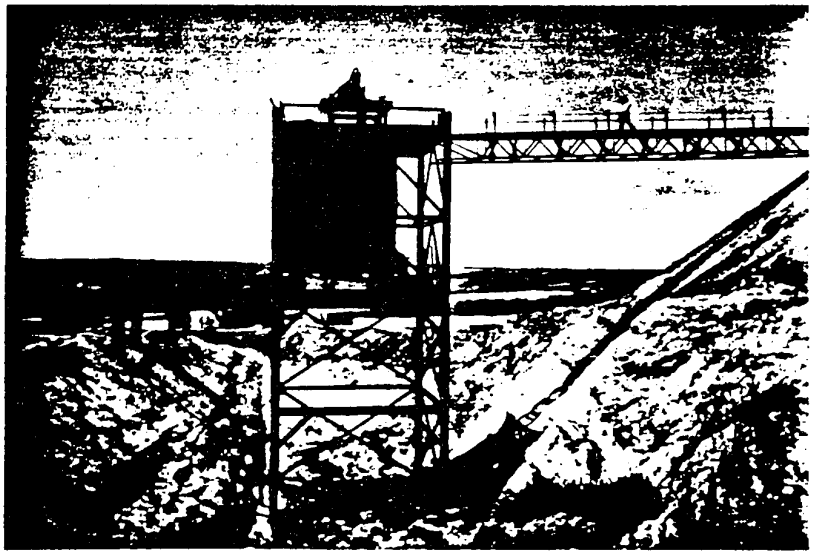

Figure 3. Photograph of DRI Test Facility

TABLE 1. TEST RESULTS

Test	Impact Conditions	Final Location of Penetrator in SUCC		Percent Difference of Depth of Penetration into Target	Percent Difference of Depth of Penetration Through Sand and Concrete
		Pretest Predictions	Test Results		
TTF3	928 ft/sec 90° trajectory angle 0° angle of attack	Nose embedded 6 inches into floor of bottom section	Nose within 1 inch of exiting floor of bottom section (no HDAS data)	- 1%	- 2%
TTF4	928 ft/sec 90° trajectory angle 0° angle of attack	Nose embedded 6 inches into floor of bottom section	Nose extends 4 inches below ceiling of bottom section (hits exterior wall) (no HDAS data)	29%	12%
TTF5	928 ft/sec 90° trajectory angle 0° angle of attack	Nose embedded 6 inches into floor of bottom section	Nose extends 2 inches into floor of bottom section (HDAS data)	2%	8%
TTF6	928 ft/sec 80° trajectory angle 0° angle of attack	Nose within 1 inch of exiting ceiling of bottom section	Nose extends 2 inches into ceiling of bottom section (HDAS data)	1%	2%
TTF7	1,123 ft/sec 90° trajectory angle 0° angle of attack	Nose extends 3 inches into bottom slab	Nose embedded 5 inches into bottom slab (HDAS data)	- 1%	- 2%
TTF8	1,123 ft/sec 90° trajectory angle 0° angle of attack	Nose extends 3 inches into bottom slab	Nose extends 3.5 inches into floor of bottom section (HDAS data)	18%	61%
TTF9	928 ft/sec 90° trajectory angle 0° angle of attack	Nose embedded 6 inches into floor of bottom section	Nose extends 3 inches into floor of bottom section (HDAS data)	2%	6%
TTF10	796 ft/sec 90° trajectory angle 0° angle of attack	Nose extends 1 inch into ceiling of middle section	Nose extends 3 inches below the ceiling of the bottom section (HDAS data)	- 45%	- 23%
TTF11	1,123 ft/sec 80° trajectory angle 0° angle of attack	Nose within 1 inch of exiting floor of bottom section	Nose embedded 6.5 inches into floor of bottom section (no HDAS data)	0%	1%
TTF12	928 ft/sec 90° trajectory angle 0° angle of attack	Nose embedded 6 inches into floor of bottom section	Nose extends 1.5 inches into floor of bottom section (no HDAS data)	3%	9%
TTF13	928 ft/sec 90° trajectory angle 0° angle of attack	Nose embedded 6 inches into floor of bottom section	Nose extends 2 inches into floor of bottom section (HDAS data)	2%	8%
TTF14	1,123 ft/sec 90° trajectory angle 0° angle of attack	Nose extends 3 inches into bottom slab	Penetrator stops in bottom slab (HDAS data)	< 3%	< 6%
TTF15	796 ft/sec 80° trajectory angle 0° angle of attack	Nose extends 1 inch below the ceiling of middle section	Nose extends 1.5 inches into floor of middle section (HDAS data)	- 38%	- 4%
TTF16	1,123 ft/sec 70° trajectory angle 0° angle of attack	Nose extends 1 inch into ceiling of bottom floor	Nose extends 1 inch into floor of bottom section	- 25%	- 8%
TTF17	796 ft/sec 90° trajectory angle 0° angle of attack	Nose extends 1 inch into ceiling of middle section	Penetrator hits spall zone of a previous shot in the floor of the bottom section (HDAS data)	- 53%	- 24%

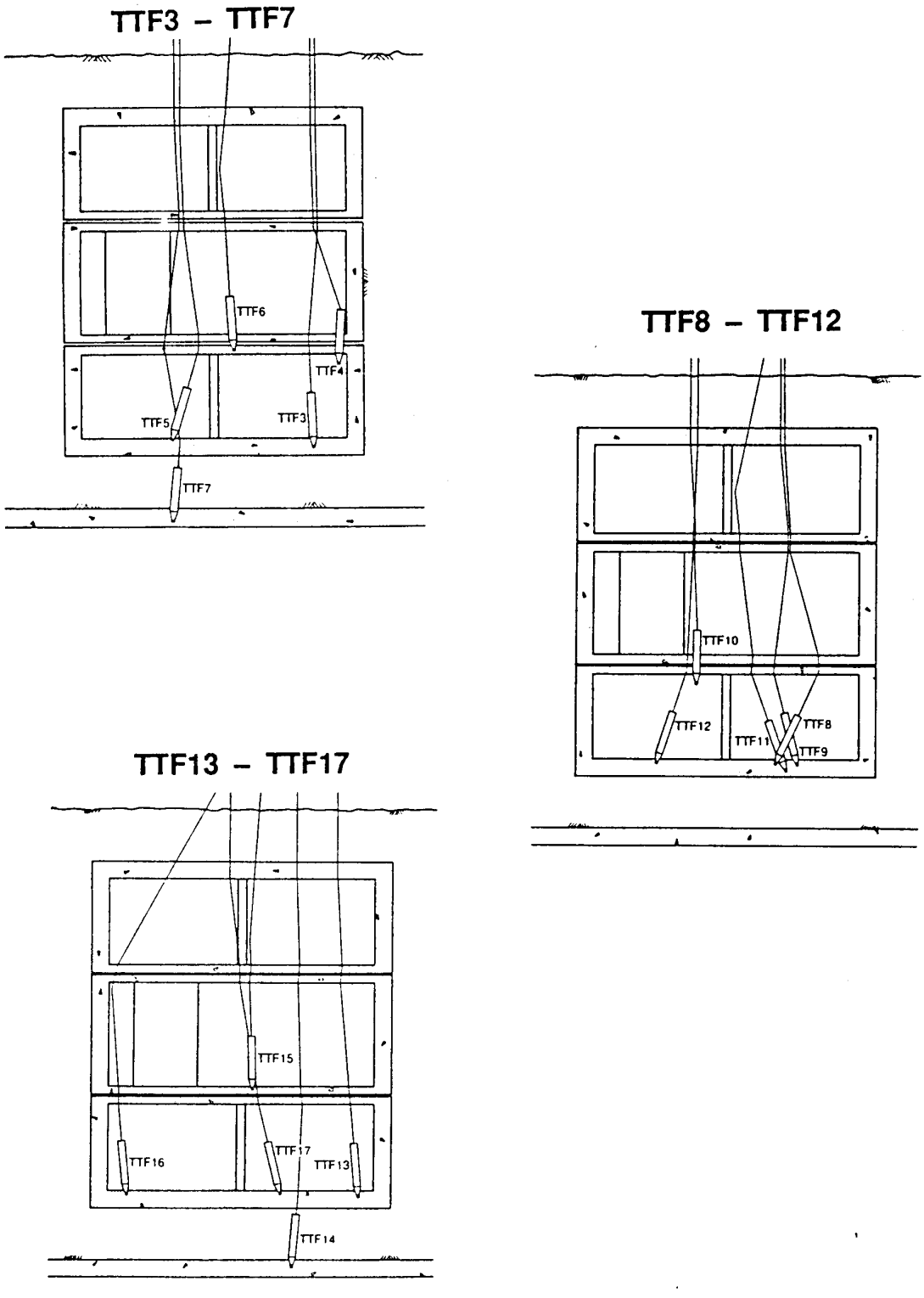

Figure 4. Section of Test Article with Trajectories Shown

POST TEST ANALYSIS

One post-test analysis was performed as of November 1, 1990. The others will be performed over the coming months. The one analysis, of TTF5, was conducted to validate the improvements to the lateral loading algorithms in the PENCO module of EVA-3D.

The velocity time history obtained from an integration of the accelerometer data for TTF5 is provided in Figure 6. It should be noted that the baseline shifts in the original data were removed. Also provided in Figure 6 is the interpreted velocity in the air voids (this was calculated from known distance traveled over known times).

Calculations using the modified PENCO-3D module of EVA-3D were made. In those calculations the reinforcing bars were placed in the actual position as occurred in the TTF5 test. The resulting velocity time is shown and compared to the test results in Figure 6.

The path of the projectile is shown in Figure 7. Note that lateral position of the projectile changes as the projectile impacts the various reinforcing bars. The actual lateral position compared well to the calculated lateral position.

CONCLUSION

The objective of the SUCC effort was to validate the terradynamics methodology embodied in the EVA-3D computer code. A series of tests were performed at the DRI test facility in Denver, Colorado. ARA performed pre-test predictions for each test condition. The calculations compared well to the test results in all areas except the lateral position of projectile. Modifications to the lateral loading algorithm in the PENCO-3D module of EVA-3D were made. The modifications were specifically related to the treatment of the loading due to the impact of reinforcing bars. A post test analysis of one test condition was made using the modified EVA-3D. The results of the analysis are encouraging. Post test analysis of the remaining tests will continue.

REFERENCES

1. Maestas, F.A., Galloway, J.C., and Collins, J.A., Development of Target Models, Vol. I, EVA-3D Version 1.0 Methodology, Draft Report to AFATL, Applied Research Associates, Inc., Albuquerque, New Mexico, 1 May 1989.

2. Maestas, F.A., Galloway, J.C., and Collins, J.A., EVA-3D Version 2.0 Methodology, Draft Report to AFATL, Applied Research Associates, Inc., Albuquerque, New Mexico, 15 May 1989.

3. Young, C.W. and Young, E.R., Simplified Analytical Model of Penetration with Lateral Loading, Sandia National Laboratories, SAND84-1635, Albuquerque, New Mexico, May 1985.

4. Luk, V.K. and Forrestal, M.J., Penetration into Semi-Infinite Reinforced Concrete Targets with Spherical and Ogival Nose Projectiles, Int. J. Impact Engineering, Vol. 6, No. 4, pg 291 - 301, 1987.

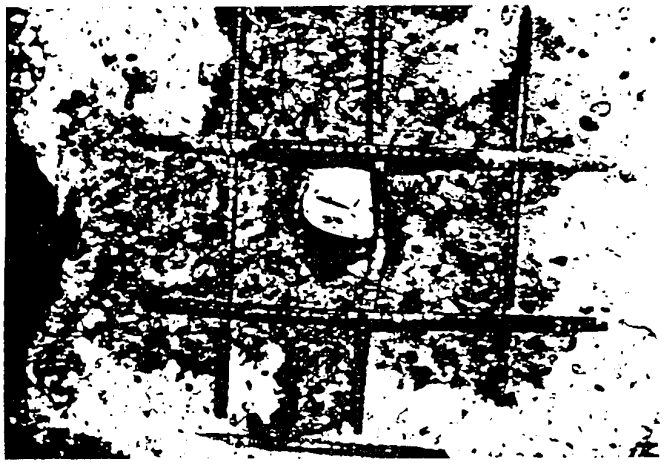

Figure 5. Photograph, Ceiling of top section on TTF3. Note the deformed reinforcing bars

Figure 6. Velocity Comparison (TTF5)

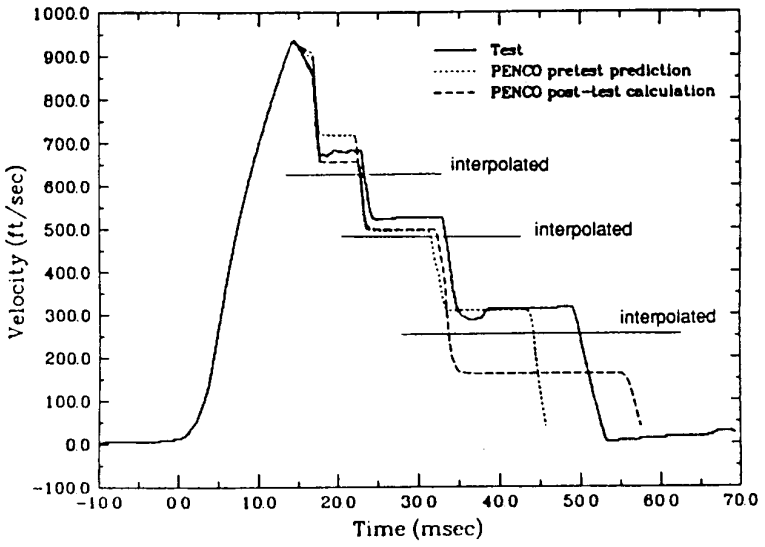

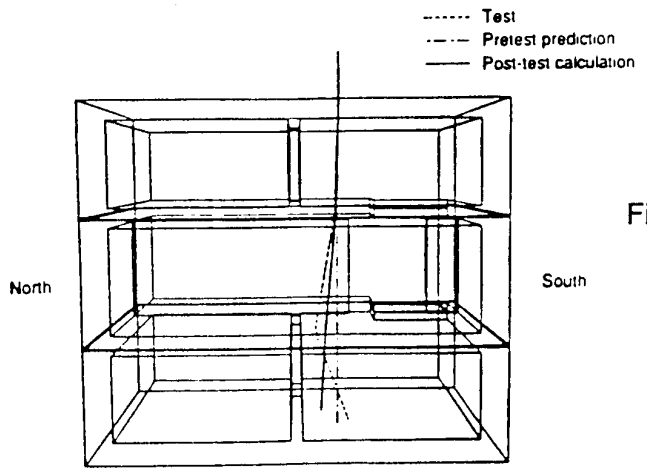

Figure 7. Position Comparison

THE EFFECT OF REBAR ON PROJECTILE PENETRATION

John A. Collins, Air Force Armament Laboratory, Eglin AFB, FL
Frank A. Maestas, Applied Research Associates, Inc., Albuquerque, NM
John C. Galloway, Applied Research Associates, Inc., Albuquerque, NM
Barry L. Bingham, Applied Research Associates, Inc., Albuquerque, NM

ABSTRACT

This paper documents the preliminary algorithms which Applied Research Associates, Inc. (ARA) developed and incorporated in to the PENCO-3D module of Effectiveness/Vulnerability Assessment in Three Dimension (EVA-3D) computer code, these EVA-3D modifications attempted to address the effect of projectile impacts on the reinforcing bars of a reinforced concrete element. Although the algorithms developed are rudimentary in nature, they do provide results that correlate well with the test comparisons made thus far.

INTRODUCTION

Existing methodology has either ignored the reinforcing bar effects on projectile terradynamics or has attempted to account for the effects by including them in the formulation of the concrete loading algorithm. In many caseloads the prevailing attitudes have assumed that the reinforcing bars merely confine the concrete and add no load themselves. The one exception has been the methodology developed by Applied Research Associates (ARA) and incorporated in the Effectiveness/Vulnerability Assessment in Three Dimensions (EVA-3D) computer code.

ARA developed this methodology in response to recent work by the U.S. Air Force under the scaled under-ground computer center (SUCC) and the Hard Target Ordinance Package (HTOP) test programs, this work has demonstrated that the reinforcing bars, if hit by a projectile, induce lateral loads onto the projectile and thus alter its trajectory. Prior to the ARA developments, EVA-3D did have a discrete algorithm for treating the effects of reinforcing bars. However, improvements were required to more accurately represent trajectory changes demonstrated by the SUCC and HTOP test efforts. This paper provides a discussion of the formulation of those algorithms.

BACKGROUND

This section provides pertinent background information on the EVA-3D terradynamic capabilities. References 1 and 2 provide detailed discussion of the methodologies embodied in the original computer code.

The weapon trajectory through a reinforced concrete target is determined by using the PENCO-3D option of EVA-3D. In this option, weapon behavior is treated in a time-marching curvilinear manner where at each time step the loads on discrete differential areas of the weapon are summed and the weapon kinematics determined. The weapon itself is a rigid non-spinning projectile. The weapon behaviors which are determined/calculated at each time step are; position, rotation, and acceleration all in three dimensions.

Within PENCO-3D, empirically-based algorithms are used to calculate the target's resistance to penetration. The resistance pressure for concrete is based on an adaption of the Sandia National Laboratory (SNL) cavity expansion model (Reference 3). Using that model, the loading stress on each element of the projectile is:

$$\sigma_n = 2.81 f_c' + 1.19 \rho_c V_n^2 \quad (1)$$

where: f_c' = the unconfined concrete strength
ρ_c = concrete density
V_n = the normal velocity component of the element

Equation (1) is a simplified version of the original SNL formulation and is based on a linear locking hydrostat value of volumetric strain of .04, concrete density of 150 lb/cf, and unconfined concrete strengths of 3000 psi to 10,000 psi.

The loading due to reinforcing bars are approximated by:

$$\sigma_s = \sigma_n + 3Y \quad (2)$$

where: Y is the yield strength of the reinforcing bars

Frictional effects are included by:

$$\sigma_t = n(\sigma_s + \sigma_n) \quad (3)$$

where n is the friction coefficient which ranges from 1% to 10%

The loading on a given element, dA_i

$$F_i = \sigma_t dA_i \quad (4)$$

MODIFICATIONS TO EVA-3D

The test programs conducted by the Air Force, SUCC and HTOP, involved penetrating weapons impacing at various trajectories on reinforced concrete targets. During those tests, when the projectile grazed reinforcing bars the projectile path was altered. Analysis of the test using the PENCO-3D module of EVA-3D correlated well with exit velocity but not with weapon position. As a result, the following modifications were made to the algorithms in the PENCO-3D module of EVA-3D.

Modification 1

The first improvements involved determining which reinforcing bar components were adjacent to individual points on the weapon surface. The goal of the search is to list the potential rebar which are in contact with the point (xeva, yeva, zeva) on the weapon. The search involves calculating the normal distance between the point on the weapon and the centerline of the rebar. If this distance is less than the radius of the rebar, then the point is defined to be in contact with the rebar.

If (X1, Y1, Z1) are the coordinates of one end of the rebar and (X2, Y2, Z2) are the coordinates of the other end, and d is the distance between these points (i.e. the rebar length), then the direction cosines for the rebar centerline are:

$$l = \frac{X2 - X1}{d} \quad (5a)$$

$$m = \frac{Y2 - Y1}{d} \quad (5b)$$

$$n = \frac{Z2 - Z1}{d} \tag{5c}$$

The equation for a plane that is perpendicular to the rebar line segment is:

$$l \cdot x + m \cdot y + n \cdot z = f \tag{6}$$

where

x, y, z = coordinates of plane points
f = an arbitrary constant

Substituting the coordinates for the point (xeva, yeva, zeva) on the weapon surface into the equation for the plane (6) will determine the value of f:

$$f = l \cdot xeva + m \cdot yeva + n \cdot zeva$$

The equation for the rebar line is:

$$\frac{x - X1}{l} = \frac{y - Y1}{m} = \frac{z - Z1}{n} = t$$

or

$$x = X1 + l \cdot t \tag{7a}$$

$$y = Y1 + m \cdot t \tag{7b}$$

$$z = Z1 + n \cdot t \tag{7c}$$

where

x, y, z = coordinates of points along the rebar centerline (ft)
t = distance between point (x, y, z) and end number 1 of the rebar (ft)

The above equations for x, y, and z (7a, 7b, and 7c) can be substituted into the equation for the normal plane (6). Solve for t to obtain:

$$t = f - l \cdot X1 - m \cdot Y1 - n \cdot Z1 \tag{8}$$

The parameter t describes the length along the rebar line where the normal plane containing the point (xeva, yeva, zeva) intersects the rebar line. If t is greater than the rebar length d,or less than zero, then the rebar is rejected. Otherwise, the coordinates (X, Y, Z) of the intersection point are calculated from equations 7a, 7b, and 7c, since t is known. The distance between points (X, Y, Z) and (xeva, yeva, zeva) is calculated and compared to the radius. If the distance is less than or equal to the rebar radius, then this point on the weapon is said to be in contact with the rebar.

Figures 1 and 2 illustrate special cases for the load application of rebar to the surface elements of a weapon that is not considered by the preceding logic. The first case is particularly applicable where the size of the weapon-surface elements are large compared to the cross-sectional area of rebar subcomponents. Notice in Figure 1 that the minimum distance, d, between the rebar centerline and the center point of a weapon-surface element is greater than the rebar radius; thus as a load applicator according to the logic discussed above it must be disallowed. However, this appears to be an obvious case where the weapon should see load application from the rebar. In order to account for these situations, additional checks were included as shown in Figure 1. The angle, Θ, between the normal vector from the element and the minimum distance vector (going from the center point of the weapon-

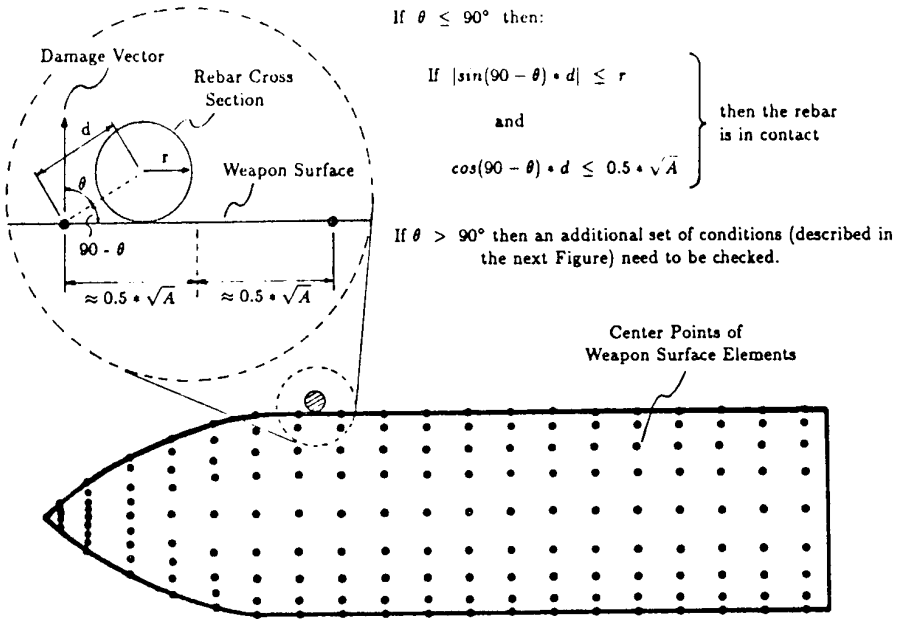

Figure 1. Condition where rebar is in between surface element center points.

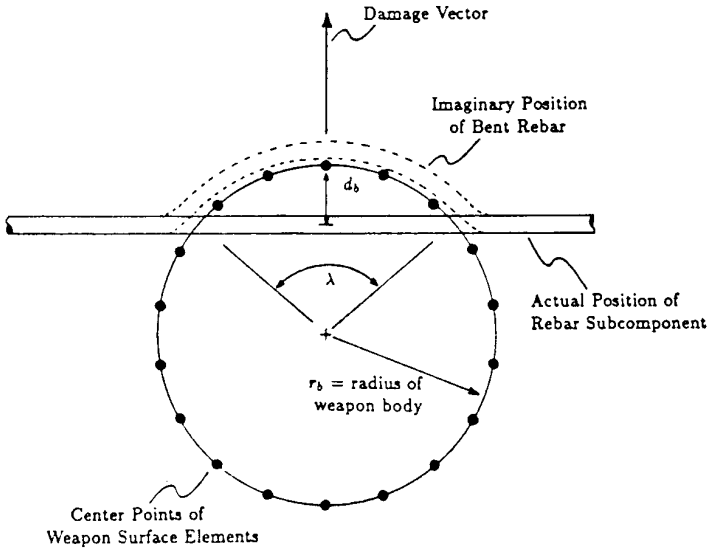

Cross Sectional View Looking Down the Longitudinal Axis of the Weapon

Figure 2. Condition where rebar is inside the weapon surface.

surface element to the centerline of the rebar) is easily calculated from vector algebra. If Θ is less than 90° (i.e. the centerline of the rebar is outside the weapon surface) and if:

$$|\sin(90 - \Theta) \cdot d| \leq r$$

and

$$\cos(90 - \Theta) \cdot d \leq \frac{\sqrt{A}}{2}$$

then the rebar loads the surface element where:

- d = minimum distance between the center point of the surface element and the centerline of the rebar
- r = rebar radius
- A = area of the weapon-surface element

If Θ is greater than 90°, then the rebar centerline is inside the weapon surface and a situation similar to that shown in Figure 2 exists. If the rebar is inside the weapon surface, then allowances should be made for rebar deflection and load to the associated surface elements. Sixty ksi steel rebar is typically very ductile; it can handle tensile strains of up to 20% and higher before breaking. A 20% strain for the imaginary rebar position shown in Figure 2 corresponds to a λ angle (see Figure 2) of approximately 120°. This corresponds to a d_b/r_b ratio of 0.5. A value of 0.5 is a default value included in EVA-3D for parameter, WRAP, which can be altered by the user. If the calculated ratio d_b/r_b is less than WRAP, then the surface element is loaded by the rebar. If the ratio is greater than WRAP, then the rebar is assumed to have broken and the rebar does not load the surface element.

In most cases, the reverse vector of the normal vector (along which the distance, d_b, is measured in Figure 2) does not intersect the rebar centerline. Therefore, a point is found along the reverse vector which is a minimum distance, d_{min}, from the rebar centerline. If the minimum distance, d_{min}, is greater than $(.5 \cdot \sqrt{A} + r)$, then the rebar is not included for load application to the surface element.

Modification 2

The second modification involved the actual loading stress used. If a steel rebar is determined to be in contact with a weapon-surface element, then a stress in addition to the concrete stress is applied to the element. The additional stress is the minimum of:

$$\sigma_s = \rho_s C_s V_n \left(\frac{A_r}{A}\right)$$

and

$$\sigma_s = f_u \left(\frac{A_r}{A}\right)$$

where:

- σ_s = stress application from steel contact
- ρ_s = density of steel (.000741 lb-s^2/in^4)
- C_s = loading wave velocity of steel (200,000 in/s)
- V_n = normal velocity of the weapon at the location of the surface element
- f_u = ultimate strength of steel (assumed to be 100 ksi for 60 ksi steel)
- A_r = cross-sectional area of the steel rebar
- A = area of the surface element

The A_r/A ratio limits the stress transmission from small-diameter rebar against large-area, weapon-surface elements. If the normal velocity, V_n, is less than zero (i.e. the weapon-surface element is moving away from the steel) then the stress application is set to zero.

Modification 3

The third modification is associated with reducing the numerical oscillations that occur from the use of equation (1). The main problem with the equation (and consequently the source of unwanted oscillations) is that the stress remains high (a minimum of 2.81 f_c') at low velocities. Theoretically, stress application from the concrete should never be higher than that described by a perfectly-elastic encounter:

$$\sigma_{ce} = \rho_c C_c V_n$$

where

σ_{ce} = stress application from the concrete if the concrete remains elastic
C_c = elastic seismic velocity of the concrete

The oscillation problem is solved by limiting the stress application to σ_{ce}, when σ_{ce} is less than σ_n. This typically applies at relatively low velocities of less than 40 ft/s. Even though the weapon may be travelling at a much faster velocity, large weapon sections could exist with normal velocities less than 40 ft/s. If the normal, slap velocity is less than zero, then stress application is set to zero.

Modification 4

The final modification involved free-surface effects and the use of a damage vector. A damage vector is of a specific length that is normal to the weapon surface elements. If the tip of the damage vector is beyond the concrete, then the concrete is assumed to spall, thus reducing the load on the weapon. All of the above discussion applies to cases where the tip of the damage vector lies within the confines of the concrete component (case A in Figure 3). If the tip of the damage vector lies outside of the concrete component (case B in Figure 3, then the stress application to the weapon-surface element is reduced by a factor of three to the minimum of either:

$$\sigma_c = 0.94 f_c' + 0.33 \rho_c V_n^2$$

or

$$\sigma_c = 0.33 \rho_c C_c V_n$$

The factor of three reduction places the stress application close to the unconfined compressive strength of concrete at low velocities.

SUMMARY

This paper provides the rudimentary algorithms developed and included in the PENCO-3D module of EVA-3D to treat the effects of reinforcing bars in a reinforced concrete target on weapon terradynamics. The algorithms have been verified by comparing the results of the EVA-3D calculations to exit conditions from the SUCC and HTOP tests (Reference 4).

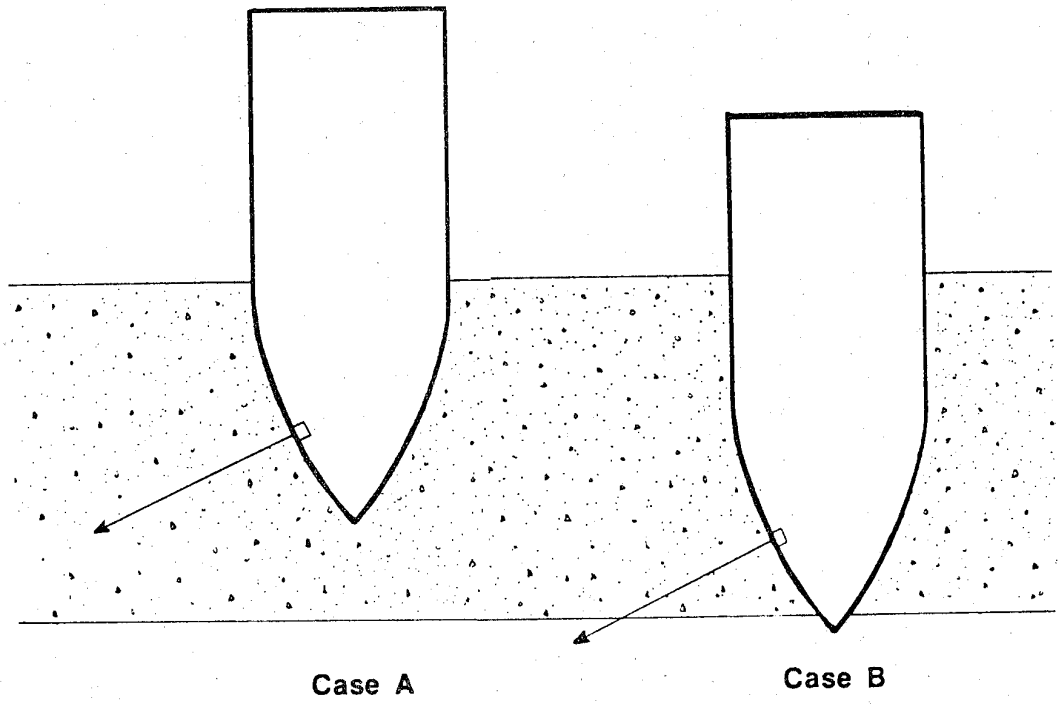

Figure 3. Cases where the tip of a damage vector is within and outside the confines of a concrete component.

REFERENCES

1. Maestas, F.A., Galloway, J.C., and Collins, J.A., Development of Target Models. Vol. I. EVA-3D Version 1.0 Methodology, Draft Report to AFATL, Applied Research Associates, Inc., Albuquerque, May 1989.

2. Maestas, F.A., Galloway, J.C., and Collins, J.A., EVA-3D Version 2.0 Methodology, Draft Report to AFATL, Applied Research Associates, Inc., Albuquerque,15 May 1989.

3. Luk, V.K. and Forrestal, M.J., Penetration into Semi-Infinite Reinforced Concrete Targets with Spherical and Ogival Nose Projectiles, Int. J. Impact Engineering, Vol. 6, No. 4, pg 291-301, 1987.

4. Maestas, F.A. and Galloway, J.C., Effects of Rebar on Penetration, Briefing to AFATL, Applied Research Associates, Albuquerque, October 1990.

Gruppe für Rüstungsdienste
Groupement de l'armement
Aggruppamento dell'armamento
Defence Technology and Procurement Agency

Dr. Daniel Favarger

Kurzfassung

Impact of Bombs on Hard Layers

A simple 2D-Model simulates the impact behaviour of bombs on hard layers. It points out the most important parameters which enhance their ricochetting or capsizing and prevent therewith a confined explosion in the protective layer.

The bombs are made of two rigid parts held together by a hinge, which has rigid ideal plastic caracteristic corresponding to the yield bending strength of both the GP and AP bombs. This way the deformation of the impacting bombs is taken roughly in account.

The comparison between the results of the model and these of the full scale tests shows good agreement. The rock rubble layers offer a very high protection against GP bombs, but are not hard enough to prevent the penetration of AP bombs in all cases.

COMPUTER MODELLING OF SMALL ARMS PENETRATION OF CONCRETE

Dr M J Iremonger
School of Mechanical, Materials and Civil Engineering
Royal Military College of Science
Shrivenham
Swindon SN6 8LA
UK

ABSTRACT

Results are presented of the numerical simulation of the penetration of a 5.56 mm NATO SS109 bullet into thick concrete and the perforation of thin concrete slabs. The two-dimensional finite difference code AUTODYN was used for these analyses with a linear elastic Lagrangian discretisation of the hardened steel bullet core and a Eulerian discretisation of the concrete targets. Reasonable agreement with experimental penetration depths and residual bullet velocities were obtained with an elastic-perfectly plastic concrete model by using enhanced static strength data.

INTRODUCTION

Experiments have been reported (Iremonger, Claber and Ho, 1989) which quantify the penetration of concrete by 5.56 mm calibre L2A1 (NATO SS109) bullets.

An opportunity has been taken to compare some of this database of experimental results with predictions from a numerical computer code for non-linear dynamic analysis (AUTODYN). In particular, an evaluation has been made of the use of such a code on a Personal Computer (PC) using limited material properties data.

NUMERICAL COMPUTER CODES (HYDROCODES)

The numerical simulation of the ballistic penetration of targets by projectiles has been widely studied (see Jonas and Zukas, 1978 and Brown,1986). The projectile and target are spatially discretized and the field equations of continuum physics are approximated using finite difference or finite element techniques. With a Lagrangian approach the computational grid is fixed in the material and moves with the motion of the continuum. In an Eulerian approach, the grid is fixed in space and the continuum passes through it. Contact laws are used to model, with slidelines, the interaction between the projectile and target. Step by step time integration is then used to simulate the event as it progresses with time.

These procedures are applicable to a wide range of impact problems. The case of a projectile impact which causes a deep and narrow penetration path in the target does, however, present problems. With a Lagrangian representation of the target there are severe mesh distortions

around the penetration path of the projectile. The consequent reduction in mesh dimensions reduces the computational time step which is controlled by the necessity to ensure that a stress wave does not traverse a cell during a single time step. More severe distortions cause mesh tangling with consequent failure of the analysis. To alleviate this problem it is necessary to rezone the mesh and remap the variables at intervals during the computational procedure. Techniques to overcome these difficulties with Lagrangian hydrocodes include the introduction of a narrow pilot hole in the target along the penetration path of the projectile (Schwer, Rosinsky and Day, 1987) and the use of erosion algorithms which delete elements when they are highly strained whilst retaining their mass (Sewell, Ong and Hallquist, 1990). An alternative approach, used in this paper, is to represent the target by a Eulerian discretisation and the projectile by a Lagrangian grid. This approach can handle the large deformations inherent in ballistic penetration but the material interfaces are less well defined and the computational requirements are greater than with a purely Lagrangian analysis.

By their nature, these numerical procedures are computer intensive in terms of both storage and processing requirements. They have been historically associated with large computers, in particular the so-called supercomputers. Such an association is still valid for large, complex analyses but the rapid advances in computer hardware give the opportunity for a more 'down-market' approach using a PC. The capacity of personal computers has been limited by the 640 kB restriction of the DOS operating system. However, recent 386 and 486 models have extended memories of typically 4MB or 8Mb. In addition, the processing speeds of current models are more than ten times faster than their recent predecessors. These factors together with its good graphics capability, single user environment and relatively low cost gives the PC considerable potential for dynamic simulation analyses.

The analyses reported in this paper have been performed with the two-dimensional AUTODYN finite difference code (Birnbaum and Cowler,1987). This code has been implemented on machines up to supercomputer level. For the present work, use has been made of the PC DOS version of the code with a limit of 1000 nodes (the latest PC DOS release with additional features has a limit of 850 nodes) and the Extended DOS version with a limit of 5000 nodes (4 MB internal memory) or 10000 nodes (8 MB internal memory). All versions of this code have both Lagrangian and Eulerian processors.

EXPERIMENTAL RESULTS

The experimental results reported by Iremonger et al (1989) are based on firing trials conducted in an indoor range at RMCS, Shrivenham. The tests were done at a range of 10.5 m.

The 5.56 mm calibre NATO L2A1 (SS109) bullet considered in this paper is shown in Fig 1a. The core comprises an air gap in front of a flat-tipped hardened steel core weighing 0.495 grams and of minimum hardness 600 HV (Vickers). The rear part of the core is a 90% lead/10% antimony alloy. The core is encased in a gilding metal (90% copper, 10% zinc) envelope. The total bullet mass is 4.00 grams.

A full description of the concrete target characteristics is given by Iremonger et al. Table 1 lists the measured and derived properties data which form the 'starting point' for the numerical studies described later. The apparent precision of this data masks the inherent variation in the properties of concrete.

Nominal Grade	15	30	45	60
Average Density (Kg/m^3)	2219	2250	2315	2321
Compressive (Cylinder) Strength (MPa)	23.1	40.1	54.1	58.4
Tensile Strength (MPa)	2.9	3.4	3.8	4.1
Bulk Modulus (GPa)	12.1	15.2	18.1	18.8
Shear Modulus (GPa)	9.1	11.4	13.6	14.1

Table 1: Typical data for 150 mm thick targets made with 20mm - 5mm coarse limestone aggregate.

The data for 150 mm thick coarse limestone aggregate targets given in Table 1 were not exactly replicated at other target thicknesses but they do serve as a self consistent set that is broadly representative of all the target thicknesses.

The experimental variation of penetration depth with concrete properties is shown in Fig 2. Each 'point' on this graph represents an average of 3 shots which gave, typically, a penetration depth range of about 5 mm. It should be noted that Claber (1987) obtained penetrations up to 10 mm greater for 10 mm down limestone aggregate concrete than the results of Ho (1988) which are shown in Fig 2. A further cause of variation in penetration depth is deviation and tumbling of the steel core which remained intact and undeformed and was considered to be the primary penetrator.

A set of 8 firings by Claber against 20 mm thick slabs of grade 30 concrete with 10 mm down limestone aggregate gave a average velocity loss of 166 m/s (ie from 923 m/s impact velocity to 757 m/s residual velocity) when perforating the targets. The velocity loss ranged from 142 m/s to 197 m/s with a standard deviation of 18 m/s.

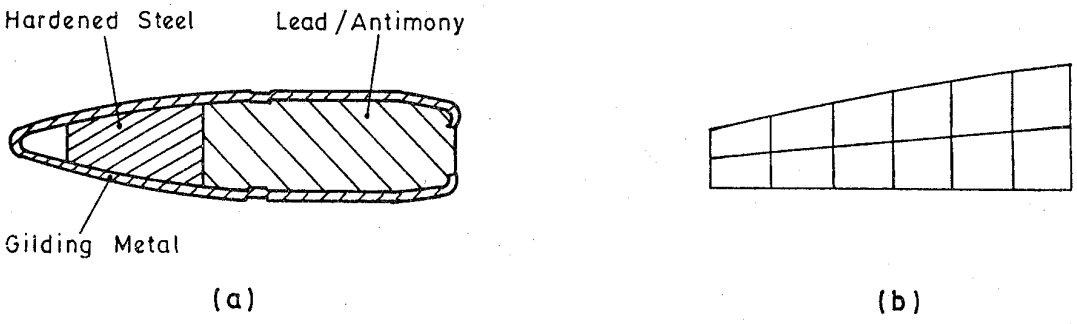

Fig 1: NATO SS109 (L2A1) bullet: (a) cross-section (b) 7x3 finite difference grid

COMPUTER MODELLING

Problem Idealisation

All the analyses are based on two-dimensional axisymmetric idealisations. The bullet is naturally axisymmetric. Square concrete targets were used in the experimental trials but the highly localised nature of the penetration process (observed both experimentally and in the numerical simulations) renders the target boundary shape unimportant. The size of the concrete grid was, however, considerably reduced compared with that used experimentally (100 mm diameter instead of 400 mm side length) in order to limit the number of grid points. A boundary condition was used at the side of the concrete grid (Figs 3 and 4) which allows stress waves normal to the boundary to be transmitted without reflection. The axisymmetric assumption implies a straight penetration path which was often not observed in practise.

On the basis of experimental observations reported by Iremonger et al (1989) only the hardened steel core of the bullet shown in Fig 1a was modelled as the projectile. It was idealised as a linear elastic material using a Lagrangian discretisation. A 21 node (7x3) finite difference grid is shown in Fig 1b. A finer grid with 144 nodes (21x7) was used for some analyses. Because the bullet grid determines the computational time step, use of the coarser mesh reduced the analysis time by more than three times.

The concrete targets were modelled with Eulerian grids. The total number of grid points was varied both to study the influence of mesh density and to change the target thickness. Similar ground rules were used for all the idealisations: a uniform square grid was maintained out to a radius of 20 mm throughout the target thickness with a graded mesh beyond that radius increasing in size with a typical geometric ratio of 1.05. A mesh of 'void' material was positioned in front of and behind the target to allow the concrete material to flow into these regions. Figures 3 and 4 show the basis of meshes for, respectively, a 1292 node grid representing a 20 mm thick concrete target and a 4898 node grid representing a 150 mm thick target. These figures indicate the I and J line numbers at critical grid co-ordinate positions. A grid consists of parallel I (column) and J (row) lines forming square or rectangular cells.

Concrete Properties

A material in AUTODYN requires an equation of state (EOS) and a strength model. Most analyses were conducted with the concrete being idealised as an elastic-perfectly plastic material because appropriate experimental data was available (see Table 1). With this model the linear EOS is characterised by density, bulk modulus and a hydrostatic tensile limit. The concrete tensile strength was used for this latter parameter which results in a cell no longer supporting tension when the limit is reached. The von Mises strength model is characterised by a shear modulus, yield strength and ultimate strain. The concrete compressive strength was used to define the yield strength with the ultimate strain being given a high value.

It is not uncommon to represent concrete as an elastic-plastic solid (Marti et al,1982) though more complex models have been used with, for example, a compaction equation of state and a Mohr-Coulomb strength model or post-cracking models (Broadhouse and Neilson,1987). It is recognised that strength and stiffness parameters are enhanced by dynamic loading though data for concrete is sparse. Allen Ross et al (1989) report tensile strength enhancements of more than 3 at high strain rates (3.5 at a strain rate of 10 per sec) with much lower increases in compressive strength (typically 1.5). Yamaguchi et al (1989) report a dynamic bulk modulus increase of about 2 at a strain rate of 10 per second.

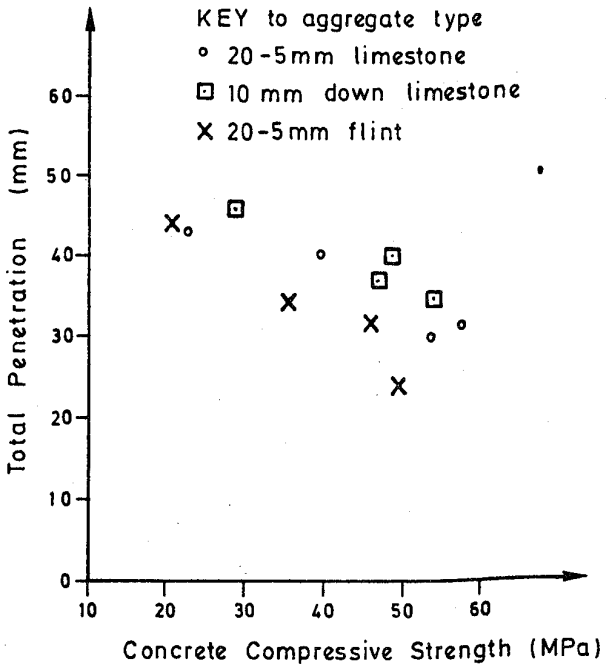

Fig 2: **Penetration deptch of SS109 bullets into 1500 mm thick concrete slabs.**

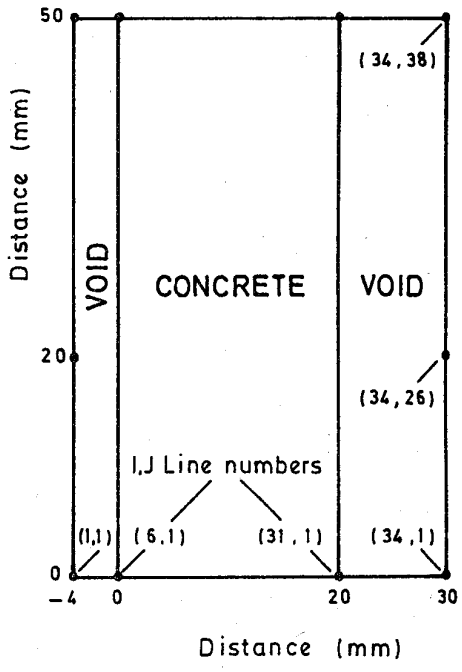

Fig 3: **AUTODYN finite difference grid for 20 mm thick concrete target: overall dimensions, column (I) and row (J) numbers**

Perforation of Thin Slabs

A number of analyses were conducted for a 20 mm thick slab. Grade 30 concrete was modelled with a bullet impact velocity of 923 m/s. Various meshes were constructed with the overall dimensions shown in Fig 3. A typical time history of projectile velocity is shown in Fig 5 from which the velocity loss could be estimated. The residual velocity was affected by both bullet and target mesh densities and the concrete material properties.

Using static material properties, a 21 node bullet grid and a 462 node target grid, the bullet velocity loss was 143 m/s. This compares with the average of 166 m/s observed experimentally. With strength properties enhanced by 50% the loss increased to 150 m/s and target meshes of 1292 and 1886 nodes gave almost exact agreement with the experimental results. Additional mesh refinement, however, further increased the velocity loss (to 175 m/s with a 7189 node target mesh). The relative analysis times were approximately 1 to 3 to 12 for the 462, 1292 and 7189 node grids respectively. The values of velocity loss were also increased by refining the bullet mesh (by about 15 m/s with a 144 node mesh).

Increasing the elastic properties (by 2) and the tensile limit (by up to 4) had little effect on the residual velocity. This indicates that the behaviour is not sensitive to the equation of state. This was confirmed by an analysis with a polynomial EOS using data for a different concrete. The velocity loss was much more sensitive to changes in yield (compressive) strength which indicates the importance of the strength model. No adequate data was available with which to assess the Mohr-Coulomb strength model.

The extent of failed material given by cells that exceeded the hydrostatic tensile limit generally overestimated the volumes of spall and cratering damage observed in practise.

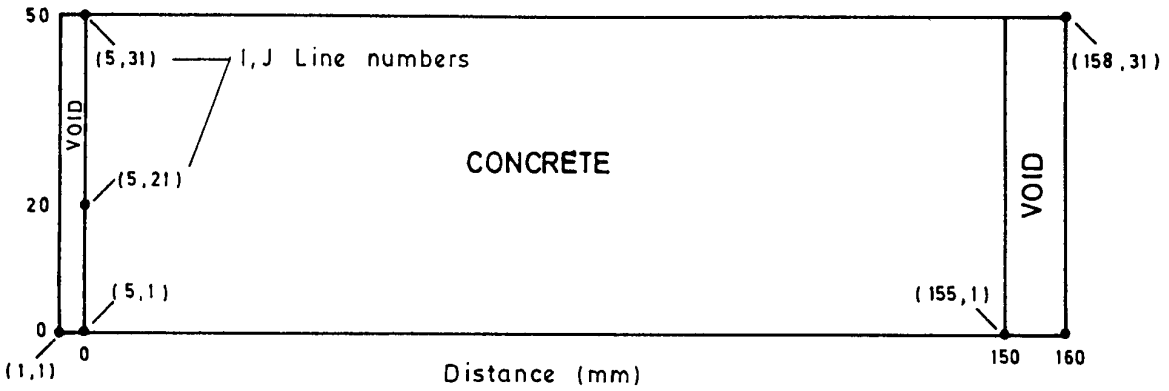

Fig 4: AUTODYN finite difference grid for 150 mm thick concrete targets: overall dimensions,column (I) and row (J) numbers.

Penetration into Thick Slabs

Penetration into 150 mm thick targets was simulated with the 4898 node mesh shown in Fig 4 for all the grades in Table 1. The results could be compared with the experimental data in Fig 2. With a 21 node bullet (Fig 1b) and static material properties, simulated penetration depths were almost double those observed in practise. Using enhanced strength values, the penetration depths reduced - to some 50% high for a 50% strength enhancement and 10% high if both tensile and compressive (yield) static strengths were multiplied by three. As with the perforation studies described above, changes in yield strength had far more effect than changes in tensile strength and changes in elastic properties had little effect (a 10% reduction in penetration for a twofold increase in bulk and shear modulus). Fig 6 shows the variation of velocity and penetration with time for a grade 60 concrete with 50% strength enhancement. This typical plot shows that the projectile deceleration reduces with increased penetration. This behaviour, which was assumed by Poncelet in 1829 (Vretblad and Nash,1989), means that penetration estimates based on the initial near-constant deceleration are inadequate.

It should be noted that the uniform square cell region for these analyses was comparatively coarse, being equivalent to an 886 node mesh for a 20 mm thick target. A grid of 9837 nodes (which is slightly finer than the 1886 node grid for a 20 mm thick slab) was used for a 100 mm thick target. Experimentally, the penetration depths were very similar for 100 mm and 150 mm targets and a finer mesh could be used for the thinner target. With elastic properties enhanced by times 2, compressive (yield) strength by 1.5 and tensile strength by 5 the penetration depth was 49 mm for a grade 30 concrete. This compares with an average value of 40 mm observed experimentally (Fig 2). Analysis time was approximately 48 hours on a 486/25 PC. It should be noted that, the predicted penetration depth would be lessened by using a more refined computational grid and also that, in reality, penetration is reduced by projectile tumbling and deviation.

The variation of penetration depth with velocity was studied for grade 30 concrete with three times strength enhancement. A power law with an exponent of 1.35 gave a good fit to these results. This value is similar to the 1.33 used in the BRL formula though most predictive formulae use higher values (Brown, 1986).

Fig 2 shows that there is a variation of penetration depth with aggregate type which is independent of concrete strength. This variation will not be accounted for in analytical or numerical models which use only the overall concrete strength properties.

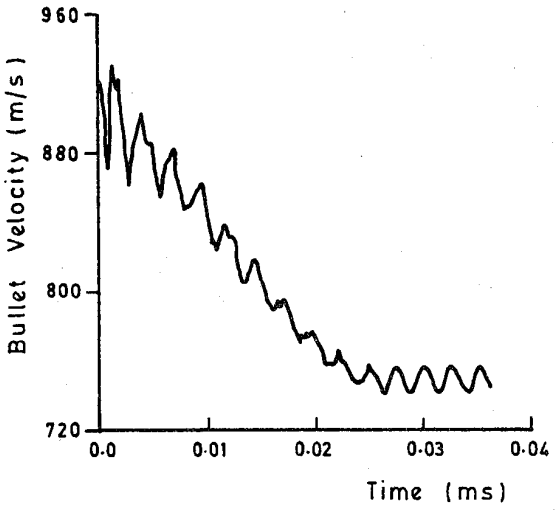

Fig 5: **Velocity v time for a 20 mm thick concrete slab**

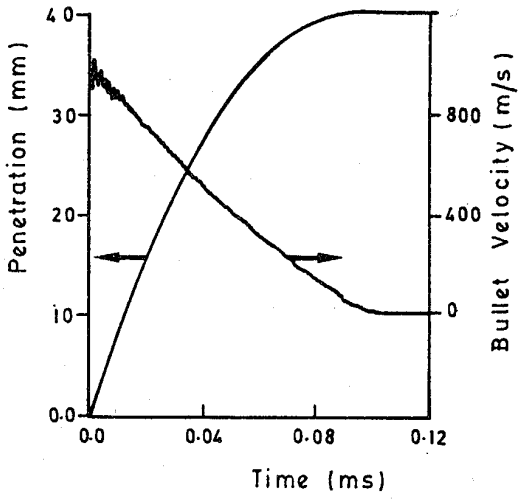

Fig 6: **Velocity and penetration v time for a 150 mm thick concrete slab**

CONCLUDING REMARKS

Numerical simulation is not an efficient competitor to simple formulae for the prediction of residual velocity or penetration depth. It is more costly and no more reliable. It can, however, provide a useful background to their development. The sensitivity to parameter variations can be studied and the development of material models itself is a means to better understand the penetration process. Also, like a perfectly instrumented experiment, a large number of variables can be monitored.

The present study has shown that reasonable predictions can be made with an elastic-plastic concrete model using enhanced strength values. Accurate penetration depth estimates needed at least a threefold enhancement of compressive (yield) strength with the relatively coarse grids that were mainly used. With finer grids, however, enhancement factors supported by the literature were satisfactory. It is worthy of note that the Recht equation (Iremonger et al, 1989) gives excellent predictions of penetration depth for all four concrete grades using static data enhanced by 1.5 (compressive strength - Allen Ross,1989), 2 (bulk and Young's moduli - Yamaguchi et al,1989) and 3 (shear strength cf tensile strength - Allen Ross,1989). The Recht predictions are, incidentally, more sensitive to changes in elastic properties than are the numerical simulations.

For absolute accuracy a finer mesh (ie more grid points) would have been desirable for the analyses of the 150 mm thick concrete slabs. A PC cannot cope with large complex analyses but it can provide a cost effective means for small problems and for the development of modelling techniques. Its ease of use with programs such as AUTODYN is a significant advantage and non-trivial problems can be tackled with the latest generation of microcomputers and overnight runs.

ACKNOWLEDGEMENTS

The author wishes to acknowledge the support of the Procurement Executive, Ministry of Defence and the MSc studies of Maj KJ Claber RE and Mr KQ Ho which provided the experimental data on which the numerical simulations are based.

REFERENCES

C Allen Ross, ST Kuennen & WS Strickland 'High strain rate effects on tensile strength of concrete' 4th Int. Symp.Interaction of Non-nuclear Munitions with Structures, Florida, USA, 1989

NK Birnbaum & MS Cowler 'Numerical simulation of impact phenomena in an interactive computing environment' IMPACT 87, Bremen, FRG, 1987

BJ Broadhouse and AJ Neilson 'Modelling reinforced concrete structures in DYNA3D' DYNA3D User Group Conference, London, UK, 1987

SJ Brown 'Energy release protection for pressurised systems, Part 2: Review of studies into impact/terminal ballistics' ASME Appl Mech Rev 39,2,177-201, 1986

KJ Claber 'The penetration of mild steel and concrete composite targets by small arms fire' No1 BLAST MSc Thesis, RMCS,Shrivenham, UK, 1987

KQ Ho 'Effects of concrete properties on the protective capability of concrete targets in withstanding small arms fire' No2 BLAST MSc Thesis, RMCS, Shrivenham, UK, 1988

MJ Iremonger, KJ Claber & KQ Ho 'Small arms penetration of concrete' 4th Int. Symp. Interaction of Non-nuclear Munitions with structures, Florida, USA, 1989

GH Jonas & JA Zukas 'Mechanics of penetration:Analysis and experiment' Int J Engng Sci 16,879-903,1978

J Marti, G Kalsi, VM Trbojevic & I Attalla ' Three-dimensional dynamic non-linear modelling of reinforced concrete under impact loads' Symposium on Concrete Structures under Impact and Impulsive Loading, Berlin, 1982

LE Schwer, R Rosinsky & J Day 'A Lagrangian technique for predicting earth penetration including penetrator response' 3rd Int. Symp. Interaction of Non-nuclear Munitions with Structures', Mannheim, FRG, 1987

DA Sewell, ACJ Ong & JO Hallquist 'Penetration calculations using LS-DYNA2D' DYNA3D User Group Conference, Bournemouth, UK, 1990

H Yamaguchi, K Fujimoto & S Nomura 'Strain rate effect on stress-strain relationships of concrete' 4th Int. Symp. Interaction of Non-nuclear munitions with structures', Florida, USA, 1989

PENETRATION MITIGATION FOR THEATER AIR BASES

Frank A. Maestas, Applied Research Associates, Inc., Albuquerque, NM
John C. Galloway, Applied Research Associates, Inc., Albuquerque, NM
James C. Partch, Applied Research Associates, Inc., Albuquerque, NM
Lt. Col. Carlos Rubio, Defense Nuclear Agency, Alexandria, VA
Capt. Rayment E. Moxley, Waterways Experiment Station, Vicksburg, MS

ABSTRACT

This paper presents a penetration mitigation concept formulated by Applied Research Associates, Inc. (ARA) under contract to the Defense Nuclear Agency (DNA). The Waterways Experiment Station (WES) has performed a preliminary scaled test using the concept. Those test results and the results of the Effectiveness/Vulnerability Assessment in Three-Dimensions (EVA-3D) comparison are presented in this paper.

INTRODUCTION

Conventional penetrating weapons are being designed for increased accuracy and increased depth of penetration into targets. Typically, tactical air base facilities have been designed against specified NATO criteria that do not adequately consider the conventional threat; existing air base assets are extremely vulnerable to advanced penetrating weapon designs. Previous research in protection from penetrating weapons has concentrated around the use of burster slabs or rock-rubble fields. Although a twenty foot thick concrete burster slab or rock-rubble field would be an excellent penetration countermeasure, these options are expensive and typically not practical for field use.

The objective of this effort is to develop a cost effective countermeasure technique to deflect, stop, or fail penetrating weapons. Emphasis is being placed on deflecting and/or failing the incoming penetrating weapon.

For penetrating weapons to be of maximum effect, they are designed to impact a target orientated so that the penetrator axis is aligned with its velocity vector. This results in maximum loading resulting from the impact to be applied to the penetrator nose and minimizes any lateral loading along the body or at the tail. The weapon may be diverted or possibly fail if high-stress levels are applied to the sides and tail of a penetrator. Lateral loading applied in a nonsymmetrical manner can induce a trajectory change and also an angle of attack (AOA) change of the penetrator (Figure 1). A trajectory change of the penetrator causes it to move away from its intended burst point. An AOA change of the penetrator will also result in an increase in the bending stress that is applied to the penetrator. As a result of the penetrator bending failure, the weapon will be unable to reach its desired depth of burst, or if the failure is great enough, may fail to burst.

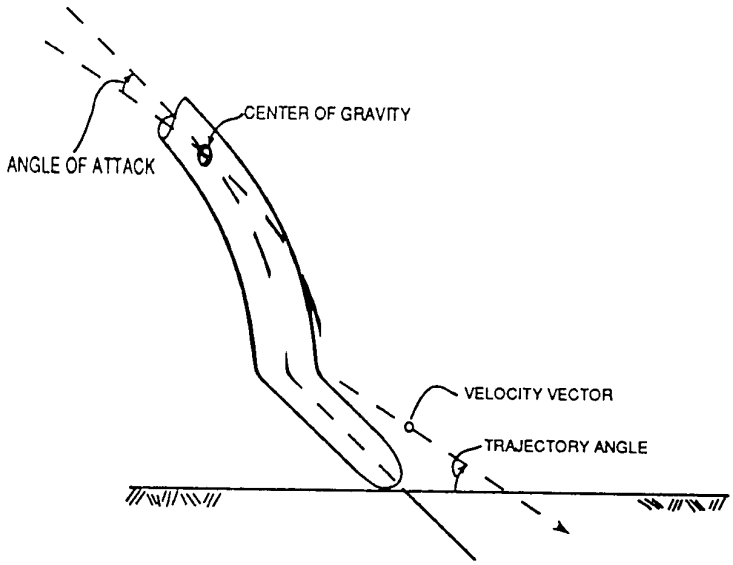

Figure 1. Impact Conditions Definitions.

A cost-effective system that induces a significant amount of AOA change on the penetrator is needed to achieve the objective of deflecting or failing a penetrating weapon. A system that has a series of extremely hard, thin, oblique surfaces will be investigated for inducing the AOA changes. The system must also include a strong "catcher" panel on which the penetrator will fail. In order to evaluate the merit of the selected countermeasure system, a computer simulation of a penetrator impacting a sequence of oblique surfaces is required to numerically predict the axial and lateral stresses, tensile and compressive bending stresses, changes in velocity, AOA, and penetrator trajectory. The simulation tool Effectiveness/ Vulnerability Assessment in Three Dimensions (EVA-3D), which includes the PENCO-3D (Reference 1) module (References 2 and 3), was modified to include new weapon loading algorithms and the Simplified Analytical Method of Penetration with Lateral Loading (SAMPLL) (Reference 4) bending failure algorithm. A more detailed description of EVA-3D is found in References 2 and 3.

A series of scaled tests are to be conducted to evaluate the countermeasure concept and provide a measure for validation of the computer simulations. The targets are to be constructed and tested at the WES located in Vicksburg, MS. The tests series began with one preliminary test in which a penetrator was fired into the baseline countermeasure system target. After a review of the initial test results, 12 additional target configurations will be constructed and tested. This paper provides the countermeasure system and the preliminary test results.

CONCEPT

Various combinations of materials, orientations, and configurations of obstacles which might be used to mitigate weapon penetration into an air base facility were investigated. Two basic evaluation criteria were used in the selection process: effectiveness and practicality. Under effectiveness, each candidate concept was evaluated with regard to its ability to divert, fail, or stop a penetrating weapon. Under practicality, each concept was evaluated with regard to the availability of construction materials, the ease of field construction, the relative cost of the individual units, and the difficulty of post-attack repairs and maintenance.

As a result of this evaluation process, a system consisting of layers of the hollow triangular beams was identified as the most promising mitigation concept. Figure 2 provides a sketch of the hollow triangular concrete beam concept.

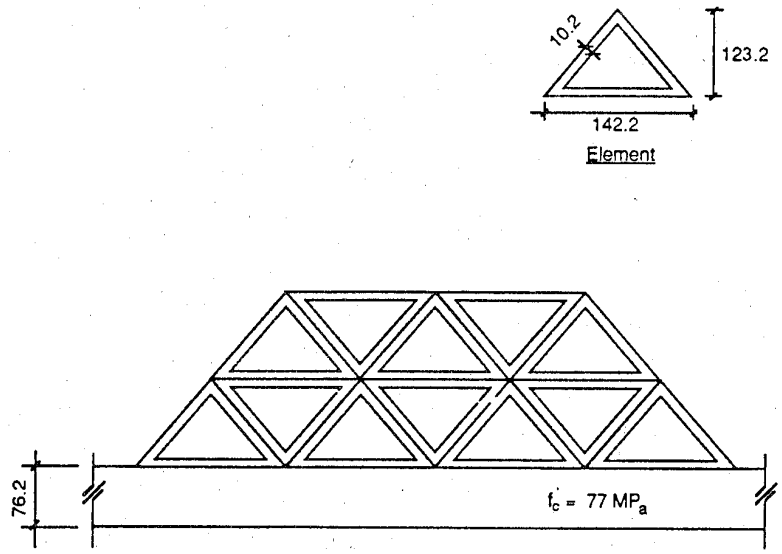

All linear dimensions are in centimeters

Figure 2. Hollow Triangular Concrete Beam Concept.

TEST PROGRAM

The scaled tests are to be performed by WES. The WES Projectile Penetration Test Facility houses an 83 mm ballistic range. WES will build, test, and provide measurement devices necessary for the testing of the baseline mitigation candidate concept. This section provides the test setup and results from the preliminary test.

ARA defined the baseline concept to be tested and WES performed the preliminary test in their Vicksburg test facility.

A. Target

The test target consisted of two high-strength (77 MPa) grout panels each 24.7 cm thick and 100 cm by 100 cm with a 30 mil piece of aluminum sheet metal placed between the two panels to act as a witness plate. The triangular prisms in the test panels were located perpendicular to each other.

B. Test Projectile

The subscale generic semi armor-piercing (SAP) projectile was fabricated from 4340 steel, heat treated to Rockwell hardness of 43-45 C and machined to the final dimensions shown in Figure 3. The projectile was placed in a three-piece high linear density polypropylene sabot which was aerodynamically stripped prior to impact.

C. Test Setup and Results

The projectile was fired into the test target at a velocity of 313 m/sec (Figure 4).

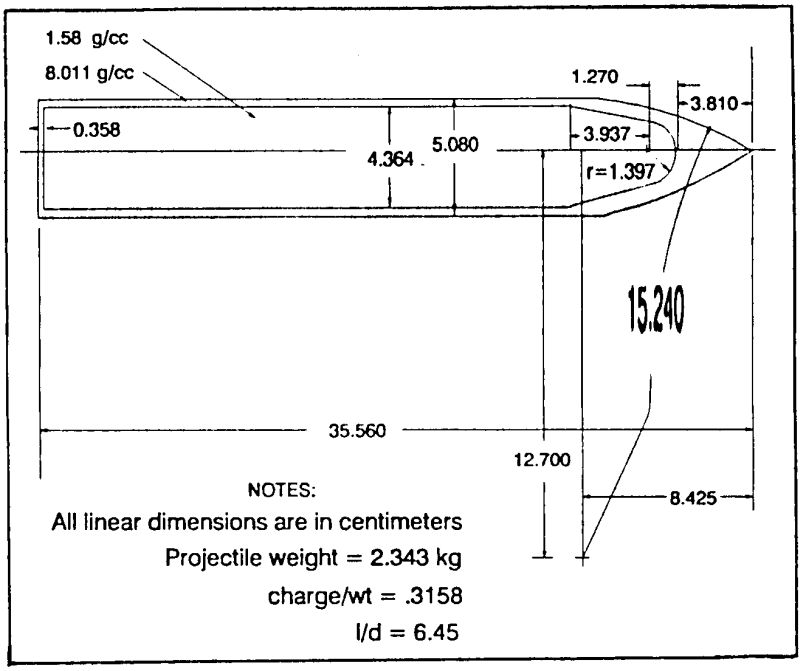

Figure 3. SAP Projectile.

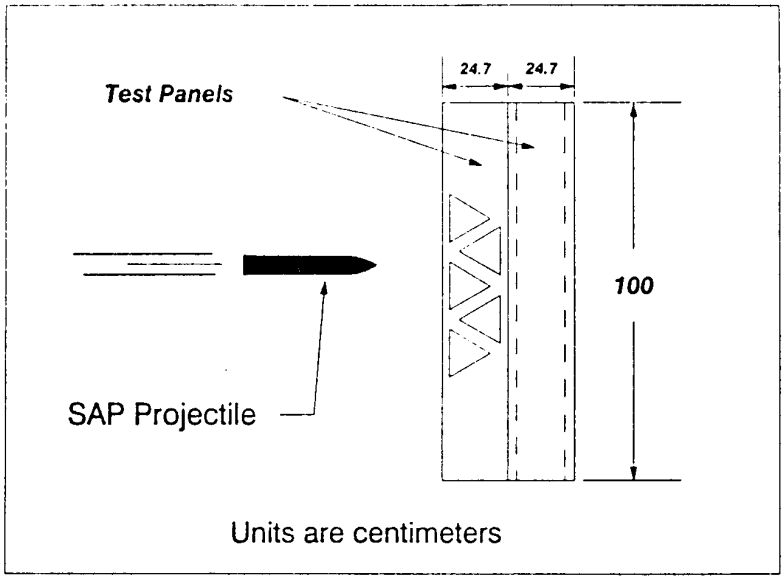

Figure 4. Plan View of Test Setup.

The projectile exit velocity as measured by high-speed film was 177 m/sec. Time motion analysis of the projectile by direct measurements of the high-speed film revealed the yaw rate to be about 3.4°/msec. By successive integration of the rotational equation of motion (Equation 1), and neglecting

$$M = J\ddot{\Theta} \quad (1)$$

air drag, it can beshown that the projectile yaw is linear with distance (Equation 2) for several body lengths of travel after exit (Reference 5), where M = turning moment, J = projectile moment of inertia, Θ = rotational (yaw), $\dot{\Theta}$ = rotational velocity, $\ddot{\Theta}$ = rotational acceleration, θ_i = initial yaw at exit, V_e = exit velocity, and L = projectile travel distance after exit.

$$\Theta \approx \frac{\dot{\theta}_i}{V_e} L + \theta_i \quad (2)$$

Figure 5 shows a plot of the projectile travel distance versus the yaw from high-speed film measurements which corroborates the theoretical linear relationship between the two variables. As seen from Equation 2, the yaw rate can also be calculated from Figure 5 as the product of the exit velocity and the slope of the line. This theoretical yaw rate is about 3.6°/msec which is close to the measured value of 3.4°/msec.

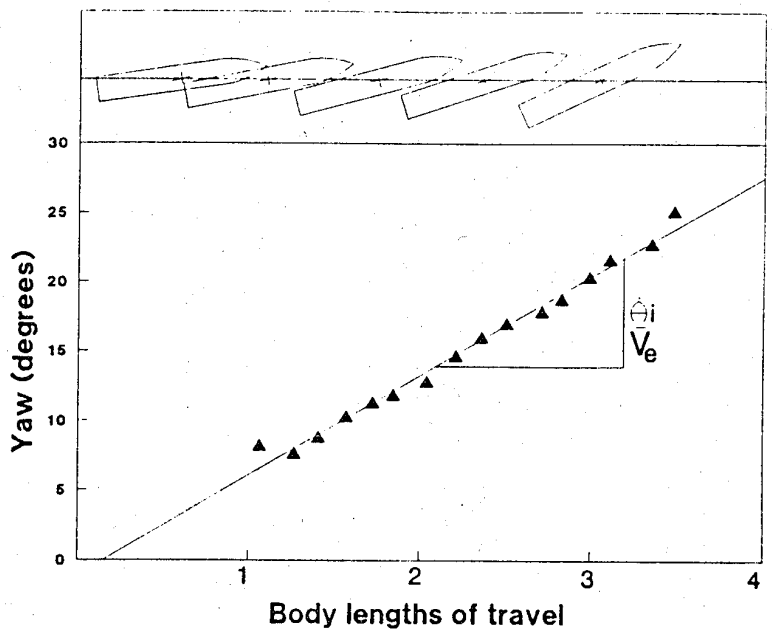

Figure 5. Projectile Yaw Versus Travel Distance After Exit.

ANALYSIS

EVA-3D with the modified PENCO-3D module will be used to perform pre-test predictions and post-test analysis of each test performed. The post-test analysis of the preliminary test effort is provided in this section.

A subscale baseline target model, similar to that used in the WES preliminary test, was built using the PADL-3D constructive solids modeler (Reference 6). The target model, like the preliminary WES test target, did not have a concrete base at the bottom of the target. A large block of air was added to the bottom of the target model so that the penetrator would be able to fully exit the target before the code stopped the simulation. The penetrator used for this analysis was a subscale version of the SAP. The initial velocity was 313 m/sec. The trajectory angle at target impact was 90° with a 0° AOA.

Initial calculations showed the penetrator stopping in the bottom layer after having traveled in a nearly straight path. This directly contradicted the WES test results which showed an exit velocity of 177 m/sec

with significant angular rotation of the penetrator. It was hypothesized that the lack of turning was due to an over estimate of the lateral loading on the body and tail sections of the penetrator. The computer program assumed that the penetrator remained in full contact with an undamaged target as it passed through the target. The target was constructed of thin sections of high-strength concrete with no steel reinforcement. This configuration would result in a very hard but very brittle target that would tend to offer only minimal lateral loading to the aft section once the nose section has passed through. As a result, EVA-3D/PENCO-3D was modified to eliminate the lateral forces on the body and tail sections of the penetrator. The results of this calculation closely match the test results. The comparisons are provided in Figure 6. The projectile position is also shown in Figure 6; note the weapon is rotating. The lack of lateral loading on the aft sections of the penetrator permits it to rotate both within the target and after it exits.

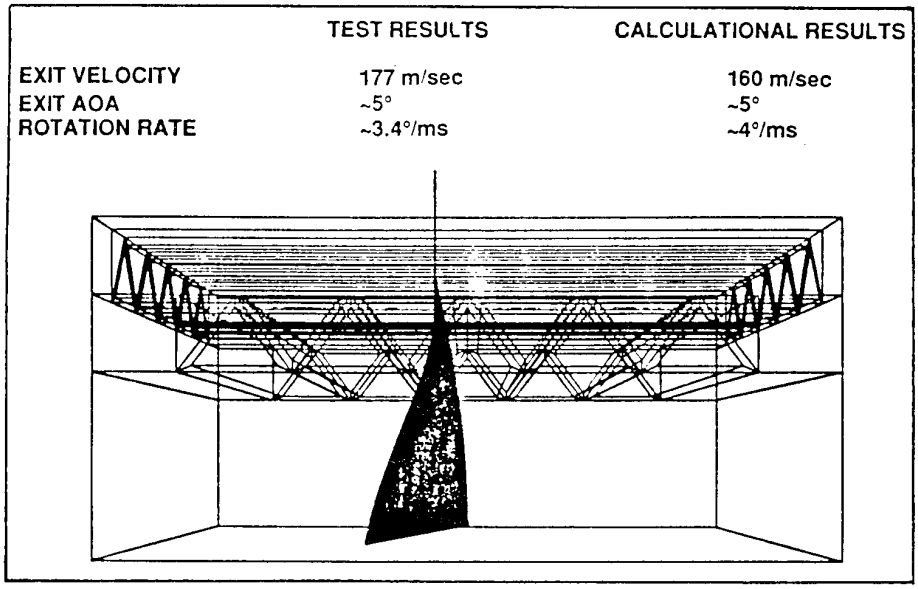

Figure 6. Calculation and Test Results for Preliminary Test Effort.

Figure 6 indicates a large amount of rotation was induced as the penetrator struck the oblique surface within the target. Evaluation of the stress and excess compressive impulse time histories indicate that the penetrator was subjected to a great deal of stress as it passed through the target but the accumulated excess impulse remained fairly small. The residual rotational velocity in the penetrator as it exited the target was quite large. The result of these two pieces of information indicates that the penetrator would probably not fail within the target, but would be rotating rapidly once it exited. Observations of the actual test indicate that the calculation was able to predict the exit velocity of the penetrator (160 m/sec in the calculation), as well as the tendency for large rotation after exit.

SUMMARY

A layered hollow triangular element configuration over a concrete slab has been chosen as the most promising penetration mitigation concept. This concept was chosen based upon its anticipated construction ease, cost, maintenance needs, and effectiveness. Evaluation of the effectiveness of various orientations and layer configurations has been made using the EVA-3D computer code. The analysis tool produced results similar to those of a preliminary test performed by WES. The calculational results suggest that the concept will be successful.

REFERENCES

1. Creighton, D.C., Three-Dimensional Projectile Penetration in Soil and Rock: User's Guide for Computer Code PENCO3D, Report in Preparation, U.S. Army Engineer Waterways Experiment Station, Vicksburg, MS, November 1989.

2. Maestas, F.A., Galloway, J.C., and Collins, J.A., Development of Target Models, Vol. I, EVA-3D Version 1.0 Methodology, Draft Report to AFATL, Applied Research Associates, Inc., Albuquerque, NM, 1 May 1989.

3. Maestas, F.A., Galloway, J.C., and Collins, J.A., EVA-3D Version 2.0 Methodology, Draft Report to AFATL, Applied Research Associates, Inc., Albuquerque, NM, 15 May 1989.

4. Young, C.W. and Young, E.R., Simplified Analytical Model of Penetration with Lateral Loading, Sandia National Laboratories, SAND84-1635, Albuquerque, NM, May 1985.

5. Cargile, J.D. and Cummins, T.K., Effectiveness of Steel Bars for Inducing Yaw in the Flight Path of a Subscale Armor - Piercing Projectile, Report in Preparation, U.S. Army Waterways Experiment Station, July 1990.

6. Hartquist, E.E. and Marisa, H.A., PADL-2 User's Manual, Report UM-10/2.2, Cornell Programmable Automation, Cornell University, Ithaca, NY, November 1988.

EIN SEMIEMPIRISCHES PROGRAMM ZUR STRUKTURAUSLEGUNG VON PENETRATOREN

ERNST ROTTENKOLBER

MESSERSCHMITT-BÖLKOW-BLOHM GMBH
Postfach 1340
D-8898 Schrobenhausen

Kurzfassung:

Bei der Auslegung von sprengstoffgefüllten Penetratoren gegen Erd- oder Betonziele sind im allgemeinen die Penetrationsleistung, die Bahnstabilität und die Strukturfestigkeit zu gewährleisten. Diese Probleme können im Prinzip mit numerischen Finite-Elemente-Simulationen gelöst werden. Solche Verfahren erfordern aber auch heute noch einen so großen Aufwand, daß sich ihr Einsatz nur zur Behandlung ausgewählter Fragestellungen lohnt. Auf der anderen Seite geben einfache empirische Formeln zu ungenaue Antworten auf die Frage nach Eindringbahnen und Strukturfestigkeit.
Es wird hier ein semiempirisches Prgramm vorgestellt, das vor allem im Hinblick auf Penetrator-Strukturauslegung und einfache Handhabbarkeit (bei geringen Rechenzeiten) entwickelt wurde. Es erlaubt die Behandlung von rotationssymmetrischen Penetratoren und geschichteten Zielen aus Beton, Sand, Erde oder ähnlichen Materialien. Die Ziele werden durch wenige empirische Parameter beschrieben. Die Wechselwirkung Ziel/Penetrator wird aus der lokalen Penetratorgeschwindigkeit berechnet, ohne Modellierung der Zieldynamik.
Um dem Schwerpunkt "Strukturauslegung" gerecht zu werden, muß die Penetratordynamik (einschließlich elastisch-plastisches Materialverhalten) ausreichend genau beschrieben werden. Die Hauptbelastung der Struktur besteht aus Stauchung und Biegung, die über die gesamte Penetratorlänge kontinuierlich variieren. Unter der Vernachlässigung lokaler Effekte wird deshalb der Penetrator in axiale Abschnitte unterteilt, deren elastisch-plastisches Verhalten balkentheoretisch beschrieben wird.
In den abschließend gezeigten Berechnungsbeispielen werden die Möglichkeiten der dargestellten Methode demonstriert.

Sprengstoffgefüllte Penetratoren werden vor allem zur Bekämpfung von Bunkern, Sheltern oder Startbahnen verwendet. Dabei müssen sie aufgrund ihrer kinetischen Energie Materialien wie Beton, Schotter, Sand oder Erde durchdringen. Bei der Auslegung solcher Penetratoren müssen Penetrationsleistung, Bahnstabilität und Strukturfestigkeit berücksichtigt werden.

Zur Ermittlung der Penetrationsleistung gibt es eine Fülle von empirischen Formeln (z. B. [1]). Die Genauigkeit von Vorhersagen hängt von der Güte der Schätzung von Ziel- und Penetratorparametern ab. Nicht ideale Auftreffbedingungen, gekrümmte Bahnen oder Penetratorverformungen gehen in solchen Formeln überhaupt nicht ein.

Auf der anderen Seite gibt es heute dreidimensionale Finite-Elemente-Codes, mit denen alle physikalischen Prozesse bei der Penetration beschrieben werden können. In der Praxis ist die Anwendbarkeit dieser Codes aber immer noch sehr aufwendig. Zur Erzielung guter Ergebnisse müssen vor allem die Zielmaterialen gut bekannt sein. Da das meistens nur nach Penetrationsversuchen der Fall ist, sind FE-Codes als Vorhersageinstrumente für Penetrationstiefen oder Bahnstabilität auch nur wenig besser als empirische Methoden. Die Stärke der FE-Codes liegt dagegen in Penetrator-Strukturuntersuchungen.

Zur Berechnung von Eindringbahnen werden seit längerer Zeit semiempirische Programme erfolgreich eingesetzt [2]. Das von MBB 1981 entwickelte Programm modelliert den Penetrator als starren Körper mit 6

Freiheitsgraden. Zur Integration der Bewegungsgleichungen werden auf diskreten Oberflächenelementen empirische Ziel-/Penetrator-Wechselwirkungskräfte angesetzt ("differential area force law"). Die Parameter zur Berechung dieser Kräfte wurden für verschiedene Zielmaterialien aus Penetrationsversuchen abgeleitet. Seither hat sich dieses Programm bei der Berechnung von Eindringbahnen (Tiefe, Stabilität) gut bewährt.

Es lag also nahe, für einen Code zur Sturkturauslegung die Vorzüge der FE-Methode und des Eindringprogramms zu kombinieren. Das Ziel wird demnach empirisch beschrieben, die Penetratorstruktur aber mit Finiten Elementen modelliert. Allerdings werden nicht wie in den üblichen 3D-Codes Volumenelemente verwendet, sondern der Penetrator wird durch Balkenelemente mit Kreisrohrquerschnitt idealisiert. Damit wird zwar auf die Beschreibung von örtlich auftretenden Verformungen verzichtet, aber die Hauptbelastungen (Biegung und Stauchung) des Penetratores werden adäquat berücksichtigt. Zur Erzielung möglichst geringer Rechenzeiten wurde ferner auf eine komplette dreidimensionale Beschreibung verzichtet, die Bewegung des Penetrators findet nur in einer Ebene statt, damit besitzen die Knoten des FE-Modells nur 3 Freiheitsgrade.

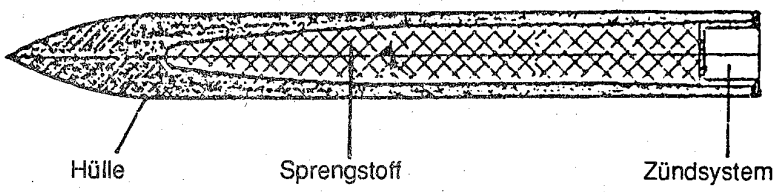

Figur 1: Typischer Penetrator

Im Programm kann eine Vielzahl von rotationssymmetrischen Penetratoren modelliert werden. Typisch ist jedoch ein Aufbau gemäß Figur 1. Die Penetratorhülle verhält sich im allgemeinen elastisch plastisch, wobei die Grenzspannung für plastisches Fließen auch dehnungs- und dehnratenabhängig sein kann. Vom Material der Füllung (z. B. Sprengstoff, Zündsystem) geht nur die Masse, nicht die Festigkeit in die Berechnung ein. Das Ziel kann aus mehreren Schichten bestehen. Die zur Beschreibung notwendigen Parameter liegen für einige Arten von Beton, Sand und Schotter vor. Die Auftreffbedingungen in der Bewegungsebene sind durch die Penetratorgeschwindigkeit, den Bodenwinkel, den Gierwinkel (siehe Figur 2) und die Drehrate festgelegt. Die Ergebnisse eines Rechenlaufs bestehen aus der Eindringbahn (Ort, Geschwindigkeit, Beschleunigung) und der Penetratorverformung (Spannung, Dehnung, Dehngeschwindigkeit). Alle Größen können zeitabhängig oder entlang der Penetratorachse für einen festen Zeitpunkt dargestellt werden.

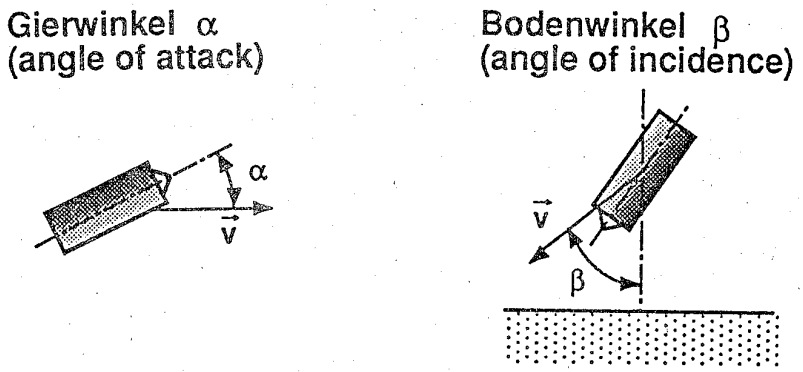

Figur 2: Definition der Winkel

Zur Integration der Bewegungsgleichungen werden zwei Diskretisierungen eingeführt: die Strukturdiskretisierung durch Finite Elemente und die Zerlegung der Oberfläche in Flächenelemente zur Berechnung der Oberflächenkräfte, die in Figur 3 dargestellt ist. Die dort angegebenen Zielparameter können im allgemeinen abhängig sein vom Ort, der Elementgeschwindigkeit und der Elementorientierung. Damit können besonders Randeinflüsse für feste Zielmaterialien wie Beton richtig modelliert werden. Die Bestimmung der benötigten Parameter geschieht am besten, wie bereits erwähnt, anhand von Penetrationsexperimenten.

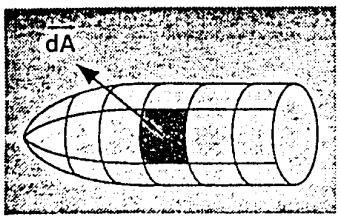

Modellierung des Penetrators durch diskrete Oberflächenelemente $\vec{dA}$

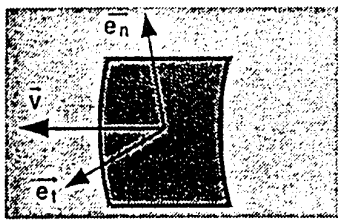

$\vec{v}$ = Oberflächenelementgeschwindigkeitsvektor

e_n, e_t = Einheitsvektoren

$$\frac{\vec{dF}}{dA} = (p_s + c_n v^2)\vec{e}_n + (\mu + c_t v^2)\vec{e}_t + \vec{G}$$

p_s = **Bodendruck**

μ = **Reibungskoeffizient**

c_n, c_t = **Strömungswiderstände (winkelabhängigkeit!)**

$\vec{G}$ = **Sondereffekte (z.B. Oberflächeneffekt, Strömungsschatten)**

Figur 3: Berechnung der Oberflächenkräfte

Zur Diskretisierung der Struktur wird der Penetrator in (möglichst gleich lange) Abschnitte zerlegt. Üblicherweise genügen 10 bis 20 Elemente über die Penetratorlänge. Der Verschiebungsansatz für die Elemente wird wie in der Balkentheorie üblich gewählt (siehe z. B. [3]). Das elastisch-plastische Materialverhalten wird in 15 Integrationspunkten pro Element berechnet (3 axial, 5 über den Querschnitt). Damit werden rein elastische Verformung, rein plastische Dehnungen und rein plastische Biegungen exakt (im Sinne der Balkentheorie) integriert. Die Zeitintegration erfolgt explizit. In jedem Zeitschritt werden zuerst die Oberflächenkräfte ermittelt und den benachbarten Strukturknoten zugeordnet. Dann erfolgt die Berechnung der Spannungen und der Knotenverschiebungen.

Daß mit dem kurz skizzierten Verfahren die wesentlichen Penetrationsphänomene erfaßt werden, zeigen die folgenden Beispiele. Ein guter Test für den Kraftansatz ist die Simulation von Ricochet-Verhalten. Bei diesem Problem spielen nicht nur die axialen Kräfte eine Rolle, sondern vor allem die lateralen Kräfte auf die Penetratornase entscheiden über Eindringen oder Abgleiten. In Figur 4 sind drei Rechenergebnisse dargestellt. Sie zeigen eine Änderung der Penetratorbahn in Abhängigkeit von Auftreffgeschwindigkeit und Auftreffwinkel, wie sie auch in Experiment beobachtet wird.

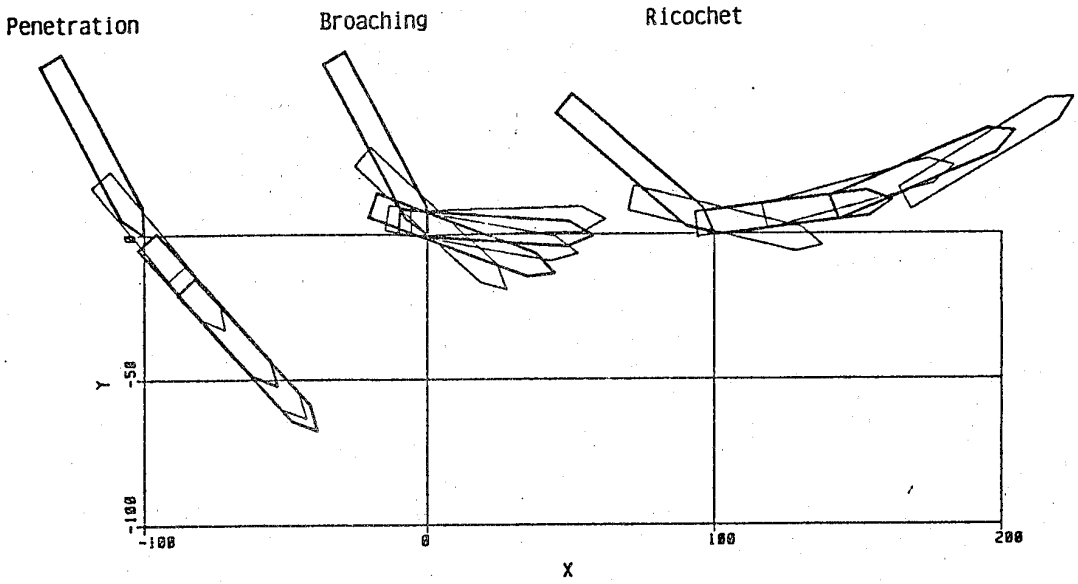

Figur 4: Eindringbahnen bei unterschiedlichen Auftreffbedingungen
links: Penetration
Mitte: Broaching bei verminderter Auftreffgeschwindigkeit
rechts: Abgleiten bei vergrößertem Auftreffwinkel

Der Effekt verschiedener Nasenformen wird in Figur 5 demonstriert. Es zeigt sich, daß ih lockerem Sand der Penetrator mit der stumpferen Nase (bei gleicher Masse und gleichen Auftreffbedingungen) besser eindringt. Der geringere Eindringwiderstand der spitzen Nase kommt nicht zur Geltung, weil der Penetrator instabil fliegt, sich querstellt und dadurch abgebremst wird.

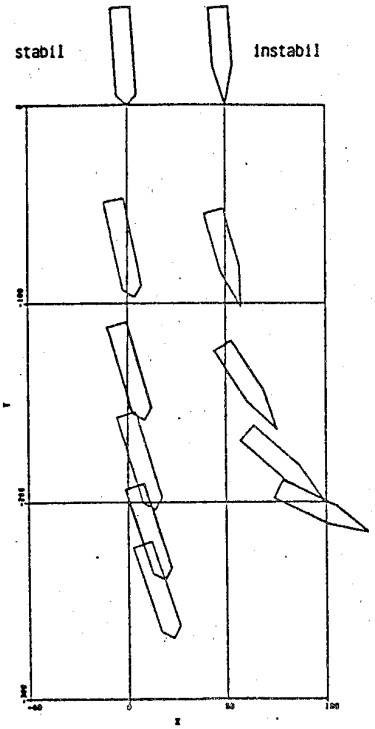

Figur 5:
Vergleich von Eindringbahnen mit unterschiedlicher Nasenform

Daß sich die lokalen Beschleunigungen im Penetrator stark von der mittleren oder Schwerpunkt-Beschleunigung unterscheiden können, zeigt Figur 6. Hier ist ein senkrechter Schuß auf ein geschichtetes Ziel simuliert, wobei der Effekt von zwei Betonplatten deutlich zu sehen ist. Ergebnisse dieser Art können zur Auslegung von mechanischen Verbindungen oder Komponenten des Zündsystems dienen. Im vorliegenden Fall war vor allem die Form des Beschleunigungssignals wegen der Verwendung als Zündkriterium interessant.

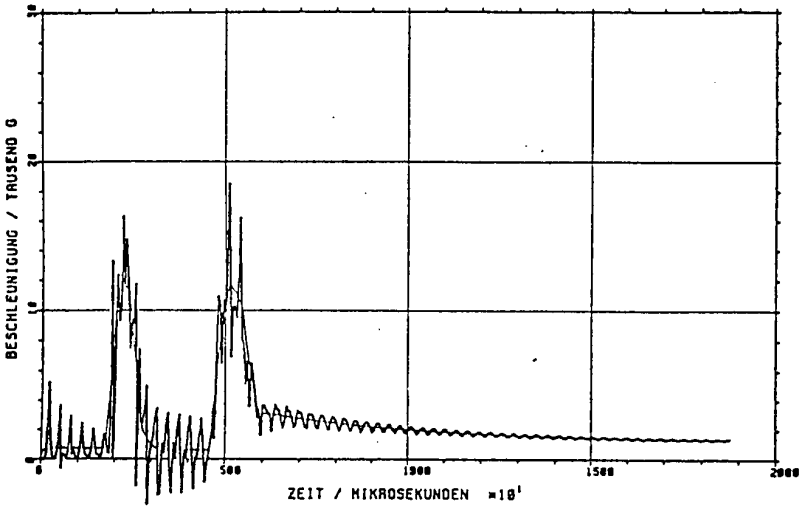

Figur 6: *Berechnete lokale Beschleunigungen (dicke Kurve: Penetratorheck) verglichen mit der Schwerpunktbeschleunigung (dünne Kurve)*

Eine Strukturberechnung mit starker plastischer Verformung zeigt Figur 7. Das Eindringen eines Penetrators mit relativ großem Anstellwinkel in ein Betonziel wurde hier verglichen mit ideal senkrechtem Eindringen. Anhand der plastischen Dehnung in Endzustand kann die kritische Stelle herausgefunden werden. Ein Vergleich der berechneten Penetratorform mit einem nach Verschuß geborgenen Penetrator in Figur 8 belegt die Brauchbarkeit des vorgestellten Programms zur Strukturauslegung.

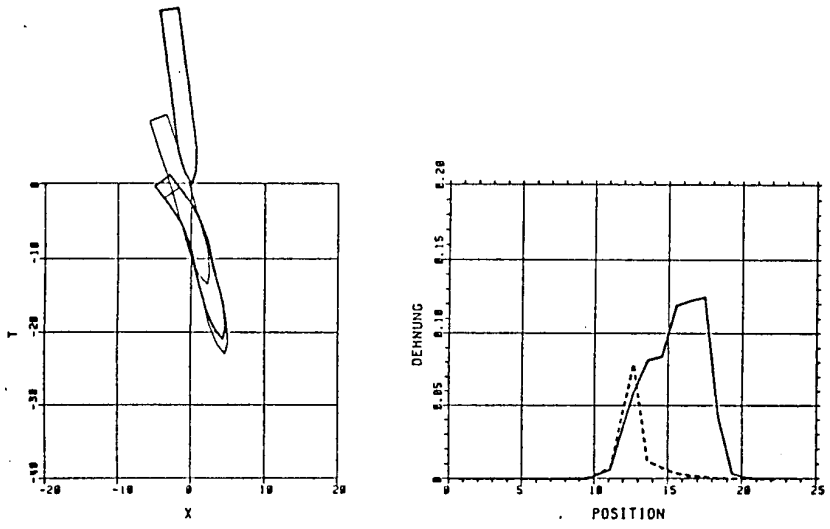

Figur 7: *Berechnete Penetratorverformungen (links) und zugehörige plastische Dehnungen auf beiden Penetratorseiten (rechts)*

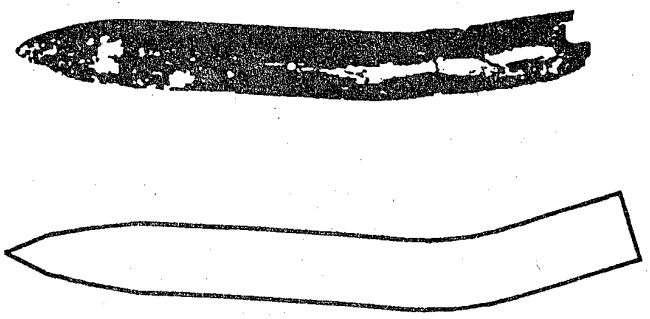

Figur 8: Vergleich von berechneter Penetratorform (unten) mit einem Versuchsmuster (oben)

Literatur

[1] C.W. Young, Empirical Equations for Predicting Penetration Performance in Layered Earth Materials for Complex Penetrator Configurations, 1972

[2] D. Henderson:, Impact and Penetration Technology Program Parametric Study, 1976

Ch. Helwig: HEIDI-Hydrodynamischer Erdeindringcode in dreidimensionaler Integrationsdarstellung, MBB TN AG 1251-498/81, 1981

[3] M. Link: Finite Elemente in der Statik und Dynamik, Teubner, Stuttgart, 1984

PROJECTILE PENETRATION INTO CONVENTIONAL AND HIGH-STRENGTH CONCRETE

by

L. E. Tidwell and B. Rohani

Civil Engineer and Research Civil Engineer
U.S. Army Engineer Waterways Experiment Station
3909 Halls Ferry Road, Vicksburg, Mississippi, USA 39180-6199

ABSTRACT

This paper summarizes the results of a large number of model experiments involving the penetration of a semi-armor-piercing (SAP) projectile into conventional and high-strength concrete targets. The purpose of these experiments was to determine what is to be gained in penetration resistance by using high-strength concrete, and our ability to analytically predict the performance of the projectile against such targets. The experiments involved both normal and oblique impacts within a velocity range of approximately 239 to 468 m/sec. The test results are analyzed and compared with corresponding computer simulations including both depth of penetration and projectile structural dynamic analyses.

Under normal impact (a) at lower velocities the projectile rebounded out of the conventional concrete targets but was embedded at the higher velocities, (b) the projectile rebounded out of the high-strength concrete targets after partial penetration, (c) the high-strength concrete caused the projectile to deform, and at higher velocities to break up, and (d) the impact crater and spall regions were greater in the high-strength concrete at lower velocities, but were of the same approximate size for both targets at higher impact velocities.

Under oblique impact (a) in the case of conventional concrete targets, the projectile's tail was flattened as a result of side impact with the target within the velocity range of 270 to 363 m/sec, (b) for higher velocity impacts into conventional concrete targets, the projectile had moderate bending towards the center of its aftbody, (c) the projectiles were completely destroyed at all velocities impacting the high-strength concrete targets, and (d) the impact craters were small and contained very few cracks for both the high-strength and conventional concrete targets.

LOCAL RESPONSE OF CONCRETE SLABS TO LOW VELOCITY IMPACT

David Z. Yankelevsky*

ABSTRACT

In missile impact of concrete slabs both local and structural response occur. The first part refers to the penetration, perforation, crushing and spallation, all of which affect only the small area near the point of impact; this part is treated in this paper.

The problem of a rigid cylinder or pipe, which impacts perpendicularly a concrete slab at low velocities ranging between 10-100m/sec, is considered. There exist full scale test data and empirical formulae which are applicable mainly for high velocities. Moreover, the empirical formulae provide the penetration depth which is somehow related to material and impactor properties, through an empirical constant, but do not provide any insight of the response, and further data such as time-history, shape of the damaged slab, etc.

In an attempt to gain better undertstanding of the local response of concrete to low velocity impact, a model has been developed to analyse the local concrete resistance mechanism, and introduce this mechanism to interact with the impacting cylinder. The model considers both the contributions of concrete and steel rebars.

The model predicts the cylinder's time history and maximum penetration depth, and if breaching of slabs occurs, the shape of failure surfaces is calculated.

The paper presents comparisons with test data, as well as empirical equations and computer code analysis.

---

* Faculty of Civil Engineering & National Building Research Institute, Technion - Israel Institute of Technology, Haifa 32000, ISRAEL.

Probabilistische Verfahren/Bedrohung

Probabilistics/Threat

Ein probabilistisches Schutzraum-Risiko-Modell

Erwin Kessler, Dr Ing, CH-9546 Tuttwil

Bernard Anet, dipl Ing, AC-Laboratorium, CH-3700 Spiez

1. Einleitung

Response-Spektren als Schock-Prüfkriterien lassen ziemlich willkürliche Testbedingungen zu [1] und führen zu einer Schein-Sicherheit. Ueber die tatsächliche Ueberlebenswahrscheinlichkeit der so geprüften Objekte unter realistischen Bedingungen in Schutzbauten geben solche Prüfungen keine Auskunft. Das kann sich verhängnisvoll auswirken, denn oft ist die Gebrauchsfähigkeit eines Schutzraumes von der Funktionsfähigkeit einer Reihe funktionell verketteter Objekte abhängig und unter Umständen schon beim Ausfall einer einzelnen Komponente zusammenbrechen. Das hier vorgestellte Schutzraum-Risiko-Modell stellt ein Mittel dar, diese Aspekte bei der Schutzraum-Planung und Komponenten-Prüfung systematisch zu berücksichtigen.
Damit wird es möglich, die Komponentenprüfung optimal in die Gesamtplanung von Schutzbauten einzubinden (maximale Schutzwirkung für minimalen Aufwand) und verbleibende Schwachstellen bei der Planung zu eliminieren. Zusammen mit einem fortgeschrittenen stochastischen Prüfkonzept [1,2] wird eine durchgehende probabilistische Behandlung der Schutzraumplanung möglich.

2. Versagenswahrscheinlichkeit von einzelnen Komponenten

Die Methodik zum Bestimmen der Versagenswahrscheinlichkeit eines Schutzraum-Einbauteiles unter Waffenwirkungen basiert auf Analyse-Verfahren, wie sie sich für die Risiko-Analysen (Probabilistic Risk Assessment) von Kernkraftwerken durchgesetzt haben [3,4,5,6,7,8]. In einer für die analoge Fragestellung in der Schutzbautechnik angepassten Form wird zunächst die Bedrohung bzw Belastung der betrachteten Komponente in durch Wahrscheinlichkeitskurven sogenannten Bedrohungskurven dargestellt. Dann wird die Versagenswahrscheinlichkeit betrachtet unter der Bedingung, dass eine bestimmte Bedrohung (Belastung) tatsächlich vorliegt: die sogenannte bedingte Versagenswahrscheinlichkeit, dargestellt in Komponenten-Empfindlichkeits-Kurven. Die effektive Komponenten-Versagenswahrscheinlichkeit wird dann mittels einer stochastischen Simulation aus der Bedrohungskurve und der bedingten Versagenswahrscheinlichkeit ermittelt. Schliesslich ergibt sich durch Betrachtung aller Schutzraum-Komponenten und deren Verkettungen die Versagenswahrscheinlichkeit der gesamten Anlage.

Am Beispiel der Ausfallursache "Schock" soll das Vorgehen näher erläutert werden.

2.1 Bedrohungskurven

Die Kurven geben an, mit welcher Wahrscheinlichkeit eine bestimmte vertikale Support-Geschwindigkeit (oder Beschleunigung) an der Decke überschritten wird. Die in Figur 1 gezeigten Bedrohungskurven basieren auf umfangreichen Schockberechnungen für typische Schweizer Zivilschutzbauten [1,2].

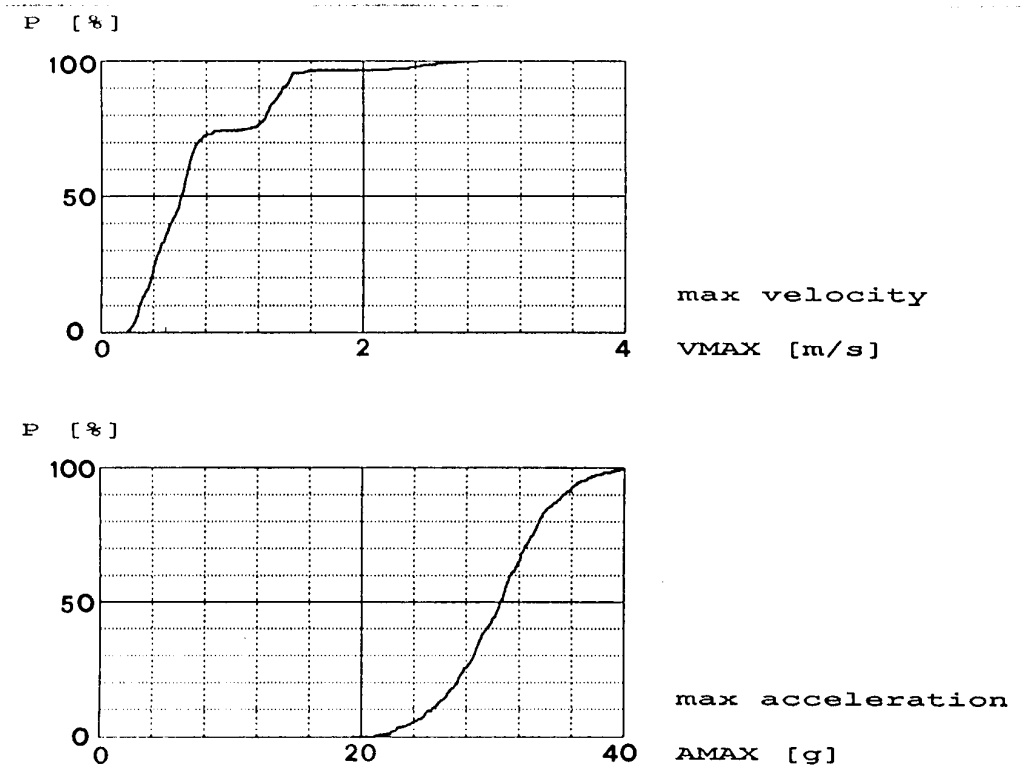

Figur 1. Bedrohungs-Kurven (hazard curves) für die Decke eines 3-bar-Schutzraumes nach Schweizer Normen

2.2 Komponenten-Empfindlichkeits-Kurven

Die Kurven der bedingten Versagenswahrscheinlichkeiten (= Empfindlichkeits-Kurven) definieren für die betrachtete Komponente (Einbauteil) die Versagenswahrscheinlichkeit bei einer gegebenen Supportgeschwindigkeit vmax. Solche Kurven werden aufgrund von Prüfdaten, Literaturangaben und - wo dies nicht ausreicht - aufgrund von Experten-Meinungen (expert opinion) geschätzt. Eine Bestimmung dieser Kurven durch Versuche allein ist in der Regel zu aufwendig. Zur Auswertung von Experten-Umfragen gibt es besondere statistische Methoden [9,10].

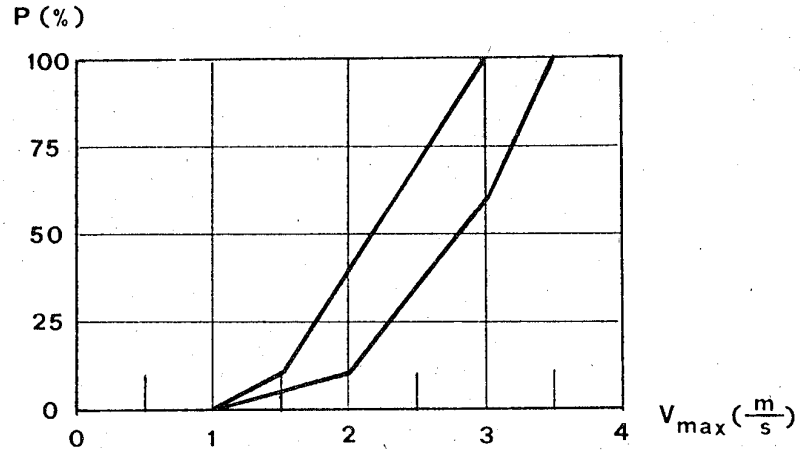

Figur 2. Komponenten-Empfindlichkeits-Kurve (component fragility curve) für ein Belüftungsgerät VA 2400, mit Median (50%-) und 5%-Nicht-Ueberschreitungs-Wahrscheinlichkeiten (nach Experten-Schätzung, gestützt auf langjährige Schockprüferfahrung)

2.3 Probabilistisches Modell zur Berechnung der Komponenten-Versagenswahrscheinlichkeiten

Wird zB der Schockparamter vmax als massgebender Bedrohungsparameter gewählt, dann kann der kritische Wert V von vmax, bei dem ein bestimmtes Einbauteil versagt, wie folgt formuliert werden:

$$V = V_m \cdot e$$

mit V_m = Median (V).

e ist eine stochastische Variable, welche die statistische Variabilität darstellt und gewöhnlich als lognormal verteilt angenommen wird mit der logarithmischen Standardabweichung ß.

Für eine gegebene Geschwindigkeit v ist die bedingte Versagenswahrscheinlichkeit [4]:

$$Pr(v>V) = F[(\ln v - \ln V_m)/ß] = F[(\ln v/V_m)/ß],$$

wobei F() die Standard-Gauss-Verteilung ist (standard Gaussian cumulative distribution function).

Diese Verteilung ist festgelegt, wenn der Medianwert V_m und die logarithmische Standardabweichung ß gegeben, bzw geschätzt sind.

Zur Vermeidung sehr grosser Prüfserien können Erfahrungsdaten (fragility data base) mit aktuellen Prüfergebnissen so kombiniert werden, dass der Medianwert V_m aus den Prüfungen genommen wird, die Standardabweichung ß aus den Erfahrungsdaten.

Bei der Verwendung bedingter Versagenswahrscheinlichkeits-Daten aus der Literatur sind die Voraussetzungen sorgfältig zu prüfen. So wurde zum Beispiel festgestellt, dass die Schockempfindlichkeiten von Schutzraum-Komponenten (ausgedrückt durch einen charakteristischen Wert der bedingten Ausfallwahrscheinlichkeit) nach [11] wesentlich ungünstiger liegen als aufgrund der Schockprüf-Erfahrungen in der Schweiz. Der Unterschied lässt sich damit begründen, dass den amerikanischen Daten offenbar beliebige handelsübliche, nicht schockisolierte Geräte zugrundeliegen, während in der Schweiz durch die Schockprüfung eine relativ strenge Auswahl getroffen wird und Schockisolations-Massnahmen als fester Bestandteil des Gerätes betrachtet werden.

Zur Berechnung der Komponenten-Versagenswahrscheinlichkeit aus der Bedrohungs-Kurve und aus der Verteilung der bedingten Versagenswahrscheinlichkeiten wurde das folgende Fortran-Programm FRAGSIM erstellt. Es berechnet aus der Bedrohungs- und aus der bedingten Versagens-Verteilung je 1000 stochastische Werte und vergleicht sie paarweise. Ist der Bedrohungswert grösser als der Versagenswert, liegt ein Ausfall vor. Die Häufigkeit der Versager (Anzahl Versager dividiert durch die totale Anzahl Fälle, also 1000) wird als Komponentenversagenswahrscheinlichkeit unter der gegebenen Bedrohung interpretiert.

FRAGSIM

```
      PROGRAM FRAGSIM
*****************************************************************
*     FRAGSIM is a stochastic simulation program to determin the *
*     failure probability, ie the probability of Z = F - H < 0   *
*     where F and H are stochastic variables defined by there    *
*     cumulative frequency distribution. H represents the hazard *
*     and F the fragility (conditional failure).                 *
*                                                                *
*     The distribution functions are defined on input file FRAGIN*
*     with 8 points. First Hazard, then Fragility. First line    *
*     velocity [m/s], second line cumulative probability.        *
*                                                                *
*     This program is in standard Fortran77 and applies IMSL     *
*     mathematical and statistical library.                      *
*                                                                *
*     Author: Erwin Kessler, consultant, CH-9546 Tuttwil         *
*     Last update: 1990/01/15                                    *
*****************************************************************
      REAL TBL(8,5),H(1000),F(1000)
      ISEED=24183
      CALL RNSET(ISEED)        Initialisation of random generator
      IZ=1000
      OPEN(3,FILE='FRAGIN')
      OPEN(2,FILE='OUTPUT')
      READ(3,10)  (TBL(I,1),I=1,8)
      READ(3,10)  (TBL(I,2),I=1,8)
10    FORMAT(8F10.3)
      CALL RNGCT(IZ,8,TBL,8,H)      random generator (Gauss)
      READ(3,10)  (TBL(I,1),I=1,8)
      READ(3,10)  (TBL(I,2),I=1,8)
      CALL RNGCT(IZ,8,TBL,8,F)
      N=0
      DO 100 I=1,IZ
        IF(F(I)-H(I).LT.0.)N=N+1
100   CONTINUE
      PF=FLOAT(N)/1000.
      PRINT*,'PROBABILITY OF FAILURE =',PF
9999  END
```

3. Gebrauchsfähigkeit einer ganzen Schutz-Anlage nach Waffenwirkungen

Anhand der Versagenswahrscheinlichkeiten der einzelnen Komponenten kann die Wahrscheinlichkeit beurteilt werden, mit der eine ganze Anlage nach Waffenwirkungen noch gebrauchsfähig ist. Dabei ist die funktionelle Verkettung verschiedener Komponenten von grosser Bedeutung: Funktioniert ein System nur, wenn alle hintereinandergeschalteten Komponenten funktionieren, dann strebt die Versagenswahrscheinlichkeit bei mit zunehmender Anzahl Komponenten rasch gegen 1, das heisst das System versagt mit an Sicherheit grenzender Wahrscheinlichkeit. Beispiel: Eine nicht von Hand betreibbare Belüftung funktioniert im Gasfall bei Ausfall der Netzspeisung nur, wenn jede einzelne der folgenden Komponenten funktioniert: Starter-Batterien für den Notstrom-Generator, Steuerschrank, Notstromaggregat, Hauptverteiler, Unterverteiler, Vorfilter, Luftverteilleitungen, Gasfilter, gasdichte Klappen, Belüftungsgerät. Alle diese Komponenten werden einzelnen schockgeprüft, müssen aber alle zusammen gleichzeitig funktionstüchtig bleiben, damit die Belüftung nicht versagt.

Das Komplement der Versagenswahrscheinlichkeit ist die Ueberlebenswahrscheinlichkeit. Damit lässt sich hier einfacher rechnen. Für die Ueberlebenswahrscheinlichkeit P_k der k-ten SR-Komponente gilt nach den Regeln der Wahrscheinlichkeitsrechnung:

$$P_k = P_i \; P_{ki}$$

wobei k = Komponenten-Nummer
i = Versagensursache

Versagensursachen (Bedrohungen):

i=1 : Luft- und Erdstossbelastung aus nuklearen oder konventionellen Detonationen
i=2 : Penetration von Geschossen
i=3 : Schock/Erschütterung
i=4 : Bruch oder Verschiebung benachbarter Komponenten (Kollision)
i=5 : Versagen der Befestigungen
i=6 : Trümmer auf Zugang und Luftfassung
i=7 : Brand (Gase, Hitze)
i=8 : EMP
i=9 : Planungs- und Ausführungsfehler
i=10: Alterungs- und Stillstandschäden, Unterhaltsmängel

Es ist kaum möglich und wohl auch nicht nötig, alle diese Versagensursachen mit Bedrohungskurven oder auf andere Weise im Detail zu analysieren. Für wenig bedeutende Nebeneinflüsse können die Versagenswahrscheinlichkeiten durchaus direkt geschätzt werden. Das ist immer noch besser, als sie vollständig ausser acht zu lassen.

Planungs- und Ausführungsfehler (i=9) können sich bei Schutzbauten - wo in der Regel keine Sicherheitsfaktoren angewendet werden und wo nicht laufend aus Fehlern gelernt werden kann - unmittelbar auswirken und werden deshalb explizit erfasst, obwohl ihre quantitative Bedeutung schwierig zu schätzen ist. Es wird aber dadurch ermöglicht, die Optimierung des Kosten/Nutzen-Verhältnisses für Qualitätssicherungsmassnahmen in die Gesamtbetrachtung einzubeziehen.

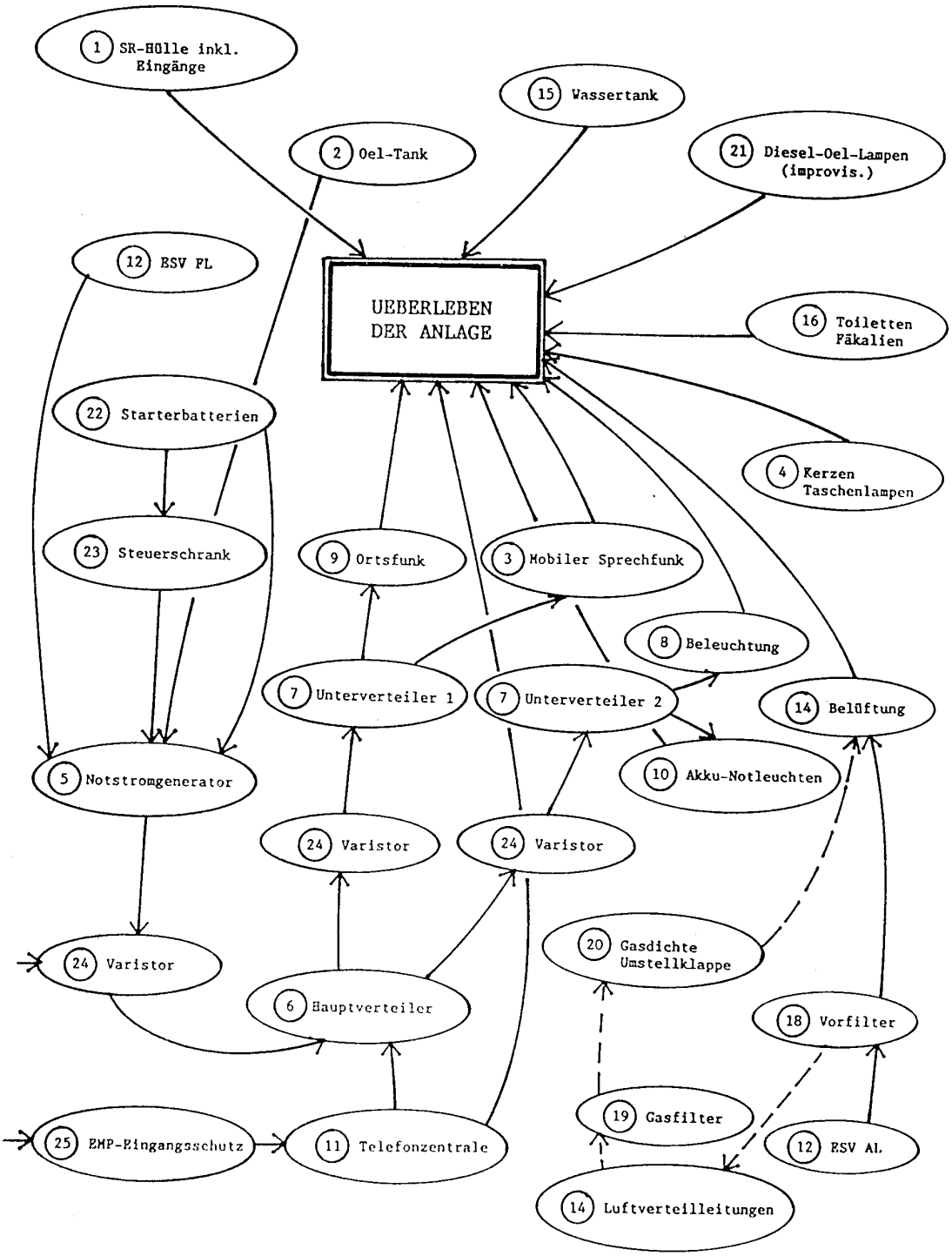

Figur 3. Ueberlebens-Schema

Für die Berechnung der totalen Versagenswahrscheinlichkeit aus den Komponenten-Versagens-Wahrscheinlichkeiten und den Verknüpfungen gemäss dem Schema in Figur 3 wurde ein Fortran-Programm namens SURVIVAL erstellt. Die zum Teil nur rudimentär bekannten einzelnen Versagensursachen verhindern, dass auf diese Weise zuverlässige absolute Versagenswahrscheinlichkeiten berechnet werden können. Die Durchrechnung vieler Beispiele mit unterschiedlichen Annahmen (Sensitivitäts-Analysen) liefert jedoch nützliche Einsichten in die relative Bedeutung der einzelnen Komponenten für die Gebrauchsfähigkeit einer ganzen Schutzanlage. Damit lassen sich Schutzmassnahmen gezielt dort treffen, wo sie die grösste Wirkung haben. Das dient der Ausgewogenheit und Wirtschaftlichkeit der Schutzbauten.

Beispiele zur praktischen Anwendung dieser Methodik werden bei nächster Gelegenheit publiziert. Den Schockspezialisten des AC-Laboratoriums Spiez, P. Hunziker und K. Waber, sind die wertvollen Erfahrungsdaten der Schockprüfung zu verdanken, welche diesem Schutzraum-Risiko-Modell zugrunde liegen.

Literatur

[1] Kessler: Stochastic Simulation of Shelter Equipment Vibrations due to Nuclear Explosions, 8th International Symposium on Military Applications of Blast Simulation (MABS 8), 1983

[2] Anet/Hunziker/Kessler: Statistics of Stochastic Shelter Shock Motions Induced by Nuclear Explosions, MABS 9, 1985

[3] Holman/Chou: Using Component Test Data to Develop Failure Probabilities and Improve Seismic Performance, 9th SMIRT-Conference, 1987

[4] Kennedy/Ravindra: Seismic Fragilities for Nuclear Power Plant Risk Studies, Nuclear Engineering and Design 79, 1984

[5] Hwang: Fragility Assessment for Seismic PRA Studies, 8th SMIRT-Conference, 1985

[6] Gou: Some Studies on the Estimation of Structural Fragility, 8th SMIRT-Conference, 1985

[7] Bohn et al: Application of the SSMRP Methodology to the Seismic Probabilistic Risk Analysis at the Zion Nuclear Power Plant, 7th SMIRT-Conference, 1983

[8] Bohn et al: A Simplified Seismic Risk Methodology Applied to Generic Shutdown Heat Removal Issues for US Reactors, 8th SMIRT-Conference, 1985

[9] Mosleh/Apostolakis: On the Derivation of Fragility Curves From Expert Opinion, 9th SMIRT-Conference, 1987

[10] Mosleh/Apostolakis: A Method for Estimating Fragility Curves Using Expert Opinions, 7th SMIRT-Concerence, 1983

[11] TM5-855-1: Fundamentals of Protective Design for Conventional Weapons, Technical Manual, November 1986, Washington

RELIABILITY-BASED DESIGN OF R/C STRUCTURES FOR PROTECTION AGAINST PROJECTILES AND FRAGMENTS

Sues, Robert H.; Hwang, Chii-Wha; Twisdale, Lawrence A.; Lavelle, Francis M.

Applied Research Associates, Inc., 6404 Falls of Neuse Road, Suite 200, Raleigh, NC 27615, USA

ABSTRACT

This paper summarizes the results of research to develop new reliability-based methods for the design of reinforced concrete (R/C) protective structures from the threat of penetrating projectiles and the effects of bomb fragmentation. The design methods are presented in an easy to use format, using reliability-based design factors (RBDFs). RBDFs are used in the same manner as traditional design safety factors, except that the safety factors are based on a specified level of survival probability. Traditional design methods provide no information on the degree of conservatism inherent in the design. A second important product of this research, is a systematic assessment of key uncertainties and identification of areas where further research can have the most significant benefit.

INTRODUCTION

Current protective construction design methods provide very limited information on the level of conservatism or safety inherent in a design and very limited guidance on the selection of an appropriate design safety factor. The purpose of this research is to systematically study the conservatisms/unconservatisms and uncertainties inherent in current design methodology as represented in the recently published *Protective Construction Design Manual* (*PCDM*) [Drake, *et al*, 1989] in order to develop new reliability-based design methods. These new methods provide reliability-based design factors (RBDFs) that are similar to traditional safety factors except that factors are provided for different levels of survival probability. This research is also providing a systematic assessment of key uncertainties and identification of areas where further research can have the most significant benefit.

The research presented in this paper is part of a program being conducted by the U. S. Air Force Engineering and Services Center. A companion paper provides an overview of this research program [Twisdale, *et al*, 1991]. This paper presents the results of research into development of RBDFs for design of reinforced concrete (R/C) against projectile penetration and bomb fragmentation. For projectile penetration, four phenomena are relevant to R/C protective construction design: (1) depth of penetration into a semi-infinite target; (2) spalling of a finite-thickness target; (3) perforation of a finite-thickness target; and (4) residual velocity after penetrating a finite-thickness target. Design against bomb fragments requires a systematic treatment of randomness since for a given standoff there are large uncertainties associated with the number of fragments that will hit the structure, the mass distribution of the fragments, the striking velocity of the fragments, and finally, whether or not the fragments will penetrate. All these factors will affect the survival probability of the structure contents and are treated in the development of a new simplified method for selection of design fragments and the required RBDFs. Due to space limitations, this paper emphasizes spall and perforation analysis; brief summaries are presented for depth of penetration, residual velocity, and fragmentation effects.

PENETRATION DATA

Penetration data collected from two data bases served as data sources for this study. Both databases provide data on penetrator characteristics, target characteristics, and penetration performance. The first information source for this study is a database that was developed for the U. S. Air Force Armament Laboratory (AFATL) [Weeks and Raspberry, 1987]. The Air Force database was taken primarily from test results by Beth and Stipe [1943]. These results were

predominantly for small projectiles impacting massive concrete targets. In total 712 data records were compiled by the Air Force. A second data source used was the database created by Sandia National Laboratories [Christensen, 1988], which catalogs over 900 penetration tests. The database encompasses data from soil, rock, ice, ocean sediments, permafrost, and concrete penetration tests. Of these tests, 147 are concrete penetration tests, some of which are also in the AFATL database.

All of the data items from both databases were reviewed and selectively reduced to eliminate obvious errors, unclear results, and duplications. Finally, 710 data records were selected. Note that, not all of these records contain sufficient information or are relevant to all four phenomena of interest. For analysis of depth of penetration 534 records were selected; for analysis of spall and perforation 703 records were selected; and for analysis of residual velocity 45 records were selected. A detailed statistical analysis of all input and output variables for all records was performed in order to qualify the range of applicability of the analysis and reliability-based models developed herein.

SPALL AND PERFORATION OF REINFORCED CONCRETE

The reliability-based design procedure for spall and perforation is developed using the dichotomous regression technique [Cox and Snell, 1989; Hosmer and Lemeshow, 1989; Veneziano and Liao, 1984]. The dichotomous regression technique uses penetration testing data to find the probability of spall or perforation as a function of penetrator and target characteristics.

For this analysis 703 records were selected from the data base. The distributions of penetrator weight and striking velocity are shown in Figure 1. As seen in the figure, most of the data are from small projectile testing, however, the data set does include a number of large projectiles. The impact velocities are distributed over a range from 400 to 3300 fps, with approximately 70% of the impact velocities in the 700 to 2000 *fps* range. The concrete compressive strengths used in the tests are centered around 5000 *psi*, and the data set encompasses a range of values that are representative of compressive strengths used in protective construction.

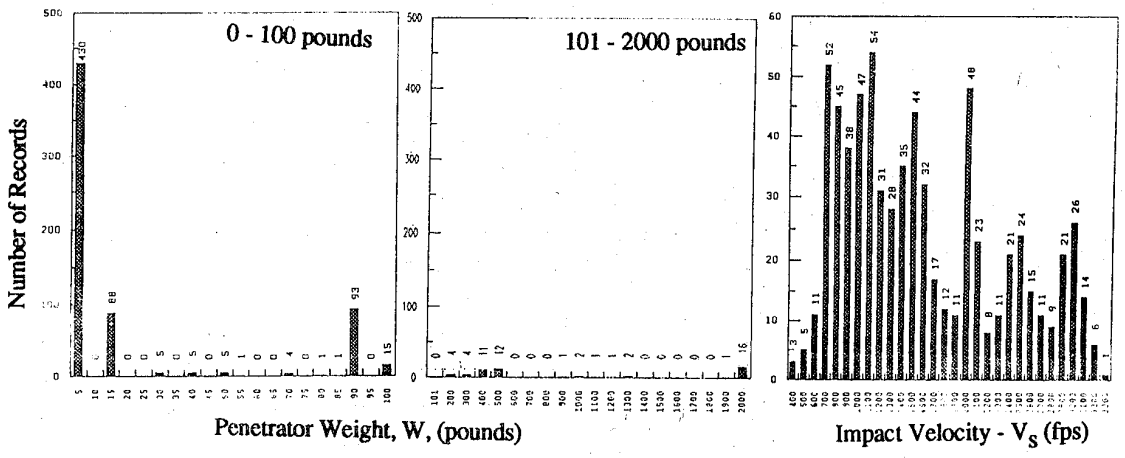

Figure 1. Distributions of Penetrator Weight and Striking Velocity in the Data Records Selected for Spall and Perforation Analysis

Dichotomous Regression. The dichotomous regression method develops a probability-based prediction model using the method of maximum likelihood. The term dichotomous refers to the fact that the observed data are categorized as either "fail" or "no-fail." For example, the spall data are categorized as either "spall" or "no-spall."

For dichotomous regression, a logistic form is often used for the probability distribution, since it allows for a mathematically tractable treatment. It is selected for the damage model herein since it was also found to fit the data exceptionally well. The logistic form used in this study is:

$$P_F = \frac{exp\left[G\left(\underline{x}\right)\right]}{1 + exp\left[G\left(\underline{x}\right)\right]} \tag{1}$$

where $\underline{x}$ are the set of problem parameters (*i.e.*, penetrator and target characteristics) and the function $G(\underline{x})$ is a linear combination of given functions of the problem parameters, $\underline{x}$, *i.e.*

$$G(\underline{x}) = A_0 + \sum_{i=1}^{n} A_i\, g_i(\underline{x}) \tag{2}$$

Different logistic models correspond to different choices of the functions $g_1, g_2, \ldots, g_n$, whereas the coefficients, A_i, are determined from data.

The Statistical Analysis System [1990], procedure LOGISTIC is used to perform the maximum likelihood estimation of the parameters for the dichotomous regression. Once the parameters are estimated, statistical measures are presented to quantify goodness-of-fit and to compare the different models. These measures include [Venezicno and Liao, 1984; SAS, 1990]: (1) Percent Correctly Predicted; (2) Likelihood Ratio Statistic; (3) Akaike Information Criterion; (4) Schwartz Criterion; and (5) Chi-Square test for Covariates.

Reliability-Based Design Model. For spall and perforation, the problem parameters (x's in Eq. 2) can be any physical or mechanical properties of the penetrator and target, *e.g.* wall size, concrete strength, penetrator size, and impact velocity, *etc.*, and the G function (which is now an indicator of the likelihood of spall or perforation), can take a number of very general forms. A simplified approach, however, is to base the *G* function on the deterministic predictors given in the *PCDM* [Drake, *et al.*, 1989]. In this way the reliability-based method can be used with the existing deterministic methodology. This approach is not as accurate as using a more general form for the G function, but it will suffice if the existing deterministic model is a reasonably good predictor. As will be shown below, this approach was found to be accurate for prediction of perforation and spall probability.

In the *PCDM*, the minimum thickness of a concrete wall required to prevent spalling, t_s, and perforation, t_p, due to projectile impact are given as:

$$t_s = \begin{cases} 7.91x - 5.06x^2/d & x < 0.65d \\ 1.36x + 2.12d & 0.65d \le x \le 11.75d \end{cases} \tag{3}$$

$$t_p = \begin{cases} 3.19x - 0.718x^2/d & x < 1.35d \\ 1.24x + 1.32d & 1.35d \le x \le 13.5d \end{cases} \tag{4}$$

where t_s and t_p are in *inches*, d is the projectile diameter (*in*) and x is the depth of penetration in massive concrete (*in*) given as:

$$x = \frac{26.8\sqrt{NW}\, v_s^{0.9}}{f_c'^{0.25} d^{0.4}} \qquad x \le 2d$$

$$x = \frac{180\, NW (v_s/d)^{1.8}}{f_c'^{0.5}} + d \qquad x > 2d \tag{5}$$

in which W, d, N, v_s, and f_c' are respectively: penetrator weight (*lbs*), penetrator diameter (*in*), penetrator nose shape factor, striking velocity (*kfps*), and concrete unconfined compressive strength (*psi*).

If these models were exact predictors, then spall would occur whenever $t_s >$ the wall thickness, t, and perforation would occur whenever $t_p > t$. Hence, we can define G functions in terms of t_s/t and t_p/t in the dichotomous regression. For spall:

$$G(x) = A_0 + A_1 \ln (t_s/t) \tag{6}$$

and for perforation:

$$G(x) = A_0 + A_1 \ln (t_p/t) \tag{7}$$

The estimated G functions and their goodness-of-fit statistics for perforation and spall are shown in Table 1. For both cases, models wherein A_0 is set to 0 were also fit. It can be seen from Table 1 that all models fit equally well and are statistically significant (since the probability of exceeding the Chi-Square is almost zero). Interestingly, this indicates that the *PCDM* prediction method is essentially median centered and unbiased. That is, it is neither conservative nor unconservative. The plots of the logistic probability distributions for both spall and perforation are

TABLE 1. G FUNCTIONS FOR MODELING CONCRETE SPALL (t_s/t), PERFORATION (t_p/t), AND ASSOCIATED GOODNESS-OF-FIT STATISTICS (703 DATA POINTS)

Goodness of Fit Measure	SPALL		PERFORATION	
	$G = 0.007 + 6.27\ ln\left(\frac{t_s}{t}\right)$	$G = 6.27\ ln\left(\frac{t_s}{t}\right)$	$G = -0.34 + 6.27\ ln\left(\frac{t_p}{t}\right)$	$G = 6.78\ ln\left(\frac{t_p}{t}\right)$
Percent Correctly Predicted	0.927	0.927	0.898	0.929
Likelihood Ratio	541.7	541.7	462.0	457.0
Akaikie Information Criterion	371.3	369.3	305.8	308.8
Schwartz Criterion	380.4	373.8	314.9	313.3
Chi-Square	541.7	607.3	462.0	667.8
Pr > Chi-Square	0.0001	0.0001	0.0001	0.0001

shown in Figure 2. The abscissa is the value of the G function. Also shown on the figure are the actual data points, where observations of spall (or perforation) are plotted as 1.0, and observations of no spall (or no perforation) are plotted as 0.0.

Using these models, we can develop the RBDFs for spall and perforation based on the design manual equations (Equations 3 and 4 here). Given that all problem inputs are known, the reliability of a wall of thickness t to resist spall can be determined from:

$$R\left(t_s/t\right) = 1 - P_F\left(t_s/t\right) = 1 - \frac{exp\left[G\left(t_s/t\right)\right]}{1 + exp\left[G\left(t_s/t\right)\right]} = \frac{1}{1 + exp\left[G\left(t_s/t\right)\right]} \tag{8}$$

where t is the wall thickness and t_s is the spall thickness given by Equation 3. By substituting the second model for spall (Table 1) into the above equation, we obtain

$$R\left(t/t_S\right) = \frac{1}{1 + exp\left[-6.27\ ln\left(t/t_S\right)\right]} = \frac{1}{1 + \left(t/t_S\right)^{-6.27}} \tag{9}$$

Similarly, for perforation,

$$R\left(t/t_p\right) = \frac{1}{1 + \left(t/t_p\right)^{-6.78}} \tag{10}$$

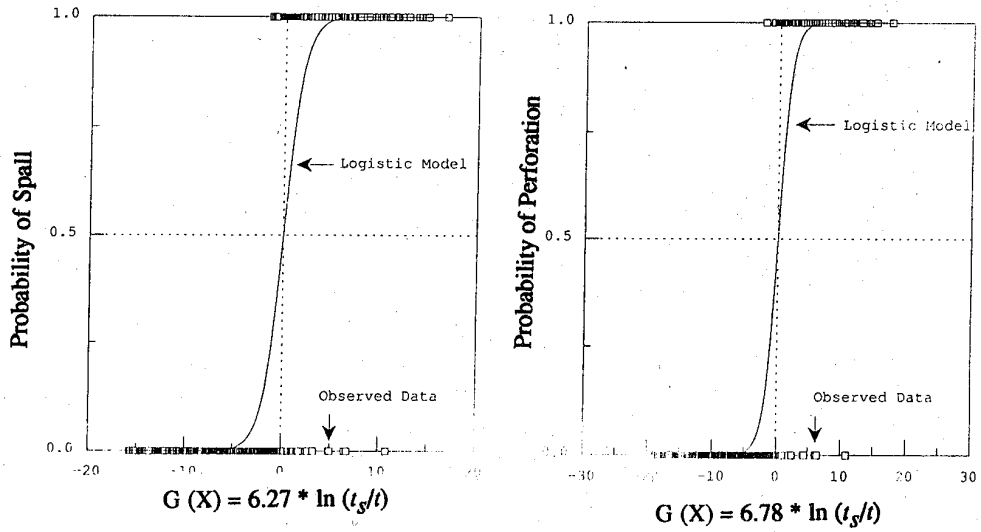

a. Spall b. Perforation

Figure 2. Logistic Probability Model for (a) Concrete Spall and (b) Concrete Perforation

TABLE 2. RELIABILITY OF WALL THICKNESS TO PREVENT SPALL AND PERFORATION[1, 2]

Reliability	$P_F(x)$	$G(x)$	RBDF	
			Spall t/t_s	Perforation t/t_p
0.01	0.99	4.60	0.48	0.51
0.05	0.95	2.94	0.63	0.65
0.10	0.90	2.20	0.70	0.72
0.25	0.75	1.10	0.84	0.85
0.50	0.50	0.00	1.00	1.00
0.75	0.25	-1.10	1.19	1.17
0.90	0.10	-2.20	1.42	1.38
0.95	0.05	-2.94	1.60	1.54
0.99	0.01	-4.60	2.08	1.97

[1] t_s, t_p as defined by Equations 3, 4, respectively

[2] Assumes all inputs to Equations 3 and 4 are deterministic

Using Equations 9 and 10, Table 2 lists the reliability-based design factors, t/t_s and t/t_p, and their associated reliabilities that account for the spall and perforation model error. Again, note that for $t/t_s = 1.0$ and $t/t_p = 1.0$, the reliability = 0.50, indicating that the design manual predictions are essentially unbiased.

To complete the reliability analysis, it is necessary to consider uncertainty in the problem inputs, that is, f'_c, W, v_s, N and d. The depth of penetration predicted by the design equation is not very sensitive to the concrete compressive strength and, in light of other uncertainties, it can be shown that the random uncertainty in concrete compressive strength will not contribute significantly to the prediction uncertainty. Also, for design, we neglect the uncertainty in concrete compressive strength prediction error; hence, concrete compressive strength need not be considered further for the reliability-based prediction model.[1] The remaining variables, W, d, N, and v_s, are weapon descriptors. We assume here that the weapon threat is specified so that there is no prediction error in these variables. Also, for a specified weapon threat the random uncertainty in W, N, and d will be the result of manufacturing tolerances and will be small with respect to the effect of striking velocity uncertainty. Hence, W, N, and d are treated deterministically. Table 3 presents load factors that should be applied to the best estimate striking velocity, for spall and perforation, respectively. The factors were obtained using Monte-Carlo simulation analysis techniques. The factors are given as a function of the desired reliability level and the coefficient of variation of striking velocity. For example, for perforation, if the striking velocity coefficient of variation is 0.30, and the desired reliability is 90%, then the specified striking velocity (which should be the mean-centered best estimate for the specified threat) is multiplied by 1.16.

TABLE 3. STRIKING VELOCITY LOAD FACTORS FOR PREDICTION OF CONCRETE SPALL AND CONCRETE PERFORATION

	CONCRETE SPALL					CONCRETE PERFORATION				
	COEFFICIENT OF VARIATION					COEFFICIENT OF VARIATION				
P_s	0.1	0.2	0.3	0.4	0.5	0.1	0.2	0.3	0.4	0.5
0.01	0.95	0.86	0.66	0.36	0.24	0.95	0.81	0.55	0.28	0.16
0.05	0.96	0.90	0.77	0.63	0.51	0.96	0.87	0.70	0.55	0.42
0.10	0.97	0.91	0.81	0.72	0.64	0.97	0.89	0.77	0.66	0.57
0.25	0.98	0.95	0.90	0.84	0.81	0.98	0.94	0.87	0.81	0.78
0.50	1.00	1.00	1.00	1.00	1.00	1.00	1.00	1.00	1.00	1.00
0.75	1.02	1.05	1.08	1.12	1.19	1.03	1.06	1.08	1.12	1.20
0.90	1.04	1.09	1.16	1.24	1.33	1.04	1.10	1.16	1.24	1.35
0.95	1.05	1.10	1.18	1.28	1.42	1.06	1.12	1.19	1.29	1.46
0.99	1.06	1.13	1.27	1.38	1.60	1.09	1.18	1.31	1.43	1.65

[1] For a targeting study, prediction uncertainty would be treated by assigning subjective probability weights to assumed values of the mean concrete strength and performing the penetration analysis for the different mean values to achieve a final probabilistic result.

The reliability-based design procedure then is:

1. Set required reliability.
2. Multiply best estimate striking velocity by the load factor from Table 3.
3. Compute t_s and/or t_p using *PCDM* equations (Equations 3 and 4 here) with the factored striking velocity from Step 2.
4. Select RBDF (t/t_s and/or t/t_p) values from Table 2.
5. Obtain design wall thickness by multiplying result of Step 3 by RBDF from Step 4.

Design Example. Design, the thickness of a reinforced concrete wall to resist perforation by 30*mm* A/C cannon fire with a reliability of 95%. Concrete strength is 5,000 *psi* and the striking velocity coefficient of variation is 20%. From the *PCDM* the relevant projectile characteristics are: $W = 0.90$ *lbs*; $d = 1.18$ *in*; $N = 1.10$; $v_s = 3.15$ *k fps*. For deterministic analysis, t_p is computed using these properties as 21.38 *in* (54.31 *cm*). For the reliability-based design, we first multiply the striking velocity by the factor given in Table 3. For the desired reliability of 95% and the given striking velocity coefficient of variation of 0.2, the factor is 1.12. Hence, t_p, is evaluated using a striking velocity of (1.12) (3.15) = (3.53 k *fps*). This gives $t_p' = 25.48$ *in* (64.71 *cm*). From Table 2 for 95% reliability, $t/t_p = 1.54$. Hence, the design wall thickness $t^* = (1.54)\ (25.48) = 39.24$ *in* (99.67 *cm*). Note that to achieve 95% reliability, the nominal, or deterministic, design thickness is increased by an overall factor of roughly 1.8.

DEPTH OF PENETRATION AND RESIDUAL VELOCITY

For depth of penetration, a statistical comparison analysis of prediction results vs. observed penetration data was performed on the data base using the procedure described in Twisdale *et al.* [1988]. Based on these results factors were obtained and are given in Table 4. Corresponding striking velocity factors are also given in Table 4. The RBD procedure is similar to that for spall/perforation. That is, the striking velocity is factored by a value from Table 4, penetration depth is computed (using the factored striking velocity) from Equation 5, and the resulting penetration depth is factored by a value λ from Table 4 (to achieve the desired level of confidence in the prediction). As an example application, these factors would be used in designing against an explosive penetrator, wherein it is desirable to ensure that the penetrator is stopped well within the wall. This approach can also be used for targeting analysis, to determine confidence levels for computed depths of penetration for weapons designed to explode after penetration.

TABLE 4. CONFIDENCE LEVEL OF MODEL FACTOR, λ, IN PREDICTING DEPTH OF PENETRATION AND CORRESPONDING STRIKING VELOCITY LOAD FACTORS

Reliability	λ	Striking Velocity Factors Coefficient of Variation				
		0.1	0.2	0.3	0.4	0.5
0.01	0.59	0.90	0.75	0.44	0.24	0.14
0.05	0.79	0.91	0.78	0.60	0.43	0.34
0.10	0.88	0.92	0.80	0.67	0.56	0.47
0.25	0.97	0.95	0.89	0.83	0.76	0.72
0.50	1.03	1.00	1.00	1.00	1.00	1.00
0.75	1.11	1.05	1.10	1.16	1.22	1.30
0.90	1.23	1.07	1.16	1.27	1.38	1.51
0.95	1.36	1.09	1.17	1.30	1.42	1.59
0.99	1.73	1.10	1.18	1.32	1.52	1.71

Calculation of residual velocity is very important in the design of layered systems and in cases where it is not possible to prevent complete perforation. Unfortunately, the residual velocity data base is very limited. Preliminary design factors for prediction of residual velocity have been developed, however, this is clearly an area that requires further work. The factors that we have developed to date account for the fact that data is limited. These factors exact a penalty for this lack of data. Due to space limitations these factors are not presented here.

FRAGMENTATION

For analysis of threat from bomb fragments, it is necessary to also analyze the uncertainty in predicting the fragmentation environment at the structure, considering fragment weight distribution, transport, impact probability, and penetration effects. Traditional design approaches have attempted to do this by employing a probability distribution for fragment weight known as the Mott distribution and using this distribution to select "design" fragments. It has been shown, however, that the probability levels given by the Mott distribution, are not correlated with the structure survival probability [Dass and Twisdale, 1987].

The traditional design approach is actually a misapplication of probability theory. The proper approach for design must consider the number of fragments that impact the structure (and do not ricochet), which is a function of bomb location and other parameters. Clearly, as the bomb is moved closer to the structure more fragments will hit (and stick). Hence, the probability increases that fragments large enough to penetrate will hit. A reliability-based design approach is being developed that properly accounts for the inherent randomness in predicting the bomb fragmentation environment and the likelihood of fragment damage. The approach differs from the current methodology in that the "design" fragment is not selected from the Mott distribution. Rather, the design fragment is selected from a probability distribution that is derived using extreme value theory. This is the proper approach for design and, for example, is the approach that is incorporated in design of conventional structures for wind loading. The extreme value distribution explicitly accounts for the number of non-ricochet hits and it can be shown that design fragments selected in this way, correlate with survival probability.

The simplified reliability-based design approach for bomb fragmentation can be summarized as follows:

1. Evaluate the number of non-ricochet fragments
2. Develop the design fragment extreme value distribution and select the design fragment.
3. Apply a reduction factor to the design fragment weight to account for non-standard fragment shape.
4. Obtain the mean striking velocity and apply a reduction factor to account for non-normal impact.
5. Design the structure thickness to resist perforation using the RBD procedure for penetration described above.

The process is straightforward and requires no more calculational effort than the current design methodology. As may be noted, the process does require evaluation of the number of non-ricochet fragments. For this purpose, simple design charts have been developed. An example is illustrated in Figure 3. Note that once the design fragment is selected, the design process proceeds (step 5) in a manner similar to that described above for design against a penetrating projectile. Hence, the design process treats all of the uncertainties in predicting the fragment environment at the structure and the uncertainty in the penetration prediction equations. Work is currently underway to complete development of the reduction factors used in steps 3 and 4.

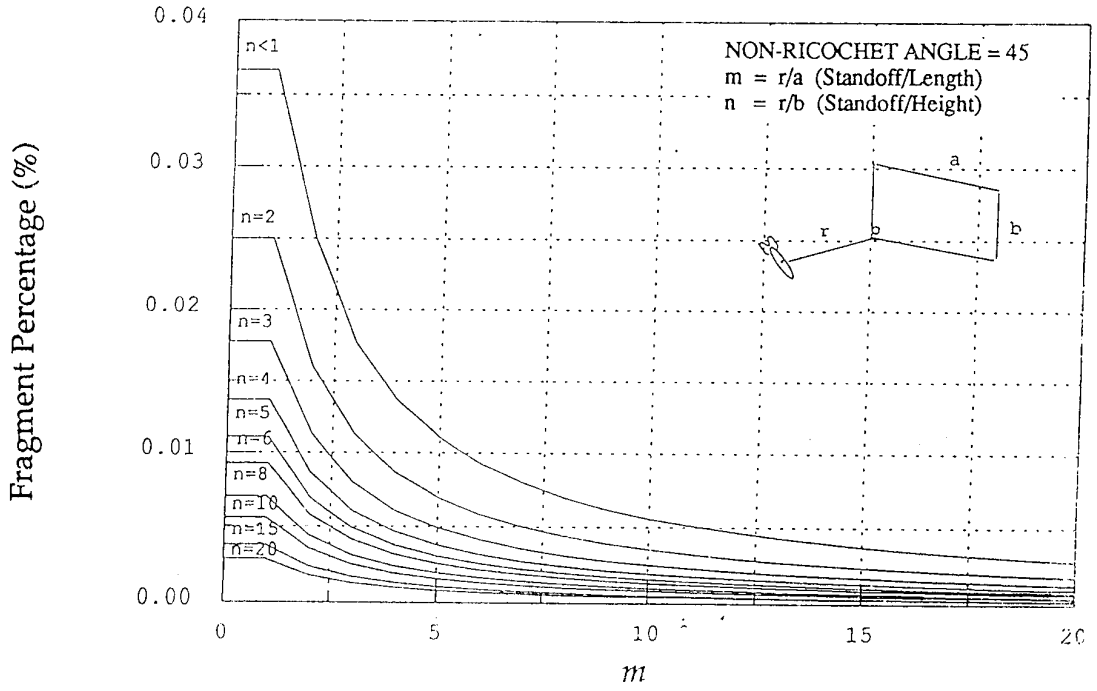

Figure 3. Design Chart for Number of Non-Ricochet (45°) Hits

SUMMARY

Simplified reliability-based design procedures are presented that do not require the designer to perform "probabilistic analyses." The procedures employ reliability-based design factors (RBDF) that are applied in the same manner as traditional design safety factors. For penetration analysis the designer simply factors the best estimate striking velocity by a tabulated load factor, computes penetration depth or spall/perforation thickness using the *PCDM* equations [Drake, *et al.*, 1989], and then factors the wall thickness (given by the design manual equations) by a

capacity safety factor. The advantage of the RBD approach is that the tabulated load and capacity factors are given as a function of survival probability, hence, the designer is provided with a quantifiable measure of safety or reliability for the design.

It is significant to note that the *PCDM* equations for prediction of depth of penetration into massive concrete and prediction of spall or perforation were found to be essentially unbiased. It was, however, found that for prediction of residual velocity there is bias and significant uncertainty. Due to the importance of estimating residual velocity (particularly for analysis of layered systems) improvements to the prediction models seems warranted.

A new methodology for the selection of design fragments was also presented. Earlier work had shown that designs using the traditional approach are not correlated to survival probability [Dass and Twisdale, 1987]. The new RBD methodology uses extreme value probability theory to obtain a design fragment that explicitly accounts for the number of non-ricochet hits (obtained from design charts) and can be shown to be correlated with survival probability.

REFERENCES

Beth, R. A., and Stipe, J. G., *Penetration and Explosion Tests on Concrete Slabs, Report I: Data*, Interim Report to the Chief of Engineers, United States Army, National Research Council, CPPAB Interim Report No. 20, January, 1943.

Christensen, B. K., *Twenty-Five Years of Penetration Records at Sandia National Laboratories, PENTDB: A Relational Database*, Sandia National Laboratories, SAND-88-1402, 1988.

Cox, D. R., and Snell, E. J., *The Analysis of Binary Data*, 2nd Edition, Chapman and Hall, London, 1989.

Dass, W.C., Twisdale, L. A., "Comparison of Design Procedures for Fragmentation Effects, "*Third International Symposium on Interaction of Conventional Munitions with Protective Structures*, Mannheim, FRG, 1987.

Drake, J. L.,Twisdale, L. A., *et al.*, *Protective Construction Design Manual*, ESL-TR-87-57, Air Force Engineering Services Laboratory, Tyndall Air Force Base, Florida, November 1989.

Hosmer, D. W., and Lemeshow, S., *Applied Logistic Regression*, John Wiley & Sons, Inc., New York, 1989.

Statistical Analysis System, *CALIS and LOGISTIC Procedures*, SAS Technical Report P-200, 1990.

Twisdale, L. A., Sues, R. H., and Miller, D., "Research to Develop Reliability-Based Design Methodology for Protective Structures," *Proc. Fifth Int Symp on Int of Conv Munitions with Protective Structures*, Germany, April 22-26 1991.

Twisdale, L.A., Sues, R.H., and Murphy, C.E., *Assessment of Reliability-Based Design Methodology for Protective Structures*, ESL-TR-88-27, Air Force Engineering & Services Laboratory Tyndall Air Force Base, Florida, December 1988.

Veneziano, D., and Liao, S., "Statistical Analysis of Liquefaction Data," *Proceedings of ASCE Specialty Conference on Probabilistic Mechanics and Structural Reliability*, Berkeley, California, January 1984.

Weeks, David L., and Raspberry, Everett T., *Hard Target Vulnerability Databases*, Analysis and Strategic Defense Division, Air Force Armament Laboratory, Eglin Air Force Base, Florida, AFATL-TR-87-48, December 1987.

absichtlich
freigelassen

blank

RESEARCH TO DEVELOP RELIABILITY-BASED DESIGN METHODOLOGY FOR PROTECTIVE STRUCTURES

Twisdale, Lawrence A.[1]; Sues, Robert H.[1]; Lavelle, Francis M.[1]; Miller, Diane B.[2]

[1]Applied Research Associates, Inc.
6404 Falls of Neuse Road, Suite 200,
Raleigh, NC 27615, USA

[2]Engineering and Services Laboratory
Air Force Engineering and Service Center
Tyndall Air Force Base, FL 32403

INTRODUCTION

The reliability of a structural system for a single failure mode is the probability that the load effect (*e.g.*, moment, deflection, etc.) is less than the structure capacity. Due to the uncertainties in the prediction of loads and structural response, the load effect E and structural capacity C are uncertain, and are represented by probability density functions $f_E(e)$ and $f_C(c)$, respectively. The probability of unacceptable performance, P_f, is simply

$$P_f = P(C - E < 0) \tag{1}$$

which can be expressed as

$$P_f = \int_{-\infty}^{\infty} F_C(x)\, f_E(x)\, dx \tag{2}$$

where $F_C(x)$ is the cumulative distribution function. By conducting research to identify and analyze the uncertainties in load and structural response, Equation 2 can be solved and the uncertainties evaluated for nominal (deterministic) analysis/design procedures. In this manner, the safety margin in the nominal load, denoted $\bar{E}$, and nominal capacity, $\bar{C}$, can be quantified.

This approach logically leads to the concept of reliability-based design (RBD) for protective structures and the use of reliability-based design factors (RBDF), or safety factors, as an integral part of the analysis/design process, just as for conventional structures. Once the research is completed, the analyst/designer does not perform "probabilistic" analysis, but simply uses the resulting probability-based safety factors. Hence, the design equation counterpart to Equation 1 for acceptable structural performance is

$$\psi \cdot \bar{C} \geq \lambda \cdot \bar{E} \tag{3}$$

where ψ = RBDF on capacity and λ = RBDF on load effect. In some cases, a load factor of unity may be appropriate, whereas in others the load and capacity factors may be combined into a single factor. In general, a table of ψ and λ values are provided corresponding to different levels of design survivability, P_s, where $P_s = 1 - P_f$, for each failure mode. A value of P_s is selected consistent with the design requirements, considering the consequences of failure and cost-survivability tradeoffs. A key advantage of the RBD approach is that optimized safety designs can be more easily developed than with the traditional approach, which produces unknown safety margins.

This paper summarizes research underway to develop probability-based design methods and RBDFs for reinforced concrete protective structures. The load modeling and structural analysis procedures used to develop the nominal $\bar{C}$ and $\bar{E}$ are based on the methods given in the recently published *Protective Construction Design Manual* (*PCDM*) [Drake *et al.*, 1989]. These uncertainties are analyzed by comparing load and structure response *PCDM* predictions to available test data and experimental measurements. These detailed comparisons provide the basis for quantifying systematic (model) prediction errors and random uncertainties needed to characterize ψ and λ for use with $\bar{C}$ and $\bar{E}$. In this manner, the degree of conservatism or unconservatism inherent in the *PCDM* analysis methods are established and the RBDF produced. The load and capacity effects considered include: (1) airblast environment prediction; (2) above-ground structure response; (3) buried structure response (structure-media interaction analysis); (4) projectile penetration; and (5) bomb fragmentation effects. This paper presents an overview of the completed work in each of

these areas, with an emphasis on the airblast environment prediction. This current research effort is funded by the U.S. Air Force Engineering and Services Center and will be completed by mid 1991.

AIRBLAST ENVIRONMENT

Uncertainties in predicting free field airblast pressure and impulse and reflected pressure and impulse from a near miss general purpose bomb are quantified using data from the Conventional High-Explosive Blast and Shock (CHEBS) Test Series [Carson, *et al.*, 1984, 1987]. The CHEBS test series involved 16 general purpose (Mk 82 and Mk 83) bomb tests with airblast data obtained over a range of standoffs applicable to protective structure design. Half-scale aboveground structure tests [Coltharp, *et al.*, 1985] are used to analyze the uncertainty in predicting airblast reflection factors.

Incident Airblast Prediction Methodology. The prediction methodology in the *PCDM* are based on the airblast parameter polynomials for uncased TNT hemispherical surface bursts of Kingery and Bulmash [1984]. The effective TNT weights used to predict the CHEBS observations are a function of the type of explosive and bomb depth-of-burial. The four groups of CHEBS tests considered for this study are described in Table 1. The data groups have been formed by pooling together observations from tests having identical bomb orientations. Group II, for example, consists of pressure and impulse readings from all of the tests in which the bomb was vertical and half-buried. Differences in the bomb sizes within each group (Mk 82 *vs.* Mk 83) are accounted for by scaling the standoffs and incident impulses according to the equivalent TNT weights.

Although the data presented in the CHEBS reports [Carson, *et al.*, 1984, 1987] was screened to eliminate bad gage readings, further editing of the database was necessary. Data was deleted if (1) excessive noise was visible in the pressure plots, (2) the high pressure region of the signal was unusually wide or narrow compared to other similar gages, (3) the pressure curve was unusually smooth, or (4) clipping occurred in the signal. Additional screening of the CHEBS data set was required for the horizontal bomb tests (Groups III and IV). For these tests, only the gages oriented at 90 *degrees* to the bomb axis are retained. Gages oriented at other angles are excluded because peak pressures and impulses decrease significantly at angles closer to the nose or tail of cylindrically-cased explosives. Eliminating the non-normal gages in Groups III and IV also results in a more consistent set of data groups, since all of the data in the vertical bomb tests (Groups I and II) are for gages at 90 *degrees* to the bomb axis. Although a considerable number of data points are eliminated from Groups III and IV as a result of this analysis, a relatively large data set still remains. A total of 325 peak pressures and 320 positive impulses at scaled ranges varying from 0.5 to 2.6 $m/kg^{1/3}$ (1.25 to 6.5 $ft/lb^{1/3}$) have been retained. By retaining only the 90-*degree* gage data, we address the critical loading case for above-ground structures subjected to standoff bursts.

TABLE 1. CHEBS TEST GROUPS

Group	Test Numbers	Bomb Orientation	Number of Observations	
			Pressure	Impulse
I	9,10,16	Vertical, Nose Tangent	85	83
II	5,6,14,15	Vertical, Half-Buried	146	143
III	1	Horizontal, Surface Tangent	5	7
IV	2-4,7,8,12,13	Horizontal, Half-Buried	89	87

Statistical Analysis of Incident Airblast Data. Denoting the j^{th} observation of pressure and impulse in each data group by ρ_{sj} and i_{sj} and the respective predictions by $\hat{\rho}_{sj}$ and $\hat{i}_{sj}$, the prediction error ξ for the j^{th} observation is simply

$$\xi_{\rho sj} = \rho_{sj} / \hat{\rho}_{sj} \tag{4a}$$

$$\xi_{isj} = i_{sj} / \hat{i}_{sj} \tag{4b}$$

The statistics of $\xi_{\rho sj}$ and ξ_{isj} allow us to quantify the systematic and random components of the *PCDM* airblast parameter prediction errors. The mean of ξ provides a measure of the systematic component of the prediction error and the higher moments (variance, etc) indicate the random uncertainty. Plots of the prediction error ratios for each data group are shown in Figure 1. Also shown on these plots are linear regression fits of the data in log-log space. Statistics of the observed prediction error ratios, as well as tests for systematic bias and lognormality, are given in Table 2. For each hypothesis test, the p-value is the probability of obtaining a more extreme value of the test statistic given that the hypothesis is true. In general, the hypothesis is rejected if the p-value is less than 0.05. For

example, the hypothesis that the mean impulse prediction error ratio is actually equal to one should be rejected for each of the impulse data groups as well as for the combined impulse data set. As a result, it can be concluded that the prediction methodology is biased towards underpredicting incident impulse.

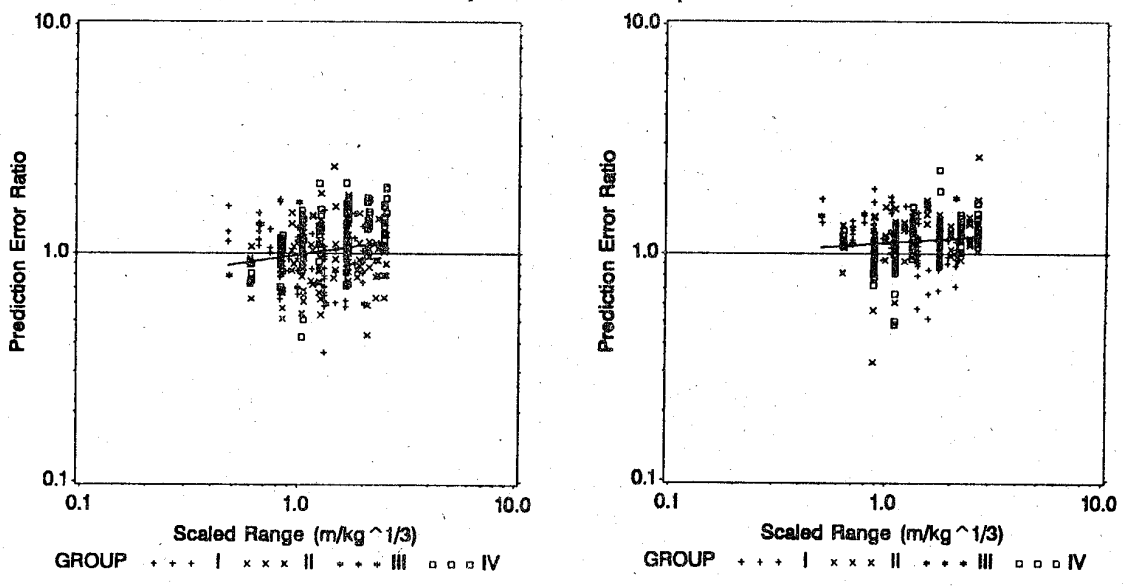

(a) Peak Pressure

(b) Peak Impulse

Figure 1. CHEBS Prediction Error Ratio Scattergram

Statistics for the log-log regression fits shown in Figure 1 indicate that, in most cases, there is a significant range dependence; however, a relatively small percentage of the prediction error variability is "explained" by each regression line. Hence, a range independent model is used in the development of free-field airblast load factors.

TABLE 2. STATISTICS OF THE PREDICTION ERROR RATIOS

		Prediction Error Ratio, ξ			ln (ξ)			
				p-value for H_O:			p-values for H_O:	
Parameter	Group	Mean	COV	Mean=1	Mean	$\sigma_{\ln(N)}$	Mean=0	Lognormal
Pressure	I	0.973	0.289	0.372	-0.069	0.290	0.032	0.727
	II	1.049	0.298	0.058	0.006	0.294	0.820	0.989
	III	1.005	0.490	0.984	-0.089	0.479	0.700	0.261
	IV	1.220	0.288	0.0001	0.155	0.304	0.0001	0.192
	I-IV	1.075	0.308	0.0001	0.026	0.310	0.135	0.781
Impulse	I	1.130	0.241	0.0001	0.093	0.243	0.0008	0.445
	II	1.199	0.198	0.0001	0.161	0.211	0.0001	0.0001
	III	1.291	0.184	0.018	0.242	0.170	0.009	0.068
	IV	1.142	0.236	0.0001	0.105	0.241	0.0001	0.063
	I-IV	1.168	0.220	0.0001	0.130	0.229	0.0001	0.0001

In order to have the largest data base possible and to simplify the development and implementation of reliability-based design procedures, the data Groups I through IV have been combined into two data sets - one for peak pressure and one for positive impulse. The process of pooling the individual data sets can be justified if it is determined that the difference between the groups is not statistically significant. An analysis of the group to group variability reveals that Group IV is significantly different from the other peak pressure data groups and Group II is significantly different from the other incident impulse data groups. These differences can most likely be attributed to the fact that Groups II and IV consist of data from half-buried bomb tests. The use of an effective TNT weight for half-buried bombs as one-half the weight of a similar surface-tangent bomb appears to be slightly unconservative. Having noted the modeling of half-buried explosives as a potential area for improvement, the pooled data Groups I through IV are accepted as being representative prediction error ratios for the purposes of this study.

Incident Airblast Load Factors. The current research on incident airblast load factors is nearly complete, and is summarized as follows:

1. The peak pressure and positive impulse prediction error statistics support the use of lognormal distributions. For pressure, the computed *p*-value shown in Table 2 give no indication that the lognormal hypothesis should be rejected. For positive impulse, both Group II and the combined data produce *p*-values that suggest that the lognormal model should not be used. However, Groups I, III, and IV do not fail the test for lognormality when taken individually, or when combined together. Based on the results for Groups I, III, and IV, the lognormal model for incident impulse is used in this study.
2. Based on the statistics of the combined data sets, the recommended lognormal model parameters for pressure and impulse prediction error are given in Table 3 and the incident airblast load factors for various reliability levels are given in Table 4. The load factors are applied directly to the *PCDM* predictions for a given range and explosive weight. For example, multiplying the *PCDM* prediction for positive impulse by 1.75 will result in an incident impulse which is exceeded by approximately 5 *percent* of the CHEBS observations.
3. The statistics of the combined pressure and impulse data sets (Groups I - IV) are taken to be representative of all of the bomb orientations tested in the CHEBS series for gages oriented at 90 *degrees* to the bomb axis. Although some significant differences between data groups have been identified, the advantages of pooling the groups into combined data sets for the purposes of reliability-based design outweigh the negative aspects of the statistical differences. In general, pooling dissimilar groups leads to an increased estimate of the variance, which will ultimately result in larger, more conservative RBDFs.

TABLE 3. RECOMMENDED INCIDENT AIRBLAST UNCERTAINTY MODEL

Lognormal Model	Pressure, ζ_{ρ_S}	Impulse, ζ_{i_S}
Mean	1.1	1.2
Coefficient of Variation	0.3	0.25

TABLE 4. RECOMMENDED INCIDENT AIRBLAST RELIABILITY-BASED LOAD FACTORS

	Load Factor, λ	
Reliability	Pressure	Impulse
0.05	0.65	0.78
0.10	0.72	0.85
0.25	0.86	0.99
0.50	1.05	1.16
0.75	1.28	1.37
0.90	1.54	1.60
0.95	1.71	1.75
0.99	2.09	2.06

Incident Airblast Example. The incident airblast prediction model is compared to an independent set of incident pressure and impulse data in the box plots given in Figure 2. The experimental data was obtained in half-scale tests of vertical, surface-tangent, cylindrically-cased explosives [Coltharp, *et al.*, 1985]. The data consist of 12 pressure observations and 10 impulse observations. It can be seen that the box-plots of the observed data agree reasonably well with the factored *PCDM* predictions using the developed lognormal distributions.

Reflected Airblast Parameters. The prediction error models generated from the statistical analysis of the CHEBS test data provide a rational basis for estimating the uncertainties in predicting peak overpressures and incident impulses. However, the loading parameters that directly impact the analysis of aboveground structures are reflected pressure and impulse. Unfortunately, the test data available for these parameters at scaled standoffs applicable to protective structure design is not comparable in quality or quantity to the free field data base. As a result, it is beneficial to approach the problem of estimating uncertainty in reflected airblast parameters by examining the uncertainty in airblast reflection factors.

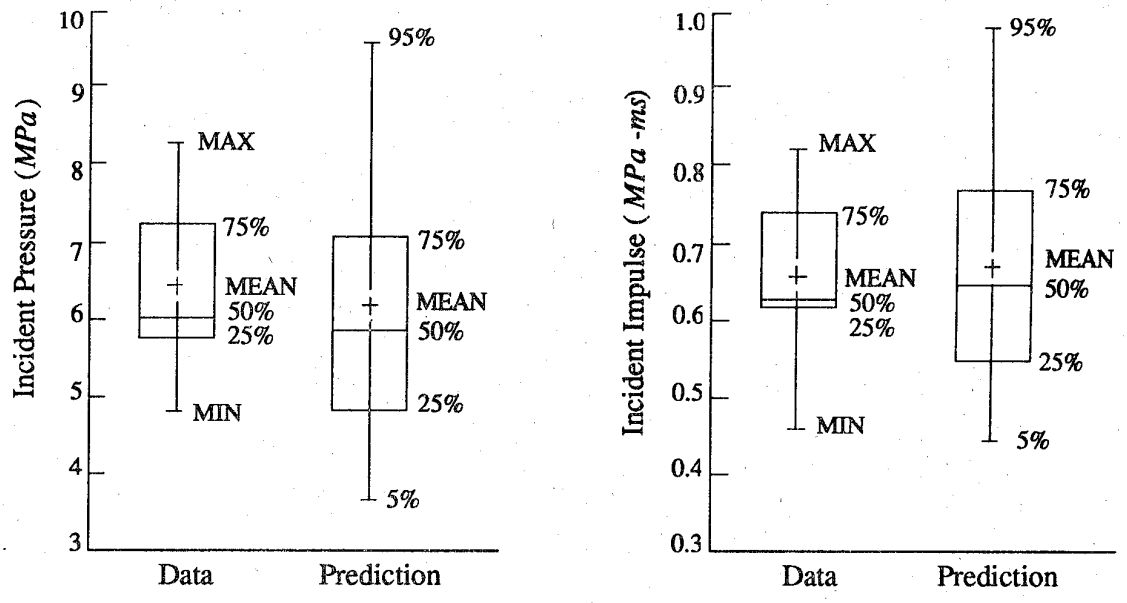

Figure 2. Incident Airblast Observations from Coltharp, *et al.* [1985] *vs.* Predictions for Various Reliability Levels.

Reflection factors are ratios of the reflected airblast parameter to the incident airblast parameter (at the same scaled range). Thus, the uncertainty in reflected airblast can be treated as a free field uncertainty compounded by the reflection factor uncertainty. In the reliability-based design procedure, a load factor is applied to the predicted free field airblast parameters which are then multiplied by a scaled-up reflection factor. The "factored" reflection factor accounts for the uncertainty in the design manual reflection factor prediction. An advantage of this approach is that the relative importance of free field prediction error and reflection factor prediction error on the overall reflected airblast prediction error can be identified. This knowledge can be used to more efficiently plan future experimental research efforts.

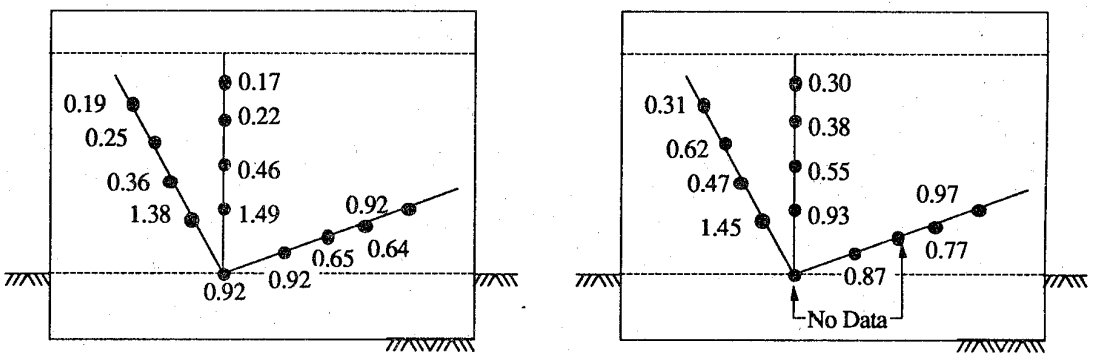

(a) Peak Pressure (b) Impulse Error Ratios

Figure 3. Mean Reflection Factor Prediction Error Ratios

In order to isolate the reflection factor uncertainty from the free field uncertainty, it is necessary to compare reflected and incident airblast parameters obtained from the same blast and at the same scaled range. As an example, data from half-scale aboveground structure tests [Coltharp, *et al.*, 1985] is considered. In these tests, reflected airblast data at various locations on an aboveground wall have been collected as well as free field data at a gage located directly opposite the bottom center-line wall gage. Figure 3 illustrates the mean reflection factor prediction error ratios (observed/predicted) for peak pressure and positive impulse. At most locations, the *PCDM* reflection factor predictions significantly overestimate the mean measured reflection factors (i.e., $\xi < 1$). The measured reflection factors at gages other than the bottom center-line location have been estimated by scaling the free field observation to the range of each wall gage and by approximately accounting for the non-normal incidence at these gages. In spite of these corrections (which both tend to improve the prediction error ratios), significant biases are still present and further work is needed. Possible explanations include clearing time effects near the edges of the wall and the use of hemispherical surface burst data to predict the reflection factor for cylindrically cased explosives.

ABOVEGROUND STRUCTURE RESPONSE

The preferred method for quantifying structural response uncertainty is to compare response predictions computed using measured loads to measured response data. By using the measured loads, the structural response prediction error is isolated from the loading uncertainties. However, this approach requires accurate observed airblast loading data as well as fragmentation impulse data for cased explosives. To illustrate the methodology, aboveground structural response prediction error ratios have been computed for several half-scale aboveground R/C wall tests in which the walls responded predominantly in a one-way slab bending mode [Coltharp, *et al.*, 1985]. Because fragmentation impulse data is not available for these tests, the fragmentation impulse has been estimated using the procedure given in the *PCDM*. In Table 5 response prediction error ratios are given for three different loading conditions: (1) one-way estimated loads applied vertically along the center strip of the wall (directly opposite the bomb), (2) observed airblast loads obtained from the vertical center strip of the wall, and (3) two-way estimated loads which consider the reduction in airblast intensity in the horizontal direction. In all cases, the loads have been transformed into equivalent uniform loads in accordance with the simplified analysis procedure. The loadings considered are airblast impulse only or airblast plus fragmentation impulse. Both the one-way and two-way estimated loads significantly overestimate the wall deflections. Since the airblast reflection factors discussed in the previous section were consistently overpredicted by the *PCDM* methods, actual loading data is important for the separation of the structural response uncertainties from the load prediction uncertainties. When the measured airblast impulse is used, the mean structural response prediction error ratio improves due to the reduction in the loading uncertainty. The coefficients of variation for the prediction error ratios range from about 25 to 50 *percent*.

Clearly, there are significant difficulties involved in characterizing the structural response uncertainty based on test data alone. An alternative to this method is to compare the design manual type predictions to predictions based on a more sophisticated structural response analysis (such as finite element computations). This approach allows the exclusion of all loading uncertainties from the structural response uncertainties. However, there are still some unknown structural modeling uncertainties associated with the response analysis which can not be accounted for. As a result, a practical characterization of the structural response uncertainties may require a combination of both experimental prediction error data and finite element computations.

Work is currently underway to finalize quantification of the structural response uncertainty and development of the reliability-based capacity factors. These factors will be used in the conjunction with the airblast load factors for the overall reliability-based design procedure for aboveground structures.

TABLE 5. ABOVEGROUND WALL DEFLECTION PREDICTION ERRORS

Test	Steel %	Observed Deflection	Predicted Error Ratios[1]					
			Estimated Loads[2] (One-Way)		Observed Loads[3] (One-Way)		Estimated Loads[2] (Two-Way)	
			Air	Air + Frag[4]	Air	Air + Frag[4]	Air	Air + Frag[4]
I6	0.25	0.46"	0.43	0.19	0.81	0.31	0.65	0.28
II5	0.25	1.75"	0.51	0.23	1.10	0.37	0.77	0.33
II9	0.25[5]	0.95"	0.27	0.12	1.19	0.29	0.42	0.18
I2	0.50	0.91"	0.53	0.24	1.17	0.39	0.81	0.34
II4	0.50	0.79"	0.45	0.20	0.31	0.15	0.69	0.29
I1	1.00	0.61"	0.66	0.30	1.91	0.58	1.00	0.43
		Mean	0.48	0.21	1.08	0.35	0.72	0.31
		COV%	27	29	48	40	26	26

[1] Observed/predicted deflection
[2] Estimated airblast loads from Drake, Twisdale, *et al.* [1989]
[3] Observed airblast loads used
[4] Preliminary estimates of fragmentation load
[5] Closed stirrups, all other walls use open stirrups for shear reinforcing

BURIED STRUCTURE RESPONSE

Development of reliability-based design factors for buried structures subjected to ground shock requires characterizing the uncertainty in predicting free field ground shock and characterizing the uncertainty in predicting structure response to the incident ground shock (including SMI effects). Collection of free field ground shock data from both conventional and contained nuclear explosions has been completed and statistical analysis to quantify ground shock prediction is currently underway. The techniques being used are similar to those described previously. A preliminary quantification of the uncertainty in predicting structure response has also been conducted. For this evaluation, predictions made with the structure-media interaction model given in the *PCDM* were compared against a number of tests conducted by the U. S. Army at Fort Polk and Fort Knox. The test data included observations of rotations (and breach) of concrete walls with L/t (clear span-to-thickness) ratios ranging from 5 to 10. The model

TABLE 6. STRUCTURE RESPONSE UNCERTAINTY CHARACTERIZATION PRELIMINARY RESULTS[1]

	Model Prediction Error[2]			
	Design Resistance[3]		Best Estimate Resistance[3]	
	SDOF	2DOF	SDOF	2DOF
Mean	0.43	0.60	0.51	0.82
COV (%)	30	35	35	30
Number of Data Points	12	10	10	12

[1]Fort Polk and CONWEB test
[2]Observed/prediction rotation
[3]Design = design conservative resistance; Best Estimate = improved resistance function

prediction error statistics presented in Table 6 below do not make use of the cases in which breach occurred. (However, in all of these cases, the prediction methods indicated that the wall would have failed.) As shown in Table 6, the predictions were made using two different resistance functions to model the nonlinear inelastic behavior of the tested walls [Drake, *et al.*, 1989b]. These are labeled Design Resistance and Best Estimate Resistance. The Design Resistance is conservative and has three response regions: (1) elastic; (2) perfectly plastic; and (3) tensile membrane. The Best Estimate Resistance includes compressive membrane forces that increase the ultimate capacity of the wall. Also, two different structural models were used: a single-degree-of-freedom model (labeled SDOF) and a two degree-of-freedom model (2DOF). The 2DOF model accounts for possible rigid body motion (or support movement) during the test and, therefore, results in a smaller prediction of wall rotation.

These models generally overpredict the wall rotation. This overprediction is due in large part to the very short L/t ratios for the tested walls. As expected, use of the Best Estimate Resistance and the 2DOF model results in less overprediction. This improvement is strictly systematic; as, there is no significant reduction in the response variability. Additional research is needed to reduce the systematic bias in computing the response of short, thick walls. The randomness in the prediction, however, is not large and likely will not be significant when compared with the random prediction error for free field ground shock. Hence, simple SMI models may be sufficiently accurate for design of the short thick walls typical of protective construction, if the source of systematic overprediction can be identified and corrected.

The results presented in Table 6 will be combined with the uncertainty in predicting freefield ground shock to form the basis for development of a reliability-based design procedure for buried structure flexure response. The large uncertainties in predicting freefield ground shock may dominate the response prediction.

PROJECTILE PENETRATION AND FRAGMENTATION EFFECTS

For projectile penetration into reinforced concrete, four effects are considered: (1) depth of penetration into a semi-infinite target; (2) spalling of a finite-thickness target; (3) perforation of a finite-thickness target; and (4) residual velocity after perforation of a finite-thickness target. Fragment penetration effects have been treated by considering the large uncertainties associated with the number of fragments that will hit the structure (and not ricochet), the mass distribution of the fragments, the striking velocity of the fragments, and fragment penetration. The key results of this area of RBD research are summarized as follows:

1. Simplified reliability-based design procedures are developed that are robust for a wide range of cases and are no more difficult to use than the traditional deterministic procedures.

2. Design safety factors are developed for the penetrator striking velocity and the penetration resistance. For a desired level of reliability, the analyst simply factors the best estimate striking velocity by a tabulated load factor, computes penetration depth or spall/perforation thickness using the design manual equations, and then factors the wall thickness (given by the design manual equations) by a capacity factor.

3. It was found that the *PCDM* procedures for prediction of depth of penetration into massive concrete and prediction of spall or perforation are essentially unbiased, *i.e.* the mean of $\overline{C} \approx 1.0$.

4. Although the available residual velocity data base is very limited, preliminary safety factors have been developed, that take into account the data limitations. Due to the importance of estimating residual velocity (particularly for layered systems), improvements to the prediction models seems warranted.

5. A new methodology for selection of design fragments is being developed. Earlier work has shown that designs using the traditional approach are not correlated to survival probability [Dass and Twisdale, 1987]. The new RBD methodology uses extreme value probability theory to obtain a design fragment that explicitly accounts for the number of non-ricochet hits (obtained from design charts) and can be shown to be correlated with survival probability.

A summary of these results, including RBDFs for penetration, perforation, and spall effects, are presented in Sues *et al.*, [1991].

SUMMARY

Although there are many uncertainties in the analysis and design of protective structures, probability-based analyses are not always expedient for design, particularly when the structural analyst does not have a background in probabilistic methods. For this reason, RBDF are developed as a research product for application by the analyst, much as safety factors are used in traditional design. A research effort is underway to systematically evaluate and analyze the uncertainties in the analysis methods given in the *PCDM*, *vis a vis* experimental measurements and test results. RBDF are being developed for use with the reinforced concrete design equations in the *PCDM* for the following failure modes and effects: penetration depth, spall, perforation, single layer residual velocity, fragment penetration, peak free-field airblast pressure, free-field airblast impulse, pressure and impulse reflection factors, aboveground structure flexure response, free-field ground shock, buried structure wall flexure response. The analysis associated with the development of these factors has pointed out quantitatively the key uncertainties associated with current prediction procedures, allowing a prioritization of research areas. Use of the RBD research results could produce fundamental improvements in protective design by facilitating cost-effective, safety-optimized, and balanced designs concepts.

REFERENCES

Carson, J. M., and Morrison, D., 1987. *Conventional High-Explosive Blast and Shock (CHEBS) Test Series: Mark-83 General-Purpose Bomb Tests*, Air Force Weapons Laboratory, AFWL-TR-86-53, Parts 1-3, January 1987.

Carson, J. M., Morrison, D., and Hampson, R. J., 1984. *Conventional High-Explosive Blast and Shock (CHEBS) Test Series: Mark-82 General-Purpose Bomb Tests*, Air Force Weapons Laboratory, AFWL-TR-84-27, June 1984.

Coltharp, D. R., Vitayaudom, K. P., and Kiger, S. A., 1985. *Semihardened Facility Design Criteria Improvement*, Final Report ESL-TR-86-32, U. S. Army Engineer Waterways Experiment Station, June 1985.

Dass, W. C., and Twisdale, L. A., 1987. "Comparison of Design Procedures for Fragmentation Effects," *International Symposium on the Interaction of Conventional Munitions with Protective Structures*, Mannheim, FRG, March 1987.

Drake, J. L., Twisdale, L. A., *et al.*, 1989. *Protective Construction Design Manual*, ESL-TR-87-57, Air Force Engineering and Services Center, Tyndall Air Force Base, November 1989.

Drake, J. L., Walker, R. E., Slawson, T. R., 1989b. *Background of Test Data and Prediction Methods for the Analysis of Below-Grade Walls Subjected to Ground Shock Loads*, U. S. Army Engineer District, Omaha, Contract No. DACA-4589-0096, May 1989.

Kingery, C. N., and Bulmash, G., 1984. *Airblast Parameters from TNT Spherical Air Burst and Hemispherical Surface Burst*, ARBRL-TR-02555, Ballistic Research Laboratory, April 1984.

Sues, R. H., Hwang, C-W, Twisdale, L. A., and Lavelle, F. M., 1991. "Reliability-Based Design of R/C Structures for Protection Against Projectiles and Fragments," *Proceedings of the 5th International Conference on the Interaction of Non-Nuclear Munitions with Structures*, Mannheim, Germany, April 1991.

Twisdale, L. A., and Sues, R. H., 1989. "Reliability-Based Design Methods for Protective Structures Subjected to Non-Nuclear Munitions Effects," *Proceedings of the Fourth International Symposium on the Interaction of Non-Nuclear Munitions with Structures*, Panama City Beach, Florida, April 17-21, 1989.

Schock im Bauwerk

Instructure Shock

Conventional Weapon-Induced Shock Environment in a Prototype Structure

James W. Ball and Stanley C. Woodson
U.S. Army Engineer Waterways Experiment Station, Vicksburg, MS

Sam A. Kiger
University of West Virginia, Morgantown, WV

Abstract

Shock isolation for equipment in blast-resistant structures can be a costly and uncertain procedure for conventional weapon threats, especially for aboveground structures with combined airblast and fragment loading. A series of NATO Semihardened Design Criteria Full-Scale tests conducted by the Air Force Engineering and Services Center and the U.S. Army Engineer Waterways Experiment Station during the summer of 1987 indicated that relatively simple isolation methods may be effective in isolating equipment.

For further evaluation, four full-scale test shots were conducted in August 1988 on the semihardened test structure used for the 1987 tests at Tyndall AFB, FL. Several pieces of equipment were placed throughout the structure. The equipment either sat on the floor unattached or was bolt-attached to the floor (hard-mounted), or one of three simple shock isolators was used. The equipment and floor slab of the structure were instrumented with accelerometers for purposes of measuring the shock transmitted from general-purpose bombs.

Evaluation of the data obtained in August 1988 indicates that the isolators were ineffective in attenuating the shock loads transmitted to the equipment inside the structure. Results indicated that any equipment not restrained against movement, i.e., simply sitting on the floor or isolator pads, will undergo significant rigid-body displacements. This, in turn, presents a real danger of injury to personnel located inside the structure, and may result in higher shock loading (because of impact) than would have occurred in the hard-mounted configuration. These developments indicate that a great deal of effort may be wasted on shock isolation in protective construction.

Die Schockbelastung von Schutzbauten infolge konventioneller Waffenwirkungen

Peter Hunziker, AC-Laboratorium, CH-3700 Spiez

Erwin Kessler, Dr Ing, CH-9546 Tuttwil

Zwei unter einer Schutzschicht angeordnete Schutzbauten wurden mit inerten und scharfen Fliegerbomben beschossen. Das AC-Laboratorium Spiez hatte den Auftrag, die dabei in den Schutzbauten auftretenden Erschütterungen zu messen.
Bei Volltreffern mit scharfen Bomben wurden in den Schutzbauten Beschleunigungsspitzen bis 100 g, Geschwindigkeiten bis 46 cm/s und Verschiebungen bis 6 mm gemessen. Die Schäden in den Schutzbauten beschränkten sich auf Risse mit Weiten bis zu 2 mm und einigen kleinen Abplatzeffekten.
Im Zusammenhang mit diesen Versuchen wurden theoretische Studien zur Abschätzung der Schockwirkungen in Schutzbauten infolge konventioneller Volltreffer durchgeführt.

EINLEITUNG

Die beschleunigte Entwicklung konventioneller Waffensysteme, mit erhöhter Treffergenauigkeit, lässt das Bedürfnis nach dem Schutz gegen **konventionelle** Volltreffer drastisch steigen. Ueber die **Schockwirkungen** solcher konventioneller Belastungen auf Schutzbauten ist aber sehr wenig bekannt. Entsprechende Publikationen fehlen oder sind nicht zugänglich.

Das AC-Laboratorium Spiez hatte in den letzten Jahren Gelegenheit, diese spezifische Schockwirkung in zwei mit inerten und scharfen Fliegerbomben beschossenen Schutzbauten zu messen und erste theoretische Ansätze für deren Berechnung zu formulieren.

Vorliegender Beitrag beschreibt die Durchführung und typische Resultate der Erschütterungsmessungen sowie einige theoretische Betrachtungen über die Schockwirkungen infolge konventioneller Volltreffer.

EXPERIMENTELLE UNTERSUCHUNGEN

Das Schweizerische Militärdepartement (EMD) hat in den vergangenen Jahren zwei unter einer Schutzschicht angeordnete Schutzbauten mit inerten und scharfen Fliegerbomben beschossen (vergl. in diesem Zusammenhang auch [6]). Dabei hatte das AC-Laboratorium Spiez den Auftrag, die in den Schutzbauten auftretenden Erschütterungen oder Schockwirkungen zu messen.

In diesen Versuchen wurden die folgenden Bombentypen verwendet:

BOMBENTYP		INERT	SCHARF
Sprengbombe	Bb 81/225 kg	3	2
Sprengbombe	Bb 70/450 kg	4	1
Panzerbombe	Bb 71/450 kg	4	7
Sprengbombe	MK 82/550 lb	2	1
Sprengbombe	MK 84/2000 lb	2	-

Versuchsanordnung

Die Bomben wurden vom Flugzeug auf eine 22 x 24 m grosse, über den Schutzbauwerken angeordnete **Schutzschicht** abgeworfen. Die Schutzschicht über dem Schutzbau 1 besteht aus einer Zerscheller- und einer Erdschicht, während die Decke von Schutzbau 2 direkt unter der Zerschellerschicht plaziert ist.

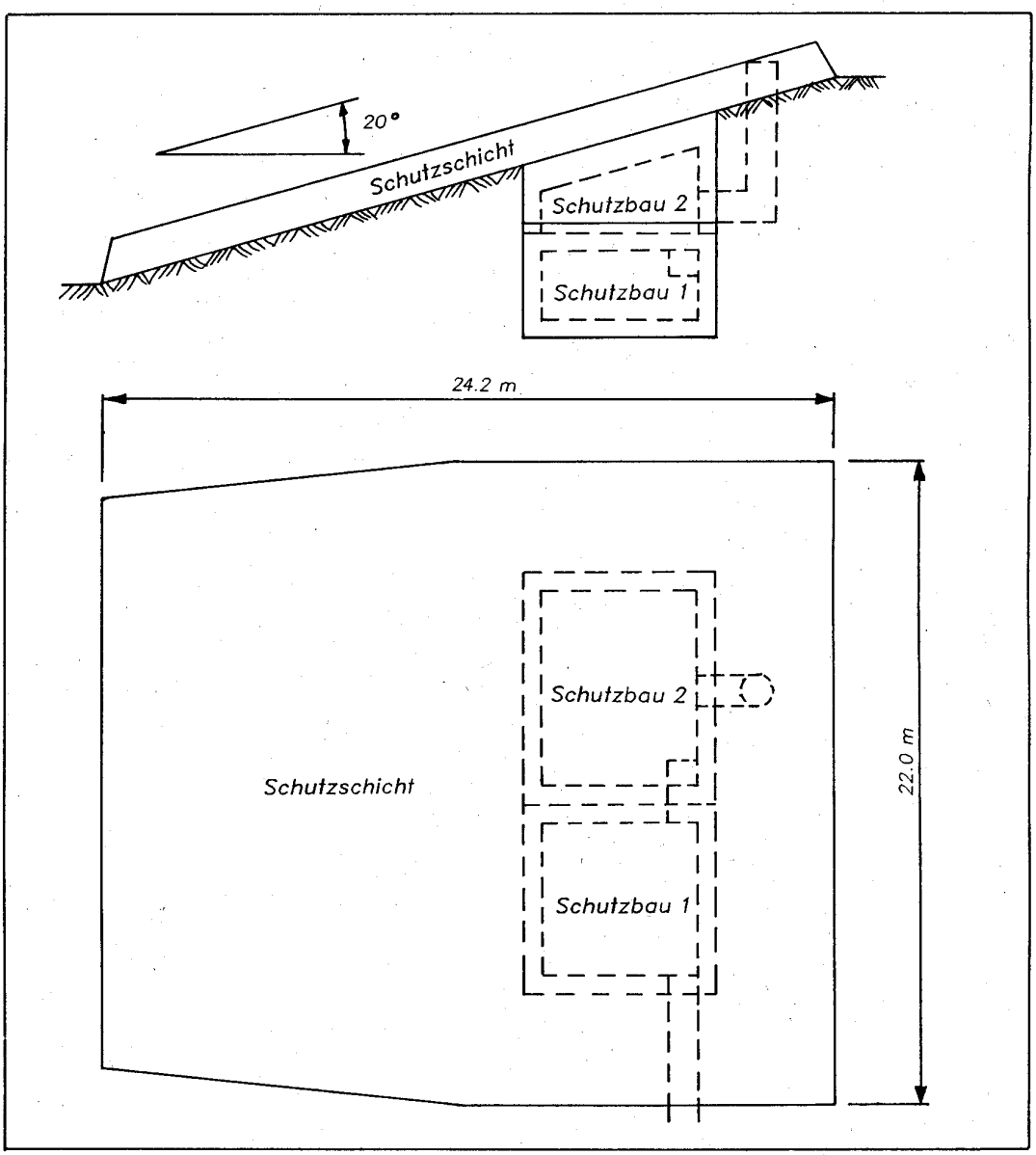

Bild 1: Zieldispositiv

Diese aus groben Felsblöcken bestehende Zerschellerschicht ist um 20° gegen die Anflugachse geneigt, um einen möglichst steilen Bombenauftreffwinkel zu erreichen.
Die Innenabmessungen des Schutzbauwerkes mit einer Erdschicht zwischen der Decke und der Zerschellerschicht betragen 5 x 5 x 2,5 m. Die Grundfläche des andern Schutzbauwerkes misst 7 x 5 m, während die lichte Höhe wegen der geneigten Zerschellerschicht zwischen 0.35 und 2.34 m variiert.
Konstruktion und Bewehrung beider Schutzbauten entsprechen den Vorschriften des EMD.

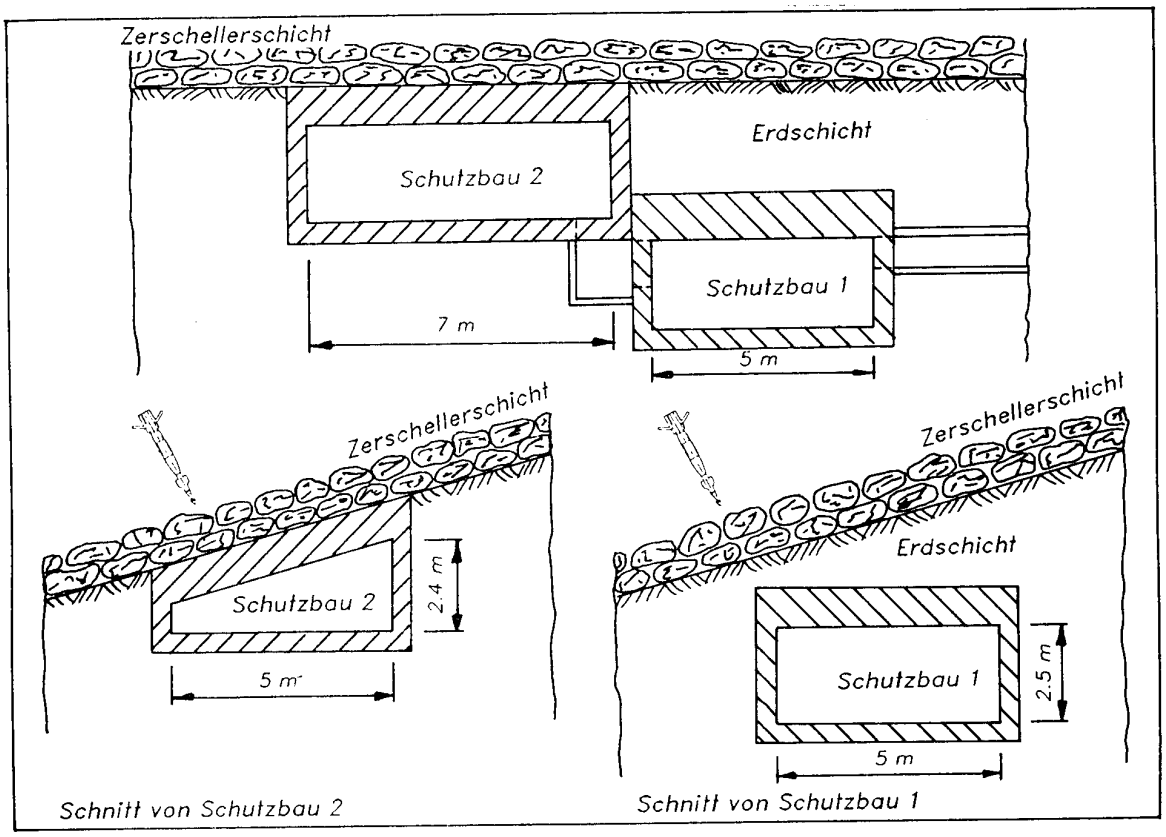

Bild 2: Versuchsanlage

Messeinrichtung

Die Erschütterungen von Boden, Decke und Wänden der beiden Schutzbauten wurden mit der in **Bild** 3 schematisch dargestellten Messeinrichtung erfasst und registriert. Die auftretenden Beschleunigungs-Zeitverläufe wurden vorwiegend in der Hauptbelastungsrichtung der Schutzbauwerke, der **vertikalen Achse** mit bis zu 12 piezoelektrischen Beschleunigungsaufnehmern erfasst. Zum Schutz vor hochfrequenten Schwingungskomponenten wurden diese auf ein **mechanisches Filter** montiert. Das verwendete mechanische Filter wirkt wie ein Tiefpassfilter; die hochfrequenten Schwingungsanteile werden unterdrückt. Dadurch kann gesichert werden, dass der Aufnehmer im linearen Bereich arbeitet. Dank der Flankensteilheit des Filters von 40 dB/Dekade im oberen Frequenzbereich werden die Resonanzüberhöhungen von etwa 30 dB auf rund 3-4 dB reduziert.

Durch Zusatzmassen zwischen Beschleunigungsaufnehmer und mechanischem Filter kann die obere Eckfrequenz des Filters beeinflusst werden. Für die hier beschriebenen Messungen wurde die Zusatzmasse so gewählt, dass die obere Eckfrequenz des Filters 2.5 - 3 kHz betrug.
Ladungsverstärker sorgten für die notwendige Signalumwandlung und -verstärkung. Um das Messignal auf den gewünschten Frequenzbereich zu beschränken, wurden die Ladungsverstärker ausgangsseitig zusätzlich mit einem aktiven Tiefpassfilter (fg = 330 Hz) ausgerüstet. Für die Digitalisierung und Registrierung der Signale wurde ein 12-kanaliger Transient-Recorder verwendet. Für die Speicherung und die erste Auswertung der Messdaten wurde ein HP-300-Computer eingesetzt. Anschliessend wurden die Daten auf einen VAX 11/750 Computer überspielt, wo die weitere Auswertung (Basislinien-Korrektur, Integration, Doppel-Integration) und die Darstellung der Resultate erfolgte.

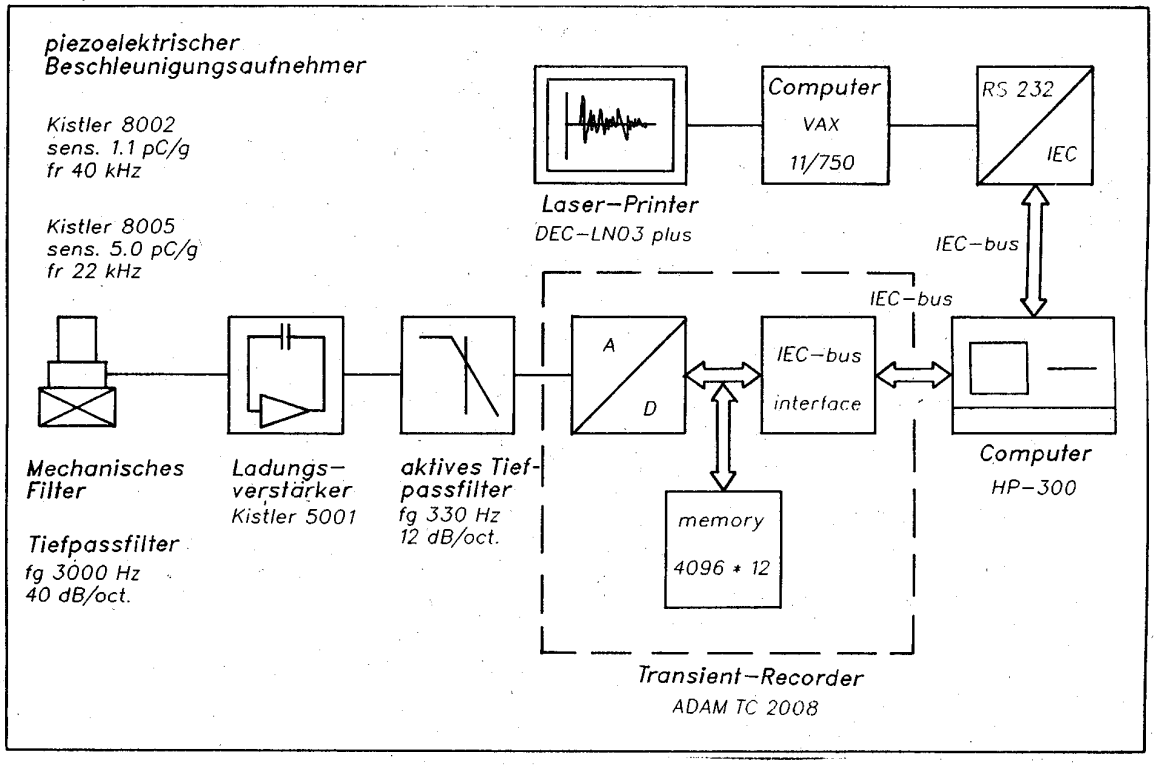

Bild 3: Messeinrichtung

Versuchsresultate

In Verlauf dieser Versuche wurden **15 inerte** und **11 scharfe** Bomben vom Flugzeug abgeworfen und mit Laser in das Ziel auf der Schutzschicht gelenkt. Von den Schutzbauten her gesehen wurden dabei **16 Nahtreffer** und **10 Volltreffer** verzeichnet. Volltreffer infolge **inerter** Bomben bewirkten in den Schutzbauten Beschleunigungsspitzen bis 10.0 g, Geschwindigkeiten bis 4.0 cm/s und Verschiebungen bis 0.6 mm. Bei **scharfen** Volltreffern wurden in den Schutzbauten Beschleunigungsspitzen bis 100.0 g, Geschwindigkeiten bis 46.0 cm/s und Verschiebungen bis 6.0 mm registriert. Bombentreffer, welche mehr als 5 m von den Schutzbauten entfernt lagen, bewirkten nur sehr kleine, vernachlässigbare Erschütterungen in den Schutzbauten.
Als Beispiel sind auf den folgenden zwei Seiten die in **vertikaler Achse** gemessenen Schock-Zeitverläufe eines scharfen Volltreffers dargestellt.

TEST F7 Panzerbombe 450 kg scharf

Situation

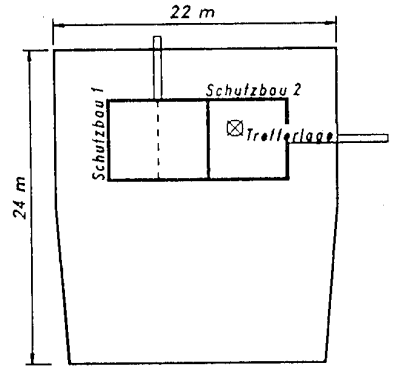

Messstellen

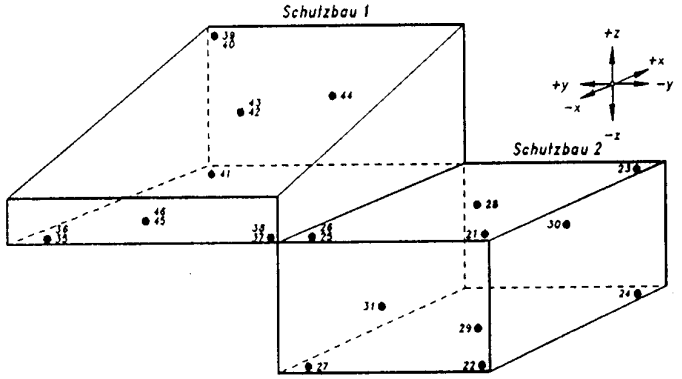

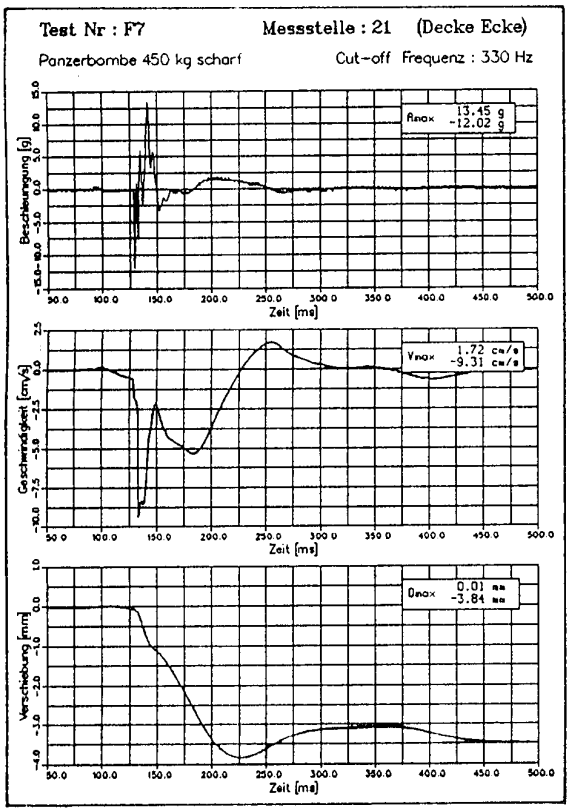

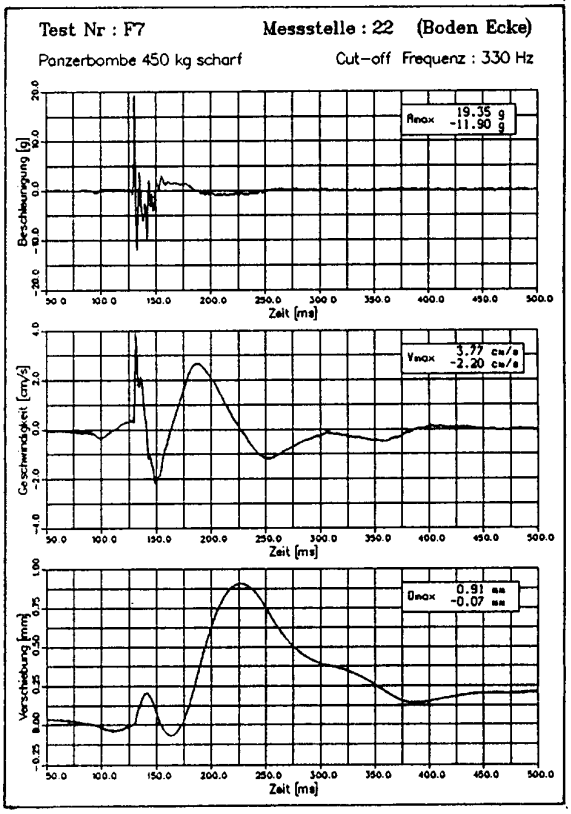

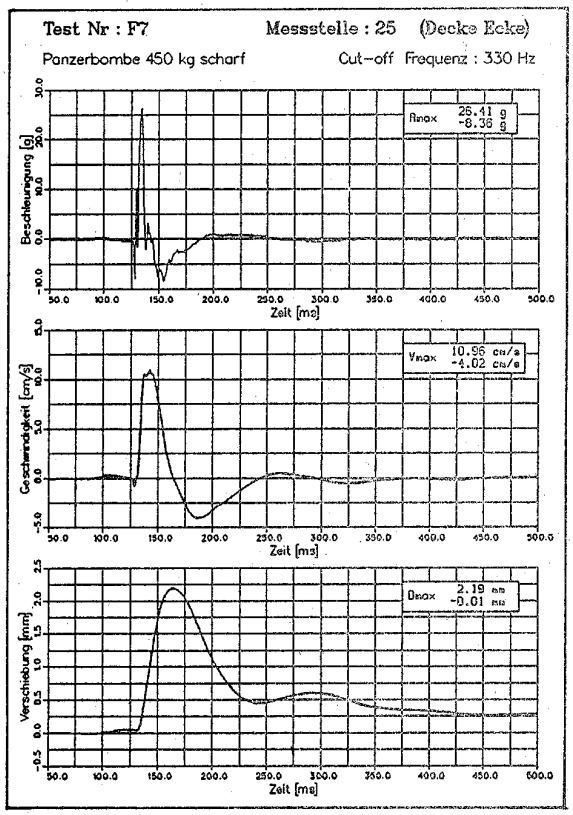
Test Nr : F7
Messstelle : 25 (Decke Ecke)
Panzerbombe 450 kg scharf
Cut-off Frequenz : 330 Hz
Amax 26.41 g -8.36 g
Vmax 10.96 cm/s -4.02 cm/s
Dmax 2.19 mm -0.01 mm
Beschleunigung [g]
Geschwindigkeit [cm/s]
Verschiebung [mm]
Zeit [ms]

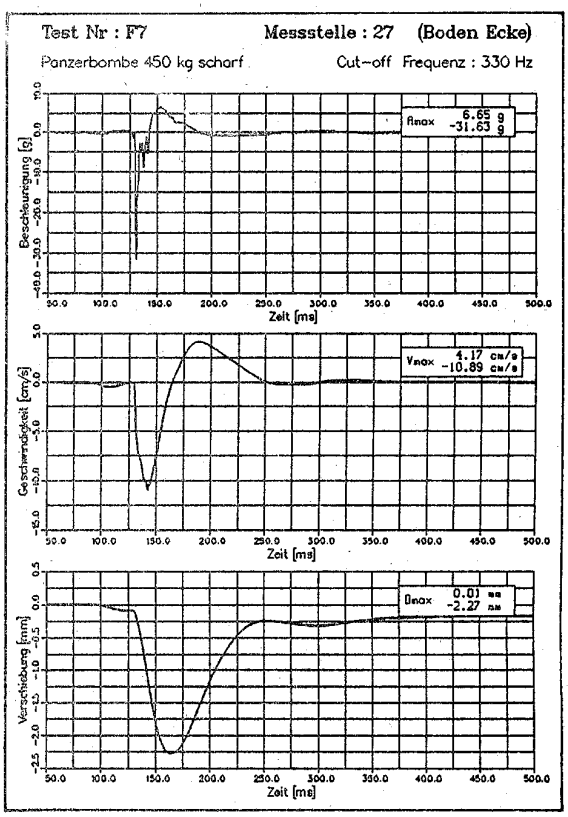
Test Nr : F7
Messstelle : 27 (Boden Ecke)
Panzerbombe 450 kg scharf
Cut-off Frequenz : 330 Hz
Amax 6.65 g -31.63 g
Vmax 4.17 cm/s -10.89 cm/s
Dmax 0.01 mm -2.27 mm
Beschleunigung [g]
Geschwindigkeit [cm/s]
Verschiebung [mm]
Zeit [ms]

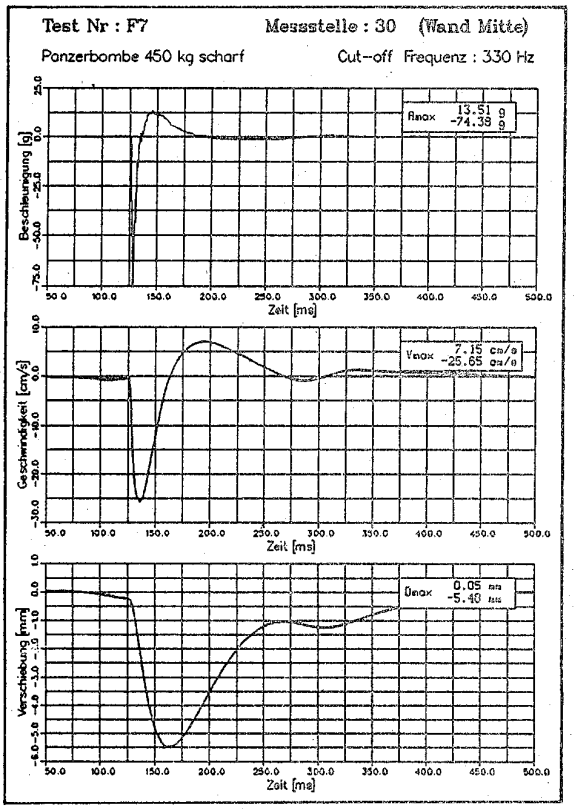
Test Nr : F7
Messstelle : 30 (Wand Mitte)
Panzerbombe 450 kg scharf
Cut-off Frequenz : 330 Hz
Amax 13.51 g -74.38 g
Vmax 7.15 cm/s -25.65 cm/s
Dmax 0.05 mm -5.40 mm
Beschleunigung [g]
Geschwindigkeit [cm/s]
Verschiebung [mm]
Zeit [ms]

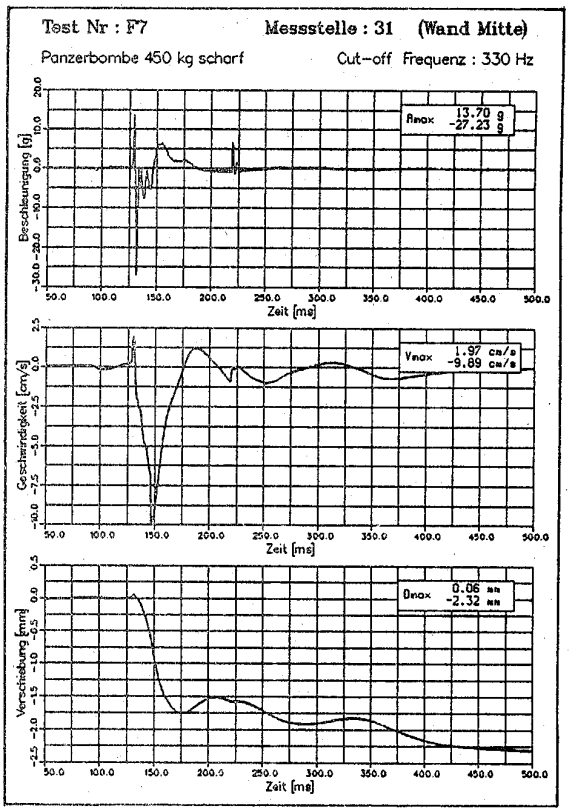
Test Nr : F7
Messstelle : 31 (Wand Mitte)
Panzerbombe 450 kg scharf
Cut-off Frequenz : 330 Hz
Amax 13.70 g -27.23 g
Vmax 1.97 cm/s -9.89 cm/s
Dmax 0.06 mm -2.32 mm
Beschleunigung [g]
Geschwindigkeit [cm/s]
Verschiebung [mm]
Zeit [ms]

Aufgetretene Schäden

Dank der gut konstruierten Schutzschicht, welche das Eindringen der Bomben verhindert hat, beschränkten sich die Schäden in den Schutzbauten auf Risse in Böden, Decken und Wänden mit Weiten bis zu 2 mm. Abplatzeffekte konnten nur in dem direkt unter der Zerschellerschicht liegenden Schutzbau 2 beobachtet werden.

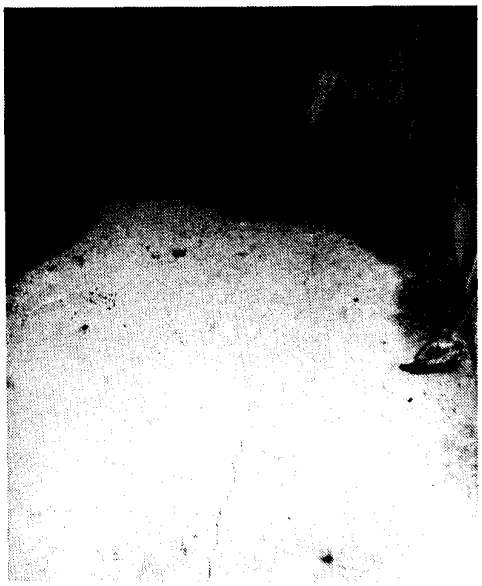

Bild 4: Risse in Boden und Wand

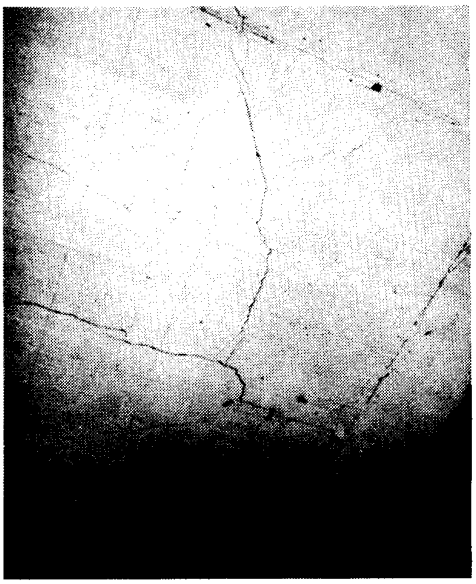

Bild 5: Risse an der Decke

THEORETISCHE UNTERSUCHUNGEN

Für die Ermittlung der Schutzbauerschütterung infolge konventioneller Volltreffer sind keine Bemessungsgrundlagen vorhanden oder erhältlich. Die im USA-Standardwerk TM 5-855-1 [1] angegebenen Formeln für die Schockparameter beschränken sich auf Nahtreffer und geben keine Auskunft über den zeitlichen Schockverlauf. Ihre Extrapolation auf Volltreffer führt zu unvernünftigen Resultaten.
Im Zusammenhang mit den hier beschriebenen Versuchen wurden nun erste Ansätze zur rechnerischen Erfassung des **konventionellen** Schocks entworfen. Dabei wurde das bereits bestehende Simulationsprogramm **'SHOCK'** [2] zur stochastischen Generierung von Bauwerkserschütterungen infolge **nuklearer** Belastung für die Berechnung des **konventionellen Schocks** erweitert.
Bei der hier dargestellten Versuchsanordnung zeigte sich, dass die Schutzbaureaktionen auf konventionelle Volltreffer eine starke Aehnlichkeit zu den Reaktionen auf eine nukleare Belastung aufweisen. Die Schutzbaubelastungen unterscheiden sich aber in einigen **grundlegenden** Punkten:

BELASTUNG	**NUKLEAR**	**KONVENTIONELL**
Luftstoss	etwa konstante Verhältnisse über dem Bauwerk	örtlich stark variierend
Erdstoss	ebene Welle	sphärische oder noch komplexere Wellenfront
Bombenaufprall	keiner	Impuls = Aufprallgeschwindigkeit x Bombenmasse

Vom **phänomenologischen Standpunkt** her gesehen setzt sich die Belastung eines unterirdischen, durch konventionelle Volltreffer belasteten Schutzbauwerkes wie folgt zusammen:

- Luftstoss-Belastung der Decke (Detonationsdruck)
- Luftstossinduzierte Erdstossbelastung der Wände
- Belastung der Wände durch den direkten Erdstoss, verursacht durch die Detonation einer in das Erdreich eingedrungenen Bombe
- Impuls-Belastung durch den Bombenaufprall

Diese Belastungen verursachen die folgenden Schutzbaureaktionen:

- Starrkörperbewegung (Bewegung des Schutzbau-Schwerpunktes)
- (In)elastische Deformationen von Decke, Boden und Wänden
- elastische Bauteil-Vibrationen

Im Prinzip kann die Gesamtbelastung des Schutzbauwerkes durch Integration der spezifischen Luft- und Erdstossimpulse berechnet werden. Dies führt aber zu Problemen, da die üblichen Formeln [1] für die Bestimmung der flächenspezifischen Impulse und Drücke wegen Divergenz nicht anwendbar sind. Im Nahbereich unterscheiden sie sich ferner quantitativ um Grössenordnungen.
Das erarbeitete Modell erlaubt also vorläufig nur eine Abschätzung der durch konventionelle Volltreffer verursachten Schutzbauerschütterungen. Für die Entwicklung einer zuverlässigen Berechnungsmethode sind weitere Studien notwendig.

SCHLUSSFOLGERUNGEN

Die bei der Schockprüfung von Einbauteilen für Schutzbauten verwendeten Prüfkriterien berücksichtigen in erster Linie die nukleare Belastung. Diese Versuche haben jedoch gezeigt, dass die durch konventionelle Volltreffer verursachten Schutzbauerschütterungen wesentlich höher sind.
Trotz der insgesamt 26 Bombentreffern traten dank der wirksamen Schutzschicht nur geringe Schäden in den Schutzbauten auf.
Mit den durchgeführten theoretischen Arbeiten bestehen heute erste Ansätze zur rechnerischen Erfassung des konventionellen Schocks, aber noch keine geschlossene, praxistaugliche Methode.

Die Verfasser danken Herrn Bernard Anet, AC-Laboratorium Spiez, für die fachtechnische Unterstützung dieser Arbeiten und allen bei der Durchführung dieser Versuche beteiligten Mitarbeitern für ihren engagierten Einsatz.

SCHRIFTTUM

[1] Fundamentals of Protective Design for Conventional Weapons, Technical Manual TM 5-855-1, Headquarters, Department of the Army, 1986

[2] E. Kessler: 'Stochastische Simulation von Schutzraumerschütterungen infolge Nuklearexplosionen' Dissertation Nr. 7597, ETH Zürich

[3] B. Anet, P. Hunziker, E. Kessler: 'Statistics of Stochastic Shelter Motions induced by Nuclear Explosions', MABS 9, 1985

[4] E. Kessler, H. Brauchli: 'Step Load Response Analysis by Generalized Functions', J. of Engrg. Mechanics ASCE, No 112/3, March 1986

[5] E. Kessler: 'Entwurf für ein Computer-Modell zur Simulation der Bauwerkserschütterungen infolge von konventionellen Waffenwirkungen', Report 127-1, AC-Laboratorium Spiez, Schweiz, 1989

[6] Proceedings des Internationalen Symposiums 'Interaktion konventioneller Waffen mit Schutzbauten', Mannheim, 1987 (Seite 209)

UNTERSUCHUNG DER SCHOCKSICHEREN LAGERUNG, AUFSTELLUNG UND BEFESTIGUNG VON AUSSTATTUNGSTEILEN IN SCHUTZBAUTEN BEI HOHER, KURZZEITIGER BELASTUNG.

Oberstleutnant Dipl.-Ing. Hans-Georg Mett

Amt für Studien und Übungen der Bundeswehr
Bereich Sonderaufgaben-Infrastruktur

KURZFASSUNG

Bei fünf 1:1-Versuchen wurden größere konventionelle Ladungen in unmittelbarer Entfernung zu einem teilgehärteten Schutzbau unterirdisch und oberirdisch zur Detonation gebracht.Es wurde sowohl das Verhalten schutzbauspezifischer Ausrüstungs- / Ausstattungsteile infolge des auftretenden hohen, kurzzeitig wirkenden Gebäudeschocks wie auch die Anwendbarkeit und Zuverlässigkeit unterschiedlicher handelsüblicher und selbstentwickelter Befestigungs- und Dämpfungsmittel untersucht. Bauwerksbewegungen und -belastungen aus Waffenwirkung wurden mittels umfangreicher Meßtechnik dokumentiert. Die Auswertung der Versuchsergebnisse führt zu ingenieurmäßig verwertbaren Erkenntnissen und Verfahren zur schocksicheren Aufstellung bzw. Montage von Schutzbauausstattungsteilen. Ausgewählte Ergebnisse werden vorgestellt.

1.0 EINFÜHRUNG

1.1 Allgemeines

Schutzbauten, die konventioneller Waffenwirkung ausgesetzt werden, sind u.a. gegen kurzzeitige, hohe Schocklasten zu bemessen. Neben einzelnen Baugruppen eines Bauwerkes werden vor allem Ausstattung und Installationen im Schutzbauinnern durch diese Stoßlasten gefährdet; eine Realität, die bei Schutzbauentwürfen in der Vergangenheit nicht immer sachgerecht berücksichtigt wurde.
Der Bereich Sonderaufgaben-Infrastruktur des AStudÜbBw untersucht seit 1988 in Originalversuchen das Verhalten unterschiedlicher Schutzbauausstattungen und Befestigungs- sowie Stoßisolationsmittel nach Beaufschlagung mit hohen, kurzen Schocklasten.

1.2 Vorversuche

Mehrere Vorversuche an auskragenden, in den Boden eingespannten, schutzbauüblichen Stahlbetonwänden ergaben wertvolle Orientierungsdaten für weitere Versuchsvorhaben.
Die Vorversuche wurden bereits beim 4. Symposium 1989 in Panama City vorgestellt.[Lit 1]

1.3 HAUPTVERSUCHE / Versuchziele

Die hier präsentierten Hauptversuche hatten folgende Zielstellungen ...

... Untersuchung des Verhaltens des gesamten Schutzbaus und der charakteristischen Schutzbauausstattung nach Nahdetonation einer großen Sprengladung im Boden bzw. im Freien;
... Erprobung von handelsüblichen Befestigungsmitteln unter hohen dynamischen

Lasten im Zugbereich der belasteten Baustruktur bis hin zum Versagen;
... Untersuchung und Erprobung der Wirksamkeit und Anwendbarkeit einfacher handelsüblicher und selbstentwickelter Stoßdämpfungsmittel;
... Feststellung der Bewegungsgrößen an definierten Bauteilpunkten und an der installierten Ausstattung;
... Bodendruckmessungen;

2.0 VERSUCHSDURCHFÜHRUNG

2.1 Konzeption

Die Zieldefinition der Versuche war eindeutig praxisorientiert. Wegen begrenzter Mittel und Zeit konnten sich die Untersuchungen nur auf eine relativ eng umrissene Aufgabenstellung konzentrieren. Der Anspruch auf allgemeine, wissenschaftlich fundierte Gültigkeit der Versuchsergebnisse war nicht Inhalt der Zielstellung.
Das untersuchte Lastspektrum erfaßt den "worst case" einer definierten militärischen Bedrohung für einen bestimmten Schutzbautyp. Die folgenden Ausführungen sollten daher nur unten dem Aspekt der Beziehungen zwischen den gemessenen Bewegungsgrößen bzw. Lastgrößen und den beobachteten Einzelreaktionen des Bauwerks bzw. der Installationen / Befestigungen bewertet werden.
Die aus den Versuchen gewonnenen Erkenntnisse sollen dem mit Schutzbauten befaßten Ingenieur Hilfe zur praxisnahen Auftragsdurchführung sein.

2.2. Versuchsbeschreibung / Versuchsergebnisse

In diesem Beitrag werden 5 von 8 Einzelversuchen eines geschlossenen Untersuchungskomplexes vorgestellt.
Bei dem untersuchten Schutzbau handelt es sich um den auf 1/3 der Länge verkürzten Flugzeugschutzbau der 3. Generation, der mittels Nahdetonationen großer Sprengladungen in unterirdischer und oberirdischer Konfiguration belastet wurde.
Im Innenraum des Schutzbaus wurden schutzbaueigentümliche Ausstattungsteile sowohl in unmittelbare Nähe zur Detonationsquelle als auch an die normal vorgesehenen Positionen gestellt bzw. an den Außenwänden befestigt.

2.2.1 Vordimensionierung der Befestigungselemente

Die versuchsvorbereitenden Maßnahmen erforderten eine Vordimensionierung der vorgesehenen Befestigungs- und Schockdämpfungsmittel. Ziel war u.a. auch die Erreichung des Grenzzustandes.

(1) Befestigungsmittel
Die Reaktion der Stahlbetonbauteile war schwierig zu beurteilen, so daß ausschließlich die Eigenschaften der gewählten Befestigungselemente zur Vordimensionierung genommen wurden. Das sind in erster Linie das Arbeitsvermögen der Befestigungsmittel und die vom Hersteller angegebenen zulässigen Lasten für die Zug- und Druckzone unter Einrechnung der inhärenten 4 bis 7 - fachen Sicherheit. Der maßgebende dynamische Lastverlauf bzw. die ableitbaren Energieparameter wurden aus den Vorversuchen herangezogen.[Lit 1]
Das Bolzenarbeitsvermögen wurde nach folgendem Ansatz für die Schraubengüte 8.8 A4 ermittelt:

$$W_{bolz} = A_s * \sigma_{di} * \delta_{zul} * L_{bolz} \quad [J]$$

A_s [mm^2] Bolzenspannungsquerschnitt

σ_{di} [MPa] idealisierte, dynamische Fließspannung
δ_{zul} [%] zugelassene Bolzendehnung
L_{bolz} [m] maßgebende Bolzenlänge

Tabelle -1- zeigt die Ergebnisse der Vordimensionierung im Vergleich zu den Versuchsergebnissen.

(2) Schockdämpfungselemente
Mit den aus Vorversuchen ermittelten Beschleunigungsverläufen wurde unter Anwendung eines SDOF-Rechenverfahrens die Verformung der Ringabsorber während der maßgeblichen Stoßphase ermittelt. Die Federkennwerte der Ringabsorber im elasto-plastischen Bereich wurden mit Hilfe der Ansätze aus Lit[2;3;4] ermittelt.
Tabelle -2- stellt Vordimensionierung und Versuchsergebnisse gegenüber.

2.2.2 UNTERIRDISCHE ANSPRENGVERSUCHE (Versuche 2 und 4)

2.2.2.1 Versuchsaufbau

Der FSB wurde in einer ersten Versuchsserie mit 2 Bodendetonationen beaufschlagt. Die 190 kg PETN Sprengladungen detonierten in etwa 4.5 m Tiefe in der Mitte der FSB-Längsseiten. Der Untergrund bestand aus mitteldichtem, feinem Sandboden.
Untersuchungsobjekte im Shelterinneraum waren .....

(1) .. die FSB-Bodenplatte, die aus einem massiven, umlaufenden Fundamentbalken und einer 0.30 m starken Bodenplatte bestand;
(2) .. eine mit ausgewählter, scharfer Munition beladene Unterflur-Munitionsbox mit einer hydraulisch angetriebenen, nicht verriegelten Stahlhohlplatte als Abdeckung;
(3) .. das FSB-Haupttor;
(4) .. ein mobiles und ein stationäres, schockgedämpftes, am Boden mit Dübeln befestigtes Lenkflugkörpergestell mit scharfen Raketen und Dummies;
(5) .. spezifische Schutzbauausstattung, wie Werkzeugschränke, Regale, Personalbau usw.;
(6) .. ein im FSB untergestelltes Flugzeug;

Wesentliche Untersuchungsobjekte und ausgewählte Positionen im FSB wurden mit Meßtechnik zur vertikalen und horizontalen Messung der Bewegungsgrößen bestückt.

2.2.2.2 Ausgewählte Ergebnisse (Tabelle -3-)

(1) Die Bodendetonationen erzeugten Erdkrater von etwa 10 m Durchmesser und 3-4 m Tiefe. Sie reichten bis zu 2 m unter die Fundamentplatte.
(2) Der Spitzenbodendruck unter der Bodenplatte, 5 m von der Detonationsstelle entfernt, betrug 7 MPa, bei einer Wirkzeit von etwa 10 ms.
(3) An der Bodenplatte im Munitionsboxbereich wurde die maximale vertikale Spitzenbeschleunigung mit 354 g bei ≈ 5 ms Wirkzeit und die horizontale mit 181 g bei ≈ 8 ms Wirkzeit gemessen.
Diese Werte wurden bei beiden Versuchen etwa gleich ermittelt.
Massenverteilung, die örtliche Bauteilsteifigkeit und die individuelle Entfernung der Meßpositionen zum Detonationsort beeinflußten diese Bewegungsgrößen wesentlich, was zu erwarten war.
Im dünneren Bodenplattenbereich mit relativ geringer Steifigkeit ergaben sich in vergleichbarer Entfernung zum Detonationsort höhere Beschleuni-

gungswerte.

(4) Unbefestigte Ausstattungsteile wurden abhängig von ihrem Standort beschleunigt und bewegten sich unkontrolliert im Schutzbauinnenraum.

- Die aufgelegte Abdeckung der Munitionsbox, schwere Munitionsteile, der Personalbau, das mobile Flugkörpergestell sowie Werkzeugschränke und Regale wurden etwa 0.8 bis 1,5 m hochgeschleudert. Das bedeutet Abgangsgeschwindigkeiten zwischen 4 m/s und 6 m/s.
- Die Spitzen der auf mobilem Gestell gelagerten Raketen brachen ab.
- Die Innenausstattung des Personalbaus wurde aus den Halterungen gerissen und disloziert, der Bau selber teilweise verformt.
- Werkzeugschränke und weiteres abgestelltes Arbeitsgerät stürzten um bzw. wurden leicht verschoben.
- Der Flugzeugrumpf (keine repräsentative Masse) wurde ca. 30 cm aus der Parkstellung verschoben. Das Feder-Dämpfersystem des Bugfahrwerks schlug etwa 8 cm durch.

(5) Das an der Bodenplatte über Isolatoren befestigte FK-Gestell zeigte keinen wesentlichen Schaden. Die FK waren äußerlich unbeschädigt, zeigten aber nach röntgenologischer Untersuchung Risse im Festtreibstoff. Die Isolatoren waren an der detonationsabgewandten Seite ≈ 4 cm, an der detonationszugewandten Seite ≈ 1 cm zusammengedrückt. Bei den stärker verformten Isolatoren vergrößerte der Aufprall des Personalbaus die Verformung.

(6) Beide 140 to Torhälften waren aus den Schienen gesprungen und etwa 0.20 m nach außen versetzt. Die Torverriegelung war verklemmt. Das Tor konnte in angemessener Zeit wieder fahrbar gemacht werden.

(7) An der Schnittstelle FSB-Bodenplatte / Torfahrbahn entstand eine Höhendifferenz von 0.12 m mit einer Breite von 0.07 m.

(8) Die Rissbildung an der intakten Bodenplatte war mit 2-3 mm Rissbreite gering.

(9) 4 Schwerlastdübel Fischer FA 16, mit denen die Hydraulikpumpe zum Fahren des Mun-Boxdeckels an der Bodenplatte befestigt war, wurden etwa 2 cm aus dem Beton gezogen.

2.2.3 OBERIRDISCHE ANSPRENGVERSUCHE (Versuche 1, 3 und 5)

2.2.3.1 Versuchsaufbau

Rückwand und Seitenwände des FSB wurden in einer 2. Versuchsserie mit 3 oberirdischen Ladungen angesprengt. Dabei handelte es sich um Nahdetonationen umhüllter 230 kg TNT Ladungen mit einem L/D Verhältnis von 5.5 .

Versuchobjekte im einzelnen waren .....

(1) .. direkt oder isoliert angebrachte Massen zwischen 1000 kg und 0.5 kg. Als Befestigungselemente wurden handelsübliche, dynamisch belastbare Ankersysteme verschiedener Fachfirmen verwendet.
Als Isolatoren dienten unterschiedliche, selbstgefertigte und vorbemessene Ringisolatoren aus handelsüblichem Stahlrohr sowie Ganzmetallpuffer der Firma STOP-CHOC (Abb -1-);

(2) .. ein gefüllter 3 m^3 Wasserbehälter mit 8 x M16 Fischer Zykonanker an der beaufschlagten Wand befestigt sowie ein frei abgestellter 3 m^3 Wasserbehälter;

(3) .. in der Wandnähe abgestellte FSB-Ausstattungsteile, Personalbau, Werkzeugschränke und Regale;

(4) .. ein mobiles FK-Gestell mit 3 Dummies und 1 scharfen Rakete;

(5) .. ein mittels Ringabsorbern an der Bodenplatte befestigtes FK-Gestell, gleichfalls mit 3 Dummies und 1 scharfen Rakete beladen;
(6) .. zwei Behälter für Abwurfmunition in geschlossener MUN-Box;
(7) .. ein an der FSB-Decke befestigtes Lüftungsrohr, Länge 6 m und Durchmesser 0.3 m;

2.2.3.2 Ausgewählte Ergebnisse (Tabelle -4-)

(1) Der Wandbereich vor der Detonationsquelle wurde mit Spitzenbeschleunigungen im Bereich zwischen 33000 g und 10000 g beaufschlagt.(Abb -2-)
(2) Zwei mit 4 Ringabsorbern und M16 bzw. M20 Ösenmuffen an der Wand befestigte 1000 kg Massen blieben sicher an der Wand. Die Ösenmuffen wurden teilweise etwa 4 cm aus der Wand gezogen, die Ringabsorber waren je nach Position zwischen 0.4 cm und 3.8 cm plastisch verformt. Beachtenswert war, daß bei symmetrischer Last- und Massenanordnung, die jeweils entsprechenden Ringabsorber gleiche Verformungen aufwiesen.
(3) Von 28 direkt an der Wand angebrachten 1000 kg bis 0.5 kg -Massen ohne Schockisolatoren blieben 24 in sicherer Lage. Davon waren zwei 1000 kg Massen derart gelockert, daß in der Praxis eine Reinstallation notwendig wäre. Die Massen im 200 bis 0.5 kg Band blieben fest installiert.
(4) Zwei kleine Massen, - 1 bis 0.5 kg - , fielen mit der Betonüberdeckung etwa 0.5 m vor die Wand. Die Dübel blieben teilweise fest in der abgeplatzten Betonüberdeckung.
(5) Eine mit 4 x M16 Fischer-Zykon-Hinterschnittanker hart angebrachte 100 kg Masse fiel direkt vor die Wand, nachdem zwei obere Dübel herausgezogen und zwei untere abgerissen worden waren.
(6) Eine mit 3 x M12 Liebig-ULTRAPLUS Vorspannanker hart montierte 50 kg Masse fiel ebenso vor die Wand, nachdem 2 Dübel herausgezogen worden waren und 1 Dübel abgerissen war.
(7) Der Personalbau sowie die abgestellten Regale und das aufgelegte Werkzeug wurden kaum bzw. nur geringfügig verschoben. Ein Schaden trat nicht auf.
(8) Das mobile FK-Gestell wurde nicht verschoben bzw. beschädigt; die FK blieben funktionsfähig. Das gleiche galt für das stationäre FK-Gestell.
(9) Eine am Boden befestigte Wasserpumpe blieb fest verankert und unbeschädigt.
(10) Eine Deckenkranbahn mit Laufkatze zeigte keine Schäden.
(11) Der 2 m^3 Wasserbehälter (M ≈ 3000 kg) blieb fest an der Wand verankert. Der abgestellte, volle Wasserbehälter blieb am Ort; Wasser wurde nur geringfügig herausgeschleudert.

3.0 KURZAUSWERTUNG / PRAKTISCHE EMPFEHLUNGEN

(1) Die Versuche haben die zwingende Notwendigkeit bestätigt, daß bei der Erstellung von Schutzbauten die schocksichere Aufstellung und Befestigung von Ausstattungsteilen einzeln nachzuweisen ist.

(2) Die Befestigung massiger Teile an Außenwänden muß vermieden werden. Sollte das nicht möglich sein, sind Isolationsmaßnahmen vorzusehen. Die Versuche haben gezeigt, daß bereits einfache Mittel einen beträchtlichen Teil der Schockwirkung wegnehmen.

(3) Es sollten grundsätzlich tief in Bauteile eingelassene Befestigungsmittel in Rasterform geplant werden.

(4) Ringförmige Isolatoren (Rohrteile) sind billig und wirkungsvoll. Sie können unter nachstehenden Bedingungen eingesetzt werden :

- bei unempfindlichen, robusten Ausstattungsteilen
- bei größeren Massen zur Dämpfung hoher, kurzer Schocklasten
- zur Vermeidung von abgehenden Massen (Sekundärtrümmer)

(5) Für Dübel / Anker ist eine Mindestsetztiefe von 10 cm vorzusehen.

(6) Abplatzschutzbleche haben sich voll bewährt und eine stützende Wirkung für Befestigungselemente bewiesen.

(7) Für die Zugzone und für dynamische Lasten zugelassene handelsübliche Befestigungsmittel können unter bestimmten Bedingungen auch unter extremer Stoßwirkung genutzt werden. Die Versuche ergaben keine wesentlichen Qualitätsunterschiede bei den unterschiedlichen Ankerfabrikaten.
Ausgehend von den Versuchsergebnissen können für die militärische Praxis folgende Montageempfehlungen gegeben werden:

MASSE kg	BEFESTIGUNGSMITTEL Größe	Typ	DÄMPFUNGSMITTEL Typ
250	1 x M24	Liebig ULTRAPLUS	--
	1 x M20	Hülsenanker mit Betonrippenstahl und Winkelende	Ringabsorber D1 oder verformbarer Montagerahmen
	1 x M20	Krückstockanker	
50	1 x M16	Hinterschnittanker	Ganzmetallpuffer D3
	1 x M16	Hülsenanker mit Betonrippenstahl und Winkelende	Ringabsorber D2 " "
25	1 x M16	Hinterschnittanker	Ganzmetallmatte
	1 x M16	Hülsenanker mit Betonrippenstahl und Winkelende	Ganzmetallpuffer D3 " "
10	1 x M12	Hinterschnittanker	--
5	1 x M10	Hinterschnittanker	--
	2 x M8	Hinterschnittanker	--
3	1 x M8	Hinterschnittanker	--
1 - 2	1 x S12	Kunststoffdübel	--
0.5	1 x S10	Kunststoffdübel	--

4.0 SCHLUSSBEMERKUNG

Die bisherigen Versuche ergaben brauchbare praktische Hinweise und Daten zur Dimensionierung und Gestaltung der Befestigungstechnik schockbeaufschlagten militärischen Schutzbauten.
Noch laufende Versuche befassen sich mit Schockwirkungen aus Kontaktdetonationen auf Schutzbauinstallationen.
Es ist beabsichtigt, eine Zusammenfassung der wesentlichen Versuchsergebnisse (Meßschriebe usw.) zu einem späteren Zeitpunkt zu veröffentlichen.

.....

Literatur :

[1] Mett,H.G.
" Empirische Untersuchung der Wirkung von Schocklasten auf Einrichtungsteile und deren Befestigungselemente in Flugzeugschutzbauten "
4.Internationalen Symposiums zur "Interaktion Konventioneller Waffen mit Schutzbauten", Panama City, USA, April 1989

[2] Neubert,V.H.
" Analysis of Energy-Absorbing Shock Mounts "
The Shock and Vibration Bulletin, USA, Mai 1981

[3] Fortuna,R.E; Neubert,V.H.
" SHIP SHOCK - Two-Dimensional Shock Response of a Mass on Energy-Absorbing Shock Mounts "
The Pennsylvania State University, USA,1984

[4] Burns,A.B.
" Guide for the Selection & Application of Shock Mounts for Shipboard Equipment ", Contract No. Nobs-78963,
Department of the Navy, BuShips Code 423, USA, Sept 1961

.....

Abb: - 1 - BEFESTIGUNGSMITTEL / SCHOCKABSORBER
Fig: - 1 - SHOCK - ABSORBING BUMPERS / MOUNTS

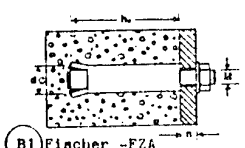

B1 Fischer -FZA
ZYKON- Anker

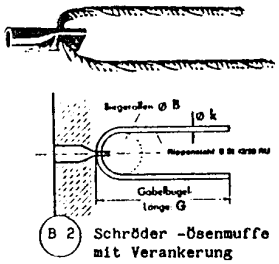

B 2 Schröder -Ösenmuffe
mit Verankerung

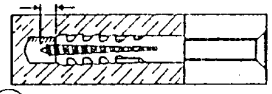

B4 Fischer - S
Kunststoffdübel

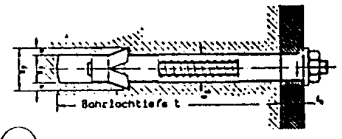

B3 Liebig -ULTRAPLUS
Vorspannanker

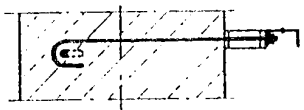

B5 Krückstockanker
mit Querstab

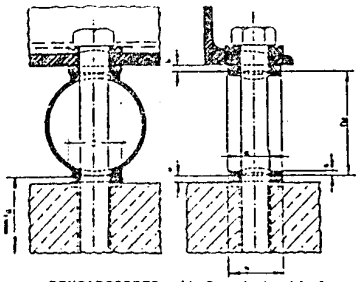

RINGABSORBER mit Durchsteckbolzen
D1 Rohr 127 x 7.1 DIN 2458
D2 Rohr 127 x 4 DIN 2458

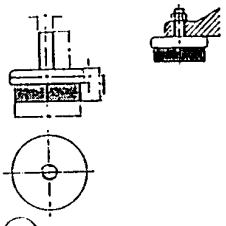

D3 STOP-CHOC
Ganzmetalldämpfer
Typ: SP 553 W

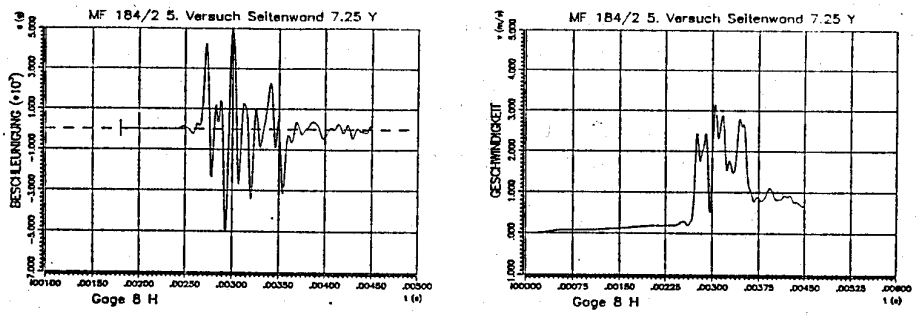

Abb.: - 2 - Typischer Beschleunigungsverlauf im Wandbereich

TABELLE: - 1 - DÜBEL- / ANKER - BELASTBARKEIT
Vordimensionierung und 'kurzzeitige Versuchslasten'

TYP	A_s (m^2)	L (m)	Vordimensionierung Wb (J)	P_{zul} zz (KN)	P_{zul} dz	s	P_{max} zz (KN)	P_{max} dz	Versuchswerte Wvm (J)	Pvm (KN)	Ivm (Ns)	Tvw (ms)
Fischer FZA												
M 8	36.6	0.050	179	2.5	4.35	4	10	17	14	117	8	.13
M10	58.0	0.060	341	3.5	5.95	4	14	24	87	462	29	.20
M12	84.3	0.080	661	6.0	10.20	4	24	41	4128	4075	329	.15
M16	157.0	0.100	1539	9.0	15.30	4	36	61	3025	6847	550	.02
Fischer 'S'												
S10	-	0.05	-	-	1.3	7	-	9.3	1.4	12	1	.20
S12	-	0.06	-	-	1.6	7	-	11.4	60	96	11	.20
Liebig ULTRAPLUS												
M 8	36.6	0.095	341	6.0	-	4	24	-	16	140	10	.13
M12	84.3	0.140	1157	13.0	-	4	52	-	174	924	329	.15
M16	157.0	0.190	2923	21.0	-	4	84	-	256	2440	160	.20
M24	353.0	0.280	9686	52.0	-	4	204	-	15126	24115	2750	.08
Schroeder ÖSENMUFFE, dickwandig												
M16	157.0	0.077	-	15.9	-	4	63.6	-	4805	24525	1550	.08
M20	245.0	0.092	-	20.8	-	4	83.2	-	6480	1523	1800	.15

A_s = Spannungsquerschnitt; L = Bolzenlänge
Wb = rechnerisches Arbeitsvermögen des Ankers/Dübels
P_{zul} = zulässige Dübelbelastung nach Werksangabe
P_{max} = maximale Dübelbelastung unter Einrechnung der Sicherheit
Wvm = maximale, kurzzeitig aufzunehmende Energie aus der Versuchsreihe
P_{vm} = maximale, kurzzeitig auftretende Last aus der Versuchsreihe
I_{vm} = maximaler, kurzzeitig auftretender Impuls aus der Versuchsreihe
Tvw = maßgebende Wirkzeit im Versuch ; s = Sicherheitsbeiwert
zz = Zugzone ; dz = Druckzone

TABELLE - 2 - VORDIMENSIONIERUNG der ISOLIERUNGSELEMENTE
- Vergleich: Rechnung / Versuch -

DÄMPFUNGSELEMENT 'Ringabsorber' Typ	Material	Vordimensionierung Pe,d (KN)	Pp,d (KN)	Wd (J)	Ivor (Ns)	svor (cm)	Versuch Ivers (Ns)	svers (cm)	Nachrechnung srech (cm)
D1	Rohr 127 x 7.1 x 120	29	44	5.5	1013	4.7	1218	3.8	6.8
D2	Rohr 127 x 4.0 x 100	4	6	1.5	202	6.8	120	2.9	2,5

$P_{e,d}$ elastische Grenzlast mit dynamischen Materialkennwerten
$P_{p,d}$ plastische Grenzlast mit dynamischen Materialkennwerten
W_d maximal aufnehmbares Arbeitsvermögen
I maßgebender Impuls ; s Dämpferverformung
vor -- Vordimensionierung ; vers -- Versuch ; rech -- Rechnung

TABELLE: - 3 - UNTERIRDISCHE ANSPRENGVERSUCHE
- ausgewählte Ergebnisse -

Test Nr.	V E R S U C H S - O B J E K T	A max (g) hor	A max (g) vert	T wirk (ms) hor	T wirk (ms) vert	V max (m/s) hor	V max (m/s) vert	e aufn (J/kg) hor	e aufn (J/kg) vert
2	*MUN-Box*								
	-Seitenwand	181	354	7.5	4.8	5.2	6.4	14	21
	-Boden	117	320	4.8	5.1	3.0	6.8	4.5	23
2	*Munition*								
	Masse 250 kg	75	160	8.2	6.8	3.6	1.8	6.4	1.6
2	*Bodenplatte*								
	sdet = 9 m	0	5.9	0	17.9	0	0.56	0	0.16
	sdet = 15 m	0	3.3	0	12.6	0	0.23	0	0.03
4	*Bodenplatte*								
	sdet = 6 m	0	38	0	26	0	4.7	0	11.1
	sdet = 9 m	0	69	0	46	0	2.7	0	3.7
	sdet = 15 m	0	231	0	86	0	0.52	0	0.14
4	*Wandfuß*								
	sdet = 3.0 m	0	169	0	22	0	3.2	0	5.1
	sdet = 5.8 m [1]	0	143	0	24	0	3.7	0	6.9
	sdet = 5.8 m	0	75	0	70	0	1.2	0	0.72
4	*Seitenwand*	77	154	--	--	1.6	3.4	1.3	5.8
4	*Personalbau*	0	87	0	20	0	3.3	0	5.5
4	*LFK-Gestell*								
	- mobil	47	230	0	10		7.9		31.2
	- stationär+RA	93	310	0	10				
4	*Batteriesatz,fest*	0	253	0	8	0	4.8	0	11.5

[1] FSB-Ecke; **sdet** = Abstand vom Detonationsort; **RA** = Ringabsorber
hor = horizontal ; **vert** = vertikal; **e** = aufzunehmende Energie
A = Beschleunigung; **V** = Geschwindigkeit; **T wirk** = Wirkzeit

TABELLE: - 4 - ERGEBNISZUSAMMENSTELLUNG der OBERIRDISCHEN ANSPRENGVERSUCHE
-- maximale Bewegungsgrössen aus den Messverläufen --

TEST Nr.	OBJEKT	BEFESTIGUNGEN ISOLATOREN	Amax [1] (g)	Amax [2]	Vmax [1] m/s	Vmax [2]	F	L/s	A/u	SCHADEN/VERFORMUNGEN BEMERKUNGEN
1	Masse 1000 kg	B5 - 4xM20	9833		11.0		X			M aus Rahmen gerissen, Anker fest
1	Masse 1000 kg	B2 - 4xM20	10000	621	6.2	7.2		X		3 Ösenmuffen herausgerissen
1	Masse 1000 kg	B3 - 4xM24	9833	665	11.0	5.7		X		untere Anker sind stark gelockert
3	Masse 1000 kg	B2 - 4xM20 + D1	29000		17.3			X		Isolatoren stark verformt,1-4 cm
3	Masse 1000 kg	B2 - 4xM16 + D1	13960		10.0			X		Isolatoren stark verformt,1-4 cm
1	Masse 200 kg	B1 - 4xM16	5674		1.8		X			
1	Masse 200 kg	B3 - 4xM16	5674		1.8		X			
5	Masse 200 kg	B2 - 4xM20	3796	1352	2.9	4.3	X			Rahmen etwas verformt
5	Masse 200 kg	B2 - 4xM16 + D3	3796	241	2.9	5.2	X			Ösenmuffe leicht herausgezogen
5	Masse 200 kg	B1 - 4xM16	13960	2888	11.0	8.5	X			Muttern gelockert
5	Masse 200 kg	B3 - 4xM16 + D2	4976	3612	3.2	3.4	X			Isolatoren: 1.7 - 2.9 cm verformt
5	Masse 200 kg	B3 - 4xM16	4976	1782	3.2	1.6	X			eine Mutter gelockert
1	Masse 100 kg	B1 - 4xM16	2200		1.2		X			[3]
1	Masse 100 kg	B3 - 4xM16	2200		1.2		X			[3]
3	Masse 100 kg	B1 - 4xM16	29000		17.3				X	2 Anker gezogen;2 Anker abgerissen
3	Masse 100 kg	B3 - 4xM16	13960		11.0			X		M aus Rahmen gerissen,Anker fest
3	Masse 50 kg	B1 - 4xM12	33230		25.7		X			
3	Masse 50 kg	B3 - 3xM12	33230		25.7				X	2 Anker gezogen;1 Anker abgerissen
3	Masse 20 kg	B1 - 4xM10	9424		5.9		X			
3	Masse 20 kg	B3 - 2xM12	9424		5.9		X			
5	Masse 20 kg	B1 - 4xM10	4751		3.3		X			
5	Masse 20 kg	B3 - 2xM12	4751		3.3		X			
3	Masse 10 kg	B1 - 3xM10	9424		5.9		X			
3	Masse 10 kg	B3 - 1xM12	9424		5.9		X			
5	Masse 5 kg	B1 - 2xM8	4751		3.3		X			
5	Masse 5 kg	B3 - 2xM8	4751		3.3		X			
5	Masse 3 kg	B3 - 1xM8	4751		3.3		X			Anker etwa 2.8 cm gezogen
1	Masse 2 kg	B4 - 1xM12	9833		11.0			X		
1	Masse 1 kg	B4 - 1xM12	9833		11.0				X	mit Betondeckung herausgefallen
5	Masse 1 kg	B1 - 1xM8	4751		3.3		X			
1	Masse 0.5 kg	B4 - 1xM12	9833		11.0				X	mit Betondeckung herausgefallen
5	Masse 0.5 kg	B4 - 2xM10	4751		3.3		X			
1	Wasserbeh. 3 to	B1 - 8xM16	1467	600	0.8	3.5	X			
1	LFK-Gestell,sta	B1 - 4xM12 + RA	72		0.3		X			
3	Wasserpumpe		194		1.7		X			

[1] an der Wand neben der Masse gemessen ; [2] direkt an der Masse gemessen ; [3] Wert linear interpoliert
F = fest ; **L/s** = locker/sicher ; **A/u** = Abgang/unsicher

Entwicklung von Schockprüfständen zur Simulation konventioneller Waffenwirkungen im Hochschockbereich

Development of Shock Test Stands for the Simulation of Shocks from Conventional Weapons in the High-Shock Region

F. Rischbieter, P. Corvin
Battelle Motor- und Fahrzeugtechnik GmbH
D-6000 Frankfurt am Main

Abstract

With close-in detonations of conventional weapons, the outer walls of protective structures are loaded by shocks in the high-shock region. Methods and test stands for high-shock testing of equipment had to be developed meeting the following requirements:

- Peak accelerations in the range of 500 g to 5000 g with durations from 2 ms to 0.2 ms, respectively.
- Realistic setup for the attachment of test objects, e.g. with dowels in concrete. Therefore, the test stands should be made of concrete.

Two types of test stands with loading by explosives were designed. For producing shocks with pulse durations of 1 to 2 ms, loading by water-tamped explosions (Figs. 1 and 2), for shocks with pulse durations of approx. 0.2 ms explosions in air (Fig. 3) were used. Velocity and acceleration as a function of charge weight for the two configurations are shown in Figs. 4 and 5, shock diagrams in Figs. 6 and 7.

1 Einleitung

Die in der Bundesrepublik Deutschland bestehenden Prüfeinrichtungen und Prüfvorschriften für Schocktests an Geräten und Einrichtungen in Schutzbauten sind für Schocks aus nuklearer Waffenwirkung ausgelegt, wobei von einer Dauer des Beschleunigungspulses von ca. 10 ms, von Spitzenbeschleunigungen bis maximal 40 g und Geschwindigkeiten bis maximal 4 m/s in der höchsten Schockklasse ausgegangen wird. Damit sind im allgemeinen auch Schocks abgedeckt, die im Innern von Schutzbauten an nicht exponierten Stellen bei

konventioneller Waffenwirkung auftreten.

Anders verhält es sich dagegen mit Geräten und Einrichtungen, die an Umfassungsbauteilen installiert sind, wenn sie durch Detonationen im Nahbereich beaufschlagt werden. Dies kann vor allem Infrastruktureinrichtungen des Schutzbaus, wie Teile von Lüftungs- und Klimaanlagen, Versorgungsleitungen, Kabel usw. betreffen, die für das Funktionieren des Systems Schutzbau notwendig sind.

Für diese Schockbelastungen war eine Prüfmethode zu entwickeln, wobei der Bereich der zu erzielenden Schockparameter grob innerhalb der folgenden Grenzen liegen sollte:

Dauer der Beschleunigungsphase	ca. 0,2 ms	bis	2 ms
Maximale Beschleunigung	ca.5000 g	bis	500 g
Maximaler Weg	ca. 10 mm	bis	100 mm
Maximale Geschwindigkeit		bis ca.	4 m/s

In der Phase I wurden in einer theoretischen Studie zwei sprengtechnische Methoden zur Schockerzeugung ausgewählt, die in der Phase II zunächst in Modellversuchen auf ihre Eignung untersucht wurden. In der Phase III wurden zwei Prüfstände im Originalmaßstab erprobt und eine erste Serie von Gerätetests durchgeführt. Die Untersuchungen wurden im Auftrag des Bundesamtes für Wehrtechnik und Beschaffung, KG IV 3, von der Wehrtechnischen Dienstelle 71 der Bundeswehr und der Battelle Motor- und Fahrzeugtechnik durchgeführt. Wesentlicher Gegenstand des Vortrages sind die Methoden der Schockerzeugung sowie Funktionsweise und Konstruktion der Prüfstände.

2 Anforderungen an die Schocksimulation

Mit den angestrebten Spitzenbeschleunigungen wird der Hochschockbereich erreicht, woraus sich einige besondere Anforderungen an die Prüfsystematik und, daraus folgend, auch an die Auslegung der Prüfstände ergeben:

- Die Befestigung und Montage der Geräte (Dübel, Schienen, Schrauben, Schockabsorber) spielt eine wesentliche Rolle für die Schockresistenz des Gesamtsystems. Montage und Befestigung sind daher bei den Tests realitätsnah auszuführen, d.h. der Prüfstand oder zumindest die die Testobjekte tragenden Teile sind aus Beton auszuführen.
- Die Beanspruchung der Prüfstandskonstruktion ist so zu begrenzen, daß die Prüfstände für eine große Anzahl von Tests zu verwenden sind. Dazu sind die zu beschleunigenden Massen möglichst klein zu halten, die anregenden Kräfte großflächig zu verteilen, um Spannungskonzentrationen zu vermeiden, und die Stoßwellenspitzen der Sprengung durch Dämpfungsschichten zu reduzieren.
- Die Testobjekte sind vor sekundären Auswirkungen der Sprengungen (Luftstoß, Wasserauswurf, Wurfstücke) zu schützen.

3 Methoden zur Schockerzeugung

In der theoretischen Vorstudie (Phase I) wurde festgestellt, daß Schocks mit kurzen Pulsdauern der Größenordnung 0,2 ms und entsprechend hoher Spitzenbeschleunigung der Größenordnung 5000 g durch Abstandsdetonation einer Sprengladung in Luft vor einer Betonplatte, die zur Aufnahme der Testobjekte dient, erzeugt werden können. Bei einem Abstand der Ladung von ca. 1 m von der Platte ist dazu eine Ladung bis zu ca. 10 kg TNT-Aequivalent erforderlich.

Mit Ladungen dieser Größenordnung läßt sich ein normaler Versuchsbetrieb auf einem Sprengplatz durchführen. Die Testobjekte müssen jedoch vor der Einwirkung der Luftstoßwelle geschützt werden. Die Auslegung der Sprengkonfiguration basierte auf den bekannten Wirkungsdiagrammen von TNT-Detonationen in Luft.

Für längere Pulsdauern ist diese Methode nicht praktikabel, da die dann erforderlichen großen Ladungen zu hohem Aufwand an Sprengmitteln und zu Sicherheitsproblemen führen. Stattdessen wurde eine wasserverdämmte Sprengung gewählt, deren Konfiguration schematisch in Bild 1 dargestellt ist. Die Funktion der einzelnen Komponenten der Anordnung ist folgende:

- Bei der Detonation erzeugt der Sprengstoff im umgebenden Luftvolumen heiße Sprengstoffschwaden unter hohem Druck.Diese expandieren gegen das Wasser, wobei der Schwadendruck auf das Wasser übertragen wird. Der Druck bricht zusammen, wenn die Sprengstoffschwaden den Wassermantel außen durchbrechen.
- Das Wasser verteilt den durch die Ausbreitung abgeschwächten Druck auf die Wand. Durch die Massenträgheit des Wassermantels wird die Pulsdauer verlängert und und der von Sprengstoff abgegebene Impuls besser ausgenutzt.
- Durch die Dämpfungsschicht wird die Spitze der primären Stoßwelle abgebaut, die unmittelbar nach der Detonation durch das Luftvolumen auf das Wasser übertragen wird. Die Stahlplatte diente zum zusätzlichen Schutz der Betonoberfläche.

Bei der praktischen Auslegung wurde eine zylindrische Geometrie mit einer langgestreckten Ladung gewählt, da damit eine gleichmäßigere Druckverteilung zu erreichen ist als mit einer konzentrierten Ladung bei sphärischer Geometrie. Die Sprengladung wurde zur Zentrierung in Schaumstoff eingebettet, der das Luftvolumen darstellt, und dieser zum Schutz gegen das Wasser in ein Plastikrohr eingebracht.

In der theoretischen Vorstudie wurde das dynamische Verhalten des Systems Sprengstoff-Luftvolumen-Wasser mit einem numerischen Rechenprogramm simuliert. Die Zusammensetzung der Dämpfungsschicht wurde in den Vorversuchen optimiert. Als am besten geeignet verwies sich eine kombinierte Dämpfungsschicht aus Spanplatten auf der Wasserseite und einem Hartschaum auf der Wandseite.

4 Aufbau der Prüfstände

Der Prüfstand für den Antrieb durch wasserverdämmte Sprengungen ist halbschematisch in Bild 2 gezeigt. Der eigentliche Prüfstand besteht aus einem Betonkasten ("Schocktisch"), der auf einer geschmierten stählernen Gleitbahn beweglich ist. Zur Gewichtsersparnis ist die Betonkonstruktion oben und hinten

offen, die Testobjekte werden gegen den Wasserauswurf durch einen leichten Stahldeckel geschützt. Wegen der Wasserverdämmung sind die Luftstoßbelastungen der Umgebung und der Testobjekte minimal, im Innern des Schocktisches traten bei den Vorversuchen nicht mehr als 50 mbar Überdruck auf.

Die Testobjekte können an der Stirnwand und am Boden des Schocktisches befestigt werden. Zur Aufnahme der Testobjekte steht ein lichter Raum von je 1,80 m Breite und Höhe und 1,60 m Länge zur Verfügung.

Im Wasservolumen waren, um die Belastung auf der Stirnwand möglichst gleichmäßig über die Breite zu verteilen, zwei vertikal stehende Ladungen angebracht. Die Gesamtladung, aufgeteilt auf die beiden Ladungssäulen, bewegte sich bei den Versuchen zwischen 800 g und 2400 g PETN.

Das Schemabild des Prüfstands mit Antrieb durch eine Sprengung in Luft ist in Bild 3 dargestellt. Als Träger der Testobjekte dient die pendelnd aufgehängte Betonplatte, die durch die Stoßwelle der Sprengung beschleunigt wird. Zur seitlichen Führung der Platte sind Stahlstäbe in Hülsen durch die Platte geführt. Der dahinter liegende Betonkasten nimmt den Impuls der Platte auf und dient zum Schutz der Testobjekte gegen den Luftstoß.Die Sprengstoffmengen bewegten sich bei den Versuchen zwischen 0,8 kg und 12 kg TNT in 0,8 m bis 1 m Abstand von der Platte.

Zur Wegbegrenzung und Energieaufnahme sind bei beiden Prüfständen zylindrische Gummipuffer eingesetzt

Als Standardinstrumentierung wurde bei allen Versuchen eingesetzt:

- Mehrere Beschleunigungsgeber für die Beschleunigung in Stoßrichtung
- Ein Weggeber am Schocktisch und zwei Weggeber an der Betonplatte
- Mehrere Dehnungsmeßstellen auf der Bewehrung an der Stirnwand des Schocktisches und an der Betonplatte

Die Geschwindigkeit wurde aus den Beschleunigungs- und Wegsignalen durch Integration bzw. Differentiation berechnet. Beschleunigungsmeßstellen an den Testobjekten wurden nach den jeweiligen Erfordernissen angebracht.

5 Ergebnisse der ersten Versuchsreihen

Die Geschwindigkeit und die Beschleunigung in Abhängigkeit von der Ladungsgröße sind in den Bildern 4 und 5 für die Orte dargestellt, die für die Anbringung von Testobjekten in Frage kommen:

- Mitte der Stirnwand des Schocktischs
- Bodenplatte des Schocktischs
- Mitte der Betonplatte.

Aus dem Vergleich der Relation zwischen Ladungsmenge und Geschwindigkeit bei der wasserverdämmten Sprengung am Schocktisch und der Sprengung in Luft an der Betonplatte ist ersichtlich, daß durch die Wasserverdämmung die Ladung effektiver zur Impulserzeugung ausgenutzt wird. Dabei ist noch zu beachten, daß die Masse des Schocktischs ca. 12500 kg, die der Betonplatte nur ca. 4000 kg beträgt. In Bild 6 und 7 sind Schockpolygone der erzielten Schocks für typische Ladungsgrößen im Schocknetz aufgetragen.

Bei den höchsten verwendeten Ladungsmengen traten Beschädigungen sowohl am Schocktisch als auch an der Betonplatte auf, wodurch die Anzahl der möglichen Tests begrenzt wurde.Ferner waren im Innenraum hinter der Betonplatte die Drücke der Blastwellen, die durch den offenen Spalt zwischen Platte und Schutzgehäuse eindringen konnten, noch zu hoch.

6 Schlußfolgerungen

Die angestrebten Schockwerte für die Simulation konventioneller Waffenwirkungen auf Schutzbauten konnten erreicht und teilweise übertroffen werden. Aufgrund der gesammelten Erfahrungen und der Auswertung der Schadensbilder an den Prüfstandsstrukturen können die Auslegung der Prüfstände verbessert und Ladungsgrenzen für den sicheren Dauerbetrieb angegeben werden. Auch das Problem der Blastwelleneinwirkung auf die Prüfobjekte in der Betonplatte ist mit relativ einfachen konstruktiven Mitteln beherrschbar.Damit sind dann Serientests an Prüfobjekten möglich, die in der nächsten Phase vorgesehen sind.

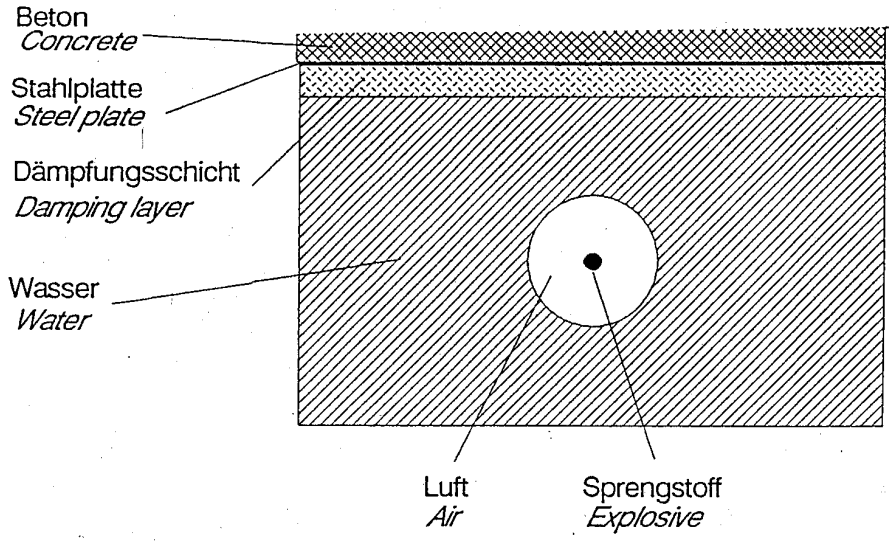

Bild 1: Prinzipieller Aufbau der wasserverdämmten Sprengung

Fig. 1: Scheme of the water-tamped explosion

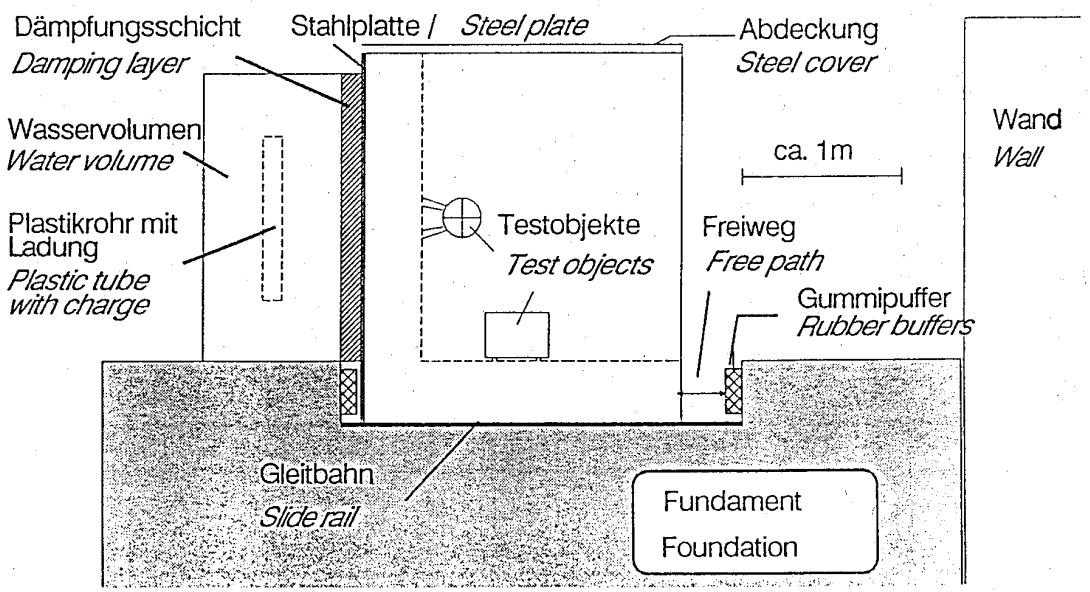

Bild 2: Schocktisch mit Antrieb durch wasserverdämmte Sprengung (halbschematisch)

Fig. 2: Shock table with loading by water-tamped blasts (half schematic)

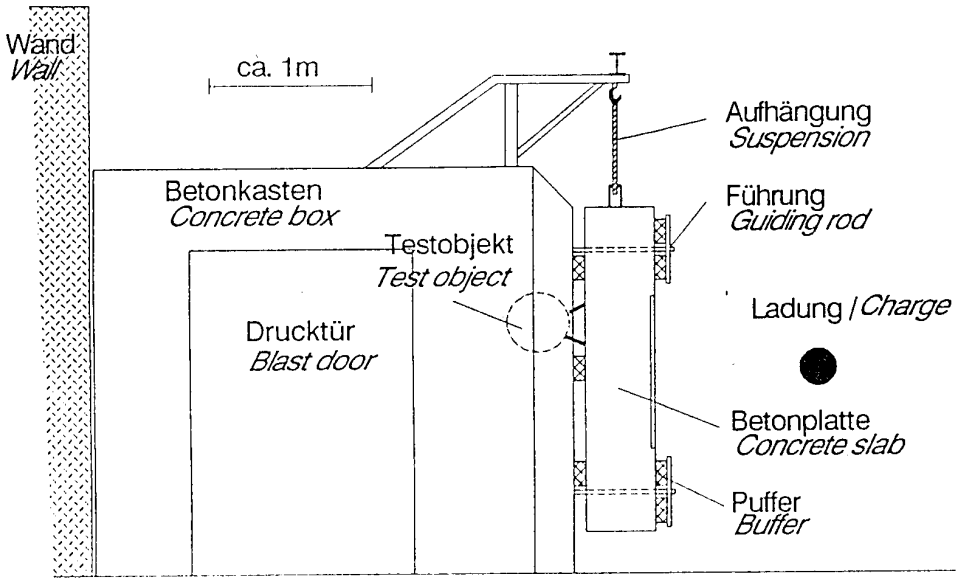

Bild 3: Prüfstand mit Betonplatte und Antrieb durch Sprengung in Luft

Fig. 3: Test stand with concrete slab and loading by air blast

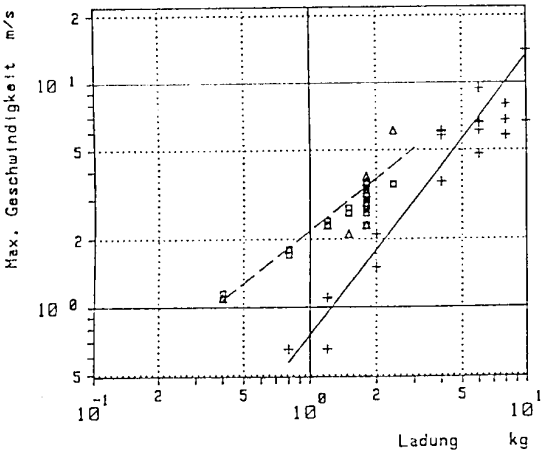

Bild 4: Maximale Geschwindigkeit in Abhängigkeit von der Ladung

Fig. 4: Peak velocity as a function of charge weight

□ △ ---------- Schocktisch

÷ —·—·— Betonplatte

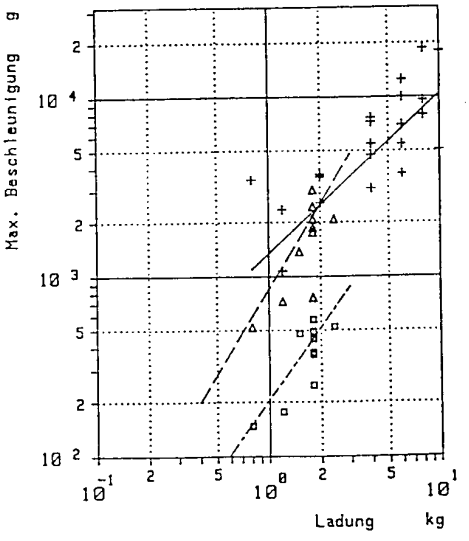

Bild 5: Maximale Beschleunigung in Abhängigkeit von der Ladung

Fig. 5: Peak acceleration as a function of charge weight

□ ---------- Bodenplatte Schocktisch

△ ---------- Stirnwand Schocktisch

÷ —————— Betonplatte

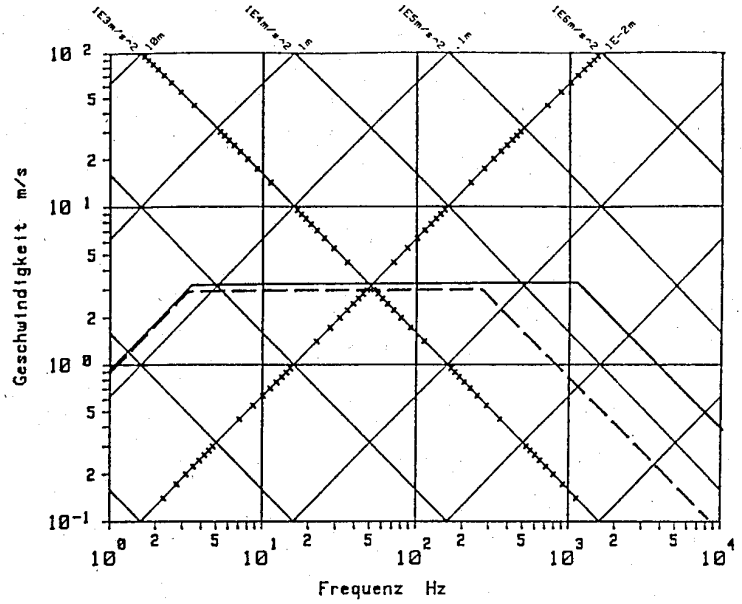

Bild 6: Typische Schockdiagramme am Schocktisch bei 1,8 kg Ladung

Fig. 6: Typical shock diagrams of the shock table for 1.8 kg charge weight

——————— Stirnwand

- - - - - - - - - - - - - - - Bodenplatte

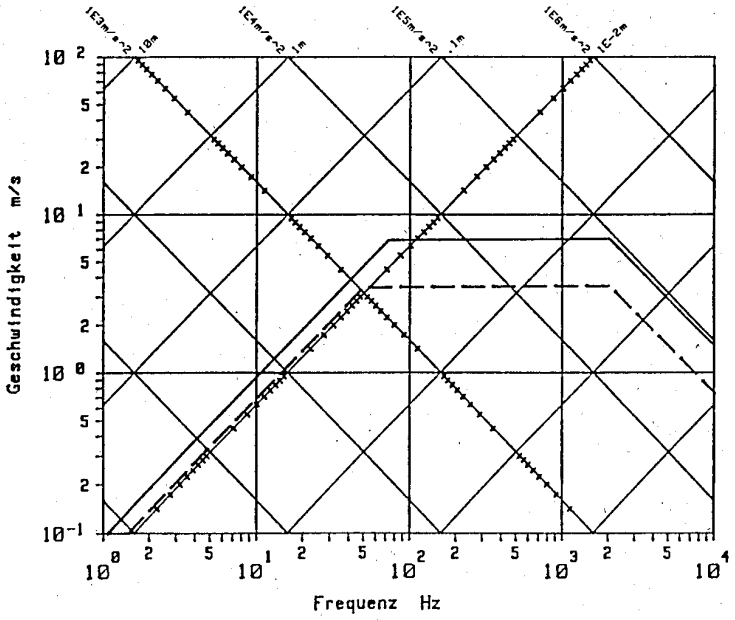

Bild 7: Typische Schockdiagramme an der Betonplatte

Fig. 7: Typical shock diagrams at the concrete slab

——————— Ladung 8 kg

- - - - - - - - - - - - - - - Ladung 4 kg

ISOLATION OF LARGE DISPLACEMENT STOCHASTIC SHOCK LOADINGS

Jyrki Ronkainen
Temet Oy
SF-00810 Helsinki, Finland

ABSTRACT

In a hardened facility it is customary to protect mechanical and electrical equipment and installations against weapon induced shock effects by means of shock isolators based on either elastic or plastic deformation of the isolator element.

This paper describes development and testing of VTV-100 shock isolator system. The system design criteria was the requirement for capability of attenuating stochastically excited shock loadings with limit quantities of motion of 6.5 g, 0.65 m/s and 100 mm in such a manner that the transmitted shock will not exceed the value of 1.2 g.

The design approach based on letting the isolated unit swing freely and transforming this low frequency swinging motion into vertical compressive motion of progressive coil spring isolators is discussed in details, studies and test program to verify the system dynamic stability for stochastic shock excitation as well as to check its shock attenuation efficiency are presented and test results are evaluated.

BACKGROUND

Conventional elastic shock isolators are usually dimensioned assuming the shock motion to be caused by harmonic excitation and defining the operational range of the isolator from shock spectra. This approach does not consider the real nature of weapon induced shock loadings. Additionally, these standard elastic isolators are usually designed for a motion displacement not exceeding 30 ... 35 mm. Since there has been a request for elastic shock isolators applicable for soft soil conditions without the above restrictions, it had become necessary to develop a commercially viable shock isolation system that can handle stochastically excited shock loadings with relatively large motion displacement.

DESIGN APPROACH

Years of experience in design of shock isolated installations in shelters was applied in the basic isolator element and suspension system design. A series of coil springs with progressive stiffness was designed as the isolator element. Suspension of the unit to be isolated was arranged by fixing the spring to a support bracket and suspending the shock isolated mass by means

of a flexible steel wire as shown on Figure 1. The steel wire is guided through a teflon bearing on the support bracket which acts as the pendulum point for the free part of the wire. Thus also the horizontal swing motion of the isolated mass will be converted into vertical displacement of the spring.

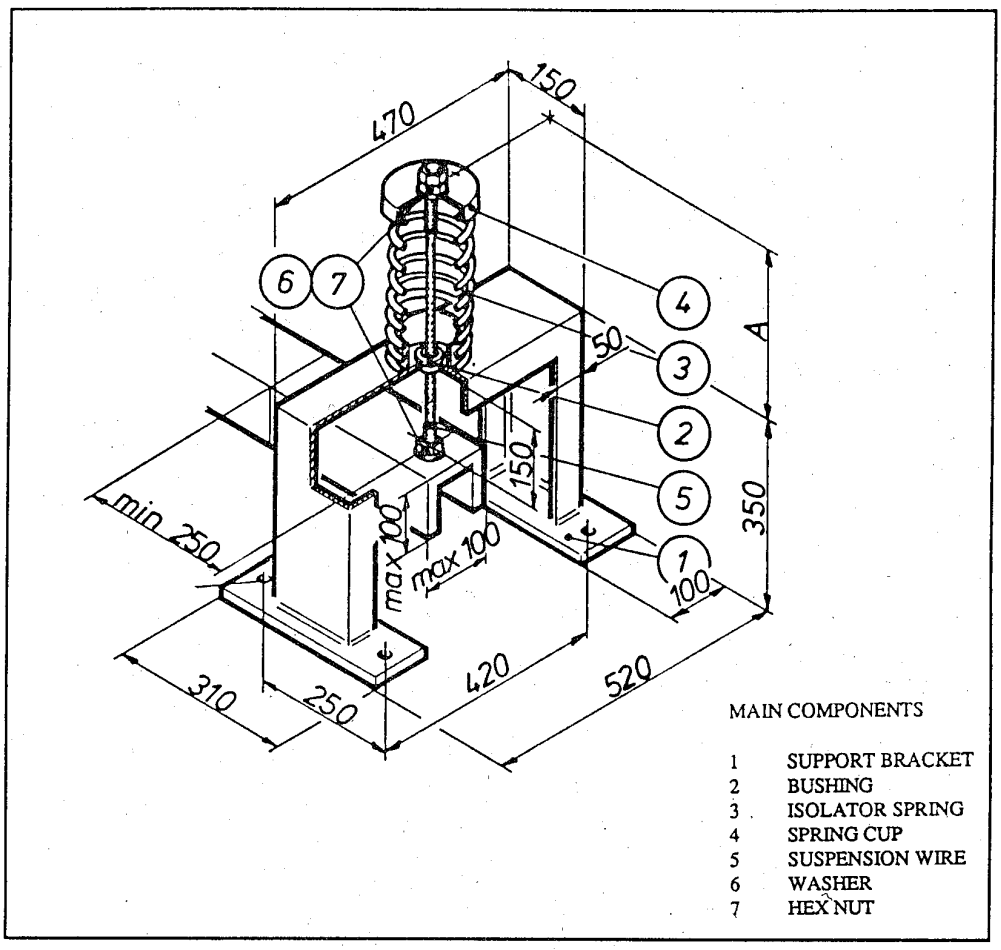

Figure 1. VTV-100 Shock Isolator System Design

From our previous experience with shock mount design it was deemed necessary to select a minimum of eight different spring units to sufficiently cover the static load range of the equipment normally installed in shelters. The static load range of the spring is defined as the range between minimum and maximum static load in which the spring is designed to perform. The minimum load restriction is set due to the fact that by decreasing the mass beyond the limits, the system natural frequency will increase thus decreasing the efficiency of shock attenuation. The maximum load restriction is naturally set to avoid impact caused by solid compression of the spring coils together. On the other hand, by designing the stiffness of the springs to be substantially progressive, a sufficiently wide load range was obtained. The spring series with minimum and maximum static loads are featured in Table 1.

Isolator type code	Minimum load N	Maximum load N
VTV100-35	20	35
VTV100-75	35	75
VTV100-150	75	150
VTV100-300	150	300
VTV100-550	300	550
VTV100-1100	550	1100
VTV100-2250	1100	2250
VTV100-4500	2250	4500

Table 1. Minimum and maximum static loads of the isolator springs

SYSTEM STUDIES AND TEST PROGRAM

As a soft isolation system is known for its effectiveness in attenuation of the transmitted shock, the study was more focused on its dynamical stability. Theoretically, it is possible that the vertical, horizontal and rotational vibration modes are superimposed under continuous stochastic excitation leading into uncontrollably large movements (overshooting) of the isolated unit.

The system stability was first theoretically analyzed for a single shock with the following parameters:

$a_{max} = 6.5\ m/s^2$
$v_{max} = 0.65\ m/s$
$d_{max} = 0.1\ m$

corresponding to the shock resistance requirements for equipment in the Central European 1 bar shelter class. The system modelling was based on a realistic mechanical installation (a cooling tower) having its shape and location of center of gravity such that it was suspect to dynamical instability. The system was first analyzed as two degrees of freedom system, and then the most critical horizontal shock direction was studied with a two dimensional three degrees of freedom system including the mass rotation. By solving the systems equations of motion using computer coded algorithms it was found that all system quantities of motion remain within acceptable limits.

After theoretical study for single shock excitation, the actual testing program to cover stochastic support motion was planned. The testing installation comprised two steel frames. The lower one was fixed on the floor and had two parallel hardened round steel bars as a slideway for the upper movable frame. This was attached to the bars with bush bearings. The angle between the direction of the rectilinear movement of the frame and horizontal plane was 45 degrees. In reality a structure will move in any direction during a ground shock. However, it is not practical to test the installation in all directions. Since support motion in 45 degrees sideways direction was considered to excite all dominant vibration modes, it was chosen as test direction.

The uppermost structure of the frame was horizontal and made up the support for the test installation which was a 900 mm long, 600 mm wide and 1200 mm high steel plate box. The box was made of 8 mm thick plate and welded on the bottom plate. The structure was suspended on four isolator

springs VTV100-1100. The total mass provided was 287 kg thus exerting a static load of approximately 700 N per isolator. The center of gravity was measured to be 530 mm above the upper surface of the bottom plate measuring roughly 315 mm above the support level. The mean static deflection of the springs was 34.0 mm and the length of an unloaded spring about 220 mm. The test arrangement is shown in Figure 2.

Movement of the upper structure was produced by a servo controlled loading system. Input signal was produced by a desk-top computer and D/A converter. Stochastic nature of the movement was achieved by selecting the time interval of the loading system input signal randomly between 0 and 1.0 seconds (the system period for the lowest vibration mode was estimated to be 1.0 s) and positioning the shaft of the hydraulic cylinder randomly between 0 and 100 mm.

The test instrumentation was such that the following displacements and accelerations were measured:

- stroke of the hydraulic cylinder considered as the support motion (DT1)
- horizontal and vertical acceleration of the moving frame (AM3 and AM4)
- deflection of two springs (DT2 and DT3)
- relative displacement between the support and the mass in horizontal and vertical direction
- horizontal and vertical acceleration of the mass (AM1 and AM2)

Displacements were measured using inductive transducers (DT1 thru DT4) and a potentiometer type transducer (DT5) and carrier frequency amplifiers. Accelerations were measured with piezoelectric accelerometers with charge amplifiers. Recording and signal processing requirements were met by an 8-channel direct writing oscillograph, a 14-channel video cassette data recorder and a 2-channel digital signal analyzer. Location of measuring points is also featured in Figure 2.

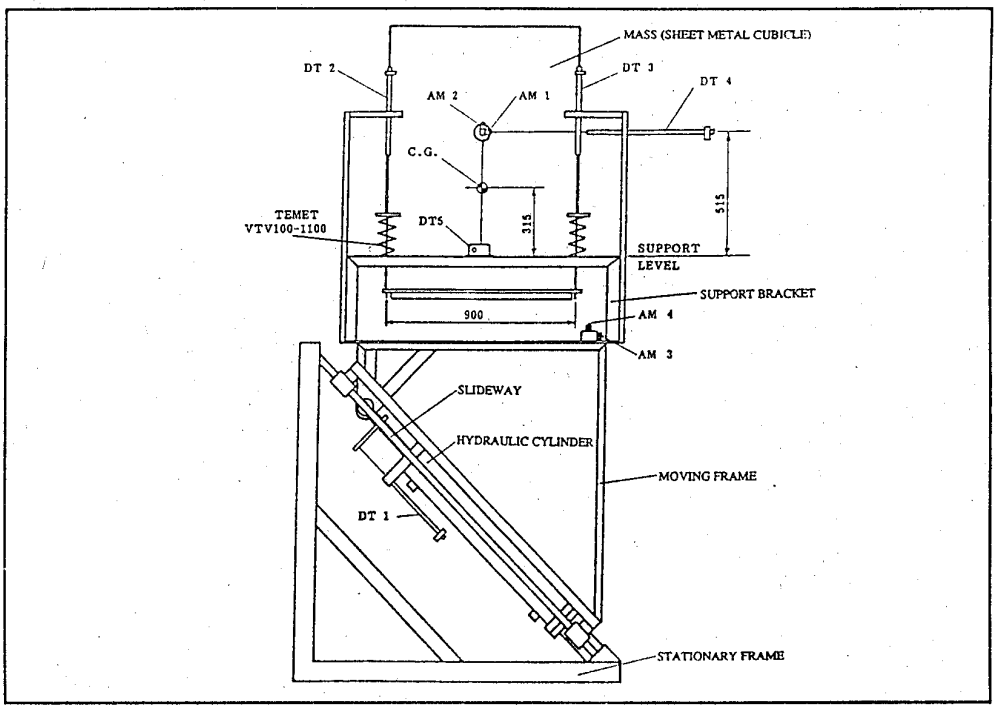

Figure 2. Test installation and location of measuring points

RESULTS:

The lowest natural frequency of 0.9 Hz of the installation corresponds to that of the pendulum mode as was expected. The second one of 1.6 Hz was that of the rotational mode around the vertical axis. This mode showed itself temporarily during the tests probably excited by latent asymmetrics of the installation. The natural frequency of the translational mode in vertical direction was 2.6 Hz and that of the rotational mode in the plane of the support motion 2.8 Hz. The frequency response function of the test installation is shown in Figure 3.

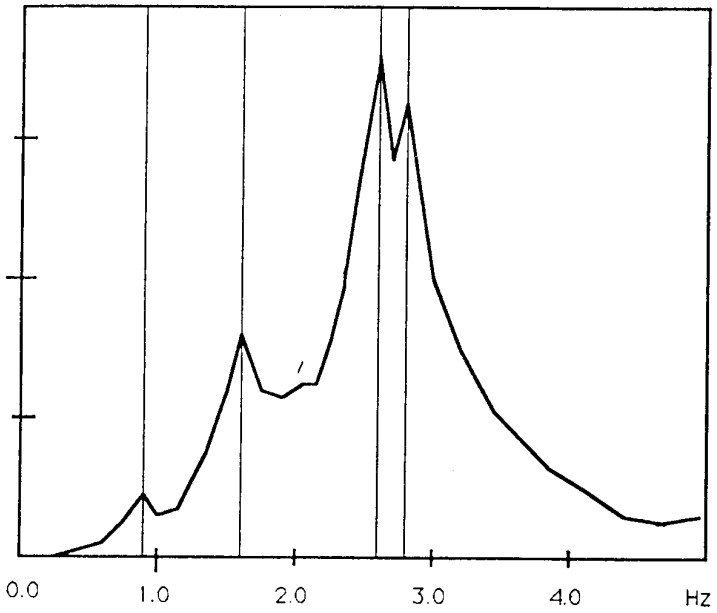

Figure 3. Frequency response function of the test installation

A typical recording from the test series is shown in Figure 4. A closer examination of the recordings reveals that the peak acceleration at the moving frame was in the range of 50 m/s^2. Mainly due to flow restrictions in the loading system servo valves, the full 6.5 g peak acceleration was not achieved with the available test set up. Regarding the system attenuation, it was observed that even in vertical direction the isolated mass did not experience acceleration in excess of 10 m/s^2. Amplitude of the mass displacement remains within 100 mm even in the more critical horizontal direction. The maximum recorded compression of the springs was about 45 mm leaving a clear safety margin for solid spring compression (spring coils hitting each other) that would require approximately 70 mm compression.

The overall system dynamic stability and movements were also studied by video recording the test performance. As could already be seen from the graphic recordings no exotic phenomena were found in terms of the system behaviour. The system retained its stability and no hard bangs against stationary supports occurred, since the large movements were accounted for in the bracket design.

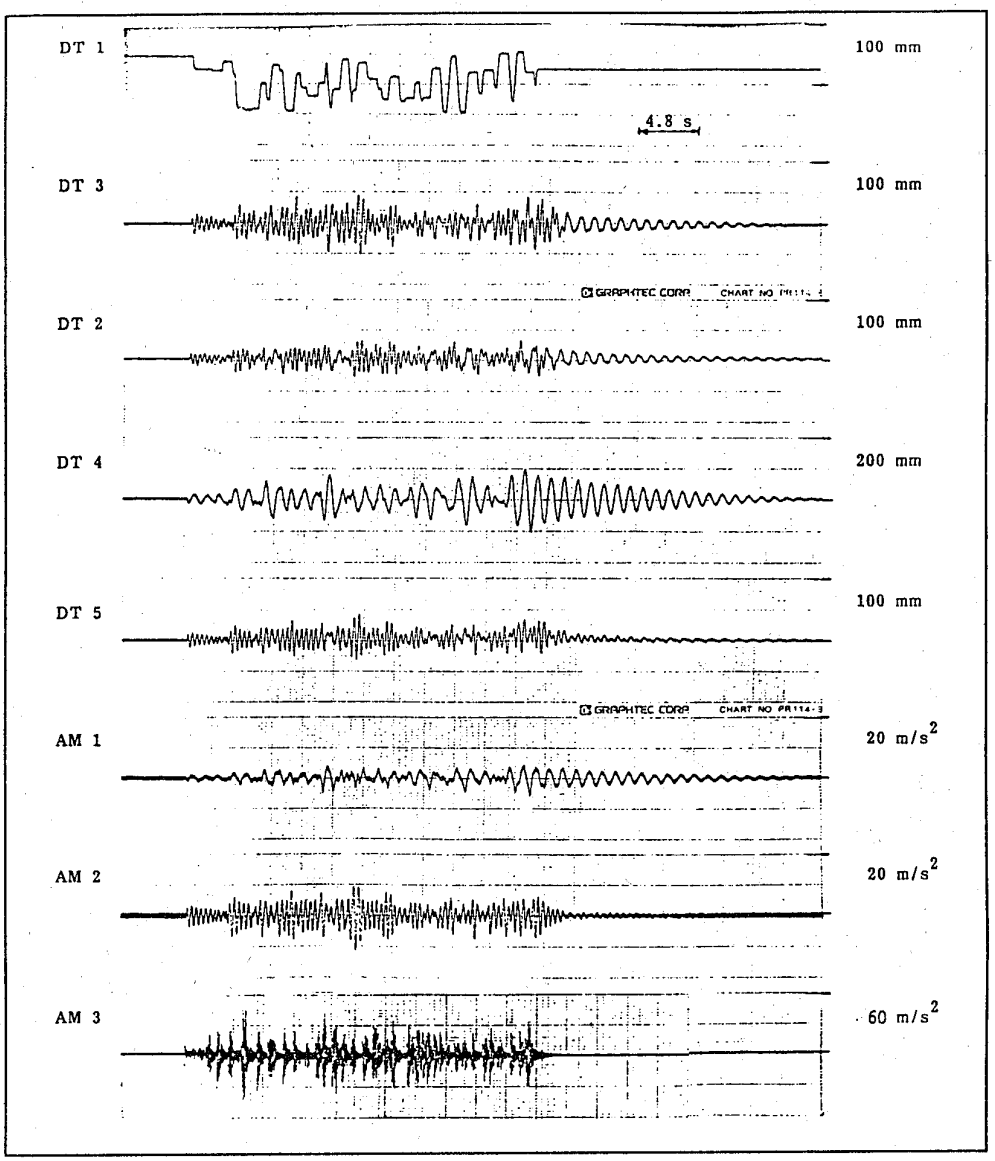

Figure 4. Typical time recording from the test

SUMMARY

It was established by testing that a soft isolation system can handle a stochastic shock excitation without problems provided sufficient free space around the isolated, moving equipment is accounted for in the system design. By keeping the natural frequencies of all vibration modes sufficiently low, preferably below 4.0 Hz, excellent shock attenuation properties are also achieved. The tested system has already been developed into a commercially available shock isolation system with numerous completed installations.

ACKNOWLEDGEMENTS

We acknowledge with thanks the great assistance and support provided by Helsinki University of Technology, Laboratory of Strength of Materials in every aspect of the analyses and performance of the tests.

A SIMPLIFIED TWO-DIMENSIONAL METHODOLOGY FOR PREDICTING IN-STRUCTURE SHOCK FOR COMPLEX STRUCTURES

Joseph L. Smith and Paul F. Mlakar
JAYCOR, Structures Division
1201 Cherry Street
Vicksburg, MS 39180

This paper presents a design methodology for predicting the in-structure shock response for structures subjected to dynamic loadings. The methodology uses a two-dimensional frame code which includes a soil-structure interaction model to predict the structural motions at locations of interest. This allows the modeling of both the flexural and rigid body components of motion. The results predicted by this method compare favorably with available test data. In addition, the shock spectra for complex geometries and for non-symmetrically located burst locations can be accurately predicted. Examples are provided.

INTRODUCTION

The primary objective in the design of a hardened facility is to prevent structural failure and collapse due to the given threat scenarios. To the structural engineer or structural dynamicist, this precept of design intuitively equates to keeping stresses, deflections, and/or rotations of critical structural elements to within accepted criteria. Experience has shown, however, that a facility may be impaired or prevented from performing its intended function at shock levels much less than that required to produce significant structural damage. This is especially true for protective command and control centers which rely on sensitive equipment such as sophisticated electronic gear, computers, pumps, generators, and a host of other mission-critical equipment. In order to determine if special shock isolation devices are required, and if so, the design of such devices, the internal shock environment must be defined with some confidence. This paper presents a methodology for accurately predicting the internal shock for above ground and buried structures subjected to blast and shock loadings.

The model developed in this paper to predict structural response is much more sophisticated than a simplified rigid body approach but less complex than a soil island finite element calculation typically used to generate response spectra. An attempt was made to develop and validate a model which would be relatively easy to use and require short run-times (less than 2 hours) on commonly available personal computers while retaining the salient features of response and an acceptable level of accuracy.

CALCULATION METHODOLOGY

The computer code STABLE (STructural Analysis of Blast Loading Effects) was used to model the structures discussed in this paper. This program is a 2-dimensional frame code capable of non-linear dynamic computations (Reference 1). While STABLE possesses a rather sophisticated, state-of-the-art concrete model, the structural members are modeled as non-linear, hysteretic beam elements with simplified elasto-plastic or elastic-reduced stiffness resistance functions. In addition, a linear interaction diagram is employed as illustrated in Figure 1. The value of k/5 for the second branch of the bilinear resistance function was chosen to approximate the "post yielding" behavior of a fixed end beam (Reference 2). This simple model was used to improve computational efficiency.

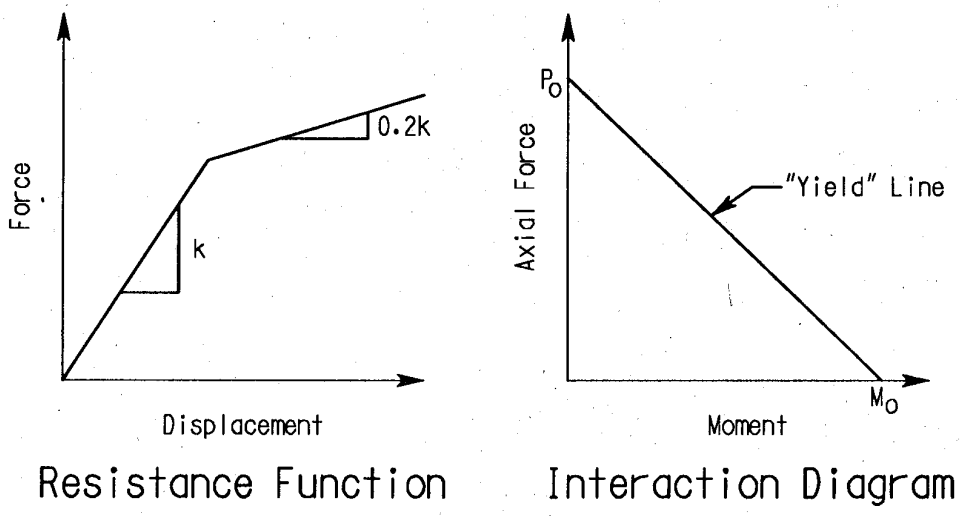

Figure 1. Typical resistance function and interaction diagram.

The interaction between the structure and supporting media, such as soil, is recognized to be a complex phenomenon that is extremely difficult to model and analyze even in detailed finite-element analyses. The soil-structure interaction (SSI) model chosen for this study was a simplified, velocity proportional, decoupled approach. The model is summarized below.

$$\sigma_{in} = \sigma_{ffn} + \rho c\,(V_{ffn} - V_{sn}) \qquad V_{sn} < \sigma_{ffn}/\rho c + V_{ffn}$$

$$\sigma_{in} = 0 \qquad V_{sn} > \sigma_{ffn}/\rho c + V_{ffn}$$

$$\sigma_{it} = \rho c_s V_{fft} \pm \rho c_s\,(V_{fft} - V_{st}) \qquad |\sigma_{it}| \le co + \sigma_{in}\tan\phi$$

where:

σ_{in} = Normal interface stress.
σ_{ffn} = Normal free-field stress.
σ_{it} = Tangential interface stress.
V_{ffn} = Normal free-field soil velocity.
V_{sn} = Normal structure velocity.
V_{fft} = Tangential free-field soil velocity.
V_{st} = Tangential structure velocity.
ρ = Mass density of the soil media.
c = Soil seismic velocity.
c_s = Soil shear wave velocity.
co = Cohesion of the soil.
ϕ = Friction angle of the soil.

By assuming one-dimensional, plane-wave shock propagation in an homogeneous elastic half-space (e.g., normal incidence of the shock front and no free-surface reflections), it can be shown that:

$$\sigma_{ffn} = \rho c V_{ffn}$$
$$\sigma_{in} = 2\sigma_{ffn} - \rho c V_{sn}$$

This SSI approach was chosen because it allows rigid body motions (unlike rigid supports) and utilized a soil acoustic impedance (ρc) which is more easily estimated than the traditional spring and damper coefficients. A complete discussion of the structure-media interaction model is presented in Reference 3.

The STABLE model allows for numerous dynamic loading options. Free-field stress, pressure or motion time-histories from measured data (in the case of test structures) or calculated waveforms using any accepted method such as that outlined in TM 5-855-1 (Reference 4) may be used. Free-field pressures do not need to be modified to account for reflections as this is accounted for in the SSI model. If interface pressure data is available it may be used in place of the free-field loading. In this case the SSI model is disabled at the points where interface loadings are provided. At locations where the structure is expected to move into the soil (support points) a dummy load (zero pressure) is applied along with the SSI model. This will provide a support force proportional to the structure velocity.

The calculation of in-structure shock proceeds as follows. First, the structure is modeled in the frame code in accordance with the above procedures. The STABLE models should be chosen to provide a reasonable compromise between calculation accuracy and problem size. As such, element lengths are varied to provide finer resolution at the loaded areas and points of interest. A cruder model is employed for the rest of the structure to reduce computation time and complexity. Care must be taken to insure that errors are not introduced by the model selection (i.e., non-symmetric model for a symmetric structure). A node must be provided at each point for which a shock spectra is desired. The frame code is then run and a time history of the structural acceleration at the points of interest are extracted from the output. These acceleration histories can then be used with any SDOF code to calculate the response spectra for the desired range of frequencies and damping. A special purpose SDOF code SPECTRA was created for this study (Reference 5).

EXAMPLES

Experimental Rectangular Structure

The first example problem consists of a rectangular, buried concrete box. This structure was used as one of the validation problems of the methodology. A series of tests known collectively as ESSEX V examined two such structures (Reference 6). Structure 3D was selected for presentation in this paper. The loading was generated by the detonation of 21 lbs of TNT placed six feet from the structure in a side-on configuration. This loading was selected since it fully exercised the longitudinal section of the structure but did not cause a structural failure. The structure geometry, burst location, and the location where the response spectra were obtained are shown in Figure 2. The structure was buried in backfill which was partially excavated and replaced after each test event. The placement of the backfill after each test was not rigidly controlled.

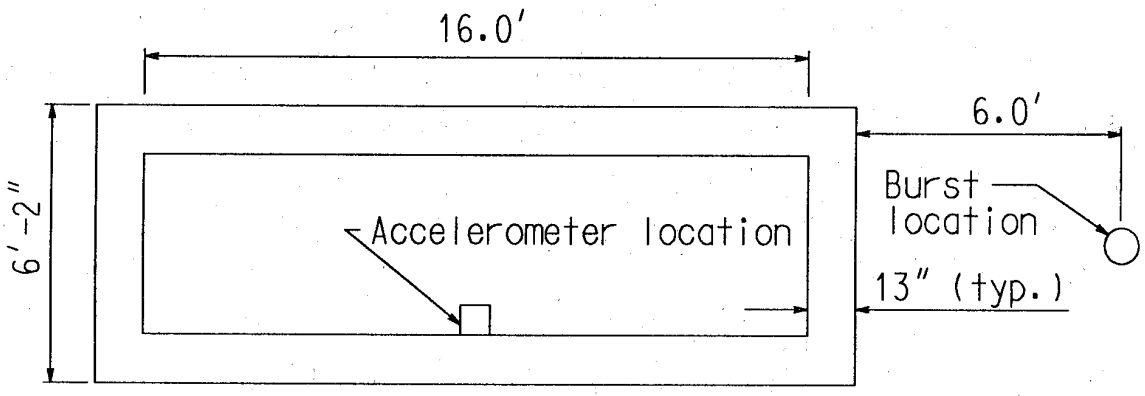

Figure 2. ESSEX structure 3D.

Calculations were performed using both measured and predicted loads as input. Free-field velocities from the test were used as input for the calculation using measured data (STABLE-MEASURED). TM 5-855-1 was used to predict free-field motions as input for the second calculation in a simulation of the actual design process (STABLE-TM). In both calculations, unreflected free-field waveforms were used since the STABLE SSI model automatically accounts for the interaction between the structure/soil media and the dynamic load.

Two frame analyses were conducted using the STABLE computer code and in-structure accelerations were obtained at the point of interest. The measured response spectrum was calculated using the measured in-structure motions and spectral amplification factors given in Reference 6. All three response spectra are shown in Figure 3 for zero percent damping. The agreement between all three spectra is excellent through the low and middle frequencies and good at higher frequencies. It is thought that the use of a finer mesh in the frame analysis would lead to even better results in the high frequency range.

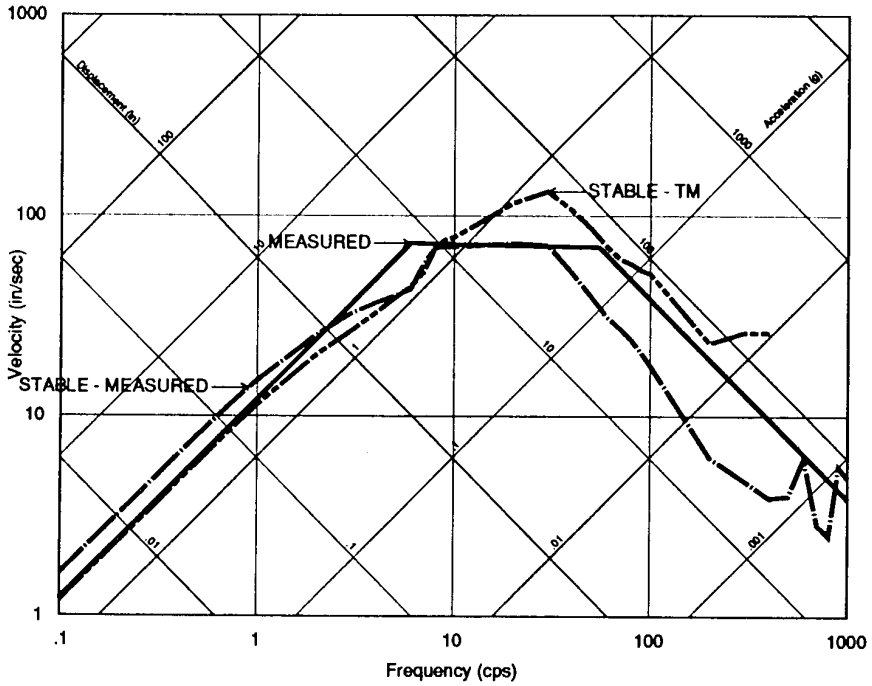

Figure 3. ESSEX structure shock spectra.

Bermed L-Shaped Structure with Burster Slab

The second example problem is an L-shaped buried concrete structure which was chosen to demonstrate the application of the methodology to complex structural geometries. The facility chosen for analysis is a three-bay, buried reinforced concrete structure. Two bays are one story in height while the third bay consists of two unequal stories. The entire structure is buried under ten feet of sand and a burster slab. The foundation of the two story bay rests on a competent rock layer while the remainder rests on sand backfill. A detonation of 526 lbs of TNT was chosen for analysis. The structure configuration and burst location are shown in Figure 4.

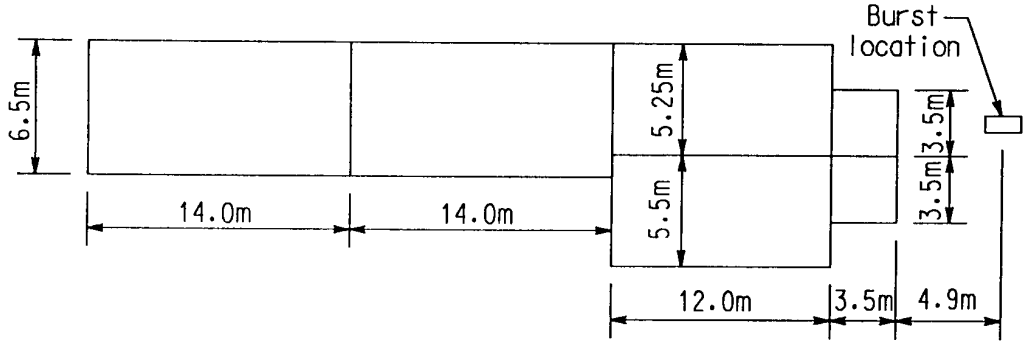

Figure 4. L-shaped structure.

Horizontal and vertical response spectra were calculated for the middle floor in the two story section. These spectra were calculated by extracting the acceleration time histories for the specified node from the STABLE calculations and using them as input for the SPECTRA computer code. Both spectral calculations were performed assuming zero percent damping. The response spectra are shown in Figure 5. Although no measured data is available for comparison, the results obtained using STABLE seem reasonable compared to the results obtained for similar complex structures and loadings. The importance of this example is that reasonable values were obtained in a case for which the current design tool (TM 5-855-1) is inapplicable. Moreover, these results were obtained in a fraction of the time that would be required if a soil island finite element analysis was performed.

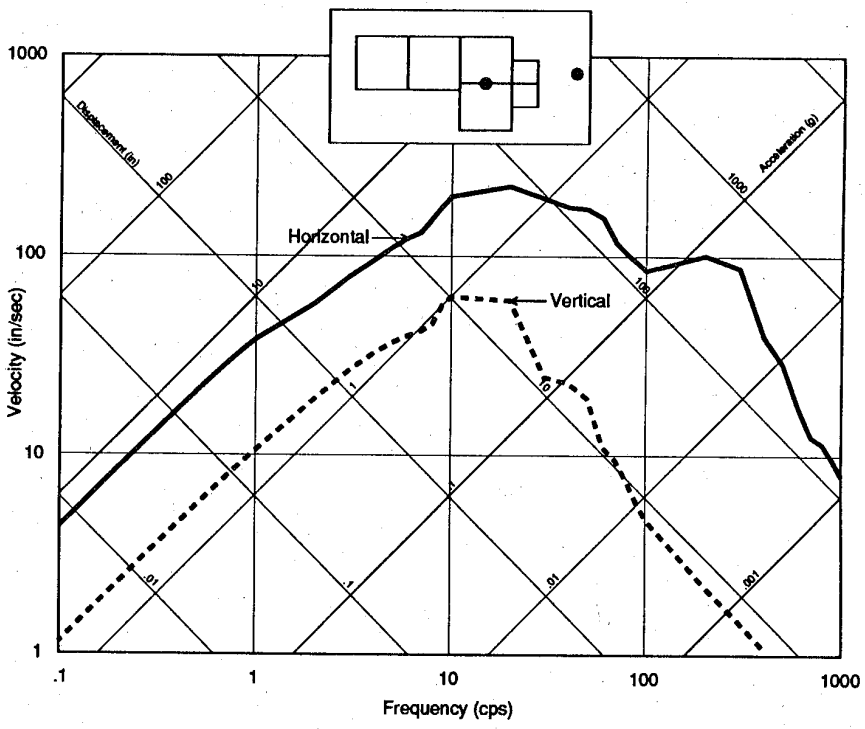

Figure 5. L-shaped structure shock spectra.

Structure Within a Protective Dome

The final example is a three story, reinforced concrete facility housed in a hardened, reinforced concrete spherical dome which is covered with a soil and rock-rubble layer. The foundation of the sheltered facility rests on a competent rock layer with a seismic velocity of about 3500 m/sec. A 2000 lb general purpose bomb with a TNT explosive equivalent warhead of 1195 lb was used as the design threat. A sketch of the facility showing the detonation location and the point of interest within the structure is provided in Figure 6. The horizontal shock spectra calculated at this point in the facility is shown in Figure 7.

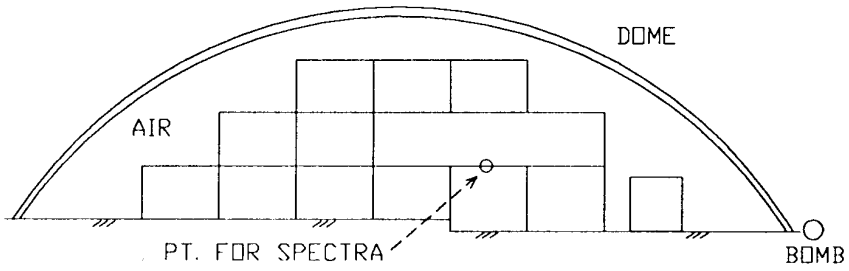

Figure 6. Structure within a protective dome.

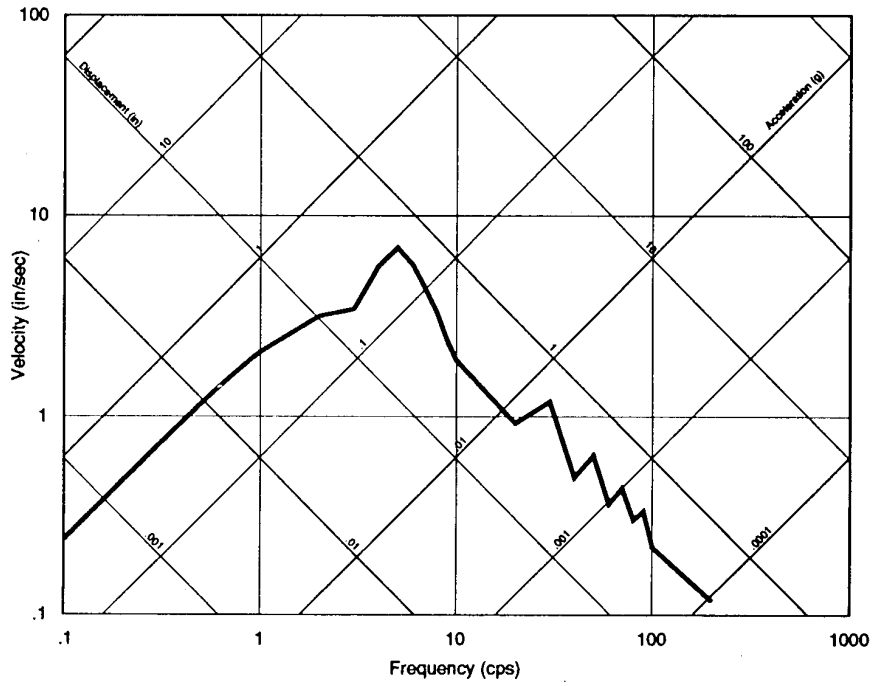

Figure 7. Horizontal shock spectra.

The spectra shown in Figure 7 was calculated using zero percent damping. The horizontal acceleration time history used to drive the spectra calculations is shown in Figure 8. This figure also shows the structural displacement waveform which peaks at about 0.4 in. at 180 msec. Based on this analysis, it was determined that the equipment proposed for use in the large open bay area of the sheltered facility did not require special shock isolation devices. This example demonstrates the ability of the methodology to handle facilities with rock, soil and air interfaces.

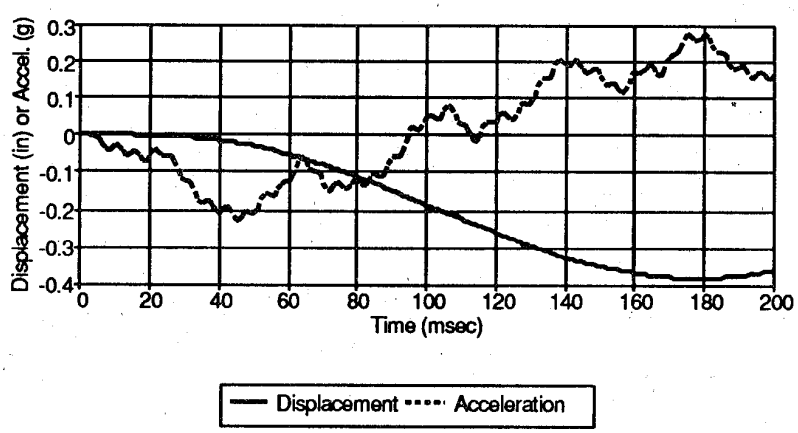

Figure 8. Horizontal structural motions.

CONCLUSIONS

The design methodology presented in this paper provides a reasonable alternative to a full soil island calculation. The calculation can be performed quickly and inexpensively, while providing more complete control over the problem definition and a wider range of applicability than simpler approaches. The approach discussed herein has been successfully applied in the analysis of a number of more complex structures to include non-rectangular facilities with combinations of rock, soil and air interfaces. This method provides a capability to confidently predict the in-structure shock environment for complex structures using a frame code.

REFERENCES

1. S. D. Campbell and L. M. Bryant, "Structure Analysis for Blast Loading Effects, STABLE Computer Program, Version 2.0, User's Manual," Report J650-89-008, JAYCOR, Vicksburg, MS, April 1989.

2. J. M. Biggs, Introduction to Structural Dynamics, McGraw-Hill Book Company, New York, NY, 1964.

3. L. M. Bryant and S. D. Campbell, "Structure Analysis for Blast Loading Effects, STABLE Computer Program, Version 2.0, Final Formulation Report," Report J650-89-010, JAYCOR, Vicksburg, MS, April 1989.

4. Headquarters, Department of the Army, "Fundamentals of Protective Design for Conventional Weapons," TM 5-855-1, Washington, DC, November 1986.

5. S. D. Campbell, "SPECTRA Computer Code," JAYCOR, Vicksburg, MS, July 1989.

6. S. A. Kiger and G. E. Albritton, "Response of Buried Hardened Box Structures to the Effects of Localized Explosions," Technical Report SL--80-1, U. S. Army Engineer Waterways Experiment Station, Vicksburg, MS, March 1980.

Tragverhalten von Bauteilen

Bearing Capacity of Construct. Members

STAHLBETONPLATTEN UNTER STOSS UND EXPLOSIONSEINWIRKUNG

Prof.Dr.-Ing. J. Eibl

Institut für Massivbau und Baustofftechnologie
Universität Karlsruhe, D-7500 Karlsruhe

Seit geraumer Zeit werden am Institut des Verfassers experimentelle und theoretische Stoßuntersuchungen an Balken, Stützen und Platten aus Stahlbeton durchgeführt [1-7], [10]. In jüngster Zeit werden auch Computersimulationen von Stahlbetonplatten unter der Einwirkung von Explosionen vorgenommen [11].

Im einzelnen wurden zuletzt nahe Explosionen studiert und Näherungsberechnungen für Kontaktexplosionen durchgeführt (Bild 1). Die resultierenden Drücke infolge von nahen Explosionen wurden entsprechend Bild 4 angesetzt (vgl. hierzu die einschlägige Explosionsliteratur [1]). Sie können näherungsweise auch für Kontaktexplosionen kleiner Ladungen verwendet werden, da bei diesen noch keine nennenswerte Beeinflussung der Detonation durch die Reflexion der Stoßwellen an der Betonoberfläche stattfindet. Die numerische Simulation erfolgte mit Hilfe der FE-Technik nach Bild 2. Besonderer Wert wurde auf das Studium einer zweckmäßigen Bewehrung gelegt. Der Werkstoff Beton wurde mit Hilfe des Triax-Stoffgesetzes von Ottosen [13] unter Berücksichtigung des strain-rate Effekts abgebildet (Bild 5). Vor dem Ausfall eines Elements wurden nach [6] ein Radialriß und drei Umfangrisse zugelassen. Die Ansätze für den Bewehrungsstahl bedürfen keiner besonderen Erläuterung. Bei Abbildung des Verbundes zwischen Stahl und Beton wurde die Mitwirkung des Betons zwischen den Rissen entsprechend Bild 3 berücksichtigt.

Wie auszugsweise in Bild 6 dargestellt, konnten US-Damage Kurven, die durch Schweizer Experimente weiter verifiziert worden waren [12], gut nachvollzogen werden. Gleiches gilt für Versuche mit Kontaktexplosionen [12], wie sie in Bild 7 dargestellt werden. Bild 8 zeigt typische Ergebnisse der rechnerischen Untersuchungen.

Diese und die vorab erörterten Stoßuntersuchungen haben immer wieder erkennen lassen, daß die numerische Behandlung derartiger Probleme von Seiten der Algorithmen her kein grundlegendes Problem mehr darstellt. Entscheidend ist vielmehr, daß bis heute immer noch nicht konstitutive Beziehungen in hinreichendem Maße zur Verfügung stehen. Aus diesem Grunde wird seit geraumer Zeit an der experimentellen Erforschung solcher Zusammenhänge gearbeitet.

Es wird versucht, Zusammenhänge zwischen der Momentanfestigkeit und der Last- bzw. Dehngeschichte aufzustellen. Die üblichen finiten Beziehungen $\sigma = f(\epsilon, \dot{\epsilon})$ geben z.B. keine vernünftige Antwort auf die Frage, wie etwa der qualitative Abfall von der „dynamischen Festigkeit“ β_{Dyn} bei einer Dehnungsrate von $\dot{\epsilon} = const$ auf die „statische Festigkeit“ β_{Stat} für $\delta\epsilon/\delta t = 0$ bei bilinearer $\epsilon = \epsilon(t)$-Funktion aussehen könnte (Bild 9).

---

[1] wird wegen der notwendigen Beschränkung des Umfanges hier nicht aufgeführt

Ungeklärt ist weiter die Frage, welche deviatorischen Spannungen bei extrem hohen Drücken, wie sie im Falle von Kontaktexplosionen auftreten, aufgenommen werden können. Nimmt der deviatorische Anteil der Versagensfläche (Bild 10) mit zunehmendem hydrostatischen Druck wieder ab bis hin zur Phasenumwandlung, geht er gegen eine Asymptote oder nimmt er sogar noch zu ?

Reibungsversuche (Bild 11 und 13), wie sie auch für Kontakt-Stoßprobleme interessieren, sollen bei der Aufklärung helfen. Es ist die Frage zu beantworten, ob mit zunehmender Strukturzerstörung bei extremen hydrostatischen Drücken der Reibungskoeffizient im Sinne eines Coulombschen Reibungsansatzes abnimmt oder – wie vielfach angenommen – tatsächlich konstant bleibt. Ebenfalls wird die rate-Abhängigkeit überprüft.

Derzeit werden bereits abgeschlossene, statische Versuche zur Herleitung von Druck-Volumen Beziehungen, bei denen Drücke von bis zu 10.000 bar erzeugt wurden, durch Detonationsversuche zur Bestimmung von Hugoniot-Kurven für Beton ergänzt (Bild 12 und 14).

LITERATUR

[1] Eibl, J., Block, K.: Zur Stoßbeanspruchung von Balken und Stützen bei hartem Stoß (Impact). Bauingenieur 1981, S. 369-377.

[2] Block, K.: Der harte Querstoß – Impact – auf Balken aus Stahl, Holz und Stahlbeton. Dissertation, Universität Dortmund, 1983.

[3] Eibl, J.: The Design of impact endangered concrete structures. Transactions 8th SMIRT Conference, Amsterdam 1985, Vol. H, pp. 265-270.

[4] Eibl, J., Kreuser, K.: Versuche zum Verhalten unterschiedlicher Stahlsorten in stoßbeanspruchten Platten. DAfStb Heft 369, Berlin, Ernst & Sohn, 1986.

[5] Eibl, J., Schlüter, F.-H.: Local behaviour of thick reinforced concrete slabs under impact loading. Transactions 9th SMIRT Conference, Rotterdam 1987, Vol. J.

[6] Schlüter, F.-H.: Dicke Stahlbetonplatten unter stoßartiger Belastung – Flugzeugabsturz –. Dissertation, Universität Karlsruhe, 1987.

[7] Eibl, J.: Soft and hard impact. First international conference on concrete for hazard protection. Edinburgh, 1987.

[8] Curbach, M.: Festigkeitssteigerung von Beton bei hohen Belastungsgeschwindigkeiten. Dissertation, Universität Karlsruhe, 1987.

[9] Eibl, J., Curbach, M.: Behavoiur of concrete under high tensile loading rates. Transactions 9th SMIRT Conference, Vol. H, Rotterdam, 1987.

[10] Feyerabend, M.: Der harte Querstoß auf Stützen aus Stahl und Stahlbeton. Dissertation, Universität Karlsruhe, 1988.

[11] Yi, Pingli: Explosionseinwirkungen auf Stahlbetonplatten. Dissertation, Universität Karlsruhe, 1991.

[12] FMB Zürich: Lokale Schadenwirkung auf Armierte Betonplatten bei der Explosion von Sprengladungen und Granaten. Forschungsinstitut für militärische Bautechnik Zürich, FMB 79-13, Dezember 1979.

[13] Ottosen, N.S.: Failure criterion for concrete. Journal Engineering Mechanics Division, ASCE, Vol.103 (1977), Vol. EM4.

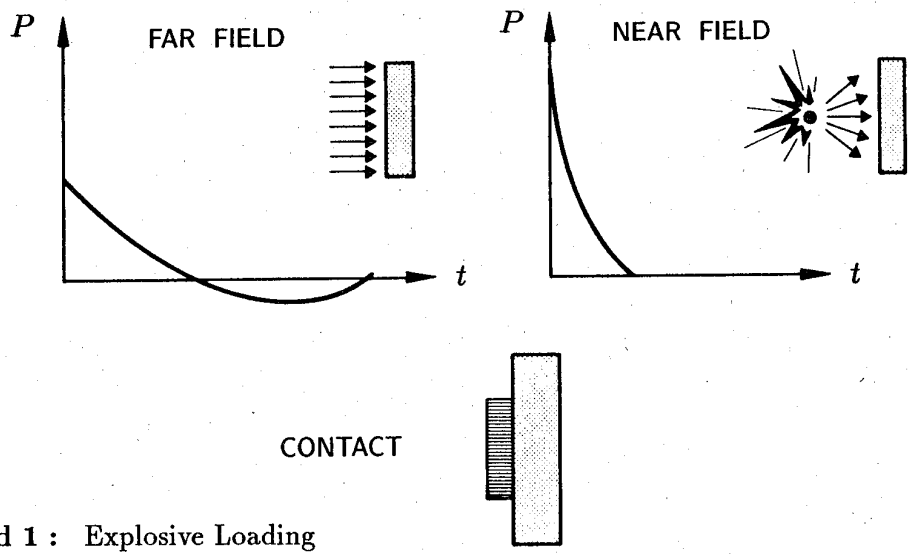

Bild 1 : Explosive Loading

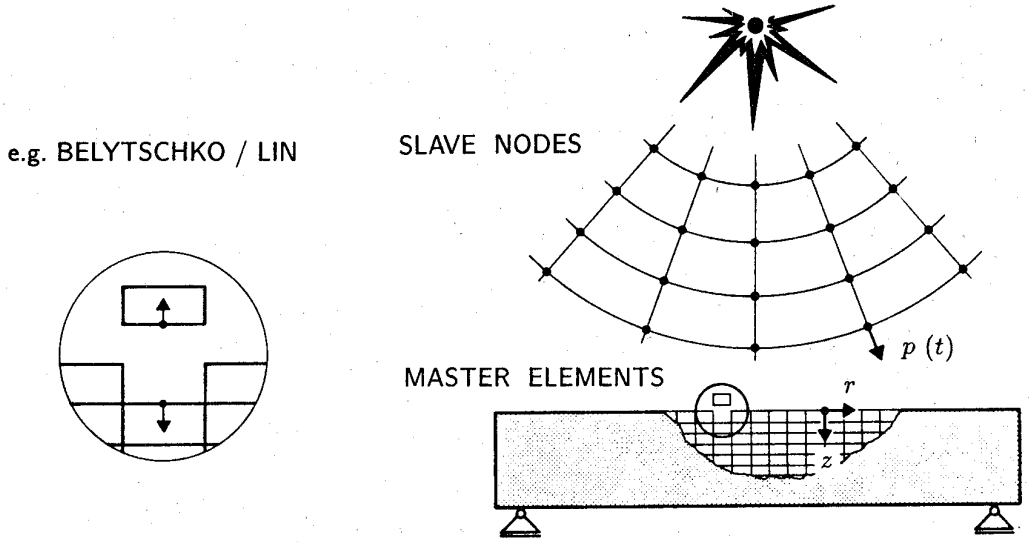

Bild 2 : Contact-Treatment (Master-Slave Algorithm)

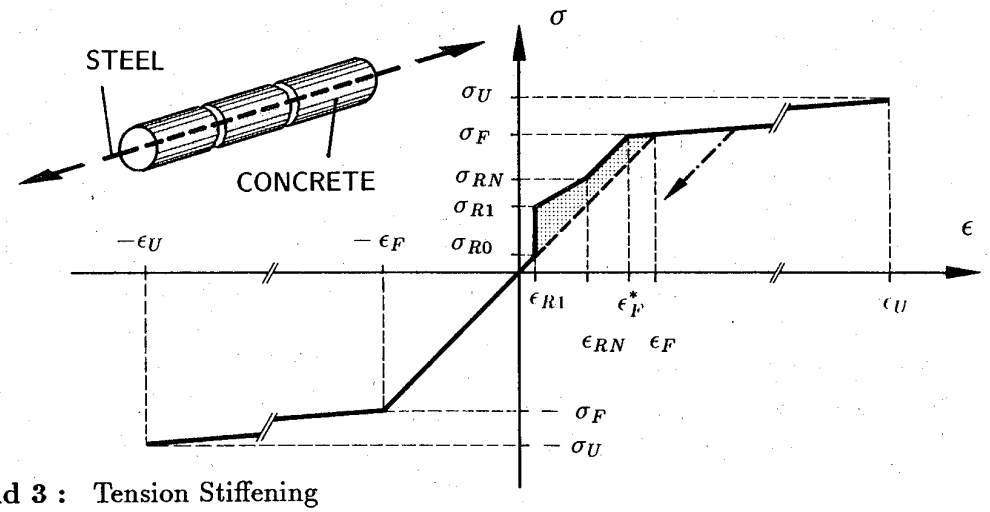

Bild 3 : Tension Stiffening

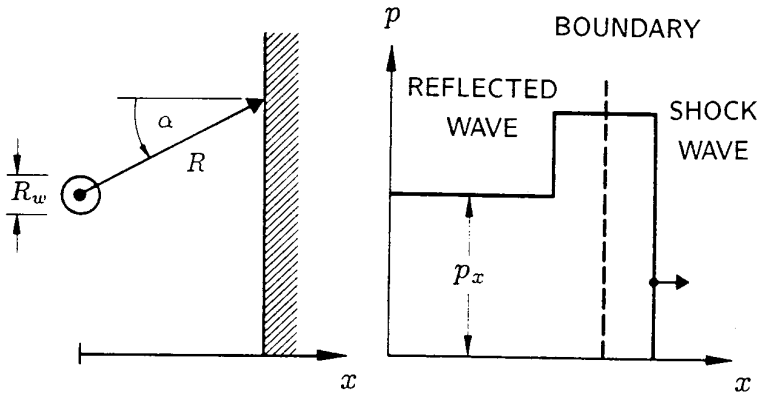

$$\frac{p_x}{p_x^*} = \left(\frac{R_w}{R}\right)^2 \cdot \left(1 - \frac{t}{\tau}\right)^2 \cdot \cos\alpha$$

$$\tau = R_w \cdot \left(\frac{1}{U_x} + \frac{1}{N_{xw}}\right)$$

U_x = PARTICLE VELOCITY IN AIR

N_{xw} = VELOCITY OF BOUNDARY SURFACE

p_x^* = REFERENCE PRESSURE EXPLOSION IN CLOSED VOLUME

Bild 4 : Pressure for Nearby Explosion

FAILURE SURFACE

$$A' \frac{J_2}{|f_c|^2} + \lambda \frac{\sqrt{J_2}}{|f_c|} + B' \frac{I_1}{|f_c|} - 1 = 0$$

STRESS – STRAIN RELATIONSHIP

$$\frac{\partial \sigma_i}{\partial \epsilon_i} = E_S \qquad E_S = f(\beta)$$

$$\beta = \frac{\sigma_3}{\sigma_{3,f}} \qquad \sigma_1 = \sigma_2 \geq \sigma_3$$

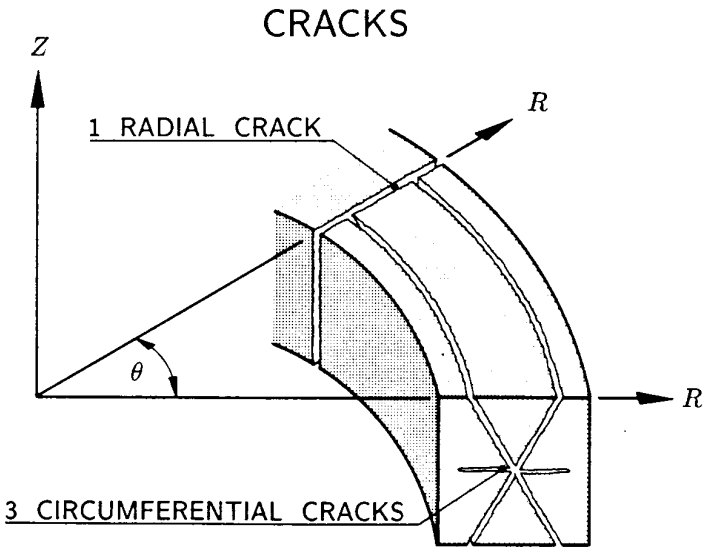

Bild 5 : Constitutive Laws

1 LIGHT DAMAGE — SMALL DEFORMATIONS, INITIAL CRACKING

2 MEDIUM DAMAGE — CRACKING, SPALLING, FORMATION OF SHEAR CONE

3 HEAVY DAMAGE — PUNCHING FAILURE, CONCRETE CRUSHING, PENETRATION, SCABBING

4 COLLAPSE — PERFORATION, HEAVY SCABBING, EXTREME BENDING OF REINFORCEMENT

Example No.	*Spalling*	Radius [cm]	Depth [cm]	Cracks Radial	Cracks Circumferential	*Scabbing*
SIMNAH1	no	–	–	beginning	beginning	–
SIMNAH2	yes	48.0	6.0	strong	strong	light
SIMNAH3	yes	34.0	6.0	strong	strong	strong
SIMNAH4	no	–	–	light	light	beginning
SIMNAH5	yes	48.0	4.0	strong	strong	strong
SIMNAH6	yes	34.0	4.0	very strong	very strong	very strong

USA – DAMAGE CURVES

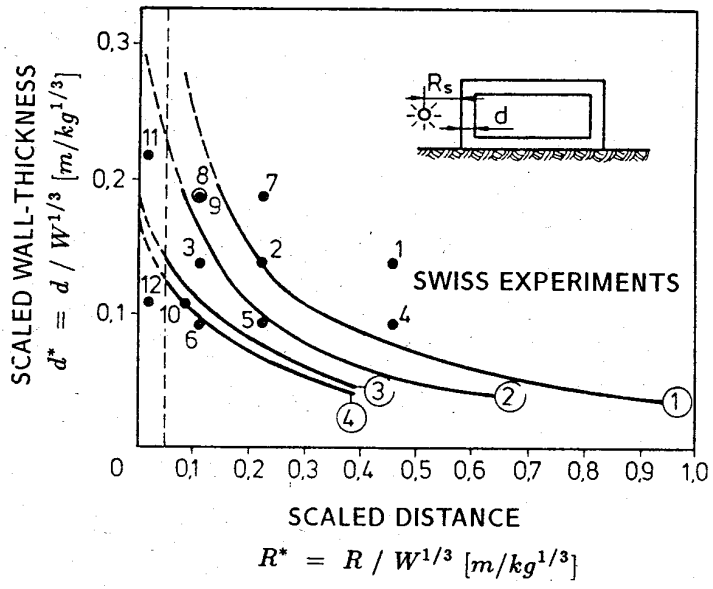

Bild 6 : Numerical Simulation of Nearby Explosion

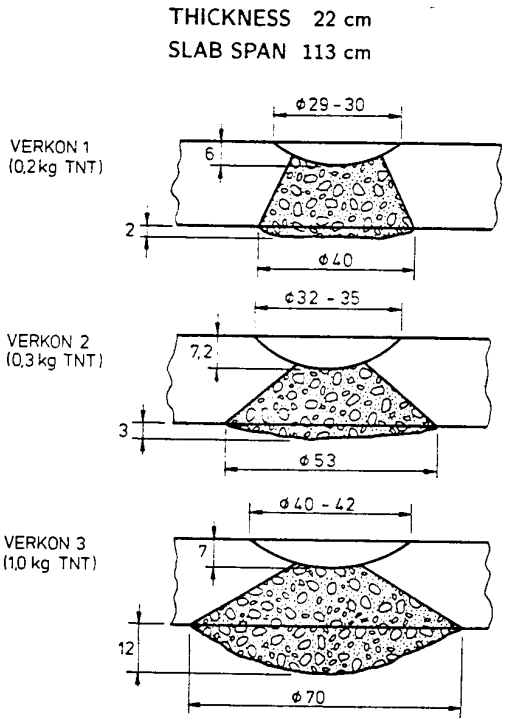

Example No.	*Spalling*	Diameter [cm]	Depth [cm]	Cracks Radial	Cracks Circumferential	*Scabbing*
SIMKON1	yes	28.0	4.4	strong	strong	strong
SIMKON2	yes	32.0	4.4	strong	strong	strong
SIMKON3	yes	48.0	4.4	very strong	very strong	very strong

Bild 7 : Numerical Simulation of Contact-Explosion

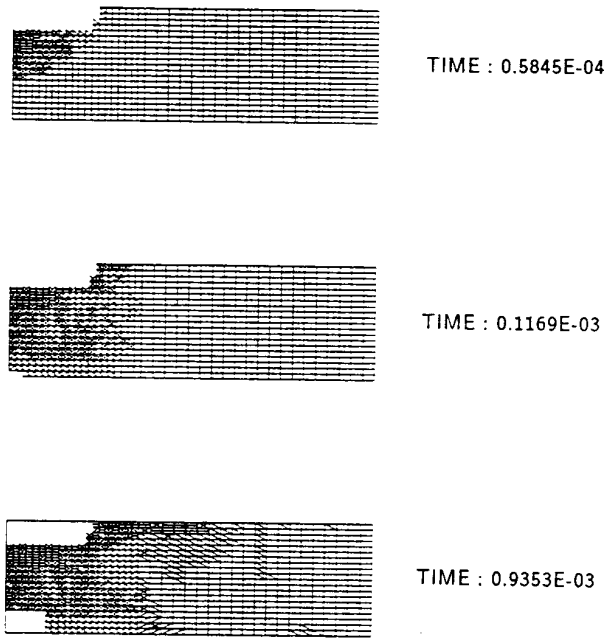

TNT CHARGE :	0.3 kg	BLANK :	SPALLING / SCABBING
DISTANCE :	CONTACT	/ :	RADIAL CRACKS
THICKNESS :	0.22 m	\ :	CIRCUMFER. CRACKS
SLAB SPAN :	1.13 m	— :	CONCRETE CRUSHING

Bild 8 : Typical FE-Result

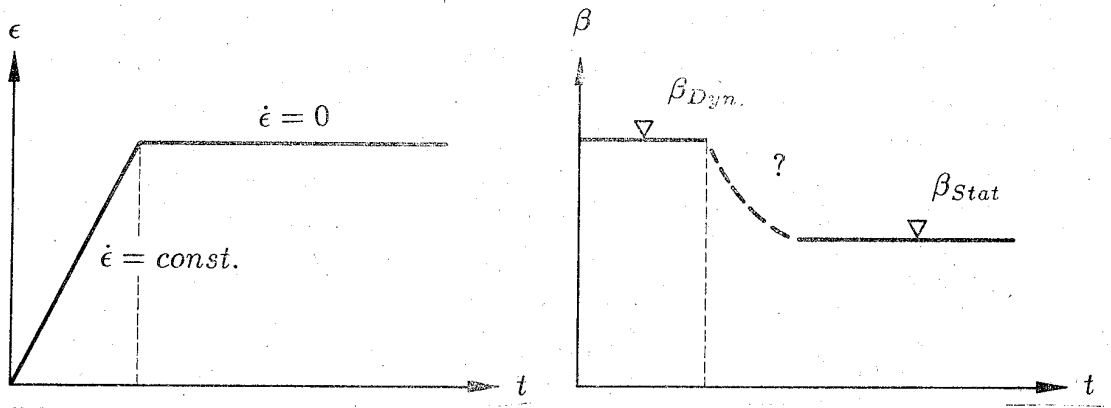

Bild 9 : Strain Rate and Dynamic Strength

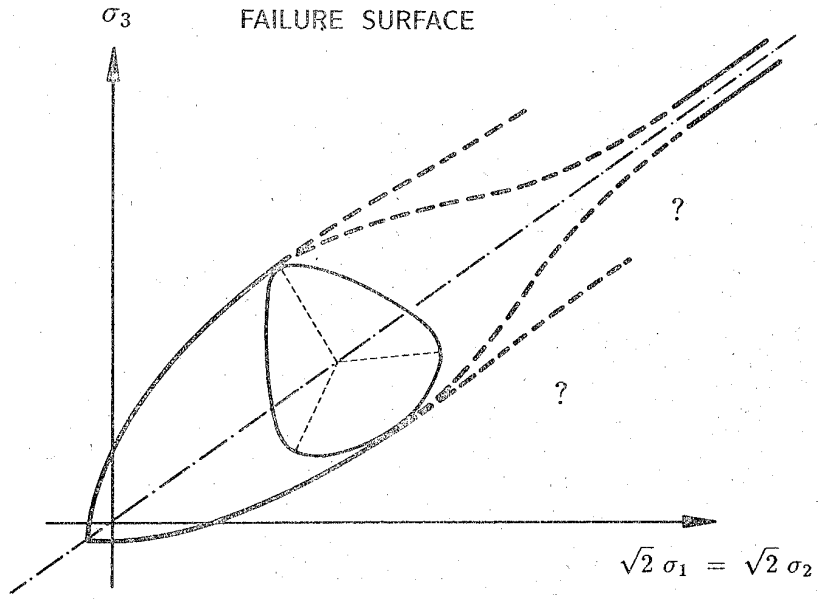

Bild 10 : Failure Surface for Concrete

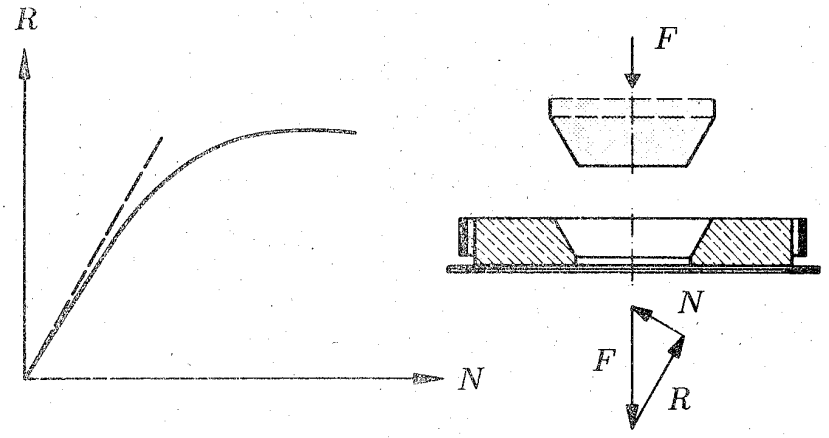

$$\text{OR} \quad \begin{aligned} R &= \mu\,(N) \cdot N \\ R &= \mu \cdot N^{\,t} \end{aligned}$$

Bild 11 : Contact – Friction

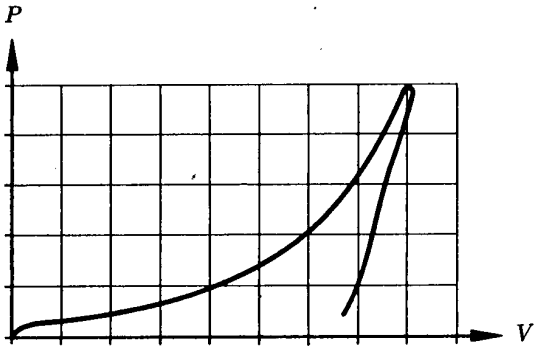

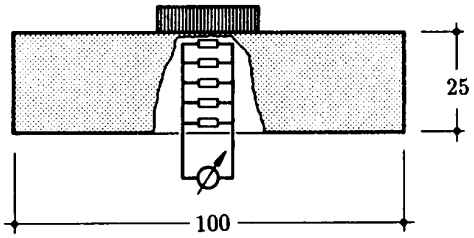

CONSERVATION LAWS

$$\rho_0 \, U_s = \rho \, (U_s - U_p) \qquad \text{MASS}$$

$$\rho_0 \, U_s^2 + p_0 = \rho \, (U_s - U_p)^2 + p \qquad \text{MOMENTUM}$$

$$\boxed{\frac{\rho_0}{\rho} = 1 - \frac{p}{\rho_0 \cdot U_s} = \frac{V}{V_0}}$$

Bild 12 : Shock-Wave Experiments

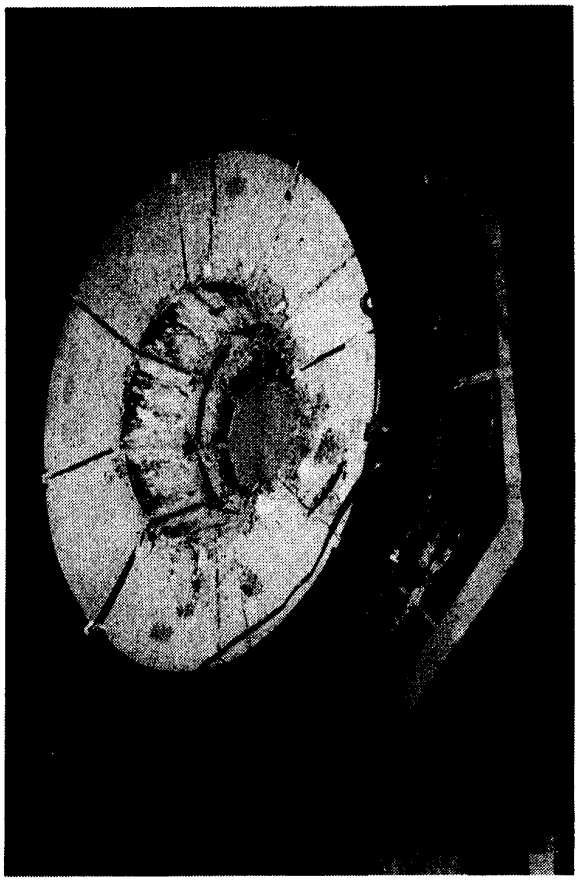

Bild 13 : Test Specimen for Friction Experiments

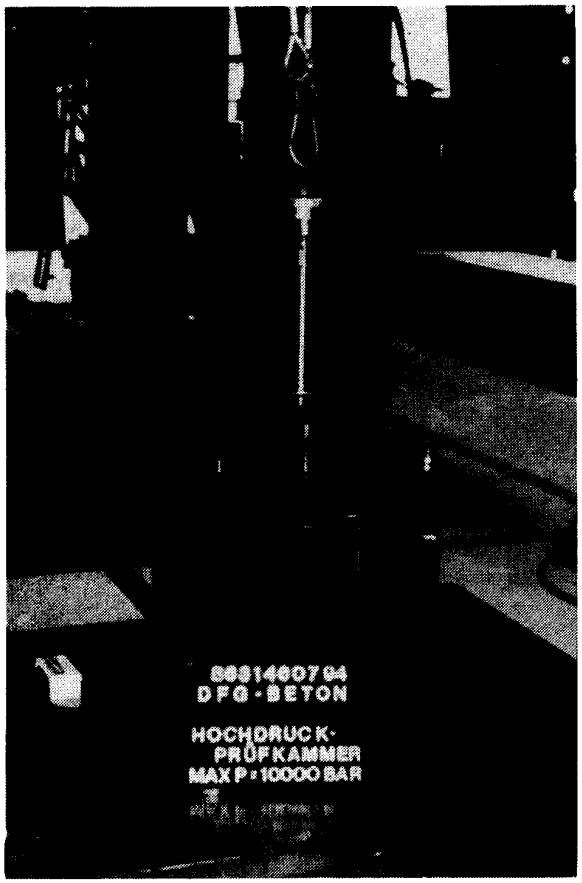

Bild 14 : Containment for Static High-Pressure Experiments

The Effect of Stiffeners at the Deformation of Steelplates at Impulsive Blast-Loading

Die Wirkung von Versteifungen bei der Verformung von Stahlplatten unter impulsartiger Blastbelastung

Gerhard H. Guerke

Fraunhofer - Institut fuer Kurzzeitdynamik

Ernst - Mach - Institut

Freiburg, Germany

Abstract

Blast loading as an effect of a nearby detonation is a danger to relative lightweight structures of large surface. Examples of this type of structure are ship panels above the water-line and containers.

Large plastic deformation of steel-plates at high impulsive blast-loading has been experimentally investigated. The rectangular steel-plates at an aspect ratio of 1 : 2 were clamped along all edges to a rigid support. Homogenous plates and stiffened plates were tested. The impulsive load was produced by the detonation of 1 kg HE-spheres at scaled distances 0.5 to 1.0 m / kg $^{1/3}$ from the plate's center. Contrary to their importance in static loading as well as in relatively slow dynamic loading situations, do the stiffeners not have any positive effect in reducing damage at impulsive loading. The stiffeners buckle or are torn off the plate. The permanent deflection is identical to that of homogeneous plates of identical mass.

Introduction

Blast loading as an effect of a nearby detonation is a danger to relative lightweight structures of large surface. Some structures, such as ship-panels above water-line, or containers, may be impulsively loaded by blast from HE-charges at charge masses from 1kg to several 100 kilogram. The aim of this study was to show basically the effect of impulsive loading at steel plates in contrast to static loading. And to find measures, that allow the structure to absorb impulsive load without tearing off.

Large plastic deformation of steel-plates at high impulsive blast-loading has been experimentally investigated. The rectangular steel-plates at an aspect ratio of 1 : 2 were clamped along all edges to a rigid support. Model plates at the dimension of 0.25m*0.5m and 1mm thickness and 0.125m*0.25m and 0.5mm thickness were tested. Homogeneous plates were tested. Linear profile steel has been welded to the rectangular steel-plates at constant distances parallel to the short side, in order to get stiffened structures. The mass of the stiffeners is relatively small compared to the mass of the plates. The impusive load was produced by the detonation of 1 kg HE-spheres at scaled distances 0.5 to 1.0 m / kg $^{1/3}$ from the plate's center.

Contrary to their importance in static loading as well as relatively slow dynamic loading situations, do the stiffeners not have a positive effect in reducing damage at impulsive loading. The stiffeners buckle or are torn off the plate. The permanent deflection is nearly identical to homogeneous plates of identical mass. This effect is explained by the fact, that at impulsive loading the mass of the structure is the most important parameter. The mass determines the amount of kinetic energy that is imparted to the plate from the reflected airblast impulse. The plate deforms until the work done in deformation equals the kinetic energy. There is not much work done in order to buckle the stiffeners.

The experimental test program was supported by a numerical simulation by a method of finite elements. A very fine discretisation and small time steps allow impressive insight into the mechanism of deformation.

Impulsive Load

Impulsive loading has to do with a shock. It is characterized by a force that applies momentary and acts on the structure for such a short time that nearly no deflection occurs. The impulsive force is caused in these tests by the blast-impulse.

The force does not work along a way. The material strength was not activated in order to withstand the impulsive force. When the material strength is activated a moment later, the load has already disappeared. It is actually important to think of a force, that acts for a short time, contrary to the more familiar forces that act along a way.

Statics generally handel forces acting on a structure in the position of rest. At any moment is the material strength activated and keeps the structure in rest. If there is a displacement, it is caused by forces, that act along a way. **Statics never handel structures that are in motion.**

There is no motion as long as the impulsive force acts on the structure but, **impulsive forces generally set structures in motion!** The motion starts, when the force has already disappeared. It is caused by the impulse, that was imparted to the structure. The impulse can be replaced by an initial velocity, by equating the total blast impulse to the change of momentum of the plate. At that moment does the plate contain a certain amount of kinetic energy.

The amount of impulse, that is imparted to the plate by a blast-impulse (per unit area) depends on the plate's area. **The kinetic energy, that the plate contains after the impulsive loading, depends on it's mass** (per unit area). The physical relation of mass and kinetic energy is inverse linear. For example, at identical blast impulse, a plate of 2 times the thickness (2 times the mass per unit area) contains 1 / 2 of the kinetic energy. As a result only 1 / 2 of the energy must be dissipated. **A principle in designing a structure to withstand impulsive loading is to add mass.** But ship-structures or containers must be relatively lightweight und mass must not be added. Therefore other measures must be investigated for structures of that type in order to withstand impulsive loading.

A small amount of energy can be dissipated by elastic motion of the structure. The damped elastic vibration finally transforms kinetic energy into heat. Vibration is not an effective mechanism to transform the kinetic energy of impulsive loading.

A more effective mechanism to transform kinetic energy into heat is the movement of an objekt against the frictional resistance. This principle may be effective for some structures, but cannot be used at ship-structures or containers.

Several thousand times the energy of vibration can be dissipated by means of plastic deformation in steel structures. **Plastic deformation is the only measure at ship-structures and containers, that can be used in order to withstand impulsive loading.** The kinetic energy must be transformed into work done in deformation. At the end of an impulsive loading situation remains a plastically deformed structure. If the structure was designed in order to tolerate a certain amount of deformation, it must not fail.

Stiffeners are used in ship design. They strengthen the structure according to static forces and relatively slow acting dynamic forces. **At stiffened structures the same amount of kinetic energy must be transformed into work done in deformation.** The design property, that a stiff structure will not allow deformation, results in extremely high peaks of stress. They are localized along any stiffener and especially along the edges, where the plate is connected to the stiff support. The stress easily reaches the ultimate yield stress. The stiffeners will be torn off the plate, as may be seen in the Figures 5 and 6.

The only way to find a design in order to withstand impulsive loading is, to make the structure "weak". The frame must not be too stiff and the edges must not be sharp. A certain amount of deformation must be tolerable without complete destruction.

Test Results

The test arrangement is shown in Figure.1. A spherical 1 kg-charge, made of the high explosive PETN, detonates at distances between 0.5m and 1.0m above the test object. The test objekt is a rectangular plate at an aspect ratio of 1 : 2. The material of the plate is mild steel. The plates is clamped along all edges to a rigid support. The axis of the test plate is turned 90 degree to the axis of the support. The highest stress acts at the center of the long span of the test plate. If this span is turned to the corner of the frame, then the frame is really rigid. The test plates were strengthened along all edges,in order to avoid drawing out of the clamp.

A very obvious result is shown schematically in Figure 2. The shape of the impulsively deformed plate is different from the shape of the plate, that was deformed statically by slowly increasing overpressure. The static load results in a parabolical element, whilst the shape of the impulsively loaded plate can be approximated by a pyramid. The work done in deformation may be very similar in both situations. But if the deformation results in different shape, then it may be concludet, that different forces acted. The zones of maximum stress and maximum strain may be different in static and impulsive loading situations. As a result, measures that prove successful in order to strengthen statically loaded structures must not be successful at impulsive loading.

The evaluation of permanent deflection profiles is shown in Figure 3. Profiles are drawn through the center of the plate parallel to the long span and along 3 sections parallel to the short span. The profiles were compared to the results of finite element calculations in Reference 1. The numerical result was in good conformity with experimental results.

Photos of 3 plates are shown in the Figures 4, 5 and 6. All three test plates were plastically deformed in the same test arrangement at identical impulsive load. It is emphasized here, that the overall shape is very similar. The outer band of the plates was clamped to the support. Just the inner rectangle is deformed. A homogeneous plate was tested in Figure 4. The stiffeners, that were welded to the plates in Figures 5 and 6, are essentially torn off. This is true along the edges. It is concluded, that the strain is at its maximum along the edges. The strengthening of the plate along all edges by sheet-metal strips can be seen in Figure 5. The strips stands out a

view Millimeters into the deformed area and prevents the plate from shearing along the sharp edge of the frame. It also effects, that the plate is not torn out of the bolts at the support. The holes all around the edge look round after the test. This was not true at plates without strengthening in earlier tests.

It is demonstrated in Figure 7, that the maximum deflection is identical at plates with and without stiffeners. Two plates rest on a spirit level, that is levelled horizontally. A second spirit level rests at the points of maximum deflection at both plates. Also the upper spirit level is horizontally levelled. It may be concluded, that there is no effect of the stiffeners as far as the maximum deflection is concerned.

References

1. Buecking,P.W.:
Numerische Simulation der Druckstoßwirkung einer detonierenden Sprengstoffladung auf eine versteifte Schiffstruktur.
Bericht des Ernst-Mach-Instituts, No.7/90, Aug.1990

2. Buecking,P.W., Guerke,G.H., et al.:
Experimentelle Untersuchungen zum Versagen schifftechnischer Bauteile unter Blastbelastung.
Bericht des Ernst-Mach-Instituts, No.E7/87, Jun.1987

3. Guerke,G.H.:
Large Plastic Deformation of Steel Plates at Impulsive Blast Load.
Proceedings 4. Int. Symp. Non-nuclear Munitions, Panama City Beach, Apr.1989

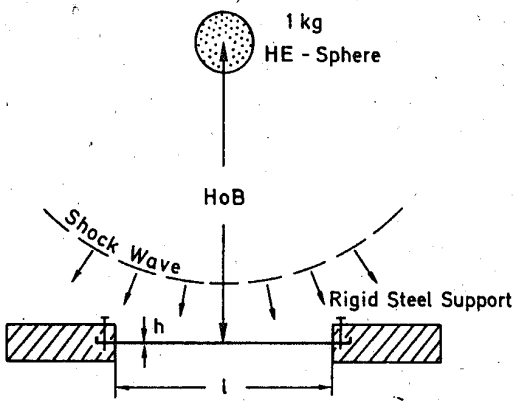

Fig. 1 Test Arrangement

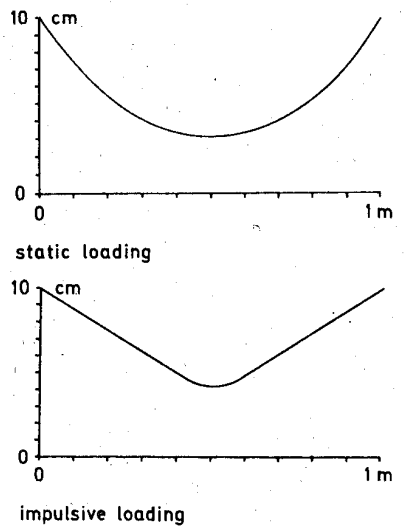

Fig. 2 Typical Shape of Steel Plates at Static and Impulsive Loading

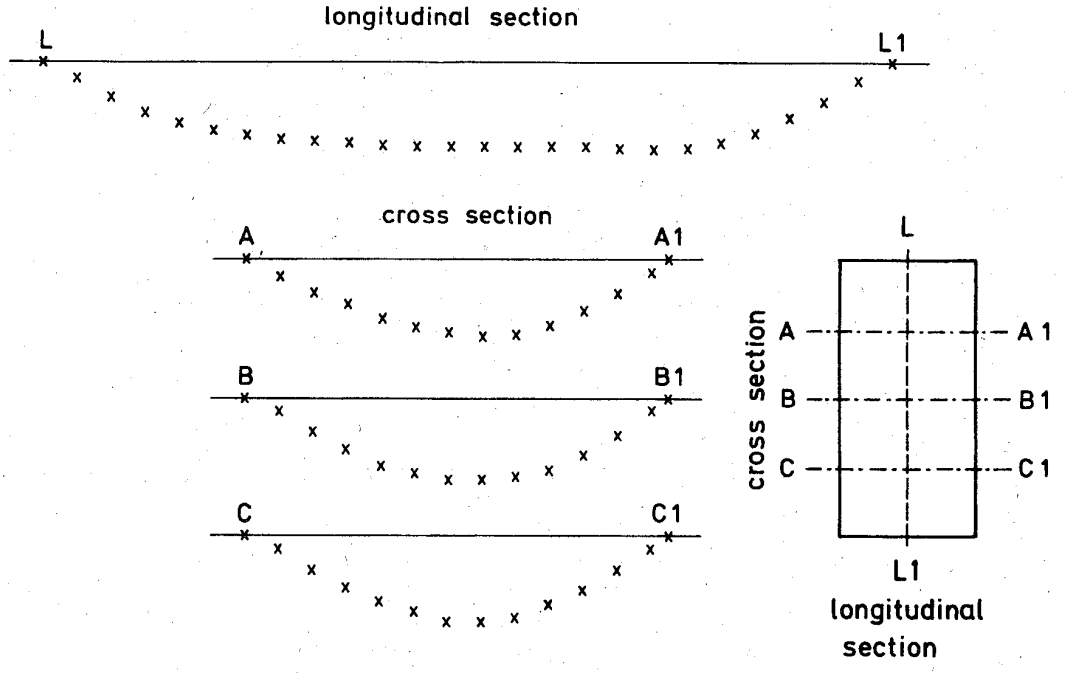

Fig. 3 Evaluation of Permanent Deflection Profiles
Long Span 0.25m, Short Span 0.125m, Thickness 0.5mm
Charge Mass 1 kg PETN, HOB 1.0m
Maximum Deflection 25mm

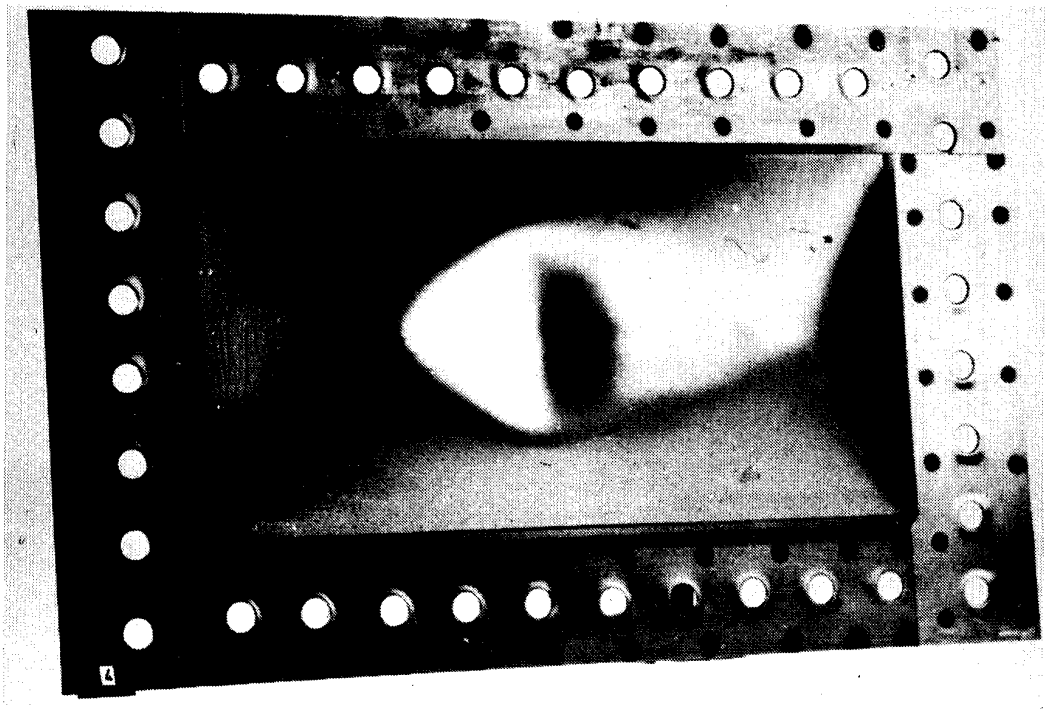

Fig. 4 Homogeneous Steel Plate after Impulsive Loading

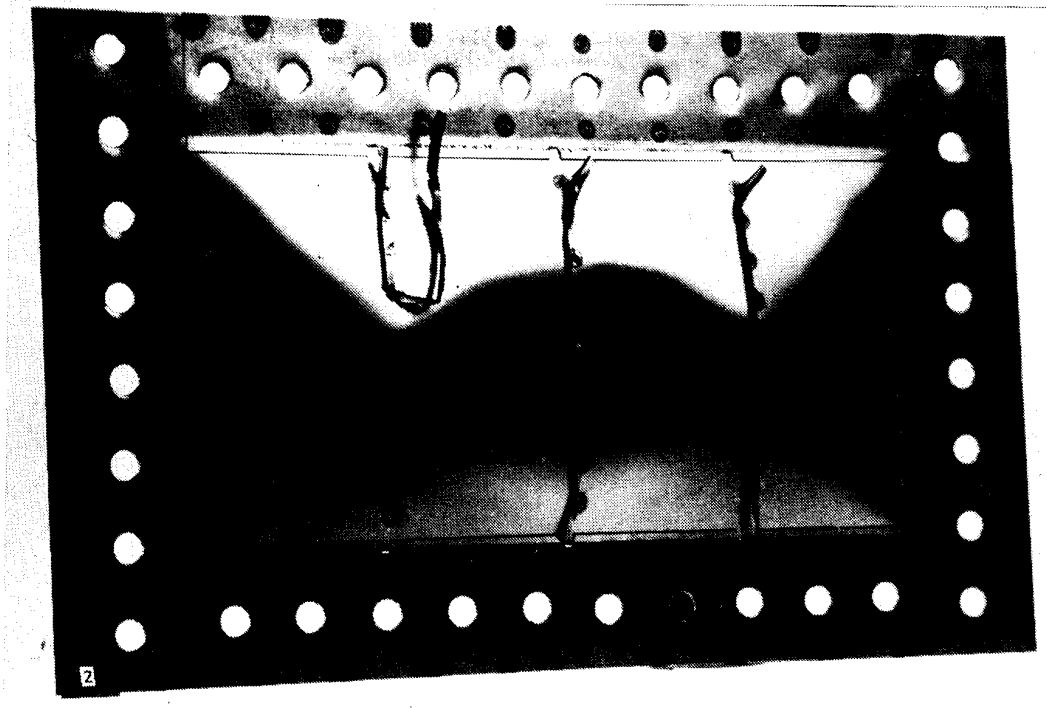

Fig. 5 Steelplate with 3 Stiffeners after Impulsive Loading

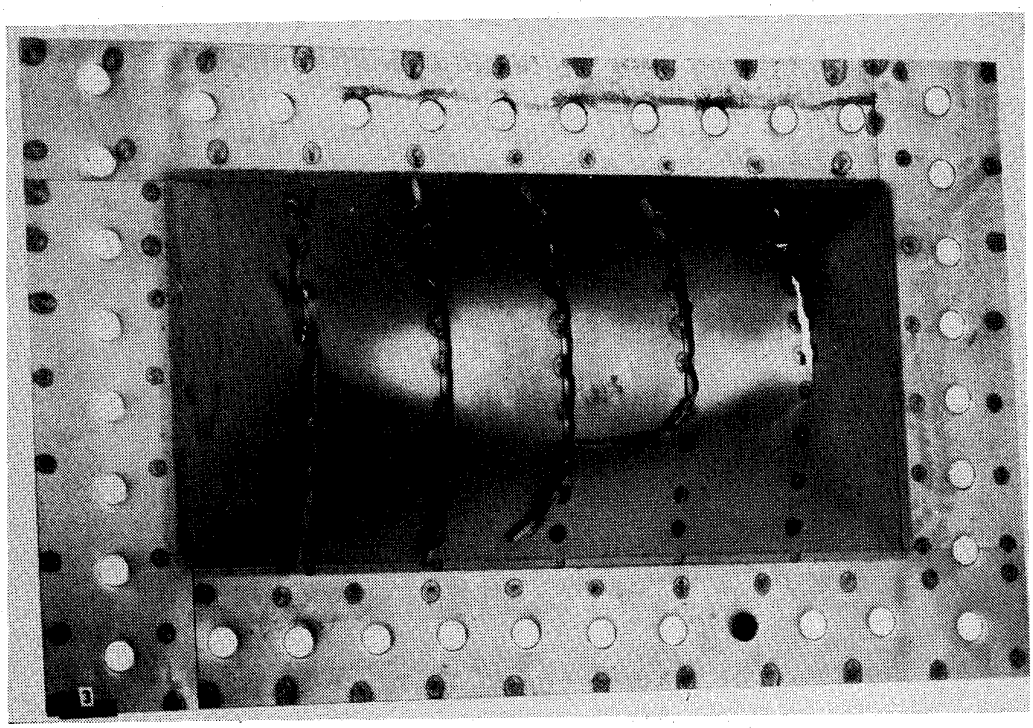

Fig. 6 Steelplate with 5 Stiffeners after Impulsive Loading

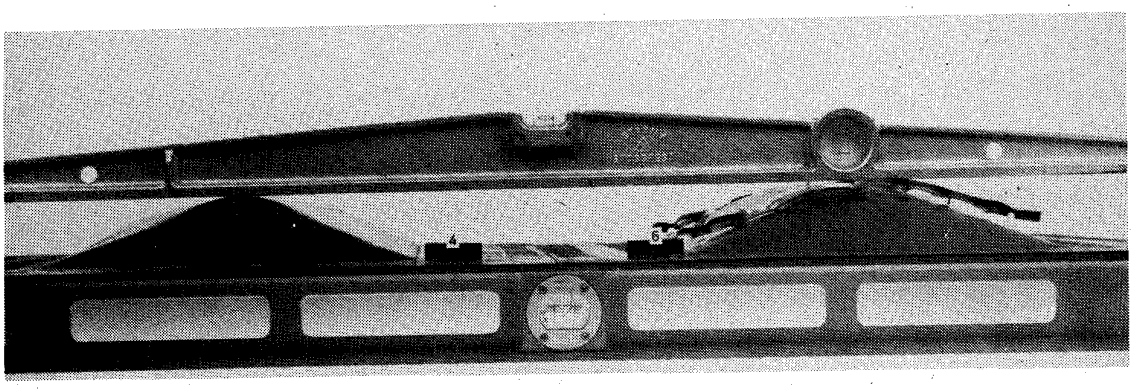

Fig. 7 Demonstration of Identical Deflection of Plates without and with Stiffeners

An Abstract for a Paper Entitled:

Localized Failure of Concrete and Fibrous Concrete Slabs--Some Wave Propagation and Panel Damage Studies

by:
Kirk A. Marchand
Luis M. Vargas
Southwest Research Institute, San Antonio, Texas, USA
and
LT James Underwood
Air Force Engineering and Services Center, Tyndall AFB, Florida, USA

Background--In the design and analysis of protective structures designed to resist the attack of modern conventional weaponry, many methods are available for the prediction of dynamic response of the structure of concern (Ref. [1],[2],[3],[4]). Additionally, several methods for the prediction of projectile and fragment penetration are available for these same structural varieties. What is missing, and is typically not addressed in a design or simplified analysis reference, is the effect of combined load types such as simultaneously applied impact and non-impact, yet impulsive, loadings.

It can be shown that simultaneous impact and blast loads applied to a structure can cause responses that in some cases are more severe than the sum of the damage generated in the structure through the independent application of the loads. Hence, this simultaneous loading is considered to be *synergistic* in the sense that the simultaneous damage is greater than the sum of the impact and non-impact loadings.

Test Program--Southwest Research Institute (SwRI) is currently conducting a study to consider and define the synergism of blast and fragment impact on structures, and the resulting structural damage modes and response (Ref. [5]). This work is being performed in the form of a combined structural test series and analysis program.

The objective of this program is to determine the synergistic effects of blast and fragments on construction materials. This required the conduct of a test series to determine the structural loads and the actual failure mechanisms induced by blast loads, fragment loads and the combinations of both. The first series of tests was conducted to quantify the loads generated by the cased weapon and to establish an equivalent bare explosive charge with the same impulse distribution as the cased weapon. The second series of tests was performed in conjunction with analyses efforts to determine and compare the response

---

1. Fundamentals of Protective Design For Conventional Weapons - TM 5-855-1", prepared by the U.S. Army Waterways Experiment Station, Vicksburg, Mississippi, 1982.

2. Crawford, R.E., et al., "Protection from Nonnuclear Weapons," Technical Report No. AFWL-TR-70-127, Air Force Weapons Laboratory, Kirtland AFB, NM, 1971.

3. Whitney, M.G., et al., "Structures to Resist the Effects of Accidental Explosions Volume II, Blast, Fragment, and Shock Loads," Special Publication ARLCD-SP-84001, U.S. Armament Research, Development and Engineering Center, Dover, NJ, 1986.

4. Baker, W.E., et al., "A Manual for the Prediction of Blast and Fragment Loadings on Structures," DOE/TIC-11268, U.S. Department of Energy, Pantex Plant, Amarillo, TX, 1980.

5. Marchand, K.A. and Vargas, L.M., "The Synergistic Effects of Combined Blast and Fragment Loadings: Test Report," SwRI Project 06-2821, Contract No. FO8635-89-C-0195, Air Force Engineering and Services Center, Tyndall AFB, FL., May 1990.

Abstract
for
Interaction of Conventional Munitions
with Protective Structures

Protective Glazing for Blast and Fragment Loadings

by
Gerald Meyers, P.E.
U.S. Department of Energy
EH-322
Washington, D.C. 20585
(301) 353-3190

Glazing that can resist blast, ballistic or fragment loading has become critical as critical facilities face chemical and biological threats superimposed upon standard conventional arms threats. The only glazing material capable of resisting the threat spectrum is a glass - polycarbonate composite. Currently no validated design procedure exists for the design procedure for the design of this class of glazing.

The proposed paper will present a design procedure for glass clad polycarbonate. The design theory will be based upon composite action of non - linear plates. Membrane stress and inelastic behavior of the polycarbonate will be factored. Criteria for framing and pane edge engagement will be included. Finally, the design criteria will be validated by actual blast test data on glass clad polycarbonate panes. The final design curves can also be adapted to design safer industrial safety shields and viewports.

"Analysis of the Response of Reinforced Concrete to Severe, Close-in Explosive Loading"

Charles J. Oswald, P.E.
Kirk A. Marchand, P.E.

Southwest Research Institute
San Antonio, Texas, USA

Abstract

Two test series were recently performed at Southwest Research Institute (SwRI) which investigated severe local explosive loading of reinforced concrete walls. A variety of parameters were varied within the two test series including wall reinforcement and concrete strength, charge weight, charge casing weight, charge geometry, and test scale factor. Maximum debris velocity, spall area, and breach area of the walls were measured. The affects of each of the varied test parameters on the measured local wall response parameters are discussed.

1.0 Introduction

Two test series were recently performed at Southwest Research Institute (SwRI) which investigated severe local explosive loading of reinforced concrete walls. A variety of parameters were varied within the two test series including wall reinforcement and concrete strength, charge weight, charge casing weight, charge geometry, and test scale factor. This paper will discuss the observed effects of these variations on local and global wall response. The test series were not large enough to derive qualitative empirical relationships for each parameter. However there are obvious trends in the data which show the relative importance of the parameters which were varied on the local concrete response. Some of the trends noted in the tests are supported by limited analytical study. These trends are important because they indicate what subjects must be better understood before accurate, quantitative relationships are available for predicting local concrete response parameters such as the maximum debris velocity from the locally loaded wall area and the wall breach dimensions. The tests also showed that the amount of global response can be related to the amount of local response. Therefore, it is important understand the local wall response of walls subjected to severe close-in loading in order to understand the global response of these walls.

The two test series were conducted to investigate different aspects of local wall response. The first test series was conducted to gain a better understanding of reinforced concrete wall breakup so that the dispersion of the wall debris could be quantified better /1/. Maximum debris velocity was measured from walls tested at different scale factors with varying amounts of reinforcing steel and concrete strength. This work was funded primarily by the U.S. Department of Energy (DOE). The second test series investigated the combined effect of fragment and air blast loading from close-in detonations on reinforced concrete wall response /2/. Maximum debris velocity, spall area, and breach area were measured from walls with varying amounts of reinforcement tested with explosives of varying shape and amount of casing. This project was performed for the U.S. Air Force Engineering and Services Center at Tyndall Air Force Base. Together, the tests from the two series provide a database of twenty-two tests which can be used to see the effects of a wide variety of parameters on the local response of concrete walls.

2.0 Description of Observed Structural Response

The response of the unloaded side of many of the test walls from the first test series was filmed with a high speed camera. These walls were subjected to a non-confined, close-in loading at scaled standoffs between 0.5 ft/lb$^{1/3}$ and 1.0 ft/lb$^{1/3}$. In most of the tests, the wall region nearest the charge responded locally very quickly and was either severely spalled or breached by the applied load. Later in time, a global response occurred. During the global response, the wall rotated at the supports and a center yield line formed through the locally loaded region. The primary loading on the walls can be characterized in two steps; 1) most of the energy from the charge is applied into region of the wall opposite the charge, 2) a portion of this load was transmitted through the reinforcement into the rest of the wall. The rest of the wall also responded to the less intense directly applied blast loading. The wall response can be idealized as a two degree of freedom system which interacts through the reinforcement. Most of the load is applied very quickly into the region of the wall nearest the charge. This section of the wall absorbs some of the load and, as it responds, transmits load into the wall regions which were not locally loaded. These regions of the of the wall respond to the tranmitted load and, to a lesser extent, to the directly applied load.

This type of response was not unexpected. The most unexpected and interesting part of the test programs was the sensitivity of the local response to the charge and wall parameters varied in the tests. The rest of the paper will concentrate on this subject while discussing the results from each of the test programs separately.

3.0 Discussion of Results from the First Test Series

Table 1 summarizes the response of a representative number of the reinforced concrete walls subjected to close-in loading during the first test series. All the test walls summarized in this table were tested with bare, spherical charges of C-4. The table shows the applied load, wall strength parameters, the measured maximum debris velocity, and gives a brief description of the damage. Most of the tests in this program modeled a "lightly reinforced" concrete wall - that is a 12" thick wall reinforced with 1/2" diameter bars spaced at 12" each way, each face, at different scale factors. The walls in groups A, B, and C were supported on three sides and free at the top. Group D consisted of walls supported only on the two vertical sides. No walls were laterally restrained.

Table 1. Wall Damage from First Test Series

Category	Scale	Charge Weight (lbs)	Standoff (ft)	Ultimate Resistance (psi)	Concrete Strength (psi)	Max Measured Debris Velocity V max (fps)	$\frac{V\ max}{V\ wall}$	$\frac{V\ max}{V\ spall}$	Damage
A1	1/2	25	1.5	23	6400	92	0.72	0.82	Breach
A2	1.4	3	0.75	23	5800	54	0.44	0.50	Spall
A3	1/4	3	0.75	23	1600	108	0.88	0.69	Breach
B1	1/4	2	0.75	1.8	5400	82	0.55	0.9	Breach
B2	1/4	2.5	0.75	4.5	5000	58	0.5	0.55	Breach
B3	1/4	2	0.75	15	5800	46	.47	0.51	Spall
C1	1/4	3	1.5	8	2600	48	0.64	1.23	Spall
C2	1/2	2.4	3	8	3300	55	0.73	1.5	Breach
D1	1/4	0.4	0.37	6.5	5000	17	0.26	0.14	No Spall
D2	1	25	1.5	6.5	4500	32	0.5	0.25	Spall

In order to investigate the effect of scaling on wall response and breakup, several series of tests were performed which were identical except for the scale factor. Test groups A (A1 and A2 only), C, and D in Table 1 are nearly identical except for the scale factor. The tests in Group B are very similar except for the amount of reinforcing steel. The amount of reinforcing steel in this group of tests increases from B1 to B3. Local response is described qualitatively in terms of breaching, spalling, etc. in Table 1 and quantitatively in terms of the maximum measured debris velocity. The wall debris was filmed with a high speed camera against a background grid so that debris velocities could be determined. The ratio of the maximum measured debris velocity to both the peak calculated spall velocity and the peak calculated wall velocity are shown for comparison in Table 1. The peak calculated wall velocity is the quotient of the specific impulse at the point on the wall directly across from the charge divided by the wall specific mass. In other words, it is the velocity of a local section of the wall across from the charge responding as an impulse plug. Reflections from the ground and off the test structure were included in the calculated impulse. The peak spall velocity is calculated assuming that the peak applied pressure is also the peak pressure reflected off the back face of the wall. In other words, it is calculated assuming no attenuation occurs in the wave as it propagates through the wall thickness. The peak local pressures on the test walls ranged from 25,000 psi (for groups A and D) to 8,000 psi (for group C.)

The amount of impulse which is absorbed or dissipated by the local wall response is "measured" by the ratio of the actual maximum debris velocities to the theoretical upper bounds on the maximum velocity described above which assume no material energy absorption or attenuation. The assumption is that the lower these ratios, the greater the amount of impulse which is "absorbed" by the wall response. Energy absorbed by the wall, as it is meant here, is local applied blast energy which is converted into strain energy during as the concrete responds to the local stress wave, or is dissipated into the less highly loaded areas or the wall, and is not converted into debris kinetic energy.

The ratios of the maximum measured debris velocity to theoretical upper bounds on this velocity (the spall velocity and the peak wall velocity) indicate that a considerable amount of the applied impulse (or applied energy) is "absorbed" within the locally loaded region since the ratios are often much less than 1.0. It is true that some locally applied energy is transmitted into the surrounding parts of the wall through the reinforcement as the wall responds locally. However, the films of the wall response showed that the maximum velocity debris left the walls very quickly, before substantial global response had occurred. Therefore, the reduction in measured maximum debris velocity from theoretical upper bound values must be due to energy absorption mechanisms within the locally loaded region. One possible strain absorbing mechanism in this region is the local stretching of the reinforcement which occurred during some tests. All tests with breaching also included significant local stretching of the steel reinforcement. However, Table 1 shows that the ratios of actual velocity to theoretical velocity increase (approach 1.0), rather than decrease, for the cases where breach occurs. If anything, the relative amount of "absorbed" local energy is inversely related to the amount of local stretching which occurs in the reinforcement. Therefore, the energy absorbing mechanism which is limiting the maximum debris velocity must be the material response of the concrete itself.

It is believed that the amount of absorbed energy or impulse is sensitive to the shape of the applied blast shock wave. This hypothesis is rooted in the observation that, as Table 1 shows, the maximum debris velocity does not "scale". That is, the maximum debris velocity does not vary according to replica scaling laws even though the wall dimensions and material properties, and the loading, were varied according to replica (and Hopkinson-Cranz) scaling laws. Numerous previous test series of explosively loaded structural components have shown this scaling approach gives scaled results for tests on ductile materials./3/,/4/ However, investigators have also noted that replica scaling does not work well for local response of brittle

materials to close-in explosive loading (such as reinforced concrete and masonry)./5/ The parameters within the locally loaded region of the wall which changed between the scaled tests were the shock loading duration and the wall thickness. The concrete strength and peak shock pressure did not change. Therefore, it was concluded that these two parameters which vary with the scale factor may be affecting the concrete response in a manner which does not conform to replica scaling laws. Also the observations that replica scaling laws predict the response of ductile materials much better than non-ductile materials implies that the concrete response, rather than the reinforcing steel response, is responsible for the energy absorption which is not scaling.

Some analytical studies also show that these two parameters, shock duration and wall thickness, can significantly affect the attenuation of a shock wave as it propagates through concrete. A recent one-dimensional finite element study compared the attenuation in peak pressure for two triangular shock waves with differing duration as they propagated through concrete./6/ The peak applied pressure for both waves was greater than the dynamic compression strength of concrete as is the case for close-in explosive loading. The calculated attenuation in the peak stress of the short duration wave was much greater than that of the long duration wave for the same distance of travel. The attenuation in both waves increased with the distance of travel. A small analytical study at SwRI using a one-dimensional hydrocode found the same relationship to be true. The study also showed that a very noticeable decrease in the impulse of the applied shock wave was apparent after several reflections of the wave within a twenty-four inch concrete wall. Both of these studies idealized concrete as a material with an infinite ultimate strain so that any energy absorption associated with fracture initiation or propagation was not considered. Also, since the studies were one-dimensional, no two-dimensional dissipation of the locally applied stress wave was considered.

An empirical approach was undertaken at SwRI to qualitatively relate the measured maximum debris velocity to important concrete material and loading properties based on the results from the test series. Figure 1 shows the data from Table 1 plotted in the form of the empirical relationship which was developed. The results from each test are plotted with the test designation symbol used in Table 1. The vertical axis is simply the inverse of the ratio of the measured maximum debris velocity to the peak wall velocity shown in Table 1. This empirical relationship shows the same trend as the theoretical studies discussed above. The reduction in debris velocity increases as the shock duration decreases and as the mass per unit area increases. The mass per unit area varies proportionally with thickness so that it is a measure of the wall thickness. In general, the relationship shown in Figure 1 indicates that as the charge overwhelms the wall (as i/m, as described in Figure 1, increases), as the loading duration increases (as the scaled standoff and/or the charge weight increases), and as the concrete strength decreases, the maximum debris velocity approaches its theoretical maximum value. It is important to note that this relationship is only fit through the limited data gathered in this test series.

It is interesting that when the reduction factor is based on the theoretical maximum debris velocity set equal to the peak wall velocity, rather than equal to the peak spall velocity, it provides a good empirical fit with the test data. This suggests that the very high applied pressures, which must cause local back face spalling, do not, in general, cause enough trapped impulse in the spalled debris to cause them to move faster than the wall itself. Evidently, the wall velocity propels the spalled debris for some distance until the wall slows down and the spalled debris continues with the peak wall velocity. It is true that, for some of the cases in Table 1, the peak spall velocity is nearly the same as the peak wall velocity. However, a plot similar to Figure 1 using a reduction factor based on the ratio of measured maximum debris velocity to peak spall velocity had far greater scatter than Figure 1.

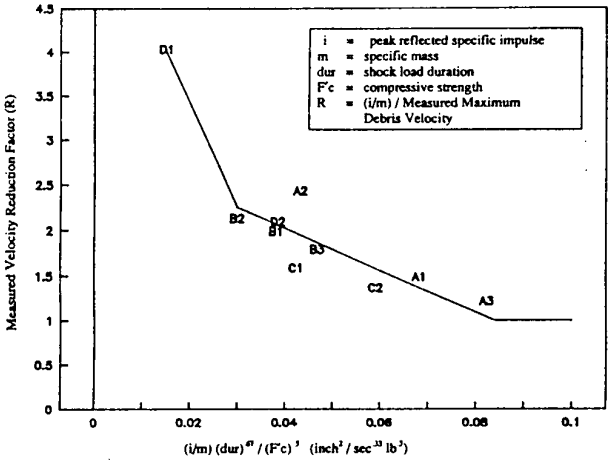

Figure 1. Reduction Factor for Maximum Debris Velocity of Concrete Walls with Close-in Loading

Films of the wall response show that the maximum velocity debris comes from a very local section of the wall opposite the charge. Therefore maximum debris velocity is a very local measure of the response of the locally loaded portion of the wall. Breach diameter and spall area, which provide a measure of wall response over a larger area of the locally loaded portion of the wall, were measured in the second test series. Therefore, this test program gives a more general measure of local wall response.

4.0 Discussion of Results from the Second Test Series

Table 2 shows the results from the second test series. In this test series four inch thick reinforced concrete walls, which were fixed along the two vertical supports and free top and bottom, were loaded with the following four types of charges; Type 1 - a lightly cased charge (simulating a MK-82 500 lb. bomb), Type 2 - a heavily cased charge (simulating a AN-MK1 1600 lb. bomb), and Types 3 and 4 - "equivalent" uncased charges which caused approximately the same impulse as the combined fragment and pressure loading from the lightly, and heavily, cased charges. Thus, Type 3 loading is comparable to Type 1 loading and Type 4 loading is comparable to Type 2 loading. The tests replicated loadings from the two bombs at a 2' standoff from a 17' by 23' by 17" thick wall in 1/4.3 scale. More specific information is available in Reference 2. The equivalent uncased charge weights were selected based on the results from a preliminary series of tests on the cased charges which measured fragment energy and side-on blast pressures at three standoffs. All charges were cylindrical and loaded the wall along their long axis except for a single case. This case was loading Type 5, which was identical to Type 4 loading, except that the charge was spherically shaped.

Three different levels of wall reinforcement were tested; 1) Type A - light reinforcement (a reinforcement ratio of 0.2% considering the reinforcing grids at both faces) spaced at 3" on center, 2) Type B - heavy reinforcement (a reinforcement ratio of 0.9%) spaced at 1.5" on center, and 3) Type C - fiber reinforced concrete (SIFCON) with very light reinforcement (a reinforcement ratio of 0.1%) spaced at 3" on center. All the walls had shear reinforcement (single leg stirrups) in proportion to the amount of flexural reinforcement. Table 2 shows three measures of local wall response - breach area, spall area, and maximum debris velocity. In all the tests the walls responded globally by hinging at the two vertical supports and at a hinge line at midspan. One measure of this global response is also shown - wall rotation. Since there are five types of loads (types 1 through 5) and three types of wall reinforcement (types A through C), the tests are designated in Table 2 by the appropriate numeral and letter.

Table 2. Panel Damage from Second Test Series

Test Designation	Breech Area (Wid. X Ht.)(in.)	Spall Area (Wid. X Ht.)(in.)	Maximum Debris Velocity (ft/sec)	Rotation (in.)
A1	20 x 14	32 x 25	n/a	5.75
A3	14 x 7	38 x 24	168	8.00
A2	28 x 12	32 x 21	336	5.25
A4	14 x 8	36 x 34	140	14.00
B1	21 x 18	30 x 35	210	1.75
B3	14 x 10	22 x 37	140	2.00
B2	28 x 24	35 x 41	201	1.75
B5	---	---	120	2.25
C1	---	Sm Raised Section	0	0.75
C3	---	Sm Raised Section	0	2.00
C2	12 x 8	24 x 13	288	.88
C4	---	---	155	1.25

The results of these tests show the relative importance of the concrete and the reinforcing steel in absorbing locally applied energy or impulse. A comparison of walls with identical loads and differing amounts of reinforcement (comparison of A1 to B1, A2 to B2, etc.) shows that the reinforcement has a minor effect on local wall response (the increased reinforcement causes a maximum of 10% to 15% reduction in the measures) and has a major effect on the one measure of global wall response (the increased reinforcement causes a 200% to 300% reduction in hinge rotation). A comparison of walls with identical loads but different "types" of concrete (wall types A or B compared to wall type C) shows that the change in concrete properties had a significant response on both local and global wall responses.

These results also show the effects of two loading parameters which were varied, charge geometry and the amount of charge casing. A comparison of the results from different geometries of the same bare charge weight applied to the walls A and B in Table 2 (case A4 compared to case B5) shows that the cylindrical charge causes more local and global damage than the spherical charge. It is interesting that wall breaching and spalling were much more severe for the case of cylindrical charge loading than for spherical charge loading, but the maximum debris velocities for these two cases differed by only 15%. Since the maximum velocity debris is usually emitted immediately across from the charge, it seems likely that very local wall response is not significantly affected by the change in charge geometry. However, the overall response within the locally loaded region is obviously greatly affected by the difference in charge shape. This may be caused by the cylindrical geometry placing more charge surface area closer to the wall and causing a more directional application of the charge energy into the wall. The rectangular shape (rather than square or circular) of the breach areas in Table 2 also shows the directionality of the impulse applied by the cylindrical charges. It is true that, for the above comparison, the cylindrical charge is applied against a less heavily reinforced wall than the spherical charge. However, a comparison of breach and spall diameters between cases A3 and B3, where only the wall type is different, shows that breach and spall diameter are not significantly affected by the difference in reinforcement between wall types A and B.

The results in Table 2 also show that combined air pressure and casing fragment loading causes more local and global damage than an air pressure loading alone with the same impulse. The presence or lack of casing affects the manner in which the charges apply impulse to the wall rather than the total amount of applied impulse as described above. The effects of the fragments and the blast pressure are applied essentially simultaneously and generate a much higher pressure, shorter duration loading than the loading caused by the equivalent base charge.

The important comparison is that for an equivalent impulse (tests A1 and A3, A2 and A4, B1 and B3) more damage results when the higher combined pressure generated by the simultaneous application of blast and impact loading occurs.

Another important observation is that, for very close-in loadings like those of Table 2 where i/m (see Figure 1 for definition of i and m) is very large, less global response is exhibited when the local damage is severe. This is probably due to several factors. First, when a large breach occurs early in time, less impulse is transferred structurally from the local section into the rest of the wall because a significant amount of the impulse is converted into debris kinetic energy. Secondly, the cased charges apply less impulse to the regions of the wall which are not locally loaded. The cased and uncased charges only apply similar impulses locally. All the impulse applied by the casing goes into the locally loaded portion of the wall while the comparable amount of explosive in the uncased charge applies some load to the entire wall. The importance of the first factor is probably much greater than that of the second.

5.0 Comparison of Results from the Two Test Series

The one measured wall response parameter which is common to both test series is the maximum debris velocity. The relationship plotted in Figure 1 shows the relationship between maximum debris velocity and wall loading and material properties based on the test results from the first test series. It indicates that the maximum debris velocity decreases with the duration of the applied shock wave for a given impulse. In the second test series the combined fragment and airblast loading causes the same impulse as the comparable uncased loading over a shorter duration as discussed above. Therefore, according to the relationship in Figure 1, the maximum debris velocities for the combined loadings should be less than those for the comparable uncased loadings. However, the combined loadings cause a much higher maximum debris velocity in identical walls.

The explanation for this is that Figure 1 only applies to airblast loading at scaled standoffs between 0.5 $ft/lb^{1/3}$ and 1.0 $ft/lb^{1/3}$. The maximum debris velocity for the one case of a wall loaded with a bare spherical charge in the second test series (B5) does fit the relationship in Figure 1. The fact that the relationship does not apply to the case of fragment loading indicates that fragments and airblast loading do not fail the wall in the same manner. This is probably caused by the much different shape of the stress wave which is induced in the walls by the two different loading cases. Pressure measurements from gages cast into the concrete during the second test series showed that the combined airblast and fragment loading caused peak concrete stresses up to four times greater than those measured for the equivalent uncased charges. The arrival times of the airblast and fragments may have coincided to cause this large peak pressure. Therefore, the high measured peak pressures and large measured breach areas for the cases of combined airblast and fragment loading may be dependent on the particular standoff used during all the tests in the test series. In any case, the reason the relationship for maximum debris velocity identified in the first test series does not apply to fragment loading may be the large increase in peak stress caused by the fragment loading. Spall, which is very sensitive to peak stress, was probably the mechanism causing the maximum debris velocities in cases where combined fragment and airblast loading occurred whereas this did not seem to be the case for the first test series where only airblast loading occurred. In the first test series the wall velocity seemed to control the maximum debris velocity as discussed previously.

6.0 Conclusions

The tests discussed in this paper show that the shock wave impulse and duration, the amount of fragments from the charge, and the wall concrete strength and thickness, can significantly influence local wall response. The amount of reinforcing steel does not seem to significantly influence the local wall responses measured in the test series. A empirical relationship based on most of these variables has been developed from the data for bare, spherical charges, and it implies trends that also have been observed in simplified analytical

studies. For close-in loading, the local concrete response is quite sensitive to charge shape and the amount of charge casing, and this may be due to the manner in which these variables can combine to cause very high peak pressures in the stress wave applied to the concrete. It is thought that general, quantitative relationships predicting local wall response must consider the propagation of the applied stress wave through the concrete and how the stress wave dissipates and is absorbed by the concrete response in order to obtain accurate results.

References

1. P.M. Bowles, C.J. Oswald, L.M. Vargas, and W.E. Baker, "Debris Hazard Evaluation, Task 3: Test Program and Predictive Model Refinement," Draft Final Report, prepared for Bernard Johnson Inc. under Mason & Hanger Silas Mason, Inc., Contract H0760103, U.S. Government Contract DE-AC04-76DP-00487, September 1990.

2. K.A. Marchand, L.M. Vargas, J.D. Nixon, "The Synergistic Effects of Combined Blast and Fragment Loadings", Interim Technical Report, SwRI Project 06-2821 prepared for AFESC, Tyndall Air Force Base, Florida, Contract No. FO 8635-89-0195, under Munitions Systems Division, Eglin AFB, Florida, June 1990.

3. W.E. Baker, P.S. Westine, F.T. Dodge, "Similarity Methods in Engineering Dynamics, Theory and Practice of Scale Modeling, 4th ed. Rochelle Park, New Jersey, Hayden Book Co, Inc., 1973.

4. W.E. Baker, P.A. Cox, P.S. Westine, J.J. Kulesz, R.A. Strehlow, "Explosion Hazards and Evaluation", Elsevier Scientific Publishing Co., Amsterdam, 1983.

5. C.J. Oswald, "Development of Predictive Methods from Test Data for Breakup of Building Components Subjected to Colse-in Explosive Loading," paper presented at the Twenty-fourth Department of Defense Explosives Safety Seminar, St. Louis, Missouri, August 28-30, 1990.

6. J.W. Tedesco, "Stress Wave Propagation in Layered Media," Final Report, Air Force Office of Scientific Research, Washington, D.C., August 1988.

Response of Reinforced Concrete Slabs to Close-In Explosive Loads.

by
James E. Tancreto
Naval Civil Engineering Laboratory
Port Hueneme, CA 93043

Dynamic blast load tests were conducted on twelve 2-way reinforced concrete slabs (7.5'x 7.5' spans) to verify their structural response to close-in blast loads and to verify design criteria for tensile membrane action at large deflections. The scaled standoff distance, Z, of the bare explosive charge (60 to 80 lbs of spherical C4) was between 0.65 to 1.10 $ft/lb^{1/3}$. Test specimen variables included main steel percentage (0.15% to 2.54%), type of shear reinforcement (lacing, stirrups, and no reinforcement), spacing of stirrup reinforcement (d/2 to d), slab thickness (4.5" to 10"), and l/d ratios (10 to 30).

This paper provides a complete test report on twelve tests (the test results for the first 6 slabs were presented at the 23rd DDESB seminar in August 1988), and compares test results to predicted response. Deflections up to 10" with support rotations up to 12.2^{o} were obtained. A few slabs were loaded to incipient breaching. Findings include the verification of new design criteria in the recently revised U.S. tri-service design manual "Structures to Resist the Effects of Accidental Explosions" (Army TM 5-1300, NAVFAC P-397, and AFM 88-22) and recommendations for less conservative criteria for stirrup spacing and breaching.